CAMBRIDGE ASTROPHYSICS SERIES 46

Lee Hartmann

Accretion Processes in Star Formation

Second Edition

CAMBRIDGE www.cambridge.org/9780521531993

ACCRETION PROCESSES IN STAR FORMATION

Second Edition

Our understanding of the formation of stars and planetary systems has changed greatly since the first edition of this book was published. This new edition has been thoroughly updated, and now includes material on molecular clouds, binaries, star clusters and the stellar initial mass function (IMF), disk evolution and planet formation.

This book provides a comprehensive picture of the formation of stars and planetary systems, from their beginnings in cold clouds of molecular gas to their emergence as new suns with planet-forming disks. At each stage gravity induces an inward accretion of mass, and this is a central theme for the book. The author brings together current observations, rigorous treatments of the relevant astrophysics, and 150 illustrations, to clarify the sequence of events in star and planet formation. It is a comprehensive account of the underlying physical processes of accretion for graduate students and researchers.

LEE HARTMANN is Professor of Astronomy at the University of Michigan and a Vice-President of the American Astronomical Society. He is an expert in the field of star formation and protoplanetary disk evolution.

Cambridge Astrophysics Series

Series editors:

Andrew King, Douglas Lin, Stephen Maran, Jim Pringle and Martin Ward

Title available in the series

10. Quasar Astronomy
by D. W. Weedman
18. Plasma Loops in the Solar Corona
by R. J. Bray, L. E. Cram, C. Durrant and R. E. Loughhead
19. Beams and Jets in Astrophysics
edited by P. A. Hughes
22. Gamma-ray Astronomy 2nd Edition
by P. V. Ramana Murthy and A. W. Wolfendale
24. Solar and Stellar Activity Cycles
by Peter R. Wilson
25. 3K: The Cosmic Microwave Background Radiation
by R. B. Partridge
26. X-ray Binaries
edited by Walter H. G. Lewin, Jan van Paradijs and Edward P. J. van den Heuvel
27. RR Lyrae Stars
by Horace A. Smith
28. Cataclysmic Variable Stars
by Brian Warner
29. The Magellanic Clouds
by Bengt E. Westerlund
30. Globular Cluster Systems
by Keith M. Ashman and Stephen E. Zepf
32. Accretion Processes in Star Formation
by Lee Hartmann
33. The Origin and Evolution of Planetary Nebulae
by Sun Kwok
34. Solar and Stellar Magnetic Activity
by C. J. Schrijver, C. Zwaan
35. The Galaxies of the Local Group
by Stanley van den Bergh
36. Stellar Rotation
by Jean-Louis Tassoul
37. Extreme Ultraviolet Astronomy
by Martin A. Barstow and Jay B. Holberg
38. Pulsar Astronomy 3rd Edition
by Andrew G. Lyne, Francis Graham-Smith
39. Compact Stellar X-ray Sources
edited by Walter Lewin, Michiel van der Klis
40. Evolutionary Processes in Binary and Multiple Stars
by Peter Eggleton
41. The Physics of the Cosmic Microwave Background
by Pavel D. Naselsky, Dmitry I. Novikov, Igor D. Novikov
42. Molecular Collisions in the Interstellar Medium 2nd Edition
by David Flower
43. Classical Novae 2nd Edition
edited by Michael Bode and Aneurin Evans
44. Ultraviolet and X-ray Spectroscopy of the Solar Atmosphere
by Kenneth J. H. Phillips, Uri Feldman and Enrico Landi
45. From Luminous Hot Stars to Starburst Galaxies
by Peter S. Conti, Paul Crowther, Claus Leitherer
46. Sunspots and Starspots
by John H. Thomas and Nigel O. Weiss
47. Accretion Processes in Star Formation 2nd Edition
Lee Hartmann

ACCRETION PROCESSES IN STAR FORMATION

SECOND EDITION

LEE HARTMANN

University of Michigan

CAMBRIDGE
UNIVERSITY PRESS

CAMBRIDGE UNIVERSITY PRESS
Cambridge, New York, Melbourne, Madrid, Cape Town, Singapore, São Paulo

Cambridge University Press
The Edinburgh Building, Cambridge CB2 8RU, UK
Published in the United States of America by Cambridge University Press, New York

www.cambridge.org
Information on this title: www.cambridge.org/9780521531993

First published in print format 2008

ISBN-13 978-0-511-46512-3 eBook (NetLibrary)

ISBN-13 978-0-521-53199-3 paperback

In memory of Alice Lewis Hartmann

Contents

Preface to the first edition

The topic of star and protoplanetary disk formation touches almost every area of astrophysics, from galaxy formation to the origin of the solar system. Our understanding of the early evolution of stars has advanced substantially in the last few years as a result of improved observational techniques, particularly in the infrared and radio spectral regions. Although many fundamental problems of star formation remain to be solved, so much has been learned in the last decade about pre-main-sequence accretion processes that an attempt to outline the emerging picture of low-mass star formation seems justified.

In this book I have tried to provide a discussion of accretion in early stellar evolution which can be used at a variety of levels: as an introduction to the subject for advanced graduate students; as a reference for researchers in star formation; and as an overview for scientists in other, related fields. The text assumes a basic familiarity with astronomical concepts and graduate-level physics, though I have made some effort to include some astronomical definitions and references to fundamental physical equations needed for my development. I have adopted a point of view close to that of my own research, which is generally near the interface between theory and observation, and so have tried to discuss basic physical concepts in relation to observational results. Many plausible and even aesthetically pleasing theories have been constructed which have failed to meet observational tests. Conversely, observations by themselves are not very meaningful unless (or until) they are placed into a physical context. I have also tried to include a substantial number of references, but I warn the reader that my selection is necessarily incomplete and probably biased in such a rapidly evolving subject; my intent is mainly to provide entry points into the literature for further research.

I especially hope to stir the interest of specialists in other fields where accretion disks are important. There are of course direct applications of pre-main-sequence disk physics and evolution to the study of planet formation, which has taken on added importance with the discovery of extrasolar planets. Beyond this, much of what we currently know about astrophysical disks is based on studies of accreting binary systems, and the accretion disks probably present in active galactic nuclei may have points of similarity to protostellar disks, in that they both exhibit powerful jets and dusty infalling envelopes. One hopes that the similarities among and differences between astrophysical accretion disks will yield further insight into accretion processes.

In writing this book I found myself continually revising material to take current important developments into account. Although this can be problematic, since very recent ideas or results may not have been fully tested, it is difficult to avoid incorporating new material in

such a rapidly developing field. Specialists will recognize that many new results have not been included, and I can only ask for their understanding in view of the rate at which the literature is expanding.

I have tried to express a point of view which is not always that of the "standard models" if the observations do not support these models. In discussing these matters I have tried to be evenhanded and to provide enough information for the reader to make his or her own judgements, although this can be difficult in addressing current areas of contention. Although some of the issues of today may be of transient importance, the conflict between opposing views seems to me to be part of the excitement of science, and the means by which we sharpen our understanding of astrophysical objects. I have also indulged in a little historical discussion to provide a faint hint of how science is actually done. In an area of rapidly evolving research such as star formation, texts such as the present one serve not simply to define the current state of knowledge, but to challenge readers to do better.

Cambridge, Massachusetts L.H.
October 6, 1997

Preface to the second edition

Initially it seemed like a good idea to revise this book, because so much has been learned about star and planet formation over the last ten years. It eventually became clear that it was a bad idea to revise this book, because so much has been learned about star and planet formation over the last ten years. By then I was halfway through and it was too late to back out.

I therefore beg the reader's indulgence for things I have left out or treated schematically. At some point in a project like this "the best is the enemy of the good", as Voltaire apparently said; just give up and send it off. Perhaps there is some value in having a treatment that does not try to cover everything in an enormous tome, but instead provides accessible points of departure. As was the case for the first version, I hope that this will be a useful reference for non-specialists as well as a starting point for researchers entering the field.

Ann Arbor, Michigan L.H.
February 27, 2008

Acknowledgments

This book could not have been written without the generous support and encouragement of many people and institutions. The first edition was written at the Smithsonian Astrophysical Observatory and at the Centro de Investigaciones de Astronomía, Mérida, Venezuela, where Gustavo Bruzual, Nuria Calvet, and Gladis Magris provided me with a very hospitable and supportive climate in which to do research. Most of the revisions and extensions of this second edition were written as a member of the Astronomy Department of the University of Michigan.

Many friends and colleagues helped me by reading and commenting upon the manuscript. Nuria Calvet, Neal Evans, Charles Gammie, Erik Gullbring, Phil Myers, Cesar Briceño, and James Muzerolle were especially helpful in reviewing the first edition, and Javier Ballesteros-Paredes, Nuria Calvet, Catherine Espaillat, Fabian Heitsch, John Tobin, and Zhaohuan Zhu provided important comments and corrections on this edition. Special thanks go to Catherine Espaillat, John Tobin, and Zhaohuan Zhu for building the index.

I also wish to thank Doug Lin for suggesting that I write this book, and the people at Cambridge University Press for their patience. As a practical matter, I also wish to cite the Astrophysics Data System's abstract service, without which I could not have finished this effort in my remaining lifetime.

Many people including Joao Alves, Phillippe André, Sean Andrews, Matthew Bate, Claude Bertout, Aaron Boley, Chris Burrows, Roger Chevalier, Laird Close, Tom Dame, James Di Francesco, Suzan Edwards, Neal Evans, Carol Grady, Stephane Guilloteau, Pat Hartigan, Lynne Hillenbrand, Jeremy Lim, Kevin Luhman, Michel Mayor, Phil Myers, Joan Najita, Debbie Padgett, Nimesh Patel, Bo Reipurth, Gerald H.M. Schieven, Glenn Schneider, Mike Simon, Karl Stapelfeldt, Jim Stone, Derek Ward-Thompson, Russel White, and Fred Vrba kindly gave permission to use their figures and/or provided copies. Figures 1.6, 1.7, 1.8, 1.10, 2.3, 2.4, 2.5, 2.6, 2.7, 2.10, 3.1, 3.2, 3.3, 4.3, 4.4, 5.2, 5.8, 5.10, 5.11, 5.12, 5.13, 5.14, 5.16, 5.19, 5.20, 6.5, 6.8, 7.8, 7.9, 8.2, 8.3, 8.5, 8.7, 8.9, 8.10, 8.11, 8.12, 8.16, 8.18, 8.19, 8.20, 9.3, 9.4, 9.10, 9.11, 9.12, 10.1, 10.2, 10.4, 10.5, 10.6, 10.7, 10.8, 10.12, 10.13, 10.14, 11.1, 11.2, 11.3, 11.5, 11.7, 11.10, and 12.3 are reproduced by permission of, and copyright by, the American Astronomical Society. Figures 3.7, 6.1, 6.9, 8.4, and 11.7 are reproduced by permission of, and copyright by, Astronomy and Astrophysics. Figure 6.3 is reproduced by permission of, and copyright by, Wiley-Blackwell. Figures 9.8, 9.9, and 9.10 are reproduced with permission from the Annual Review of Astronomy and Astrophysics, Vol. 34, copyright 1996, by Annual Reviews Inc.

1

Overview

Much of what we presently know or surmise about the physical processes involved in star formation is derived from the detailed study of a few nearby molecular cloud "nurseries". Stars in the solar neighborhood are formed from the gravitationally induced collapse of cold molecular gas. Typical molecular gas clouds must contract by a factor of a million in linear dimensions to form a star. Because of this dramatic (and rapid) reduction in size, any small initial rotation of the star-forming cloud is enormously magnified by conservation of angular momentum during collapse. In this way a modestly rotating gas cloud produces a rapidly rotating object – a disk – in addition to a small, stellar core at the end of gravitational collapse. Probably most of the material of a typical star is accreted through its disk, with a small amount left behind to form planetary systems.

Advances in observational techniques spanning the electromagnetic spectrum have been essential in developing our present understanding of star formation. The launch of the *Infrared Astronomy Satellite* (*IRAS*) in 1983 led to the recognition that dusty disks are common around young stars. The *ISO* infrared satellite provided detailed mid-infrared spectra of many bright disks. The *Spitzer Space Telescope*, the latest in this line of infrared observatories, has now detected mid-infrared disk emission in very large samples of stars spanning a wide range of ages. During the same period, radio-wavelength interferometry developed to a state where it could provide high spatial resolution images of cold dust and gas in outer disks, along with estimates of disk masses. The forthcoming Atacama Large Millimeter Array (ALMA) is expected to produce a major advance in imaging at mm and sub-mm wavelengths. Optical studies using large ground-based telescopes have produced better estimates of stellar masses and ages for large samples of stars, as well as providing new insights into the accretion flows of young stars. The *Hubble Space Telescope* (*HST*) has provided remarkable images of disks in a wide variety of environments, and even has produced important constraints on accretion rates from ultraviolet observations.

Concurrently, our theoretical insight into star formation processes has improved, driven in important ways by the remarkably rapid increase in computing power. The analytic and steady-state models of the previous generation, which served the field so well for many years, are now being supplemented by time-dependent numerical simulations of the complex physical processes involved in star formation and protoplanetary disk evolution.

While a coherent picture of star formation is emerging, many mysteries remain. We do not yet have a conclusive theory explaining the stellar initial mass function, though many ideas have been advanced. Disk accretion is clearly an important part of the star (and planet) formation story; although much progress has been made lately in understanding

angular momentum transport mechanisms which drive accretion, theories do not yet have predictive power. The powerful, highly collimated outflowing jets observed from young stars were totally unexpected, and additional surprises are probably yet in store. Finally, we now know that extrasolar planetary systems can differ dramatically from our own, providing new challenges to theories of planet formation.

This book attempts to survey our present understanding of the accretion processes involved in star formation, with an extension to a few aspects relevant to planet formation. The present chapter contains a brief outline of the processes discussed in more detail in the rest of the book.

1.1 Molecular clouds

Young stars are not distributed at random in the Milky Way, but are generally found close to or within clouds of relatively dense molecular gas. The Milky Way is a spiral galaxy, probably with a central bar (e.g., Blitz & Spergel 1991; López-Corredoira *et al.* 2007). Most of the gas in the galaxy is distributed near the plane of its disk with most of its molecular gas of the galaxy concentrated to inner regions in the "molecular ring" about 3–5 kpc distant from the center. The most luminous star-forming regions of the galaxy are found in the molecular ring. The surface density of gas near the solar circle is lower than that of the molecular ring; locally, most of the gas is in atomic hydrogen rather than in molecular clouds (e.g., Dame 1993). Our detailed understanding of star formation, which arises from studies of nearby regions, is therefore somewhat biased toward low-density regions with relatively low star formation rates; such regions are probably not typical of the sites where most stars in the galaxy form. While exploring the formation of stars in very dense and active environments is probably best done by studying external galaxies, the solar neighborhood provides by far the most stringent tests of general star formation theory.

The sizes and masses of molecular clouds in the Milky Way span a large range, from giant star-forming molecular cloud complexes of masses $\sim 10^6\ M_\odot$ and sizes $\sim$100 pc to clouds of $\lesssim 10^1\ M_\odot$ and $\lesssim$1 pc and smaller. Three of the best-studied (and closest) molecular cloud complexes forming stars are: Taurus, at a distance of $\sim$140 pc, with a mass $\sim 10^4\ M_\odot$ extending over a region 30 pc or more (Ungerechts & Thaddeus 1987; Figure 1.1); Ophiuchus, at a distance similar to that of Taurus, and with a similar mass and overall size, but with much denser concentrations of gas (DeGeus *et al.* 1990; Loren *et al.* 1990); and the Orion complex, at a distance of $\sim$450 pc, with a mass $\sim 10^5\ M_\odot$ spread over a region $\sim$100 pc, and also possessing very dense star-forming regions (Bally *et al.* 1987; Genzel & Stutzski 1989). An overview of galactic molecular clouds can be found in Dame *et al.* (2001), and references therein.

Most of the gas in a molecular cloud is in H_2, but this species is observable only with great difficulty; other molecules, especially CO, are used as tracers of the dense gas. Figure 1.1 shows a map of ^{12}CO emission from the Taurus molecular cloud complex, with the young stellar population superimposed. The ^{12}CO ground state rotational spectral line at $\sim$2.7 mm becomes optically thick at modest column densities, thus highlighting relatively low-density material. Rarer isotopes of CO, such as ^{13}CO and C^{18}O, or other, less abundant, species are used to probe the densest regions of clouds, which occupy relatively small volumes. The temperatures of the molecular gas are generally in the range 10–20 K, unless the material is quite close to luminous stars.

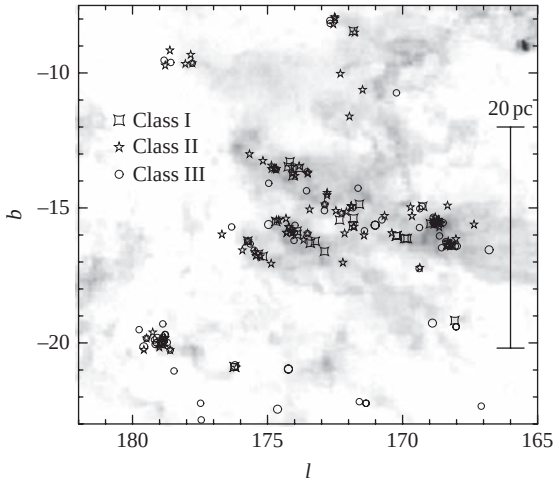

Fig. 1.1. The Taurus–Auriga molecular cloud complex. Grayscale shows integrated ^{12}CO emission, taken from Megeath *et al.* (2001). The positions of known young stars (ages ∼1 Myr) have been superimposed. The pre-main-sequence stars (Classes II and III) are generally clustered near regions of high gas column density; the likely protostars (Class I) are found only in high density regions (e.g., Onishi *et al.* 1998).

The formation of a star requires that gravity overcome the resisting forces of thermal gas pressure, turbulent motions, and magnetic fields. It is therefore not surprising that stars form in dense, cold molecular cloud regions which exhibit reduced turbulent motions. The substantial dust extinction in many molecular cloud complexes (Cernicharo 1991) may play an important role in condensing protostellar gas clouds (e.g., McKee 1989) by shielding the radiative heating by luminous stars and therefore lowering the internal temperature. Dust absorption of external photoionizing radiation fields also strongly reduces the level of ionization in the interiors of molecular clouds. For some time it was thought that this reduced ionization played an important role in star formation by enabling gas to diffuse across magnetic field lines, reducing the magnetic forces which can counteract gravity (Shu *et al.* 1987); however, it now seems more likely that protostellar clouds require little if any magnetic flux loss to allow gravitational collapse.

Molecular clouds have complex spatial structure (Falgarone 1996; Falgarone *et al.* 1998); line-of-sight motions often exceed the local sound speed by as much as an order of magnitude. Supersonic "turbulence" is an important component of the energy balance of molecular clouds (e.g., Larson 1981). The gas from which stars form is highly filamentary in many places. The origin of this structure is not well understood at present, though dynamical and thermal instabilities plus gravitational collapse probably play roles.

Substructure within molecular clouds is clearly related to the formation of stars. Older observational estimates suggested that the number of molecular cloud clumps with mass M_c is $dN_c/dM_c \propto M_c^{-1.5}$ (Blitz 1991). This cloud mass spectrum differs strongly from the initial mass function (IMF) of stars (see next section). More recent studies (Bontemps *et al.* 2001; see also Ward-Thompson *et al.* 2007) have suggested a closer correspondence between the densest and smallest clumps – called "cores" – and the stellar IMF. Comparisons between cloud and stellar masses are made difficult by uncertainties in the defining boundaries of actual star-forming clouds (Williams *et al.* 1994).

Molecular cloud "cores" are condensations in molecular gas with densities $\gtrsim 10^3\,\mathrm{cm}^{-2}$, and are thought to be the predecessors of low-mass stars. Cores are typically found from radio-frequency surveys of spectral lines of NH_3 and other molecules which are excited only at relatively high gas densities. In Taurus, cloud cores found in NH_3 have densities $\gtrsim 10^4\,\mathrm{cm}^{-3}$ and are typically ~ 0.1 pc in size (Myers & Benson 1983; Myers & Goodman 1988a,b). At such high densities, the expected gravitational collapse timescales are only a few hundred thousand years, so that star formation could proceed quite rapidly from these cores. This expectation is borne out by observations which indicate that almost half of these cloud cores in Taurus have heavily extincted (presumably recently formed) stars within their boundaries (Beichman *et al.* 1986).

Bok globules, visually opaque clouds found by their extinction of background stars, were long ago proposed as sites of low-mass star formation (Bok & Reilly 1947). The globules vary in properties, but typically have masses of a few times that of the Sun, with radii of order a few tenths of a pc in size (Clemens & Barvainis 1988). Many of these globules have young stars within them (Yun & Clemens 1990) and some may be undergoing collapse (Wang *et al.* 1995). Molecular cloud cores may be essentially equivalent to dense Bok globules, but have not been catalogued as such because they are superimposed upon regions of generally large visual extinction, and so are difficult to detect optically.

1.2 The IMF, clusters, and binaries

The frequency with which stars of a given mass are produced is called the stellar initial mass function (IMF). The general form of the galactic IMF is that of a broad distribution peaking near $\sim 0.3\,M_\odot$ (Miller & Scalo 1979; Scalo 1986; Kroupa *et al.* 1993; Chabrier 2003). At high masses, the number of stars N of mass M in logarithmic bins appears to follow a nearly power-law shape, with $\xi = d\log N/d\log M \approx -1.35$, the so-called "Salpeter slope". The form of the IMF at low masses is more uncertain, but it is clear that there is a turnover in ξ at masses below about $1\,M_\odot$. Studies of the brown dwarf or substellar mass regime (usually taken to be $0.08\,M_\odot \lesssim M_* \lesssim 0.01\,M_\odot$, bodies which will never fuse hydrogen in their interiors) suggest that the IMF *may* be relatively flat down to planetary masses ($\sim 0.01\,M_\odot$, or about 10 M(Jupiter)).

It is difficult to tell whether the IMF is truly universal, given the difficulty of obtaining sufficient statistics on the high-mass end without studying distant clusters where counts of the much more numerous low-mass population are incomplete due to faintness, crowding, etc. One unresolved issue is whether high-mass stars can form in low-density environments, though it seems unlikely, given the necessity of accreting a large mass from a finite volume. What *is* clear is that low-mass stars are formed in all environments (e.g., Herbig & Terndrup 1986). At present there are many explanations of the IMF; as yet none are wholly satisfying or convincing.

Completely isolated star formation seems to be the exception rather than the rule, though perhaps as much as 30% of all stars currently form in "distributed" rather than clustered environments, if the Orion A cloud is any indication (Figure 1.2; S.T. Megeath, personal communication). In the solar neighborhood, about 10% of recently formed stars are found in clusters of $\sim 10^3$ stars or larger, i.e., open clusters (which can remain gravitationally bound for timescales of order 100 Myr; Adams & Myers 2001). Most nearby stars are probably formed in clusters of 10^2–10^3 members (e.g., Lada & Lada 2003), although much larger clusters may be found near the galactic center. A small fraction of stars appear to be formed

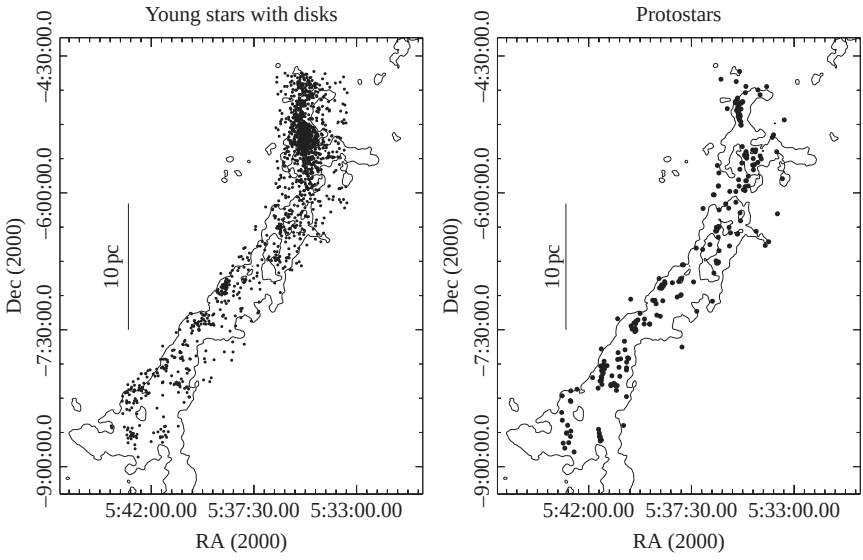

Fig. 1.2. Young stars in the Orion A molecular cloud (shown by contours outlining the main molecular emission) identified via their infrared excesses detected with the *Spitzer Space Telescope*. The left panel shows stars with disk emission, while the right panel shows likely protostars (§§1.4, 1.5). Most of the stars in the cloud reside in the clustered northern region (the Orion Nebula Cluster), but a significant fraction are "distributed" along the cloud. From Megeath *et al.* 2008 (in preparation).

in low-density environments like Taurus. Even in Taurus, the stars are not randomly distributed, but most are situated in extended filaments (Figure 1.1); such regions constitute the closest approximation to isolated star formation.

Most young solar-type stars are members of binary or multiple stellar systems (Ghez *et al.* 1993; Leinert *et al.* 1993; Reipurth & Zinnecker 1993; Mathieu 1994; Simon *et al.* 1995). The multiplicity of solar-type (F–G main sequence) field stars, the sample for which we have the best statistics, is roughly 57:38:4:1 single:binary:triple:quadruple (Duquennoy & Mayor 1991). The distribution of binary orbits is roughly Gaussian, with a median semi-major axis of order 30 AU; this result may be affected by tidal disruption of wide binaries with separations $\gtrsim$1000 AU over time. The mass ratios in multiple systems are not well constrained, but are roughly consistent with the companion being drawn randomly from the IMF. Observations of low-density star-forming regions suggest that, within certain separations, the frequency of binaries may be higher than in the field (Simon *et al.* 1995), while studies of dense clustered regions like the Orion Nebula Cluster suggest a smaller binary fraction (Köhler *et al.* 2006). Binary frequencies among very low-mass stars may be considerably lower (e.g., Ahmic *et al.* 2007).

1.3 Young stars

Young low-mass stars were originally recognized as a subset of optical emission-line objects, typically exhibiting strong hydrogen (Balmer α or Hα) line emission at $6563\,\text{Å} = 0.6563\,\mu\text{m}$. The youth of these stars was suggested by their spatial correlation with reflection nebulae and dark clouds (Joy 1945), which could be remnant natal material,

and by their concentration near associations of high-mass stars which must necessarily be young (Ambartsumian 1947). This grouping is now understood as the result of star formation in molecular clouds; stars of ages $\lesssim 10^6$ yr cannot travel far from their formation sites with typical small velocities ($\lesssim$1–2 km s^{-1}) relative to the molecular gas (Herbig 1977a; Jones & Herbig 1979; Hartmann *et al.* 1986).

Objective prism surveys for stars with strong emission lines (mostly Hα) led to the first extensive catalogs of young stars. With the advent of infrared techniques, many additional objects (heavily obscured by dust at optical wavelengths) were found. Some of the densest known clusters of newly formed stars were only detected once infrared arrays were employed to image molecular cloud complexes (Lada *et al.* 1991). X-ray emission has also been used to identify many additional young objects, especially stars which do not exhibit strong excess infrared or optical emission (e.g., Montmerle *et al.* 1983; Feigelson *et al.* 1987; Walter *et al.* 1988).

Stellar luminosities and effective temperatures, or equivalently positions in the Hertzsprung–Russell (HR) diagram, provide important clues to the evolutionary states of young stars. Effective temperatures are determined from spectroscopic measurements of optical (and now infrared) absorption line strengths; usually, spectral line ratios are used to determine the stellar spectral type and luminosity class, which can be associated with the stellar surface effective temperature and surface gravity. Stellar luminosities are determined from observed optical and infrared fluxes corrected for the dimming and reddening effects of intervening dust. Using these methods, many surveys of the properties of young stellar populations have been made (e.g., the seminal work of Cohen & Kuhi (1979)).

Many low-mass stars associated with molecular clouds lie above the hydrogen-fusion main-sequence in the HR diagram (Figure 1.3); their low masses M_* and moderately large radii R_* indicate central temperatures too low to fuse hydrogen into helium (since the internal temperatures tend to scale as M_*/R_*). Deuterium fusion can occur at lower temperatures than hydrogen fusion; but because the deuterium abundance is relatively low, the luminosities of typical young stars can be powered by deuterium fusion for only a million years or less. Without fusion energy release, the young star must contract, generating gravitational potential energy to replace the energy lost by the radiation of the stellar photosphere. This contraction corresponds to moving downward in the HR diagram (Figure 1.3), and thus the positions of young stars in the HR diagram can be used to estimate ages. (Stars with masses $\gtrsim 0.8\,M_\odot$ eventually develop radiative cores, at which point they contract in radius but increase slowly in luminosity, moving mostly right to left in the HR diagram, as shown in Figure 1.3.) Contraction stops when stars arrive on the main sequence, at which point hydrogen fusion energy release replaces the energy radiated into space by the stellar photosphere. Thus the ages of stars near the "zero-age main sequence" (ZAMS) are difficult to determine, especially when uncertainties in stellar luminosities due to distance and dust extinction errors are taken into account.

The lowest-mass stars, the so-called "brown dwarfs" (usually taken to have masses between 0.08 and 0.01 $M_\odot$), exhibit slightly different behavior. By definition, brown dwarfs never fuse hydrogen in their interiors; thus, apart from a brief energy release from deuterium fusion, they can only replace the energy radiated from their surfaces by contracting, as with the higher-mass stars. Instead of halting contraction with the onset of hydrogen fusion, internal degeneracy pressure eventually slows brown dwarf contraction, with a final cooling at a roughly constant radius, of the order of the size of Jupiter. Evolutionary tracks for

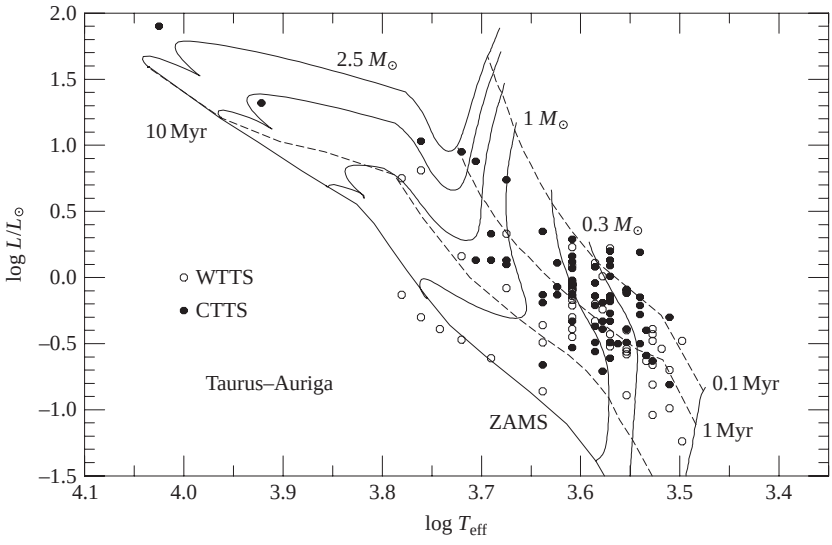

Fig. 1.3. HR diagram positions of young stars lying within the Taurus–Auriga molecular cloud complex (Figure 1.1). For comparison, theoretical evolutionary tracks for pre-main-sequence stars of masses 2.5, 2.0, 1.5, 1.0, 0.5, 0.3, and 0.1 $M_\odot$ are shown. The dashed lines are isochrones for ages of 10^5, 10^6, and 10^7 yr (0.1, 1, and 10 Myr), with the hydrogen-fusion "zero-age main sequence" or ZAMS shown as the lowest line running from upper left to lower right. The open circles refer to weak-emission T Tauri stars (WTTS; see text), while the filled circles denote the positions of the classical T Tauri stars (CTTS). Stellar properties taken from Kenyon and Hartmann (1995); evolutionary tracks are from D'Antona and Mazzitelli (1994).

these objects are particularly uncertain due to the difficulty in treating the complex molecular opacities in the atmospheres of these objects; representative calculations are shown in Figure 1.4. The rapid cooling of brown dwarfs means that it is much easier to detect them when they are very young and proportionately much brighter.

Low-mass ($M \lesssim 2\ M_\odot$), pre-main-sequence stars, having stellar spectral types F–M (corresponding to surface effective temperatures ∼7000–3000 K), are called "T Tauri" stars (Joy 1945; Herbig 1962; Bertout 1989); higher-mass ∼2–10 $M_\odot$ pre-main-sequence stars are labeled "Herbig Ae/Be" stars (Herbig 1960) to distinguish them from other types of emission-line A-B stars (effective temperatures ∼8000–30 000 K) which are presumably more evolved. (The mass ranges are not exact because the classification depends upon the optical stellar spectral type or effective temperature, which can vary substantially as a ∼2 $M_\odot$ star evolves; see Figure 1.3.) The rapidity with which massive stars evolve makes study of their pre-main-sequence evolution more difficult. Stars with masses $>2\ M_\odot$ are typically found near the ZAMS (Figure 1.3; Hillenbrand *et al.* 1992); age estimates for these objects are especially uncertain.

The old systematic catalog of pre-main-sequence stars, that of Herbig and Bell (1988 = HBC), is very useful for the best-studied pre-main-sequence stars, but it is now highly incomplete given the vastly increased number of young stars since discovered. Many

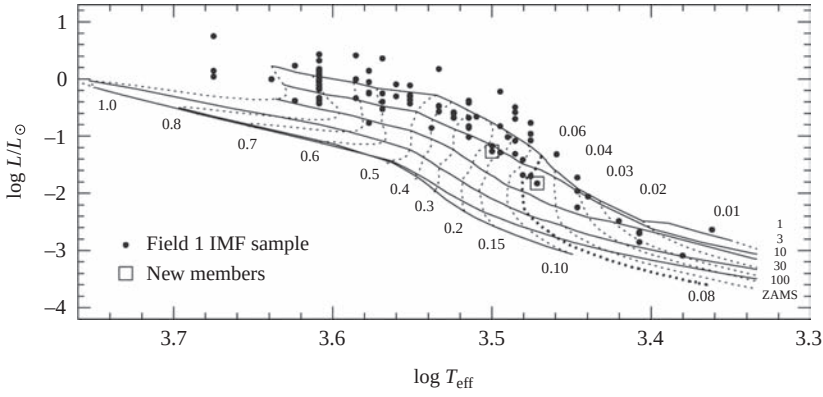

Fig. 1.4. A recent placement of the low-mass population of Taurus on an HR diagram, with evolutionary tracks from Baraffe *et al.* (2002). Modified from Luhman (2004).

young stars have only been detected as infrared sources, so their effective temperatures, masses, and often luminosities are poorly known.

The term "young stellar objects", or YSOs (Strom 1972), was coined partly in the recognition that the appearance of young stars may be strongly affected or altered by their circumstellar material. It also serves as a relatively neutral term to identify objects whose underlying nature – T Tauri star, Herbig Ae/Be star, protostar (§1.3), pre-main-sequence accretion disk (§1.4) – is not yet understood. In this book the term YSO is used sparingly, since it does not discriminate clearly between objects which can be intrinsically quite different.

The T Tauri stars originally were identified as late-type stars with strong emission lines and irregular light variations associated with dark or bright nebulosities (see Bertout 1989 for a discussion). Since that time, the term "T Tauri star" has come to be synonymous with low-mass pre-main-sequence stars, whether or not they are associated with nebulosity or have strong emission lines. Most of the variable stars first identified as T Tauri stars are currently called "strong-emission" or "classical" T Tauri stars (CTTS), to distinguish them from "weak-emission" pre-main-sequence stars (WTTS). The distinction between strong and weak emission stars is usually made on the basis of Hα emission. The original definition assigned the WTTS label to stars with Hα equivalent widths less than 10 Å but we now know that the boundary between weak- and strong-emission stars depends upon spectral type (White & Basri 2003). It appears that the excess emission of many WTTS can be explained in terms of enhanced solar-type magnetic activity (Walter *et al.* 1988), while the extreme levels of excess emission at optical and infrared wavelengths of many CTTS require an external energy source. *Accretion* from a circumstellar disk appears to supply the energy needed for the non-photospheric emission of CTTS (§1.7).

High-mass stars are by definition young, since they exhaust their hydrogen rapidly via fusion. It appears that early B and O stars start their lives near or on the zero-age main sequence, although it is difficult to say more because of the rapidity with which these stars form and would pass through any pre-main-sequence phase. In addition, there are severe observational difficulties in studying very young massive stars because they are generally

heavily extincted. Moreover, the scarcity of massive stars results in the need to study these objects at much larger distances than those of the nearest low-mass star-forming regions. These problems have made it difficult to tell whether the accretion disk paradigm of low-mass stars applies to high-mass stars as well. Recent interferometric studies have yielded indications of the presence of disks around some young massive stars (Shepherd *et al.* 2001; Patel *et al.* 2005; Reid *et al.* 2007), as well as bipolar outflows suggesting collimated flows from accretion disks (e.g., Shepherd & Churchwell 1996).

1.4 Protostars

Dramatic improvements in infrared detector technology over the last three decades have enabled astronomers to find YSOs hidden by dust absorption at optical wavelengths. The measurement of far-infrared emission, which can penetrate through the most opaque dust clouds, was enormously enhanced by the launch of the *IRAS*. In orbit, *IRAS* could be more effectively shielded from the intense thermal emission of the Earth than was possible with ground-based telescopes, and it was actively cooled to liquid He temperatures. *IRAS* produced a survey of the sky at wavelengths of 12, 25, 60, and 100 μm with enough sensitivity to detect many pre-main-sequence stars; the launch of the *ISO* satellite produced further advances in characterizing infrared excess objects.

One of the major results of *IRAS* was the discovery of infrared sources with luminosities typical of T Tauri stars, but with spectral energy distributions peaking at 60–100 μm (Beichman *et al.* 1986). Most of these objects are now generally identified as protostars, with dusty envelopes that absorb energy from the central star at short wavelengths and re-emit this energy at far-infrared wavelengths, where the envelope is sufficiently transparent for the radiation to escape (Figure 1.5). The protostellar phase of star formation is thought to involve the free-fall collapse of dusty material to stellar dimensions, resulting in very large extinctions toward the central energy source (e.g., Larson 1969a,b; Appenzeller & Tscharnuter 1974). Theoretical models of the dust emission from protostellar envelopes in gravitational free-fall can reproduce the observed infrared emission of these heavily extincted young stellar objects (Adams *et al.* 1987 = ALS; Butner *et al.* 1991; Kenyon *et al.* 1993). So far it has not been easy to demonstrate that these dusty envelopes are actually falling in, although continuing efforts to observe small velocity shifts in radio-wavelength emission lines have provided additional support for the collapse model (Walker *et al.* 1986; Hayashi *et al.* 1993; Zhou *et al.* 1993; Zhou & Evans 1994; Mardones *et al.* 1997; Di Francesco *et al.* 2001).

IRAS surveys of Taurus (Beichman *et al.* 1986; Cohen *et al.* 1989; Kenyon *et al.* 1990, 1994; Beichman *et al.* 1992) indicate that the number of protostellar sources is $\approx$10% of the total pre-main-sequence population. This suggests that the time for protostellar collapse is similarly about 10% of the age of the pre-main-sequence stars in the region. The resulting estimate of $\sim 10^5$ yr for the protostellar infall phase is roughly consistent with the expected timescale of collapse for the formation of a typical low-mass T Tauri star (Larson 1969a,b; Shu 1977). Forthcoming results on embedded stellar populations from the *Spitzer Space Telescope* should add to these results, but are unlikely to result in major revisions.

The behavior of high-mass protostars is much less clear, due in part to the observational problems mentioned in the previous section. Nevertheless, observations of the so-called "hot cores" (e.g., Kurtz *et al.* 2000) show that massive stars are formed in very dense clouds.

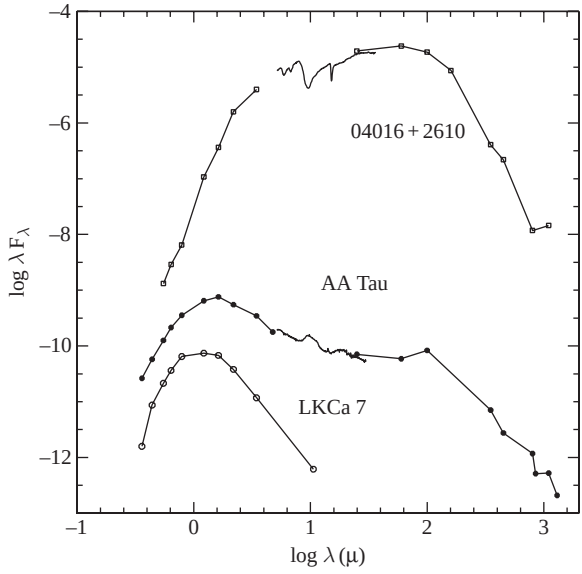

Fig. 1.5. Spectral energy distributions (SEDs) of three young stellar objects which typify the infrared classification system. The vertical axis is the flux at the Earth in arbitrary units. The Class I object IRAS 04016 + 2610 is a protostar hidden at optical wavelengths by its dusty infalling envelope; the dust absorbs the radiation from the central regions and re-emits it in the far-infrared. The CTTS or Class II object AA Tau is optically visible, but exhibits long-wavelength dust emission generally attributed to a circumstellar disk (see text). The WTTS or Class III object LkCa 7 does not exhibit detectable dust emission; its SED is nearly that of a single temperature blackbody, and is typical of the photospheric emission of low-mass pre-main-sequence stars. Note the 10 μm silicate feature, which is in absorption in the Class I object and in emission in the Class II star AA Tau (and the 15 μm CO_2 ice feature absorption in 04016 + 2610). Data from Kenyon and Hartmann (1995) and IRS Spitzer spectra from Furlan *et al.* (2006).

1.5 Long-wavelength emission: dusty envelopes and disks

YSOs are frequently classified in the literature based on the shape of the emitted spectrum from near- to far-infrared spectral regions, which emphasizes the properties of circumstellar dust (Lada & Wilking 1984; Lada 1987). The emitted spectrum is usually discussed in terms of the "spectral energy distribution" or SED, which is a frequently used shorthand for either the flux distribution λF_λ observed at the Earth, or the luminosity distribution λL_λ, depending upon the context.*

The infrared classification scheme depends upon the spectral index s of the emitted flux F of the object, $\nu F_\nu = \lambda F_\lambda \propto \lambda^s$, typically measured between $\lambda \sim 2\,\mu$m and ∼50–100 μm. Class I sources correspond to objects with $s > 0$, i.e., the SED rises toward long wavelengths. An example of such a Class I source is the Taurus YSO IRAS 04016 + 2610 (shown in Figure 1.5); this heavily extincted object is one of the protostar candidates discussed in the previous section. The SEDs of such objects can be explained with emission from dusty infalling envelopes.

* In this book we follow the typical astronomical convention of using cgs units. Thus, the flux λF_λ has units of erg cm^{-2} s^{-1}, while the luminosity λL_λ has units of erg s^{-1}.

Class II sources have $-4/3 \lesssim s \lesssim 0$, which is frequently identified as the spectrum produced by a dusty, optically thick circumstellar disk. A typical example of a Class II source is the T Tauri star AA Tau, shown in Figure 1.5. The CTTS AA Tau exhibits much more infrared radiation than the WTTS Taurus object LkCa 7 (Figure 1.5); the latter is a Class III source, because it has the Rayleigh–Jeans distribution $s \sim -3$ expected at long wavelengths for a star without infrared excess emission from circumstellar dust.

Since this classification scheme was introduced, a further modification has been suggested by the introduction of the "Class 0" sources (André *et al.* 1993). Class 0 sources are very red objects, with large amounts of sub-mm emission relative to their total luminosities. Evidence is accumulating that the Class 0 sources have especially large amounts of gas and dust in their immediate environs, as might be expected if they represent a generally earlier phase of protostellar evolution than Class I sources (e.g., Bontemps *et al.* 1996). It is difficult to plot a typical Class 0 SED on Figure 1.5 because the spectral information available is usually incomplete at shorter wavelengths.

ALS suggested that the infrared classification scheme can be interpreted in terms of an evolutionary sequence. Protostars are Class I (or 0) sources, surrounded by (roughly spherical) dusty infalling envelopes. The angular momentum of the infalling material causes it to pile up in a rotating, flattened disk. After envelope infall has ceased, the dusty disk can still produce substantial infrared emission, as it can be heated externally by radiation from the central star and internally by viscous dissipation; however, because the disk is flat, it does not intercept most lines of sight to the central star, and thus the latter is optically visible. This combination of large amounts of dust in a disk geometry produces a Class II source. Eventually, the disk dust is dissipated or coagulated, and one is left with only detectable emission from the central star – a Class III object.

We may divide the Class III objects into additional categories due to the vast increase in infrared sensitivity over the years. In addition to the so-called "debris-disk systems", stars with small amounts of optically thin dust (presumably similar in origin to our zodiacal dust), we now recognize a small group of stars with weak or absent near-infrared emission, but strong mid- to far-infrared emission – the "transitional disks". Both debris and transitional disks provide evidence of inner disk clearing, presumably by large gravitating bodies – companion stars or giant planets.

Surveys of the Taurus molecular cloud suggest that roughly half of the pre-main-sequence stars have dusty circumstellar disks at ages of 1–3 Myr (Strom, K.M. *et al.* 1989; Beckwith *et al.* 1990; Skrutskie *et al.* 1990; Strom, S.E. *et al.* 1993). There is some indication that binary T Tauri stars exhibit less long-wavelength dust emission than single stars, which may be the result of disk disruption by the tidal forces in the binary system (Jensen *et al.* 1994, 1996; Osterloh & Beckwith 1995). The frequency of stars with optically thick disks decreases rapidly over typical timescales of a few Myr.

In principle, the optically thin dust emission observed at wavelengths $\sim$1 mm can be used to calculate the dust mass surrounding Class II sources. In practice, masses estimated in this way are uncertain for several reasons, but principally because the dust opacity is not well understood. This is particularly a problem for circumstellar disks, where appreciable evolution of dust grain sizes is expected to occur (e.g., Weidenschilling & Cuzzi 1993). Current estimates (Beckwith *et al.* 1990; Osterloh & Beckwith 1995; Andrews & Williams 2005, 2007) suggest typical disk masses within an order of magnitude of $10^{-2}\,M_\odot$. This is comparable to the so-called "minimum mass solar nebula", i.e., the total mass of solar

composition material that would be needed to produce the observed (condensed) material in the planets. However, it is likely that these are underestimates, and that in many cases T Tauri disks are up to an order of magnitude more massive than initial estimates.

1.6 Imaging of disks

We now have a remarkably diverse set of images of circumstellar disks around young stars, some even within infalling envelopes during earliest stages of star formation. At the moment, extant images tend to emphasize structure at a few tens of AU to a thousand AU because of limited resolution. This situation is likely to change dramatically soon with the development of the ALMA.

Figure 1.6 shows optical images of young stars in the Orion Nebula taken with *HST*. Objects like the one in the left-hand panel were detected as very compact H II (ionized hydrogen) regions in optical and radio-wavelength observations. It was recognized that the most luminous central star of the Trapezium cluster, the O7 star θ^1 C Ori, could photoevaporate disks around T Tauri stars, accounting for the otherwise strange, tiny compact HII emission (Churchwell *et al.* 1987 and references therein). The lifetimes required by the source statistics, coupled with studies of the rate of evaporation of material (e.g., McCullough *et al.* 1995), suggest that these objects are gaseous disks with masses of order 10^{-1}–$10^{-2}\ M_\odot$ (Churchwell *et al.* 1987). The *HST* images confirm this picture in detail (O'Dell *et al.* 1993; O'Dell & Wen 1994); quantitative theory now exists which can account for the shape and emissivity of the material boiling off these disks around young low-mass stars in the Orion Nebula Cluster (Johnstone *et al.* 1998; Richling & Yorke 2000; Henney *et al.* 2002).

While the most spectacular structure of the ionized disks, sometimes called proplyds, is that of the ionized gas freed from the disk, in some cases one can also see the disk itself as a dark silhouette against the bright background (Figure 1.6, left). In addition, many objects in the Orion Nebula Cluster have been detected which are too far away from θ^1C to be heated and ionized, but can be seen in silhouette against the bright nebular background (McCaughrean & O'Dell 1996; Figure 1.6, right). The morphologies of these absorption structures are very suggestive of circumstellar disks, with faint, low-mass T Tauri stars detected at their centers.

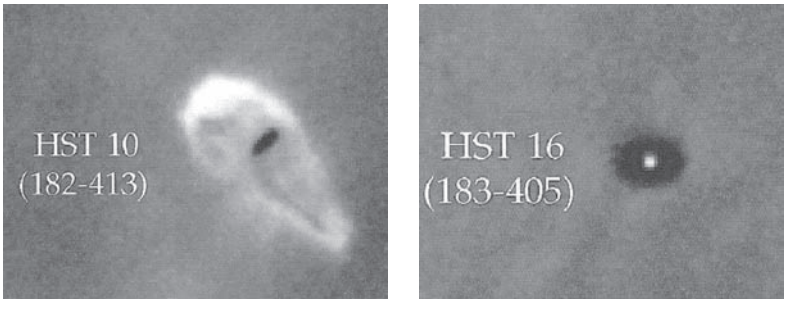

Fig. 1.6. (Left) A so-called "proplyd" in the Orion Nebula region, consisting of a dusty disk seen nearly edge-on in absorption against the bright nebular background, with an arc of ionized material created by evaporation of the disk by the hot central O7 star, and swept back around by the wind of the O star (see text). (Right) A shadow disk in the Orion Nebula, seen more face-on than the system on the left, with the central T Tauri star visible as a bright spot. From Bally *et al.* (1998).

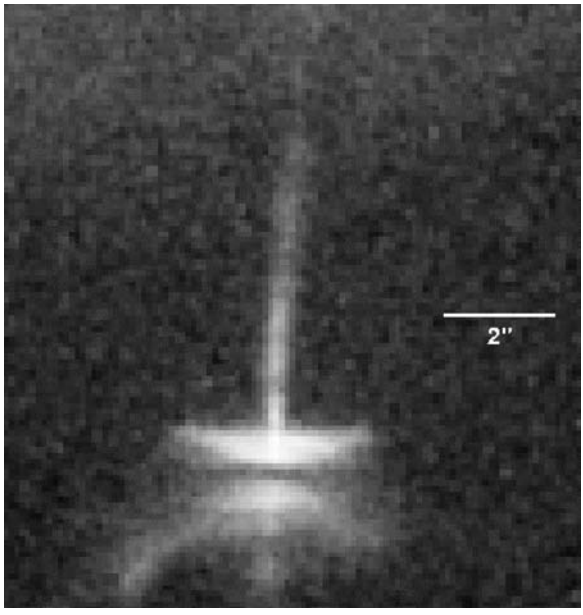

Fig. 1.7. *HST* optical image of the YSO HH 30. The double-concave reflection nebula is produced by light from a hidden central star scattering off the upper surfaces of a dusty disk seen nearly edge-on (see text), with some residual infalling material accounting for the outer scattering nebula. The dust absorption in the disk plane (central lane between the upper and the lower reflection nebulae) completely obscures the central star. The roughly vertical linear structure is a bipolar high-velocity jet, which is observed in shock-excited emission lines. At the distance of Taurus (140 pc), 2 arcsec corresponds to 280 AU. From Burrows *et al.* (1996).

Another way of improving the contrast between the disk and the illuminating central object is to use the disk to occult the central star. This should be a rare occurrence, but *HST* observations of the YSO HH 30 show such an edge-on disk (Burrows *et al.* 1996). As shown in Figure 1.7, in addition to a dark lane representing the disk shadow, the scattering surfaces of the disk are curved away from the disk midplane. Originally this structure was attributed to the disk "flaring" expected on general principles (Kenyon & Hartmann 1987), but more recent images suggest much flatter images of pure disk systems seen edge-on. The most probable explanation of the extreme flaring seen in HH 30 is that there is a remnant infalling envelope which is being evacuated by a wind (e.g., Wood *et al.* 1998). This example illustrates some of the complications involved in interpreting images of young objects. The *HST* image also shows a highly collimated, rapidly moving bipolar jet, which appears to be a common feature of low-mass star formation (e.g., Edwards *et al.* 1993); the jet is probably the central high-density, high-energy portion of a much more widely diverging outflow.

Dramatic progress in radio-wavelength interferometry has led to the detection of many dense flattened structures of dust and molecular gas around young stars (Koerner *et al.* 1993; Lay *et al.* 1994; Dutrey *et al.* 1996; Koerner & Sargent 1995; Koerner *et al.* 1995; Mundy *et al.* 1996). Perhaps most importantly, studies in molecules such as CO provide clear indications of Keplerian rotation around central stars, as well as more detailed constraints on disk structure (Dutrey *et al.* 1996) and in some cases the disk motion can be analyzed to "weigh" the central star (Simon *et al.* 2000).

1.7 Disk accretion

Relatively small amounts of dust in a T Tauri disk can efficiently absorb a substantial amount of light from the central star, and reradiate this energy effectively at infrared wavelengths. These so-called "reprocessing" or "irradiated" disks emit long-wavelength radiation simply as a result of heating by the T Tauri star, without any internal energy source. Models of irradiated disks can account for the infrared emission of many CTTS (Kenyon & Hartmann 1987; Chiang & Goldreich 1997; D'Alessio *et al.* 1999, 2001). However, some disks are much more luminous than can be explained by the amount of irradiation from the central star, and require their own energy source. Many of these T Tauri stars also exhibit strong excess optical and ultraviolet continuum emission along with broad emission lines (Bertout *et al.* 1988; Bertout 1989; Figure 1.8). This optical and ultraviolet continuum emission is dominated by hydrogen bound-free and free-free emission at temperatures $\sim 10^4$ K.

Accretion of mass from a circumstellar disk is responsible for the excess emission of the CTTS (Lynden-Bell & Pringle 1974). The dissipation of accretion energy in the disk enhances the infrared emission, while the infall of material onto the central star produces the high-temperature optical and ultraviolet continuum emission and strong optical emission lines. This conjecture is supported by the strong correlation between infrared and ultraviolet excess emission (Hartigan *et al.* 1990; Edwards 1995); YSOs with substantial near-infrared excess emission (Class II sources) generally show strong optical emission lines and continuum (i.e., are CTTS); stars without near-infrared excess emission (Class III sources) do not show strong optical excess emission (are WTTS).

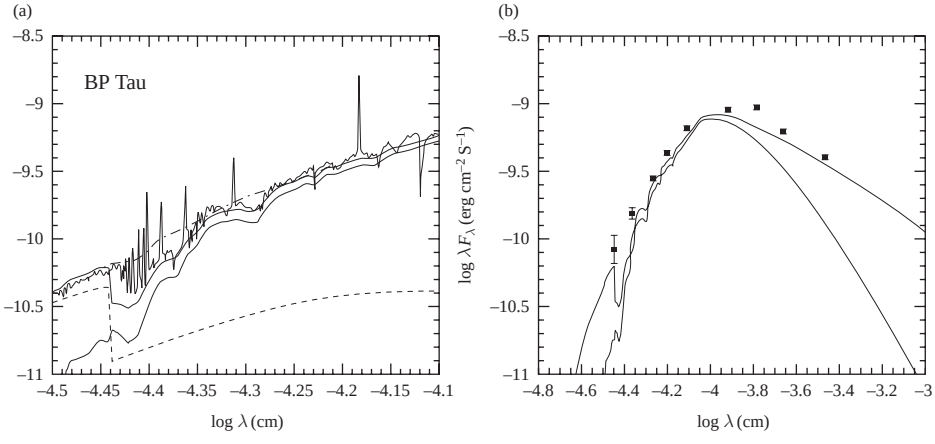

Fig. 1.8. Spectrum of the CTTS BP Tau, showing evidence for excess optical and infrared emission. The left-hand panel shows the observed spectrum (upper heavy line), which is made up of several components; a hot continuum (dashed line), the stellar photospheric emission (second curve from bottom), plus Balmer, Ca II, etc. emission lines. The right-hand panel illustrates broad-band photometry (points) of BP Tau, which indicates both optical and infrared excess emission above that expected for a normal stellar photosphere (bottom curve). The upper curve is a model including hot continuum emission and infrared disk emission. Reproduced from Basri and Bertout (1989).

In some cases the optical and ultraviolet excess continuum emission far exceeds that of the stellar photosphere. This applies to roughly 5–10% of the well-studied T Tauri stars in the Taurus molecular cloud region (Kenyon & Hartmann 1995). In these objects, the accretion energy release is the dominant luminosity source of the system. Our understanding of the evolutionary states of strong-emission CTTS is poor, because the strong hot continuum emission extends to optical wavelengths, making it very difficult to determine reliable positions of these stars in the HR diagram.

Originally, it was thought that the high-temperature emission was produced in a shear boundary layer between the rapidly rotating disk and the more slowly rotating star (Lynden-Bell & Pringle 1974). It now appears more likely that the inner disk is disrupted by the magnetic field of the central T Tauri star; this results in magnetospheric accretion, in which the disk material is channeled along magnetic field lines to crash into the star (Camenzind 1990; Königl 1991; Ostriker & Shu 1995). The continuum emission is thought to arise from the shock at the base of the magnetospheric accretion column, near the stellar surface, while the emission lines arise in the fast-moving, essentially freely infalling magnetospheric gas, which is heated to temperatures $\sim$8000 K (Calvet & Hartmann 1992; Hartmann *et al.* 1994a). The large velocity widths of the strong emission lines in CTTS apparently result from the central star's gravitational acceleration of the infalling gas lifted from the Keplerian disk. Mass accretion rates needed to explain the observed ultraviolet, optical, and infrared emission excesses of CTTS range from $\sim 10^{-9}$ to $\lesssim 10^{-6}\ M_\odot\ \mathrm{yr}^{-1}$ (Basri & Bertout 1989; Hartigan *et al.* 1991; Valenti *et al.* 1993; Hartigan *et al.* 1995; Gullbring *et al.* 1998).

In some pre-main-sequence objects the mass accretion rate increases by orders of magnitude for short periods of time (Herbig 1977b). During these "FU Orionis" outbursts, the accretion disk becomes 2–3 orders of magnitude more luminous than the central star (Hartmann & Kenyon 1996; Figure 1.9). Event statistics suggest that the average low-mass

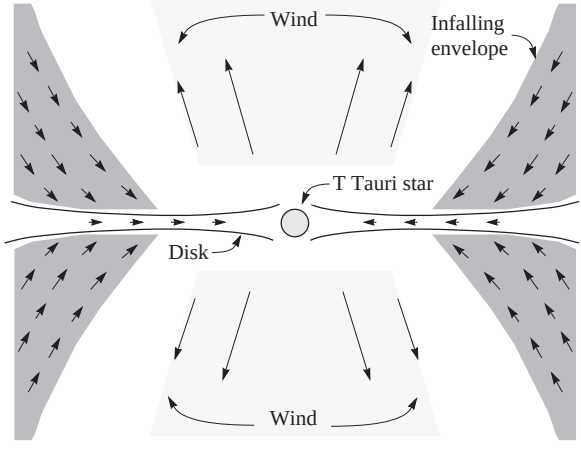

Fig. 1.9. Schematic picture of stellar accretion. Mass is fed into a circumstellar disk by the collapsing protostellar envelope with an infall rate $\sim 10^{-5}\ M_\odot\ \mathrm{yr}^{-1}$. The disk generally accretes at $\sim 10^{-7}\ M_\odot\ \mathrm{yr}^{-1}$ during the T Tauri phase, but during FU Ori outbursts this accretion rate may increase to $\sim 10^{-4}\ M_\odot\ \mathrm{yr}^{-1}$. The disk ejects roughly 1–10% of the accreted material in a high-velocity wind.

star may undergo several FU Ori outbursts during its evolution, during which perhaps 10% or more of the final stellar mass is accreted.

Disk accretion appears to produce the powerful highly collimated jets which commonly emanate from young stellar objects (Figures 1.7 and 1.9). These jets can have velocities of several hundreds of $\mathrm{km\,s^{-1}}$, with collimation angles of only a few degrees, and involve mass ejection at rates as much as 10% of the accretion rate (Dopita *et al.* 1982; Mundt & Fried 1983; Lada 1985; Bally & Devine 1994; Hartigan *et al.* 1994; Hartigan *et al.* 1995; Bally *et al.* 2007). Such jets are only observed when there is some evidence for accretion disks; WTTS do not exhibit jets or massive outflows. The collimation of the jets is probably the result of magnetic acceleration from the surface of the Keplerian disk (Pudritz & Norman 1983; Heyvaerts & Norman 1989), although the details of this process are uncertain (Königl 1989; Pelletier & Pudritz 1992; Lovelace *et al.* 1993; Shu *et al.* 1994; Najita & Shu 1994).

1.8 Disks and planet formation

Not all young stars exhibit strong infrared (and longer wavelength) excess emission from dusty disks. As mentioned above, only about half of the young stars with ages of 1 Myr or less exhibit optically thick disk emission. However, by an age of order 10 Myr, very few stars still exhibit such strong disk emission, at a frequency of ∼10% or less. Something dramatic happens to the disk during this interval.

Many older systems, with ages ∼10–100 Myr or more, are now known to possess tenuous, optically thin dust disks, with very little gas content. Figure 1.10 shows images of two of these "debris-disk" or "Vega-like" systems. Because the timescales for small dust ejection due to radiation pressure or inward drift due to the Poynting–Robertson effect in the absence of significant gas drag are very short, it is thought that the dust in these systems needs to be replenished continually, probably by the collisions of larger bodies. Most of the known debris-disk systems are intermediate-mass or solar-mass stars, due to sensitivity limits, though lower-mass nearby systems have been detected, such as the nearby K dwarf ϵ Eri (e.g., Greaves *et al.* 1998).

Figure 1.11 compares the SED of Herbig Ae/Be star of the Taurus–Auriga molecular complex, AB Aur, with that of the Vega-like or debris-disk system with the largest infrared

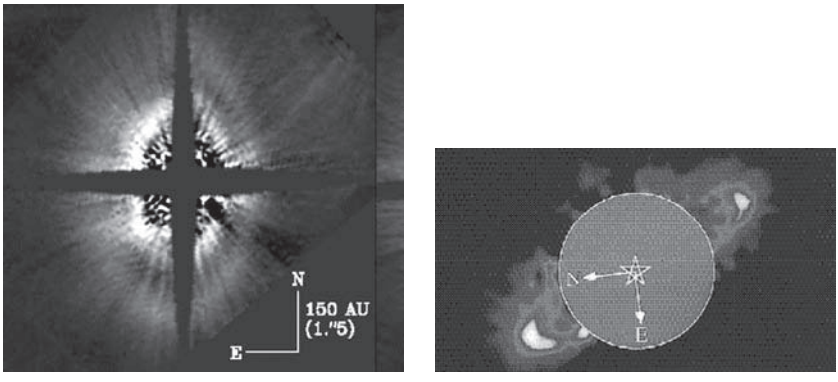

Fig. 1.10. NICMOS/HST coronographic imaging of scattered light from debris disks around HD 141569 (left) and HR 4796 (right) (from Schneider *et al.* 1999; Weinberger *et al.* 1999).

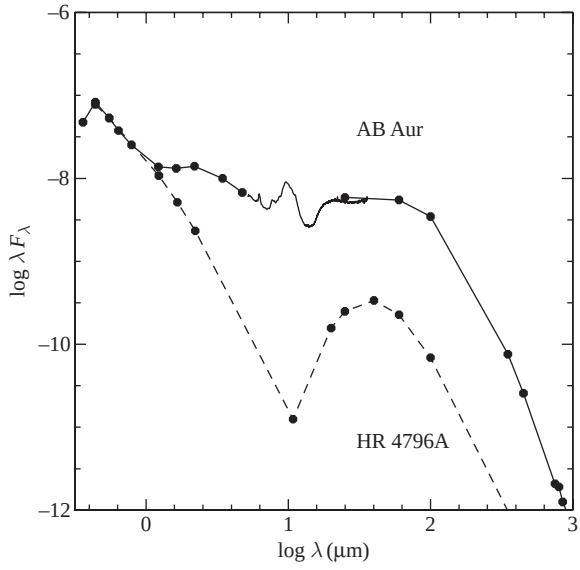

Fig. 1.11. Comparison of the SEDs (normalized to the stellar photospheres) of AB Aur, a Herbig Ae/Be star (intermediate-mass equivalent of a T Tauri star), with HR 4796, a debris-disk system – that is, a system whose dust is thought to be the product of collisions between large bodies rather than being "primordial" dust. HR 4796 (currently) has the largest known ratio of infrared excess luminosity to stellar luminosity (most other debris-disk systems have an order of magnitude or more fainter infrared excesses). The absence of any excess emission at wavelengths $\lesssim 10\,\mu$m above the stellar photosphere indicates a strong evacuation of matter at radii less than 70 AU (see Figure 1.10 for imaging confirmation). The detailed mid-infrared spectrum of AB Aur is taken from *Spitzer Space Telescope* spectra (Furlan *et al.* 2006).

excess to date, HR 4796A. Both stars have spectral types of A0, but slightly different masses, as AB Aur lies just above the main sequence; the age of AB Aur is roughly 2 Myr, while the age of HR 4796A is about 8 Myr (Stauffer *et al.* 1995). The dramatic reduction in dust emission in HR 4796A is evident, especially at short wavelengths, where the infrared excess is very low if not absent. This lack of near-infrared dust emission indicates that there is a "hole" or relative decrease of the dust content of the inner disk of HR 4796; this feature of the SED is consistent with the image (Figure 1.10), which shows a ring structure. It is plausible that this structure indicates the presence of massive bodies (planets) which shepherd this ring, just as small moons shepherd the rings of Saturn.

What happens to disk gas, which originally constituted the bulk of the mass, is not clear. In principle, extreme-ultraviolet (EUV; wavelengths shortward of the Lyman limit at 912 Å) and far-ultraviolet (FUV; typically ∼1000–2000 Å) emission can heat and drive off outer disk material (e.g., Hollenbach *et al.* 2000; Alexander *et al.* 2006a,b). This process seems to be occuring in the central regions of the Orion Nebula, due to the intense radiation field of O7 star θ^1 Ori C. However, it is not at all clear that most stars are formed near an O star which can rapidly ablate their gas disks, as in the Orion Nebula Cluster; and this might be a good thing, as the rate of disk destruction might be so rapid (Henney *et al.* 2002) as to make it difficult for planets to form. Over longer timescales, energetic radiation, particularly EUV

radiation from stellar chromospheres, may be responsible for at least some of the elimination of disk gas in low-mass stars. The other alternative is accretion, either into the central star or into massive planets.

1.9 A picture of star and planet formation

The (mostly observational) findings outlined above have led to the following scenario for low-mass stellar accretion (Figure 1.12). Cold, dark molecular gas fragments by some unknown process into self-gravitating cloudlets of a few solar masses. These cloudlets or cores evolve into a critical configuration where they cannot support themselves against gravity, and nearly collapse at free-fall. Because of the rapidity of this collapse, any angular momentum transfer must be relatively inefficient, and any initial rotation of the cloud results in collapse to a multiple star system, or to a disk, or both. Since it seems rather unlikely that

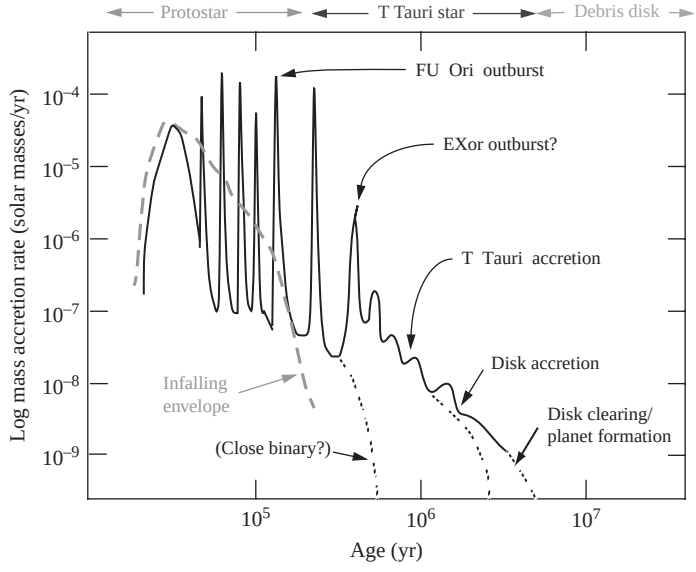

Fig. 1.12. Outline of estimated mass accretion rates during the formation of a typical low-mass (solar-type) star. In relatively cold, isolated regions of star formation, the collapse of the parent molecular cloud of a $\sim 1\,M_\odot$ star is thought to take approximately 0.1–0.2 Myr. The result of this infall is to build up a stellar core and a circumstellar disk. The disk accretes steadily onto the central star at low rates, punctuated by very brief FU Ori outbursts of rapid disk accretion. It is thought that the FU Ori events occur preferentially during the earliest phases, in which mass is still falling onto the disk from the protostellar envelope, thus replenishing the accreted material; during the outburst, as much as $10^{-2}\,M_\odot$ may be dumped onto the central star ($\dot{M} \sim 10^{-4}\,M_\odot\,\mathrm{yr}^{-1}$ for $t \sim 100\,\mathrm{yr}$). Well after the protostellar envelope has stopped adding mass to the circumstellar disk, the disk continues to accrete and evolve during the T Tauri phase. The figure indicates that disk accretion slowly decays and eventually ceases over periods of a few million years, but this timescale is uncertain, varying substantially from star to star. Many of the current WTTS probably finished accreting from their disks in timescales $\lesssim 1$ Myr, perhaps because of close binaries which disrupt inner disks, although this seems unlikely to explain all young diskless systems. The eventual cessation of accretion in many systems may signal the formation of giant planets, which can open up gaps in the disk, accreting material otherwise destined for the central star.

the initial angular momentum will be so small as to permit collapse directly to stellar dimensions, given the large difference in size between a star and its parent gas cloud, it is plausible to suppose that most of the mass initially lands on the disk(s). Disks are engines for the outward transfer of angular momentum, allowing the accretion of mass to the central star.

Disk accretion rates during early stellar evolution vary widely for typical low-mass stars. During or immediately after the protostellar phase of infall to the disk (Figure 1.12), disk masses are likely to be relatively large, and such disks could be subject to gravitational instabilities which would cause rapid accretion. The rate at which infall adds mass to the disk generally may not be the same as the natural accretion rate of the disk; a mismatch between these rates could explain the FU Ori outbursts, if matter piles up in the disk until it can be discharged in rapid accretion events.

Eventually, infall to the disk stops. At this point the disk slowly evolves and eventually becomes depleted in mass, due to accretion into the central star, and due to processes such as evaporation of gas by high-energy stellar photons. Coagulation or accretion of disk material into planets probably represent the final stages in disk clearing.

These stages of infall and disk accretion are schematically indicated in Figure 1.12. It is difficult to set a precise boundary between the protostar and the T Tauri phases, because infall from the envelope may not cease instantaneously. During the main infall phase the central protostar may accrete from its disk at generally similar rates as T Tauri stars – which suggests that if the protostar could be observed directly, it might appear quite similar to a T Tauri star, an idea supported by recent infrared spectra (Muzerolle *et al.* 1998b; Doppmann *et al.* 2005; White *et al.* 2007). Moreover, if one were to try to define a protostar as an object which has not finished accreting its final mass, then T Tauri stars would also be protostars. Definitions based on the relative amount of mass remaining in the disk/envelope vs. the amount of mass already in the stellar core are difficult to implement given measurement uncertainties. Therefore, in this book the term "protostar" is used to refer to phases where a substantial (in the sense of extinction) infalling envelope surrounds the central star (i.e., a Class 0 or Class I source).

There is reason to believe that the FU Ori outbursts are generally concentrated to early phases of evolution, while infall is still occuring, but the frequency and duration of such outbursts are poorly understood; and little is currently known about the so-called "EXor" outbursts of T Tauri stars (Herbig 1977b). Similarly, there is a wide range of accretion rates among T Tauri stars. The disk accretion rates at later times in Figure 1.12 are meant only to refer to the CTTS; the WTTS may have accreted their disks much faster, assuming that they initially did possess disks.

A further uncertainty in this picture is whether protostellar disks fragment gravitationally. It appears increasingly likely that the collapse of the protostellar cloud to a flattened rotating structure frequently results in fragmentation into binary or multiple stellar systems, which then may or may not remain gravitationally bound due to gravitational interactions between the (protostellar) fragments (e.g., Reipurth & Clarke 2001; Bate *et al.* 2002). The above picture of collapse and disk evolution then needs to be modified to account for more complex disk structure, such as truncation of the disks surrounding individual (proto)stars.

The formation of planets is thought to occur near the end of disk evolution. The most likely mechanism for initiating planet formation is the agglomeration of dust particles in the disk. Small dust is expected to eventually settle toward the disk midplane and accumulate into larger bodies. Although small (micron-sized) dust particles are likely to stick together

quite effectively, it is not clear that collisions can account for growth up to km-sized bodies, at which point the gravity of the bodies can take over in enhancing accretional growth. The timescales for planetary growth are uncertain, and are likely to vary substantially even among stars of the same mass; most probably they lie in the range of a few to 10 Myr, corresponding to the timescales for the disappearance of extensive dusty disks. Studies of extinct radioactivities in meteoritic material suggest timescales of similar magnitude for the main phase of solar system formation (Podosek & Cassen 1994). More precisely, it is thought that formation of giant planets, with substantial gas accretion, occurs over several Myr, while terrestrial planet formation is slower, taking tens of Myr.

The subject of planet formation has been revolutionized by the discovery of extrasolar planets, many of which are quite massive (Jupiter mass or greater) on very close orbits, even down to orbital periods of a few days. The presence of massive planets at radii unlikely to contain sufficient mass in the original disk, plus other indications such as large eccentricity orbits, strongly indicate that many of these planets have migrated to their present positions from larger distances. In addition to migration due to many-body interactions, gravitational interactions with their natal disks can cause planets to move inward for substantial distances. Depending upon the detailed physics of these interactions and the poorly known properties of protoplanetary disks, it is easy to develop scenarios in which most planetary embryos and/or giant planets end up in the central star; whether these scenarios are realistic or other effects prevent such planetary accretion is currently one of the major problems in planet formation.

This picture of stellar and planetary accretion is mostly the result of extensive empirical studies over the last two decades, supported by theoretical calculations incorporating expanded numerical simulations. The following chapters explore the physical arguments and observational evidence underlying this overview.

2

Beginnings: molecular clouds

Star formation in our galaxy at present occurs in dense, cold clouds of molecular gas. The efficiency of star formation is generally low. While there are localized regions of high efficiency which produce bound star clusters, typical star formation efficiencies of nearby molecular cloud complexes are a few percent by mass. For a long time it was thought that this low efficiency of converting gas to stars was due to the slowing of gravitational collapse by magnetic fields. However, most nearby molecular clouds of significant mass harbor young stars, with typical ages of a few Myr, indicating that star formation is relatively rapid and that (at least local) molecular clouds are not long-lived, casting doubt on the importance of magnetic fields. The low efficiency of star formation is not due to the slowing gravitational collapse but to the disruption of molecular gas by stellar energy input, particularly from massive stars, which disperse clouds before all the mass can collapse.

The processes by which large molecular clouds fragment into molecular cloud cores, the precursors of protostars, are not yet well understood. Lower-density gas must be concentrated into dense regions, often filamentary in structure, with low(er) "turbulent"* motions. Numerical simulations show that supersonic turbulence can create protostellar cores with the aid of rapid cooling and even thermal instability, which then gravitationally collapse. It seems increasingly likely that this turbulence is injected as part of the cloud formation process, with stellar energy input providing some additional motions before blowing clouds apart. A better understanding of molecular cloud structure and its origin is needed to develop a quantitative theory of star formation and the origin of the stellar IMF.

2.1 Large-scale properties of molecular clouds

The Milky Way is a barred spiral galaxy, although many details of the structure are hard to discern because of our disadvantaged position in its midst. Both stars and gas tend to collect in spiral arms, making them particularly important (though probably not exclusive) sites of molecular clouds forming stars. The theory of spiral density waves in galaxies (see discussion in Binney & Tremaine 1987) predicts that the gaseous material should pass through a spiral shock, and the subsequent compression is a likely starting point for cloud formation.

The molecular gas in the galaxy is strongly confined to the rotational plane, and concentrated in the inner regions. Much of the galaxy's molecular gas is concentrated in a feature known as the "molecular ring", situated at about 3–5 kpc from the center. Both the atomic and the molecular gas mass fall off with increasing radius beyond the molecular ring,

* "Turbulence" is used to refer to observations of large velocity widths of spectral lines, which may or may not be the same as the turbulence seen in numerical simulations.

with a more rapid decline in the molecular material. Near the solar circle, where we have the most detailed information about star formation, most of the gas appears to be atomic, with perhaps four times as much atomic as molecular gas in the interstellar medium (ISM) (Dame 1993).

Molecular clouds exhibit supersonic "turbulent" motions; that is, the spectral lines of CO and other low-density tracers show velocity widths much exceeding the sound speed, in some cases with complex velocity structure. The kinetic energy in these motions is typically comparable to the gravitational potential energy, as described in some of the correlations known as "Larson's laws" (Larson 1981). While such motions in principle can help prevent gravitational collapse, complex motions on smaller scales often invoked ("turbulence") tend to dissipate rapidly (e.g., Stone *et al.* 1998); thus, such motions would need to be regenerated continuously to maintain cloud support to support the cloud against gravity. Regeneration is needed if clouds are long-lived; but as discussed in §2.2, many clouds are short-lived, at least in the solar neighborhood. In addition, energy input from massive stars in the form of supernovae and stellar winds are much more likely to blow their natal cloud apart rather than keep it in some kind of quasi-equilibrium state (see, e.g., Blitz & Shu 1980). This stellar energy input can also help explain why the entire $10^9\ M_\odot$ of molecular gas in the Galaxy does not all collapse rapidly under gravity and form stars at a rate one or two orders of magnitude higher than the observed $1\ M_\odot\ \mathrm{yr}^{-1}$ (Zuckerman & Evans 1974).

Figure 2.1 shows a very large-scale view of the nearest substantial or "giant" molecular cloud, the Orion complex, as detected in ^{12}CO emission. While the molecular gas in the galaxy has an overall scale height of about 75 pc from the galactic plane, Orion extends roughly a factor of two farther below the plane. The amount of molecular gas in Orion is

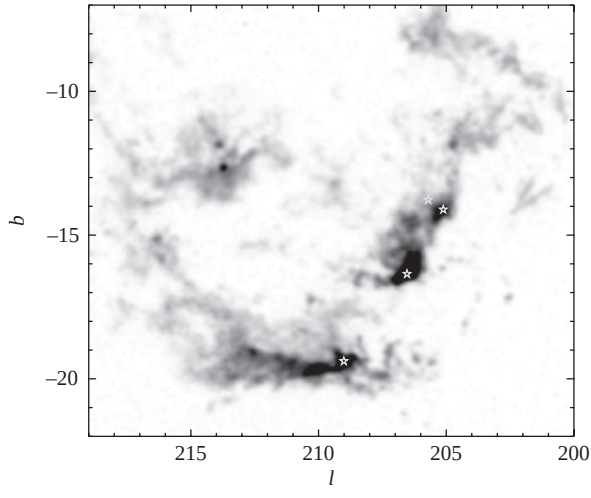

Fig. 2.1. Large-scale distribution of ^{12}CO emission in the region of Orion, plotted in galactic coordinates. The Orion A and B clouds describe an apparent broken arc of length ∼80 pc from $l \sim 204$, $b \sim -13$, $l \sim 214$, $b \sim -20$, to a distance as much as ∼150 pc below the galactic plane. Star symbols indicate the positions of dense clusters of young stars; the Orion Nebula Cluster at the northern end of the A cloud, and the NGC 2023/2024 and NGC 2068/2071 complexes at the ends of the B cloud. From Wilson *et al.* (2005).

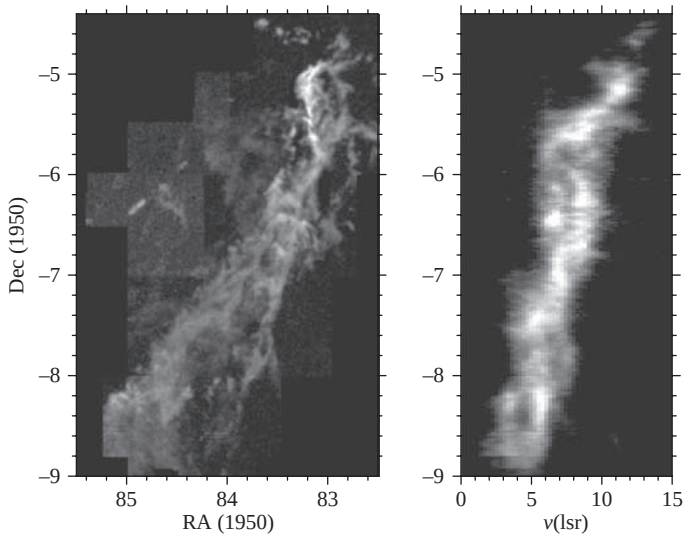

Fig. 2.2. Spatial distribution (left panel) and velocities integrated over right ascension as a function of declination (right panel) of ^{13}CO line emission. The Orion Nebula Cluster is centered in the famous integral-shaped filament at the northern end of the cloud, at about a declination of $-5.4°$ (1950). In addition to local supersonic motions of a few $\mathrm{km\,s^{-1}}$, with significant substructure all along the cloud, there is an overall radial velocity gradient of about 8 $\mathrm{km\,s^{-1}}$ from one end to the other, with an especially high-velocity gradient running from the northern end of the cloud toward the Orion Nebula Cluster. Data taken from Bally *et al.* (1987).

of order $10^5\ M_\odot$ (Bally *et al.* 1987; Genzel & Stutzki 1989), spread over a region almost 100 pc in length.

In addition to local "turbulence", molecular clouds also often exhibit large-scale motions in the form of an overall shear and/or rotational motion. For example, Figure 2.2 shows the velocity structure inferred from ^{13}CO line emission in the Orion A cloud. Beyond the small-scale motions of the order of 2 $\mathrm{km\,s^{-1}}$, there is a substantial north–south gradient of radial velocity, of about 8 $\mathrm{km\,s^{-1}}$ over a length of about $4° \sim 33$ pc at a distance of 470 pc, in a region of total mass $\sim 10^5\ M_\odot$. The rotational motion required to support an elongated cloud of half-radius $r = 16$ pc against collapse then is

$$2 \times \left(\frac{GM}{r}\right)^{1/2} \sim 10\ \mathrm{km\,s^{-1}}. \tag{2.1}$$

Thus large-scale shear or rotation plays an important dynamical role in this cloud. Similar results hold for many other molecular complexes such as Taurus (§2.6).

2.2 Turbulence and cloud lifetimes

One of the central problems in star formation theory is to understand the origin and nature of turbulence in molecular clouds (see Elmegreen & Scalo 2004 and Scalo & Elmegreen 2004 for general discussions of interstellar medium turbulence). Turbulent motions may either promote star formation by collecting additional mass into limited regions

which can then become gravitationally unstable and collapse, or inhibit star formation in principle by providing a "pressure" which resists gravitational collapse. Recent reviews of turbulence and issues related to star formation can be found in Mac Low and Klessen (2004) and Ballesteros-Paredes *et al.* (2007).

Older models of molecular clouds envisioned a sort of equilibrium or average steady-state condition, partly due to the then limitations of computing power which precluded detailed time-dependent simulations. In analogy with the thermal pressure that keeps the Sun supported against its own self-gravity, some models assumed that the pressure could be expressed (assuming isothermality for simplicity) as

$$P = \rho(c_{\rm s}^2 + v_{\rm turb}^2), \tag{2.2}$$

(Chandrasekhar & Ferni 1953), where ρ is the gas density, $c_{\rm s}$ is the sound speed, and $v_{\rm turb}$ is the turbulent velocity. The turbulent component is essential to quasi-equilibrium models; thermal pressure in (large) molecular clouds is far too low to provide substantial support against gravity on a global scale. However, the approach of simply adding in a turbulent pressure acting as equivalent to an added thermal component is problematic, because the turbulence is in general neither time-independent nor isotropic.

Setting aside large-scale ordered motions, like rotation, smaller-scale supersonic motions in gas generally produce shocks and dissipate their energy rapidly. If molecular clouds persist for long periods of time, turbulent energy dissipation must be reduced or suppressed, or the turbulence must be regenerated. It had been suggested that magnetohydrodynamic turbulence might decay much more slowly than pure gasdynamic turbulence (Arons & Max 1975). In particular, Alfvén waves (see discussion in Shu 1992) can have supersonic motions transverse to the magnetic field direction and yet be non-compressive to first order (and thus less dissipative). However, recent numerical simulations of MHD turbulence (Mac Low *et al.* 1998; Stone *et al.* 1998) indicate that the turbulent energy dissipates rapidly, on the order of a crossing time for the particular region involved. The reason appears to be that in any realistic situation, the complicated magnetic field and density structure means that pure linear Alvenic modes cannot be sustained; they convert into other, compressive modes (fast and slow modes), resulting in rapid dissipation of wave energy and turbulence (Passot & Vazquez-Semadeni 2003). Moreover, numerical simulations suggest that supersonic turbulence more generally *promotes* star formation via the resulting strong compressions (e.g., Ostriker *et al.* 1999; Klessen *et al.* 2000; Heitsch *et al.* 2001; Padoan & Nordlund 2002).

But are molecular clouds really long-lived? Old theories of molecular cloud formation invoked a kind of agglomeration of subunits, which required timescales comparable to the galactic rotation period, $\sim 10^8$ yr. Blitz and Shu (1980) suggested considerably shorter lifetimes, of order tens of Myr at most, based on the relative absence of massive molecular clouds in interarm regions, which should be present if clouds form as they pass through the spiral density wave pattern and then linger on. However, a recent re-examination by Elmegreen (2007) of spiral arm structure suggests even shorter lifetimes.

Moreover, molecular cloud lifetimes of a few tens of Myr are much longer than the ages of the stellar populations in these clouds. The first indication of this came from the study of Herbig *et al.* (1986), who conducted a sensitive search for T Tauri stars considerably older than the typical population age of $\sim 1-3$ Myr, and found none. Subsequently, studies using X-ray surveys attempted to find the so-called "post-T Tauri stars" which ought to be present if clouds had been manufacturing stars for $\gtrsim 10$ Myr or so. It soon became clear that most of

Table 2.1. *Star-forming regions*

Region	$< t >$ (Myr)	Molecular gas?	Ref. (age)
Coalsack	–	yes	–
Cha III	–	yes	–
Pipe Nebula	–	yes	–
Orion Nebula	1	yes	1
Taurus	2	yes	1,2,3
Oph	1	yes	1
Cha I,II	2	yes	1
Lupus	2	yes	1
MBM 12A	2	yes	10
IC 348	2–3	yes	1,5,10
NGC 2264	2–3	yes	1
Sco OB2:			
Upper Sco	5	no	5,6
Lower Cen-Crux	10–15	no	7
Upper Cen-Lup	10–15	no	7
TW HyA	∼10	no	8
η Cha	∼10	no	9

Notes: (1) Palla and Stahler (2000); (2) Hartmann (2001); (3) White and Ghez (2001); (4) Herbig (1998); (5) Preibisch and Zinnecker (1999); (6) Preibisch *et al.* (2001); (7) de Geus *et al.* (1989); (8) Webb *et al.* (1999); (9) Mamajek *et al.* (1999); (10) Luhman (2001).

the young stars found in the X-ray surveys were actually much older systems, $\sim 30-100$ Myr old, and constituted a widespread population which had long ago dispersed from their parent molecular clouds (Briceño *et al.* 1997, 1998; Covino *et al.* 1997).

Table 2.1 summarizes properties of nearby molecular cloud complexes with masses in excess of $\sim 10^3\, M_\odot$. It is striking that there are no significant populations of stars in these clouds with typical ages close to 10 Myr. Conversely, young associations of ages $\sim$10 Myr are generally devoid of molecular gas. (A more systematic analysis is presented by Ballesteros-Paredes & Hartmann 2007, reaching similar conclusions.) At least in the solar neighborhood, *molecular clouds form rapidly and disperse rapidly.*

Note that this does *not* mean that older stars are not present in a given star-forming region. There are many examples where older associations abut a younger population – for example, when stellar winds, ionization, and/or supernovae pile up material, triggering a second generation of star formation (see following section). What *does* seem to be true is that once gas becomes compressed sufficiently, star formation ensues within 1 Myr or less; otherwise we would see many molecular clouds without any star formation, which is in contradiction with observations (Ballesteros-Paredes & Hartmann 2007). (Some debate remains concerning the relatively small numbers of apparently older stars in some star-forming regions; Chapter 11.)

A major factor in limiting cloud lifetimes is stellar energy input, especially when massive stars are formed. For example, in the nearest B association, Scorpius-Centaurus,

which consists of stars with ages of ∼5–15 Myr, molecular gas is not present in the older population; the large H I shells surround the three subconcentrations – Lower Centaurus-Crux, Upper Centaurus-Lupus, and Upper Scorpius – which are probably the result of the dispersal of association molecular gas by stellar winds and supernovae (de Geus 1992). As de Geus (1992) showed, the action of a single supernova would be sufficient to remove the gas in the 5-Myr-old Upper Scorpius subassociation (see also Preibisch & Zinnecker 1999), while the molecular gas at the eastern end of the region remains as the Ophiuchus cloud, with young stars (of ages ∼1 Myr or less) and forming protostars.

Short lifetimes mean that supersonic turbulence *within* a molecular cloud need not be regenerated, because clouds are dispersed rapidly (Ballesteros *et al*. 1999; Elmegreen 2000). Moreover, rapid dispersal leads to an alternate explanation of the low galactic star formation rate: clouds are simply inefficient at forming stars because they don't live long enough for all the turbulence to decay. Indeed, it has been known for a long time that star formation occurs with an efficiency of only a few percent, averaged over entire complexes (e.g., Cohen & Kuhi 1979).

As noted above, the gravitational collapse timescale in the absence of resisting forces is of order one to a few Myr at the typical densities of molecular clouds; the ages of the stellar populations shown in Table 2.1 are comparable. The rapidity of star formation emphasizes that molecular cloud formation and dissipation processes are crucial to understanding the processes of protostellar core formation.

2.3 Molecular cloud formation and dispersal

The molecular clouds harboring these young stellar populations are generally quite elongated (e.g., Figure 2.2), such that the lateral "crossing time", defined as the largest linear dimension of a molecular cloud complex divided by either a velocity dispersion or a velocity gradient, is often considerably longer than the characteristic age of the stellar population in the cloud. For example, in the Orion A cloud most of the stars have ages $\sim 1-2$ Myr, though the crossing time from a local velocity dispersion would be of order 10 Myr, or 4 Myr using the overall velocity gradient (Figure 2.2). As another example, in Taurus the velocity dispersion of ~ 2 km s^{-1} implies a crossing time over the >20 pc projected extent of the cloud of >10 Myr; yet the stellar population is mostly of ages $1-4$ Myr (Table 2.1; Hartmann 2002). A more striking example of this is provided by the Sco OB2 association mentioned above, a nearby ($\sim 120-140$ pc) massive assemblage containing about 150 B stars (and presumably thousands of other, low-mass stars; e.g., de Geus 1992, Preibisch & Zinnecker 1999, and references therein). Proper motions measured by the Hipparcos satellite for the more massive members indicate a velocity dispersion of $\lesssim 1.5$ km s^{-1} in one dimension (de Bruijne 1999), comparable to typical velocity dispersions of molecular clouds. The lateral crossing time of this complex of 150 pc in length is then ∼100 Myr, while the age spread of the stellar population is at most 15 Myr (Table 2.1). Thus something must be coordinating or triggering molecular cloud and star formation over large distances.

The crossing time requirement implies that molecular clouds are the product of large-scale flows. Figure 2.3 shows a simple example of how this works. Stellar energy input from a cluster of stars – predominantly winds from massive stars and supernova explosions – blow out a bubble in the ISM (see also Franco *et al.* 1988). Eventually, enough material is accumulated in the bubble periphery that star formation can occur (left figure), being "triggered" by the pile-up of gas becoming gravitationally unstable (e.g., Elmegreen & Lada 1977). Star

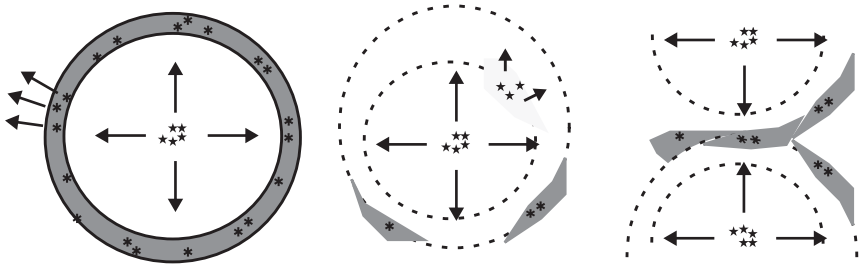

Fig. 2.3. Schematic illustration of the formation of a young stellar population in a molecular cloud, with the population age being much shorter than the lateral cloud-crossing time. Winds and supernovae from a star cluster blow out a bubble; at some point material along the bubble wall becomes self-gravitating and forms stars (left). The molecular gas is dispersed rapidly, and other regions form later on (center). In general, the situation is not as simple as this, because bubbles from differing sites can and will collide. From Hartmann *et al.* (2001).

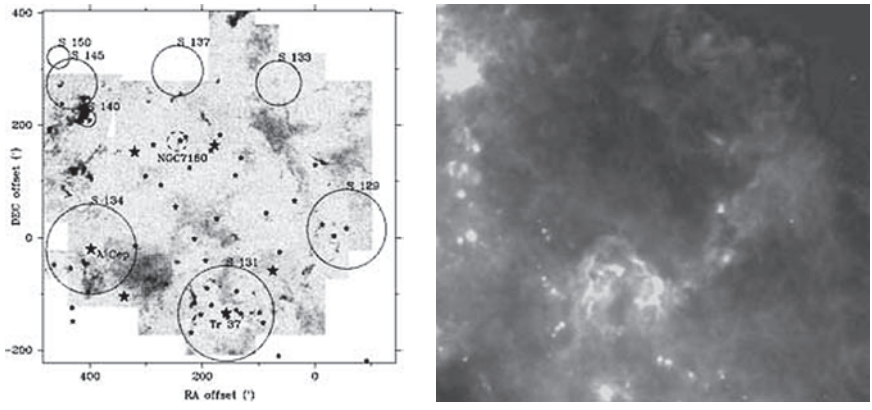

Fig. 2.4. Overview of the Cep OB2 association. The region contains a large bubble of approximately $3 \times 10^5\ M_\odot$ of atomic gas; about $1 \times 10^5\ M_\odot$ of molecular gas resides at a radius of about 50 pc. The left panel shows molecular gas in the region, with clusters indicated; the right panel is the 100 μm *IRAS* map, showing the bubble structure more clearly in the warm dust. Near the middle of the bubble resides the ∼10 Myr-old cluster NGC 7160; younger clusters lie along the periphery. The cluster Tr 37 has an age of about 3 Myr; other stars more embedded in the molecular gas are younger. The circles denote H II regions. From Patel *et al.* (1998).

formation can proceed nearly simultaneously along the bubble wall; as no information is being propagated laterally, there is no problem with the star formation episode being faster, and dispersing the molecular gas faster, than the lateral crossing time (middle figure). Thus, one can consider molecular clouds as "accidental collections" of dense gas.

An example of this process with differing stellar energy sources is provided by the Cep OB2 association (Figure 2.4). The region contains a roughly circular shell of molecular gas of approximately 50 pc radius and mass $\sim 10^5\ M_\odot$; there is a similar structure in atomic hydrogen, though extending to larger distances, with mass $\sim 3 \times 10^5\ M_\odot$ (Patel *et al.* 1998 and references therein). The cluster NGC 7160 and other hot stars of age ∼10 Myr reside

near the center of this bubble. Along the periphery of the bubble are several H II regions heated by groups or clusters of young stars with ages $\lesssim 3$ Myr (e.g., Marschall *et al.* 1990; Patel *et al.* 1998).

The scenario outlined by Patel *et al.* (1998) to explain the observations is that stellar winds and supernovae from NGC 7160 swept up the bubble, and that after a period of several Myr enough mass had been accumulated to result in star formation. The arc of molecular gas along which stars are forming is many tens of pc, yet the stellar populations have ages ranging from $\sim 1-3$ Myr (e.g., Sicilia-Aguilar *et al.* 2005, 2006). Thus Cep OB2 is a particularly direct example of the mechanism envisaged for making molecular clouds in Figure 2.4.

The passage of gas through shocks at spiral density waves can also have the same effect as stellar winds and supernovae. However, it is clear from Cep OB2 and other regions that the density wave shocks cannot be the only sites of compression needed to form stars. The example of Cep OB2 shows that even a few OB stars can have dramatic effects on the local gas, dispersing the molecular gas rapidly once massive stars are born.

The effects of stellar energy input can be oulined quantitatively using the simplest version of the theory of interstellar bubbles by Castor *et al.* (1975). We ignore the initial stages in which massive stars photodissociate molecular gas and then photoionize the atomic material, leading to an expanding H II region.

Assume that a massive star ejects a steady high-velocity wind with a luminosity $L_{\rm w} = (1/2)\,\dot{M} v_{\rm w}^2$, with $\dot{M}_{\rm w}$ and $v_{\rm w}$ being the mass loss rate and wind velocity, respectively, into a uniform medium of density $\rho_\circ$, with mean molecular weight μ. The mass of the bubble is assumed to be mostly swept-up material; for bubble radius R_s,

$$M_s = 4\pi\rho_\circ \frac{R_s^3}{3}. \tag{2.3}$$

The fast wind (typical velocities $\sim 1000-3000$ km s^{-1}) shocks and creates a hot bubble. Calculations show that the interior of the bubble has a nearly uniform temperature T_b. Assuming a perfect gas, the energy within the bubble is

$$E_{\rm b} = \frac{4}{3}\pi R_s^3 \rho_{\rm b} \times \frac{3}{2}\frac{kT_b}{\mu m_H} = 2\pi R_s^3 P_{\rm b}, \tag{2.4}$$

where P_b is the pressure of the interior of the bubble. This pressure drives the bubble outward; the momentum equation is

$$\frac{dM_s v_s}{dt} = \frac{d}{dt}\frac{4\pi\rho_\circ}{3} R_s^3 \frac{dR_s}{dt} = \frac{\pi\rho_\circ}{3}\frac{d^2 R_s^4}{dt^2} = 4\pi R_s^2 P_{\rm b}. \tag{2.5}$$

The energy equation, neglecting radiative losses, is then

$$\frac{d}{dt} 2\pi R_s^3 P_{\rm b} = L_w - 4\pi R_s^2 P_{\rm b}\frac{dR_s}{dt}. \tag{2.6}$$

Taking $L_{\rm w}$ to be constant, one can eliminate $P_{\rm b}$. We then look for a similarity solution, one in which the radius of the shell $R_s \propto t^n$. Substituting this form, one finds after some algebra

$$R_s = \left(\frac{125 L_w}{154\pi\rho_\circ}\right)^{1/5} t^{3/5}. \tag{2.7}$$

Using fiducial units of $10^{36}\,\mathrm{erg\,s^{-1}}$ for L_w (typical for an O star wind), ambient hydrogen density $n_\circ$ in units of $\mathrm{cm^{-3}}$, and the time t_6 in Myr,

$$R_s = 27 L_{36}^{1/5}\, n_\circ^{-1/5}\, t_6^{3/5}\,\mathrm{pc}. \tag{2.8}$$

Alternatively, we may consider driving by a hot bubble produced by a supernova explosion. Following Spitzer (1968), we calculate the bubble expansion during the phase where most of the mass in the bubble wall is swept up from the interstellar medium, but the bubble has not lost a significant amount of its energy through radiation. Let K_1 be the fraction of the total energy E which is in heat energy, and denote the pressure immediately behind the shock front (post-shock gas) by p_2. We further set p_2 to be K_2 times the mean pressure of the heated gas within the bubble (we expect K_1 and K_2 to be constants of order unity). For a perfect gas with $\gamma = 5/3$ the thermal pressure is 2/3 of the mean thermal energy density; therefore,

$$p_2 \sim K_2 \frac{2}{3}\frac{3K_1 E}{4\pi R_s^3}. \tag{2.9}$$

For an adiabatic shock with a large Mach number (highly supersonic), the density contrast is $\rho_2 = 4\rho_1$ and the pressure is $p_2 = (3/4)\rho_2 v_s^2$ for a perfect gas with $\gamma = 5/3$ (Spitzer 1968). Thus the shock velocity is

$$v_s = \frac{2K_1 K_2 E}{3\pi\rho_\circ R_s^3}. \tag{2.10}$$

We then solve for R_s,

$$R_s = \left(\frac{2}{5}\right)^{2/5} \left(\frac{2K_1K_2E}{3\pi\rho_\circ}\right)^{1/5} t^{2/5}. \tag{2.11}$$

Setting $K_1K_2 = 1.53$ from detailed calculations,

$$R_s = \left(\frac{2}{5}\right)^{2/5} \left(\frac{2K_1K_2E}{3\pi\rho_\circ}\right)^{1/5} t^{2/5}. \tag{2.12}$$

Putting in fiducial values,

$$R_s = 50\,\mathrm{pc}\, E_{50}^{1/5}\, n_\circ^{-1/5}\, t_6^{2/5}, \tag{2.13}$$

where E_{50} is the supernova kinetic energy in units of 10^{50} erg.

Now consider an application to Cep OB2 (Figure 2.4). The amount of molecular mass in the $\sim$50 pc radius shell is $\sim 1 \times 10^5\ M_\odot$; if this mass has been swept up from material originally within the volume, the average initial hydrogen density would need to have been $\sim 5.5\,\mathrm{cm^{-3}}$ for self-consistency. Inserting this value into equation (2.8) and assuming the presence of a single massive O star, with $L_{36} \sim 1$, $R_s = 50$ pc at $t_6 = 5$. This is reasonably consistent with the $\sim$10 Myr age of the central NGC 7160 cluster, and the ages of secondary clusters around the periphery of the molecular shell (though it must be noted that equation (2.8) overestimates the expansion at late times ($\sim$5$-$10 Myr) because of the neglect of radiative losses). Alternatively, if we assume that a supernova originally within NGC 7160 has gone off, $R_s \sim 50$ pc at 5 Myr for $E_{50} \sim 0.2$, easily produceable by a single supernova.

Detailed models of populous star clusters with typical initial stellar mass functions suggest that the total energy input from winds and supernovae is relatively constant over timescales of 10 Myr (Leitherer *et al.* 1992), with supernovae dominating the energy input at later times.

Overall, supernovae likely dominate the energy input to the ISM, because wind mass loss rates decline rapidly below $M \sim 20\ M_\odot$, while stars of masses $M > 8\ M_\odot$ can become supernovae; thus there are many more stars which become supernovae than have strong winds.

Based on these calculations, even a small number of massive stars can efficiently disrupt molecular clouds. While the general situation is more complex than can be treated by equation (2.8) because most molecular clouds are neither uniform nor spherical, the amount of energy and momentum available will clearly have major effects in dissipating molecular (star-forming) clouds.

In summary, formation of massive stars will result in rapid cloud dispersal (perhaps after some initial triggering of star formation in compressed regions), helping to explain the short lifetimes of local molecular clouds; there is no reason why the energy injected should be so finely tuned as to precisely balance cloud self-gravity, given typical escape velocities of a few $\mathrm{km\,s^{-1}}$. On larger scales, the effect of winds and supernovae will be to drive flows which pile up material and thus trigger star formation. The Orion molecular cloud complex, with its arc-like shape and its large distance from the galactic plane (Figure 2.1), may be a prime example of large-scale flow-driven formation.

The reasons for dispersal of low-mass star-forming clouds are less clear. The youngest low-mass YSOs exhibit powerful bipolar outflows powered by disk accretion. Although the narrow "jets" seen from such systems will not be very effective in disrupting a molecular cloud, given the small swath they cut, it is likely that some additional ejection of material over wider solid angles accompanies each jet, and this material could be responsible for disrupting low-mass star-forming regions, which are probably less gravitationally bound than the high-mass regions. Alternatively, supernovae in nearby massive star-forming regions are likely eventually to disrupt low-mass clouds.

2.4 Flows, magnetic fields, and cloud formation

Magnetic fields can have important dynamical effects on cloud formation and subsequent evolution. The average magnetic field B in the ISM, with a strength $\sim 6\,\mu\mathrm{G}$ (Beck 2001; Heiles & Troland 2005), has a pressure $B^2/8\pi \sim 1.4 \times 10^{-12}\,\mathrm{dyne\,cm^{-2}}$, comparable to the turbulent and cosmic ray pressures of the ISM (e.g., Boulares & Cox 1990). The magnetic field tends to increase as the gas is compressed, resisting the formation of higher-density condensations. However, because the magnetic field is not isotropic, it does not act in the same way as a thermal pressure. Even in the limit of "flux freezing" (§3.6), where the gas is confined to flow within magnetic flux "tubes", gas can accumulate locally along field lines until inertia or even gravity can dominate the resisting magnetic forces, to the extent of bending the field lines (see Ostriker *et al.* 1999, 2001, and Heitsch *et al.* 2001).

Numerical simulations are essential to understanding the dynamic development of clouds. An early attempt to look at cloud formation on a large scale was made by Passot *et al.* (1995). These ideal MHD calculations have limitations, among which are that they treated only a two-dimensional layer of the ISM in the plane of the galaxy, adopted a schematic heating term due to stellar winds but not supernova explosions, and had a limited dynamic range in density. Nevertheless, the treatment of a large region (1 kpc square) produced interesting results.

Figure 2.5 shows a simulation with a 1 kpc square slice intended to represent the plane of the Galactic disk, in a "shearing box" approximation which treats galactic differential

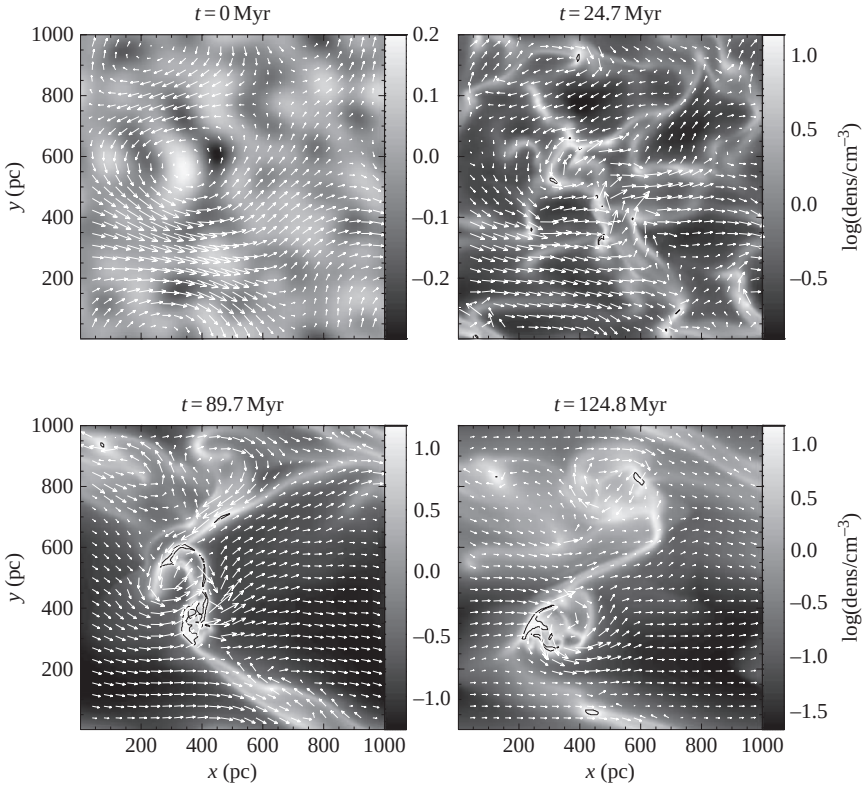

Fig. 2.5. Simulation of cloud evolution at four times, (a) t = 0, (b) t = 24.7 Myr, (c) t = 89.7 Myr, and (d) t = 124.8 Myr. Vectors indicate magnetic field directions and strengths. The grayscale denotes the density in logarithmic units, as indicated in the grayscale bars. "Clouds", defined as regions where the density exceeds 15 cm^3, are denoted by the black isocontours. After about 10 Myr, "star formation" occurs in the model (when local densities increase to the threshhold level; see text), adding energy to the simulation. Clouds are built up by flows along field lines (bending the field lines in dense regions) over scales of hundreds of pc, concentrating most of the mass into a small fraction of the computational region. From Hartmann *et al.* (2001).

rotation as a shear in the *y*-direction (Passot *et al.* 1995). An initial set of random velocity and density perturbations are introduced into a uniform density region of 1 cm^{-3} with an initial uniform magnetic field component of 1.6 μG and a random component of 5 μG; then the system is allowed to evolve. When a threshhold density is reached, an energy source is introduced locally to simulate the energy input of massive stars. After several tens of Myr, large-scale flows have been set up, mostly in the direction of galactic rotation. The magnetic field similarly gets more ordered in the direction of rotation, though with significant distortions. There are relatively few cloud structures in this region. Simulations which include more energy input from supernovae tend to yield more bubble-like substructure (e.g., de Avillez & Mac Low 2001; Wada & Norman 2001).

The left panel of Figure 2.6 shows the evolution of energies within the entire computational region. The gravitational energy (solid line) has been given the opposite sign

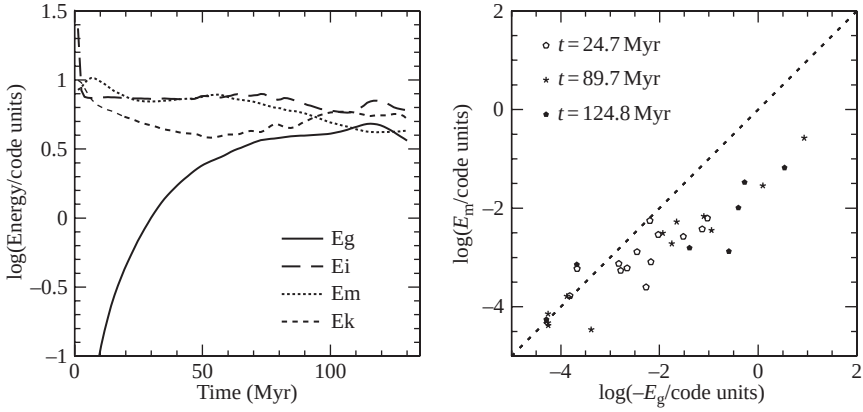

Fig. 2.6. Left panel: Evolution of (negative) gravitational (E_g, solid line), thermal (E_i, long dashed line), magnetic (E_m, dotted line), and kinetic (E_k, short dashed line) energies for the whole computational domain. Note that the internal energies are larger than the gravitational energy, indicating that the whole computational domain is supported against collapse. Right panel: Magnetic vs. gravitational energy for clouds in the last three timesteps in Figure 2.5 (t = 24.7, 89.7, and 124.8 Myr). Note that while the energies are comparable, and correlated, the gravitational energy is somewhat larger for more massive clouds, implying that they are magnetically supercritical (see text). From Hartmann *et al.* (2001).

to facilitate comparison. The magnetic and (internal) energies remain nearly constant for the first 50 Myr of the simulation, decaying slightly thereafter. The overall kinetic energy decreases slightly at first due to dissipation, and then eventually steadies or even rises due to stellar energy input. The main evolution is in the gravitational potential energy in the volume, which rises rapidly until it becomes roughly comparable to the other energy terms. This agrees with many observations suggesting rough equipartition of various energies within clouds (e.g., McKee 1989; Ballesteros-Paredes 2006).

The right panel in Figure 2.6 compares the magnetic and gravitational energies of clouds (defined as connected grid cells above a certain critical density). While the magnetic and gravitational energies are correlated, the larger clouds are gravitationally dominated, while the smallest clouds tend to have comparable or even higher magnetic energy than gravitational potential energy. One can understand this behavior in a qualitative way: denser/higher-pressure gas, especially that with higher gravitational compression, can confine magnetic fields more strongly, leading to a correlation between field and gas, while strong magnetic fields resist compression, so that low-density regions are more likely to have relatively higher magnetic than other energies. The general equipartition of magnetic energy with gas dynamic/thermal energy in the diffuse ISM probably reflects the origin and maintenance of the field by the gas; a much stronger field could not be contained by the ISM but would cause the material to expand to a much larger configuration which would result in a state closer to force balance.

2.5 Gravity and fragmentation

Star formation is the result of the collapse of gravitationally bound cloud fragments. The so-called “Jeans length” or “Jeans mass” can provide a useful guide to the scales over which gravitational instabilities can grow and produce a mass concentration.

The physical basis of the Jeans instability can be understood from the following simple argument (Binney & Tremaine 1987). Consider an isothermal, initially uniform gas with sound speed c_s, density $\rho_\circ$, and pressure P. In this state, there are no net pressure or gravitational forces. Suppose a spherical region of this gas is slightly compressed so that its density is higher by an amount $\chi\rho_\circ$ within a radius r. There will now be an outward pressure force, of order of magnitude per unit mass

$$F_P \sim \nabla\frac{P}{\rho} \sim \chi\frac{c_s^2}{r}. \tag{2.14}$$

The higher density leads to an inward gravitational force per unit mass of

$$F_G \sim GM\frac{\chi}{r^2} \sim G\rho_\circ\chi r, \tag{2.15}$$

where M is the mass of the cloud. Thus, gravity wins on large scales such that

$$r^2 \gtrsim \frac{c_s^2}{G\rho_\circ}. \tag{2.16}$$

A detailed analysis (Appendix 2) leads to a critical Jeans length

$$\lambda_J = \left(\frac{\pi c_s^2}{G\rho_\circ}\right)^{1/2}, \tag{2.17}$$

and a critical Jeans mass

$$M_J = \lambda_J^3\rho_\circ = \left(\frac{\pi c_s^2}{G}\right)^{3/2}\rho_\circ^{-1/2}. \tag{2.18}$$

According to this analysis, length scales larger than the Jeans length, or masses greater than the Jeans mass, will be unstable to gravitational collapse. Assuming a molecular hydrogen gas with a mean molecular weight of 2.36,

$$M_J \sim 540\ M_\odot\, T_{10}^{3/2}\, n_{H_2}^{-1/2}, \tag{2.19}$$

where T_{10} is the temperature in units of 10 K and N_{H_2} is the molecular hydrogen density in units of cm^{-3}.

Equation (2.18) implies that as gas condenses to higher densities, the Jeans mass decreases. This dependence of the Jeans mass on density suggests the possibility of *fragmenting* ever smaller masses out of the original larger self-gravitating cloud, a scenario for fragmentation into star-sized clouds originally proposed by Hoyle (1953). But this does not work in a simple manner, as discussed by Larson (1985). The basic problem is illustrated by the dispersion relation for the Jeans analysis (Appendix 2). Assuming density perturbations of the form $\delta\rho \propto \exp[i(\omega t - kx)]$, the dispersion relation is

$$\omega^2 = c_s^2(k^2 - k_J^2), \quad k_J^2 = 4\pi G\frac{\rho_\circ}{c_s^2}. \tag{2.20}$$

When the wavenumber $k = 2\pi/\lambda$ is smaller than the critical wavenumber k_J, i.e., the wavelength of the perturbation is larger than the Jeans length $\lambda_J = 2\pi/k_J$, ω is imaginary, and there is an exponentially growing (unstable) mode. The growth rate $-i\omega$ increases monotonically with decreasing k, and is *largest* as $\lambda \to \infty$. In other words, the largest scales

have the fastest growth rates and thus the fastest collapse times. This faster collapse of the larger scales makes it very hard for the cloud to fragment into smaller pieces (Larson 1985) – unless one starts with large density perturbations to begin with.

A related difficulty of applying the Jeans analysis in the uniform density case is that a uniform self-gravitating medium cannot be static, invalidating a central assumption of the analysis. This inappropriate assumption is sometimes described as the "Jeans swindle" (Binney & Tremaine 1987; Appendix 2). Some theories have assumed that "turbulent" supersonic motions exert an isotropic pressure, equivalent to a thermal gas pressure with a higher temperature; however, the generally anisotropic and time-dependent nature of real turbulent flows renders this assumption implausible (Ballesteros-Paredes 2006).

Even ignoring the difficulties posed by supersonic turbulence, and adopting the most optimistic view, the above argument against fragmentation shows that the Jeans mass is at best a *lower limit* to gravitationally bound condensations; larger condensations have no problem collapsing. Thus, the Jeans criterion is a useful indicator of the minimum scales which can collapse gravitationally, but it is not a useful means of estimating the characteristic masses into which a cloud will fragment.

2.6 Sheets and filaments

The picture of cloud formation by large-scale flows discussed in the previous section suggests that clouds might initially be parts of "bubble" walls, or approximately sheet-like. In addition, molecular clouds generally show filamentary structure, with the youngest stars (especially protostars) found in these filaments. For example, Figure 1.1 shows that many of the stars in Taurus lie in banded structures, with the Class I objects and protostellar cores aligned even more clearly with high-density filaments such as traced by ^{13}CO (Schneider & Elmegreen 1979; Scalo 1990; Mizuno *et al.* 1995; Figure 2.7). This kind of distribution extends even to clustered regions; as illustrated in Figure 2.8, protostars are generally found in more spatially concentrated distributions, often along dense gas filaments, while the T Tauri (older) stars are more widely distributed.

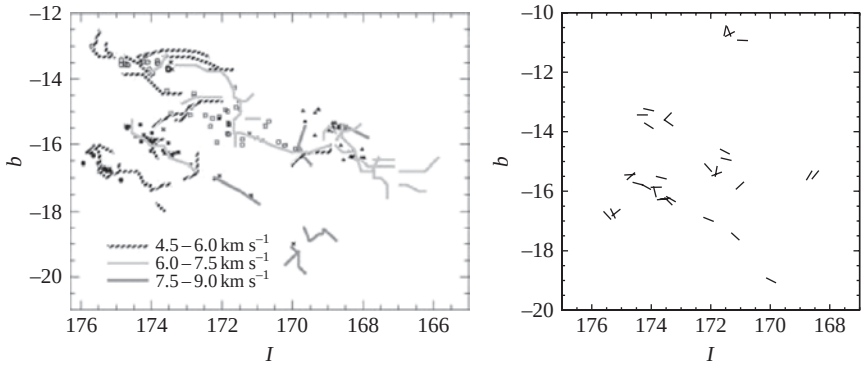

Fig. 2.7. Left panel: schematic positions and velocities of dense gas (^{13}CO) in Taurus, following Mizuno *et al.* (1995). Right panel: position angles of the optically selected molecular cloud cores, from Lee and Myers (1999). The cores are generally elongated in the direction of the filament that they lie within (see Chapter 3). From Hartmann (2002).

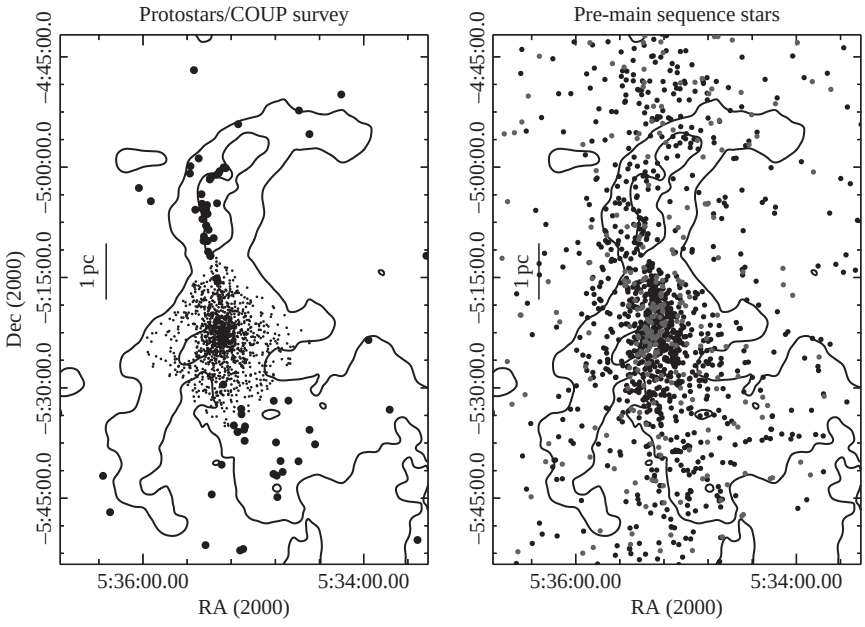

Fig. 2.8. Relative distribution of pre-main-sequence stars and Class I sources (protostars) in the vicinity of the Orion Nebula Cluster. Left: Protostars detected with the IRAC and MIPS instruments on the *Spitzer Space Telescope* (large black dots) compared with a deep X-ray survey for young stars, most of which will be Class II/III objects (small dots: Feigelson *et al.* 2005). The protostars are clearly more concentrated spatially; bright nebular emission prevents their detection in the innermost regions of the ONC. Right: IRAC Class II sources (T Tauri stars with disks; dark circles) along with Class III/WTTS stars identified from variability (light circles: Carpenter *et al.* 2001). Contours show the $A_V \geq 3$ area. Courtesy S.T. Megeath.

The frequent observation of star formation in filaments have led to theoretical investigations of gravitational fragmentation in such structures. *Infinite* sheets and filaments *are* equilibrium solutions to the equations of motion and thus can satisfy the Jeans assumption. Consider an isothermal thin sheet with a surface mass density $\Sigma_\circ$. As shown in Appendix 2, the dispersion relation indicates that surface density perturbations can grow exponentially in time at a rate Γ, where

$$\Gamma^2 \;=\; 2\pi G \Sigma_\circ k \;-\; c_{\rm s}^2 k^2. \tag{2.21}$$

There is a critical wavenumber,

$$k_{\rm c} \;=\; 2\pi G \frac{\Sigma_\circ}{c_{\rm s}^2}, \tag{2.22}$$

above which no exponential growth is possible; i.e., there is a minimum wavelength (a "Jeans" length) for gravitational instability. However, there now is a wavenumber with a maximum growth rate, because the growth rate is zero at both $k_{\rm c}$ and $k \rightarrow 0$. Differentiating equation (2.21) with respect to k, we find the wavenumber at which the exponential growth is fastest,

$$k_{\rm f} \;=\; \pi G \frac{\Sigma_\circ}{c_{\rm s}^2} \;=\; \frac{k_{\rm c}}{2}. \tag{2.23}$$

This result suggests that the sheet will break up into fragments of preferred mass (Larson 1985)

$$M_f \;\sim\; \lambda_{\rm f}^2 \Sigma \;=\; \frac{4c_{\rm s}^4}{G^2\Sigma_\circ}, \tag{2.24}$$

where $\lambda_{\rm f} = 2\pi/k_{\rm f}$.

Although the assumption of an infinitely thin sheet is unrealistic, analysis of an isothermal, self-gravitating sheet in hydrostatic equilibrium also shows instability, with critical and preferred wavenumbers half those of the corresponding values of the infintely thin sheet,

$$k_{\rm c} \;=\; \frac{\pi G \Sigma_\circ}{c_{\rm s}^2} \;=\; H^{-1}. \tag{2.25}$$

where the scale height H is defined by (Spitzer 1978)

$$H \;=\; \frac{c_{\rm s}^2}{\pi G \Sigma_\circ}, \tag{2.26}$$

for the hydrostatic equilibrium density distribution in the coordinate z perpendicular to the midplane

$$\rho(z) \;=\; \rho(0)\,{\rm sech}^2\left(\frac{z}{H}\right). \tag{2.27}$$

A similar result holds for infinite cylindrical filaments, where again the Jeans length is a few scale heights (see Appendix 2):

$$\lambda_{\rm J} \sim \frac{2\pi}{0.8} H, \tag{2.28}$$

where the filament scale height is given by

$$H \;=\; \frac{c_{\rm s}^2}{2G\Sigma_0}. \tag{2.29}$$

One attraction of this picture is that it predicts a minimum fragment length larger than the radial scale height of the filament, e.g., it predicts that self-gravitating cores would tend to be elongated in the direction of the filament; and that is observed in Taurus (Figure 2.7, right panel). In addition, this estimate of the characteristic scale of fragmentation in filaments bears some resemblance to observed fragmentation lengths (Hartmann 2002; Teixeira *et al*. 2006). Unfortunately, this analysis *also* suffers from the "Jeans swindle", because *finite* sheets and filaments (the only ones there are) *do not* constitute an equilibrium configuration. Global gravitational modes tend to overwhelm any linear perturbations.

To illustrate the importance of global gravity in a simple way, we follow Burkert and Hartmann (2004) and consider an infinitely thin, uniform density circular sheet of radius R, for which gas or magnetic pressure support is negligible (i.e., the case of a cloud containing a large number of initial Jeans masses). The gravitational potential at a point r from the center of this sheet is (Wyse & Mayall 1942)

$$\Phi = -4G\Sigma R\, E\left(\frac{r}{R}\right), \tag{2.30}$$

where Σ is the surface density and E is the second complete elliptic integral. The gravitational acceleration toward the center at r is

$$a_r = -\frac{\partial \Phi}{\partial r} = 4G\Sigma \frac{R}{r}\left[K\left(\frac{r}{R}\right) - E\left(\frac{r}{R}\right)\right], \tag{2.31}$$

where K is the first complete elliptic integral. The acceleration goes to infinity at $d = R$, which would not occur in a sheet with finite thickness; thus we restrict use of this equation to regions considerably more than a sheet thickness from the edge.

Figure 2.9 shows the acceleration in units of $4G\Sigma$ as a function of r/R. The steep increase of inward acceleration as $r \rightarrow R$ implies that the sheet, initially at rest, will immediately proceed to collapse, with material piling up most rapidly at the outer edge (limited by gas pressure gradients which are ignored in the calculation).

It is useful to estimate the timescale of global collapse for comparison with numerical results. Using the expansions of the K and E integrals (Abramowitz & Stegun 1972), equation (2.31) can be written as

$$a_r = \frac{1}{2}\frac{dv^2}{dr} = \pi G\Sigma\left[\frac{r}{R} + \frac{3}{8}\left(\frac{r}{R}\right)^3 + \frac{45}{192}\left(\frac{r}{R}\right)^5 + \cdots\right]. \tag{2.32}$$

Ignoring pressure support, a collapse timescale t_c can be estimated for a subregion of size δr lying in the inner region of the sheet of radius R. Integrating equation (2.32) using only the linear term, starting from rest, and assuming that Σ does not change significantly within the inner region (see §3.1), a typical infall velocity of the subregion is

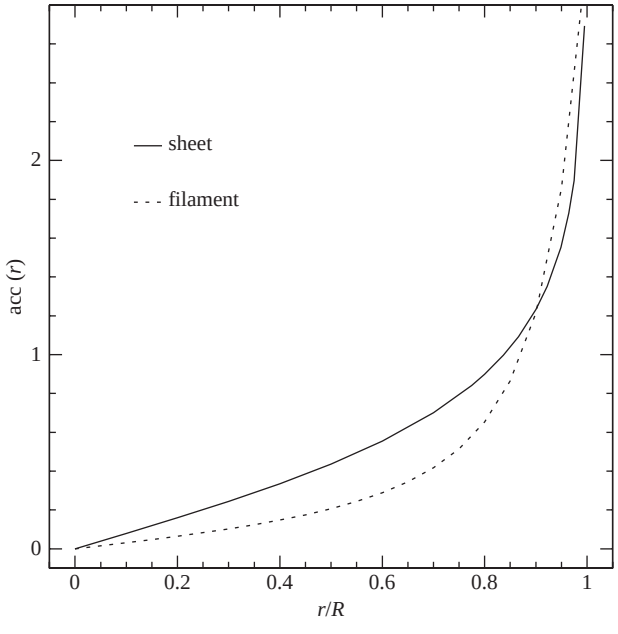

Fig. 2.9. Gravitational acceleration toward the center of a thin sheet (solid curve) or filament (dotted curve) as a function of position in units of the sheet radius R or filament length $2l$ (measured from the filament center). From Burkert and Hartmann (2004).

$$v^2 = \frac{\pi G \Sigma}{R} (\delta r)^2, \tag{2.33}$$

and thus

$$t_c = \frac{\delta r}{v} = \left(\frac{R}{\pi G \Sigma} \right)^{1/2}. \tag{2.34}$$

This estimate reproduces the numerical results for of the time it takes for the edge of the circular sheet to fall to the center.

The important feature is that t_c is independent of the size of the region δr; this means that *larger* scales must be moving at *larger* velocities, which makes it difficult to fragment on small scales. Indeed, the situation is similar for free-fall collapse in spherical geometry (§4.1). In their simple simulations, Burkert and Hartmann (2004) found no fragmentation due to linear perturbations, except at the edge of the sheet where in effect non-linear perturbations result from the high local acceleration (Figure 2.9). The overall infall of the sheet leads to "swallowing" linear perturbations in the interior by the collapsing edge.

Without rotation or some other motion, the ultimate fate of this circular sheet is to collapse entirely to the center. While the inner regions have a linear acceleration (dashed lines) and so might be stablized by a Hubble-type expansion or a solid-body rotation with centripetal acceleration $a(c)_r = -\Omega^2 r \propto r$, where $\Omega =$ constant, the non-linear acceleration as $r \rightarrow R$ shows that such rotation cannot stop the edge from collapsing to a ring whose dimensions are set by angular momentum. Moreover, the uniformly rotating sheet, whether in the non-equilibrium case of constant surface density, or in the equilibrium case of $\Sigma \propto [1 - (r/R)^2]^{1/2}$ (Mestel 1963), is unstable to large-scale perturbations (Hunter 1963), and generally results in large-scale redistribution of material with a concentration of mass to the center (see, e.g., Binney & Tremaine 1987, pp. 374–375). Conversely, large rotation (such as indicated by the upper dashed curve) could prevent the inner region from collapsing, but only at the expense of having the interior expand and the edge collapse to an outer ring (Burkert & Hartmann 2004).

Given the complexity of velocity fields of real clouds (Figure 2.2), it is implausible that massive clouds can be stabilized *everywhere*. In view of the observations indicating that star formation occurs rapidly upon cloud formation, the difficulty of preventing collapse is actually a desirable feature.

Molecular clouds obviously are not circular sheets in any approximation. As shown in Figure 2.10, the collapse of a simple elliptical sheet (the next most complicated figure) also piles up material at its edge, but with extra concentrations of density at each end. The eventual result of the collapse of the elongated sheet is to produce a filament. This filament contains non-linear clumps resulting from small initial non-uniformities (basically, sampling an elliptical cloud edge on a square grid), which become highly magnified during the collapse. It may be that given a spectrum of non-linear fluctuations in filaments, equation (2.28) may yet provide a useful guide to the minimum scales of gravitational collapse.

The importance of large-scale gravity acting on geometry for clouds encompassing many initial Jeans masses means that it is difficult to imagine a velocity field which prevents not only local but even global collapse. In the rapid star formation picture, even global molecular cloud collapse can be accomodated. To demonstrate this more directly, Hartmann and Burkert (2007) examined the collapse of an elliptical sheet with an overall density gradient

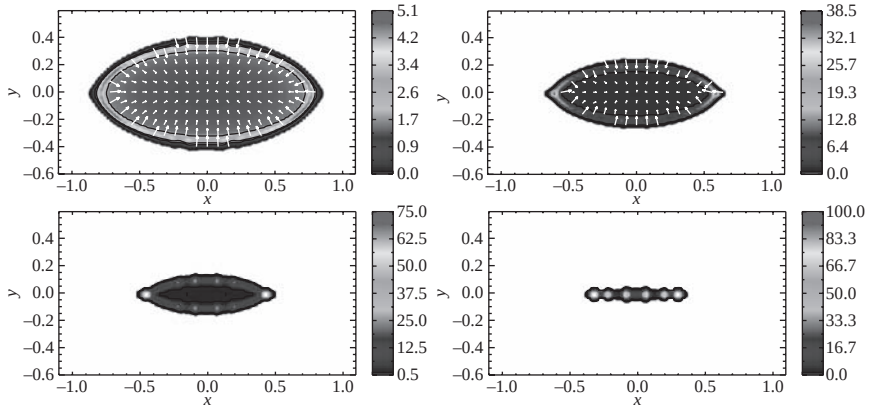

Fig. 2.10. Collapse of an initially elliptical, static, uniform sheet in two dimensions, shown at four different times. The grayscale indicates surface density. Material piles up at the edge early during the collapse, with extra mass concentrations at the ends of the ellipse. In the bottom right panel, the sheet has collapsed into a filament with non-linear perturbations of density that result from the magnification of initial structure in the ellipse boundary, which was sampled on a square grid. From Burkert and Hartmann (2004).

from one end to the other, set into rotation in the plane of the sheet. The collapse sequence (Figure 2.11) results in a cloud morphology remarkably similar to that of Orion A seen in ^{13}CO (Figure 2.2), with a dense concentration near the upper end suggesting the accumulation of large amounts of mass to form a large cluster like the ONC. Moreover, the ridges of increased density along the lower part of the cloud appear to have at least one corresponding feature in Orion A, as indicated by the higher concentration of younger stars on the north-western edge (Figure 2.8). Remarkably, the entire collapse sequence takes only 1.7 Myr, consistent with the ages of the embedded stellar populations. The velocities implied in this model are also roughly consistent with observation, taking into account the two-dimensional nature of the model and the fact that we only observe radial velocities and not proper motions.

Global collapse also seems plausible in the flow-driven model of cloud formation. There is no reason why a cloud formed by large-scale flows (§2.3) should be formed in approximate equilibrium. Lateral collapse could also help in understanding the rapid transition from atomic to molecular gas (Bergin *et al.* 2004), by concentrating the gas and making H_2 formation faster than in one-dimensional models. More generally, global velocity fields will either promote cloud expansion or contraction, with equilibrium unlikely; selecting dense clouds obviously favors contraction rather than expansion. In bubble-driven cloud formation, one would expect that expansion dominates early, but that as the bubble ages, it will slow down and accumulate mass, eventually reaching the point where gravity can overcome expansion.

If, however, clouds are collapsing, why have investigators usually found roughly virial motions? This is actually a natural result of collapse. Near free-fall velocities are only a factor $\sim 2^{1/2}$ larger than equilibrium velocities, a difference well below the geometric, kinematic, and mass uncertainties in assessing equilibrium (Vazquez-Semadeni *et al.* 2007; see Ballesteros 2006 for a discussion of problems with applying virial equilibrium to real clouds). More generally, it seems quite clear that molecular clouds are not equilibrium

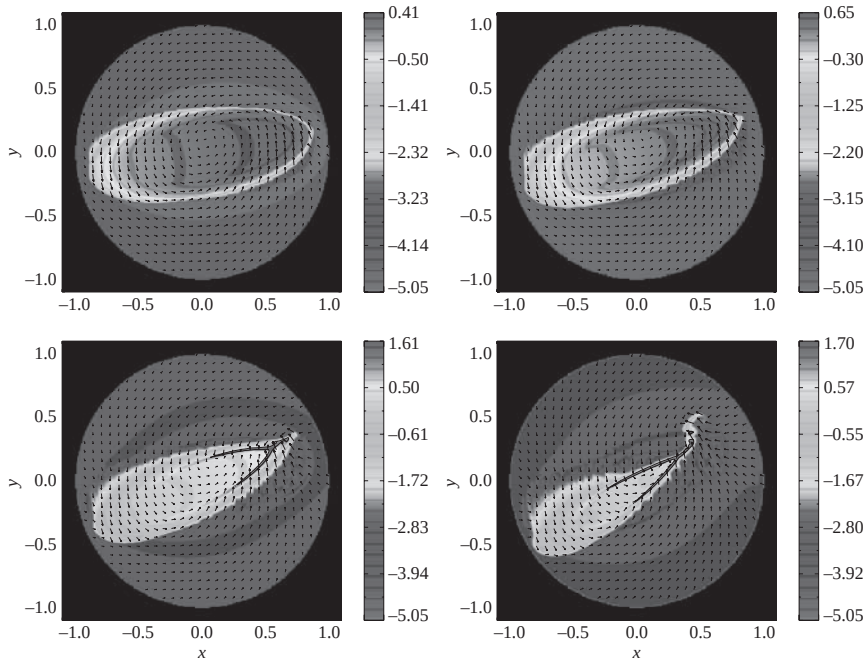

Fig. 2.11. Evolution of an elliptical sheet with rotation. The cloud begins contracting in the upper left panel, begins to form dense ridges as a result of the edge acceleration in the upper right panel (Figure 2.10), forms a filament at the upper/denser end of the sheet and a "wishbone" density structure, and finally forms dense blobs at the upper end and a twisted filament structure (compare with Figure 2.2). Scaling this isothermal model to the mass and size of the Orion A cloud, the entire evolution requires only 1.7 Myr. Modified from Hartmann and Burkert (2007).

bodies, considering both the crossing-time problem (§2.3) as well as the complexity and irregularity of their observed structure. Given that free-fall velocities are modestly higher than equilibrium velocities, "near-equilibrium" is not equivalent to equilibrium.

This picture of global collapse requires rapid dispersal of the molecular gas to avoid high star formation efficiencies and thus galactic star formation rates higher than observed (§2.2). However, the most luminous star in Orion A, θ^1 Ori C, is rapidly evaporating the molecular gas in its vicinity (O'Dell 2001), and will probably remove the neighboring molecular gas on a timescale of order 1 Myr. Furthermore, there are many examples of associations with large H I shells around them, representing in part the dispersal of molecular gas by the energy input of the massive stars (e.g., De Geus 1992), showing that this is a common occurence.

The collapse model for Orion A is neither unique nor conclusive, but it points out the need to consider the global effects of gravity in developing more realistic models of star-forming molecular clouds.

2.7 Turbulence and cloud structure

Molecular clouds exhibit turbulence on a variety of scales (e.g., Figure 2.2; Larson 1981; Elmegreen 1997; Falgarone *et al.* 1998), with supersonic motions seen on all but the smallest scales. These supersonic motions can shock and condense material, in principle

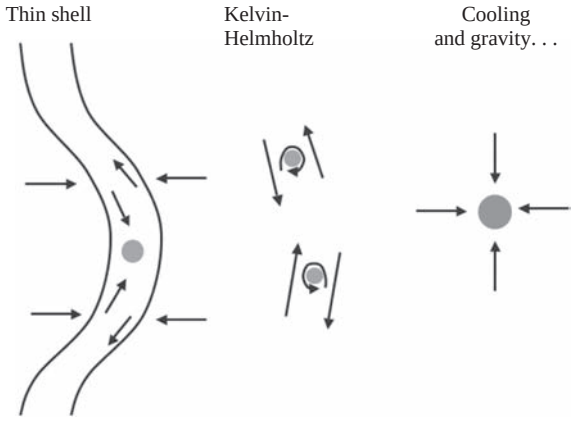

Fig. 2.12. Schematic illustration of some instabilities that molecular clouds may be subject to. Ripples in a thin post-shock region can be subject to the non-linear thin shell instability, which can concentrate material due to deflections in oblique shocked material. Kelvin–Helmholtz instabilities can also generate turbulence at shear flow interfaces. Finally, regions of overdensity can exhibit rapid or even runaway contraction due to thermal instability or rapid radiative cooling, leading to the formation of gravitationally unstable concentrations.

producing protostellar cloud cores. Some simulations assume that gravitational attraction becomes important only after flows have built up cores to a significant size, so that the core mass spectrum is mostly the result of turbulence (e.g., Padoan & Nordlund 1999; Klessen & Burkert 2000, 2001; Klessen 2001; Padoan *et al.* 2001). The adequacy of these assumptions is not clear because gravity is a long-range force and probably begins to operate quite early (Heitsch *et al.* 2008; Vazquez-Semadeni *et al.* 2007). Other simulations also assume an initial spectrum of velocity fluctuations but include gravity at all stages (Bate *et al.* 2002, 2003). The problem is that the precise nature of turbulent velocity and density fields present as initial conditions for the numerical simulations is far from clear.

A promising recent suggestion is that various instabilities are generated in the post-shock accumulating flow which produces the molecular cloud; these instabilities may then provide the seeds for star formation (Heitsch *et al.* 2005, 2006; Vazquez-Semadeni *et al.* 2007; Figure 2.12). As a specific example, Heitsch *et al.* (2005, 2006, 2007, and references therein) considered the formation of clouds as a result of colliding supersonic flows in the atomic interstellar medium. (One can apply this picture to the supersonic sweeping-up of material by transforming into the rest frame of the shock.) Heitsch *et al.* found that small perturbations of the shock interface lead to dynamical instabilities which concentrate mass; rapid cooling then leads to extreme concentrations (see also Hennebelle & Audit 2007 and Vazquez-Semadeni *et al.* 2007).

Figure 2.13 shows one such simulation of flows seen edge-on. The initial small perturbation of the interface (left panel) rapidly results in the formation of "fingers" of material which then contract due to thermal instability and other rapid cooling into large blobs of material. The resulting structure can be characterized as dense regions with subsonic internal motions surrounded by low-density regions with supersonic "turbulence" – with velocities smaller than that of the initial shock, but larger than that of the rapidly cooling postshock gas.

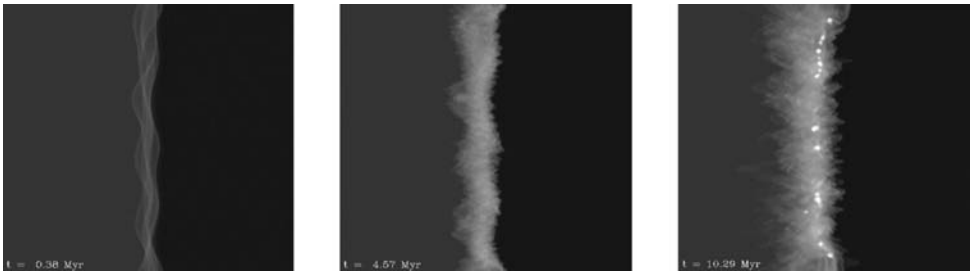

Fig. 2.13. Generation of turbulent substructure as a result of instabilities in post-shock gas produced by colliding flows, entering the computational box in the horizontal direction. The right-hand inflow has a higher density, intended to simulate the collision of swept-up dense material with lower-density atomic interstellar medium (e.g., Figure 2.4). Modified from Heitsch *et al.* (2007).

The outlines of these and similar calculations appear to be quite promising in explaining the observed structure of molecular clouds. What remains to be seen is whether the mass spectra of the gas clumps is consistent with the protostellar core mass function – can a relatively universal power-law distribution of core masses be produced from a turbulent cascade? While some simulations suggest that this is the case, limited dynamic range remains a difficulty. In addition, turbulence by itself is unlikely to produce a turnover in the stellar IMF (§1.2); what role do thermal effects play? What is the role of gravity in coalescing individual concentrations? Simulations in the near future may provide more conclusive answers to these questions.

3

Initial conditions for protostellar collapse

Low-mass stars tend to form in dense concentrations called "cores" in which the supersonic turbulent motions typical of molecular clouds are lowered or are suppressed in some fashion. In the limit that turbulence can be neglected, and thermal gas pressure is the principal force which counteracts gravity, the relationship between the mass $M_{\rm cl}$ and radius $R_{\rm cl}$ of a core in or near hydrostatic equilibrium is

$$\frac{GM_{\rm cl}}{R_{\rm cl}} \sim c_{\rm s}^2 = \frac{kT}{\mu m_{\rm H}}\,, \tag{3.1}$$

where $c_{\rm s}$ is the sound speed and $m_{\rm H}$ is the mass of the hydrogen atom. Taking a mean molecular weight $\mu = 2.3$, appropriate for molecular hydrogen plus helium, and a typical cold molecular cloud temperature of $T = 10\,{\rm K}$, equation (3.1) implies that a solar mass molecular cloud core must have a radius $R_{\rm cl} \sim 0.1\,{\rm pc}$. Encouragingly, observations suggest that many molecular cloud cores have roughly these properties. YSOs are detected as infrared sources within many cores, indicating that star formation proceeds rapidly once cores are formed.

The simple thermally supported model of molecular cloud cores is a useful limit. However, many cores are irregularly shaped, suggesting important departures from hydrostatic equilibrium. More generally, it appears to be difficult to produce truly static structures in molecular clouds, because thermal energy is not trapped efficiently, but instead is rapidly radiated away; this makes it difficult to build up gas-pressure forces except at very high densities on very small (essentially stellar) size scales. The short lifetimes of molecular cloud complexes discussed in the previous chapter imply rapid evolution and fragmentation, which also tends to suggest that cores are not generally in hydrostatic equilibrium, though internal motions are mostly subsonic.

It had been suggested that magnetic fields might provide the restraining forces necessary to slow dynamical evolution of clouds, rendering them more amenable to static or quasi-static treatments; however, observations and simulations suggest that magnetic pressures can modify, but generally do not strongly control, overall dynamics.

3.1 Molecular cloud cores

The properties of dense molecular gas clouds have mostly been inferred from observations of cm- and mm-wavelength spectral lines. Emission from the ^{12}CO molecule provides the most extensive and sensitive tracer of molecular gas, because the (much more abundant) H_2 molecule is difficult to observe directly except when heated by shocks or ultraviolet radiation fields. The lowest rotational spectral line transitions of ^{12}CO are usually

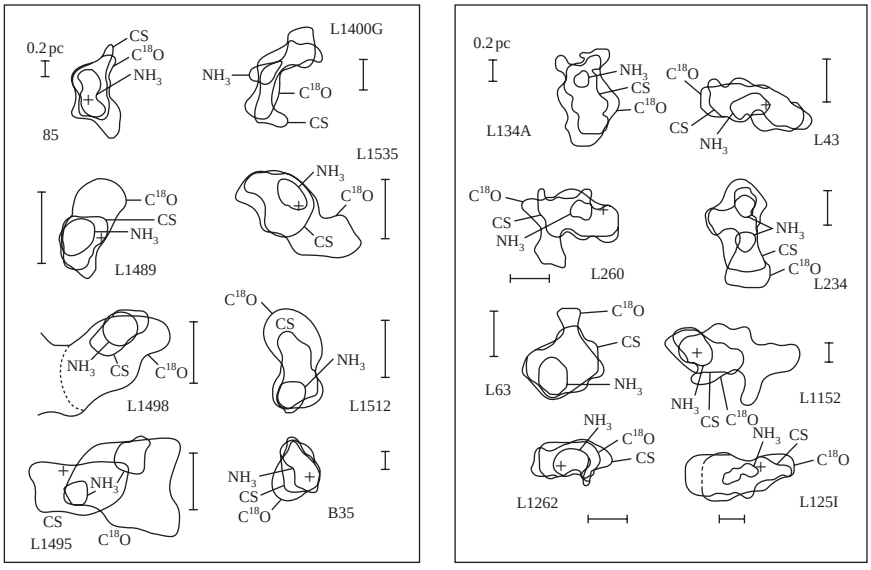

Fig. 3.1. Half-maximum intensity contours for a sample of dense molecular cloud cores, as observed in a variety of molecular species. For each core a linear dimension of 0.2 pc is indicated. Crosses indicate associated star (*IRAS* source). From Myers *et al.* (1991).

extremely optically thick in many molecular cloud regions, making it difficult to use these lines to study the densest regions of gas. It is necessary to use other tracers whose transitions are more strongly excited at high densities, such as NH_3 or CS, or to use rare isotopes of CO, which are less optically thick, to study dense molecular cloud cores.

Observations of molecular cloud cores in the $NH_3\,(J, K) = 1 - 1$ inversion transition in nearby star-forming regions (Myers 1983; Benson & Myers 1989) indicate typical molecular hydrogen number densities between 2×10^3 and 2×10^5 cm^{-3}, velocity dispersions between 0.2 and 0.9 km s^{-1}, and median masses $\sim 10\,M_\odot$. On the smallest scales, the velocity dispersions of these cores approach thermal values. The median size of these objects is a few $\times$ 0.1 pc (Figure 3.1).

The properties of cores depend somewhat on which molecular tracer is being used to define the object. Different species and transitions reflect differing density and temperature ranges (Zhou *et al.* 1989; Fuller & Myers 1993; Butner *et al.* 1995), and yield somewhat different results for velocity widths and sizes (e.g., Figure 3.1). In addition, chemical evolution can affect the appearance of cores in differing tracers (e.g., Bergin *et al.* 2002). Observations suggest that some of the smallest, least turbulent, protostellar molecular cloud cores are not very far from hydrostatic equilibrium (Myers & Goodman 1988b; Fuller & Myers 1992; Figure 3.2). It is difficult to prove this, however, since the difference in energy between static and unbound systems is only a factor of two, which is within the uncertainties in estimating masses, magnetic field pressures, appropriate velocity moments, appropriate geometry, etc.

Magnetic fields are difficult to measure in cloud cores; most observations are made in lower-density environments. For example, in one dark cloud in the Perseus molecular complex, B1, with a size $\sim$1 pc and an estimated average density $\sim 10^3$ cm^{-3}, the measured magnetic field is $\sim 30\,\mu$G (Goodman *et al.* 1989). Recent compilations of available

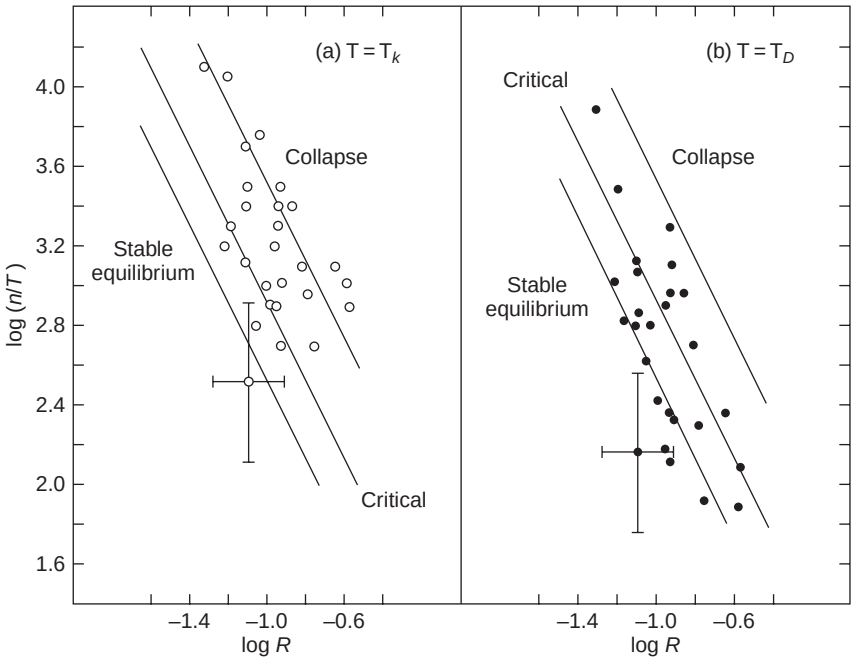

Fig. 3.2. Comparison of cloud core density, temperature, and radius with the requirements for hydrostatic equilibrium. The left-hand panel assumes that only thermal pressure supports the cloud, while the right-hand panel incorporates a pressure due to non-thermal motions indicated from the velocity widths of the spectral line profiles. The solid lines are based on a model of an isothermal pressure-bounded equilibrium sphere. Points above the upper line correspond to conditions for which no hydrostatic equilibrium is possible; the equilibrium is unstable if the data point lies above the middle line (§2.3). Typical estimated uncertainties for the data points are shown by the error bars. The results suggest that most cores are near equipartition of energies, but do not necessarily indicate equilibrium (§3.4). From Myers and Benson (1983).

results for molecular clouds (Crutcher 1999, 2005) suggest that magnetic field pressures are comparable to turbulent pressures, and that they are generally magnetically supercritical (self-gravity larger than magnetic forces; §2.4) by a small factor (also Bourke *et al.* 2001). More generally, it is suggested that the gravitational, magnetic, and thermal plus "turbulent motion" energy densities are roughly comparable (Myers & Goodman 1988a,b). On small scales in dense cores, the mass motions appear to be dominated by thermal motions and velocity dispersions are small (Myers & Goodman 1988b; Figure 3.3). In contrast, on large scales, velocity dispersions can be dominated by non-thermal motions (Larson 1981).

Most molecular cloud cores exhibit modest projected spatial velocity gradients corresponding to $\sim$0.3–3 km s^{-1} pc^{-1} (Goodman *et al.* 1993). At the upper end of this range, the rotation or shear at the outer edge of a cloud core of radius 0.1 pc would be $\sim$0.3 km s^{-1}, comparable to the thermal support velocity, but most clouds surveyed seem to have slower rotation than this. In general, rotation does not appear to provide much support for molecular cloud cores against their self-gravity.

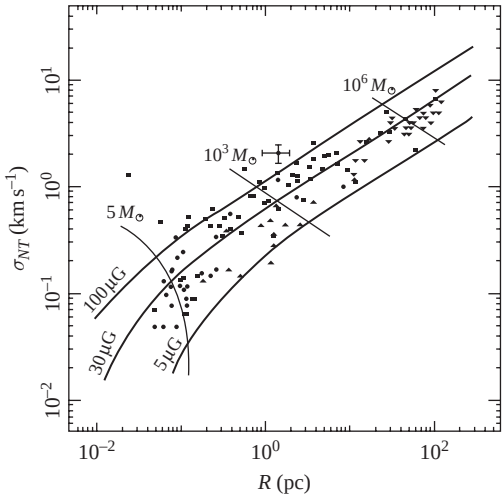

Fig. 3.3. Non-thermal velocity dispersion vs. size of cloud cores. The curves show predictions for energy equipartion models for an assumed gas temperature of 10 K (see following sections). Contours of constant mass and assumed magnetic fields are indicated. From Myers and Goodman (1988b).

Current surveys suggest that, at least in the Taurus molecular cloud complex, many known cores are associated with heavily extincted YSOs (Beichman *et al.* 1986). The high frequency of association of known cores with young stars indicates that many cores may be observed in a stage of collapse, because the star is presumably the result of some core material having collapsed already (Fuller 1994). It is not known whether all cores without stars will eventually form stars (e.g., Bonnell *et al.* 1996a).

Many molecular cloud cores seem to be elongated rather than spherical (e.g., Figure 3.1). The observed ratios of major to minor axes in Taurus core maps are ∼2 (Myers *et al.* 1991). Several studies have analyzed the observations in the context of a random distribution of inclinations to infer that cores are more nearly prolate than oblate (Myers *et al.* 1991; Jones *et al.* 2001; Curry 2002; Jones & Basu 2002), although their detailed structure is probably more complicated. As discussed in the previous chapter, the cores in Taurus are preferentially aligned along filaments (e.g., Figure 2.7), which almost certainly means that the cores themselves are more prolate than oblate (but in detail neither), and that this elongation is a remnant of their origin in filaments (Curry 2002; Hartmann 2002; §2.6).

3.2 Virial theorem and cloud stability

The classical analysis of gravitational stability of clouds starts by imagining cores to have reasonably well-defined outer boundaries. In its simplest form, the analysis proceeds using the virial theorem. The equations of momentum and mass conservation (e.g., Shu 1992; Appendix 1) can be combined to yield

$$\rho \frac{D\mathbf{v}}{Dt} = -\nabla P - \frac{1}{8\pi}\nabla B^2 + \frac{1}{4\pi}\left(\mathbf{B}\cdot\nabla\right)\mathbf{B} - \rho\nabla\phi\,. \tag{3.2}$$

Since

$$\frac{D^2 r^2}{Dt^2} = \frac{D^2 \mathbf{r}\cdot\mathbf{r}}{Dt^2} = 2\left(\dot{\mathbf{r}}\cdot\dot{\mathbf{r}} + \mathbf{r}\cdot\ddot{\mathbf{r}}\right), \tag{3.3}$$

taking the dot product of the momentum equation with the position vector $\mathbf{r}$, and integrating over a volume V which has a closed surface S, the left-hand side becomes

$$\frac{1}{2}\frac{D^2}{Dt^2}\int r^2 dm - \int dm\, v^2 = \frac{1}{2}\frac{D^2 I}{Dt^2} - 2E_{\rm k}, \tag{3.4}$$

where $E_{\rm k}$ is the bulk kinetic energy of the material and the D/Dt operator is the time derivative following the motion. The generalized moment of intertia, I, is the integral of r^2 over the mass element $dm = \rho dV$.

Because translational motion does not affect the basic analysis, we set $E_{\rm k} = 0$ and consider the volume to be at rest. After further manipulation and use of vector identities, we have the virial theorem,

$$\begin{aligned}\frac{1}{2}\frac{D^2 I}{Dt^2} = &\int_V dV\, 3P + \int_V dV\, \frac{B^2}{8\pi} - \int_S \left(P + \frac{B^2}{8\pi}\right)\mathbf{r}\cdot d\mathbf{S} \\ &+ \frac{1}{4\pi}\int_S (\mathbf{r}\cdot\mathbf{B})\,(\mathbf{B}\cdot d\mathbf{S}) - \int_V dV \rho \mathbf{r}\cdot\nabla\phi\,.\end{aligned} \tag{3.5}$$

The integrals are taken over the closed surface S or the volume V which is enclosed by S; the unit vector normal to the surface, d$\mathbf{S}$, is taken to be pointing outward. The first term on the right-hand side is a volume integral of the internal thermal energy, the second term is the magnetic energy, and the last term is the gravitational potential energy. The third and fourth terms constitute surface pressure effects; the magnetic field enters in two different ways because the force involved can be separated into pressure and tension terms (e.g., Priest 1984).

To apply this relation in a simplified way, consider the case of a spherical, isothermal, uniform, unmagnetized cloud in virial equilibrium, i.e., $D^2 I/Dt^2 = 0$. (Note that the adoption of uniform density is not consistent with hydrostatic equilibrium and thus violates the assumption of virial equilibrium, but this simplifies the problem to its essence.) The cloud has a radius $R_{\rm cl}$ and mass $M_{\rm cl}$, and the external medium exerts a pressure $P_\circ$ at its surface. With these assumptions equation (3.5) reduces to (Spitzer 1978)

$$4\pi R_{\rm cl}^3 P_\circ = 3c_{\rm s}^2 M_{\rm cl} - \frac{3}{5}\frac{G M_{\rm cl}^2}{R_{\rm cl}}\,, \tag{3.6}$$

where the term on the left-hand side of the equation results from the surface integral over the gas pressure in equation (3.5), the first term on the right-hand side of the equation is the integral of $3P$ over the volume, and the final term is the potential energy integral.

If the mass of the cloud and its internal temperature are fixed, equation (3.6) determines the equilibrium relationship between parameters. In the limit $R_{\rm cl} \to \infty$, gravitational forces become unimportant and equilibrium is established by a balance of the internal and external pressures. Decreasing $R_{\rm cl}$ increases the importance of gravity. For a given $M_{\rm cl}$ and $c_{\rm s}$, there is a minimum radius:

$$R_{\rm min} = \frac{1}{5}\frac{G M_{\rm cl}}{c_{\rm s}^2}\,, \tag{3.7}$$

below which there is no possible equilibrium state. This equation simply expresses the inability of thermal pressure forces to support a cloud against gravity if it is too small for its mass (e.g., equation (3.1)).

In practice this minimum radius is not the critical condition, because not all equilibria are stable. This can be seen by considering the relationship between the external pressure and the cloud radius in more detail. In equilibrium, the derivative of $P_\circ$ as a function of radius is

$$\frac{dP_\circ}{dR_{\rm cl}} = \frac{1}{4\pi}\left(-\frac{9c_{\rm s}^2 M_{\rm cl}}{R_{\rm cl}^4} + \frac{12}{5}\frac{GM_{\rm cl}^2}{R_{\rm cl}^5}\right) . \tag{3.8}$$

At large $R_{\rm cl}$, $dP_\circ/dR_{\rm cl} < 0$, so an increase in external pressure causes the radius of the cloud to shrink. However, there is a maximum external pressure in equilibrium, because equation (3.8) changes sign at a critical radius. The maximum pressure, from equation (3.8), occurs when the cloud has an equilibrium radius slightly larger than $R_{\rm min}$,

$$R_{\rm crit} = \frac{4}{15}\frac{GM_{\rm cl}}{c_{\rm s}^2} ; \tag{3.9}$$

the corresponding maximum pressure from equation (3.6) is

$$P_{\rm crit} = 3.15\frac{c_{\rm s}^8}{G^3 M_{\rm cl}^2} . \tag{3.10}$$

There is no possible equilibrium for pressures larger than this critical value. At lower pressures, collapse may still ensue if $R_{\rm cl} < R_{\rm crit}$. In this case, equation (3.8) shows that the equilibrium pressure must decrease with decreasing radius. This is an unstable equilibrium; for a fixed pressure, a perturbation decreasing the cloud radius will result in the external pressure being larger than the maximum equilibrium value, which will cause the cloud to contract further. The process runs away; the gas pressure becomes increasingly less important than gravity, and free-fall collapse eventually ensues, i.e., gravitational forces are essentially unopposed by pressure forces.

If we recast this critical condition in terms of the density $\rho_\circ$ of the uniform sphere and a "critical mass" $M_{\rm crit} = 4\pi R_{\rm cl}^3 \rho_\circ/3$,

$$M_{\rm crit} = \left(\frac{3}{4\pi}\right)^{1/2}\left(\frac{15}{4}\right)^{3/2}\left(\frac{c_{\rm s}^2}{G}\right)^{3/2}\rho_\circ^{-1/2} . \tag{3.11}$$

Thus the stability analysis can be transformed into a relationship between the mass of cloud and its internal density and temperature, in a form which differs only by constants of order unity from the Jeans mass relation (2.18). Equation (3.9) also may be converted into a more suitable form for comparison with observations,

$$\frac{\rho_\circ}{c_{\rm s}^2} = \frac{45}{16\pi G R_{\rm crit}^2} . \tag{3.12}$$

The lines labeled "critical" in Figure 3.2 approximate this relation. The observations of cloud cores suggest that many are near the critical equilibrium point (Myers & Benson 1983; Myers & Goodman 1988a,b; Benson & Myers 1989).

The existence of a maximum pressure for a cloud of given mass, or a minimum radius, arises from the assumption that the cloud internal temperature remains constant, and does not

increase under contraction. Observations and theory suggest that in typical density regimes, cloud temperatures do not vary much, and lie between about 12 K and ∼5 K (Goldsmith 1988; Boland & DeJong 1984; Cernicharo 1991; Shirley *et al.* 2005). If anything, cloud core interiors are likely to be colder than the outer layers (Hollenbach & Natta 1995; Bergin *et al.* 2006; Di Francesco *et al.* 2007, and references therein).

While this classical equilibrium analysis, like the Jeans mass, yields insights into the conditions favorable to cloud collapse, it is questionable whether it can be applied to real clouds in detail, given the difficulty in setting clear outer boundaries for some cores (e.g., Figure 3.1). Using a fixed external pressure is also problematic, since the supersonic turbulent motions observed in clouds probably dominate the pressure, and are difficult to estimate observationally, or are even ignored, leading to misleading conclusions (Ballesteros-Paredes *et al.* 1999).

3.3 Centrally concentrated clouds

The simple virial equilibrium analysis above assumed a uniform density cloud; however, such clouds are not in hydrostatic equilibrium, because there are no internal pressure gradients to balance gravity. A more appropriate equilibrium initial state can be found from solving the force balance equation. Assuming spherical geometry and no magnetic pressure, the equation of hydrostatic equilibrium is

$$\frac{dP}{dr} = -\rho \frac{GM_r}{r^2} \,, \tag{3.13}$$

where

$$\frac{dM_r}{dr} = 4\pi r^2 \rho \,. \tag{3.14}$$

For an isothermal cloud, these equations can be combined to yield

$$\frac{1}{r^2}\frac{d}{dr} r^2 c_s^2 \frac{d\ln\rho}{dr} \;=\; -4\pi G\rho \,. \tag{3.15}$$

Making the substitution $\ln(\rho/\rho_c) \equiv -u$, one arrives at the Lane–Emden equation

$$\frac{1}{\xi^2}\frac{d}{d\xi}\xi^2 \frac{du}{d\xi} = e^{-u} \,, \tag{3.16}$$

where $\xi = r/(c_s^2/4\pi G\rho_c)^{1/2}$ is the non-dimensional radial coordinate.

If ρ_c is taken to be the central density, then the boundary conditions of (3.16) are $u(0) = 0$ and $du/d\xi\,|_0 = 0$ (by symmetry). There is a family of solutions to this equation, known as Bonnor–Ebert spheres (Ebert 1955; Bonnor 1956), each distinguished by an outer radius ξ_1. The results of integrating the Emden equation are shown in Figure 3.4 for the case of critical stability (see p. 50). The limiting case, where $\xi_1 \to \infty$, is that of the singular isothermal sphere,

$$\rho = \frac{c_s^2}{2\pi G} r^{-2} \,, \tag{3.17}$$

which corresponds to an infinitely concentrated configuration. One may verify that this is a solution by direct substitution into equation (3.13). Equation (3.17) provides a convenient initial power-law density distribution which is often used in analyzing the collapse of protostellar clouds (§3.2).

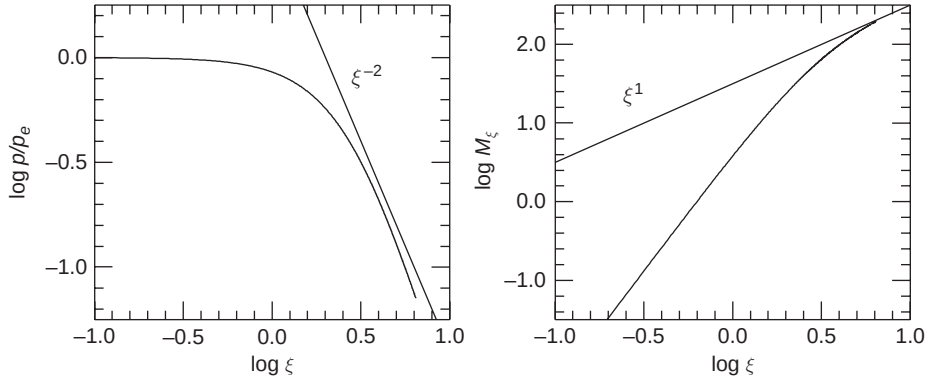

Fig. 3.4. Density and mass distributions for the critical Bonnor–Ebert sphere, i.e., with the maximum central concentration allowed by stability. The left-hand panel illustrates the density distribution with normalized radius ξ (see text), while the right-hand panel illustrates the mass enclosed within ξ. The dashed lines show the power-law dependence of the singular isothermal sphere for comparison.

Like the uniform sphere, the Bonnor–Ebert sphere also has a maximum external pressure or minimum stable radius for a given mass and temperature. The variation of P_o with $R_{\rm cl}$ for solutions of equation (3.16) has basically the same form as for the uniform cloud (3.8). The critical radius and pressure for the Bonnor–Ebert sphere exhibit the same parameter dependence as in the case of the uniform sphere, but with slightly different numerical coefficients (Spitzer 1968),

$$R_{\rm crit} = 0.41 \frac{G M_{\rm cl}}{c_{\rm s}^2} \,, \tag{3.18}$$

and

$$P_{\rm crit} = 1.40 \frac{c_{\rm s}^8}{G^3 M_{\rm cl}^2} \,. \tag{3.19}$$

Figure 3.4 illustrates the variation of density and mass with radius for this limiting solution. The density variation is similar to that of the singular isothermal sphere over roughly the outer half of the cloud. In the inner regions, the density approaches a constant. The central density is ∼5.8 times the mean density; this modest concentration explains why the limiting pressure for the critical Bonnor–Ebert sphere is not much different from that calculated with the simple uniform density assumption. (Note that the singular isothermal sphere is extremely unstable to infinitesimal perturbations, and thus cannot represent a realizable hydrostatic equilibrium.)

For a $1\,M_\odot$ cloud at $T = 10\,{\rm K}$, we have $R_{\rm crit} = 1.5 \times 10^{17}\,{\rm cm} \sim 0.05\,{\rm pc} \sim 10^4\,{\rm AU}$ and $P_{\rm crit} \sim 2 \times 10^{-11}\,{\rm dyne\,cm^{-2}}$. This external pressure is about an order of magnitude higher than typical interstellar medium pressures $P \sim 10^4\,{\rm k} \sim 1.4 \times 10^{-12}\,{\rm dyne\,cm^{-2}}$ (Elmegreen 1991). Whether internal pressure due, for instance, to turbulent motions can provide additional confining pressure is an open question, especially as such turbulence is likely to be anisotropic and time-dependent.

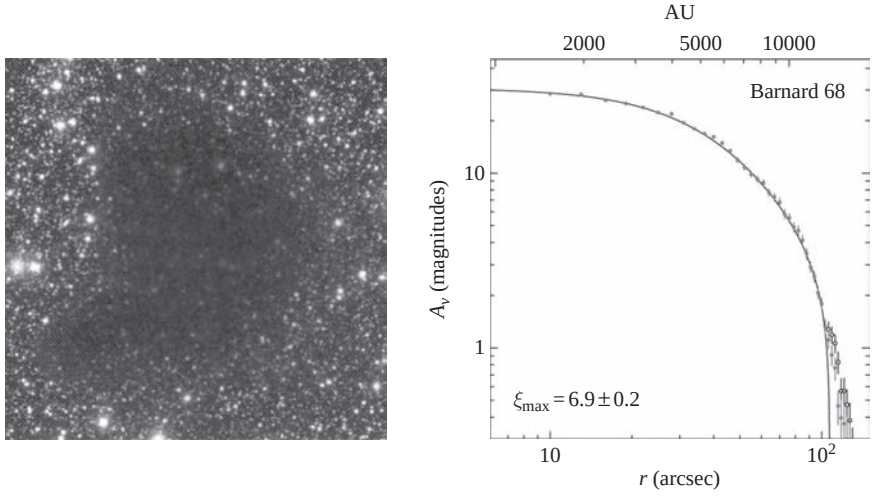

Fig. 3.5. Left panel: near-infrared image of the Bok globule B68. Right panel: azimuthally averaged column density, inferred from the extinction measurements, compared with a Bonnor–Ebert sphere of $\xi_{max} = 6.9 \pm 0.2$. From Alves *et al.* (2001).

As an application of the Bonnor–Ebert family of solutions, consider the molecular core (Bok globule) Barnard 68. B68 is an isolated object which does not lie within molecular material (left panel of Figure 3.5); probably it is situated within low-density warm atomic ISM, as envisaged in the boundary condition for Bonnor–Ebert spheres. Alves *et al.* (2001) derived column densities along the line of sight from near-infrared extinction measurements, and then compared the circularly averaged column density profile (ignoring the south-east projection) with Bonnor–Ebert solutions. As shown in the right panel of Figure 3.5, the measurements fit a slightly (gravitationally) supercritical object ($\xi_{max} \sim 6.9$) very well (the critical limiting value for stability is $\xi_c = 6.5$).

While the fit in Figure 3.5 is quite good, it should be emphasized that it was achieved by circular averaging, which minimizes the more complex structure of the actual object. To illustrate this in a graphic way, consider the "Bonnor–Ebert rectangle". Figure 3.6 shows how a filamentary distribution of mass can be turned into something qualitatively resembling a Bonnor–Ebert sphere by inappropriate circular averaging followed by misinterpreting the density distribution as that of a sphere. Circular averaging of a uniform density filament on scales less than the width of the filament will produce a flat central surface density; but on larger scales, the inferred surface density will behave as $\Sigma \propto r^{-1}$ because the mass grows as r while the area grows as r^2. Interpreting this surface density in terms of the volume density of a spherical object results in a flat inner density distribution and a spurious $\rho \propto r^{-2}$ on large scales. Averaging in this way produces a very powerful smoothing which can eliminate important features of the real object. While B68 is far from being a filament, circular averaging makes it look much more regular than it really is. Other cores are much more filamentary (Figure 3.7), and even more caution must be applied in analyzing their structure.

Studies of other, non-isolated molecular cloud cores often indicate a qualitatively similar density structure in the sense of having a central density plateau, with an outer falloff of

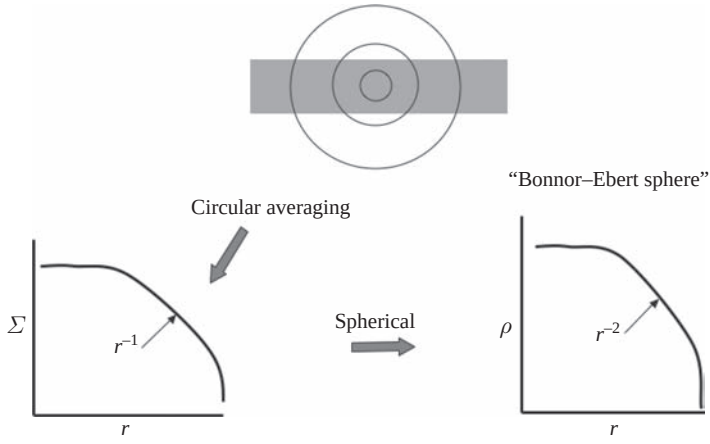

Fig. 3.6. Illustration of the dangers of assuming the incorrect symmetry. A filament (or rectangle on the sky, in the simplest terms) will show a uniform surface density on small scales by construction, but will have an apparent averaged surface density $\Sigma \propto r^{-1}$ if circularly averaged, because the mass will grow as r while the surface density grows as r^2. If one then makes the further mistake of interpreting the surface density in terms of a spherical distribution, the volume density requires a further factor of r in the outer regions, resulting in a presumed distribution $\rho \sim$ constant on small scales and $\rho \propto r^{-2}$ on large scales, resulting in an apparent Bonnor–Ebert-type structure where none is present.

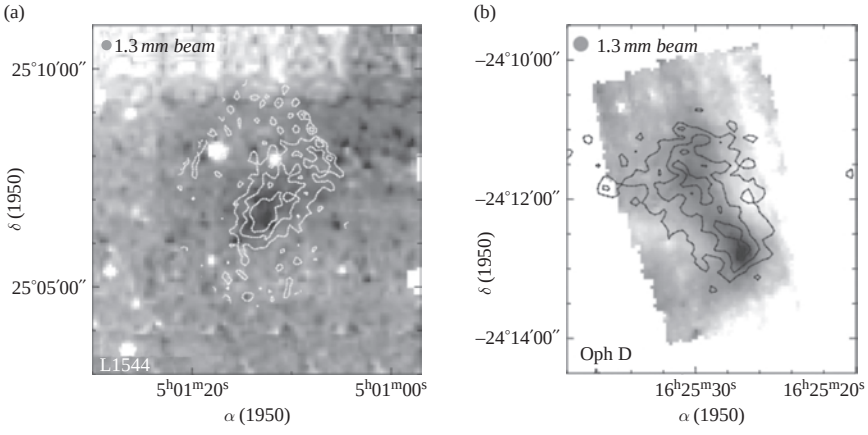

Fig. 3.7. Two starless cores, seen in exinction from ISO (grayscale) and 1.3 mm dust continuum (contours). From Bacmann *et al.* 2000.

density roughly comparable to r^{-2} (e.g., Bacmann *et al.* 2000; Figure 3.7). However, most cores are more irregularly shaped and more elongated than B68 (compare Figure 3.7 and Figure 3.1; see also Doty *et al.* 2005). Other analyses suggest that Bonnor–Ebert solutions are not strictly applicable to many cores, even after circular averaging (Harvey *et al.* 2003b, Kirk *et al.* 2005).

3.4 Core lifetimes and equilibrium

The virial stability analysis yields results within factors of order unity of the Jeans mass (equation 2.18), and the Bonnor–Ebert equilibrium models provide a reasonable starting point for analyzing molecular cloud cores. The broader question is: how relevant are equilibrium models for real cloud cores? The complex structures of many cores (Figures 3.1, 3.7) suggest that these objects are not in complete hydrostatic equilibrium. Even ignoring irregularities in morphology, the inference that most cores are more prolate or triaxial than oblate or spherical (§3.1) indicates shapes that are difficult to maintain in equilibrium (Curry 2002).

Observations of starless cores such as L1544 suggest inward motions, albeit subsonic, on scales of order $\sim$0.2 pc (Tafalla *et al.* 1998). This would seem inconsistent with an inside-out collapse model; such a widespread collapse would imply that a central star had already formed (see also Williams *et al.* 1999). Williams *et al.* 2006 showed that such indications of large-scale, slow infall are commonly present in starless cores, and made the very plausible suggestion that these motions are induced by the process of core formation. On the contrary, Ciolek and Basu (2000) argue that they can reproduce the observations of L1544 very well with a magnetically supported model, though they assume that it is being observed at a special epoch, when the core is just barely magnetically subcritical. Whether such models can explain the frequency of slow infall found by Williams *et al.* (2006) is an open question.

For equilibrium to be satisfied, cores must last for more than one dynamical timescale to "settle down" from their time-dependent, probably anisotropic, formation processes. The lifetimes of cores are generally estimated using statistical arguments. It is generally assumed that the protostellar phase (Class 0 plus Class I) lasts roughly one dynamical timescale, corresponding to essentially free-fall gravitational collapse (§4.1); then the ratio of starless cores to protostars yields the lifetime of the starless core phase in units of dynamical or free-fall times. The assumption of a dynamical timescale for the Class I phase is supported by studies in Taurus, where the 1:10 ratio of Class I objects to T Tauri stars, coupled with a median age of Taurus of 2 Myr, results in a Class I lifetime of order $\sim 2 \times 10^5$ yr, very consistent with theory (Kenyon *et al.* 1990, 1994).

Because incompleteness strongly affects results, studies of nearby star-forming regions are most conclusive. Initial studies of nearby star-forming regions indicated that about half of the known molecular cloud cores in Taurus contain YSOs (Beichman *et al.* 1986); this suggested that starless cores do not last more than one or two dynamical times. A survey of optically selected cores by Lee and Myers (1999) encompassing several regions estimated that approximately 1/3 of the cores have embedded YSOs, so that the starless core lifetime is approximately two dynamical timescales.

A detailed study of cores in Taurus and Ophiuchus by Kirk *et al.* (2005) suggests dense (sub-mm detected) core lifetimes of about 3×10^5 yr (see also Onishi *et al.* 2002). They estimated this is about $\sim$3 times the free-fall timescale, which might require a retarding force opposing gravitational collapse, possibly magnetic fields (see following sections). However, Kirk *et al.* use a "minimum central density" rather than an average (lower) density to estimate the free-fall timescale, which is likely to be an underestimate of the true collapse timescale (§4.1). Another estimate of the appropriate dynamical timescale is the time taken for a sound wave to pass across the core – the minimum time needed to establish hydrostatic equilibrium (assuming support is dominated by thermal pressure). Taking the median FWHM of the

longest projected core dimension in this sample, ∼0.05 pc, and using a typical sound speed of 0.2 km s^{-1} result in a median crossing time of ∼2.5 × 10^5 yr. Then the Kirk *et al.* results indicate persistence of sub-mm cores for little more than one dynamical timescale.

This example indicates some of the difficulties in making precise estimates of core lifetimes for the purposes of understanding whether they are truly equilibrium objects or not. Nevertheless, the weight of the evidence suggests that cores are generally not very dynamically old.

3.5 Stability of magnetized clouds

Magnetic fields can help support clouds against their self-gravity. To simplify the analysis, Spitzer (1978) assumed a uniform density spherical cloud with a uniform internal magnetic field. Spitzer also assumed that the cloud resides in a low-density medium of negligible mass, and that the magnetic field outside the cloud falls off as $B = B_{\rm cl}(R_{\rm cl}/r)^3$, which roughly reproduces the variation of energy density with radius in a dipole magnetic field. These assumptions make it possible to take a large control volume with a surface sufficiently far away that the magnetic surface terms are negligible. In general, these are not good assumptions for cores other than isolated objects like B68, because most cores are situated in regions of substantial molecular mass, with much more matter outside of cores than in cores. However, removing these assumptions does not change the essential behavior of the result.

Taking the bounding surface S to be far outside the cloud at a radius $R_{\rm b} \gg R_{\rm cl}$, the magnetic surface integral terms become negligible by assumption. Then the terms in equation (3.5) are

$$0 = 3c_{\rm s}^2 M_{\rm cl} + \int_{R_{\rm cl}}^{R_{\rm b}} dV\, 3P_\circ - 4\pi R_{\rm b}^3 P_\circ + \frac{1}{6} B_{\rm cl}^2 R_{\rm cl}^3 + \int_{R_{\rm cl}}^{R_{\rm b}} dV\, \frac{B^2}{8\pi} - \frac{3}{5}\frac{GM_{\rm cl}^2}{R_{\rm cl}} - \int_{R_{\rm cl}}^{R_{\rm b}} dV\, \rho r \nabla\phi\,. \tag{3.20}$$

The very last term in (3.20) can be written as $\int dM(r\nabla\phi)$, and since (again by assumption) the mass exterior to the cloud is negligible, we may set this term to zero. It is straightfoward to show that the integral of the magnetic energy density outside of the cloud equals the volume integral inside the cloud as $R_{\rm b}/R_{\rm cl} \to \infty$. Finally, the volume integral of the external pressure term outside the cloud is $4\pi P_\circ(R_{\rm b}^3 - R_{\rm cl}^3)$. With this result, equation (3.20) becomes

$$4\pi R_{\rm cl}^3 P_\circ = 3c_{\rm s}^2 M_{\rm cl} - \frac{3}{5}\frac{GM_{\rm cl}^2}{R_{\rm cl}} + \frac{1}{3} R_{\rm cl}^3 B_{\rm cl}^2\,. \tag{3.21}$$

When the gas is sufficiently conducting, the magnetic flux passing through a given parcel of gas remains constant (e.g., Priest 1984). This "flux-freezing" condition requires that the magnetic flux $\Phi_B = \pi R_{\rm cl}^2 B_{\rm cl}$ remains constant. Under this condition, the gravitational and magnetic terms in equation (3.21) both vary as $R_{\rm cl}^{-1}$, i.e., they remain in the same ratio. Thus, with magnetic flux freezing, if magnetic forces do not prevent collapse at one time, they will not be able to prevent collapse at any later time. Conversely, flux-freezing implies that clouds in which magnetic forces dominate (and therefore resist) gravity will always maintain this relationship and therefore gravitationally induced collapse cannot occur.

The gravitational energy term in equation (3.21) exceeds the magnetic energy term if the mass of the cloud is larger than a critical value, which depends upon the magnetic flux through the cloud,

$$M_B = \frac{1}{\pi}\left(\frac{5}{9G}\right)^{1/2}\Phi_B\,. \tag{3.22}$$

This result can also be written in terms of the mean density of the cloud ρ_c,

$$M_B = \frac{5^{3/2}}{48\pi^2}\frac{B_{cl}^3}{G^{3/2}\rho_c^2}\,. \tag{3.23}$$

Gravitational collapse can occur only if $M_{cl} > M_B$. As in the case of the non-magnetized sphere, the external pressure at the critical equilibrium point is

$$P_{crit} = \frac{3.15c_s^8}{G^3 M_{cl}^2[1-(M_B/M_{cl})^{2/3}]^3}\,. \tag{3.24}$$

Comparison with equation (3.10) illustrates the effect of the magnetic field in resisting collapse. Clouds with masses $>M_B$ are termed "magnetically supercritical"; those with masses $<M_B$ are called "magnetically subcritical".

More sophisticated calculations allowing departures from uniformity and sphericity (which must be present since the magnetic field is not isotropic) have been made which exhibit the same basic behavior as this simple model, but differ modestly in numerical coefficients. Calculations of flattened, centrally condensed, equilibrium clouds suggest that equation (3.22) is more accurately written as (Mouschovias & Spitzer 1976)

$$M_B \sim \frac{0.13}{G^{1/2}}\Phi_B\,. \tag{3.25}$$

From equation (3.25) we find immediately that the maximum magnetic flux that a $1\,M_\odot$ cloud core can have and still contract gravitationally is $4\times10^{30}\,\mathrm{G\,cm^2}$; for a typical cloud core of radius $\sim$0.1 pc, the critical field strength is $B\sim10\,\mu$G.

Alternatively, we may write

$$M_B \sim 3.5\times10^{-3}\frac{B_o^3}{G^{3/2}\rho_c^2} \approx 70\ M_\odot\left(\frac{B_{cl}}{100\,\mu\mathrm{G}}\right)^3\left(\frac{N_{H_2}}{10^4\,\mathrm{cm^{-3}}}\right)^{-2}, \tag{3.26}$$

where we have assumed that the gas is entirely composed of molecular hydrogen and has a mean molecular weight of 2.3. At typical cloud core densities $10^4\,\mathrm{cm^{-3}}$, a $M_{cl}\sim1\,M_\odot$ core will be able to collapse only if $B_{cl}\lesssim20\,\mu$G. With this magnetic field, and assuming an internal core temperature of 10 K, the ratio of gas pressure to magnetic pressure is $\beta = \rho_c c_s^2/(B_{cl}^2/8\pi)\sim1$, i.e., the magnetic energy (pressure) is roughly in equipartion with the thermal energy (pressure).

3.6 Ambipolar diffusion of magnetic flux

The classical view of low-mass star formation recognized the potential of magnetic fields to prevent gravitational collapse. However, the effects of magnetic fields can be reduced if the field is not perfectly "frozen" to the gas. The large extinctions through a molecular cloud core can prevent the ultraviolet radiation field of the galaxy (or of the nearby hot stars) from penetrating into the core interior. These radiation fields photoionize

species, and the resulting ions help couple the gas to the magnetic field. In a dark cloud interior, where the external ionizing radiation fields do not penetrate, the ion fraction drops to very low values. Although the ions are "frozen" to the magnetic fields by the Lorentz force (e.g., Priest 1984), the neutral species are not. The neutrals are affected by the magnetic field only indirectly through collisions with ions, which are following the field. If the frequency of collisions between ions and neutrals is sufficiently low, as may occur in dark cloud cores, the neutral gas can "slip" through the field lines on interesting timescales. In principle, this process of "ambipolar diffusion" represents a means by which the molecular gas can be slip through the field lines; gravity pulls material mass in through the resisting magnetic field, concentrating the cloud as the magnetic field is slowly "left behind".

To illustrate this process in an approximate way, we follow Spitzer (1978) in considering an infinite cylinder of uniform density molecular gas. We distinguish between the neutral particles, which have a mass density $\rho_n = n_n m_{\rm H} \mu$, where μ is the mean molecular weight, and the ions, which have a number density n_i. Assuming the neutral particles comprise most of the mass, Gauss' law (e.g., Priest 1984) applied to the cylindrical configuration yields the gravitational force per unit mass

$$-\nabla\phi = 2\pi\, R\, G\rho_n\,, \tag{3.27}$$

where ϕ is the gravitational potential and R is the distance measured from the cylinder's axis. For simplicity we assume that the magnetic field is responsible for providing the balancing force against gravity. In this situation the neutrals do not directly feel the magnetic restoring force, but are affected indirectly by collisions with the ions, which are tied to the field. The momentum transfer to the neutrals from the ions is

$$\rho_n\,(n_i\ <u\sigma>)\,w_D\,, \tag{3.28}$$

where u is the relative velocity (assumed to be a thermal or random velocity) between ions and neutrals, σ is the collisional cross-section, and w_D is the drift velocity of the neutrals relative to the ions. The term in brackets is the net collision rate. Balancing this force against gravity, and solving for a characteristic diffusion time,

$$t_D \equiv \frac{R}{w_D} = \frac{<u\sigma>}{2\pi G m_{\rm H}\mu}\left(\frac{n_i}{n_{\rm H}}\right)\,, \tag{3.29}$$

where we have scaled the neutral density in terms of the density of hydrogen atoms n_H. Often $<u\sigma>$ varies slowly with temperature. Taking $<u\sigma> \sim 2\times10^{-9}\,{\rm cm^3\,s^{-1}}$,

$$t_D \sim 5\times10^{13}\left(\frac{n_i}{n({\rm H_2})}\right)\,{\rm yr}\,, \tag{3.30}$$

now incorporating a scaling to the number density of neutral hydrogen molecules $n({\rm H_2})$ since these are likely to be the dominant constituents of regions where ambipolar diffusion may be applicable. It is clear that the ambipolar diffusion process will be important for star formation only if $n_i/n({\rm H_2}) \lesssim 10^{-7}$. Typical estimates based on cosmic-ray ionization of the molecular gas suggest $n_i/n({\rm H_2}) \sim 10^{-7}(n({\rm H_2})/10^4\,{\rm cm^{-3}})^{-1/2}$ (McKee 1989). Thus it appears that in conditions representative of molecular cloud cores, ambipolar diffusion can remove a substantial amount of magnetic flux over timescales of $\sim 10^7$ yr (see also Umebeyashi & Nakano 1990).

3.7 The magnetic flux "problem(s)"

The idea of a magnetic flux "problem" in star formation dates to Mestel and Spitzer (1956), who pointed out that the (then) recent recognition of galactic interstellar magnetic fields in the diffuse ISM implied critical masses of order $10^3\ M_\odot$ (using equation 3.26), and then argued ambipolar diffusion had to take place before clouds of stellar mass could collapse. This idea was developed by Shu and coworkers (e.g., Shu *et al.* 1987 and references therein; also Nakano 1984 and Mouschovias 1991) into a detailed picture of slowly evolving magnetically supported cloud cores. The diffusion time was assumed to be much longer than the free-fall time (see previous section); thus, this model predicted slow star formation in relatively long-lived molecular clouds, explaining the low rate of galactic star formation.

As discussed in Chapter 2, current observational evidence suggests that molecular clouds are not long-lived; that the onset of star formation closely follows cloud formation; and that the low rate of galactic star formation is the result of low efficiency rather than slow evolution. In addition, as discussed previously in this chapter, the irregular, complex structure observed for nearby cores strongly suggests they are not equilibrium, long-lived objects, consistent with the evidence for short lifetimes discussed in §3.4. Thus, the modern evidence suggests that ambipolar diffusion is either not needed or provides only a small delay prior to cloud collapse. What happened to all the magnetic flux?

As discussed in §2.4, simulations of the large-scale flow of material in the ISM show that cloud masses tend to be accumulated along magnetic flux tubes; that is, the mass is concentrating along the field, increasing mass-to-flux ratios naturally. This mechanism was dismissed by Mestel and Spitzer (1956), who argued that the length over which mass needed to be accumulated from the diffuse ISM (hundreds of pc) would greatly exceed the Jeans length and thus the medium would fragment into "sub-cylinders". However, the accumulation of material from the diffuse ISM occurs in supersonic flows, which are not describable by Jeans analyses. In any event, it is worth noting that giant molecular clouds, as a whole, are thought to be magnetically supercritical (McKee 1989; McKee & Ostriker 2007); the increase in the mass-to-flux ratio from the diffuse ISM cannot be due to ambipolar diffusion, given the high ionization state of the medium; instead, it must be the result of flow along field lines, with possibly some enhancement due to reconnection.

The fundamental reason why massive clouds, both observationally and theoretically (e.g., Figure 2.6), tend to be magnetically supercritical can be seen schematically from the terms in equation 3.21. A magnetically subcritical cloud, by definition, is one in which the final term on the right-hand side (the magnetic term) exceeds in magnitude the second term on the right-hand side (the self-gravitational term). To attain anything close to equilibrium, the external pressure (left-hand side of the equation) *must* be sufficiently large *to prevent the cloud from expanding*. Adding in the internal thermal support term (or, in real clouds, any turbulent or rotational or shearing motions) makes the demand on the external pressure even worse. A substantially subcritical cloud requires an external pressure of the same order as the gravitational acceleration to confine the cloud; otherwise it will simply expand away (see Figure 3.8). Invoking external turbulent pressure confinement is problematic, given its general time-dependence and anisotropy. Invoking a strong external magnetic field to provide the confinement simply displaces the problem of rooting the magnetic fields in gas to larger scales.

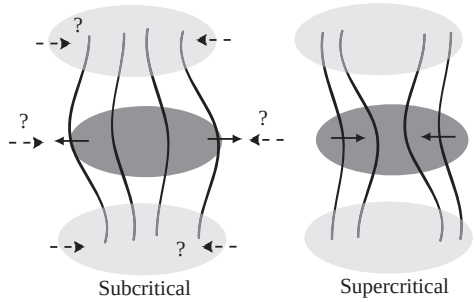

Fig. 3.8. Schematic illustration of the difficulty with making subcritical dense cloud regions (left figure). Because the internal pressure (magnetic plus gas) exceeds gravity, there must be some confining pressure to prevent the cloud from expanding. As by definition the surroundings are less dense, and therefore of lower thermal pressure, there must be in general some kind of external turbulent or magnetic pressure (dashed arrows) to confine the cloud. Providing this high external pressure using low-density regions is problematic. On the contrary, supercritical clouds can be held together by gravity, without the need for confining pressure in the outer, lower density regions (right panel).

Note also that, given the tendency of material to collapse along field lines, one would expect clouds to be elongated perpendicular to the field; this would require the confining pressure to be applied at the elongated ends of the cloud to prevent expansion. Such a requirement is hardly credible given, for instance, the morphology of the Orion clouds (Figures 2.1, 2.2). On the contrary, if massive molecular clouds are magnetically supercritical, then gravity can hold the cloud together without requiring a dynamically significant external pressure. This is why molecular clouds are estimated to be supercritical, given typical estimates of pressures in the surrounding ISM.

A globally supercritical cloud must have more mass in supercritical regions than subcritical regions, by definition. One might expect that subcritical regions would tend to resist collapse, so that the supercritical regions would be the ones to form stars, at least first; and as star formation is rapid, these most favorable sites would constitute the majority, or even all, of the star formation.

Recent attempts to retain aspects of the ambipolar diffusion picture show that the observational constraints may be explained if cores are only slightly subcritical initially (e.g., Ciolek & Basu 2001). In other words, if the amount of magnetic flux that must be lost is small, the ambipolar diffusion timescale is reduced by a similar amount, to the point where it has at most a modest impact on evolutionary timescales. Whether this is an important modification to the overall picture of cloud core evolution and collapse is an open question. In the context of near-critical clouds, turbulent motions may play some role in removing magnetic flux from subregions (Fatuzzo & Adams 2002; Nakamura & Li 2005).

Sometimes another stellar magnetic flux "problem" is considered. The critical magnetic flux for a $0.5\,M_\odot$ star, $\Phi_B \sim 2 \times 10^{30}\,\mathrm{G\,cm^2}$, corresponds to a magnetic field of $\sim 3 \times 10^7\,\mathrm{G}$ at the radius of a typical pre-main-sequence star. Current estimates for T Tauri stars suggest much lower stellar surface magnetic fields, a few kG (Basri, Marcy, & Valenti 1992). In the absence of diffusive or reconnective processes, this stellar field strength implies a very low magnetic field strength at the point of cloud core collapse; once the collapse gets underway,

the free-fall time is so much shorter than the diffusion time that the magnetic field is effectively dragged in with the gas (e.g., Galli & Shu 1993a,b). It is implausible that ambipolar diffusion continues until the magnetic flux is three or four orders of magnitude below values that would permit collapse (Mouschovias 1991). Other processes which occur after collapse must be responsible for the low magnetic fields of T Tauri stars.

One possibility is that the magnetic field decouples from the infalling material because of the decrease in ionization fraction at high densities; calculations suggest this may occur in the very innermost regions of the collapsing cloud, where densities are $\sim 10^{10}$–10^{12} cm^3 (Umebeyashi & Nakano 1990). In addition, magnetic reconnection may play an important or even dominant role in reducing the magnetic flux which remains in pre-main-sequence stars. If most of the mass of stars is accumulated by accretion from a circumstellar disk, as seems very likely (Chapter 4), the bulk of magnetic field loss could occur through reconnection and diffusion in the disk. However, the details of this evolution in magnetic flux passing through the disk are very complicated and uncertain (e.g., Shu *et al.* 2006).

Early theoretical investigations of star formation emphasized the potential role of the magnetic field of the molecular cloud in solving the "angular momentum problem" (Ebert *et al.* 1960; Mestel 1965) by transferring core angular momentum to the external cloud. However, many observed molecular cloud cores do appear to retain significant angular momentum, in amounts that are not important in supporting the core against gravity (Goodman *et al.* 1993), but are much larger than would permit collapse to stellar dimensions.

Once dynamical collapse begins, the angular momentum should be retained (because the free-fall time is necessarily comparable to or shorter than the angular momentum transport time; Shu (1995)). This retention of angular momentum during collapse now does not seem to be a problem for two reasons: first, the outcome of collapse must in general be a binary system (at least for stars of solar and larger masses); and second, *accretion disks* are present around many young stars. As discussed in Chapters 7–9, observed disks are likely to posess enough angular momentum to solve much of the angular momentum "problem" for star formation.

4

Protostellar cloud collapse

The developments described in the previous chapter suggest that molecular cloud cores may evolve into gravitationally unstable configurations, because of the inability of the cloud cores to heat up as they contract. One may anticipate the general nature of the collapse for a thermally supported spherical molecular cloud core by estimating that the initial infall velocity should be of the order of the free-fall velocity from the outer cloud radius,

$$v_{\rm in} \sim \left(\frac{GM}{R}\right)^{1/2} \sim c_{\rm s}\,; \tag{4.1}$$

therefore, the collapse time is of order $t_{\rm in} \sim R/c_{\rm s}$ and the mass infall rate is

$$\dot{M} \sim \frac{M}{t_{\rm in}} \sim \frac{c_{\rm s}^3}{G}\,. \tag{4.2}$$

The collapse can be halted basically for one of two reasons. First, if the gas temperature increases to the point that the sound speed is comparable to the escape velocity, the thermal pressure will become large enough to combat gravity. Numerical simulations indicate that this can occur only on distance scales much smaller than the initial cloud, where the optical depths become large enough to trap the radiant energy released by infall. It is likely that in many cases a second reason is more important in stopping collapse, namely the angular momentum of the infalling material, which causes it to fall out onto a rotating disk, a possible site for the formation of multiple stars as well as planets.

In this chapter we review some simple physical models for collapsing protostellar clouds. The predictions of these and similar models are compared with observations of likely protostars in Chapter 5.

4.1 Free-fall collapse of a uniform cloud

The simplest model one might imagine of a molecular cloud core is that of a spherical cloud of uniform density. As discussed in Chapter 2, cloud cores can become gravitationally unstable because the internal pressure forces can no longer balance gravity. As a limiting case, consider the collapse of a uniform, spherical cloud with no gas pressure to counteract gravity. The equation of motion of a shell of material which starts at radius $r_\circ$ is

$$\frac{d^2r}{dt^2} = -\frac{GM_r}{r^2} = -\frac{4\pi G\rho_\circ r_\circ^3}{3r^2}\,, \tag{4.3}$$

where $\rho_\circ$ is the initial density and M_r is the mass interior to radius r. Here we have taken advantage of Newton's result that, for a spherical mass configuration, only the mass interior to the point in question has any gravitational effect. Multiplying through by dr/dt and

integrating once with respect to time, and then making the substitution $r/r_\circ = \cos^2\beta$, the resulting solution is

$$\beta + \frac{1}{2}\sin 2\beta = \left(\frac{8\pi G\rho_\circ}{3}\right)^{1/2} t\,, \tag{4.4}$$

where t is the time from the beginning of the collapse (when $r = r_\circ$).

At a given time t, β is fixed no matter what the original starting radius $r_\circ$ was. Therefore, the shells do not cross, and they all reach the center at the (same) "free-fall" time,

$$t_{\rm ff} = \left(\frac{3\pi}{32G\rho_\circ}\right)^{1/2} \sim \frac{3.4\times 10^7}{N_{\rm H_2}^{1/2}}\ {\rm yr}\,, \tag{4.5}$$

where $N_{\rm H_2}$ is the number density of molecular hydrogen in a gas of solar composition.

A $\sim$1 $M_\odot$ cloud core in hydrostatic equilibrium maintained by thermal pressure support at $\sim$10 K has a radius of approximately 0.1 pc (Chapter 2). If for some reason the supporting gas pressure were "turned off", equation (4.5) implies a free-fall time of $\sim 5\times 10^5$ yr. Even with pressure forces retarding the infall, it is clear that the protostellar collapse phase is likely to be fairly rapid.

The free-fall result also helps provide some insight into the Jeans stability results of Chapter 2. The pressureless collapse calculation becomes increasingly relevant on the largest scales, where pressure forces are relatively unimportant. Because the free-fall time scales as $t_{\rm ff} \propto \rho_\circ^{-1/2}$, a (pressureless) uniform density sphere collapses with material from all radii arriving at the center simultaneously. This means that the outermost radii must fall in fastest, i.e., must have the fastest growth rates, as illustrated by the dispersion relation for the standard Jeans analysis.

4.2 Similarity solution for collapse

The simple free-fall collapse discussed above is not directly applicable to the general problem of protostellar collapse, because pressure forces are likely to be important initially. Numerical solutions of protostellar cloud collapse have been presented by Larson (1969a,b), Appenzeller and Tscharnuter (1974), Bodenheimer (1978), Winkler and Newman (1980a,b), Boss and Black (1982), and others. If considered in its full generality, the problem is made difficult by the need to treat both the very large scales of the initial cloud and the very small scales of the resulting stellar core, placing great demands on the accuracy of numerical solutions (see Tscharnuter 1991). Moreover, the collapse of real clouds must have many complicating factors which are difficult to incorporate. It is therefore worth developing simple models which illustrate the basic features of collapse.

As discussed in §2.5, the density distribution in the outer layers of an isothermal sphere in hydrostatic equilibrium approaches $\rho \propto r^{-2}$. This approach to a power-law density distribution suggests that (ignoring the inner regions) one might find a similarity solution for the collapse. In a similarity solution, non-dimensional functions for properties like the density and velocity field can be used to describe the motion at any time by some appropriate scaling. The tendency of the numerical calculations to adjust to a (roughly) self-similar structure led Larson (1969a), Penston (1969), Hunter (1977), and Shu (1977) to develop similarity solutions for the infall problem. Of course, any similarity solution for protostellar collapse must fail at early and late times, when the influence of inner and outer boundary conditions

must be felt; however, the mathematical simplicity of such solutions leads to a basic understanding of many essential physical features. We follow Shu's (1977) elegant development for the singular isothermal sphere (SIS) to illustrate the basic physics of the problem in a particularly simple and straightforward way.

Before considering the mathematical details it is useful to outline the qualitative properties of the collapse solution. If the cloud density initially has the singular form $\rho \propto r^{-2}$, then the mass interior to r is $M_r \propto r$. The free-fall time (equation (4.5)) scales as the inverse square root of the mean density, so one might guess that the mass M_r will fall in to the center after an elapsed time $t(r) \approx t_{\rm ff} \propto <\rho>^{-1/2} \propto r$. Therefore, the total amount of mass that has fallen to the center should increase linearly with time, i.e., the mass infall rate should be constant. The inner regions should collapse first because they have the shortest free-fall times (highest densities), while the outer parts of the cloud take longer to fall in. Since the mass that has already fallen in increases linearly with time, and the cloud mass increases linearly with the radius r, this "inside-out" collapse results in a free-fall zone within the original cloud whose radial extent expands linearly with time.

Now consider the detailed similarity solution. The usual equation of mass conservation in spherical symmetry,

$$\frac{\partial \rho}{\partial t} + \frac{1}{r^2}\frac{\partial}{\partial r} r^2 \rho u = 0 \,, \tag{4.6}$$

where u is the radial velocity, can be transformed into an alternative form in terms of M_r,

$$\frac{\partial M_r}{\partial t} + u\,\frac{\partial M_r}{\partial r} = 0 \,, \quad \frac{\partial M_r}{\partial r} = 4\pi r^2 \rho \,. \tag{4.7}$$

The momentum equation for isothermal flow is

$$\frac{\partial u}{\partial t} + u\frac{\partial u}{\partial r} = -\frac{c_s^2}{\rho}\frac{\partial \rho}{\partial r} - \frac{G M_r}{r^2} \,. \tag{4.8}$$

The similarity solution assumes that the outer and inner boundary conditions are unimportant, and so the only dimensional quantities in the problem are G, c_s, r, and t. Dimensional analysis gives the similarity variable $x = r/c_s t$. Then one looks for solutions of the form

$$\rho(r,t) = \frac{\alpha(x)}{4\pi G t^2} \,, \qquad M_r(r,t) = \frac{c_s^3 t}{G} m(x) \,, \qquad u(r,t) = c_s v(x) \,, \tag{4.9}$$

where α, m, and v are non-dimensional functions of the coordinate x, and the solution is subject to the boundary condition that at $t = 0$ the mass of the core $M_r(0,t) = 0$.

The equations of motion can be written in terms of the similarity variable x through suitable transformations. For the radial coordinate, the transformation is

$$\frac{\partial}{\partial r} = \frac{1}{c_s t}\frac{\partial}{\partial x} \,. \tag{4.10}$$

The partial time derivative for the similarity solution is to be taken at a constant x, which is moving with respect to the Eulerian coordinate system r. Thus, the required transformation is

$$\frac{\partial}{\partial t_r} = \frac{\partial}{\partial t_x} - \frac{x}{t}\frac{\partial}{\partial x} \,. \tag{4.11}$$

Using these relations, equations (4.7) can be written as the ordinary differential equations

$$m - (x - v)\frac{dm}{dx} = 0 \,, \quad \frac{dm}{dx} = x^2 \alpha \,, \tag{4.12}$$

or

$$m = x^2 \alpha (x - v)\,. \tag{4.13}$$

Equations (4.7) and (4.8) can be transformed into two coupled first-order differential equations,

$$[(x-v)^2 - 1]\,\frac{1}{\alpha}\,\frac{d\alpha}{dx} = (x-v)\left[\alpha - \frac{2(x-v)}{x}\right], \tag{4.14}$$

$$[(x-v)^2 - 1]\,\frac{dv}{dx} = (x-v)\left[\alpha(x-v) - \frac{2}{x}\right]. \tag{4.15}$$

An extended description of the properties of these equations is given in Shu (1977). Here we present a limited discussion, focussing on the collapse problem. One exact analytic solution of these equations is given by

$$v = 0, \quad \alpha = \frac{2}{x^2}, \quad m = 2x\,. \tag{4.16}$$

This corresponds to the singular isothermal sphere, which is static but unstable. If the velocities are initially small, i.e., if $v \to 0$ as $x \to \infty$, the asymptotic behavior of equations (4.13)–(4.15) is

$$\alpha \sim \frac{A}{x^2}\,, \quad v \sim -\frac{(A-2)}{x}\,, \quad m \sim Ax \text{ as } x \to \infty\,. \tag{4.17}$$

Here A is a constant which must be >2 for v to be negative, as required for infall. This asymptotic solution has the same power-law form for the density as the singular isothermal sphere, but if $A > 2$ there is no balance between gravity and pressure forces and so collapse begins everywhere.

One solution of particular interest is $A = 2 + \epsilon$, $\epsilon \ll 1$, so that the cloud is nearly in hydrostatic equilibrium for $x \geq 1$. A numerical solution for $A = 2.0005$ is shown in Figure 4.1, which was obtained by integrating the two equations (4.14) and (4.15) simultaneously inward. By taking $A > 2$, the outer envelope is not precisely in hydrostatic equilibrium, but the velocities for $x > 1$ are so small as to be negligible. As $\epsilon \to 0$ the external velocities become arbitrarily small, but then a singularity near $x = 1$ must be considered (see p. 64).

The principal properties of this solution can be outlined as follows. At small distances, expansion of the equations shows that

$$m \to m_\circ, \quad \alpha \to \left(\frac{m_\circ}{2x^3}\right)^{1/2}, \quad v \to -\left(\frac{2m_\circ}{x}\right)^{1/2} \text{ as } x \to 0\,. \tag{4.18}$$

For $\epsilon \to 0$ the core mass is $m_\circ = 0.975$. Since the total mass contained in the region $x \leq 1$ is $m(1) = 2$ (equation (4.16)), about 49% of the mass is in the core, while the rest is still falling in. From the scaling of equation (4.9), the central mass is

$$M_r(0,t) = 0.975\frac{c_s^3 t}{G}\,, \tag{4.19}$$

and so the limiting mass infall rate is constant,

$$\dot{M} = 0.975\frac{c_s^3}{G}\,. \tag{4.20}$$

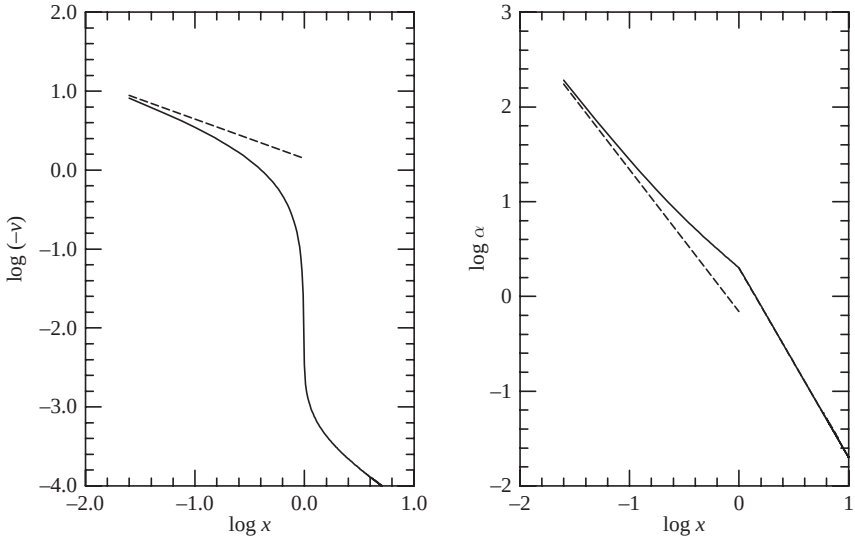

Fig. 4.1. Similarity solution for the collapse of the singular isothermal sphere, adopting the constant $A = 2.0005$ (see text). The left-hand panel exhibits the non-dimensional velocity, while the right-hand panel exhibits the non-dimensional density α. The dashed lines correspond to the case of free-fall (pressureless) collapse at a constant rate onto a core containing all the mass.

Equations (4.18) show that in the innermost regions, the self-gravity of the envelope is negligible in comparison with the gravitational field of the central mass. Because the gas pressure is also relatively unimportant in impeding the (supersonic) collapse at small radii, the infall velocity approaches the free-fall velocity $v_{\rm ff} \approx (2GM/r)^{1/2}$ (indicated as a dashed line in the left-hand panel of Figure 4.1). The density of the infalling material approaches

$$\rho_i \approx \frac{\dot{M}}{4\pi r^2 v_{\rm ff}} = \frac{c_{\rm s}^3}{4\pi r^2 G v_{\rm ff}}\,, \tag{4.21}$$

and so $\rho_i \propto r^{-3/2}$ (dashed line in the right-hand panel of Figure 4.1) because the mass infall rate is constant.

These equations have a critical point at $x - v = 1$. In the present case, the limiting solution approaches a critical point $x \sim 1$. Discussions of the significance of critical points can be found in Shu (1977) and Hunter (1977). In general, the presence of critical points depends upon the specific initial conditions adopted.

This simple similarity solution can be exploited to understand the time dependence of the infall. The variable x is transformed to physical radial distance r by $r = c_{\rm s} t x$. Therefore, at time t, the position $x = 1$, which corresponds to the boundary between the hydrostatic and infall regions (Figure 4.1), lies at $r = c_{\rm s} t$ (Figure 4.2). The mass initially contained within this radius r is $M_r = 2c_{\rm s}^3 t/G$; of this amount, $m_\circ c_{\rm s}^3 t/G$ has already fallen into the center, and the rest is in the infall region. The physical interpretation of this behavior is as follows: the collapse begins first in the inner regions, because they are densest and therefore have the shortest free-fall times. As the material in the inner region falls in, the pressure support of the overlying layers is removed, allowing these to fall in as well. Because of exact spherical

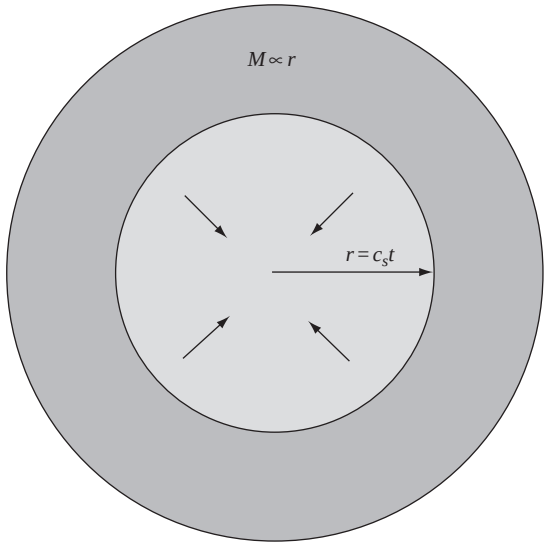

Fig. 4.2. Schematic diagram of purely spherical, "inside-out" similarity collapse. If the initial cloud is centrally condensed, the innermost regions collapse first because they are densest and have the shortest free-fall times. The outermost regions remain nearly unchanged because they cannot respond on short timescales, and because the spherical collapse of mass to a central point does not affect the gravitational force on large scales. As collapse proceeds, a region of radius $r = c_s t$ becomes evacuated as the material originally in this region falls onto the central mass.

symmetry, the gravitational field seen by the external material is unaffected by the collapse of inner regions. Thus, the information that inner layers have fallen in is communicated to the outer layers only by a rarefaction wave, which moves outward at the sound speed c_s. The amount of mass per unit time that loses its pressure support and begins to fall is constant, because the rarefaction wave radius is $r = c_s t$ and the isothermal sphere mass grows linearly with r (Figure 4.2).

As a specific example, we follow Shu (1977) in envisaging a cloud core of pure molecular hydrogen at 10 K bounded by an external pressure of 1.1×10^5 cm^{-3} K, which implies an initial mass 0.96 $M_\odot$ and $r = 1.6 \times 10^{17}$ cm. For a sound speed of 0.2 km s^{-1}, the expansion wave takes 2.5×10^5 yr to reach the outer boundary of the cloud, at which point 49% of the total mass has fallen in. Beyond this point in time, the similarity solution is clearly not applicable because of the effects of the boundary. In particular, one expects a compression wave to form at the outer boundary and steepen into a shock as it propagates into the interior, so the details of the infall will change from the similarity solution.

4.3 Generalized models of protostellar collapse

While the SIS similarity solution presented by Shu (1977) provides a particularly clear and elegant way of conceptualizing the basic physics of the gravitational collapse, the hydrostatic singular isothermal sphere does not represent a realizable state because it is intrinsically unstable (e.g., Whitworth *et al.* 1996). Moreover, similarity solutions must fail

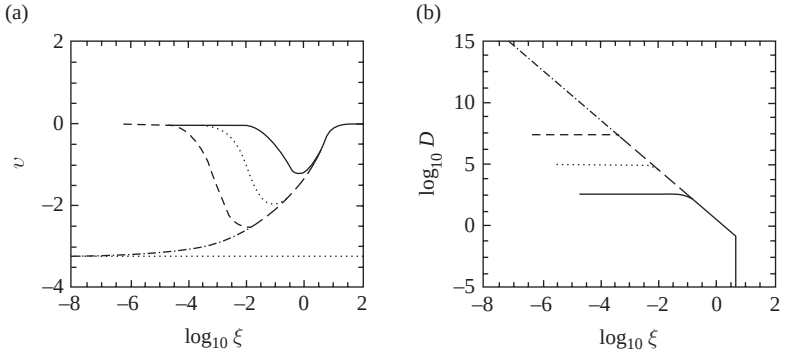

Fig. 4.3. Velocities (left) and densities (right) in the collapse of the critical isothermal sphere as a function of radius at four early times. The velocity v is measured in units of the isothermal sound speed. The density is $D = \rho/\rho_c$ and $\xi = r/(c_s^2/4\pi G\rho_c)^{1/2}$ (§3.3). The collapse begins at large radii and eventually forms a central core, with an infall velocity approaching that predicted by the Larson–Penston similarity solution (horizontal line). From Foster and Chevalier (1993).

at early and late times when the boundary conditions are important. The resulting collapse can differ from the SIS solution in interesting ways.

The collapse of isothermal Bonnor–Ebert spheres, with flattened inner density distributions, cannot be represented by similarity solutions. Foster and Chevalier (1993) followed the gravitational collapse of isothermal spheres numerically and showed some of the qualitative differences that arise from non-self-similar structure. As shown in Figure 4.3, collapse of the *critical* Bonnor–Ebert sphere (§3.3) begins on the outside; the contraction is not inside-out. The initial collapse of material to the center exhibits a velocity structure which more nearly resembles the Larson–Penston similarity solution. Finally, the mass infall rate as a function of time is not constant, as shown in Figure 4.4; at the moment of central core formation, the infall rate is very high, and decreases as the collapse proceeds, falling to near zero in a time $\sim(2/3)(R_{\rm crit}/c_s)$.

The qualitative differences between this solution and the SIS similarity solution can be understood using developments in the previous two chapters. The Jeans instability (§2.5) is stronger on large scales, where pressure support becomes less important; this explains why the infall starts at large radii. The Larson–Penston (Larson 1969a,b; Penston 1969) similarity solutions were developed for the collapse of a uniform density sphere; because the critical Bonnor–Ebert sphere has a nearly constant density in its inner regions, the Larson–Penston solution is more appropriate for the infall velocity in the early stages after core formation. The free-fall collapse of the constant density sphere results in all shells reaching the origin at the same time, formally corresponding to an infinite infall rate over an infinitely short time; this is why the Bonnor–Ebert sphere, with its flat inner density distribution, has a higher initial infall rate than the SIS similarity solution (see discussion in Henriksen *et al.* 1997).

Foster and Chevalier (1993) showed that the evolution of spheres with higher central concentration ($\xi_{\rm max} \gtrsim 20$; see §3.3) is closer to that of the SIS similarity solution, as would be expected. However, such highly concentrated objects are highly unstable to perturbations, and observations of real pre-stellar cores suggest that their inner density distributions are much flatter than the SIS model.

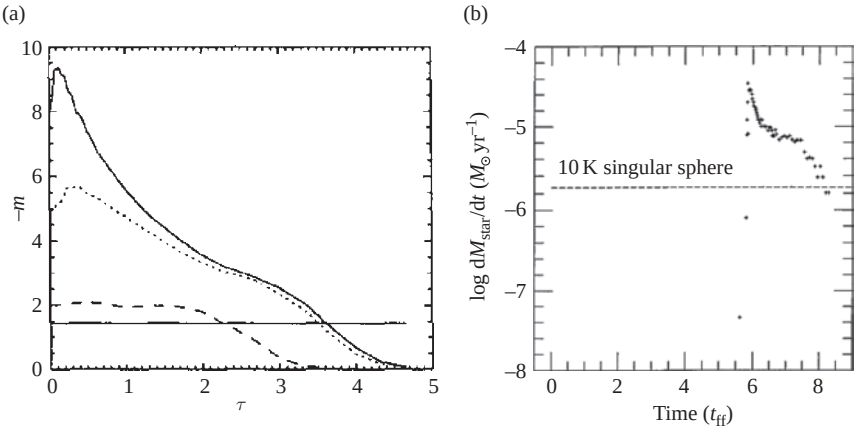

Fig. 4.4. Left: Mass infall rates $\dot{m} = Dv\xi^2$ as a function of time for the collapse of the critical isothermal sphere, measured at three radii: $\xi = 0.3$ (solid line), $\xi = 1.0$ (dotted line), and $\xi = 3$ (dashed line). The non-dimensional time is $\tau = t(4\pi G\rho_c)^{1/2}$. The infall rates are much higher than that predicted by the SIS similarity solution (horizontal line) at early times; they fall below the SIS solution at late times. From Foster and Chevalier (1993). Right: Infall rates for the collapse of the isothermal sheet. Once core formation occurs, the behavior of mass infall rate vs. time is very similar to that of the critical isothermal sphere. From Hartmann *et al.* (1994b).

The effects of magnetic fields may also be important. Galli and Shu (1993a,b) found little difference in mass infall rates for modest magnetic support. The qualitatively different feature of the Galli and Shu model is the development of what they called a "pseudodisk" in the equatorial plane. The pseudodisk arises because the magnetic field threading the spherical outer cloud tends to deflect infalling material away from the radial direction. Assuming axisymmetry, the deflected material from one hemisphere shocks with material coming in the opposite direction from the other hemisphere, resulting in a pile-up of material in the equatorial plane some distance from the central mass. Since this pseudodisk is not rotationally supported (see §4.6), it must fall in toward the star. Decoupling of the interstellar magnetic field from the inner infalling envelope might cause a "pile-up" of magnetic flux, which could also have important dynamical effects (Li & McKee 1996; see also Shu *et al.* 2007).

As discussed in Chapter 2, if gravitational fragmentation makes cloud cores, the initial conditions for cloud collapse will differ from both the singular isothermal sphere and the Bonnor–Ebert sphere. One situation which might be envisioned is fragmentation from a non-rotating isothermal sheet initially in hydrostatic equilibrium (Hartmann *et al.* 1994b), which might be taken as one of the simplest cases of the non-spherical initial cloud structure observed in nature, and which may be essential in the fragmentation of gas into multiple systems (Bonnell *et al.* 1991; Boss 1993; Nelson & Papaloizou 1993) (although a cylindrical initial condition would probably be more appropriate).

As shown in the right-hand side of Figure 4.4, a finite isothermal sheet initially in hydrostatic equilibrium, with just slightly larger than one Jeans mass, eventually collapses in a manner very similar to that of the critical Bonnor–Ebert sphere. The central mass infall rate in this simulation is never constant, but exhibits a "plateau" phase with an infall rate

approximately three times that predicted by the Shu (1977) similarity solution for the singular isothermal sphere. In fact, a comparison with the critical isothermal sphere results shows a very similar pattern of mass infall rate with time; apparently the details of the geometry are not that crucial. It can be shown from dimensional arguments that the mass infall rate for this simulation scales as c_s^3, just as in the Shu similarity solution (Hartmann *et al.* 1996). In general, model cores with flat inner density distributions exhibit initial peaks in infall rates, followed by a slower phase of mass accumulation (e.g., Henriksen *et al.* 1997).

To summarize, collapse models which include additional effects – stable initial equilibrium conditions, magnetic fields, non-spherical initial structure – exhibit many general features in common with the Shu (1977) similarity solution for the singular isothermal sphere; however, there are significant differences in the mass infall rate, which varies substantially as a function of time. The principal qualitative differences produced by magnetic forces and non-spherical initial structure are in the geometry of the collapse; magnetic forces may produce a large-scale collapsing pseudodisk, while initial flattening of the parent cloud core produces relatively evacuated cavities in the infalling envelope, increasing the observability of protostars at short wavelengths (Chapter 5).

4.4 Rotating collapse

As discussed in §2.7, if collapse occurs on a dynamical timescale, it is unlikely that the angular momentum remaining in the cloud core at the start of rapid collapse can be transferred efficiently to the external medium. The large size of the initial cloud core implies that even modest initial rotational velocities will cause the infalling material to land first on a rotationally supported disk rather than a pressure-supported star. In general, the disk may be sufficiently massive to break up or fragment into stars (Yorke *et al.* 1993; Bonnell & Bate 1994; Laughlin & Bodenheimer 1994; see review in Boss 1995). Here we concentrate on the simpler case where the disk mass does not affect the infall pattern. The simplest analysis of rotating collapse assumes that pressure forces are negligible and so the problem can be analyzed using ballistic trajectories. The results for the case of the collapse of a spherically symmetric cloud in uniform (solid-body) rotation were initially worked out by Ulrich (1976), with subsequent extension by Cassen and Moosman (1981) to disk formation and by Terebey *et al.* (1984; hereafter TSC) to the collapsing singular isothermal sphere.

Before developing the mathematical solution it is again worth making an initial estimate of its overall properties. For simplicity assume a fixed central mass of M. If material with specific angular momentum h falls in and ends up in a circular orbit while maintaining its angular momentum, then the radius R of the circular orbit is

$$R = \frac{h^2}{GM} \,. \tag{4.22}$$

In the similarity solution for "inside-out" collapse, all the material which arrives at the center at a given instant of time started from the same initial cloud radius r_o. If the protostellar cloud core is initially in uniform rotation, with angular velocity Ω, then the specific angular momentum at r_o varies with the angle θ from the rotation axis as $h = \Omega r_o^2 \sin\theta$. Thus, material falling in from different directions will have different angular momenta and arrive at the midplane (the plane perpendicular to the rotation axis) at differing radii. Material near the rotation axis will fall in close to the central star because it has low angular momentum, while mass falling in from regions near $\theta \sim \pi/2$ will fall in to a maximum "centrifugal radius"

$$r_c = r_o^4 \frac{\Omega^2}{GM} \,. \tag{4.23}$$

This material arriving at $\theta \sim \pi/2$ from "above" will collide with material arriving at the same position from "below"; this infall produces a flat structure with rotation, i.e., a disk (see § 4.6).

Now we proceed to the detailed solution. For simplicity we assume that essentially all of the mass is contained in the center, that the gas falls in from a very large distance with essentially zero total energy, so that the motion is approximately parabolic. This free-fall approximation neglects pressure forces and the mass of the inner envelope, which can be justified from the inner limits of the similarity solution (4.18).

For two-body parabolic motion around a central gravitating mass, the equation of the particle orbit in its own plane is

$$r = \frac{h^2/GM}{1 - \cos\alpha} \,, \tag{4.24}$$

where α is the direction angle of the particle measured from the origin to apastron, and h is specific angular momentum. We define θ_o as the angle between the orbital plane and the rotation axis of the system (see Figure 4.5).

The transformations to convert from (r, α) in the orbital plane to (r, θ, ϕ) are

$$\cos\theta = \cos\theta_o \, \cos\alpha \tag{4.25}$$

and

$$\tan\phi = \frac{\tan\alpha}{\sin\theta_o} \,. \tag{4.26}$$

From the standard solution for the two-body problem,

$$u \equiv \frac{1}{r} = \frac{GM}{h^2} (1 - \cos\alpha) \,, \tag{4.27}$$

$$\dot{\alpha} = hu^2 \,, \tag{4.28}$$

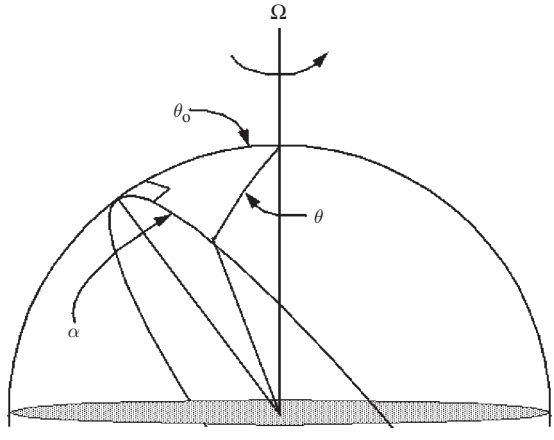

Fig. 4.5. Geometry of rotating collapse solution (see text).

$$\dot{r} = -\frac{\dot{u}}{u^2} = -\frac{\mathrm{d}u}{\mathrm{d}\alpha}\frac{\dot{\alpha}}{u^2} = -\frac{GM}{h}\sin\alpha\,, \tag{4.29}$$

so that

$$h = [GMr\,(1\,-\,\cos\alpha)]^{1/2}\,. \tag{4.30}$$

The radial velocity is

$$v_r = \dot{r} = -\left(\frac{GM}{r}\right)^{1/2}\left(1+\frac{\cos\theta}{\cos\theta_\circ}\right)^{1/2}\,. \tag{4.31}$$

The meridional velocity is given by

$$v_\theta = r\dot{\theta} = r\frac{\mathrm{d}\theta}{\mathrm{d}\alpha}\dot{\alpha} = \frac{h}{r}\frac{\mathrm{d}\theta}{\mathrm{d}\alpha}\,, \tag{4.32}$$

which can be rearranged to the form

$$v_\theta = \left(\frac{GM}{r}\right)^{1/2}(\cos\theta_\circ - \cos\theta)\left(\frac{\cos\theta_\circ + \cos\theta}{\cos\theta_\circ\,\sin^2\theta}\right)^{1/2}\,. \tag{4.33}$$

Finally, the azimuthal velocity is

$$v_\phi = r\sin\theta\dot{\phi} = r\sin\theta\left(\frac{\mathrm{d}\phi}{\mathrm{d}\alpha}\right)\dot{\alpha} = \frac{h}{r}\sin\theta\frac{\mathrm{d}\phi}{\mathrm{d}\alpha}\,, \tag{4.34}$$

which after some manipulation can be written as

$$v_\phi = \left(\frac{GM}{r}\right)^{1/2}\left(1-\frac{\cos\theta}{\cos\theta_\circ}\right)^{1/2}\frac{\sin\theta_\circ}{\sin\theta}\,. \tag{4.35}$$

It is straightforward to verify that $v^2 = v_r^2 + v_\theta^2 + v_\phi^2 = 2GM/r$.

The quantity h is the specific angular momentum measured around the axis perpendicular to the orbital plane. It is convenient to introduce the specific angular momentum of the particle relative to the overall cloud rotation axis,

$$H_l = h\sin\theta_\circ\,. \tag{4.36}$$

Then the trajectory of the particle is given by

$$r = \frac{H_l^2}{\sin^2\theta_\circ}\frac{1}{GM(1-\cos\alpha)} = \frac{H_l^2}{\sin^2\theta_\circ}\frac{1}{GM(1-\cos\theta/\cos\theta_\circ)}\,. \tag{4.37}$$

The particle lands on the (thin) disk at $\theta = \pi/2$, at a radial distance

$$r(\pi/2) = \frac{H_l^2}{\sin^2\theta_\circ\,GM}\,. \tag{4.38}$$

For the ballistic solution to be valid, one requires that the streamlines of particles with different $\theta_\circ$ do not intersect; otherwise, shocks would result. It is clear from equation (4.38) that $H^2/\sin^2\theta_\circ$ must be a monotonically increasing function over $0 \le \theta_\circ \le \pi/2$ to avoid such intersections.

One simple rotation law which satisfies this condition is

$$H_l^2 = r_\circ^4\Omega_\circ^2\sin^4\theta_\circ\,, \tag{4.39}$$

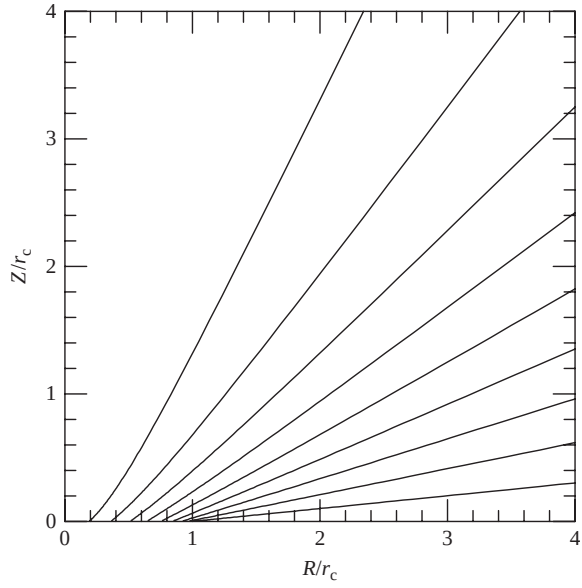

Fig. 4.6. Streamlines for the rotating collapse solution described in the text. Distance scales for the polar axis z and the cylindrical radius R are given in units of the centrifugal radius r_c. The streamlines shown are in steps of 0.1 in $\cos\theta_\circ$, with the lowest streamline for $\cos\ \theta_\circ = 0.9$. Since equal intervals in $\cos\theta_\circ$ correspond to equal intervals of mass in the outer cloud, the tendency of the material to pile up at the outer edge of the initial disk ($R \sim r_c$) is evident.

which corresponds to uniform rotation of a sphere of radius $r_\circ$ at an angular velocity $\Omega_\circ$. Defining $r_c = r_\circ^4 \Omega_\circ^2 / GM$, the particle trajectories in the meridional plane can be written as

$$\frac{r}{r_c} = \frac{\sin^2\theta_\circ}{1\ -\ \cos\theta/\cos\theta_\circ}\,. \tag{4.40}$$

Figure 4.6 shows the streamlines of particles in the meridional plane, which are labeled by $\theta_\circ$. With the assumption of solid-body rotation, particles falling near the rotational axis have little angular momentum, and thus fall nearly radially. Particles with larger $\theta_\circ$ have larger angular momentum and thus fall to the disk at larger radii. All of the streamlines intersect the disk plane interior to r_c.

The density can be evaluated by assuming that the mass infall rate is steady. If $r_\circ >> r_c$, $\cos\theta \approx \cos\theta_\circ$ (equation (4.40)) and the flow is radial. Assuming that the cloud at $r_\circ$ is nearly spherical, the mass flow in a flow tube spanned by $d\theta_\circ$ is

$$d\dot{M} = \frac{2\pi r^2 \sin\theta_\circ\, d\theta_\circ\, \dot{M}}{4\pi r^2} = \frac{1}{2}\sin\theta_\circ\, d\theta_\circ\, \dot{M}\,. \tag{4.41}$$

The density at r, θ can be found by following the streamlines corresponding to $\theta_\circ$ and $\theta_\circ + d\theta$,

$$\rho = \frac{d\dot{M}}{2\pi r^2 \sin\theta\, d\theta\, |v_r|} = \frac{1}{2\pi r^2 \sin\theta\, |v_r|}\left(\frac{d\dot{M}}{d\theta_\circ}\right)\left(\frac{d\theta_\circ}{d\theta}\right)\,. \tag{4.42}$$

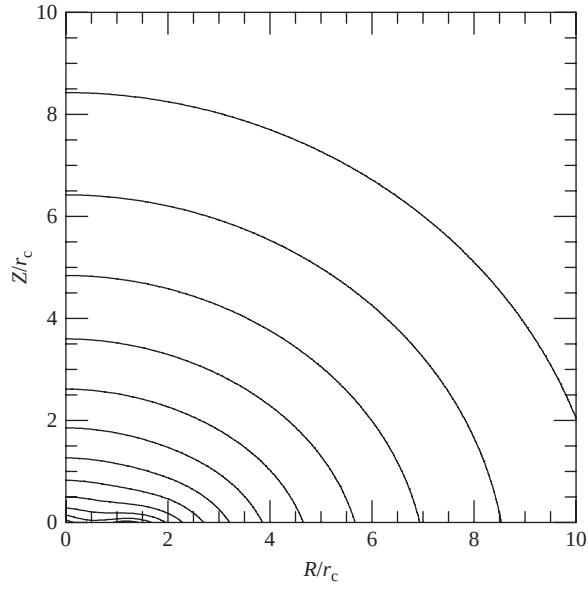

Fig. 4.7. Contours of constant density for the rotating collapse solution. Distance scales for the polar axis z and the cylindrical radius R are given in units of the centrifugal radius r_c. Each contour represents a factor of $2^{1/2}$ difference in density, with the outer contours representing the lowest densities. The flattening of the density distribution near the disk is evident.

Using equations (4.31) and (4.40), this becomes

$$\rho = \frac{\dot{M}}{4\pi(GMr^3)^{1/2}}\left(1+\frac{\cos\theta}{\cos\theta_\circ}\right)^{-1/2}\left(\frac{\cos\theta}{\cos\theta_\circ}+\frac{2\cos^2\theta_\circ}{r/r_c}\right)^{-1}. \tag{4.43}$$

In Figure 4.7 we show contours of constant density in a meridional plane for this infall solution. The density is nearly spherically symmetric at large distances, where the effects of rotation are small. At distances $\lesssim r_c$, the density distribution becomes quite flattened, as material falls non-radially onto the disk. This behavior can be seen directly from equation (4.43) in its limits. For $r \gg r_c$, $\theta \to \theta_\circ$, and

$$\rho \sim \frac{\dot{M}}{4\pi(2GM)^{1/2}} r^{-3/2}, \tag{4.44}$$

which is precisely the density distribution for free-fall at a constant mass infall rate toward a point mass M. For $r \ll r_c$, the streamlines are nearly vertical and so $\cos\theta_\circ \approx 1$; therefore,

$$\rho \sim \frac{\dot{M}}{8\pi r_c(GM)^{1/2}}(1+\cos\theta)^{-1/2} r^{-1/2}. \tag{4.45}$$

This limit of equation (4.43) illustrates an important effect of rotation on the infall density distribution; inside r_c, the density increases less rapidly with decreasing radius than the $\rho \propto r^{-3/2}$ expected for spherically symmetric collapse. To emphasize the point, we consider

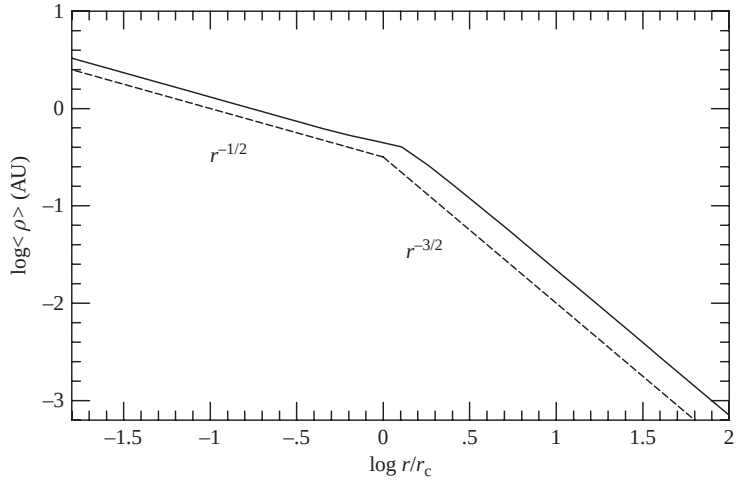

Fig. 4.8. The spherically averaged density distribution of the rotating collapse solution as a function of radial distance in units of the centrifugal radius r_c. The dashed lines denote pure power-law distributions of $r^{-1/2}$ and $r^{-3/2}$ for comparison. The density distribution follows the spherical free-fall result outside of r_c, but departs at smaller radii as material falls onto the disk.

the spherical average of the density distribution, i.e., the average density at a given radius r, which can be written as (Adams & Shu 1986)

$$< \rho(r) >= \int_0^{\pi/2} \rho(r,\theta) \sin\theta d\theta = Cr^{-3/2} A\left(\frac{r}{r_c}\right) , \tag{4.46}$$

where

$$A(u) = (2u)^{1/2} \ln\left[\frac{1+(2u)^{1/2}}{(1-u)^{1/2}+u^{1/2}}\right], u \leq 1 ; \tag{4.47}$$

$$A(u) = (2u)^{1/2} \ln\left[\frac{1+(2u)^{1/2}}{(2u-1)^{1/2}}\right], u \geq 1 , \tag{4.48}$$

with $u = r/r_c$ and $C = \dot{M}/[(4\pi(2GM)^{1/2})]$.

Figure 4.8 shows this angle-averaged density distribution. There is a break at $r \sim r_c$ between the $\rho \propto r^{-1/2}$ and the $\rho \propto r^{-3/2}$ regimes, because the angular momentum of the infalling material causes it to fall onto a disk at $\theta = \pi/2$, $r \leq r_c$, and material "disappears" from the infall solution. In effect, the mass infall rate across any sphere of radius $r < r_c$ decreases with decreasing radius because of the deposition of material into the disk. This behavior has an important effect on the observable emission from infalling protostellar envelopes.

4.5 Time evolution of rotating collapse

In an important and influential paper, TSC used a perturbative analysis to include the effects of rotation (§4.4) as a small perturbation to the dynamics of the initial singular isothermal sphere (§4.2). The TSC solution can be used to follow the evolution of the collapse during the period when the approximation of self-similarity is valid. While the details

of the mathematics are complicated, the basic evolution can be understood qualitatively as follows. The protostellar cloud initially approximates a singular isothermal sphere in structure. The cloud has a small uniform rotation at large scales at angular frequency $\Omega_\circ$, so that departures from spherical symmetry on large scales are small. Collapse can proceed along the lines of the similarity solution presented in §4.2 on large scales; at small radii, rotation becomes important, and the results of §4.4 may be used. At any instant of time, equation (4.43) or its angle-averaged form (4.46) may be used to estimate the density distribution interior in the collapsing region. The estimate (4.44) for large scales is not exact, because it has been derived for the case where all of the mass is in the central star, whereas the mass in the infalling envelope is generally not negligible (cf. §4.2). Nevertheless, since most of the protostellar emission is concentrated toward the central regions (Chapter 5), equation (4.43) provides a reasonable approximation to the more detailed TSC result.

In the similarity solution the central mass varies with the elapsed time after the beginning of collapse as $M = m_\circ c_s^3 t/G$ (4.19), where $m_\circ = 0.975$. This mass was contained within a radius $r_\circ = (m_\circ/2)\, c_s t$ in the original singular isothermal sphere configuration. The specific angular momentum of the material relative to the axis of symmetry at this radius was

$$H^2 = r_\circ^4 \Omega_\circ^2 \sin^4\theta_\circ = m_\circ^4 c_s^4 t^4 \Omega_\circ^2 \sin^4 \frac{\theta_\circ}{16}\,. \tag{4.49}$$

This is the angular momentum of the material that is arriving at (near) the origin at the present time t. The material along the streamline $\theta_\circ = \pi/2$ lands at the largest disk radius, given by

$$r_c(t) = \frac{m_\circ^4}{16}\,\frac{c_s^4 t^4 \Omega_\circ^2}{GM} = \frac{m_\circ^3}{16}\, c_s t^3 \Omega_\circ^2\,. \tag{4.50}$$

Thus, the centrifugal radius increases rapidly with time, $r_c \propto t^3$. Initially most of the mass falls close to the center, because the material that falls in first has small angular momentum. As collapse proceeds, and material from larger radii is added to the central core, r_c increases rapidly with time, and material is added to the disk rather than to a central star (see Figure 4.6).

4.6 Disk formation

In the simple infall model discussed above, where the initial cloud is spherically symmetric and exhibits axisymmetric rotation, the infall solution has complete symmetry above and below the equatorial plane $\theta = \pi/2$. With this assumption, the momentum fluxes of infalling material on either side of the disk (equatorial) plane perpendicular to the disk are equal in magnitude and opposite in direction. The result is that the infalling gas must pass through a shock at the equator, which dissipates the kinetic energy of motion perpendicular to the equatorial plane. If the shocked gas cools rapidly, as expected for many plausible (though not necessarily all) conditions (Neufeld & Hollenbach 1994), the result is that material accumulates in a thin structure in the equatorial plane, i.e., a disk.

After the energy dissipation in the shock removes most of the velocity component normal to the disk plane, the shocked gas initially retains its velocity parallel to the disk plane. In general, this parallel velocity is not consistent with circular motion at the radius of entry into the disk. The result is that the shocked material must mix with existing material; further dissipation of energy and angular momentum transport must occur before ending up with a

disk in circular rotation (Yorke *et al.* 1993; Cantó *et al.* 1995). If the initial magnetic field structure of the cloud produces a "pseudodisk" (§4.3), there will be additional material near the equatorial plane falling in from larger radii. Thus, the point at which envelope material enters the disk cannot represent its final orbital radius (Cassen & Moosman 1981).

It is instructive to use the TSC model to explore some qualitative and semi-quantitative aspects of disk formation. We can evaluate the centrifugal radius as a function of the mass in the central object by combining equations (4.50) and (4.19), with the result

$$r_{\rm c}(M) = \frac{G^3 \Omega_\circ^2}{c_{\rm s}^8} M^3 \,. \tag{4.51}$$

From this equation one can infer that the surface density of the disk will *initially* have a dependence $\Sigma \propto M r^{-2} \propto r^{-5/3}$ (which may then be modified quickly depending upon the rate of angular momentum transfer within the disk; Cassen & Moosman 1981).

Numerically,

$$r_{\rm c}(M) \sim 9\,{\rm AU}\, T_{10}^{-4}\, \Omega_{-15}^2 \left(\frac{M}{M_\odot}\right)^3 , \tag{4.52}$$

where T_{10} is the gas temperature in units of 10 K (we also assume a mean molecular weight of 2.3 for molecular hydrogen plus helium) and Ω_{-15} is measured in units of $10^{-15}\,{\rm rad\,s^{-1}}$. The fiducial value of $\Omega_\circ$ chosen here is quite small, corresponding to a velocity gradient of $\sim$0.03 $\rm km\,s^{-1}\,pc^{-1}$, which is smaller than that typically seen at the outer edge of rotating cores (e.g., Ward-Thompson *et al.* 2007). From this result one sees that very low-mass stars *might* have very small or even negligible initial disks, but that it would be very difficult for massive stars not to collapse most of their mass into disks initially, unless the initial core temperature was extremely high (or the magnetic/turbulent support was extremely high). Also note that these equations represent the centrifugal radius at the time the expansion wave hits the outer disk radius; at this point only a little less than half the cloud mass has been accrete, and so the eventual object will be twice as massive and have an outer centrifugal radius about eight times as large. In other words, these results provide essentially the initial half-mass radius of the disk. (The details are not precise for the collapse of all the cloud because the similarity solution is not really applicable at late times.)

Another useful way of looking at this result is to place it in terms of how fast the cloud originally rotates relative to the breakup velocity at its outer equatorial radius R,

$$\Omega_K^2 = \frac{GM}{R^3} \,. \tag{4.53}$$

Here we use the fact that the mass interior to radius r of the SIS solution is (e.g., equation (4.16)),

$$M(r) = \frac{2c_{\rm s}^2}{G} r \,. \tag{4.54}$$

Substituting these two relations into equation (4.23), we have

$$r_{\rm c}(M) = \frac{8GM}{c_{\rm s}^2} \left(\frac{\Omega_\circ}{\Omega_K}\right)^2 = 16R \left(\frac{\Omega_\circ}{\Omega_K}\right)^2 . \tag{4.55}$$

Thus, unless the initial cloud rotation is $\lesssim 10^{-3}$ of breakup, the initial disk radius will be much larger than typical stellar radii.

The point here is simple; because stars are so much smaller than molecular cloud cores, it is impossible to avoid having most of the cloud mass fall onto a disk unless angular momentum can be transferred faster than the material falls in, or has an extremely small initial rotation. The former is very difficult to achieve if clouds must be magnetically supercritical to collapse, because this essentially means that the Alfven speed is smaller than the infall speed; this in turn means that magnetic waves cannot escape easily from the collapse to connect to the ambient medium, which is needed for spindown (e.g., Ebert *et al.* 1960). The latter is inconsistent with observations of cloud core velocity gradients. Thus, disk formation is nearly inevitable, at least for most systems. This *also* implies that stars accrete most of their mass *through* disks; thus disk evolution is an essential part of star formation.

Ultimately disk material will be redistributed by the processes of angular momentum transport and energy loss which drive disk accretion. The rapidity with which initial conditions are altered depends upon the rate of angular momentum transfer (e.g., Cassen & Moosman 1981), which may be sufficiently fast to eliminate "memory" of the initial state of the disk on relatively short timescales (Chapter 7).

4.7 Massive protostars

The developments in the previous sections must be modified to consider the formation of the most massive stars. Luminous, hot protostars can exert strong outward forces on their environments through the ram pressures of their fast winds, the thermal pressure of any ionized gas (H II region) produced by their photoionizing fluxes, and the pressure of their stellar photospheric radiation on the surrounding dust grains (which are closely coupled to the gas for typical conditions). Radiation pressure appears to be the most important of these effects, and has been suggested to set the maximum masses of stars (Larson & Starrfield 1971; Kahn 1974).

As discussed by Wolfire and Cassinelli (1986, 1987a,b), the dust in a collapsing envelope around a luminous protostar will become so hot that it evaporates at some radius; the gas can then proceed inward to accrete onto the central star (Figure 4.9). Now, dusty protostellar envelopes are extremely opaque at the ultraviolet wavelengths at which most of the energy of hot massive stars is emitted; thus the radiation from a massive protostar is first absorbed within a thin shell at the inner edge of the envelope (Figure 4.9). The absorbed energy is then reradiated by this inner shell of dust. This dust has lower temperatures than that characteristic of the central star, and thus it reradiates the energy at longer wavelengths, which can travel larger distances outward through the envelope before being absorbed, because the dust opacity is lower at longer wavelengths. Even so, the radiant energy of the central protostar is usually absorbed and reradiated several times before ultimately escaping. We defer a more detailed discussion of the transfer of radiation in protostellar envelopes to the following chapter; here we focus on conditions near the inner edge of the dusty infalling envelope, which addresses the essential physics of the problem.

For simplicity assume spherical infall, and further assume that the grains are spherical and absorb and emit as blackbodies, and that they all have the same sublimation (or evaporation) temperature, $T_{\rm sub}$. Then the radius $r_{\rm s}$ of the inner edge of the dusty envelope is set by the condition (e.g., Wolfire & Cassinelli 1987)

$$\frac{L_*}{4\pi r_{\rm s}^2}\,\pi a^2 = 4\pi a^2 \sigma T_{\rm sub}^4\,, \tag{4.56}$$

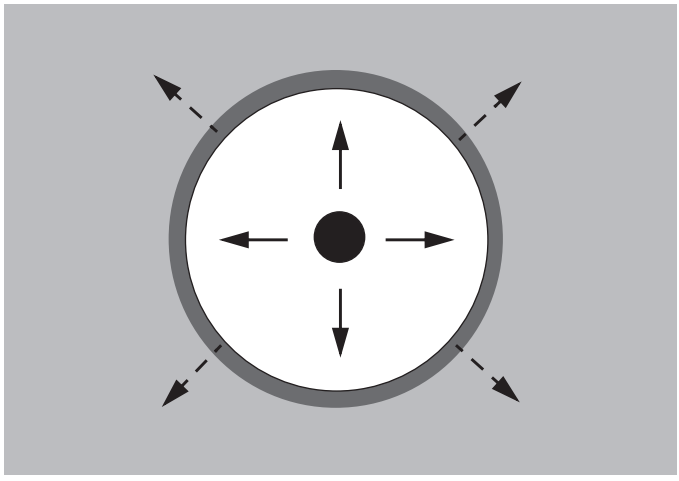

Fig. 4.9. Schematic illustration of a protostellar envelope surrounding a hot star. The dust in the envelope is vaporized inside a certain radius (clear or white region), rendering the infalling matter essentially transparent to the effects of radiation pressure. Most of the (ultraviolet) luminosity of the star is absorbed in a thin layer near the inner edge of the dust envelope (darker region). The dust in this innermost layer reradiates the absorbed energy at longer wavelengths (dashed arrows), some or all of which may be absorbed in the outer layers of the infalling envelope (light gray region), and then reemitted at even longer wavelengths.

where L_* is the stellar luminosity and a is the grain radius. Rearranging,

$$r_s = \frac{1}{4\pi}\left(\frac{L_*}{\sigma T_{sub}^4}\right)^{1/2} . \tag{4.57}$$

For a $60\,M_\odot$ star with luminosity typical of its main sequence value, $L \sim 10^6\ L_\odot$, and assuming a sublimation temperature of $\sim$1500 K, the sublimation radius is $r_s \sim 3 \times 10^{14}$ cm, or about 20 AU; this is much larger than the expected radius of the protostar, $\lesssim$0.1 AU.

Next, consider the magnitude of the dust opacity. Figure 4.10 shows the standard opacity of dust in the diffuse interstellar medium, in units of area per mass, $\mathrm{cm^2\,g^{-1}}$. We adopt this opacity law as representative, although there is evidence for departures in dense regions, particularly in the ultraviolet region (e.g., Mathis 1990). This figure shows that only a very small mass is required to absorb the (ultraviolet-dominated) radiation from a hot star. Therefore, we can expect essentially all of the direct protostellar radiation will be absorbed within a thin shell just exterior to the dust sublimation radius.

The entire momentum flux L/c of the stellar radiation field is thus absorbed in this thin shell. The amount of mass in the shell is negligible, so gravitational acceleration is not sufficient to overcome the outward radiative force. The shell will expand outward, and infall to the protostar will be prevented, unless the ram pressure of the infalling material (schematically exerted on the outside of this shell) exceeds the radiative force. If the infall velocity at r_s is u, and using the equation of mass conservation $\dot{M} = 4\pi r_s^2 \rho u$, the requirement that the infall ram pressure overcomes radiation pressure becomes (Wolfire & Cassinelli 1987b)

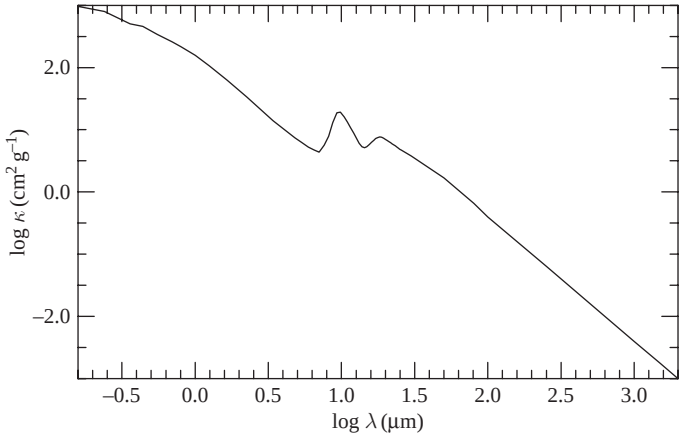

Fig. 4.10. Dust opacity for typical interstellar material, given per gram as a function of wavelength. From Draine and Lee (1984).

$$\frac{L_*}{4\pi r_s^2 c} < \rho u^2 \sim \frac{\dot{M}}{4\pi r^2}\left(\frac{2GM_*}{r_s}\right)^{1/2}, \tag{4.58}$$

where we have estimated the infall velocity u as the free-fall velocity, which ignores any slowing of the external envelope due to the transfer of radiation through it. Rewriting this, we have

$$\dot{M} > \frac{L_*}{c(2GM_*/r_s)^{1/2}}\,. \tag{4.59}$$

For the 60 $M_\odot$, 10^6 $L_\odot$ protostar, the mass infall rate must exceed $\dot{M} > 3 \times 10^{-4}\, M_\odot\,\mathrm{yr}^{-1}$ if the protostar is to continue to accrete mass. This infall rate is very much larger than those predicted by the SIS model; for typical starless cloud core temperatures 10–25 K, $c_s^3/G \sim 2 \times 10^{-6}$–$10^{-5}\, M_\odot\,\mathrm{yr}^{-1}$. Indeed, rapid mass infall is observationally required to form high-mass stars before they leave the main sequence; indeed, high-mass stars seem to be formed on timescales similar to that of the low-mass stars surrounding them, typically 1–2 Myr (§2.2).

As discussed in §4.3, much higher infall rates can be achieved during the collapse of non-SIS models such as the Bonnor–Ebert sphere; but these very high infall rates occur mostly in the earliest phases, long before most of the cloud mass has collapsed. The initial "Bonnor–Ebert" cloud mass would have to be much larger than the (final) stellar mass to achieve the required high infall rates. A much more plausible solution to this problem is to assume that the mass of the initial protostellar cloud was much larger than a single Jeans mass. With thermal pressure forces much weaker than gravity, the situation asymptotically resembles the pressureless free-fall collapse (§4.1), for which the entire cloud collapses to (small scales) essentially at the same time, rather than flowing in uniformly as in the singular isothermal sphere collapse. Very rapid collapse from a non-equilibrium cloud core also helps explain how massive stars can form on roughly the same timescales as low-mass stars – and, for the most massive stars, form before they leave the main sequence.

Returning to the issue of force balance, Kahn (1974) and Wolfire and Cassinelli (1987b) showed that the momentum balance at the inner edge of the envelope is a necessary, but not sufficient, condition to allow collapsing protostellar envelopes of massive central stars; the radiative force throughout the infalling envelope must also be taken into account. Neglecting thermal pressure forces, and assuming spherical symmetry, the equation of motion can be written as

$$v\frac{dv}{dr} = -\frac{GM}{r^2} + \frac{\kappa_F L}{4\pi c r^2}\,, \tag{4.60}$$

where M is the mass interior to r, L is the luminosity, and

$$\kappa_F = \frac{\int d\nu \kappa_\nu F_\nu}{\int d\nu F_\nu} \tag{4.61}$$

is the mean opacity per unit mass, weighted over frequency by the radiant flux F (see Appendix 3), and $\int d\nu F_\nu = L/(4\pi r^2)$. For infall to occur, the first term on the right-hand side must exceed the second; thus,

$$\Gamma_R \equiv \frac{\kappa_F L}{4\pi c G M} < 1 \tag{4.62}$$

is the criterion for infall to occur.

The essential aspects of the problem can be understood using the following simplified analysis. Consider the innermost region of the dusty envelope. As discussed above, a thin region at the inner edge absorbs all of the direct protostellar radiation, and reradiates it at a lower temperature. To first order, we can consider this shell as radiating like a blackbody at or just below the dust sublimation temperature, with the same luminosity as that of the protostar (in steady-state). We may then examine the force of this radiation field on dust just outside the inner shell. In principle, we should examine the force balance as a continuous function of distance throughout the dusty envelope. However, as the radiation is absorbed and reemitted outward, the characteristic dust temperature becomes lower, and thus more of the luminosity is emitted at ever-increasing wavelengths (see §5.2). As shown in Figure 4.10, the dust opacity decreases with increasing wavelengths; we can expect the product $\kappa_F L$ to decrease outward as well. In addition, the self-gravity of the dense envelope becomes more important at larger radii. Therefore it suffices to examine Γ_R in the inner regions.

Take for example the $60\,M_\odot$, $10^6\,L_\odot$ protostar. For this object, $\Gamma_R \sim 1.3\kappa_F$; therefore, $\kappa_F \lesssim 1\,\mathrm{cm^2\,g^{-1}}$ for infall to occur. But examination of Figure 4.10 shows that such low opacities occur only for wavelengths $\lambda > 30\,\mu\mathrm{m}$. This poses a problem. Dust sublimation temperatures are estimated to be (of order, depending upon the species) $\sim$1500 K; by the Wien law, a blackbody with this temperature has a maximum in its spectrum at $\lambda_{\max} \sim 3000\,\mu\mathrm{m}/T \sim 2\,\mu\mathrm{m}$! The near-infrared dust opacity for the standard dust extinction law is more than an order of magnitude too large to allow our $60\,M_\odot$ protostar to continue accreting from its infalling envelope. Indeed, Wolfire and Cassinelli (1987) found that, assuming the standard dust opacity of the diffuse interstellar medium, the maximum protostellar mass was only $\sim 7\,M_\odot$.

To explain stars with masses larger than $7\,M_\odot$, Wolfire and Cassinelli suggested that the total dust mass must be depleted, and the size distribution of particles must be modified, in regions which form massive stars. While this is possible, it is more usual to find substantial modifications of dust extinction in the ultraviolet, while the near-infrared – the essential

opacity for this analysis – remains relatively unchanged (Mathis 1990). Fortunately another option is available: departures from sphericity, which can modify the situation profoundly. The angular momentum of the protostellar cloud will cause it to "fall out" onto a disk which is much larger than the star, or even the nominal dust sublimation radius. As discussed in §4.4, most of the mass falls onto the disk near the centrifugal radius; thus r_c becomes the effective inner limit of the envelope instead of r_s. If r_c is large enough, the dust temperature can become low enough that the flux-mean opacity decreases such that $\Gamma_R < 1$.

In addition, departures from sphericity in the rotating, collapsing envelope also modify the transfer of radiation in important ways. In any non-spherical envelope there will be a tendency for the radiation to escape along paths of lesser optical depth. Thus, radiation will preferentially escape out the rotational axes, where mass column densities and thus optical depths are low. This means that the more equatorial regions, where most of the mass infall is concentrated (Figure 4.7), will see weaker radiation fields. Thus there will be "shielded" regions in the flattened collapsing envelope in which the radiative force is greatly reduced or even absent; infall can occur relatively unimpeded in these directions. This leads to a picture schematically shown in Figure 4.11. Radiation escapes preferentially in the lower-density, "polar" regions, such that the radiative force is even larger than that estimated for the spherical case; material in these regions can be blown away by radiation pressure quite

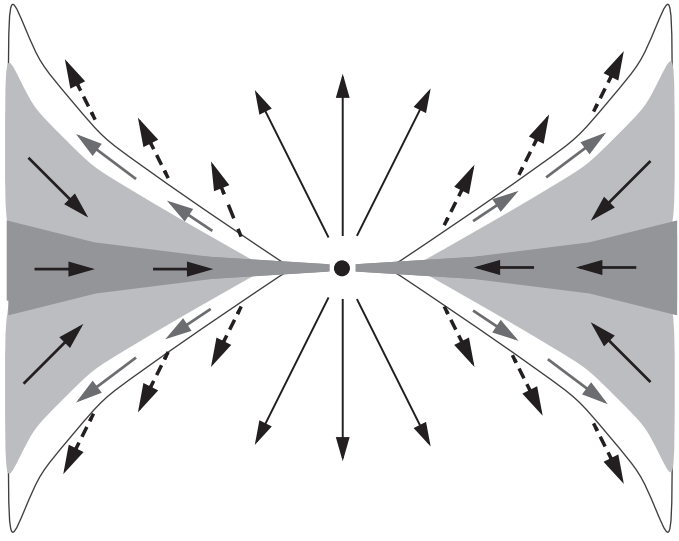

Fig. 4.11. Schematic model of accretion and outflow for a massive, luminous protostar. The combination of initially flattened structure and rotation leads to infall at high rates in a flattened envelope (light gray region) and accretion through a dense circumstellar disk (dark gray region). The high optical depths of these regions result in scattering and reradiating much of the stellar luminosity out low-density "polar" regions; this so-called "flashlight effect" (e.g., Yorke & Sonnhalter 2002) shields most of the infalling material from the effects of radiation pressure. Surface layers of the infalling envelope are driven outward (light area with outward arrows) through the combined effects of radiation pressure, wind ram pressure, and photoionization; if the stellar wind (long arrows) does not have a high ram pressure, the ionization/photodissociation-induced expansion of material (dashed arrows) may further confine the wind.

easily, but this does not constitute the main mass infall. Meanwhile, the "shielded" material arriving along "equatorial" regions falls in readily. As long as the "ablated" polar material mass loss rate is significantly smaller than the infall rate in the shielded region, massive stars can be formed. Of course, this requires the central star to be built up primarily via disk accretion; but this is likely to be the case for all stellar masses (§4.6).

Yorke and Sonnhalter (2002) made numerical calculations of the collapse of massive cores including radiation pressure and departures from sphericity due to rotation. They adopted an approximate radiative transfer method, but incorporated the full frequency dependence, which is essential given the strong variation of dust opacity with wavelength. Yorke and Sonnhalter demonstrated that the effects of non-sphericity on the radiative acceleration described above were important in allowing larger protostars to form. They were able to form protostars of 30–40 $M_\odot$ despite using the standard interstellar dust opacity, in contrast to the results of Wolfire and Cassinelli. Yorke and Sonnhalter described this as the "flashlight effect", i.e., the tendency of radiation to be focussed out polar holes in the density distribution, and pointed out that the effect was especially important for light with the shortest wavelengths, which in turn dominate the radiation pressure forces.

While the Yorke and Sonnhalter results represent a clear step forward in understanding the formation of massive protostars, they were unable to make objects much larger than about 40 $M_\odot$, even when starting with an initial core of 120 $M_\odot$; eventually the radiative acceleration halted collapse. Here one may conjecture that the problem is with the initial conditions adopted by these authors; specifically, the singular isothermal sphere. It seems plausible that by starting with a flattened core and allowing it to collapse, the "flashlight effect" will be stronger, and more material will be shielded from the radiation from central regions.

This discussion ignores the effects of stellar winds and expanding H II regions. Because the winds of young massive stars are driven by radiation pressure, and much or most of the radiation escapes without driving mass loss, the wind ram pressure generally is only a correction of order unity. The effects of the central star in ionizing infalling gas and thus producing an outward pressure are important when there is sufficient radiation to ionize a large enough region that the local infall velocity is smaller than the 10 $\mathrm{km\,s^{-1}}$ thermal velocity (Keto 2003). However, both winds and H II region expansion will also be affected by departures from sphericity in the same way as radiation pressure; the net effect probably will be to blow away and/or "ablate" material from the low-density directions. Thus, inclusion of H II region expansion should not qualitatively change the picture of Figure 4.11, adding photoionization/photodissociation of atomic and molecular material along the infalling envelope's surface (and a corresponding outflow). Growing evidence for disks around massive young stars (§5.9) has provided additional support for this schematic of high-mass star formation.

5

Protostellar collapse: observations vs. theory

As described in the previous chapter, theory predicts that the protostellar envelope should collapse at near free-fall velocities to form the stellar core and disk. It is not easy to detect this collapse directly; on large scales, the infall velocities are small and difficult to isolate from the complex supersonic motions in the surrounding cloud, while freeze-out or other chemical effects remove some of the standard tracers in the inner envelope. In addition, the presence of high-velocity bipolar outflows cause further confusion. Nevertheless, an increasing body of evidence generally supports the rapid collapse model of protostar formation.

Infrared imaging and spectroscopy have provided the most broadly based indications of protostellar collapse. While dust emission does not directly measure infall motion, the presence of dust in the near environs of very young stars, as shown either directly in scattered light or inferred through detection of warm dust emission, demands a dynamical explanation. As the material is too cold to be thermally supported, it must be either falling in or flying out (the envelopes are mostly not in flattened disks, though somewhat flattened "toroids" are observed). The required infall rates are plausible from the collapse theories discussed in the previous chapter, while wind mass loss rates would have to be implausibly large (because the same density implies a larger mass flux for a larger velocity) – and, in any event, outflows have distinctive bipolar geometries, not toroidal expansion.

The theoretical models of protostellar infall discussed so far predict that, for typical parameters, the dusty collapsing envelopes will be very opaque; thus, the radiation from the central protostellar core should be mostly absorbed in a dust "cocoon", which reradiates the absorbed energy at mid- to far-infrared wavelengths from an extended dust envelope "photosphere". For this reason, the study of protostellar sources received dramatic impetus from the launch of the *IRAS* satellite, which made possible studies of the far-infrared radiation from many low-luminosity sources. Although infrared spectra were calculated for many numerical simulations, such as Larson's (1969b), the subject took a major step forward with the application of the TSC collapse solution to the calculation of protostellar SEDs by Adams and Shu (1986) and Adams, Lada and Shu (1987 = ALS). These pioneering investigations made a compelling case for identifying *IRAS*-detected Class I sources (§1.4) as protostars (Beichman *et al.* 1986; Myers *et al.* 1987; Butner *et al.* 1991, 1994; Kenyon *et al.* 1993). In addition to results from the *ISO* satellite, we now have observations from the sensitive *Spitzer Space Telescope*, which have permitted increasingly detailed tests of infall models.

The similarity solution for thermally supported clouds at a typical molecular cloud temperature of 10 K (equation (4.20)) predicts a mass infall rate of

$$\dot{M} \sim \frac{c_s^3}{G} \sim 1.6 \times 10^{-6}\ M_\odot\ \mathrm{yr}^{-1}. \tag{5.1}$$

This suggests that a 0.5 $M_\odot$ cloud will take approximately $\sim 3 \times 10^5$ yr to collapse. The ages of the pre-main-sequence stars in Taurus are mostly ∼1–2 Myr; therefore, the collapse theory predicts that about 10–20% of the pre-main-sequence population in Taurus should be protostars (i.e., young stars still surrounded by their dusty infalling envelopes). About 25 far-infrared Class I sources have been found in Taurus out of a total population of approximately 200 pre-main-sequence objects, consistent with the identification of these objects as protostars. The study of protostellar sources in dense regions of star formation has proved to be much more difficult, not only because of large extinctions from *distributed*, non-collapsing dust, but also because most clusters contain more massive, luminous stars, which can dominate the heating of dust in the cluster environment.

The so-called "Class 0 sources", which are very heavily extincted, may be the "youngest" protostars (e.g., André *et al.* 1993). This picture is consistent with collapse from protostellar clouds with initially flat inner density distribution, as observed in many cores; the collapse of such structures should have the highest mass infall rates in the earliest phases, leading to higher extinctions of the central object. One would then expect that the later, longer-lived phases of protostellar collapse, with lower infall rates (§4.3) correspond to Class I sources.

The luminosity of a protostellar system is

$$L = L_* + L_{\mathrm{acc}} \tag{5.2}$$

where L_* is the luminosity of the central stellar core produced by gravitational contraction and deuterium fusion, and L_{acc} is the luminosity produced by accretion, which includes the dissipation of kinetic energy as the infalling material lands on the disk, the energy lost as material accretes through the disk, and finally the energy released as the accreting material lands on the central stellar core. In Taurus, the Class I sources exhibit the same luminosities ($\sim 1\ L_\odot$) as the (slowly accreting) CTTS or even the (non-accreting) WTTS (§5.1); there is little evidence for a large additional accretion luminosity component. This is surprising because the implied accretion luminosities,

$$L_{\mathrm{acc}} \sim G M_* \frac{\dot{M}_{\mathrm{acc}}}{R_*} \tag{5.3}$$

are $L_{\mathrm{acc}} \sim 8\ L_\odot$ for $\dot{M}_{\mathrm{acc}} \sim \dot{M} \sim 1.6 \times 10^{-6}\ M_\odot\ \mathrm{yr}^{-1}$, using reasonable estimates for protostellar masses and radii. The same problem seems to be present in Class 0 sources as well; although their luminosities are often an order of magnitude higher, so are the predicted mass infall rates. One possible explanation of this discrepancy between predicted and observed protostellar luminosities is that the infalling material mostly lands on a disk at vastly larger radii than R_* (§4.6). The accretion luminosity then depends upon the accretion rate through the disk $\dot{M}_{\mathrm{acc}}$ onto the star. If this can be smaller than the infall rate $\dot{M}$, the luminosity problem can be alleviated. However, this implies that mass piles up in the disk, which cannot go on indefinitely. The disk must eventually dump most of the accumulated mass onto the central star; conceivably this could occur during rapid bursts of disk accretion, such as are observed in the FU Ori objects (Chapter 9).

Spherical collapse models predict that protostellar photospheres should be basically invisible until some time near the end of the collapse phase. While many protostars are heavily extincted at wavelengths $\lesssim 2\,\mu$m, making it difficult to infer stellar properties from photospheric lines, departures from sphericity render some Class I objects detectable at near-infrared wavelengths. Rotation of the infalling envelope, which causes most of the infalling material to drop out on the disk long before reaching the star, has an important effect in reducing the extinction to the central protostar. The protostellar bipolar outflows rapidly blow away polar regions of the dusty envelope, yielding a relatively unobstructed view to the protostar if viewed along the outflow cavity. Such objects, viewed pole-on, may be difficult to distinguish from older Class II objects (Chapter 8).

5.1 Protostellar luminosities and accretion

The most thorough studies of luminosity distributions for Class I/0 objects have been undertaken for Taurus at the time of this writing (further results from *Spitzer* studies should be forthcoming). In addition to its proximity, Taurus has the advantage of being spread on the sky – reducing source confusion – and is devoid of luminous stars which heat dust to large distances and thus create difficulties in measuring far-infrared radiation from faint sources. While the distribution shown in Figure 5.1 is likely to be incomplete on

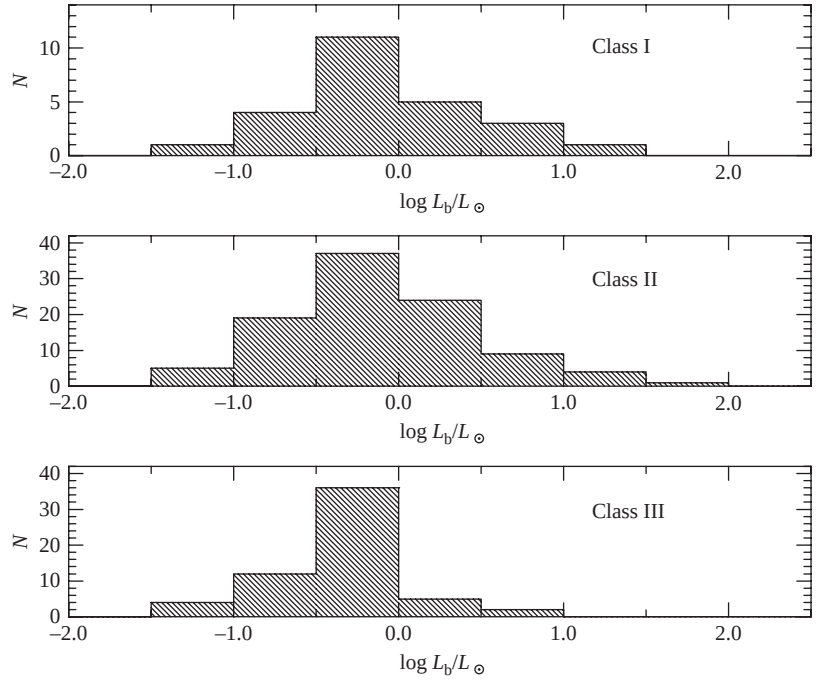

Fig. 5.1. Luminosity distributions of Class I, II, and III sources in Taurus. The Class I sources, heavily extincted and in general protostar candidates, exhibit roughly the same median luminosities as the Class II sources (CTTS or stars with inner dusty disks) and the Class III (WTTS or stars without inner dusty disks). Adapted from Kenyon and Hartmann (1995).

the low-luminosity end, as shown for instance by the recent discovery of a new very faint protostar IRAM 04191+1522 (Andre *et al.* 1999), *Spitzer* surveys do not seem to be turning up large numbers of new Class I sources in Taurus.

Figure 5.1 demonstrates that the Class I and Class II luminosity distributions are very similar. This result indicates, as discussed in the introduction to this chapter, little evidence for the large accretion luminosities expected if matter is being transferred to central protostars at the same rates as expected for envelope infall.

One might expect that star-forming regions of higher density might form higher-density cores, which in turn would collapse faster, resulting in higher accretion rates. However, the most recent surveys of the Ophiuchus cloud, which is considerably denser and more opaque than Taurus, do not provide strong evidence for significantly higher luminosities. The *ISOCAM* survey of Ophiuchus by Bontemps *et al.* (2001) suggest that the Class I, Class II, and Class III objects have similar luminosity functions, steeply rising between about 10 and 2 $L_\odot$, and roughly flat in $dN/d\log L$ between about 2 and 0.03 $L_\odot$. There are a few luminous Class I objects in the Bontemps *et al.* survey ($\sim 20-30$ $L_\odot$), but there are also Class II sources of similar luminosity – more than in Taurus, so it is not obvious that these high luminosity Class I objects exhibit rapid accretion rather than simply being more massive protostars.

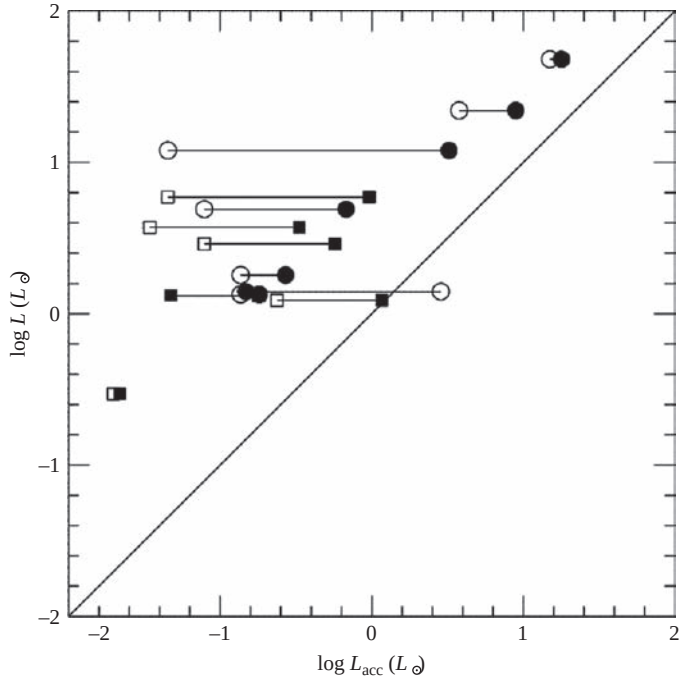

Fig. 5.2. Total luminosity (vertical axis) as a function of accretion luminosity estimated from the 2.1 μm Brγ emission line. Circles are Ophiuchus Class I sources, squares are Taurus Class I objects, and open and filled symbols are rates inferred before and after reddening correction, respectively. From Muzerolle *et al.* (1998c).

Measuring the accretion rate directly onto the central protostar is difficult given the high extinction involved. To circumvent this difficulty, Muzerolle *et al.* (1998b) attempted to use the infrared Brγ line emission of Class I objects to infer accretion rates, using a correlation developed for Class II/T Tauri stars. As shown in Figure 5.2, the reddening-corrected line fluxes (solid symbols) suggest accretion luminosities that are a modest fraction of the total, again suggesting low accretion rates for many Class I objects. White and Hillenbrand (2004) attempted to use (faint) optical continuum excess emission to study accretion in Taurus Class I stars, also finding that accretion rates in these objects do not dominate the total system luminosities, though there is some evidence that Class I objects have somewhat higher accretion rates than typical Class II objects (see also Doppmann *et al.* 2005). Preliminary results from *Spitzer* surveys in other regions also suggest that Class I objects are not much more luminous than the corresponding Class II population, suggesting lower accretion rates onto central stars than the infall rates onto protostellar disks (M. Enoch *et al.*, personal communication).

5.2 SEDs of spherical infalling envelopes

The identification of Class I sources in Taurus and Ophiuchus as protostars is basically due to the matching of the SEDs with the dust emission predicted for infalling dusty envelopes (Adams & Shu 1986; ALS; Butner *et al.* 1991). Although many hydrodynamic simulations have been used to predict dust envelope emission (e.g., Yorke *et al.* 1993; Boss & Yorke 1995), the advantage of the ALS method lies in its use of simple analytic models of the collapsing envelope at a snapshot in time. Because the thermal gas pressure (and radiation pressure) is generally negligible in the envelopes of low-mass protostars, one can decouple the hydrodynamic problem from the radiative transfer problem. The use of an analytic model allows greater freedom in handling the radiation transfer and thermal equilibrium, and makes it relatively easy to explore the effects of different envelope parameters on the emergent spectrum.

We begin with dust emission from a spherical collapsing envelope. In the following we assume a familiarity with the basic results of radiative transfer. Some essential relations are summarized in Appendix 3; others can be found in Mihalas (1978).

As discussed in §4.2, the density distribution of a spherical, collapsing, protostellar cloud can be reasonably approximated by "free-fall" behavior, where the density of the infalling matter is

$$\rho \sim \frac{\dot{M}}{4\pi r^2 v_{\rm ff}} = \frac{\dot{M}}{4\pi (2GM)^{1/2}} r^{-3/2} \tag{5.4}$$

(equation (4.21)). The radial optical depth integrated inward to radius r from the center, assuming a large outer radius, is

$$\tau_\lambda = \frac{\kappa_\lambda \dot{M}}{2\pi (2GM)^{1/2}} r^{-1/2}, \tag{5.5}$$

where κ_λ is the opacity at wavelength λ.

To make a quantitative estimate of the amount of dust extinction through the envelope, we again adopt the standard curve for interstellar dust opacity from Draine and Lee (1984), as illustrated in Figure 4.10. This extinction curve is not unique; for example, it is known that the ultraviolet dust extinction varies strongly in regions with massive star formation (e.g., Mathis 1990). Far-infrared studies also indicate larger dust opacities near 200 μm

(Hildebrand 1983). More recent studies suggest that the opacities in the sub-mm and mm range in dense protostellar cores might be a factor of 4–5 larger (Ossenkopf & Henning 1994). However, Figure 4.10 provides a starting point for exploration.

Most low-mass (T Tauri) stars have peaks in their photospheric SEDs at wavelengths $\lesssim 1\,\mu$m. The optical depth at $1\,\mu$m through the infalling envelope to a radius $r_{\rm in}$ is

$$\tau_1 \sim 10 \left(\frac{\dot{M}}{2 \times 10^{-6}\, M_\odot\, {\rm yr}^{-1}} \right) \left(\frac{M}{0.5\ M_\odot} \right)^{-1/2} \left(\frac{r_{\rm in}}{15\,{\rm AU}} \right)^{-1/2}. \tag{5.6}$$

From equation (A3.7), the light from the central star escaping along the radial direction is extinguished by a factor of $\exp(-\tau)$.* Thus, as long as the envelope extends into radii of tens of AU or less, for typical mass infall rates one expects the central star to be extinguished by a factor of $\sim 10^4$, or around 10 mag ($\Delta{\rm mag} = 1.086\tau$). This simple estimate suggests that the central star will be essentially invisible at optical wavelengths unless the dust envelope is somehow removed at radii $\lesssim 100$ AU.

Because protostellar envelopes are very optically thick at the characteristic wavelengths of radiation from the inner region, they will absorb essentially all of the light from the central source (as long as the envelope is nearly spherically symmetric). This means that, to a first approximation, the details of the central star's spectrum are not important, and the emergent spectrum seen at the Earth depends mainly upon the properties of the dust envelope. It is straightforward to show that the radiative cooling times of the grains are shorter than infall timescales, and therefore the envelope emission can be computed in the limit of radiative equilibrium.

The observed protostellar radiation at a given wavelength is a weighted sum of the radiation from several layers in the envelope. However, only a limited range of the envelope can contribute significantly, since optically thin regions contribute little flux and very few photons escape from layers at large optical depths. Crudely, one may say that the observed emission arises from a "characteristic" layer at $\tau_\lambda \sim 2/3$ (see Appendix 3). In this approximation, the dust envelope will have a "photospheric" radius r_λ, defined as the radius where $\tau_\lambda = 2/3$,

$$r_\lambda = \left(\frac{9}{4} \right) \frac{\kappa_\lambda^2\, \dot{M}^2}{8\pi G M}. \tag{5.7}$$

In the case of most stellar atmospheres, the density distribution varies so rapidly with radius that the photospheric radius is essentially fixed over a wide range of wavelengths and opacities. However, the extended density distribution of the infalling envelope produces different photospheric radii at differing wavelengths of observation. The left-hand panel in Figure 5.3 shows r_λ as a function of wavelength using the opacity in Figure 4.10 and $\dot{M} = 2 \times 10^{-6}\, M_\odot\, {\rm yr}^{-1}$.

To make an initial guess at the protostellar spectrum, we adopt the approximation that the dusty envelope emits like a blackbody with a peak wavelength λ_m. Equivalently, we

* The amount of light from the protostar escaping through the envelope is not simply the stellar emission which is not absorbed by the envelope along the line between the star and the observer. In addition, the envelope dust *scatters* protostellar emission emitted in other directions into the line of sight of the observer. In general, one cannot neglect dust scattering at optical and near-infrared wavelengths, and so equation (5.6) greatly underestimates the amount of protostellar emission that can be observed directly, especially since envelopes are not spherically symmetric (see §5.6; Figure 5.8). However, the extremely large extinctions of protostellar envelopes do make short-wavelength detections difficult.

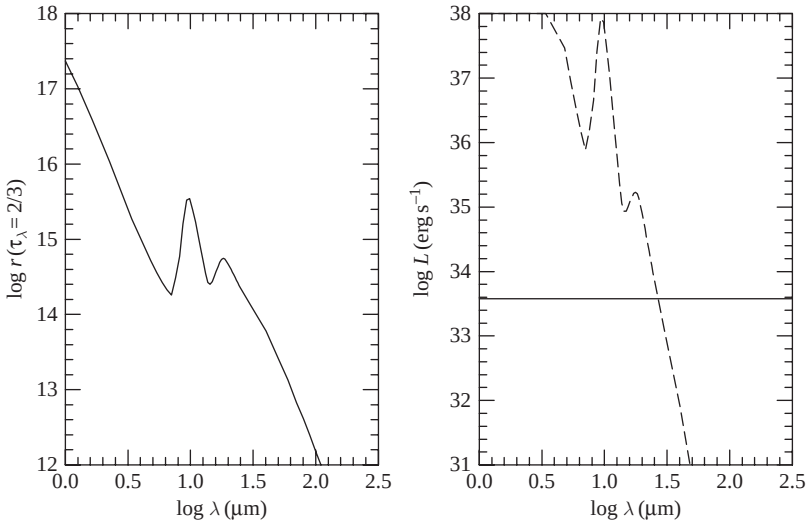

Fig. 5.3. Approximate solution for the dust "photosphere" of a protostar, as described in the text. The left-hand panel shows the photospheric radius of the spherical collapsing envelope as a function of wavelength (equation (4.8)). The dashed curve in the right-hand panel shows the estimated envelope luminosity as a function of its characteristic wavelength λ_m. The horizontal line corresponds to a typical protostellar luminosity of 1 $L_\odot$. The intersection of the two provides an estimate of the approximate λ_m.

assume that the dust emission has a characteristic effective temperature $T = 0.3/\lambda_m$ (the Wien relation). Thus,

$$L \;=\; 4\pi r_{\lambda_m}^2 \sigma\, T(\lambda_m)^4, \tag{5.8}$$

where r_{λ_m} is the radius at which $T(\lambda_m)$ occurs. If we then assume that r_{λ_m} is the "photospheric" radius and so occurs at a radial optical depth $\tau_{\lambda_m} = 2/3$, then for a given dust opacity (Figure 4.10), a mass infall rate $\dot{M}$, and total central luminosity L, one can solve for λ_m, $T(\lambda_m)$, and r_{λ_m}.

The right-hand panel in Figure 5.3 shows the results of equation (5.8) applied to the infall case for $\dot{M} \;=\; 2 \times 10^{-6}\; M_\odot\,\mathrm{yr}^{-1}$ as the dashed curve running from the upper left to the lower right. The intersection of this curve with the appropriate source luminosity provides an approximation to the photospheric radius of the dust envelope and the wavelength of peak SED emission. For an assumed luminosity of 1 $L_\odot$ (horizontal line), the intersection occurs at a wavelength $\sim$30 μm, or a characteristic temperature $T(\lambda_m)$ $\sim$100 K. Thus, the model predicts that typical protostars should mainly emit in the far-infrared.

An analytic estimate of λ_m can be made if we approximate the opacity as $\kappa_\lambda = \kappa_\circ(\lambda/\lambda_\circ)^{-\beta}$. Substituting,

$$\frac{\lambda_m}{\lambda_\circ} \;=\; \left(\frac{0.3}{\lambda_\circ}\right)^{1/(1+\beta)} \left(\frac{4\pi\sigma}{L}\right)^{1/(4+4\beta)} \left(\frac{9\,\dot{M}^2\kappa_\circ^2}{32\pi G M}\right)^{1/(2+2\beta)} . \tag{5.9}$$

If we take the far-infrared opacity to be $\kappa_\lambda = 0.2\,(\lambda/100\,\mu\mathrm{m})^{-2}$, then the peak of the spectrum occurs at

$$\lambda_m \approx 30 \left(\frac{L}{L_\odot}\right)^{-1/12} \left(\frac{\dot{M}}{2\times10^{-6}\ M_\odot\ \mathrm{yr}^{-1}}\right)^{1/3} \left(\frac{M}{0.5\,M_\odot}\right)^{-1/6} \mu\mathrm{m}. \tag{5.10}$$

Thus, the free-fall collapse picture, coupled with predicted infall rates for simple models of cloud cores, indicates that protostars will emit most of their energy in the mid- to far-infrared spectral region. This conclusion is almost independent of the assumed central luminosity, and is only moderately dependent upon the mass infall rate.

To proceed beyond these simple estimates to more detailed calculation of a protostellar spectrum requires the application of detailed radiative transfer techniques to compute the radiative equilibrium temperature structure of the dust envelope and the emergent spectrum. Detailed radiative equilibrium temperature distributions for spherically symmetric dusty envelope models are shown in Figure 5.4. Results are presented for two mass infall rates, $\dot{M} = 2\times10^{-6}\ M_\odot\,\mathrm{yr}^{-1}$, and $\dot{M} = 10^{-5}\ M_\odot\,\mathrm{yr}^{-1}$, for central source luminosities of 1 and 10 $L_\odot$.

The overall features of these temperature distributions can be understood from simple arguments. Compare, for example, the results in Figure 5.4 for $L = 1\ L_\odot$ and $\dot{M} = 2\times10^{-6}\ M_\odot\,\mathrm{yr}^{-1}$ with the results of Figure 5.3 or the approximate relations (5.10) and (5.7). The predicted value of $\log\lambda_m$ is ∼1.5, corresponding to a "photospheric" radius of about 1.5×10^{14} cm ∼10 AU. Roughly speaking, the detailed temperature distribution in Figure 5.4 changes slope near this radius, marking the transition between inner "optically thick" and outer "optically thin" behavior.

At small optical depths, the radiative equilibrium equation

$$\int \kappa_\nu (J_\nu - B_\nu)\, d\nu = 0 \tag{5.11}$$

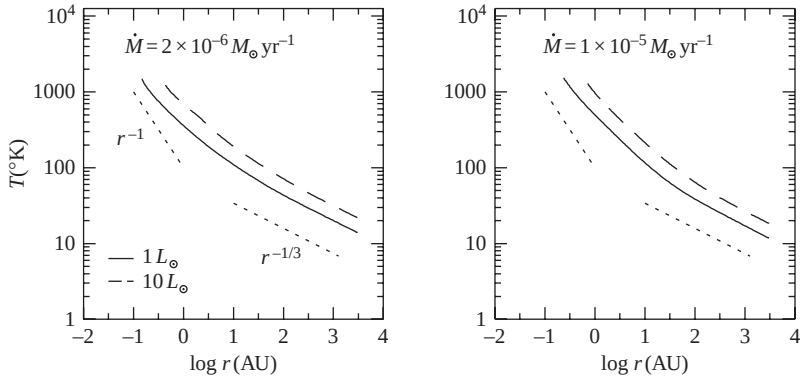

Fig. 5.4. Temperature distributions for spherical envelope models, shown for two different mass infall rates and two different source luminosities. The dotted lines exhibit the asymptotic behaviors predicted for optically thin and optically thick radiative equilibrium (see text). Courtesy N. Calvet.

(see Appendix 3) simplifies because $J_\nu \rightarrow$ constant $\times\ r^{-2}$. It is straightforward to show that the appropriate (Planck) mean opacity varies as $\kappa_P \propto T^\beta$ for $\kappa_\lambda \propto \lambda^{-\beta}$. Therefore,

$$T \propto r^{-2/(4+\beta)} \quad \text{(optically thin)}. \tag{5.12}$$

For $\beta = 2$, characteristic of the far-infrared opacity adopted (Figure 4.10), one can use equation (5.12) to show that $T \propto r^{-1/3}$. The temperature distributions in Figure 5.4 show this property at large distances. (If one adopts $\beta = 1.5$ for the long-wavelength opacity, as suggested by observational and theoretical treatments (e.g., André *et al.* 1993; Ossenkopf & Henning 1994), the results are only slightly different, $T \propto r^{-0.36}$.)

The temperature distribution changes its character inside the "photospheric" radius, where the envelope is very optically thick; trapping of radiation causes the temperature gradient to become steeper than in the optically thin case. In the limit of large optical depth, one can use the usual diffusion approximation,

$$L = -\frac{64\pi\sigma r^2 T^3}{3\kappa_R \rho}\frac{dT}{dr} \tag{5.13}$$

(Appendix 3), where κ_R is the Rosseland mean opacity. Again, for a power law dependence of opacity $\kappa_\lambda \propto \lambda^{-\beta}$, $\kappa_R \propto T^\beta$. Taking a power law distribution of density $\rho = \rho_\circ (r/r_\circ)^{-n}$, equation (5.13) can be integrated with the boundary condition that $T \rightarrow 0$ as $r \rightarrow \infty$, with the result that

$$T \propto (L\rho_\circ r_\circ^n)^{1/(4-\beta)} r^{-(1+n)/(4-\beta)}. \tag{5.14}$$

The optically thick portions of the solutions shown in Figure 5.4 pass through temperatures $\sim$300 K, where the peak of the blackbody radiation is at 10 μm; in this region, $\beta \sim 1.5$, and so we find $T \propto r^{-1}$, in reasonable agreement with the detailed calculations.

Figure 5.5 shows SEDs for spherical infalling envelopes calculated from detailed radiative transfer solutions for two values of both central source luminosities and mass infall rates. The simple scaling law described above provides a reasonable first approximation to the results, although there are obviously important spectral features, such as the silicate features near

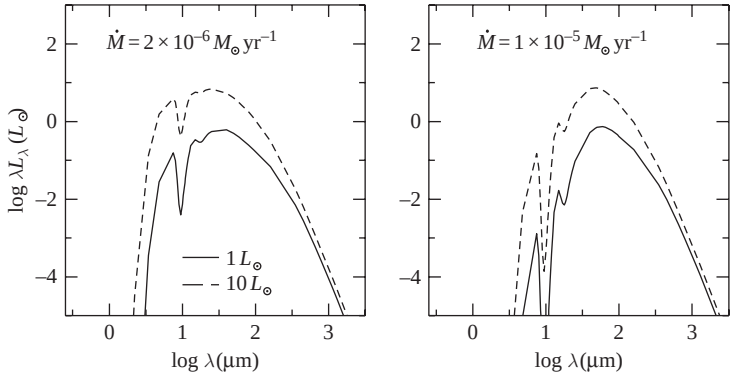

Fig. 5.5. SEDs for the spherical infall models whose temperature distributions are shown in Figure 5.4. The wavelength λ_m of the peak emission moves to longer wavelengths for higher mass infall rates, but is not very sensitive to the central source luminosity, as described in the text. Courtesy N. Calvet.

10 and 20 μm, which require detailed calculations. The resulting SEDs are slightly broader than a single-temperature blackbody distribution, because a range of temperatures is present in layers that contribute to the emission.

5.3 SEDs for rotating collapse models

The observed SEDs of Taurus Class I sources (Figure 1.5) exhibit far-infrared emission similar to that predicted by the spherical collapse models (Figure 5.5). However, the models predict far too little near- to mid-infrared emission to explain the observations, indicating that the extinction of the central hot regions must be reduced. As equation (5.5) indicates, most of the optical depth in the infalling envelope accumulates at small radii. For this reason, Myers *et al.* (1987) originally suggested that there were inner "holes" in Class I envelopes to reduce the extinction and increase the amount of short-wavelength light that escapes.

The inclusion of rotation in the envelope models of ALS produced SEDs in better agreement with the observations. Because rotation causes the infalling material to land on the disk (§4.4), it also reduces the central envelope extinction. To see this in broad terms, consider the spherical average of the TSC density distribution (Figure 4.7; §4.4). In this approximation, the density distribution inside r_c has the form $\rho \propto r^{-1/2}$ (equation (4.46)). Rotation therefore limits the column density or optical depth ($\propto \int \rho dr$) through the envelope; material drops onto the disk and is therefore removed as an opacity source.

In a radial infall model, the inner radius of the dust envelope is limited by the dust destruction radius, i.e., where temperatures become too high for dust to survive. Typical estimates suggest that the dust destruction temperature is ∼1500 K (Larson 1972; Stahler *et al.* 1980a,b; Wolfire & Cassinelli 1987). For a central star of a few solar luminosities, the dust destruction radius is of order 10^{-1} AU. Now most of the optical depth of a TSC model is accumulated near r_c; in terms of the spherical average, the total optical depth through the envelope is roughly given by equation (5.6) if r_{in} is replaced by r_c and the scaling constant is doubled. Thus, a TSC infall model with a centrifugal radius of 100 AU has a total column density roughly 30 times smaller than the corresponding radial collapse model with the same total mass infall rate.

This reduction of envelope optical depth due to rotation has a profound effect on the amount of near- and mid-infrared emission emitted by a protostellar envelope (see Figure 5.6). Adams and Shu (1986) and ALS made the initial applications of the TSC infall models to Class I sources. Because the density variation from pole to equator in the TSC model at a constant radius is generally no more than ∼ a factor of two (see Figure 4.7), ALS estimated the radiative equilibrium temperature using the spherical average of the opacity distribution in the envelope (cf. Efstathiou & Rowan-Robinson 1991). The resulting calculations showed that modest amounts of rotation in the initial protostellar cloud, consistent with the velocity gradients observed in molecular cloud cores (Goodman *et al.* 1993), could explain much of the observed mid-infrared emission of these infrared sources.

ALS found reasonable agreement of source luminosities with reasonable theoretical parameters for the assumed accretion rate. In their treatment, the central luminosity comes from both accretion onto the star and through the disk, and the accretion luminosity is generally

$$L_{acc} \sim \frac{3}{4}\frac{G M_* \dot{M}}{R_*}. \tag{5.15}$$

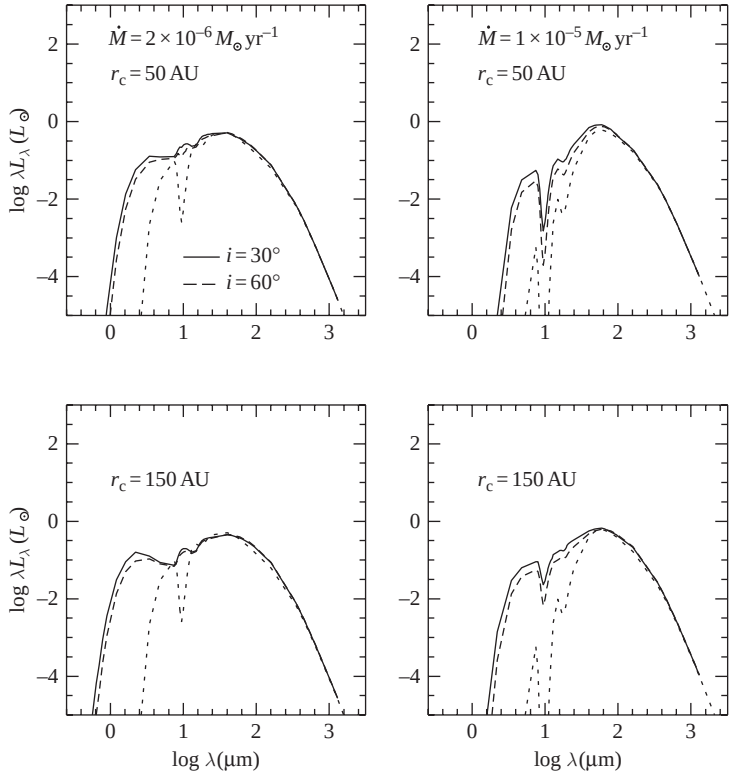

Fig. 5.6. Effects of rotation on the SEDs of infalling envelopes. The dotted lines repeat the non-rotating SEDs with $L = 1\,L_\odot$ from Figure 5.5 for comparison. The models including rotation exhibit vastly more mid- and near-infrared emission because of the reduction in inner envelope optical depth as infalling dusty material falls onto the disk. The silicate feature at $\lambda \sim 10\,\mu$m can change from the deep absorption seen in spherical models to emission for plausible infall rates and centrifugal radii r_C (§3.4). The SED and the depth of the silicate feature also depend upon the viewing angle i between the rotation axis and the line of sight in addition to the mass infall rate and centrifugal radius. Courtesy N. Calvet.

The factor of 3/4 arises from the assumption that some of the accretion energy is not radiated at the star but goes into ejecting a wind, or spinning up the star, etc. Encouragingly, ALS found that they could reproduce their Taurus source luminosities for $\dot{M} = 2 \times 10^{-6}\ M_\odot$ yr^{-1} with central masses of $\sim$0.5 $M_\odot$. However, later investigators (Kenyon *et al.* 1990, 1994) found disagreement between predicted and observed Class I luminosities, mainly because ALS modeled only some of the brightest Class I sources in Taurus and Ophiuchus; their Taurus sources have luminosities almost an order of magnitude larger than the median value.

This result emphasizes the need to obtain systematic samples of the protostellar populations. Observations of any star-forming region yield only a snapshot of protostars of differing masses in various stages of evolution. For these reasons, results for as complete a sample as possible are required to make further progress. The most systematic analyses of the SEDs of protostellar sources in a star-forming region have been performed for Taurus Class I sources, initially by Kenyon *et al.* (1993), and later updated by Furlan *et al.* (2008), including *Spitzer* IRS spectra. Kenyon *et al.* adopted the TSC model to compute dusty envelope emission,

and used the spherical average of the TSC density distribution to calculate the dust equilibrium temperature, but departed from ALS in taking the correct density distribution into account when calculating the emergent spectrum. As shown in Figure 5.6, the emergent spectrum is strongly affected by the envelope rotation; at short wavelengths, the extinction of the outer layers is much larger in the equatorial direction than along polar regions, even though the differences in column densities are modest (Figure 4.7). Kenyon *et al.* (1993) also included the effects of dust scattering in a systematic way, and, unlike ALS, assumed that the source luminosity is a free parameter. With these assumptions, the TSC SED models essentially have four fitting parameters: the source luminosity, the centrifugal radius, the viewing angle relative to the rotation axis, and a parameter setting the density of the infalling envelope. This last parameter can be related to the mass infall rate for a given assumed central mass.

Kenyon *et al.* modeled the SEDs of 21 Class I sources and found a median infall rate $\sim 4 \times 10^{-6} (M_*/0.5\,M_\odot)^{1/2}\ M_\odot\,\mathrm{yr}^{-1}$; similar values were found by Furlan *et al.* (2008) (Figure 5.7). Given the uncertainties in the calculation – departures from spherical symmetry, uncertainties in dust properties, possible role of magnetic fields, approximations in

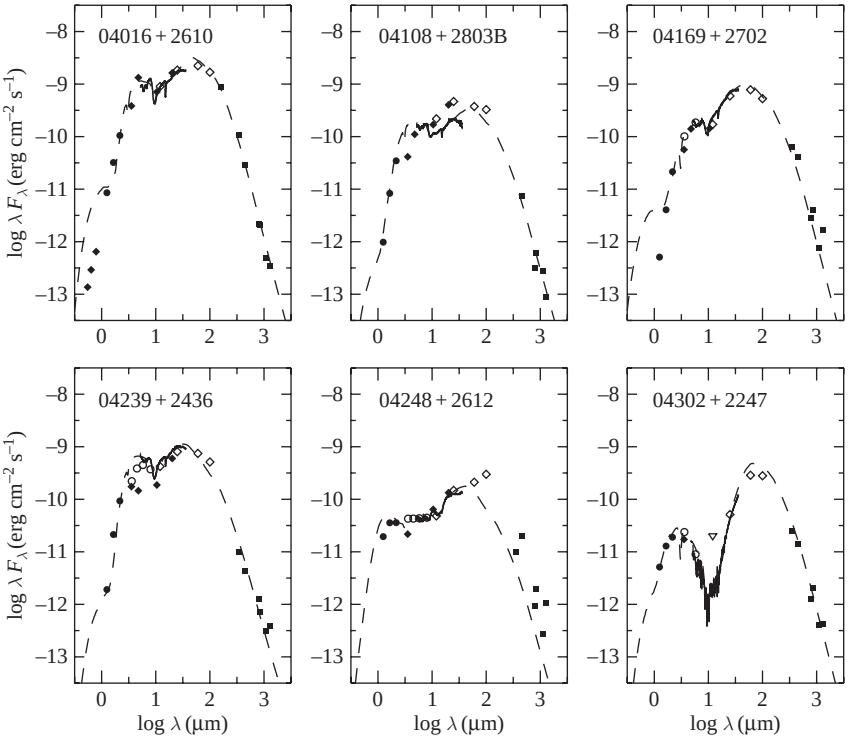

Fig. 5.7. Theoretical SEDs of rotating infall models (TSC models with outflow cavities) fitted to observations of Taurus Class I sources, including both *IRAS* and *Spitzer* IRS data. Typical mass infall rates are a few times $10^{-6}\ M_\odot$ with centrifugal radii of order $\sim$100 AU. Note the very strong 10 μm silicate absorption in IRAS 04302 + 2247. From Furlan *et al.* (2008).

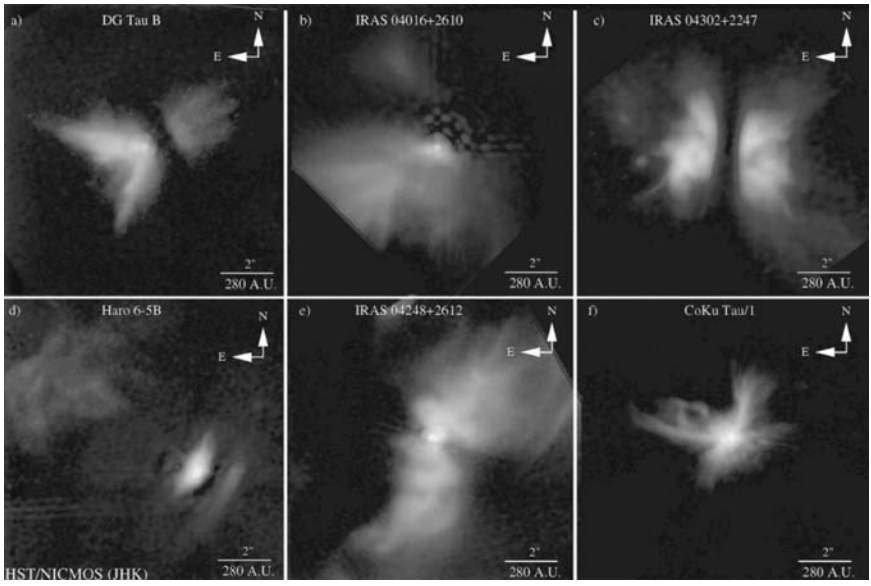

Fig. 5.8. Near-infrared images of Class I sources in Taurus taken with NICMOS. In several cases dark extinction lanes can be seen which probably denote the positions of opaque circumstellar disks, upon which envelope material falls (e.g., Figure 1.9). From Padgett *et al.* (1999).

the radiative transfer, etc. – the results are reasonably close to the $\dot{M} \sim 2 \times 10^{-6}\ M_\odot\ \mathrm{yr}^{-1}$ predicted by the singular isothermal sphere collapse for the $T = 10\,\mathrm{K}$ temperatures in Taurus.

Another source of uncertainty in interpreting SEDs is geometric. The fitting of TSC models to the Taurus data results in systematically large centrifugal radii and low inclinations; for the latter, the median inclination derived from the SED modeling is $i \sim 30°$, rather than the average value $i \sim 60°$ expected for a random distribution of inclinations. The main reason for this discrepancy is that real protostellar envelopes have "holes" or low-extinction paths through which short-wavelength light preferentially escapes, and indeed are commonly observed near highly extincted young stellar objects (e.g., Bastien & Ménard 1988). Figure 5.8 shows some examples of cavities (presumably evacuated by outflows) seen in near-infrared scattered light of several Taurus Class I sources.

5.4 A case study: L1551 IRS 5

One of the brightest Class I objects in the sky, and hence one of the best-studied systems, is L1551 IRS 5 in Taurus. The source itself is extincted by of order 100 magnitudes of visual extinction (see, e.g., Stocke *et al.* 1988) but calls attention to itself by its large scattered light nebula which is filled with a variety of shocked gas elements called Herbig–Haro objects; the cavity is driven by an outflow of material (Snell *et al.* 1980), including highly collimated jets. As shown in Figure 5.9, the region is quite complex, with many young stars being formed in the same cloud.

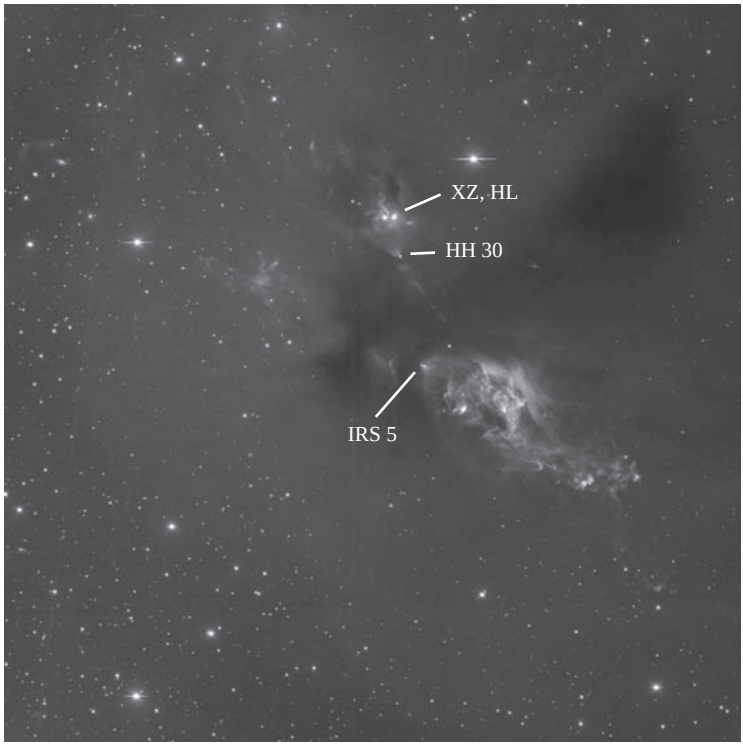

Fig. 5.9. Image of the L1551 region made by combining Hα and [S II] emission, with labels indicating some of the young objects in the region, including L1551 IRS 5, and HH 30 (note the extended scattered light indicating the presence of envelope material; compare with Figure 1.7) and HL Tau (rightmost of the XZ/HL pair; Figure 5.16). Courtesy of John Bally and Bo Reipurth.

The dusty envelope of L1551 IRS 5 extends over many thousands of AU, as would be expected for a protostellar core, but it is far from spherical; instead it appears to be roughly toriodal in shape (Figure 5.10). A hint of this flattened structure can also be seen in Figure 5.9 as a dark, extincted region running southeast to northwest. By spatially resolving this structure one can also investigate its kinematics. Saito *et al.* (1996) (Figure 5.10) inferred that this material is falling in a rate of roughly $\sim 10^{-5}\ M_{\odot}\ \mathrm{yr}^{-1}$, with also some evidence of rotation. This was followed up by a more detailed modeling study by Momose *et al.* (1998), who also found similar results for infall and rotation using a flattened cloud collapse model (Figure 5.11). Such initially non-spherical cloud models are motivated by the requirement of a seemingly more flattened envelope density distribution than can be explained by the outflow cavities, and may arise from collapse along magnetic field lines (Galli *et al.* 2006).

The proximity of L1551 IRS 5 and its relatively high luminosity and dust mass(es) has made it possible to explore the innermost regions in some detail. Keene and Masson (1990), Lay *et al.* (1994), and Ladd *et al.* (1995) found evidence for a central bright source in addition to extended emission. This central region is now shown to be (at least) a binary system (Bieging & Cohen 1985; Looney *et al.* 1997; Rodriguez *et al.* 1998), with both dust emission and strong free–free emission from jets. Rodriguez *et al.* showed that the

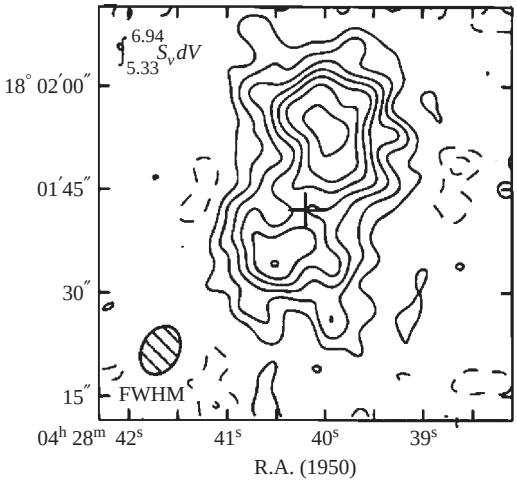

Fig. 5.10. Map of the L1551 IRS 5 region in $H^{13}CO^+$, showing the flattened, extended structure of its dense gas envelope. From Saito *et al.* (1996).

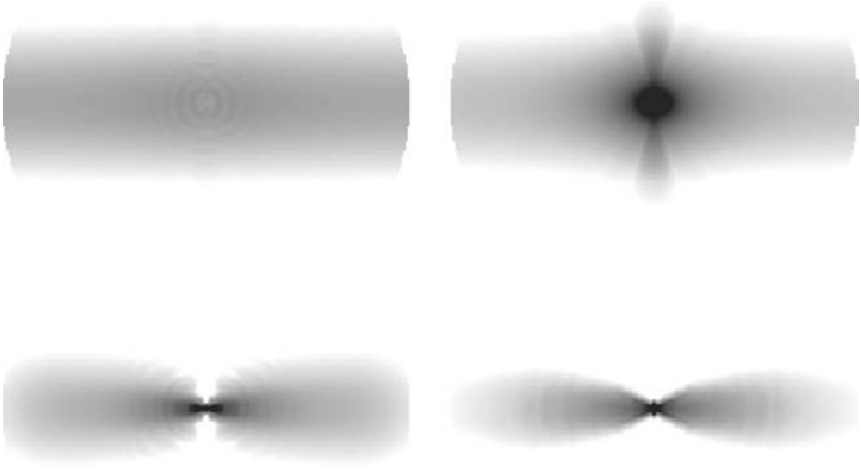

Fig. 5.11. The density distribution of a sheet collapse model shown as a logarithmic gray scale in a meridional plane. As collapse proceeds, most of the material becomes concentrated toward the equatorial plane, producing evacuated cavities in the polar directions. The resulting envelope asymmetry is very much greater than in a TSC model. A model of this type has been used to investigate the properties of the L1551 system (Osorio *et al.* 2003). (See the right panel of Figure 4.4 for the time evolution of infall for this model.) From Hartmann *et al.* (1996).

high surface brightnesses of the dusty disks require high mass accretion rates, which is at least qualitatively consistent with the relatively high luminosity of the system ($\sim$25 $L_\odot$) compared with other Taurus Class I sources.

Lim and Takakuwa (2006) used higher-resolution maps to suggest that there is a third component in the system (Figure 5.12). The two main components have disks of (detected) dimension $\sim$17 AU. Proper motions suggest orbital motion, with a separation of order

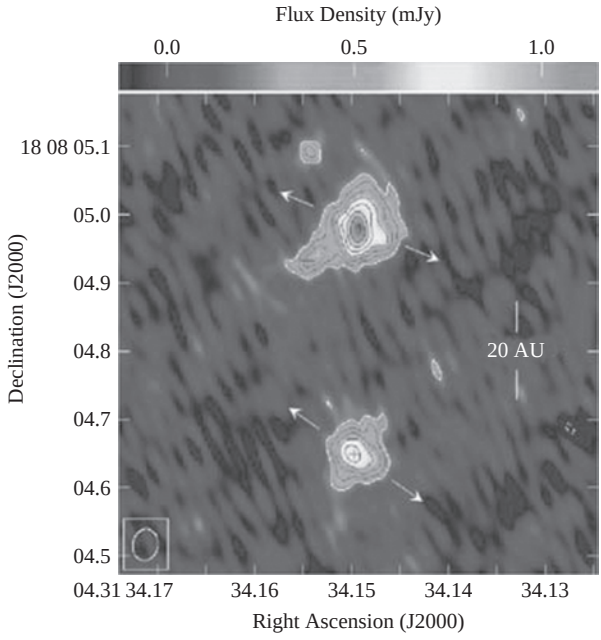

Fig. 5.12. Image at 7 mm of the L1551 IRS 5 system made at high resolution using the VLA and the PT antenna. Emission from the binary disks is evident; there may be a third source to the southeast of the brighter (northern) component. Arrows indicate the direction of jets. From Lim and Takakuwa (2006).

50 AU, a period of roughly 400 yr, and a total system mass of order 0.9 $M_\odot$. The direction of the inferred orbital motion is in the same sense as that inferred for the inner region of the toroid (Takakuwa *et al.* 2004), consistent with the idea that the angular momentum of the infalling material has led to binary formation.

Millimeter-wave observations suggest the presence of an elongated structure on radial scales of 100–400 AU (Keene & Mason 1990; Lay *et al.* 1994; Looney *et al.* 1997), which Looney *et al.* suggest may correspond to a circumbinary ring or disk. A somewhat larger structure has also been inferred from mm and sub-mm continuum observations (Ladd *et al.* 1995; Hogerheijde *et al.* 1997), but it is not obvious whether this is also part of the circumbinary disk, or perhaps just the inner regions of the infalling envelope.

Osorio *et al.* (2003) developed a model which attempted to reproduce the SED of L1551 IRS 5, using data from *ISO* and including constraints from the mm and sub-mm imaging. Figure 5.13 shows that the results of this modeling can reproduce the observed SED, albeit with a complicated set of components in addition to the envelope. In particular, the two circumstellar disks (labeled "CS") contribute at an important level in the mid- to near-infrared as well as in the mm range, while the estimated circumbinary disk (CB) contributes non-negligible flux in the far-infrared. The parameters of the Osorio *et al.* (2003) model are in reasonable agreement with other findings, except that the inferred mass infall rate of $\sim 7 \times 10^{-5}\ M_\odot\ \mathrm{yr}^{-1}\ (M/M_\odot)^{1/2}$ is somewhat higher than inferred from other measurements; the discrepancy may be due to uncertainties in the assumed envelope geometry, or possibly in the molecular abundances.

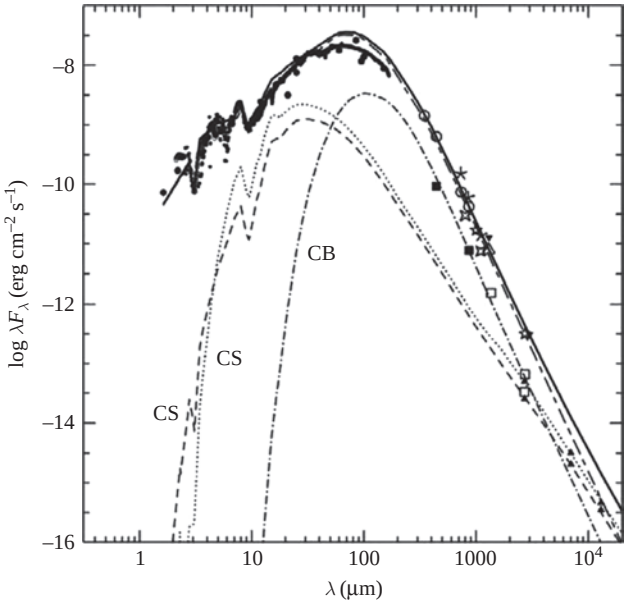

Fig. 5.13. Detailed SED fitting of L1551 IRS 5, including ice features in the mid-infrared, by Osorio *et al.* (2003). Model contributions from individual disks are labeled by "CS" and the circumbinary disk emission by "CB" (see text). Symbols indicate long-wavelength measurements through differing aperture sizes (see Osorio *et al.* 2003 for details).

While L1551 IRS 5 cannot be studied directly at optical wavelengths, the spectrum of the central source can be seen faintly in spectra of the scattered light in the extended nebula. These spectra indicate central object(s) of effective temperature ∼5000 K, with a remarkably strong, blueshifted Hα absorption component indicative of powerful wind(s) (Mundt *et al.* 1985; Stocke *et al.* 1988). As Mundt *et al.* and Stocke *et al.* point out, this type of very broad Hα absorption profile is not similar to those observed in T Tauri stars, but is typical of that seen in the FU Orionis systems, which are rapidly accreting protostellar disks. More tellingly, Carr *et al.* (1987) showed that L1551 IRS 5 exhibits very strong first-overtone absorption bands of CO in the 2 μm region, which again is typical of FU Ori systems but not at all of T Tauri stars. Coupled with the relatively large luminosity of this system, and the bright disks from mm-wave imaging, it seems clear that this system is in a state of rapid disk accretion. Whether it has always been in such a state is an open question, given the long timescales of FU Ori outbursts (Chapter 9).

5.5 The Class 0 sources

The Class 0 sources are distinguished by very "red" SEDs, peaking near $\lambda_m \sim 150$–200 μm, with typically undetectable near- to mid-infrared emission (Figure 5.14). According to equation (5.10), reproducing such SEDs requires mass infall rates $\gtrsim 4 \times 10^{-4}\ M_\odot\ \mathrm{yr}^{-1}$ for typical source luminosities $L \sim 10\ L_\odot$. For comparison, the accretion rate predicted at $T = 25$ K in singular isothermal sphere similarity solution is $\dot{M} \sim 6 \times 10^{-6}\ M_\odot\ \mathrm{yr}^{-1}$. Alternative forms for the long-wavelength opacity with a smaller value of β than (Draine &

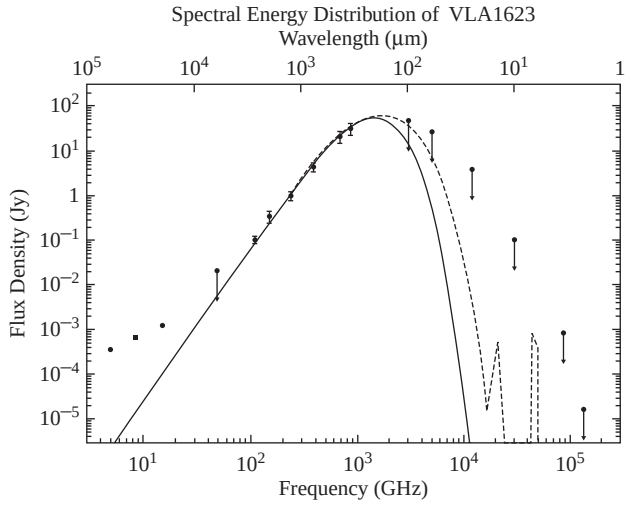

Fig. 5.14. SED of the Class 0 source VLA 1623 (see text). From André *et al.* (1993).

Lee 1984) as suggested by theoretical calculations of dust opacities including ice mantles (Ossenkopf & Henning 1994) yield only a modest reduction in the required infall rate.

A plausible explanation is that many of the Class 0 sources represent the non-similar collapse of the protostellar cloud in its initial phase (Henriksen *et al.* 1997). As discussed in §4.3, the earliest stages of the collapse of a Bonnor–Ebert sphere or other cloud with a flat innermost density distribution will exhibit much higher mass infall rates than predicted by the singular isothermal sphere similarity solution. The large masses of circumstellar material in the vicinity of Class 0 sources also suggest youth (André & Montmerle 1994). Class 0 sources tend to exhibit massive outflows seen in molecular gas which probably also indicates that a large amount of circumstellar material has not yet been blown away by the bipolar ejection.

The interpretation of Class 0 sources in many cases is complicated by the presence of substantial amounts of external material. The Class 0 sources in Ophiuchus, for example, are often found in regions ranging from 50 to 100 magnitudes of visual extinction, and much of this material is not part of any particular envelope; disentangling envelope from "external" matter is more complicated in such a case.

It should be emphasized that the departures from spherical symmetry produce SEDs that are significantly dependent upon inclination (Chapter 4; see also Yorke, Bodenheimer, & Laughlin 1993). The SEDs of toroidal-collapse models can be especially dependent upon the viewing angle (Hartmann *et al.* 1996). These effects probably are not important enough in most cases to confuse the identification between Class 0 and Class I; nevertheless, one should be cautious about inferring "evolutionary state" from SEDs, particularly from limited spectral information dependent upon extinction to the central source, which is highly dependent upon inclination (and centrifugal radius).

Although the Class 0 sources found so far are generally somewhat more luminous than the Taurus Class I sources, $\sim$10 $L_\odot$ (Andre *et al.* 2000). However, if Class 0 sources have much higher infall rates than Class I sources, there is still a "luminosity problem", because the predicted accretion luminosity should be higher still.

5.6 Flat spectrum sources

Some T Tauri stars exhibit very much flatter infrared spectra than are easily explained by disk emission. There is a small class of optically visible T Tauri stars called "flat spectrum" sources, which have spectral indices $s \sim 0$ between $\sim 3 - 100\,\mu$m. The classic example of this group is HL Tau (Figure 5.15). As discussed in §8.2, while irradiated disks

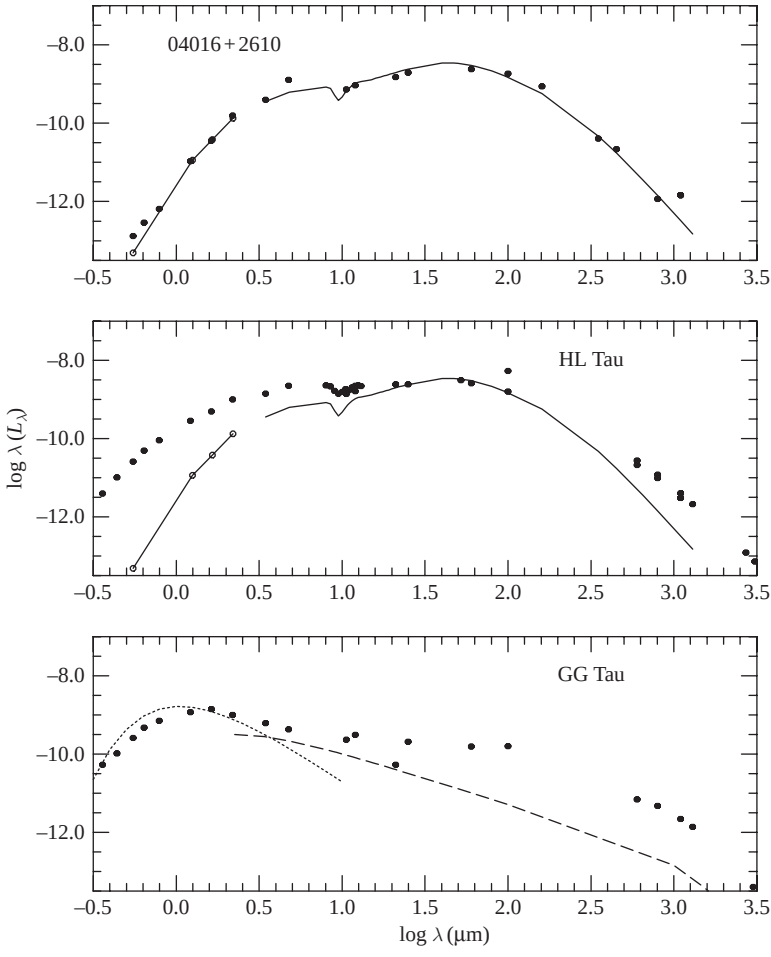

Fig. 5.15. SEDs of three representative young objects in Taurus: the Class I or protostellar source IRAS 04016 + 2610 (Figure 1.5), the "flat-spectrum" source HL Tau, and the Class II system GG Tau. The SED of HL Tau much more resembles that of the Class I source, rather than the "disk" excess of the T Tauri star (Chapter 8). The solid line connected by open circles is a model for the Class I source from Kenyon *et al.* (1993) which includes extra short-wavelength flux resulting from scattering out of envelope cavity (see Figure 5.8, top middle panel). The Class I model is repeated again in middle panel, indicating that an envelope model can explain HL Tau, as long as additional escape of scattered light occurs at short wavelengths, consistent with the near-infrared image (see Figure 5.16). The two curves in GG Tau are schematic representations of star and disk spectra. Modified from Calvet *et al.* (1994).

may exhibit flat SEDs at long wavelengths, it is difficult to achieve this in the near-infrared (compare the Class II system GG Tau in Figure 5.15).

However, if one simply compares the SED of HL Tau to a Taurus Class I object of comparable luminosity, IRAS 04016 + 2610, the similarity is immediately evident (Figure 5.15). The comparable properties of these objects extend beyond the infrared SEDs. Both 04016 + 2610 and HL Tau are completely hidden by dusty nebulae at optical wavelengths, and can only be observed in scattered light in the optical spectral region showing that a dusty envelope must surround the central source (Figure 5.8, middle upper panel; Figure 5.16). These properties strongly suggest the far-infrared emission of HL Tau arises from an infalling dusty envelope rather than a disk. Indeed, infall was independently suggested in HL Tau on the basis of scattered light analyses and high-resolution spectroscopy (Beckwith *et al.* 1989; Grasdalen *et al.* 1989), and from interferometry at radio wavelengths (Hayashi *et al.* 1993). Detailed fitting of the SED (Calvet *et al.* 1994; Hartmann *et al.* 1996) showed that the overall infrared emission plus the scattered light nebula of HL Tau could be matched quite well with an infall rate of $\dot{M} \sim 4 \times 10^{-6}\ M_{\odot}\ \mathrm{yr}^{-1}$, typical of Taurus protostellar sources.

The spatially resolved mapping of HL Tau in ^{13}CO by Hayashi *et al.* suggested that an envelope of radial extent ∼2000 AU was mostly falling in, with a small amount of rotation. The mass infall rate found for this CO cloud was very similar to that found for typical Taurus Class I sources from modeling SEDs (§4.3). The interpretation of gas kinematics is made more complicated by the fact that HL Tau resides at the edge of what appears to be a slowly expanding bubble, as seen in ^{13}CO (Welch *et al.* 2000).

At sub-mm and mm wavelengths, HL Tau exhibits very strong compact emission on a size scale ∼100 AU which is almost certainly due to a disk (Lay *et al.* 1994; Mundy *et al.* 1996). The disk may well have a nearly flat-spectrum temperature distribution, due to the backwarming effect of the infalling envelope; the opaque envelope acts like a blanket, with a tendency to equalize the disk temperature with the local envelope temperature (e.g., Keene & Masson 1990; Natta 1993; Butner *et al.* 1994; D'Alessio *et al.* 1997). The resulting extra disk heating produces higher temperatures which accounts for the strong excess emission at wavelengths $\gtrsim$100 μm, while the envelope probably dominates the system emission between ∼3–100 μm (D'Alessio *et al.* 1997).

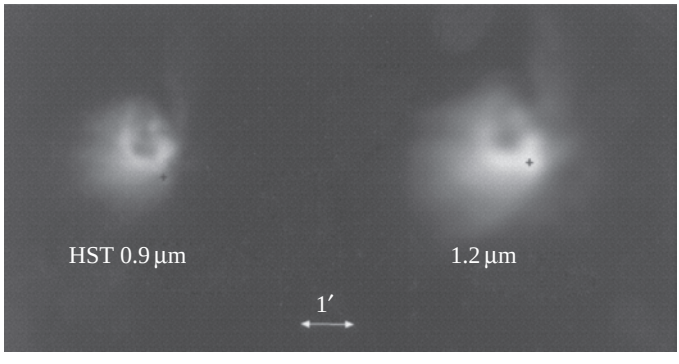

Fig. 5.16. Optical image from HST (left) and near-infrared image from ground-based adaptive optics (right) of HL Tau. From Stapelfeldt *et al.* (1995) and Close *et al.* (1997).

The example of HL Tau indicates that the flat-spectrum sources generally should be identified as protostellar-like sources with infalling envelopes, with perhaps less dense envelopes than those of typical Class I systems and/or more favorable viewing angles, allowing more short-wavelength light to escape along our line of sight. Disk emission for these systems

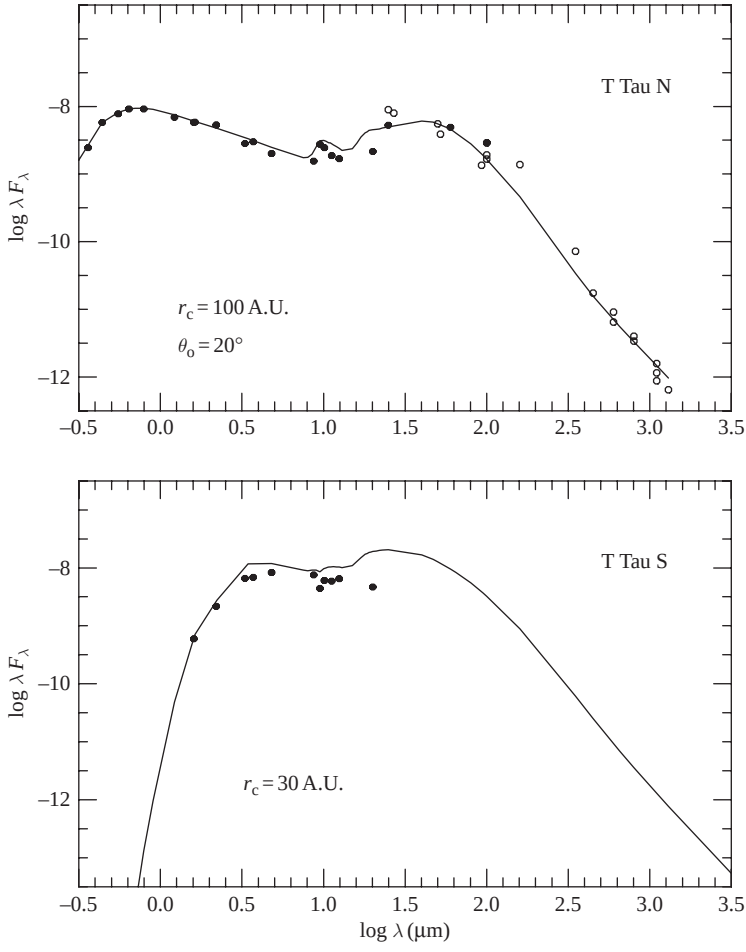

Fig. 5.17. The T Tau binary system. The measurements from ∼1–20 μm are obtained by speckle interferometry (Ghez *et al.* 1991). The optical fluxes are dominated by the northern component; it is not possible to distinguish between sources at wavelengths >20 μm for reasons of limited resolution. The curves represent models including infalling envelopes. In both cases, the models have mass infall rates $\dot{M} = 2 \times 10^{-6}(M/2\ M_\odot)^{1/2}\ M_\odot\ \mathrm{yr}^{-1}$ (the radiative transfer models depend directly only upon the density; the mass of the companion is not known, but the optical star has a mass $\sim 2\ M_\odot$). For T Tau N, the model assumes that we are viewing the object along a *hole* in the envelope; the excess emission between 2 and 10 μm is due to a disk, while the emission at longer wavelengths, including the silicate emission "bump" at 10 μm, is due to the infalling envelope. The model for the southern component assumes no envelope hole. Fitting the two components requires different centrifugal radii in the models which may reflect differing distances of the (orbiting) stars from the edges of what is presumably a common infalling envelope. Modified from Calvet *et al.* (1994).

is likely to be especially strong, both because these young disks may be quite massive and because of the backwarming effects of the envelopes.

In other cases an apparent flat SED is the result of combining the emission of an optically visible T Tauri star with that of a heavily extincted, possibly protostellar, close companion. The classic case of this is T Tauri itself. The main components T Tau N and S are separated by about 0.7 arcsec ∼100 AU on the sky. The southern component, detected only in the infrared (Dyck *et al.* 1982), is actually binary with a separation of about 0.05 arcsec or ∼7 AU. T Tau Sa is actually the most luminous source in the system, perhaps an intermediate-mass star, heavily extincted, while Sb appears to be a typical T Tauri star reddened by about 15 magnitudes of visual extinction (Duchêne *et al.* 2005). The result is that T Tau N looks like a typical T Tauri star with disk (§8.2), while T Tau S looks more like a protostellar source (Figure 5.17).

The high extinction seen toward T Tau S is usually interpreted in terms of seeing the object through an edge-on disk (Hogerheijde *et al.* 1997b, Koresko 2000, and Beck *et al.* 2004). However, as T Tau S appears to lie within a dusty region, not within the large extincted cavity seen in scattered light (Stapelfeldt *et al.* 1998b), one might consider whether some of this extinction is due to an infalling envelope. The advantage of an envelope model is that it naturally predicts significant, but not enormous, extinction, while disks can be extremely opaque seen edge-on. In any event, it is clear that more detailed observation reveals additional complexity, much of it the product of binary or multiple star formation.

5.7 Spatial distribution of emission

If the thermal dust emission from the envelope can be resolved, one can test the whether the envelope density distribution is consistent with infall, especially when observed at long wavelengths where the dust is optically thin. The observed intensity on the sky is (cf. Appendix 3)

$$I_\nu(p) = \int_0^\tau S_\nu \exp(-\tau_\nu) d\tau_\nu, \tag{5.16}$$

where the impact parameter p is the distance measured perpendicular to the line of sight from the center. The optical depth at frequency ν along the line of sight at p is

$$\tau_\nu = \int dz\, \rho \kappa_\nu, \tag{5.17}$$

where κ_ν is the dust opacity per unit mass at frequency ν and z is the coordinate along the line of sight at constant p.

One simple limit is when the envelope is optically thin. This applies at long wavelengths and large radii, where the envelope will be more spherical, and the source function will be entirely thermal. Then

$$I_\nu(p) = \int_0^\tau B_\nu d\tau_\nu = 2 \int_0^\infty B_\nu k_\nu \rho dz, \tag{5.18}$$

where B_ν is the Planck function and the factor of two takes the symmetry of the envelope into account.

If the frequency of observation is sufficiently low that the Planck function is in the Rayleigh–Jeans limit $h\nu \ll kT$, and if we take power law distributions $T = T_\circ (r/r_\circ)^{-m}$, $\rho = \rho_\circ (r/r_\circ)^{-n}$, then

$$I_\nu(p) = \frac{4\nu^2 k r_\circ T_\circ \rho_\circ \kappa_\nu}{c^2} \left(\frac{p}{r_\circ}\right)^{1-(m+n)} \int_1^\infty \frac{x^{1-(m+n)} dx}{(x^2 - 1)^{1/2}}. \quad (5.19)$$

Thus, the surface brightness depends upon both the density and the temperature gradient. For the standard case of infall in the optically thin temperature distribution, $m = 1/3$ and $n = 3/2$, $I_\nu(p) \propto p^{-5/6}$.

There are several problems with carrying out this analysis in practice. The intensity distribution is very sharply peaked at small radii (where very little of the mass resides), while the extended wings of the distribution produced at large radii (where most of the mass resides) may be difficult to distinguish from background emission. This makes it generally difficult to follow the surface brightness of the cloud out to several beam sizes; usually, comparisons are made between the main peak of the intensity distribution and the point spread function (e.g., Butner *et al.* 1991). A pure power-law distribution is scale free, so it does not have a "size"; inner and outer cutoffs play an important role in determining the apparent source "size" when convolved with a (roughly Gaussian) observational point spread function (see discussion in Terebey *et al.* (1993) and Ladd *et al.* (1991)). Finally, a central unresolved continuum source (i.e., a disk) with a shallow density law can be difficult to distinguish from a source without a disk but with a steeper density increase with decreasing radius; detectable disks at mm and sub-mm wavelengths are found even in very young objects (Keene & Masson 1990; Lay *et al.* 1994; Pudritz *et al.* 1996).

Notwithstanding these difficulties, some careful investigations of the spatial distribution of long-wavelength dust emission suggest density distributions reasonably consistent with infall (Butner *et al.* 1991; Ladd *et al.* 1991; Chandler & Sargent 1993; Terebey *et al.* 1993; Shirley *et al.* 2002). One of the best-studied objects, B335, yields an estimate of the density power law of $\sim r^{-1.6 \pm 0.2}$, including the uncertainties introduced by the possible presence of a central unresolved source (disk) (Harvey *et al.* 2003).

5.8 Detection of infall from line profiles

Although direct detection of infall motions is the clearest indication of collapse, as mentioned in the introduction to this chapter, this has been a very difficult measurement to make. In some cases (such as L 1551 IRS 5; §5.4) kinematic evidence can be found from spatially resolved observations, but even then there can be difficulties due to the presence of outflowing molecular gas (cf. Zhou & Evans (1994) and references therein). Another reason is that there is very little mass at high velocities. One can see this by noting that, in spherical infall, the mass interior to r is $M_r \propto r^{3/2}$; but since the infall velocity $v_{\rm ff} \propto r^{-1/2}$, $M_r \propto v^{-3}$. In addition, if material does drop out onto a disk of size $r_{\rm c} \sim 100$ AU, the amount of mass at velocities greater than a few $\mathrm{km\,s^{-1}}$ will be even smaller.

A more complicated analysis than presented above is needed to model the optically thick line emission from moving envelopes (Kuiper *et al.* 1978; Anglada *et al.* 1987). Again consider a spherical envelope in radial free-fall. Simplifying the situation once more, assume that only material with exactly the appropriate Doppler shift can contribute to the observed emission at a frequency shift $\Delta\nu$ from the line center frequency $\nu_\circ$. In other words, only gas with a Doppler shift in the observer's direction of $\Delta V_n = c\Delta\nu/\nu_\circ$ contributes to the flux at $\Delta\nu$. This simplifying assumption is part of the so-called "Sobolev approximation", which is used to make the treatment of line transfer in moving media much more tractable (in the radio astronomical literature, this is often called the Large Velocity Gradient or LVG

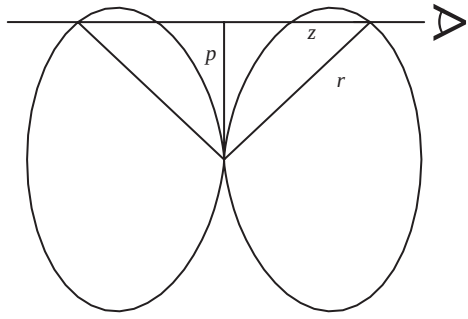

Fig. 5.18. Constant velocity surfaces for radial infall in a (meridional) plane. If the observer is on the right-hand side, the solid curve corresponds to a redshifted surface of constant projected velocity, while the dashed curve is the corresponding surface for the same velocity blueshifted. The line of sight to the observer, taken along coordinate z at impact parameter p from the center, generally intersects the constant velocity surface at two points. If the source function of the spectral line varies radially, then the differing order of radial distance at which the line of sight intersects the constant velocity surface on the blueshifted and redshifted sides produces a line asymmetry (see text).

approximation). The points in space which satisfy this requirement lie on a surface given by the equation

$$\Delta V_n = v_\circ \left(\frac{r_\circ}{r}\right)^{1/2} \frac{z}{r}, \tag{5.20}$$

where z is the distance in the observer's direction measured from the plane perpendicular to the observer's direction passing through the center.

Figure 5.18 shows typical surfaces of constant velocity (in the observer's plane). It is evident from the figure that a ray passing through the envelope at a given impact parameter p will intersect the constant velocity surface twice, and so two distinct regions will contribute to the flux at a given velocity shift. Denote these intersections as r_1, r_2, where the former corresponds to the intersection closest to the observer. We make the further assumptions of the Sobolev approximation that the source functions are slowly varying across the region near the constant velocity surface. This requirement is most likely to be met in the case where the relevant path length $dl << r$, which is most easily satisified if the medium has large velocity gradients. Then the formal solution of the equation of transfer (equation (5.16)) at impact parameter p in the direction z toward the observer is

$$I^+(\Delta v) = S(r_1)\{1 - \exp[-\tau(r_1)]\} + S(r_2)\{1 - \exp[-\tau(r_2)]\}\exp[-\tau(r_1)]. \tag{5.21}$$

That is, the specific intensity in the line of sight is given by the emission from the outer layer plus the emission from the inner layer reduced by the extinction of the overlying part of the constant velocity surface.

In the case of a static medium, the line width is $\delta v^2 = v_{\rm th}^2 + v_t^2$, where $v_{\rm th} = (2kT/m)^{1/2}$ is the thermal broadening for a species of mass m and v_t is the turbulent broadening velocity. For a static medium, this line broadening helps determine the line optical depth, but in the Sobolev limit, the line optical depths τ depend instead on the envelope velocity field. To see this, note that regions of the envelope that have the same line-of-sight velocity within δv of

v are able to contribute to the absorption at v. The path length over which the medium is in radiative contact is then

$$dl \approx \frac{v_{\rm th}}{(dv/dr)_s}, \tag{5.22}$$

where $(dv/dr)_s$ is the velocity gradient along the line of sight at the resonant position s where the line-of-sight velocity in the medium is equal to the desired velocity shift. If we approximate the line profile as square with a width given by $\delta v = v_{\rm th}$, and take the line absorption cross-section per molecule for spectral line m to be α_m, then the optical depth at velocity v through the resonant region becomes

$$\tau_m \approx \frac{\alpha_m N_s}{v_{\rm th}}\, dl = \frac{\alpha_m N_s}{v_{\rm th}} \frac{v_{\rm th}}{(dv/dr)_s} = \frac{\alpha_m N_s}{(dv/dr)_s}, \tag{5.23}$$

where N_s is the number density at the resonant position s. The velocity width of the line δv thus drops out of the optical depth determination.

Because of the symmetry of the problem, the radii of intersection and optical depths are the same at $\pm\Delta v$. However, the ordering of the intersections with the constant velocity surface differs, and this is responsible for producing a profile asymmetry for non-constant line source functions S. In many situations the source function will decrease with increasing radius, either because of outwardly decreasing temperatures, or densities, or both. Consider the limiting case of an outwardly decreasing source function, namely $S(r_1) = 0$. Then the emission from the material on the side of the envelope nearest the observer, which is redshifted and thus contributes to the long-wavelength portion of the line profile, is reduced by a factor of $\exp[-\tau(r_1)]$ relative to the emission on the correspondingly blueshifted portion of the line profile. This asymmetry holds as one sums over all impact parameters to obtain the total observed flux. Therefore the blue wing of the line is brighter than the red wing (Anglada *et al.* 1987). The centroid of the emission profile will exhibit a net blueshift. A similar effect is discussed in Chapter 10, when infall line profiles are revisited in the context of accretion onto the surfaces of T Tauri stars.

Major problems in detecting this infall asymmetry are defining the central velocity shift of the object and avoiding the effects of outflows; the latter can produce confusing effects, especially because they do not have the quasi-spherical symmetry assumed implicitly in the above discussion (Figure 5.18). The question of the central velocity is especially important, because even small errors in this parameter can affect the derived asymmetry dramatically. Initial studies (e.g., Walker *et al.* 1986) utilized absorption reversals in optically thick lines to define the central velocity (cf. Figure 5.19). The problem with this method is that it can be difficult to distinguish absorption in the outer infalling region from foreground absorption by an independent cloud with an unrelated motion. This is an especially difficult problem because the velocity shifts are small, and of the order of velocity dispersions of the objects within the cloud. The favored approach (see discussion by Zhou & Evans (1994)) is to use the emission from another optically thin spectral line which is too optically thin to show the effects of outflow and foreground low-density clouds, and therefore is more likely to define the system velocity for asymmetry analysis.

Several promising candidates for protostellar infall have been found based on line profiles, although uncertainties remain (Zhou 1994, and references therein; also Choi *et al.* 1995, Wang *et al.* 1995, Myers *et al.* 1995; Mardones *et al.* 1997). For example, in the very case of B335 shown in Figure 5.19, a higher-resolution study by Wilner *et al.* (2000) also

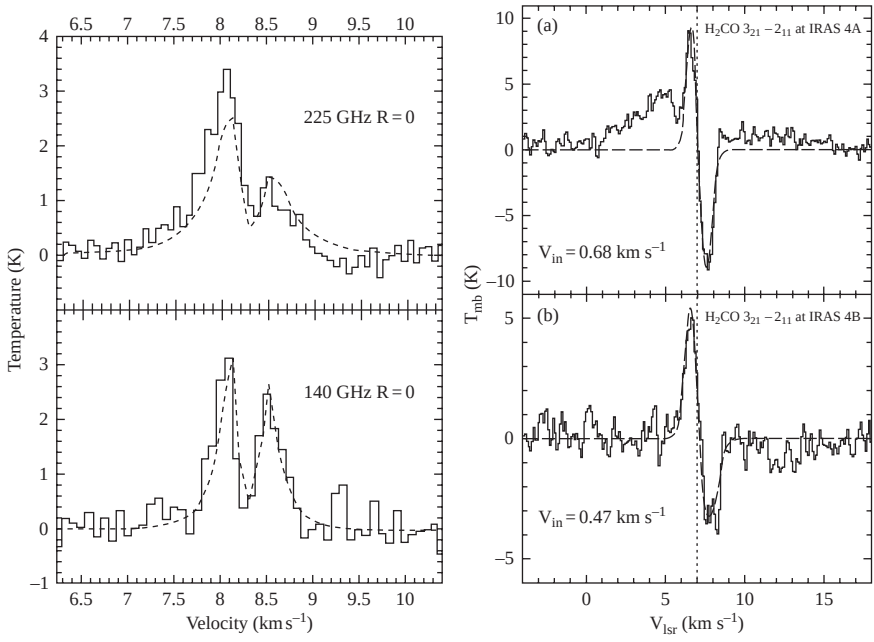

Fig. 5.19. Potential infall profiles of embedded objects. Left: Emission line profiles of H_2CO in the Bok Globule B335. The central reversal is presumed to be absorption from the outer, nearly stationary, regions, while the emission wings are asymmetric in a sense consistent with infall. The dashed lines are predicted line profiles for a simple model based on the singular isothermal sphere similarity solution for collapse (§4.2). From Zhou *et al.* (1993). Right: Infall signature detected in H_2CO lines toward the dense bright cores NGC 1333 IRAS 4A and 4B (see text). From Di Francesco *et al.* (2001).

found infall asymmetry, but the high-velocity wings predicted by collapse models were not detected, though this may be explained by freeze-out (see below). In addition, some of the blueshifted emission is due to outflow, complicating the interpretation of the profile asymmetry. Spatial resolution is important in understanding the kinematics of protostellar regions; mm-wave interferometric mapping has provided evidence for spatially resolved collapse motions in a few objects (e.g., Hayashi *et al.* 1993; Ohashi *et al.* 1996).

Some of the problems involved in establishing the system velocity can be avoided in systems for which infall can be observed seen directly in contrast against the continuum emission of inner regions; this avoids much of the complicated analysis involved in line self-absorption. The main limitation of this technique is that it requires a very bright central continuum source, and so is not generally applicable. However, Di Francesco *et al.* (2001) were able to use this method in NGC 1333 IRAS 4A and B, and detected a strong infall signature (Figure 5.19, right panel).

More generally, one might look for a statistical trend in profile asymmetries. This has been done for a sample of Class 0 and Class I cores by Mardones *et al.* (1997) and Gregersen *et al.* (2000), showing that, while an individual source may exhibit a non-infall asymmetry, most Class 0 and even Class I sources show a profile asymmetry consistent with infall (Figure 5.20).

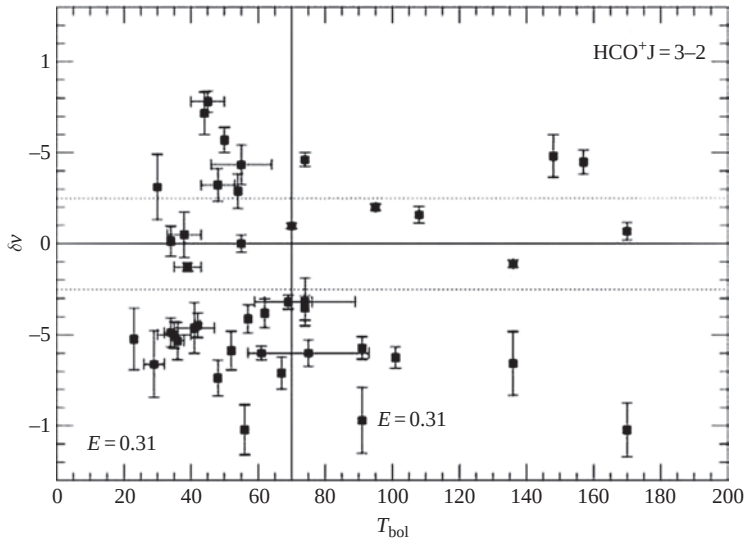

Fig. 5.20. Profile asymmetries in the HCO^+ $J = 3-2$ line of a sample of Class 0 and Class I objects. The vertical line denotes the approximate distinction between Class 0 objects (to the left) vs. Class I objects (to the right) using the "bolometric temperature", a measure of the redness of the spectrum. Objects with a negative δv have velocity shifts of emission to the blue, consistent with infall (see text). From Gregersen *et al.* (2000).

Generally, high-velocity wings predicted by infall models are not seen in typical species. Probably this is due to depletion (freeze-out) of the relevant molecular species at high densities and low temperatures (e.g., Bergin *et al.* 2002); this effect may drastically reduce the species for which the high-velocity wings of infall can be detected. One exception is the Class 0 source L1489 IRS, in which broad redshifted absorption is seen against the continuum in the fundamental rotation–vibration band of CO at 4.7 μm, with velocities of up to 100 km s^{-1}. However, this infall is likely to be highly non-axisymmetric, as it would imply an extremely large mass infall rate inconsistent with other observations. The likely special geometry in this object is also consistent with the absence of similar detections of fast infall in other systems.

Overall, it is clear that the infall model for protostellar cloud collapse and protostar formation is reasonably well supported by a wide variety of observations, including explaining SEDs, general velocity shifts, and in a few cases direct spatial resolution of infall motions.

5.9 Massive protostars

There is no reason why the overall picture of protostellar collapse in low-mass systems should not apply to higher-mass stars as well (Equation (4.52)). Indeed, as discussed in §4.7, non-spherical collapse followed by accretion through the disk may be essential to the formation of the most massive and luminous stars.

The application of the above paradigm of protostellar formation to high-mass stars has been slowed by observational difficulties. Because massive stars are much more rare than low-mass stars, they must be studied in more distant regions, placing extreme demands on

spatial resolution. In addition, massive stars perturb their environments to large distances through heating, ionization, H II region expansion, and stellar winds, and the resulting welter of phenomena tends to confuse the analysis. Finally, massive stars are frequently found in dense (proto)stellar clusters, presenting problems in understanding which source is actually responsible for which observed property.

Despite these difficulties, progress has been made in recent years; a good recent review is that of Zinnecker and Yorke (2007). High-resolution studies by Shepherd *et al.* (2001) of the compact H II region G192.16–3.82* suggested that the presumed early B star in the system has a circumstellar disk with a diameter of order 130 AU and a mass of several times solar. Zhang *et al.* (1998) found evidence for very large (5000–10000 AU) flattened rotating structure around a distant, massive young object, IRAS 20126 + 4104. This system has been extensively studied and shown to have not only evidence for the rotating disk but also a well-developed bipolar outflow (see Cesaroni *et al.* 2007 for a detailed discussion). Another example has been investigated by Patel *et al.* (2005), who found additional evidence for a dusty disk of radius ∼330 AU around a 15 $M_{\odot}$ protostar. Observations of "source I", a highly embedded source in the Orion Nebula Cluster provide a suggestive picture of protostellar collapse in a moderately massive system (Greenhill *et al.* 2005; Reid *et al.* 2007). Maser emission in source I suggests outflows along an "X" pattern, which could be cloud material entrained along cavity walls (e.g., Figure 4.11; Cunningham *et al.* 2005). Source I also exhibits evidence for a disk which is partially ionized, presumably by the ultraviolet radiation of the central source (Reid *et al.* 2007). In summary, evidence is mounting that massive stars form through disk accretion.

Other clues to the formation of massive stars come from the study of so-called "ultra-compact" (UC) H II regions. These are extremely dense, small (<0.1 pc) ionized regions surrounding what are likely to be massive young stars, if not massive protostars. In their survey of UC HII regions, Wood and Churchwell (1989a) showed that the lifetimes of these regions had to be much greater than the sound crossing time, based on number statistics. Thus these UC HII regions cannot simply be expanding into a low-density medium; somehow the ionized material must be confined (or replenished, if it is being evaporated) for timescales of order 10^5 yr or more.

Hollenbach *et al.* (1994) discussed various possibilities for resolving the problem of UC H II region lifetimes. They dismissed the possibility that the ram pressure of infalling circumstellar material confines the H II regions, because maser proper motions indicate outflow, not infall, and because ram pressure confinement is unstable, leading to either runaway expansion or collapse of the H II region. Van Buren *et al.* (1990) had argued that if the massive stars move through dense molecular gas at high speeds, of order 10 km s^{-1}, their ionizing radiation would create a bow shock ahead of the motion, consistent with the observed geometry of 20% of the observed regions (Wood & Churchwell 1989a). However, most of the resolved UC H II regions have geometries that differ from the cometary/parabolic shape predicted by this model; in addition, it seems very unlikely that most massive stars have such high velocities with respect to their ambient medium.

Yorke *et al.* (1983) suggested that some UC H II regions might be "champagne flows", where the H II region breaks out of a dense molecular cloud. This model does not

* Such regions are often identified by their galactic longitude and latitude in degrees; hence, this object is at $l = 192.16$, $b = -3.82$.

particularly address the nature or lifetime of the dense material, and may not explain the limb-brightening seen in some regions (Van Buren *et al.* 1990). The problems with the above models led Hollenbach *et al.* to propose that most UC H II regions are the photoionized and photoevaporated material coming off the circumstellar disks of very young massive stars.

De Pree *et al.* (1995) argued that the disk evaporation model of Hollenbach *et al.* (1994) would not work for most objects. The disk wind model (in most cases, not all) predicts a spectrum typical of optically thick free–free emission in an ionized wind, which De Pree *et al.* found to be inconsistent with observations of most UC H II regions. Instead, De Pree *et al.* revived the idea of pressure confinement by the ambient medium, pointing out that more recent estimates of massive core properties indicated much higher densities and temperatures than those assumed by Wood and Churchwell (1989a). De Pree *et al.* invoked cores with densities of $\sim 10^7$ cm^{-3} and temperatures of order 100 K, and showed that at such high densities the UC H II regions could be confined for timescales of order 10^5 yr.

A problem with the De Pree *et al.* model is that the postulated molecular core cannot be static. It is straightforward to show that even at temperatures of order 100 K, an object with this density and required diameters $\gtrsim$0.04 pc are gravitationally unstable, using, for example, the Bonnor–Ebert limit (equations (3.18), (3.19)). Furthermore, the only way the core can have such a high temperature is if it is heated by local massive stars, most probably the central star producing the UC H II region; thus this temperature does not reflect the initial condition, which must have been one of a much lower temperature, and thus even more susceptible to collapse. Indeed, it is difficult to believe that the surrounding core is not in the collapse state if some of it has already collapsed to form a star.

Thus one must return to the gravitational infall picture, with the ram pressure of the infalling material providing a more important restraint than the static pressure. Keto (2003) computed infall models in spherical geometry, and showed that in principle flow could continue through the H II region down to the star, with ram pressure preventing rapid expansion. However, Keto ignored the problem of radiation pressure in the infalling dusty envelope, considering only the constraint at the dust sublimation radius; as discussed in §4.7, this is problematic for stars with masses $\gtrsim$10 $M_\odot$ if the long-wavelength dust opacity is at all similar to that of the diffuse interstellar medium.

The necessity for the core to have *some* angular momentum; the likelihood that collapse is from an initially flattened core; and the need for a "flashlight" effect to form the most massive stars all point to considering UC H II formation and evolution in a non-spherical collapsing envelope. As discussed in Chapter 4, the most general configuration is one in which there are low-density (polar) regions with high-density (equatorial) regions. In such a model, it is far more likely that the poles are blown out, with evaporating H II region gas streaming out of these regions, while infall is still occurring in shielded regions to a disk. Indeed, non-spherical infall must occur if one is to form an evaporating disk, as in the Hollenbach *et al.* model if one is to use a disk. The advantages of the "evaporating toroid" picture (Figure 4.11) over the disk model are that infall must precede or be contemporaneous with disk formation, and that the infalling cloud naturally subtends a larger solid angle as seen from the star than a disk, thus capturing more ionizing photons than the disk. Perhaps most importantly, because the evaporating toroid can be much larger than the disk, the observed free–free emission at cm wavelengths is much less likely to be optically thick in the toroid model than in the disk model, potentially circumventing the problem addressed by De Pree *et al.*

Whether this type of model can account for the range of morphologies of UC H II regions is not clear; further model calculations are required. However, given that the most general collapse must be toroidal (which may be an essential requirement for forming the most massive stars), it is difficult to avoid the conclusion that this picture must apply to some UC H II regions.

Wood and Churchwell (1989b) inferred that O stars spend somewhere between 10 and 20% of their lifetimes in opaque molecular clouds; i.e., they spend between 1 and 2 Myr in clouds. This is consistent with the short lifetimes of molecular clouds (Chapter 2); it also implies that the formation timescale of massive stars is also relatively short, so that high infall rates are needed. This timescale is an upper limit to the formation timescale, because an O star can have a large-scale dust cocoon. Thus, massive star formation times probably are no longer than a few times 10^5 yr (unsurprisingly, comparable to UC HII region lifetimes).

6

Binaries, clusters, and the IMF

Virtually all stars are born with neighbors. Most stellar systems are multiple, and many if not most stars are born in groups, with a subset in clusters of substantial numbers of stars. An understanding of multiplicity is therefore an important part of theories of star formation.

The complex structure within molecular clouds, and in particular the asymmetries present in protostellar cores, may be essential to understanding the process of forming binaries. Whether the disks formed during protostellar collapse are capable of spawning multiple stellar companions rather than simply accreting onto the central object is an open question, perhaps requiring strong departures from axisymmetry in the infalling material. Observationally, we detect multiple protostellar systems which appear to lie within disks or toroids in Class I sources, indicating that stellar fragmentation occurs before infall to the disk is complete.

The early evolution of binary and multiple stellar systems is likely to be complex. The growth in mass of fragments formed early on will depend upon complicated accretion processes in disks and infalling envelopes. If more than two fragments are formed, the system can become dynamically unstable, resulting in dispersal or ejection of some members. Whether many or even any stars are initially formed as single objects, or instead were ejected from multiple systems, is currently unclear.

Probably most young stars are born in clusters or groups. Currently most stars in the solar neigborhood are born in modest-sized groups of order 10–100 members in regions of order a pc in size. Only about 10% of local star formation ends up in producing "open clusters", systems with of order 1000 members and sizes of a few pc (Adams & Myers 2001), which remain bound for one to a few hundred Myr, like the Pleiades. The small groups are likely to be weakly bound or unbound, and in any event are probably dynamically unstable, leaving only the larger clusters to resist dispersal for tens to hundreds of Myr.

It is not clear how cluster gas is accumulated, nor how it fragments into individual stars. One possibility is that the long-range effects of gravity can result in focussing material from larger scales into a small area. In such a picture, non-linear, small-scale "turbulent" structure needs to be present to fragment into stars while the global protocluster cloud collapses under its own gravity.

One of the ultimate goals of any global theory of star formation must be to understand the origin of the stellar initial mass function (IMF). There are many theories of the IMF; sorting through the various possibilities is difficult. It is plausible, though far from certain, that different mass ranges of the IMF result from differing processes. The approximate power-law distribution at high masses suggests some kind of generic process, perhaps a result of a turbulent cascade of structures, while the "peak" in the number distribution or the turnover in

the numbers of stars at smaller masses may have something to do with trapping of radiation in dense structures. Observations of star formation in extreme environments are beginning to show some indication of variation in the IMF; further studies are needed to yield clues to the mechanisms responsible for setting stellar masses.

6.1 Observations of binary and multiple systems

Any attempt to understand the binary and multiple populations of stars begins with the classic survey of field solar-type (G) dwarfs by Duquennoy and Mayor (1991; DM91). Correcting for various biases in radial velocity and visual binary studies, DM91 estimated that of all systems (or primary stars), the fraction that are single is roughly one-third, with at least ∼10% of all systems in triple and quadruple systems. These results may understate the true multiplicity, as outer members are likely to be tidally disrupted over the typical several Gyr ages of nearby G dwarfs; in addition, systems of more than two stars are generally unstable (e.g., Reipurth & Clarke 2001), being long-lasting only when the orbits are sufficiently hierarchical, for example an outer third member with a much larger orbit than that of the inner two stars.

Binary stars in the field exhibit a broad distribution of orbital periods, as shown in Figure 6.1 (left). The peak of this quasi-Gaussian distribution in period corresponds to an approximate semi-major axis of ∼30 AU. The turn-down in the numbers of binaries at long periods may partly be a result of tidal disruption, as above. Another interesting feature is the distribution of eccentricities. As shown in Figure 6.2 (right), there is quite a wide range of eccentricities in binary orbits, except for the closest systems; for these, tidal effects are likely to have helped circularize any initial close elliptical orbits (e.g., Meibom *et al.* 2006).

Given the likelihood of orbital evolution, it is of importance to try to find the initial distribution of multiple star properties. Although it is more difficult to study more distant, more heavily extincted systems, substantial progress has been made in characterizing multiplicity in YSOs, using principally near-infrared observations, especially speckle interferometry, with additional results from lunar occultations and some radial velocity studies. Simon *et al.* (1995; see also Ghez *et al.* 1993 and Leinert *et al.* 1993) summarized a survey of 47 systems

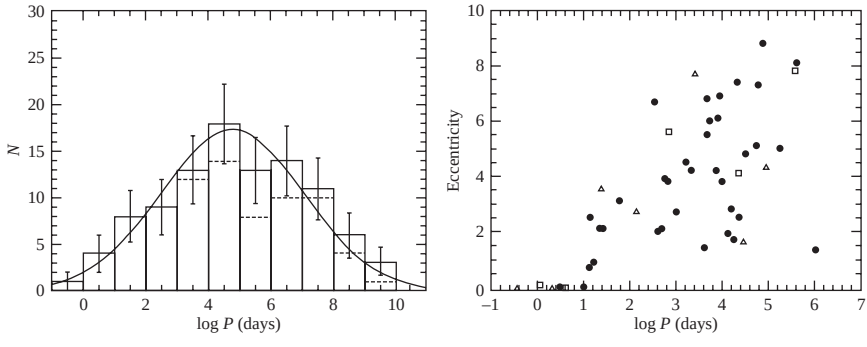

Fig. 6.1. Relative numbers of stars as a function of binary period (left) and orbital eccentricities as a function of period (right) for G dwarf systems in the solar neighborhood. From Duquennoy and Mayor (1991) (see text).

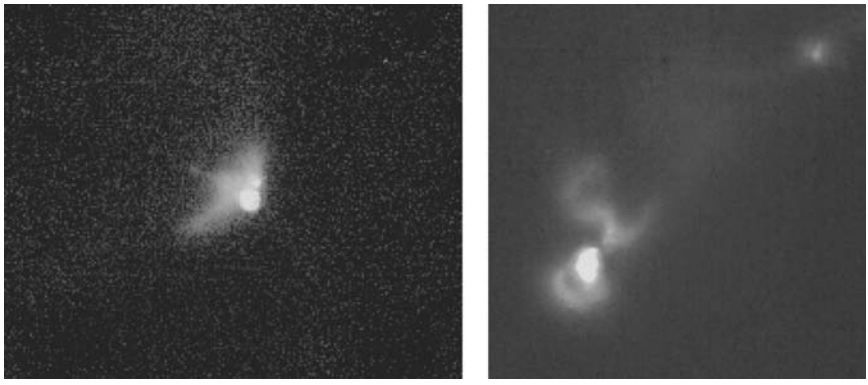

Fig. 6.2. Left: *HST* NICMOS image of the Taurus Class I source IRAS 04381 + 2540. This near-infrared (1.6 μm + 2.15 μm) image shows two protostars separated by about 0.8 arcsec, or around 110 AU. From Hartmann *et al.* (unpublished). Right: NICMOS near-infrared scattered light image of the Taurus Class I source IRAS 04325 + 2402. The central region exhibits a ring, which might be a signature of an inner binary system (see Figure 6.4). An additional low-luminosity, pre-main-sequence system is off to the upper right, at a distance of about 1150 AU from the main structure; this third system has a dark lane running through it suggestive of an edge-on disk. Modified in part from Hartmann *et al.* (1999).

in Taurus revealed 22 binaries and four triple systems; in Ophiuchus, of 35 systems 10 were binary, two were triple, and one system was quadruple. This work suggested an excess of order a factor of two in the binary frequency in Taurus relative to the field distribution in the separation range ∼18–1800 AU (with some correction for incompleteness). This factor cannot apply at all scales, because then the fraction of primaries in binaries would be greater than unity. The higher frequency of binaries in Taurus may simply indicate that Taurus-type regions do not contribute much to the field stellar population; there is some evidence that denser, more clustered regions have a more typical binary frequency (see discussion in Mathieu *et al.* 2000).

Studies of the nearby field stellar population suggest much lower binary fractions for M and later stars than for G stars (e.g., Bouy *et al.* 2003; Burgasser *et al.* 2003; Close *et al.* 2003; Gizis *et al.* 2003; Siegler *et al.* 2005), closer to 10% of all systems. However, low-mass systems are much more susceptible to disruption over time, and recent studies of young star-forming regions suggest companion fractions closer to 20% (Kraus *et al.* 2005; see discussion in Konopacky *et al.* 2006). The initial binary fraction in lower-mass stars is thus still uncertain.

Observations show that binary formation starts early, before the entire protostellar envelope has collapsed. Figure 6.2 shows two Class I sources in Taurus which are multiple and which clearly lie within infalling envelopes, as indicated by the scattered light outflow cavities. The structure in IRAS 04381 + 2540 is relatively straightforward, indicating a fairly wide-opening angle in the cavity with the binary at the base. IRAS 04325 + 2402 is clearly more complicated, with a ring-like structure around the primary source; the wide member exhibits a dark lane indicating a disk viewed nearly edge-on. The wide separation between the primary source and the faint distant object may mean that this is an accidental binary.

Other multiple systems include the well-known binary Taurus Class I source L 1551 IRS 5 (§5.4), and the archetypal T Tauri triple system, lying within a large scattered light nebula suggestive of an outflow cavity in an infalling envelope (Stapelfeldt *et al.* 1995). Thus early binary or multiple star formation is likely to be a typical outcome of protostellar core collapse.

6.2 Theories of multiple stellar system formation

One of the early ideas for binary formation was fission of a very rapidly rotating protostar. However, fission is difficult if not impossible to make work because the angular momentum of a pair of objects just touching is generally larger than the angular momentum of the most rapidly rotating star (Pringle 1991a), making this evolution difficult without some additional source of angular momentum. Moreover, fission certainly cannot explain the majority of systems with orbital semi-major axes of a few to hundreds of AU. At the extreme other end of the scale of separations, one might consider the "capture" or otherwise association of initially separate cores. This mechanism may work for the largest binary separations (e.g., Bonnell *et al.* 1991), such as for the protostellar system shown in the right panel of Figure 6.2, where the outlying protostar is about 1000 AU from the main source. However, it is difficult to make capture models work for much closer binaries (e.g., left panel of Figure 6.2); the angular momentum of the combined system must be extremely low for cores separated by a distance of order 0.1 pc to end up with most of the mass in protostars separated by tens of AU, i.e., orders of magnitude smaller orbits.

The roughly similar sizes of many circumstellar disks and median binary separations suggests that binaries typically form in some way during collapse, as a result in part of the finite angular momentum of the initial cloud core. As discussed in §§2.5 and 4.1, it is very difficult to fragment during free-fall collapse; however, once the supersonically infalling material shocks and becomes incorporated into the disk, fragmentation becomes a more realistic possibility.

Many numerical simulations of fragmentation during protostellar collapse have been conducted over the last couple of decades (see, e.g., the review by Boss 1995). One major result of the early simulations was the finding that the distribution of angular momentum was important in inducing fragmentation. Collapse of the singular isothermal sphere did not appear to lead to fragmentation in general, while so-called "Gaussian" cores (i.e., cores with a flattening of the density distribution at small radii) were capable of fragmenting. As discussed in Chapter 4, a uniformly rotating singular isothermal sphere has a mass $M(r) \propto r$ and a specific angular momentum $j \propto r^2$; hence, $j \propto M^2$. This rapid increase of angular momentum with increasing mass leads to a very centrally concentrated disk, at least initially, the opposite of what one would like to have a massive exterior fragment. In contrast, "Gaussian" cores (i.e., cores with centrally flattened density distributions) have proportionately more mass with larger angular momenta. This leads to the formation of a less centrally concentrated disk (Stemwedel *et al.* 1990), a much more favorable configuration for fragmentation into multiple objects.

The problem of protostellar fragmentation into multiple stars has historically been subject to significant numerical problems. Beyond the issue of having enough resolution in the calculation (e.g., Truelove *et al.* 1997), there are difficulties in handling energy balance sufficiently accurately to tell whether fragmentation actually occurs (S 7.7). One feature which seems clear from the work of Boss (2002, 2005, and references therein), Bodenheimer

and Burkert (1993), and others, is that a non-axisymmetric structure of the initial cloud makes fragmentation much more likely. Some early simulations introduced modest non-axisymmetric components to make binary formation easier. However, real cores are often *highly* asymmetric (e.g., Figures 3.1, 3.7), corresponding to non-linear deformations from a spherical or axisymmetric initial cloud. If cloud cores are often (roughly) prolate, with length ratios of 2:1 or even 3:1 (Jones & Basu 2002), it is easy to understand why binary formation is so frequent; if their structure is even more complex, multiple condensations may produce triple and higher order systems more efficiently. Along these lines, Boss (2002) confirmed that prolate clouds tend to fragment into binary protostars, while oblate clouds tend to fragment into more objects, with interactions and possible ejection of some objects. Thus, non-equilibrium structurings of protostellar cores may be critical to the formation of multiple star systems.

6.3 Evolution of multiple systems during accretion

If binary or multiple fragmentation occurs early during the collapse, in a compact, disk-like structure, the continuing infall of material causes the system to evolve. Initially, Bate and Bonnell (1997) investigated this evolution by assuming initial binaries of low mass, and followed the effects of infall with a smooth particle hydrodynamics (SPH) code. As shown in Figure 6.3, material infalling to these systems can be accreted through disks onto the individual stars in spiral patterns, as a result of torques imposed by the stars on the gas, similar to the transfer of angular momentum in disk gravitational instabilities (§7.7). The continuing infall of material lead to mass buildup as material ended up on one or the other of the binary stars; this suggests that early gravitational fragmentation is more likely to lead to relatively massive object formation (binaries) rather than very low-mass objects (planets).

For the most plausible case in which the later infalling material has more angular momentum than that of the initial fragments, Bate and Bonnell (1997) found that the binary separation becomes larger due to accretion (as is necessary for angular-momentum conservation). They also found a tendency for the masses to become more equal with time: if the fragments initially have a large mass ratio, the lower-mass object moves in the largest orbit, which is closer to the positions at which the infalling (higher angular-momentum) material is falling, and so preferentially captures more material; which then tends to make the orbital motions of the two protostars more equal, which tends to equalize accretion.

A more ambitious simulation was undertaken by Bate *et al.* (2002, 2003), in which an attempt was made to follow evolution from a protocluster cloud through to star formation and dynamical evolution of multiple systems. To do this, Bate *et al.* assumed a simplified energy equation, with a fixed pressure–density relation. Starting from a spherical cloud with some random velocity perturbations, local collapse ensued to smaller systems. Fragmentation into multiple systems occurred, initially for objects of a few Jupiter masses, as predicted from the simple fragmentation theory (and as had to occur given the adopted $P - \rho$ relation). Accretion leading to higher-mass objects then occurred. As shown in Figure 6.4, a wide variety of systems were formed. Many spiral-armed disks fed mass into local fragments as in the Bate and Bonnell (1997) simulation.

A distinctive feature of this long simulation was the formation of multiple systems which were dynamically unstable and led to dispersal or ejection of one or more members. Bate *et al.* found that many, though not all, of the lowest-mass stars (brown dwarfs) formed were

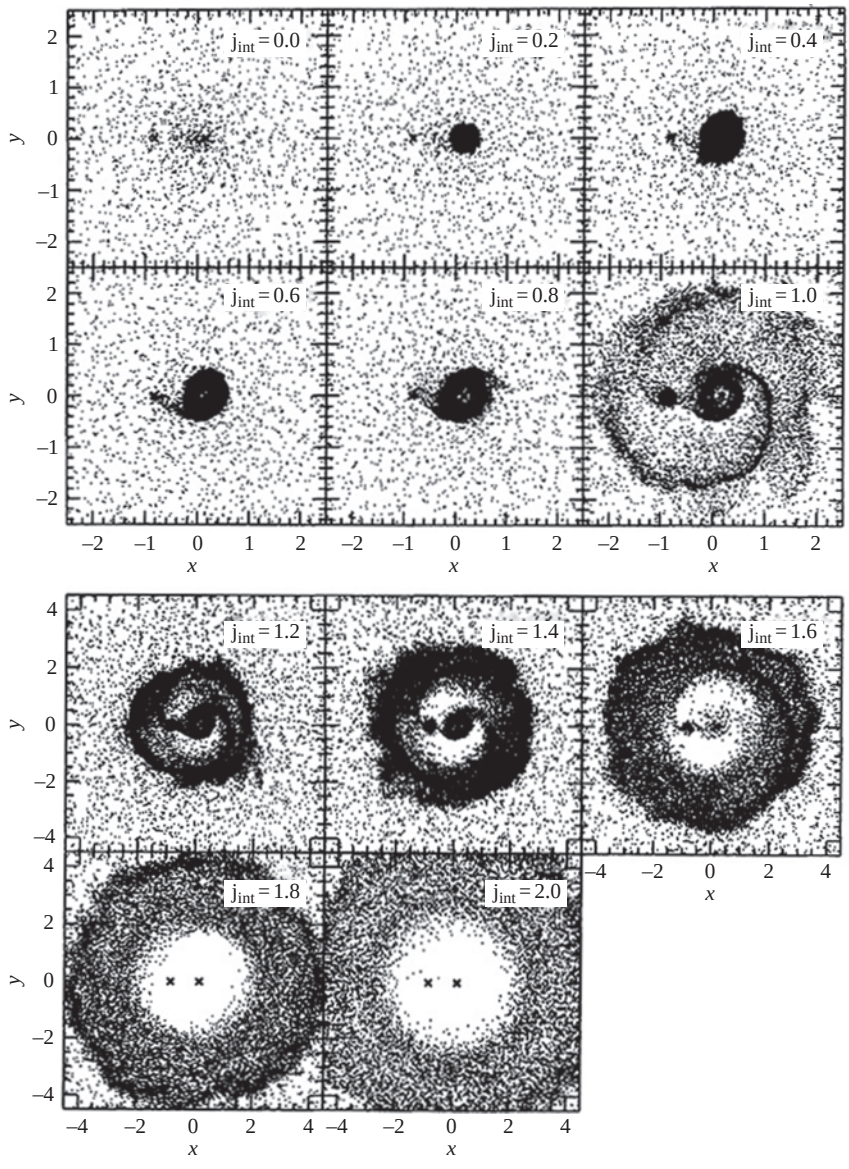

Fig. 6.3. Evolution of an initial binary system with the addition of mass of increasing angular momentum. Initially, low-angular momentum falls onto the individual systems, building up circumstellar disks around them; later on, material lands in a circumbinary disk, from which the individual objects can accrete through spiral arms. From Bate and Bonnell (1997).

ejected relatively early on from their host systems, and so had little opportunity to accrete additional mass from the continuing collapse of local material. This provided numerical confirmation of a prediction of Reipurth and Clarke (2001), who argued that fragmenting multiple stellar systems would be dynamically unstable in general, resulting in ejection of

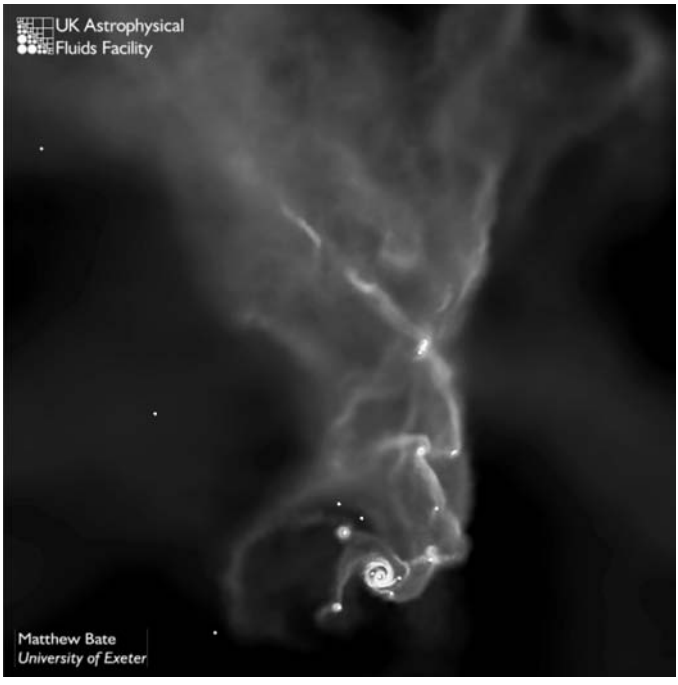

Fig. 6.4. Numerical simulation of star formation in a cluster by Bate *et al.* (2002, 2003). The complexity of the phenomena is evident; multiple unstable stellar systems lead to ejection of some members; gas streams due to the combined effects of gravity and angular momentum are evident (see text).

lower-mass members before they can accrete more mass. While it is plausible that this process occurs in some systems, its generality is not clear; surveys of Taurus and Chamaeleon I (Luhman 2004, 2007; Figure 6.5) suggest that the spatial distributions of brown dwarfs and lower-mass stars in general are not distinguishable from those of the higher-mass stars. There may also be numerical issues with the fragmentation in the SPH simulations (Klein *et al.* 2004). In any event, it seems clear that patterns of accretion will be more complex in multiple systems than simple models would suggest.

6.4 Young clusters

Most, but not all, stars in the solar neighborhood are formed in groups or clusters. In a recent review of embedded young clusters, Lada and Lada (2003) concluded that between 70 and 90% of all stars in giant molecular clouds are formed in clusters, while Allen *et al.* (2007) estimated distributed populations approaching 30% from preliminary analyses of large-scale surveys with the *Spitzer Space Telescope*. Most "clusters" in the solar neighborhood are relatively small, of order 10^2 members (Adams & Myers 2001); many stars are formed in larger clusters (Lada & Lada 2003).

The most well-studied, reasonably massive cluster is associated with the famous Orion Nebula. The nebula is ionized (mostly) by the O7 star θ^1 C Ori of the Trapezium cluster of O and early B stars. In turn, the Trapezium is near the center of a cluster of about two

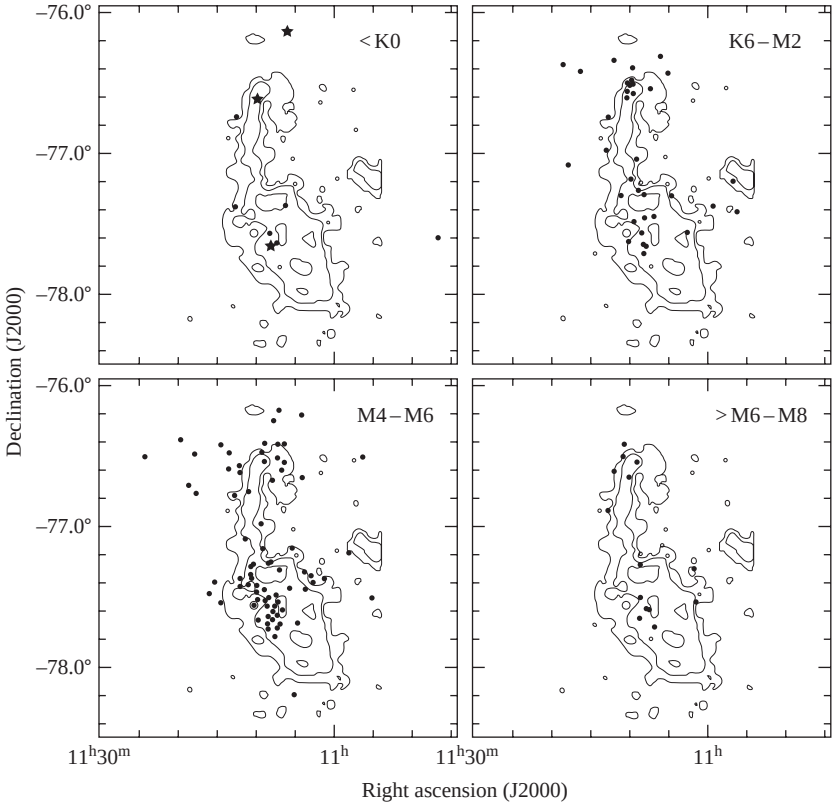

Fig. 6.5. Distribution of pre-main-sequence stars in the Cha I cloud as a function of mass. At this young age, the stars of spectral type M6.5 and later are likely to be brown dwarfs. The contours show levels of extinction, indicating the location of molecular gas. No obvious difference is seen in the spatial distributions of the lowest and highest mass stars. From Luhman (2007).

thousand lower-mass stars lying within a radius of about 2 pc (Herbig & Terndrup 1986; Jones & Walker 1988; Hillenbrand 1997). Figure 6.6 shows a plot of the brighter stars in an infrared-selected sample in the region of the Orion Nebula Cluster (ONC), superimposed upon the distribution of ^{13}CO emission (which is less optically thick than ^{12}CO and thus more clearly shows the position of the denser gas). The elongated geometry of the cluster, extended in the same direction as the overall distribution of dense gas is apparent (compare with the large-scale distribution shown in Figure 2.2).

The molecular gas "integral-shaped" filament contains about 2000–4000 $M_\odot$ of gas within a distance of about 2 pc from the center of the ONC (roughly the position of θ^1 C Ori), and is extremely opaque at optical wavelengths ($A_V \sim 50$–100 in many places). Within this region, there are approximately 2000 stars down to a mass $\sim$0.1 $M_\odot$ (right panel of Figure 6.6) (Hillenbrand 1997), about half of them optically visible; the other half are heavily extincted (McCaughrean & Stauffer 1994; Ali & DePoy 1995). There may be approximately as much mass in stars as in gas within a radius of about 2 pc of the center (Hillenbrand & Hartmann 1998). Thus, the ONC should be considered as a cluster still in the process of forming.

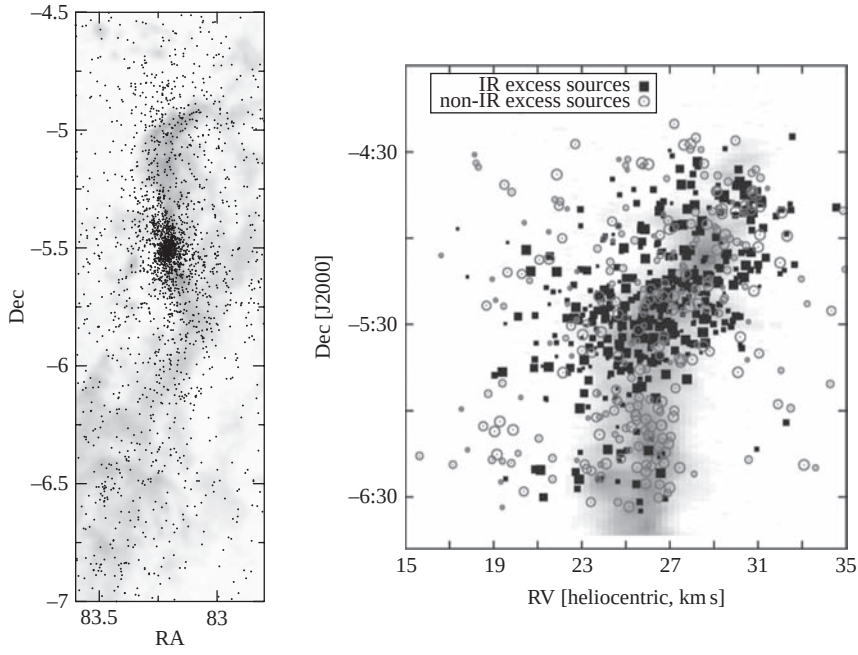

Fig. 6.6. Left: Positions of young stars, selected from the infrared survey of Carpenter *et al.* (2001) to maximize membership (including Class III stars), in the region of the ONC. The ^{13}CO velocity-integrated emission from Bally *et al.* (1987) is shown in grayscale (see also Figures 2.8 and 2.2). The dense concentration of stars is the ONC, which is elongated north, in the same direction as the dense filamentary gas. Right: Radial velocities of stars (points) and molecular gas (grayscale; compare with Figure 2.2) as a function of declination, summed over right ascension. Substantial velocity structure and gradients are seen, with the stars mostly following the gas (no correction has been made for binary motion), indicating that the stars are simply moving with the gas out of which they were born. From Tobin *et al.* (2008, in preparation).

O'Dell (2001, and references therein) and collaborators have extensively studied the properties of the Orion Nebula and have developed a compelling description of the geometry. In summary, most of the nebular emission arises from the ionized boundary of the dense molecular cloud in the region. An analysis of the surface brightness yields a picture in which θ^1 C Ori is only about 0.25 pc in front of the (irregular but roughly planar) ionized boundary of the molecular gas. As this distance is not large compared with the general extent of the cluster, it is not surprising that a significant number (roughly half, or perhaps a bit less) of cluster stars are heavily extincted, presumably lying within the molecular cloud.

Hillenbrand and Hartmann (1998; hereafter HH98) made an initial attempt to understand the structure of the ONC. They showed that the spatial distribution of the optical and infrared-only (embedded) stars was roughly similar, suggesting no particular bias in understanding the stellar distribution due to the large extinction of the molecular filament. HH98 found that even in the inner regions, the cluster is elongated, as is obvious from a larger view of the region (left panel of Figure 6.6), and could be fitted on scales less than about 3 arcmin or about 0.4 pc by ellipses with an ellipticity of $e \sim 0.3$. In the absence of a better model,

HH98 then circularly averaged the stellar distribution to find a structure with a central flattened core of size $\sim$0.16 pc and a r^{-2} density structure outside (a structure we have seen before in gaseous form; §3.3). Using a stellar cluster model of this form (a "King" model), HH98 inferred the volume density from the observed surface density, estimating a central stellar density of order 2×10^4 stars pc^{-3}. Adopting a typical stellar initial mass function (§6.6), HH98 inferred a total mass of stars of about 2000 $M_\odot$ within a radius of 2 pc. This is about half the mass required by a King model in virial equilibrium, given the magnitude of the observed proper motions (Jones & Walker 1988); the required gravitating mass to bind the cluster might be in the molecular gas.

However, the ONC is not likely to be in dynamical equilibrium. As shown in the right panel of Figure 6.6, the stars generally follow the complicated structure of the molecular gas in the region, with a sharp reversal in velocity gradient near the center of the ONC. Such a structure would not be seen in a relaxed stellar cluster. Instead, it seems plausible that the cluster is no older than about one crossing time; otherwise the gas motions would have been damped. A crossing or dynamical time of about 2 pc/2 km s$^{-1}\sim$1 Myr is consistent with the typical age of the population (Hillenbrand 1997).

As in the case of some molecular cloud cores (§3.3), circular averaging of the ONC distribution produces a misleading impression of a relaxed cluster. As in the case of the "Bonnor–Ebert rectangle", circular averaging of a filament will produce flat central surface density, followed by $\Sigma \propto r^{-1}$ on larger scales (because the mass grows as r while the area grows as r^2); interpreting this result in terms of the volume density of a spherical object results in a spurious $\rho \propto r^{-2}$ on large scales. While the ONC structure is not as simple as this, and is certainly centrally concentrated, it seems clear that the large scale $\rho \propto r^{-2}$ is mostly a product of inappropriate averaging.

Hillenbrand and Hartmann (1998) also demonstrated that the higher-mass stars are preferentially found near the cluster center relative to the lower-mass stars. The question is whether this effect is due to preferential formation of high-mass stars in deep cluster potential wells, as suggested by some theories (§6.6), or whether this is simply the result of two-body relaxation (e.g., Kroupa 2000). In the latter case, gravitational interactions between stars tend to give kinetic energy to the lower-mass objects, resulting in the higher-mass systems sinking to the center. Whether relaxation can account for mass segregation in the ONC depends upon details of the gravitational potential and the precise ages of the systems (Bonnell & Davies 1998). For instance, Henney *et al.* (2002) have argued that the disks around low-mass stars in the inner ONC are being photoevaporated so rapidly by θ^1 C Ori that this most massive member cannot be much older than about 10^5 yr, in which case its current position must be essentially its site of formation. Overall, it seems likely that initial formation rather than settling of massive stars to the bottom of the gravitational potential well is responsible for the central concentration of the more massive stars.

6.5 Cluster formation

How do star clusters form, and why are they so ubiquitous? Several numerical simulations have been undertaken to investigate fragmentation of protocluster gas (e.g., Klessen & Burkert 2000; Bate *et al.* 2003; Bonnell *et al.* 2003). Far less attention has been paid to how the protocluster gas cloud is assembled in the first place; yet, without an understanding of cluster gas accumulation, it may be difficult to establish the initial conditions leading to subsequent fragmentation.

Some models have simply assumed that protocluster gas clouds are in some kind of approximate virial equilibrium; the large densities and cloud masses are then supported by "turbulence", which in the simplest models is taken to be an additional pressure source; observations are said to support such a picture, in the sense that dense protocluster gas is highly turbulent. However, these models raise more questions than they answer; for instance, what is the source of the turbulence? How does any known source of turbulence result in an isotropic, time-constant pressure? More generally, it would seem that clusters are merely the concentrated end of a general tendency for stars to group together.

Burkert and Hartmann (2004) suggested that the on-edge structure in molecular clouds might provide a solution to this problem. As discussed in §2.6, finite sheets tend to collapse to filaments, with a pileup of material near the ends. In general, Burkert and Hartmann showed that edge regions of smaller radii of curvature can gravitationally collapse into "focal points", strongly concentrating matter. The principle of this simple idea is illustrated schematically in Figure 6.7. A more complicated case is shown in Figure 2.11, where the collapse of the rotating elliptical sheet produced a structure with a remarkable morphological similarity to that of the Orion A cloud; the dense concentration of matter at the upper end resulted from the process indicated in Figure 6.7.

In this interpretation, it is no accident that the ONC lies near the end of the Orion A cloud. Other potential examples of this process may be the dense young clusters NGC 2023, 2024, 2068, and 2071, which form a roughly double structure near the ends of the Orion B cloud (Figure 2.1). Another possible example is the Chamaeleon I cloud, with two relatively small concentrations roughly toward the ends of the molecular gas distribution (Figure 6.5). Any region of small radius of curvature can produce gravitational focusing, so that clusters need not always or only form at the ends of clouds.

The amount of mass concentrated by a gravitational focal point is not limited to the local Jeans mass. All that is required is that the cloud form relatively "fast" so that material can be piled up before the structure can collapse upon itself. Thus, the long-range effects of gravity can be used in principle to "pull in" large amounts of gas for cluster formation. The rate

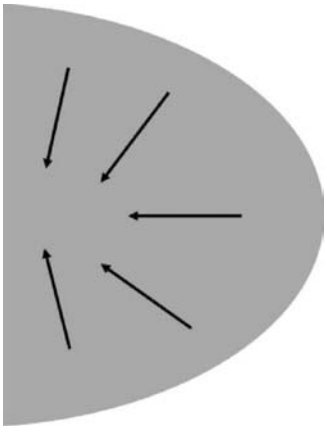

Fig. 6.7. Schematic showing how curvature of the edge of a self-gravitating cloud can result in a gravitationally focused flow, so that large masses can in principle be collected into small volumes.

of infall in this picture is not constrained by (thermal) hydrostatic equilibrium, and so the high infall rates needed to form high-mass stars can be achieved very simply (see following section). The difficulty of preventing collapse everywhere in a very massive cloud due to the effects of global gravity (Chapter 2) may be the reason for the ubiquity of star formation in clusters.

6.6 The Initial Mass Function

Salpeter (1955) estimated that the stars in the galaxy exhibited an initial mass function (IMF) which declined steeply toward higher-mass stars,

$$\xi = \frac{dN}{d\log} M \approx M^{-1.35}. \tag{6.1}$$

Empirical estimates of the form of the IMF now appear to be converging toward a high-mass power-law distribution with a slope similar to that estimated by Salpeter, with a change to a much flatter slope around 1 $M_\odot$, and perhaps a maximum in ξ at $\sim$0.3 $M_\odot$. At still lower masses, there may be a decline in ξ down to the end of the brown dwarf range at about $\sim$0.01 $M_\odot$. Stars with masses greater than about 100 $M_\odot$ appear to be rare or absent, though this is more likely due to instability in stars mostly supported by radiation pressure than some intrinsic limit of accretion (§5.9).

The exact form of the IMF, and whether or not it is universal, has been the subject of an enormous amount of work, as summarized in two recent conferences on the subject (Gilmore & Howell 1998; Corbelli *et al.* 2005). A recent important review of the subject is that of Bonnell *et al.* (2007). The methodology of deriving the IMF and the associated uncertainties has been summarized in the magisterial contribution by Scalo (1986).

The recent review of the IMF by Chabrier (2003) suggests a combined log-normal and power-law form for the average IMF:

$$\xi\left(\log\left(M/M_\odot\right)\right) \sim \exp\left[\frac{-\left(\log\left(M/M_\odot\right) - \log(0.079)\right)^2}{2(0.69)^2}\right], M \leq 1.0\ M_\odot; \tag{6.2}$$

$$\xi\left(\log\left(\frac{M}{M_\odot}\right)\right) \sim \left(\frac{M}{M_\odot}\right)^{-1.3}, M > 1.0\ M_\odot. \tag{6.3}$$

Below 1 $M_\odot$ the correction for binaries may be especially significant (Kroupa 1993); it may be convenient to define a system IMF in which the stars are lumped together,

$$\xi(\log M) = \propto \exp\left[-\frac{(\log M - \log 0.022)^2}{2(0.57)^2}\right], M < 1\ M_\odot. \tag{6.4}$$

Alternative, segmented power-law fits also have been used to represent the IMF, as discussed by, for example, Kroupa (2002).

Whether or not the IMF has a universal form has been the subject of much debate (for opposing views, see Kroupa 2002 and Scalo in Gilmore & Howell 1998). It is clear that determining the form of the IMF in differing regions is a substantial observational challenge; the distribution is very broad, so one must probe a large dynamic range in mass, and therefore selection effects can be very important. For example, initial studies of star-forming regions had suggested that perhaps star formation was bimodal, with high-mass stars and low-mass stars forming separately; but as observational techniques improved, it became apparent that

low-mass stars are present in great numbers within high-mass star-forming regions, and had simply been missed in earlier studies (e.g., Herbig & Terndrup 1986). The steep form of the IMF at high masses also presents challenges, simply in having large enough samples to have statistically significant results for massive stars. Finally, the corrections needed to account for binary or multiple companions add to the uncertainties.

The best evidence so far for variations in the IMF as a function of environment comes from studies of two very young clusters: NGC 3603 (e.g., Eisenhauer *et al.* 1998) and the Arches cluster (Stolte *et al.* 2005; Kim *et al.* 2006). The Arches cluster is only 20–30 pc from the galactic center (in projection), and is as massive as the smallest galactic globular clusters $\sim 2 \times 10^4\, M_\odot$. Studies of both clusters suggest an upper mass power-law index $\Gamma \sim -0.9$ (in units of $d \log N / d \log M$, where the Salpeter slope would be -1.35), which may span the range of 1.3–50 $M_\odot$ (Kim *et al.* 2006). However, this result on the IMF in the central regions is not clearly a constraint on the *initial* IMF, as mass segregation can occur rapidly in such a dense cluster; this would lead to an overabundance of massive stars in the central regions, which are easiest to observe against the background. Indeed, Portegies Zwart *et al.* (2007) suggest that the IMF slope of the Arches cluster was indeed close to the Salpeter value, but has evolved as massive stars have settled closer to the cluster center.

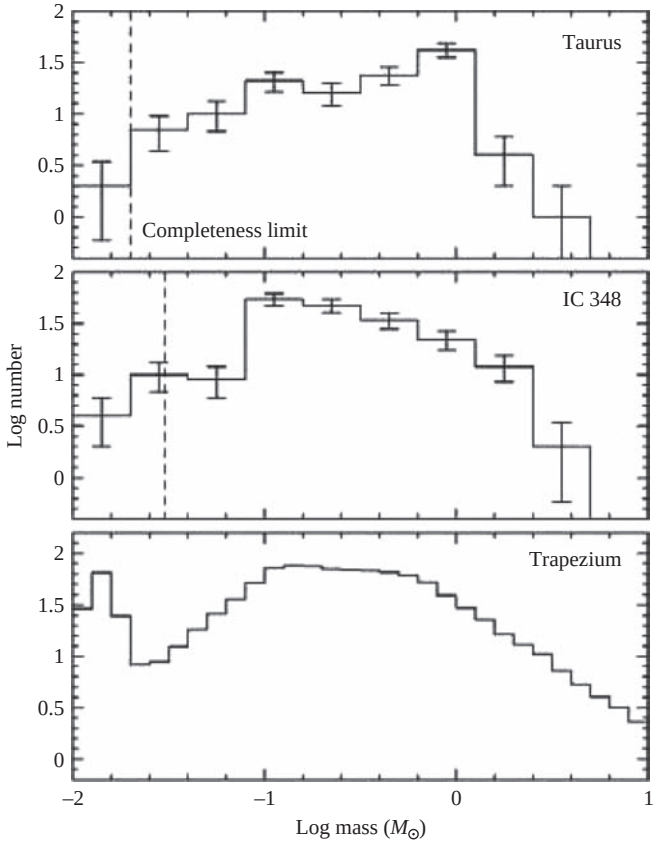

Fig. 6.8. Recent estimate of the IMFs in three nearby star-forming regions. From Luhman (2004) and Muench *et al.* (2002).

Current studies of star-forming regions suggest that in most sites, a standard IMF is present (e.g., Muench *et al.* 2002; Luhman *et al.* 2003b; Figure 6.8). The Taurus star-forming region provides evidence for a slightly different IMF, with perhaps somewhat fewer brown dwarfs and most importantly a strong peak just below a solar mass (Briceno *et al.* 2002; Luhman 2004). The Taurus results are most easily seen in terms of spectral types, which are thought to be directly translateable into stellar mass (though the absolute calibration is uncertain; Chapter 11). Taurus exhibits a strong peak at around K7-M0, whereas most other young clusters have a peak in the number of objects near M3-M4.

6.7 Theories of the IMF

The studies cited above suggest that the stellar IMF is fairly similar in a variety of regions. Overall, studies indicating that protostellar cores have a similar mass spectrum to that of stars (e.g., Motte *et al.* 1998; Johnstone *et al.* 2000; Figure 6.9) suggest that whatever determines the core masses mostly determines the stellar IMF.

A variety of explanations have been offered to explain the overall shape of the IMF, including the following.

Random processes. Adams and Fatuzzo (1996) suggested that the combination of many processes involving independent physical variables could ultimately yield a log-normal form (via the central limit theorem). This point of view is attractive, in that a range of physical conditions could easily be responsible for the broad peak in ξ for low-mass stars. However, it is not clear that the specific variables suggested by Adams and Fatuzzo are the most important parameters for star formation, nor that such parameters are necessarily independent of each other. In particular, magnetic and turbulent pressures are not likely to be static and isotropic, and it is far from clear that bipolar outflows can really remove much of the mass of a typical

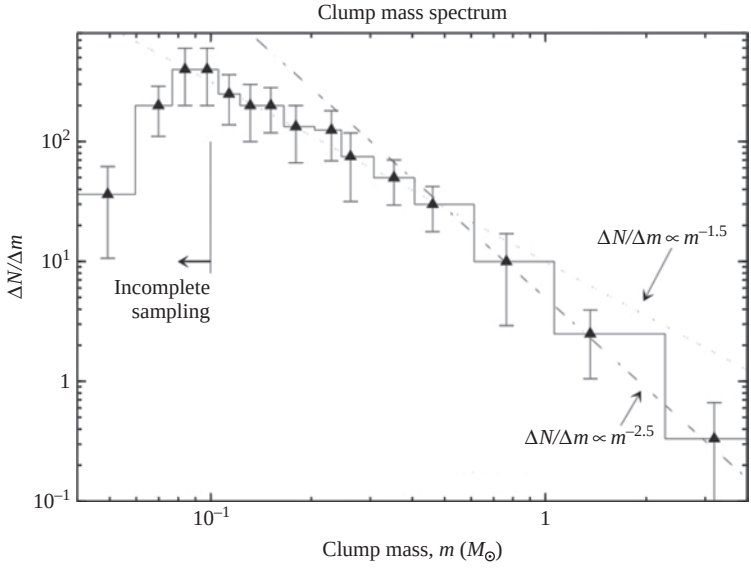

Fig. 6.9. Estimated mass function of molecular cloud cores in Ophichus. Note some similarity between the shape of the core IMF and that of the stellar IMF. From Motte *et al.* (1998).

protostellar core (Chapter 5). Finally, the random parameter model predicts something like a log-normal distribution, whereas studies of the massive end of the IMF suggest a power-law distribution (see discussion in Chabrier 2003).

Competitive accretion. Because stars tend to form in groups if not in clusters, it has been suggested that the initial cores might "compete" for accreting the leftover gas (Bonnell *et al.* 2001). This mechanism seems especially appropriate for developing the high-mass end of the IMF, where the gravitational potential of the stars can help focus mass into dense inner regions, resulting in more massive stars (e.g., Bonnell *et al.* 2004). The competitive accretion model therefore results in a mass-segregated cluster.

A strength of this model is that observations of young clusters indicate that the most massive stars form in roughly the same time as the low-mass stars. This means, for example, that a $50\,M_\odot$ star must form with an accretion rate roughly two orders of magnitude higher than a $0.5\,M_\odot$ star in the same cluster. From equation (4.20), to increase the mass infall rate by two orders of magnitude from that of a thermally supported, near-equilibrium core – whether a singular isothermal sphere or a Bonnor–Ebert sphere – would require a sound speed $10^{2/3} = 4.64$ times larger, or a temperature $\sim$22 times larger, $T \sim 220$ K. Such high temperatures seem to be achieved by the heating of an already formed massive central protostar, which therefore does not constitute an appropriate initial condition. Some have suggested turbulent velocity support to take the place of the missing thermal support, but it is far from clear that the required supersonic turbulence can be maintained sufficiently long to make equilibrium plausible. Instead, if material is being attracted into a deep gravitational potential well, perhaps due to the gravitational focusing discussed in the previous section, the high infall rates needed to make massive stars rapidly can be produced without recourse to problematic turbulent support. On the other hand, many young stars are formed in either the distributed population or on modestly sized clusters, even up to moderately massive stars ($\sim 10\,M_\odot$), which may be difficult to accomplish with competitive accretion.

"Turbulence". In principle, turbulent motions in molecular clouds can serve to collect and compress gas in sites which can eventually collapse gravitationally. Larson (1992) suggested that if stars form in linear cloud structures such as filaments or lines of clumps, and if the overall structure of clouds is sheet-like, then a slope of $\xi \propto M^{-1}$ would result. More generally, if clouds have a "fractal structure" with a dimensionality of $\sim$2.3, then the IMF slope would be comparable to the Salpeter value. A similar argument, with more detailed calculations, was made by Elmegreen (1997).

Padoan and Nordlund (2002) argued that the high-mass end of the IMF is due to the power spectrum of turbulence in molecular clouds as inferred from observations. Incorporating jump conditions for magnetic shocks, they found a mass function with slope $\sim$1.33, similar to the Salpeter slope. A turnover at lower masses resulted from the probability distribution of the gas density, which is approximately lognormal, and by thermal pressure on small scales. A recent set of detailed numerical simulations by Padoan *et al.* (2007) support these conclusions. While the turbulence in these simulations is super-Alfvenic, Padoan *et al.* argue that the magnetic field must be taken into account to obtain the correct form of the high-mass IMF.

The idea that turbulence creates the seeds of star formation is very attractive. Nevertheless, uncertainties remain due to our poor knowledge of the true nature of the motions in star-forming clouds. For example, Padoan *et al.* (2007) use random forcing in Fourier space, but there is no a priori reason why the phases of this forcing should be random. Also, Padoan

et al. ran the simulations for several dynamical times so that the turbulent motions can approach a steady state; but as discussed in Chapter 2, the rapid formation of stars upon molecular cloud formation makes it highly unlikely that a steady state is achieved. Finally, Padoan *et al.* (2007) point out that they could not achieve a statistically relaxed state with self-gravity, but as argued by Burkert and Hartmann (2004) and Heitsch *et al.* (2007), it isn't obvious that self-gravity can be neglected.

To emphasize the potential importance of global gravity, Figure 6.10 shows a numerical simulation of colliding flows (a special case of swept-up material; see also Figure 2.13). Seen end-on, initial smooth perturbations lead to substructure, which, if dense enough, cools sufficiently rapidly (in this case via thermal instability) to form dense, self-gravitating lumps which in principle can collapse into stars before the entire region collapses globally, ultimately to form a filament in this simulation. It may be that the turbulence generated by the process of cloud formation can be used to provide physically self-consistent initial conditions without the need of introducing assumptions about the turbulent spectrum, or requiring some continuous forcing (Heitsch *et al.* 2005, 2006, 2007; Hennebelle & Audit 2007; Vázquez-Semadeni *et al.* 2007; §2.7).

"*Jeans mass*". It is plausible that a turbulent cascade would set up a relatively robust power-law mass spectrum, but this does not obviously provide a turnover in the IMF at low masses. In principle, one might suspect that this has something to do with thermal pressures, which enter into the "Jeans mass" (e.g., also Klessen & Burkert 2000, 2001; Klessen 2001). The question is, which Jeans mass? Since $M_J \propto T^{3/2}\rho^{-1/2}$, even under the relatively isothermal conditions thought to be typical of local molecular clouds, low-mass objects can still be produced from concentrations with sufficiently high density. Padoan and Nordlund (2004) argued that turbulence naturally leads to high-density concentrations which can make brown dwarfs in the same manner as solar mass stars; for isothermal conditions, this requires densities (and thus pressures) two orders of magnitude larger than for 1 $M_\odot$ objects. Although many simulations show a break in the mass spectrum at some sort of "Jeans mass",

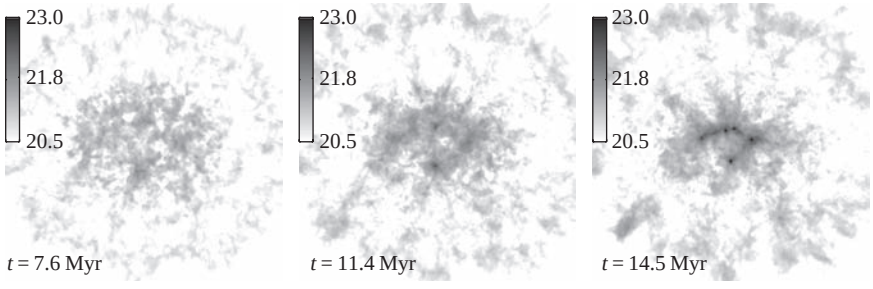

Fig. 6.10. Face-on view of two atomic colliding flows, seen at three different times as noted in the panels. Long-wavelength perturbations in the initial interface between the flows result in turbulent fragmentation; radiative cooling then makes individual protostellar lumps (right panel). The initial flows are elliptical in cross-section, with densities falling off to prevent the development of very strong edge effects (§2.6, Figure 2.10), but even so an echo of the edge forms as the accumulated material collapses under gravity. Modified from Heitsch *et al.* (2008).

the result may be affected by the resolution of the simulation (higher resolution is generally needed to detect higher-density concentrations).

Larson (2005) recently suggested that the detailed behavior of the temperature as a function of density in molecular clouds causes a change in the ease of fragmentation. Calculations and observations suggest that denser regions are cooler, due to increased shielding from external radiation and enhanced cooling, up to a certain density. Below this critical density, which Larson suggested that would occur roughly round $10^6\,\mathrm{cm}^3$, a polytropic approximation would suggest $T \propto \rho^{(\gamma-1)}$ with $\gamma \sim 0.7$; this leads to a decreasing Jeans mass with increasing density as $\gamma \sim 1.1$ due to extra heating (see below); this would lead to a smaller dependence of the Jeans mass on density, $M_J \sim \rho^{-0.35}$, which is suggested to cause less fragmentation to smaller masses, changing the slope of the IMF. Numerical simulations by Jappsen *et al.* (2005) seem to bear out the idea that changing the density–temperature relation in this way can produce something like the desired turnover in the IMF at lower masses.

The physical processes which would produce such varying polytropic behavior are unclear. Larson (2005) suggested that the temperature in the relevant density range is controlled by the balance between dust cooling and heating due to the PdV work done by dynamical compression in near free-fall. But, as discussed in §§2.5, 2.6, and 4.1, free-fall is *not* conducive to fragmentation. Using a polytropic relation, as in the simulations of Jappsen *et al.* (2005), is not the same thing as including a heating term which only becomes important at high velocity. The idea of thermal support producing a low-mass turnover in the IMF has its attractions, but the details of how this might really occur have yet to be worked out.

Opacity-limited fragmentation in disks. As discussed in §6.3, the simulations of Bate *et al.* (2002, 2003) suggest that the opacity limit for fragmentation acts in dense protostellar disks to form initial cores of a few Jupiter masses. Here the Jeans mass is much lower than in the cloud-fragmentation case discussed immediately above because of the high densities involved. The initial very low mass fragments then continue to accrete, so that the final system mass probably tends to represent the "cloud conditions" Jeans mass(es). Very low-mass objects are ejected from multiple systems before they have a chance to accrete much more mass. As discussed in §6.3, observations to date show little evidence for the differing spatial distributions of low- and higher-mass stars predicted by this picture.

The most plausible explanation of the stellar IMF in the author's opinion is that it results from a turbulent spectrum of initial perturbations, which can cool and collapse faster than (likely) global gravitational collapse. The highest-mass stars may be fed at the expense of smaller objects through competitive accretion. Thermal pressure support may produce a turnover in the IMF as it resists the collapse of lower-mass, smaller regions. Fragmentation into binary and multiple systems may occur in initial collapse to flattened, disk-like systems; this may lower the characteristic mass at which the IMF turns over. Clearly much remains to be learned both observationally and theoretically before a robust theory of the IMF emerges.

7

Disk accretion

As described in Chapters 4 and 5, the collapse of protostellar clouds with plausible amounts of angular momentum generally should result in the formation of disks as well as protostars. Disk formation during the collapse phase is then followed by a longer phase of *disk accretion* during which angular momentum is transferred to a small fraction of disk particles at large radial distances, permitting the accretion of most of the disk mass onto the central star (with some fraction possibly forming planets). The subsequent evolution of a star-disk system will be controlled by the rate at which angular momentum is transported in the disk.

Substantial progress has been made in understanding two likely mechanisms for angular momentum transport: magnetic turbulence and gravitational instability. Unfortunately, it has proved difficult to apply these mechanisms to the development of a predictive theory of disk evolution for young systems. The low ionization levels predicted for large regions of YSO disks make it unclear whether the magnetic field can couple sufficiently well to the gas for the so-called "magnetorotational instability" (MRI) to efficiently transport angular momentum. While it seems likely that the MRI operates in some regions of YSO disks, it is far from clear that it is the dominant factor in producing accretion. The effects of gravitational instability depend sensitively on disk energy balance, and local heating and cooling rates are difficult to determine.

General predictions about the emission of circumstellar disks can be made without knowing the specifics of the angular momentum transfer, as long as accretion is relatively steady, the disk is optically thick, and energy dissipation is local (true for viscous disks in which the MRI operates, but not obviously correct for disk accretion driven by gravitational waves). The essence of this result can be derived from energy conservation and blackbody radiation. If material accretes at a rate $\dot{M}$ through an annulus ΔR in a Keplerian disk at radius R from a star of mass M_*, the gravitational potential energy released by accretion must be radiated away by the disk surface; thus,

$$\frac{G M_* \dot{M}}{2R} \frac{\Delta R}{R} \sim 2 \times 2\pi R \, \Delta R \, \sigma T_{\rm d}^4, \tag{7.1}$$

and so the disk surface temperature $T_{\rm d}$ is predicted to vary as

$$T_{\rm d} \sim \left(\frac{G M_* \dot{M}}{8\pi\sigma R^3} \right)^{1/4}. \tag{7.2}$$

While this result reproduces the basic dependence of disk temperature on radial distance, one must also consider energy fluxes carried by viscous stresses to obtain the exact relation (§7.2).

To understand the temperature distributions of typical pre-main-sequence disks it is also necessary to account for the radiation from the central star intercepted by the disk; the resultant energy input can often exceed the heating resulting from accretion. In the limit of no accretion energy release, the absorption of light from the star by an optically thick disk balances the energy loss by disk radiation, so that

$$\frac{L_*}{4\pi R^2} < \cos\gamma > \sim \sigma T_{\rm d}^4, \tag{7.3}$$

where $< \cos\gamma >$ is an average angle with respect to the disk normal at which rays from the star enter the disk. With $< \cos\gamma > \sim R_*/R$, where R_* is the stellar radius, the temperature distribution for the case of disk *irradiation* is

$$T_d \sim \left(\frac{L_* R_*}{4\pi\sigma R^3}\right)^{1/4}. \tag{7.4}$$

Thus, whenever $L_* > GM_*\dot{M}/R_*$, which is often the case for T Tauri stars, disk irradiation dominates the disk temperature distribution. This is especially true for $R \gg R_*$, where the finite vertical thickness of the disk generally increases $\cos\gamma$ substantially, such that $T_d \rightarrow R^{-1/2}$.

Since the disks of pre-main-sequence stars generally have very large radial extensions, they radiate over a wide range of wavelengths, extending from the near-infrared to mm wavelengths and beyond. Simple models predict a wide variety of observed properties of T Tauri disks, but such models likely miss many details which will only become apparent with future high-resolution imaging.

In this chapter a brief sketch of disk physics is presented with emphasis on issues most important for pre-main-sequence systems. Fuller treatments of accretion disk physics in a more general context can be found in several other sources: a basic and particularly clear elaboration is given by Frank *et al.* (1992); a useful outline is presented by Pringle (1981); another good review is given by Papaloizou and Lin (1995). Applications of disk theory to observations of T Tauri stars are discussed in Chapter 8.

7.1 Energy minimization and angular momentum conservation

To illustrate some basic issues involved in disk accretion, we follow Lynden-Bell and Pringle (1974) in considering an idealized situation involving only two bodies orbiting around a central mass. Suppose that the bodies of (small) mass m_1 and m_2 are in circular Keplerian orbits about the central mass M. Then the energy and angular momentum of this system are

$$E = -\frac{GM}{2}\left(\frac{m_1}{r_1} + \frac{m_2}{r_2}\right), \tag{7.5}$$

and

$$J = (GM)^{1/2}(m_1 r_1^{1/2} + m_2 r_2^{1/2}), \tag{7.6}$$

where r_1 and r_2 are the corresponding radial coordinates of the bodies. Now suppose that the orbits are perturbed by small amounts while conserving the overall angular momentum J. Then the relation between the perturbations is

$$m_1 r_1^{-1/2}\Delta r_1 = -m_2 r_2^{-1/2}\Delta r_2, \tag{7.7}$$

and the corresponding change in the system energy, written in terms of the first body, is

$$\Delta E = -\frac{GMm_1\Delta r_1}{2r_1^2}\left[\left(\frac{r_1}{r_2}\right)^{3/2} - 1\right]. \tag{7.8}$$

Suppose we wish to reduce the energy E of the system. If body 1 is at a larger radial distance from the center than body 2, we can decrease the energy of the system by a positive displacement Δr_1, i.e., moving body 1 further away from the center. If body 1 is originally closer to the center, then the energy can be reduced by a negative displacement Δr_1, moving body 1 closer in. Thus, the energy can be reduced while conserving orbital angular momentum by moving the initially closer body in and moving the initially outer body further away. This is the basic action of the accretion disk; energy is released as material both accretes and spreads to larger distances. If mass can be transferred between bodies, one can show (e.g., Lynden-Bell & Pringle 1974) that the system energy can be minimized by transferring mass from the outer body to the inner body. With many bodies, the energy is minimized by moving most of the mass inwards as far as possible; this can be accommodated with conservation of angular momentum if some (small) mass is moved outward to very large distances.

This process requires some way of connecting different particles in the disk. One schematic way of picturing this is to imagine rings or annuli in a disk which rub against each other (Figure 7.1). In all situations considered in this book, the angular velocity of the disk system decreases outward (in the specific case of the Keplerian disk, $\Omega = (GM/r^3)^{1/2}$). This means that an inner annulus will rotate faster than its neighboring outer annulus. "Friction" between the two will try to spin up the outer annulus and spin down the inner annulus,

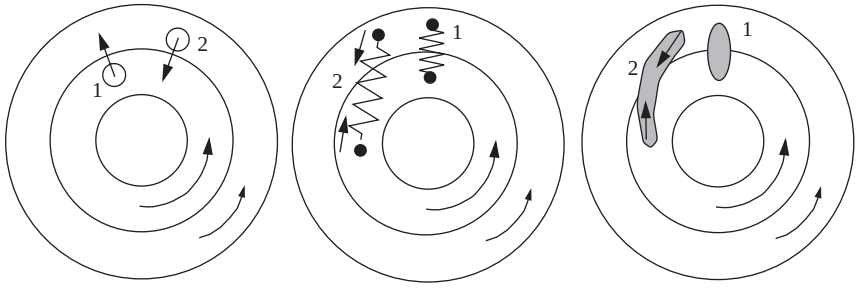

Fig. 7.1. Schematic treatment of angular momentum transfer in a shearing disk. The angular velocity is assumed to decrease outwards. If there is "friction" or communication between two neighboring annuli, the resulting torques will attempt to bring the two annuli into co-rotation; a net torque will be exerted on the outer annulus in the sense of spinning it up, i.e., gaining angular momentum. However, the simple hydrodynamic interchange of parcels of material shown in the left-hand panel does not seem to work, because the inner material being moved outward has less angular momentum, while the outer material has more angular momentum; this interchange works in the direction of moving angular momentum inward, not outward. The middle panel illustrates the potential effects of magnetic fields schematically, shown as if adjacent disk annuli are tied together by an (elastic) spring tethered at each end. Starting with an initially radial configuration (dashed line), the differing angular velocities of the annuli will cause the spring to be stretched. The restoring force of the spring works in the direction of trying to spin up the outer annulus and spin down the inner annulus, i.e., to transfer angular momentum outward. In the case of gravitational instability (right panel), an excess of material gets sheared out by the differential rotation; the gravitational attraction on the sheared excess (spiral arm pattern) exerts a restoring force in the same sense as the magnetic case, again transferring angular momentum outward.

i.e., angular momentum tends to be removed from the inner annulus and transferred outward. Because the gravitational potential constrains the orbital motion, this transfer of angular momentum results in moving material from the inner annulus inwards while outer material gaining angular momentum will move to larger radii. Energy is lost due to frictional dissipation, and this must cause the net gravitational potential energy of the system to decrease, i.e., the net motion of disk mass must be inward.

The situation is more complicated in a gaseous disk because material diffuses in both directions from all radii. One physical picture for the torque g between neighboring annuli supposes that the gas exhibits (small) turbulent, random motions which cause mixing in the radial direction. As indicated in Figure 7.1, this means that material between adjacent annuli will be exchanged. Since the material originating in the two annuli will have different specific angular momenta, this will cause a transfer of angular momentum between annuli.

The classical treatment of viscous accretion in gaseous disks postulates a kinematic, "turbulent" viscosity which is much larger than molecular viscosity, and can be treated by the same equations (e.g., Frank *et al.* 1992). The basic picture is one in which turbulent elements of the gas moving at a typical random velocity w travel a mean free path λ before mixing with other material. Unfortunately, pure hydrodynamic mixing, whether by blobs or a molecular viscosity, does not seem to be effective in transporting angular momentum outward (Ryu & Goodman 1992; Stone & Balbus 1996). To see schematically why this might be problematic, note that material interior to radius R has low angular momentum, so mixing it outward tends to move *lower* angular momentum outward (Figure 7.1, blob 1). Similarly, material exterior to R has higher angular momentum, so moving it inwards (blob 2) tends to transport angular momentum inward, the opposite of what is needed for accretion. This behavior is consistent with simulations which suggest hydrodynamic modes produce weak angular momentum transport, mainly inward (Stone & Balbus 1996).*

A (weak) magnetic field in a Keplerian disk is unstable and can produce a turbulent viscosity which can be made consistent with the simple viscous disk model (Balbus & Papaloizou 1999). We return to this in §7.5. For the following we simply assume that an appropriate viscosity can be determined and consider its effects.

7.2 The thin accretion disk

Consider a thin disk composed of particles moving essentially on circular orbits in a single plane. We suppose further that any radial motions are small and that radial pressure forces are negligible, so that the orbital motion of the disk is due entirely to equating the centripetal acceleration with gravity. Then, adopting cylindrical polar coordinates (R, ϕ, z), the circular velocity resulting from a gravitational potential $\Phi(R)$ is

$$\frac{v_\phi^2}{R} = \frac{d\Phi}{dR}. \tag{7.9}$$

The equation of mass conservation for an annulus of width ΔR at R, denoting the surface density of the disk again by Σ, is

$$\frac{\partial}{\partial t}(2\pi R \Delta R \Sigma) = v_{\rm R}(R,t)\, 2\pi R \Sigma(R,t) - v_{\rm R}(R+\Delta R,t)\, 2\pi (R+\Delta R)\Sigma(R+\Delta R,t), \tag{7.10}$$

* This discussion differs substantially from the corresponding treatment in the first edition, which used the Frank *et al.* (1992) formulation for a viscous disk with kinematic viscosity.

where v_R is the *net* radial velocity of the material. (In a turbulent viscosity model, the turbulent velocity w may be much larger than v_R, but the turbulent motions do not represent a net mass flux; §7.1.) The first term on the right-hand side of equation (7.10) is the flow of material into the annulus and the second term is the flow out. Taking the limit for small ΔR, one obtains

$$R\frac{\partial \Sigma}{\partial t} + \frac{\partial}{\partial R}(R\Sigma v_R) = 0. \tag{7.11}$$

Similarly, the equation for conservation of angular momentum can be written as

$$R\frac{\partial}{\partial t}(\Sigma R^2\Omega) + \frac{\partial}{\partial R}(R\Sigma v_R R^2\Omega) = -\frac{1}{2\pi}\frac{\partial g}{\partial R}. \tag{7.12}$$

The usual fluid mechanics definition of viscosity ν_v is

$$g = -2\pi R\Sigma\nu_v R^2\frac{d\Omega}{dR}, \tag{7.13}$$

so that

$$\frac{\partial}{\partial t}(\Sigma R^2\Omega) + \frac{1}{R}\frac{\partial}{\partial R}(\Sigma R^3\Omega v_R) = \frac{1}{R}\frac{\partial}{\partial R}\left(\nu_v\Sigma R^3\frac{d\Omega}{dR}\right). \tag{7.14}$$

The mass conservation equation can be used to eliminate v_R, with the result that

$$\frac{\partial \Sigma}{\partial t} = \frac{1}{R}\frac{\partial}{\partial R}\left[\left(\frac{d\Omega R^2}{dR}\right)^{-1}\frac{\partial}{\partial R}\left(-\nu_v\Sigma R^3\frac{d\Omega}{dR}\right)\right]. \tag{7.15}$$

Since the viscosity can be a function of local physical conditions in the disk, this is a nonlinear diffusion equation for Σ.

In many cases of interest most of the mass is contained in the central spherical star, so that the gravitational potential is that of a central point mass, and the angular velocity takes on its Keplerian value, $\Omega = (GM/R^3)^{1/2}$. Then the diffusion equation (7.15) becomes

$$\frac{\partial \Sigma}{\partial t} = \frac{3}{R}\frac{\partial}{\partial R}\left[R^{1/2}\frac{\partial}{\partial R}(\nu_v\Sigma R^{1/2})\right]. \tag{7.16}$$

It is convenient to have an equation for the mass flux as a function of radius; because

$$\frac{\partial \Sigma}{\partial t} = \frac{1}{2\pi R}\frac{\partial \dot{M}}{\partial R}, \tag{7.17}$$

we have

$$\dot{M} = 6\pi R^{1/2}\frac{\partial}{\partial R}(\nu_v\Sigma R^{1/2}). \tag{7.18}$$

By assuming circular motion and a thin disk we have in effect imposed constraints on the conservation of energy in this disk system. An annulus of width ΔR is subject to torques on its inner and outer surfaces; the net torque is

$$g(R+\Delta R) - g(R) = \frac{\partial g}{\partial R}\Delta R. \tag{7.19}$$

The rate of working by this torque, i.e., the energy added, is

$$\Omega\frac{\partial g}{\partial R}\Delta R = \left[\frac{\partial}{\partial R}(g\Omega) - g\frac{d\Omega}{dR}\right]\Delta R. \tag{7.20}$$

The first term on the right-hand side is a rate of "convected" rotational energy; integrated over the radial extent of the disk, this is just

$$g\Omega|_{\text{outer edge}} - g\Omega|_{\text{inner edge}} \tag{7.21}$$

and therefore is determined by the disk boundary conditions. The second term represents a local rate of mechanical energy dissipation. In these equations this energy is assumed to be lost from the system (i.e., radiated away). This energy loss per unit area for each of the two sides of the disk is

$$\dot{E}(R) = -\frac{g d\Omega/dR}{4\pi R} = (1/2)\,\nu_{\rm v}\Sigma\left(\frac{Rd\Omega}{dR}\right)^2. \tag{7.22}$$

The radiation of this dissipated accretion energy makes the disk self-luminous.

The evolution of the viscous accretion disk depends upon the behavior of the viscosity $\nu_{\rm v}$, which in turn can depend in complicated and unknown ways on disk properties. It is instructive to explore some simple solutions of the diffusion equation (7.16) which illustrate some general properties of accreting disks. To begin, we examine the case in which the viscosity is constant. One may proceed with generality by considering only one initial (thin) annulus of material because the assumption of constant viscosity makes the equation linear in Σ, and therefore one can construct a general solution by adding up solutions for individual annuli.

Starting with an initial density distribution representing an annulus of material at radius R_1,

$$\Sigma(R, t=0) = \frac{\delta(R-R_1)}{2\pi R_1}, \tag{7.23}$$

Lynden-Bell and Pringle (1974) showed that the solution to (7.16) for a constant viscosity $\nu_{\rm v}$ is

$$\Sigma(x, t_{\rm d}) = \frac{x^{-1/4}t_{\rm d}^{-1}}{2\pi R_1^2}\,\exp\left[\frac{-(1+x^2)}{2t_{\rm d}}\right] I_{1/4}\left(\frac{x}{t_{\rm d}}\right), \tag{7.24}$$

where $I_{1/4}$ is the modified Bessel function of fractional order and the dimensionless distance and time are $x = R/R_1$ and $t_{\rm d} = 6\nu_{\rm v}t/R_1^2$, respectively. Plots of this solution at various times are given in Figure 7.2. The net effect of the viscosity is to spread the ring of material, ultimately concentrating mass at smaller radii, while small amounts of matter are pushed to large distances to conserve angular momentum.

The evolutionary timescale of this ring is of order $R_1^2/\nu_{\rm v}$, a result which is expected on dimensional grounds. This can also be seen as the relevant timescale based on an argument using the turbulent diffusion picture. Individual elements travel a distance λ before merging with the background. The turbulent motion of a particle inward or outward then consists of a random walk process with a mean free path λ at each step. It requires $\sim N^2 \sim (R_1/\lambda)^2$ random walk "steps" for the particle to move a distance $\sim R_1$; each "step" takes a time $t_{\rm s}\sim\lambda/w$; thus the time taken, on average, for a particle to diffuse a distance R_1 is $\sim R_1^2/(\lambda w) \sim R_1^2/\nu_{\rm v}$.

Another illustrative result can be obtained with the assumptions that the viscosity is independent of time and is a power-law function of radius. Recall that in the case of free-fall collapse of an initial power-law density distribution (the singular isothermal sphere; Chapter 3), it was possible to find a similarity solution provided inner and outer boundary conditions did not become important. It is also possible to find similarity solutions to the disk evolution

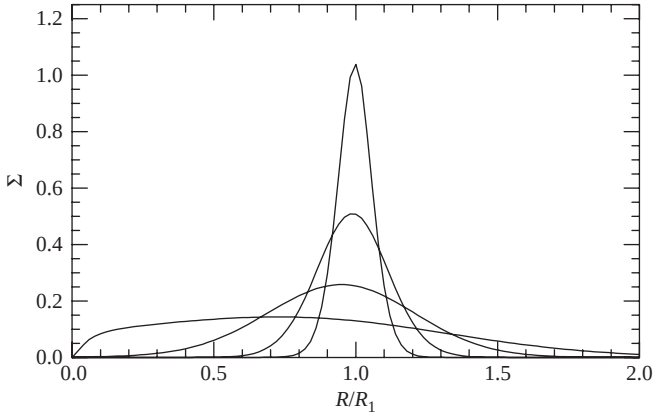

Fig. 7.2. Calculation of the diffusion of a ring of material of unit mass initially at $R = R_1$ for the case $\nu_v =$ constant. As time proceeds, the ring spreads, and distributes more and more mass to smaller radii; results are shown for multiples of 0.004, 0.016, 0.064, and 0.256 of the time measured in units of $R_1^2/(6\nu_{\rm v})$. The turn-down of the surface density at small radii is due to the inner boundary condition employed (see §7.3). After Lynden-Bell and Pringle (1974).

case for the above conditions, as shown by Lynden-Bell and Pringle (1974), and we develop one of these solutions to explore some general properties of viscous accretion disks.

It is useful to recast the equations in terms of the specific angular momentum $h = \Omega R^2$ as a variable. Expanding equation (7.12) in terms of h, and using the mass continuity equation,

$$\frac{\partial g}{\partial R} = -\dot{M}\frac{\partial h}{\partial R}, \tag{7.25}$$

where the (outward) mass flux is $\dot{M} = 2\pi R\Sigma v_{\rm R}$. This equation can be written as

$$\frac{\partial g}{\partial h} = -\dot{M}. \tag{7.26}$$

The continuity equation (7.11) becomes

$$\frac{\partial \Sigma}{\partial t} + \frac{1}{2\pi R}\frac{\partial \dot{M}}{\partial R} = 0. \tag{7.27}$$

Substituting for Σ and $\dot{M}$ with g and h, we have

$$-\frac{\partial}{\partial t}\left(\frac{g}{\nu_v R^2 d\Omega/dR}\right) - \frac{\partial}{\partial R}\left(\frac{\partial g}{\partial h}\right) = 0, \tag{7.28}$$

or

$$\frac{\partial^2 g}{\partial h^2} = -\frac{\partial}{\partial t}\left[\frac{g}{\nu_{\rm v} R^2 (d\Omega/dR) dh/dR}\right]. \tag{7.29}$$

For a central point mass dominating the gravitational potential,

$$\Omega = (GM/R^3)^{1/2}, \quad h = (GMR)^{1/2}. \tag{7.30}$$

so that

$$\frac{\partial^2 g}{\partial h^2} = \frac{4h^2}{3\nu_{\rm v}(GM)^2}\frac{\partial g}{\partial t}. \tag{7.31}$$

This equation simplifies greatly if we assume that the viscosity depends only upon R as a power law. For simplicity we take the special case $\nu_{\rm v} = \nu_\circ(R/R_\circ)$, which may be appropriate in some circumstances. Then we may write

$$\frac{\partial^2 g}{\partial h^2} = \frac{4R_\circ}{3\nu_\circ GM}\frac{\partial g}{\partial t} \equiv \kappa_g^2\frac{\partial g}{\partial t}, \tag{7.32}$$

where κ_g^2 is a constant. Note that because

$$\Sigma = -\frac{g}{2\pi R^3 \nu_{\rm v} d\Omega/dR}, \tag{7.33}$$

finding a solution for g is equivalent to solving for Σ.

Following Lynden-Bell and Pringle (1974), suppose we look for modes of the form

$$g \propto \exp(-st). \tag{7.34}$$

If we set $k^2 = \kappa_g^2 s$, the equation for a single mode is simply

$$\frac{\partial^2 g_k}{\partial h^2} = -k^2\frac{\partial g}{\partial t}. \tag{7.35}$$

For simplicity we assume that g vanishes at the origin $h = 0$, i.e., there is no central torque. Then the solutions to this equation are of the form

$$g(t,h) = \int_0^\infty dk\, e^{-tk^2/\kappa_g^2} A_k \sin(kh). \tag{7.36}$$

From the Fourier theorem, we have

$$A_{k'} = \frac{2}{\pi}\int_0^\infty \int_0^\infty A_k \sin(kh)dk\, \sin(k'h)dh = \int_0^\infty dh\, g(0,h)\sin(k'h). \tag{7.37}$$

This equation can be used to find the coefficients A_k with an initial form for the torque.

For reasons that will become apparent, we try the initial solution

$$g(0,h) = C_g h e^{-a^2h^2}, \tag{7.38}$$

where C_g and a are constants. Substituting this into the equation (7.37),

$$A_k = \frac{2}{\pi}\int_0^\infty C_g h e^{-a^2h^2}\, \sin(kh)dh\,; \tag{7.39}$$

integrating by parts, we find

$$A_k = C_g\frac{k}{2a^2}\frac{1}{\pi^{1/2}a}e^{-k^2/(4a^2)}. \tag{7.40}$$

Then substituting back into (7.36),

$$g(t,h) = \frac{C_g}{2a^3\pi^{1/2}}\int_0^\infty dk\, k\, e^{-[(t/\kappa_g^2)+(1/4a^2)]k^2}\sin(kh). \tag{7.41}$$

This integral is exactly of the same form as the one needed to determine the A_k. After some manipulation we finally arrive at the result

$$g(t,h) = \frac{C_g h}{\left[(4a^2 t/\kappa_g^2)+1\right]^{3/2}} \exp\left[-\frac{ah^2}{(4a^2 t/\kappa_g^2)+1}\right]. \tag{7.42}$$

This solution has the same form at all times, i.e., it represents a similarity solution. To see this more clearly, define

$$T_g = \frac{4a^2}{\kappa_g^2} t + 1. \tag{7.43}$$

Then we can write the solution (7.42) as

$$g = C_g h T^{-3/2} e^{-a^2 h^2/T}. \tag{7.44}$$

If we make the identification

$$a^2 = (GMR_1)^{-1}, \tag{7.45}$$

where R_1 is the appropriate length scale for the initial density distribution, we can solve for the mass flux and the surface density of the disk in terms of physical variables,

$$\dot{M} = C_g T_g^{-3/2} \exp\left(-\frac{R/R_1}{T_g}\right)\left[1 - \frac{2R/R_1}{T_g}\right], \tag{7.46}$$

and

$$\Sigma = \frac{C_g T_g^{-3/2}}{3\pi \nu_\circ (R/R_\circ)} \exp\left(-\frac{R/R_1}{T_g}\right), \tag{7.47}$$

where

$$T_g = \frac{3\nu_\circ t}{R_\circ R_1} + 1 = \frac{t}{R_1^2/3\nu_{\rm v}(R_1)} + 1. \tag{7.48}$$

Solutions for this case are plotted in Figure 7.3. The disk expands to take up the angular momentum as accretion proceeds. The disk mass decreases with increasing time, because material is flowing into the origin (onto the central star; we have ignored the change in central stellar mass in this calculation). The inner disk regions approach a constant mass accretion rate (as a function of radius); overall, the inner mass accretion rates decrease with time as the disk empties out.

Equation (7.46) shows that the mass flux changes sign at a radius $R_{\rm tr} = R_1 T_g/2$. At larger radii, the *net* flow of matter is outward; at smaller radii, the net flow of mass is inward. Eventually most of the disk mass is accreted onto the origin; however, one may show by integrating the equation for Σ with radius that most of the mass in the disk at any given instant of time is actually moving *outward*.

This *self-similar* solution scales with the scaled non-dimensional time T_g as $R \propto T_g$. This solution thus expands linearly in size with time (for $T_g >> 1$), like the singular isothermal sphere similarity solution discussed in §3.2. A qualitative difference in the nature of these similarity solutions is that in the case of the expansion-wave solution for infall, the initial

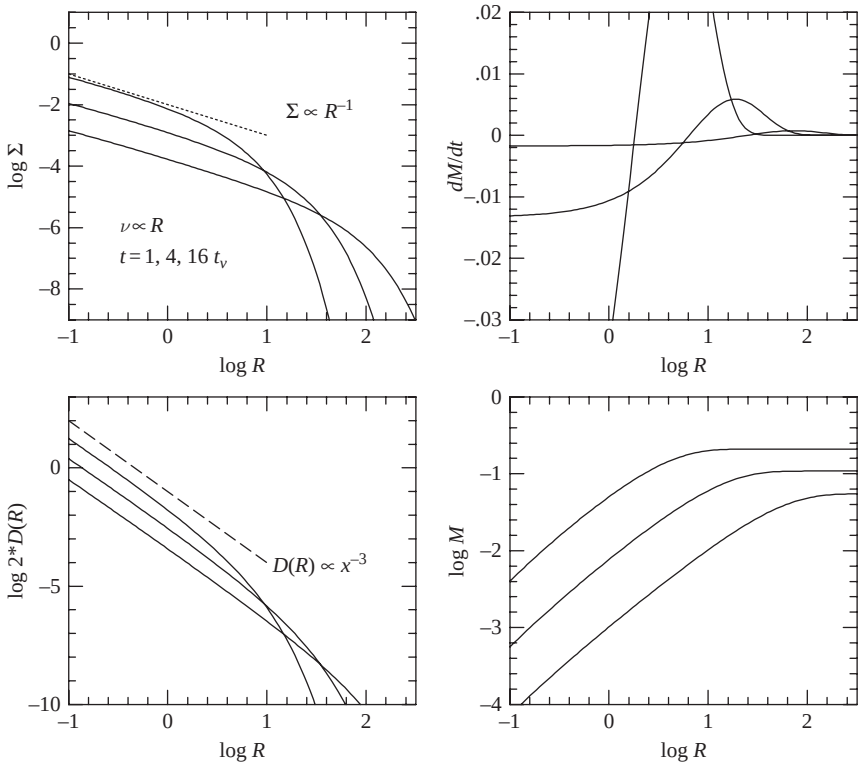

Fig. 7.3. Similarity solution for $\nu_{\rm v} \propto R$. If R is measured in units of R_1, then the solutions shown correspond to $T_g = 1, 4$, and 16 (see text). The surface density (upper left panel) exhibits the same shape at all times when scaled as discussed in the text. The mass flux (upper right) is negative at small radii (accretion) and positive at large radii (expansion). The viscous dissipation rate is shown in the lower left panel, while the disk mass shown in the lower-right panel exhibits a $T_g^{-1/2}$ scaling. The dashed lines show the $\Sigma \propto R^{-1}$ and $D(R) \propto R^{-3/4}$ scaling expected for steady accretion (§7.3).

condition is important, and at late times there is no guarantee that the similarity solution will hold (unless the initial singular isothermal sphere were truly infinite). In contrast, for the disk accretion case, the surface density approaches the similarity solution as the disk expands far beyond its initial (characteristic) radius R_1, no matter what the initial surface density distribution was. This can be seen from a Green's function analysis, which shows that the Green's function for this problem asymptotically approaches the similarity form given above with increasing time.

This similarity solution obviously is not unique; Lynden-Bell and Pringle (1974) give the general solutions for all cases where the viscosity has a power-law dependence on radius. In general one cannot expect the viscosity to scale precisely as any power-law in radius, or be independent of other disk properties. Nevertheless, this simple similarity solution illustrates some generic properties of viscous accretion disks, and provides a simple basis upon which to explore disk evolution, as discussed further in Chapter 12.

7.3 The steady optically thick disk

Given the uncertainties in understanding angular momentum transport in accretion disks, it is important to develop results which are not sensitive to ν_v. The similarity solutions shown in Figure 7.3 suggest that disks tend to evolve toward a nearly constant accretion rate (as a function of radius at a given time) in their inner regions. Using the assumption of steady flow, the emission from the accretion disk can be predicted independently of the viscosity, provided the disk is optically thick.

For steady accretion the mass conservation equation becomes

$$\dot{M} = -2\pi R \Sigma v_R, \tag{7.49}$$

where we have assumed that the constant mass flux $\dot{M}$ is inward, and the conservation of angular momentum equation can be integrated to yield

$$\Sigma R^3 \Omega v_R = \nu_v \Sigma R^3 \frac{d\Omega}{dR} + C, \tag{7.50}$$

where C is a constant of integration. Alternatively, this result can be written as

$$-\nu_v \Sigma \frac{d\Omega}{dR} = \Sigma \Omega (-v_R) + \frac{C}{R^3}. \tag{7.51}$$

Most T Tauri stars are slowly rotating, at rates much less than the Keplerian velocity. It follows that the angular velocity in the disk must eventually decrease (if the disk extends up to the stellar surface, which does not appear to be the case in general; Chapter 8). At the point where the derivative of the angular velocity goes to zero (Figure 7.4), $C = -\dot{M}\Omega R^2/2\pi$; therefore C is proportional to the angular momentum flux at the point where the radial derivative of Ω changes sign.

In simple disk theory, the point where the shear goes to zero is expected to be close to the stellar surface, for reasons outlined in §7.8. For the moment we assume this and write $C = -\dot{M}(GMR_*)^{1/2}/2\pi$, where R_* is the stellar radius, so that

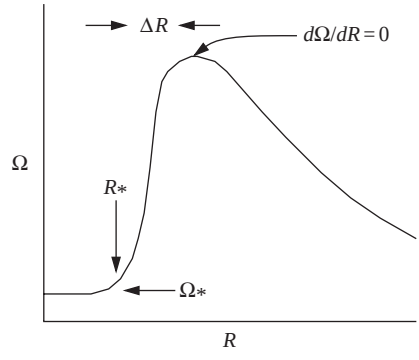

Fig. 7.4. Schematic diagram of the angular velocity in the region where the disk reaches the stellar surface. The star is assumed to be rotating at a rate Ω_* that is much less than the Keplerian velocity near the surface. Therefore, there must be a maximum in the angular velocity Ω of the disk. The point where $d\Omega/dR = 0$ is assumed to be a small distance $\Delta R << R_*$ exterior to the stellar surface. The narrow region where the disk material loses most of its rotational kinetic energy is called the boundary layer (see §7.8).

$$\nu_{\rm v}\Sigma = \frac{\dot{M}}{3\pi}\left[1-\left(\frac{R_*}{R}\right)^{1/2}\right]. \tag{7.52}$$

Far from the inner boundary condition, the steady disk has $\Sigma \propto \nu_{\rm v}^{-1}$; this is consistent with the results for the inner, nearly steady regions of the similarity solution discussed in §7.2.

To obtain the surface temperature distribution of the disk, and therefore its emission properties, we use the result that the viscosity generates dissipation of energy in the disk at a rate $D(R)$ per unit area per unit time (cf. equation (7.22)),

$$D(R) = \dot{E} = \frac{1}{2}\nu_{\rm v}\Sigma\left(R\frac{d\Omega}{dR}\right)^2 = \frac{3GM\dot{M}}{8\pi R^3}\left[1-\left(\frac{R_*}{R}\right)^{1/2}\right]. \tag{7.53}$$

Note that in the limit of constant mass accretion rate, the energy release is independent of the viscosity $\nu_{\rm v}$. Integrating the dissipated energy over radius yields the total energy release by accretion,

$$L_{\rm d} = \frac{1}{2}\frac{GM\dot{M}}{R_*}. \tag{7.54}$$

This is one-half the total accretion energy available, as can be seen by considering bringing in a parcel of material which starts out at infinite radius and therefore has zero energy; at the inner edge of the disk, the gravitational potential energy is twice the kinetic energy of the inner Keplerian orbit. A comparable amount of energy can be released if the kinetic energy of the material at the inner edge of the disk is completely dissipated as it comes to rest upon a slowly rotating star (see §7.8).

A peculiarity of this solution is that the energy released in an annulus at $R >> R_*$ is three times the energy produced locally by accretion through the annulus. The extra energy is provided by a large viscous energy flux transporting energy away from the inner boundary (equation (7.21)). There is a deficit of energy release near R_* as the viscous energy is convected outward by the action of the torque g. As discussed by Lynden-Bell and Pringle (1974), in this model the torques go to zero at the inner boundary and at infinity; thus, the torques can only redistribute the energy released by accretion in this region. It is worth emphasizing that the assumed boundary condition on the angular momentum flux may not be correct in general; for example, interaction with a stellar magnetosphere could produce different torques (Frank *et al.* 1992).

If we make the simple assumption that the disk radiates from its surface like a blackbody, then the surface or effective temperature of the disk is

$$T_{\rm d}^4 = \frac{3GM\dot{M}}{8\pi R^3\sigma}\left[1-\left(\frac{R_*}{R}\right)^{1/2}\right]. \tag{7.55}$$

The maximum temperature of the disk,

$$T_{\rm max} = 0.488\left(\frac{3GM\dot{M}}{8\pi R_*^3\sigma}\right)^{1/4}, \tag{7.56}$$

occurs at $R_{\rm max} = 49/36 = 1.36R_*$. We note that the temperature distribution given by (7.55) formally goes to zero at the inner edge of the disk. This results from the assumed boundary condition on the angular momentum, as discussed above. Although a decrease

to zero temperature is unphysical, modifications require considering the disk structure and inner boundary condition in detail.

With this result, the luminosity as a function of frequency emitted by the disk can be calculated from

$$L_\nu = \int_{R_{\rm in}}^{R_{\rm out}} \pi\, B_\nu[T_{\rm d}(R)]\, 2\pi R dR, \tag{7.57}$$

where L_ν is the luminosity and $R_{\rm out}$ and $R_{\rm in}$ are the inner and outer disk radii. As shown in Figure 7.5, at high frequencies or small wavelengths, the emission is dominated by the hot inner edge of the disk, and the spectrum has an exponential fall-off to higher frequencies. If the disk is optically thick at all wavelengths, and it has a finite outer radius (and thus a lower limit to the temperatures at which the disk emits), at very long wavelengths the spectrum varies as $L_\nu \propto \nu^2$, because the emission from all disk annuli have this spectral form at long wavelengths regardless of their temperature. In practice, this limit is not very important for disks around YSOs because the (dust) opacity falls off rapidly with increasing wavelengths, and so the long-wavelength emission of real disks tends to be optically thin.

At intermediate wavelengths, the spectrum has a characteristic power-law shape produced by the power-law temperature distribution. This can be seen by writing the temperature in terms of a fiducial value at some specified radius, $T_{\rm d} = T_\circ (R/R_\circ)^{-3/4}$, and neglecting the turn-over in the temperature near the inner edge of the disk. The integral can then be written as

$$L_\nu = \frac{16\pi^2 h R_\circ^2}{3c^2} \left(\frac{kT_\circ}{h}\right)^{8/3} \nu^{1/3} \int_{x_{\rm in}}^{x_{\rm out}} \frac{x^{5/3}\, dx}{(e^x - 1)}, \tag{7.58}$$

where $x = h\nu/kT_{\rm d}$. When the outer and inner limits are sufficiently large and small, respectively (i.e., the inner and outer disk temperatures are sufficiently different), the integral over x is nearly constant, so the spectrum varies with frequency as $L_\nu \propto \nu^{1/3}$, or $\lambda L_\lambda \propto \lambda^{-4/3}$.

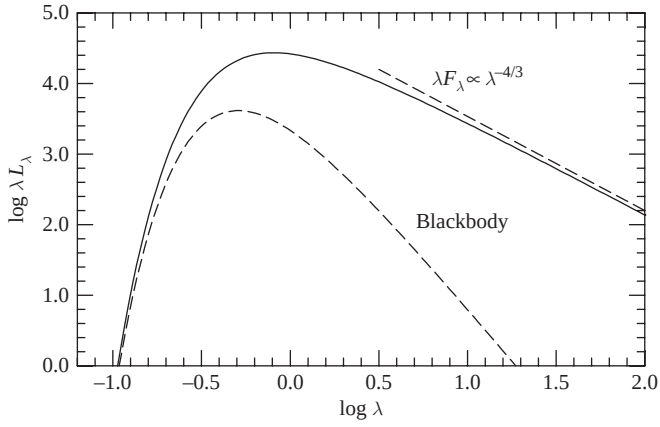

Fig. 7.5. Spectrum of the optically thick steady disk. At short wavelengths, the SED looks like a blackbody with the temperature of the hottest disk annulus; at long wavelengths, the asymptotic $\lambda L_\lambda \propto \lambda^{-4/3}$ is observed, resulting in much more emission at long wavelengths than would result from a single-temperature blackbody (dashed line).

7.4 The α disk

In the absence of a detailed theory, the viscous stress may be parameterized for comparison with observations. The usual way of doing this is through the dimensionless parameter α introduced by Shakura and Sunyaev (1973). We use the modified formalism in which the viscosity is scaled in terms of a characteristic length and a turbulent velocity. It is generally assumed that the length scale of the turbulence in a disk will be less than the scale height H, and the eddy velocity will be less than the sound speed c_s. Thus, the kinematic viscosity can be written as (cf. Pringle 1981)

$$\nu_v = \alpha c_s H, \tag{7.59}$$

where $\alpha \leq 1$. Shakura and Sunyaev also argued that this form might be expected to hold for magnetic stresses. Defining the Alfvén speed $v_A^2 = B^2/4\pi\rho$, Shakura and Sunyaev suggested that $\alpha \sim V_A^2/c_s^2$ should similarly be less than unity, a guess that is consistent with simulations of the magnetorotational instability (§7.5).

The α parameterization can be used to illustrate some features of disk structure most easily discussed in the steady disk approximation. Substituting equation (7.59) into the steady disk angular momentum equation,

$$\alpha c_s H \Sigma = \frac{\dot{M}}{3\pi}\left[1 - \left(\frac{R_*}{R}\right)^{1/2}\right], \tag{7.60}$$

produces an equation for the surface density Σ provided that some relation is found between the total energy dissipated and the central temperature, which is most appropriate for this vertically averaged form. (Note that the surface density $\Sigma \to 0$ as $R \to R_*$ using the temperature distribution of equation (7.55); again, the issue of conditions at the innermost edge of the disk must be settled by more detailed considerations.)

We may proceed a bit further by developing a relation for the scale height. Force balance in the vertical z direction, perpendicular to the disk plane, is given by a balance between the vertical component of gravity and the vertical supporting pressure gradient,

$$\frac{dP}{dz} = -\frac{GM\rho}{(R^2+z^2)}\frac{z}{(R^2+z^2)^{1/2}}. \tag{7.61}$$

For simplicity, adopt an ideal gas law $P = \rho c_s^2$, take the sound speed c_s to be constant in z, and assume that the disk is thin, i.e., $R >> z$. Then the density structure is given by

$$\rho = \rho_0 \exp\left(-\frac{z^2}{2H^2}\right), \quad H = (R^3 c_s^2/GM_*)^{1/2}, \tag{7.62}$$

where the scale height H can be written in terms of the sound speed and the Keplerian velocity v_ϕ,

$$\frac{H}{R} = \frac{c_s}{v_\phi} = \frac{c_s}{\Omega R}. \tag{7.63}$$

Again assuming isothermality in z, and neglecting the factor in brackets in equation (7.60), $T(R,z) \propto R^{-3/4}$ or $c_s \propto R^{-3/8}$. Then the scale height of the disk varies as $H \propto c_s R/v_\phi \propto c_s R^{3/2} \propto R^{9/8}$, and therefore the surface density varies as $\Sigma \propto \alpha^{-1} R^{-3/4}$.

It is worth emphasizing from this example that H/R increases with increasing R; that is, disk isodensity contours tend to curve away from the disk midplane, a feature called disk

"flaring" (Kenyon & Hartmann 1987). This property is crucial to understanding the SEDs of disks, as discussed further in §7.9 and Chapter 8.

It is also worth pointing out that for the α parameterization, the radial accretion velocity in the steady disk,

$$v_{\rm R} \sim (3/2)\alpha c_{\rm s}\left(\frac{H}{R}\right), \tag{7.64}$$

is highly subsonic, consistent with the assumptions of nearly circular motion. Finally, note that the mass accretion rate scales as

$$\dot{M} \propto \nu\Sigma \propto \alpha c_{\rm s} H\Sigma \propto \alpha c_{\rm s}^2 \Sigma\Omega \propto \left(\frac{\alpha T\Sigma}{\Omega}\right). \tag{7.65}$$

Thus, a higher value of viscosity (larger α) leads to a larger mass accretion rate for a given surface density; conversely, for a given mass accretion rate, the surface density $\Sigma \propto \alpha^{-1}$.

In general, the relationship between the central temperature and the surface temperature (or the dissipated energy) is not so simple and an energy balance equation coupled with a constitutive equation must be solved to close the equations. It is also not obvious that α is constant at all radii; indeed, given considerations of the following section, variations in α seem likely.

7.5 Sources of viscosity: the magnetorotational instability

It is evident that a complete theory of disk accretion requires a knowledge of the viscosity. However, molecular viscosity is so small that disk evolution due to this mechanism of angular momentum transport would be far too slow to be of interest. Turbulent *convection* in disks has been a popular mechanism for viscosity for some time (Lin & Papaloizou 1980); unfortunately, as discussed in §7.1, investigations suggest that convection might actually transport angular momentum *inward* more effectively than *outward* (Cabot & Pollack 1992; Ryu & Goodman 1992; Stone & Balbus 1996). Other gas dynamic waves might be important in carrying angular momentum, particularly if they are forced by some external factor, such as the gravitational field of a companion star (e.g., Vishniac & Diamond 1989; Rozyczka & Spruit 1993). However, the presence of a companion star or massive planet does not seem to be sufficiently general to account for pre-main-sequence disk accretion in many or most cases.

The favored mechanism for producing an "α" type viscosity is the "magnetorotational instability" (MRI) initially discussed by Velikhov (1959) and specifically developed for accretion disks in a series of papers by Balbus and Hawley (1991) and collaborators (related discussions were also provided by Chandrasekhar (1960) & Fricke (1969), and a recent review has been presented by Balbus and Hawley (1998)). The essence of this instability is indicated in Figure 7.1. Imagine that a magnetic field line initially connects two neighboring annuli in a radial direction, as shown by the schematic "spring" (position 1). Because these two annuli have differing angular velocities, the spring (field line) will become stretched as the shear proceeds (position 2). The magnetic field will try to oppose the shear, but if it is not initially "strong", it cannot resist. The magnetic field line will then try to straighten out, which requires speeding up the outer annulus relative to the inner annulus, i.e., transferring angular momentum outward. As the inner annulus loses angular momentum, it will fall in deeper to the potential well, increasing its angular velocity further, while the outer annulus will tend to move outward and slow down, enhancing the stretching of the magnetic

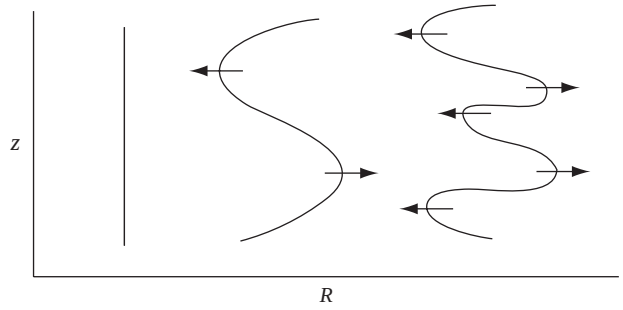

Fig. 7.6. Development of the MRI, as indicated by magnetic fields in the meridional plane for a disturbance with a finite vertical wavenumber. The field lines stretch radially as they shear toroidally (see Figure 7.1), and then break up into turbulent regions.

field. This is the essence of the instability. Three-dimensional numerical simulations suggest that the MRI results in vigorous magnetohydrodynamic turbulence, which can in principle provide the needed viscosity for accretion disks.

To see how this instability can give rise to turbulent motions, consider a magnetic field line which is initially vertical, i.e., perpendicular to the disk plane (Figure 7.6). Suppose that a small sinusoidal perturbation is applied to the field line. Then, for the reasons discussed in the previous paragraph, the outward "bulges" will tend to be stretched further outward, while the inward bulges will tend to be stretched further inward. The result is increasingly long (in the radial direction) loops of magnetic field, allowing the interchange of material moving inward and outward at different (randomly varying) levels z in the disk. This behavior is shown dramatically in the numerical simulations of Hawley *et al.* (1995) and Stone *et al.* (1996).

What if there is no magnetic field to begin with? The *stretching* of the magnetic field shown in Figure 7.1 amounts to an *amplification* of the field. The instability can amplify small (perturbation) fields to larger fields, i.e., it can exhibit dynamo activity (Tout & Pringle 1992; Vishniac & Diamond 1992; Curry *et al.* 1994; Brandenburg *et al.* 1996; Hawley *et al.* 1996; also Rincon *et al.* 2007), so the instability may arise even if there is a vanishingly small initial magnetic field. On the other hand, if the magnetic field is too strong, it can enforce co-rotation of the neighboring annuli and quench the instability. This places a limit on the magnetic field such that the magnetic pressure must be less than the gas pressure.

To place the MRI in the context of the α disk formalism (e.g., Balbus & Papaloizou 1999), consider the momentum equation for a gas with density ρ, velocity v, pressure P, gravitational potential Φ, and magnetic field B is (see Appendix 1)

$$\frac{\partial \rho}{\partial t} + \nabla \cdot (\rho \mathbf{v}) = -\nabla P - \rho \nabla \Phi + \frac{1}{4\pi} (\nabla \times \mathbf{B}) \times \mathbf{B}, \tag{7.66}$$

which can be rewritten using vector identities as

$$\frac{\partial \rho}{\partial t} + \nabla \cdot (\rho \mathbf{v}) = -\nabla P - \rho \nabla \Phi + -\frac{1}{8\pi} \nabla B^2 + \frac{1}{4\pi} (\mathbf{B} \cdot \nabla) \mathbf{B}. \tag{7.67}$$

Here we have ignored the kinematic viscosity. The azimuthal component of this equation expresses angular-momentum conservation:

$$\frac{\partial \rho R v_\phi}{\partial t} + \nabla \cdot R\left[\rho v_\phi \mathbf{v} - \frac{B_\phi}{4\pi}\mathbf{B_p} + \left(P + \frac{B_p^2}{8\pi}\right)\hat{\mathbf{e}}_\phi\right] = 0, \tag{7.68}$$

where the subscript p denotes a poloidal vector component. (We will see this equation again in Chapter 10, while discussing magnetic winds and infall.)

Now decompose the velocity into a steady circular component plus a fluctuating part $\mathbf{u}$,

$$\mathbf{v} = R\Omega\hat{\mathbf{e}}_\phi + \mathbf{u}. \tag{7.69}$$

Further assume that the mean radial velocities (i.e., accretion or expansion) are small in comparison with the fluctuating component, so that

$$|\langle \mathbf{u} \rangle|^2 \ll \langle u^2 \rangle, \tag{7.70}$$

where the averaging is done over a region larger than a scale height but not very large in comparison with R. We substitute this into equation (7.68), and take an average over azimuthal angle ϕ; this averaging eliminates the gas and magnetic pressure term. Then, ignoring u_ϕ in comparison with $R\Omega$,

$$\frac{\partial}{\partial t}\langle \rho R^2\Omega \rangle_\phi + \nabla \cdot R\left[\langle \rho R\Omega \mathbf{u}_p \rangle_\phi + \left\langle \rho\left(u_\phi \mathbf{u_p} - B_\phi \frac{\mathbf{B_p}}{(4\pi\rho)}\right)\right\rangle_\phi\right]. \tag{7.71}$$

We define the density-weighted mean of $\langle X \rangle_\rho$ as the integral of quantity ρX taken over all azimuth, over a radial distance ΔR, and over height z. Finally we define the equivalently weighted, radial component of the final term of equation (7.71),

$$W_{R\phi} = \frac{1}{2\pi\Sigma R\Delta R}\int_{-\infty}^{\infty}\int_{R-\Delta R/2}^{R+\Delta R/2}\int_0^{2\pi}\left[u_\phi \mathbf{u}_p - B_\phi \frac{\mathbf{B}_p}{(4\pi\rho)}\right]. \tag{7.72}$$

Then the equation of angular momentum conservation becomes

$$\frac{\partial}{\partial t}\langle \Sigma R^2\Omega \rangle_\rho + \frac{1}{R}\frac{\partial}{\partial R}(R^3\Omega\Sigma\langle u_R \rangle_\rho + R^2\Sigma W_{R\phi}) = 0, \tag{7.73}$$

which is of the same form as equation (7.14).

We can proceed further by using the mass conservation equation, which essentially is the same as (7.10):

$$\frac{\partial \Sigma}{\partial t} + \frac{1}{R}\frac{\partial(R\Sigma\langle u_R \rangle_\rho)}{\partial R} = 0. \tag{7.74}$$

Substituting this into equation (7.73) yields

$$\Sigma\langle u_R \rangle_\rho = \frac{1}{R}\frac{\partial}{\partial R}\left(\frac{d\Omega R^2}{dR}\right)^{-1}\frac{\partial}{\partial R}\left(-\Sigma R^3 W_{R\phi}\right). \tag{7.75}$$

Combining these, we finally arrive at the equation for the evolution of the surface density,

$$\frac{\partial \Sigma}{\partial t} = \frac{1}{R}\frac{\partial}{\partial R}\left(\frac{d\Omega R^2}{dR}\right)^{-1}\frac{\partial}{\partial R}\left(\Sigma R^2 W_{R\phi}\right). \tag{7.76}$$

This equation has the same form as (7.15), with the identification

$$W_{R\phi} = -\nu_{\rm v} R \frac{d\Omega}{dR}. \tag{7.77}$$

These equations simply exhibit a formal similarity to the α disk theory. For this to work in practice, it must be the case that the fluctuating components $u_{\rm R}$ and u_ϕ, and $B_{\rm R}$ and B_ϕ, are correlated. Moreover, because $d\Omega/dR < 0$, outward angular momentum transport requires that $W_{R\phi} > 0$, so that these fluctuations are positively correlated. One must turn to simulations to show that the MRI exhibits the necessary correlations (Balbus & Papaloizou 1999).

This suggests that suitably averaged disk behavior can be studied with the simple viscous disk theory, at least for some applications. Presciently, Shakura and Sunyaev (1973) originally developed the α disk theory in terms of a magnetic stress, parameterized by

$$W_{R\phi} = -\alpha_{\rm SS} c_{\rm s}^2. \tag{7.78}$$

The relation between the α used in the previous section and the Shakura–Sunyaev value is thus

$$\alpha c_{\rm s} H R \frac{d\Omega}{dR} = \alpha c_{\rm s}^2 \frac{d\ln\Omega}{d\ln R} = -\alpha_{\rm SS} c_{\rm s}^2 ; \tag{7.79}$$

thus, for a Keplerian disk, $\alpha_{\rm SS} = (3/2)\alpha$.

Efforts to characterize the magnitude of the MRI viscosity quantitatively are still uncertain. Three-dimensional numerical results (e.g., Brandenburg *et al.* 1996; Stone *et al.* 1996; Heyvaerts *et al.* 1996) suggest

$$\alpha \sim 0.1 - 0.01, \tag{7.80}$$

but there is uncertainty about how these values depend upon specific parameters (size of the simulated region, etc.); there may also be difficulties in running simulations long enough to construct meaningful averages (Winters *et al.* 2003). There are indications that the MRI saturates at a specific fraction of the total magnetic pressure (Sano *et al.* 2004), but how one translates this into a limit on α is not yet clear. More recently, there are concerns that numerical simulations tend to yield values of $\alpha \sim 0.01$ while observations tend to indicate larger values by as much as an order of magnitude (King *et al.* 2007).

It should be noted that in general, the MRI does not act precisely as an α viscosity, in the sense that it may not be linear in $d\Omega/dR$ as equation (7.77) indicates (Ogilvie 2003; Pessah *et al.* 2006). However, this is unlikely to be an important issue for near-Keplerian disks.

7.6 The ionization problem

A crucial issue in applying the MRI to the disks of YSOs is the requirement that the magnetic field must couple effectively with the gas. Since the magnetic field acts only upon charged particles, the efficiency with which the MRI mechanism can work depends upon whether there are enough ions in the gas; otherwise, collisions between ions and neutrals may not be frequent enough to transfer momentum effectively from the former to the latter. In the cold, dusty disks around young stars, the ionization fraction is likely to become quite low (cf. Umebeyashi & Nakano 1988; Reyes-Ruiz & Stepinski 1995; Gammie 1996b; Sano *et al.* 2000), strongly reducing the effectiveness of the MRI, or even eliminating its action altogether (Blaes & Balbus 1994).

At temperatures around $T \gtrsim 1000\,\mathrm{K}$, low-ionization-potential atoms such as K and Na can provide enough electrons for the MRI to operate under typical conditions. However, most of the mass of YSO disks is likely to reside in much colder regions. To address this problem, various mechanisms producing non-thermal ionization of disks have been suggested, the two most prominent being galactic cosmic rays (Gammie 1996a) and X-rays from the central young star (Glassgold *et al.* 1997; Igea & Glassgold 1999). It has been argued that the magnetic fields of young stars, especially in their outflows, might scatter cosmic rays away (as the solar wind does) so effectively as to strongly reduce or eliminate them as an effective ionizing agent for the disk. However, earlier-type stars (such as HAe/Be stars) apparently possess accretion disks, yet they appear to be relatively weak X-ray emitters (see §8.7).

Whether using cosmic rays or X-rays as the ionizing mechanism, it seems likely that not all regions of YSO disks are completely penetrated by the ionizing fluxes (although Fromang *et al.* 2002 argue that this may not be true, especially if small amounts of metal ions are present). The difficulty in ionizing much of typical protoplanetary disks led Gammie (1996a) to suggest that YSO disks have "dead zones", that is, regions of the disk which are inactive in terms of angular momentum transport (and magnetic/viscous energy dissipation); the MRI occurs in upper disk layers, as indicated schematically in Figure 7.7.

Fleming and Stone (2003) numerically simulated a stratified disk region, where the MRI only operated in the outermost (in z), lower density layers. They found that the turbulence generated by the MRI-active layers could penetrate into the inactive layers, developing a low level of angular momentum transport. However, it seems very unlikely that this turbulence can drive much more mass accretion than can be driven in the upper, active layers, because the mass flux is proportional to $\alpha\Sigma$ (equation (7.65)); thus, the order-of-magnitude smaller α in the dead zone found by Fleming and Stone would have to penetrate to an order of

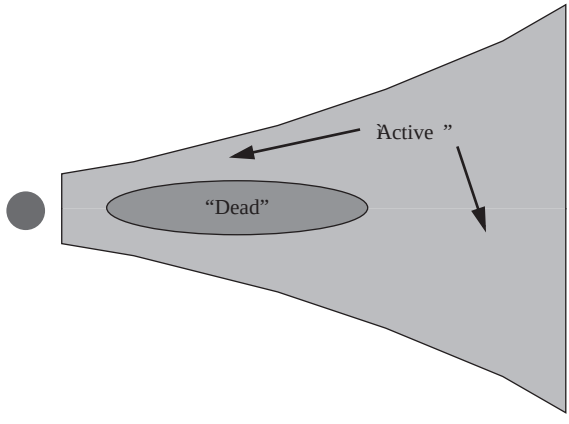

Fig. 7.7. Schematic version of a "layered" accretion disk. The innermost regions can be sufficiently ionized for the MRI to operate because the disk is warm, with estimated temperatures $\gtrsim$1000 K; the outer regions may also be the site of an "active" MRI due to non-thermal ionization by cosmic or X-rays. At intermediate radii, the disk is too cold for thermal ionization to be effective, and has too high a surface density for cosmic or X-rays to penetrate; this region may then be relatively inert, not subject to the MRI (Gammie 1996a; see text).

magnitude larger surface density than the active layer to have a significant effect on the mass accretion rate, which seems implausible.

In the simplest version of the layered theory, Gammie (1996a) suggested that the cosmic rays would magnetically activate a roughly constant (upper) surface density Σ_a. Studies of X-ray ionization by Igea and Glassgold (1999) suggest only a weak dependence of Σ_a on radius for this mechanism. If we take both α in the active layer and Σ_a as constants for simplicity, then equation 7.18 implies

$$\dot{M} = 6\pi R^{1/2} \alpha \Sigma_a \frac{\partial}{\partial R} \frac{c_s^2 R^{1/2}}{\Omega}. \tag{7.81}$$

Then if we further assume $c_s^2 \propto T \sim R^{-1/2}$ (see §7.9 and Chapter 8) as typical of irradiated T Tauri disks, $\dot{M} \propto R$. That is, the layered disk model in its simplest form is unlikely to be steady; instead, mass will tend to pile up over time in the inner regions, which might lead eventually to gravitational instabilities (Gammie 1996a; §7.7).

Another possible mechanism of magnetic angular momentum transport is the ejection of disk winds. Strong winds are associated with rapidly accreting disks, and the most plausible origin for these outflows is that they are "slung off" the disk surface by magnetic fields rooted in the disk (Chapter 10). The magnetic fields couple the disk to ejected material which carries away angular momentum. Models have been constructed in which all of the angular momentum transport needed for accretion is carried away by such winds; however, in this case all of the accretion energy is carried away as well (§10.8). Observations show that at least some disks are self-luminous due to the dissipation of accretion energy (Chapters 8, 9), and other considerations suggest that winds are not the dominant mode of angular momentum transport of pre-main-sequence accretion disks (Chapter 10).

7.7 Gravitational instability and angular momentum transport

The probability that most of the mass of a typical star initially resides in its disk suggests that disks might be self-gravitating in early phases of evolution. Gravitational instabilities may also transfer angular momentum, as can again be illustrated from the schematic drawing in the right-hand panel of Figure 7.1. Suppose that instead of a magnetic field line there is a radially extended mass concentration, as shown in the right-hand panel. If the gravitational instability can keep this mass concentration together despite the shearing effects of the disk and tidal acceleration, the excess mass can be confined to a trailing spiral arm. There are excess gravitational forces due to this mass concentration; the inner part of the spiral arm pulls on the outer part of the spiral arm, trying to accelerate the outer regions. As in the BH instability, this tendency to accelerate outer regions in the direction of motion causes a net flow of angular momentum outward, and thus in principle can produce the torque needed for mass accretion.

Under what conditions can gravitational instability arise? In Chapter 2 we discussed gravitational instabilities in a non-rotating sheet. Although we require non-axisymmetric instabilities to transfer angular momentum (cf. Figure 7.1), it turns out that the criterion for such instabilities is nearly the same as the requirement for axisymmetric instability. The dispersion relation for symmetric modes in a thin rotating disk is (Binney & Tremaine 1987)

$$\omega^2 = \kappa^2 + c_s^2 k^2 - 2\pi G \Sigma \mid k \mid . \tag{7.82}$$

This relation is similar to the result for the non-rotating sheet discussed in Appendix 2; it differs in the term involving the epicyclic frequency κ. (When the disk rotation is Keplerian, $\kappa = \Omega$, the local angular velocity.) For negative ω^2, perturbations grow exponentially and the disk is unstable. The limiting condition occurs when $\omega = 0$; the condition for axisymmetric instability is then given by the "Toomre Q" parameter,

$$Q \equiv \frac{c_s \kappa}{\pi G \Sigma} \lesssim 1. \tag{7.83}$$

The precise value at which instability sets in depends upon the specific conditions assumed. For example, in a finite thickness, isothermal disk, the stability criterion is $Q < 0.676$ (Goldreich & Lynden-Bell 1965). Differing detailed assumptions lead to differing specific values for the limiting value of Q (see, e.g., Gammie 2001), but they are always of order unity.

The above analysis applies to axisymmetric gravitational instabilities, whereas non-axisymmetric modes are required to transport angular momentum. Although disks are formally stable to all local non-axisymmetric disturbances (Goldreich & Lynden-Bell 1965; Julian & Toomre 1966), global instabilities may occur (i.e., extended spiral arms) which may be either linear or non-linear, depending upon the so-called swing amplification and boundary conditions (see §6.3 in Binney & Tremaine (1987) for further discussion). Roughly speaking, as $Q \to 1$, non-axisymmetric waves appear which can transfer angular momentum efficiently (Larson 1984; Shu *et al.* 1990; Gammie 2001).

The physical basis of the instability can be understood qualitatively from a simple argument (Toomre 1964). If a small region or fragment in a self-gravitating disk is compressed, its self-gravity is increased; but it also tends to spin more rapidly, producing a centrifugal force to oppose gravity. The balance of these two effects leads to the instability criterion, as described in the following paragraphs.

Consider a region in the disk of size ΔR which is initially in equilibrium. Suppose the mass in this region is compressed so that it is now confined within a radius $\Delta R - \delta R$. The force of gravity per unit mass is then changed to

$$F_G = \frac{GM}{(\Delta R - \delta R)^2} \approx \frac{GM}{(\Delta R)^2}\left(1 + 2\frac{\delta R}{\Delta R}\right). \tag{7.84}$$

Next, one must consider the effects of angular momentum conservation in spinning up this region or fragment around its own center. The initial specific angular momentum of the region or fragment is

$$l \sim \Omega \Delta R^2. \tag{7.85}$$

After contraction, if angular momentum is conserved, the new angular velocity is

$$\Omega' \sim \frac{l}{(\Delta R - \delta R)^2} \sim \Omega\left(1 + 2\frac{\delta R}{\Delta R}\right). \tag{7.86}$$

The centrifugal acceleration of this fragment or region around its center is

$$\frac{v'^2}{(\Delta R - \delta R)} \sim \Omega'^2(\Delta R - \delta R) \sim \Omega^2 \Delta R\left(1 + 3\frac{\delta R}{\Delta R}\right). \tag{7.87}$$

For stability the change in centrifugal acceleration must more than balance the increased gravity, so with $M = \pi \Delta R^2 \Sigma$,

$$3\Omega^2 \delta R > 2\pi G \Sigma \frac{\delta R}{\Delta R}, \tag{7.88}$$

so that

$$\Delta R > \frac{2\pi G \Sigma}{3\Omega^2}. \tag{7.89}$$

A similar analysis for small-length scales provides a constraint for gas pressure to stabilize the perturbation against gravity.

$$\Delta R < \frac{c_s^2}{\pi G \Sigma}. \tag{7.90}$$

This is basically just a Jeans analysis (Chapter 2); because pressure stabilizes on small scales, there is a minimum length scale (a Jeans length) for gravitational instabilities. If the length scale over which pressure stabilizes the gravitational perturbation is *larger* than the length scale on which rotation provides stability, then

$$\frac{2\pi G \Sigma}{3\Omega^2} < \Delta R < \frac{c_s^2}{\pi G \Sigma}, \tag{7.91}$$

or

$$\frac{3\Omega^2 c_s^2}{2(\pi G \Sigma)^2} > 1. \tag{7.92}$$

This reproduces the basic result for the Q parameter if the epicyclic frequency κ is comparable to Ω.

Another way of understanding the Q limit is to consider tidal forces. A perturbation of radius ΔR can grow if its self-gravity is greater than the tidal forces on the perturbation, i.e., the differential acceleration due to the central gravitating regions. Assuming most of the mass is in the central star,

$$\frac{GM}{R^2}\frac{\Delta R}{R} \sim \pi G \Sigma \frac{\Delta R}{R} < \frac{G \Delta M}{\Delta R^2} = \pi G \Sigma, \tag{7.93}$$

so that

$$\Delta R < \pi G \Sigma \frac{GM}{R^3} = \pi G \Sigma \Omega^{-2}. \tag{7.94}$$

Now, ΔR must be larger than the disk thickness (i.e., the scale height H) to satisfy the Jeans criterion, because by construction the gas pressure can support the disk against its own self-gravity in the z direction. Using equation (7.63) (assuming that the disk self-gravity does not markedly change the Keplerian result),

$$\frac{c_s}{\Omega} = H < \Delta R. \tag{7.95}$$

Putting these two constraints together,

$$\frac{\Omega c_s}{\pi G \Sigma} < 1 \tag{7.96}$$

once again emerges as the criterion for gravitational instability.

It is useful to develop a rule of thumb which constrains the amount of mass in the disk needed for gravitational instability. Multiplying the numerator and denominator of (7.83) by the outer disk radius R_d^2, and making the approximation that the disk mass is $M_d \sim \pi R_d^2 \Sigma$, the condition for instability becomes

$$c_s \kappa R_d^2 < G M_d. \tag{7.97}$$

Making the further approximation that the disk motion is nearly Keplerian, the requirement for instability is roughly (Pringle 1981)

$$M_d > \frac{H}{R} M_*. \tag{7.98}$$

Thus, gravitational instability occurs only when the disk has an appreciable mass in comparison with the central star (Larson 1984), as might be expected intuitively. The central stellar mass enters because it is responsible for producing the initial angular velocity of a contracting fragment; for larger central masses, Ω becomes larger, and therefore the disk mass must be larger to overcome the centrifugal resistance to contraction. The disk temperature is also important. For a given ratio of disk mass to central mass, cooler disks have smaller scale heights H and are thus more susceptible to gravitational instability.

Numerical simulations (see Tomley *et al.* (1994), Laughlin and Bodenheimer (1994), and references therein; also discussion in Lin & Pringle (1990)) indicate that gravitational instabilities can generate turbulence which appears as unsteady, wave-like, spiral density structures. These waves can transfer angular momentum provided that there is some mechanism for "cooling" the disk, i.e., a way of reducing the gas temperature. If the disk is not cooled effectively, it tends to heat up until Q increases to values slightly above the limit for stability. (Similar results were found in the case of stellar disks of galaxies, and the need for cooling for gaseous disks is related to the development of "hot" galactic stellar disks in the absence of a massive halo; see the discussion in Binney & Tremaine (1987).) Quantitative estimates of the angular momentum transport rates are still difficult to obtain, because heating and cooling rates are difficult to determine (Tomley *et al.* 1994).

Gravitational instability can also lead to fragmentation, rather than simply providing a mechanism for angular momentum transport in disks (e.g., §7.2). Gammie (2001) considered the problem by analyzing a small, local region (a "shearing box") in a very thin disk, with schematic cooling properties. Denoting the timescale for losing (radiating away) thermal energy as the cooling time t_c, Gammie found that for $t_c \lesssim 3\Omega^{-1}$, the disk fragmented (e.g., left panel of Figure 7.8), while for longer cooling times, a steady, "gravoturbulent" state is reached, with a balance between dissipating turbulence and cooling, and $Q \sim 1$; the resulting waves have the trailing structure which would result in angular momentum transport outward (right panel of Figure 7.8). The situation is more complex in situations with more complicated energy equations; Johnson and Gammie (2003) found qualitatively similar results.

The reason why the relation between the orbital period and the cooling time is critical can be seen from the following argument. In the disk, the time for a sound wave to travel a scale height is $H/c_s = \Omega$, and this is of the order of the timescale for the onset of a (small scale) gravitational perturbation to grow (since gravity must overcome the gas pressure). Consider a perturbation which locally increases the density. If the cooling time is long in comparison with this sound crossing time, the increasing temperature along with increasing

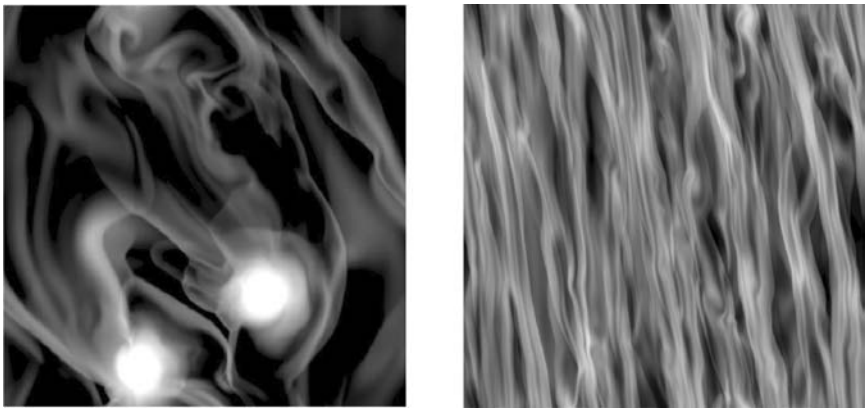

Fig. 7.8. Surface density maps for a shearing box simulation of a thin disk. Left panel: gravitational fragmentation results for a short cooling time ($t_c = 2\Omega^{-1}$). Right panel: a quasi-steady pattern of turbulence present for a long cooling time ($t_c = 10\Omega^{-1}$). The direction of rotation is from bottom to top. From Gammie (2001).

density can help support the disk against the increased gravity. Conversely, if the cooling time is short, then the thermal energy is rapidly lost and gravitational collapse can ensue (on the appropriate length scale).

In the case of YSOs, disk heating is likely to be strongly affected, if not dominated, by the absorption of radiation from the central star (§7.9). In this case the disk temperature is more likely to be fixed at a value given by the geometry of the disk and the distance from the star, and the cooling time is not relevant (effectively short). In this limit, for a similar local thin disk analysis, Johnson and Gammie (2003) found fragmentation occurs for $Q \lesssim 1.4$.

A gravitationally unstable, but non-fragmenting, disk cannot be treated as a viscous disk in general, because gravity is a long-range force, and thus can transport energy over long distances without the local dissipation assumed in the standard viscous disk theory (e.g., Laughlin *et al.* 1998). For example, low-order disturbances, such as the single-armed spiral mode, can be very effective in propagating waves over long distances (Adams *et al.* 1989; Shu *et al.* 1990). Under some circumstances a kind of α-approximation might be adequate, for example with small amplitude, tightly wound spiral disturbances as the disk hovers near the $Q \sim 1$ limit (Balbus & Papaloizou 1999; Gammie 2001).

A global calculation by Boley *et al.* (2006; Figure 7.9) suggests that gravitationally unstable protostellar disks might tend to evolve to a state where a local, effective-α treatment is reasonable over some range of disk radii, though the details depend upon the thermal properties of the disk. In general, thermal physics of disks are extremely difficult to follow in numerical simulations because, for typical parameters, the disks are very optically thick. This means that the energy loss is constrained by radiation from a geometrically thin disk "photosphere" which poses resolution problems for numerical simulations.

7.8 Disk boundary layers

A particle which moves from an orbit far from the central star to a circular orbit just above the stellar surface must lose an amount of energy per unit mass equal to $GM_*/2R_*$. Potentially, this particle can lose almost an equal amount of energy in coming to rest on the

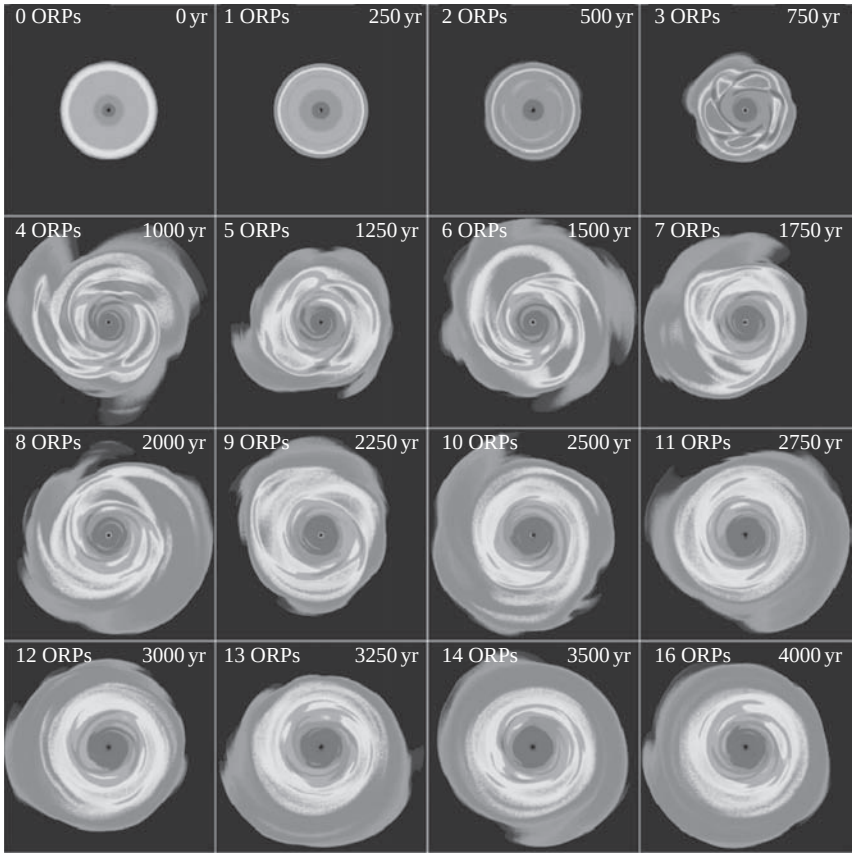

Fig. 7.9. Numerical simulation of the evolution of a gravitationally unstable disk with external irradiation. The figure shows the projected surface density seen perpendicular to the disk plane. The disk develops spiral arms which then transfer angular momentum outward (e.g., Figure 7.1); this results in inner disk material moving inward while the outer disk expands. From Boley *et al.* (2006).

surface of a slowly rotating T Tauri star. Thus, the release of energy near the stellar surface is an important part of the total accretion energy, and if a substantial fraction of this energy is radiated it can have important effects on the spectral energy distribution.

Suppose that the disk rotates at Keplerian velocities up to a small distance from stellar surface (as justified below). The angular velocity must decline as material passes from the disk to join the slowly rotating star (Figure 7.4). The region interior to the peak in $\Omega(R)$ cannot transfer angular momentum outward to the disk, because the gradient in Ω goes the wrong way (cf. equation (7.13)). If there are no other angular momentum transport mechanisms, such as a magnetically coupled wind (Chapter 10), the accreting material will transfer angular momentum to the star, which over a long enough time will spin the star up.

If material at $R_* + \Delta R$ is initially rotating at the Keplerian angular velocity $\Omega_K(R_* + \Delta R) \approx \Omega_K(R_*)$, and then slows down to the stellar angular velocity Ω_*, the change in kinetic energy per unit mass is $(\Omega_K^2 - \Omega_*^2)R_*^2$. However, not all of this energy is released as radiation; some of it goes into spinning up the star. The proportion between radiation and

spin up depends in detail upon what is assumed about the effect of adding material to the star. For a slowly rotating central star, the boundary layer luminosity is predicted to approach $L_{\rm BL} \rightarrow GM\dot{M}/2R_*$.

Now we justify the adoption of a narrow boundary layer, implicit in the assumption that the disk exhibits Keplerian rotation almost up to the stellar surface. Basically, the boundary layer is narrow in radial dimension as long as the disk is thin, i.e., $H << R$. In the radial direction the equation of motion is

$$v_R \frac{dv_{\rm R}}{dR} - \frac{v_\phi^2}{R} = -\frac{1}{\rho}\frac{dP}{dR} - \frac{GM}{R^2}. \tag{7.99}$$

Since the radial velocity is small in most cases, departures from Keplerian motion will only occur when the gas pressure forces can help balance gravity. If Ω departs significantly from Keplerian motion over a region of length $R_{\rm BL}$, then the radial force balance equation requires

$$\frac{c_{\rm s}^2}{R_{\rm BL}} \sim \frac{GM}{R^2}, \tag{7.100}$$

and, using (7.63),

$$\frac{R_{\rm BL}}{R} \sim \left(\frac{H}{R}\right)^2, \tag{7.101}$$

so that the dynamical boundary layer is thin, as assumed, as long as the disk is thin.

If the disk material in the vicinity of the boundary layer is optically thick, then even if the *dynamical* boundary layer thickness $R_{\rm BL}$ is small, the energy dissipated must diffuse in the radial direction as well as in the z direction. In an optically thick boundary layer, this diffusion must occur over a radial scale $\sim H$, since on much smaller scales the influence of the surface cannot be felt. A reasonable rule of thumb for the width ΔR of an optically thick, emitting boundary layer region is $\Delta R \sim H$ (Pringle 1989).

In either optically-thin or -thick cases the boundary layer of a disk accreting onto a slowly rotating star emits a luminosity comparable to that released in the rest of the accretion disk, but over a very small area. Therefore, the boundary layer must be much hotter than the maximum temperature in the disk proper, and so will radiate at much shorter wavelengths. For this reason Lynden-Bell and Pringle (1974) suggested that the hot optical and ultraviolet excess emission of T Tauri stars is emitted in the disk boundary layer.

However, it appears that the traditional boundary layer picture is not relevant for most T Tauri stars, because the stellar magnetic fields are generally strong enough to prevent most disks from reaching the stellar surface. The stellar magnetosphere disrupts the disk and channels the accreting material along field lines out of the disk and onto the star (Figure 8.1; §§8.11, 8.12). The stellar magnetic field absorbs the angular momentum of the accreting material, allowing it to fall inward. It appears likely that the accreting gas falls in supersonically, at nearly free-fall velocities, and then shocks at the stellar photosphere. In this model the radiation produced as material comes to rest on the stellar surface arises from this hot shock at the stellar surface. The size of the emitting region is controlled by magnetic field strengths and geometries and not by scale–height considerations for the disk. The observational support for this picture, as well as some of the physics involved, will be discussed further in Chapters 8 and 10.

7.9 Disk irradiation

In T Tauri stars the disk accretion luminosity is often less than that of the luminosity of the central star. In this case, the absorption of light from the central object can be the dominant mechanism heating the disk, a process called *irradiation* here.

The absorbed energy for an opaque, completely absorbing, flat disk can be calculated simply assuming that the star radiates uniformly and isotropically from its surface. For a point on the disk at distance R from the center of the star, we take a coordinate system in which the xy plane corresponds to the disk, the z axis is perpendicular to this plane, parallel to the disk rotation axis (see Figure 7.10). Then a direction vector to a point on the star is characterized by two angles, θ measured from the y axis, and ϕ, measured between the projection of the direction vector onto the xz plane and the x axis. In this coordinate system the direction vector is then given by

$$\hat{\imath} = -\cos\theta\,\hat{\mathbf{y}} + \sin\theta\,\cos\phi\,\hat{\mathbf{x}} + \sin\theta\,\sin\phi\,\hat{\mathbf{z}}. \tag{7.102}$$

The flux of energy from an area of the star through the disk is given by the component perpendicular to the disk of the intensity times the solid angle subtended by the stellar unit area,

$$dF_{\rm d} = I\,\hat{\imath}\cdot\hat{\mathbf{z}}d\omega = I_\circ \sin^2\theta\,\sin\phi\,d\theta\,d\phi, \tag{7.103}$$

where we take the stellar intensity $I_\circ$ to be constant. The total flux into the disk is given by the integral of $dF_{\rm d}$ over the solid angle subtended by the star,

$$F_{\rm d} = \int_0^{\pi} d\phi\,\sin\phi\int_0^{\theta_m} d\theta\,I_\circ\sin^2\theta = 2I_\circ\int_0^{\theta_m} d\theta\,\sin^2\theta. \tag{7.104}$$

The maximum value of θ occurs when the direction vector is tangent to the stellar surface, when the radial distance is R_*; thus, $\sin\theta_m = R_*/R$ and therefore

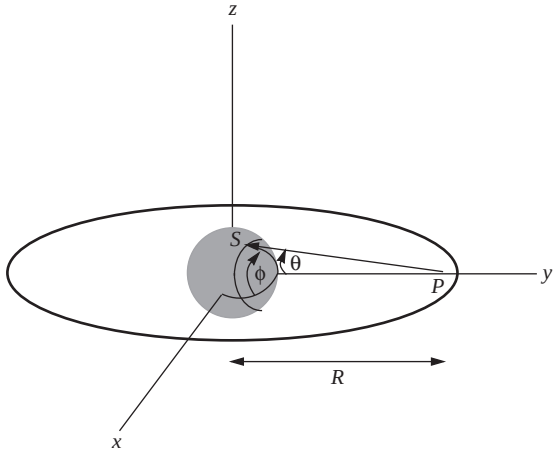

Fig. 7.10. Geometry for the calculation of the irradiation of a flat disk by the central star. The point P on the disk under consideration is along the y axis at a distance R from the star's center. The calculation is of the flux emitted along a ray from point S on the star to point P; the angle θ lies between SP and the y axis; and ϕ is the angle between this projected vector and the x axis. See text.

$$F_{\rm d} = I_\circ \left[\sin^{-1}\left(\frac{R_*}{R}\right) - \frac{R_*}{R}\left(1 - \frac{R_*^2}{R^2}\right)^{1/2} \right]. \tag{7.105}$$

In the limit that $R >> R_*$, $F_{\rm d} \propto R^{-3}$. Assuming that the disk radiates away the incoming energy in the form of blackbody emission, so that $\sigma T_{\rm d}^4 = F_{\rm d}$. As this results in a temperature distribution which asymptotically approaches $T_{\rm d} \propto R^{-3/4}$ at large radii, the optically thick, flat, irradiated disk exhibits the same wavelength dependence in its SED, $\lambda F_\lambda \propto \lambda^{-4/3}$, as the steady optically thick accretion disk (§7.3).

The total luminosity of one side of an infinite flat disk is

$$L_{\rm d} = \int_{R_*}^{\infty} 2\pi\, R\, dR\, F_{\rm d} = \frac{\pi^2 I_\circ R_*^2}{2}. \tag{7.106}$$

By assumption, the intensity $I_\circ = B = \sigma T_*^4/\pi$, so $L_{\rm d} = L_*/8$ for one side of the disk. The total emission from both sides of the disk is therefore one-quarter of the stellar luminosity. It is apparent from the above discussion that if the optically thick, steady disk has a mass accretion rate producing an accretion luminosity $\lesssim L_*/4$, it will be difficult to distinguish accretion-produced energy from irradiation-induced disk emission.

The irradiation of outer regions of a flat disk is very inefficient because the light from the central star impinges very obliquely on the disk. As shown in (Figure 7.11), the flux of stellar radiant energy entering the disk depends upon $\cos\gamma$, where γ is the angle that the impinging radiation makes with the normal to the disk surface. If we assume that the "average" radiation from the star originates at a distance $R_*/2$ from the disk plane on the stellar surface, then the radiative flux entering the flat disk at radius R is

$$F_{\rm d} \sim \frac{L_*}{4\pi R^2}\cos\gamma \sim \frac{L_*}{4\pi R^2}\frac{R_*}{2R}, \tag{7.107}$$

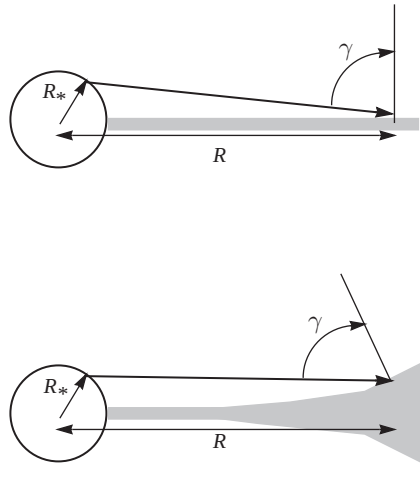

Fig. 7.11. Geometry of irradiated disks, showing how the "flaring" of the disk affects the heating (see text).

reproducing the $F_{\rm d} \propto R^3$ behavior derived for the exact solution (7.105). However, as discussed in §7.4, disk scale heights tend to increase faster than linearly with increasing R; this can lead to the effective "photosphere" for absorbing stellar radiation to curve away from the midplane (becoming "flared"), decreasing γ and thus increasing the heating of the disk. For typical parameters, T Tauri disks are likely to be highly flared at large radial distances (Kenyon & Hartmann 1987; D'Alessio *et al.* 1999).

At large R, when the disk absorbing layers are much higher above the midplane than the stellar radius, the stellar radiation is essentially radial. Thus, a wedge-shaped disk, with $H/R \sim$ constant, will asymptotically act like a flat disk; thus the entering flux at large radii is proportional to $\cos\gamma \propto dH/dR - H/R$ (Kenyon & Hartmann 1987; Ruden & Pollack 1991). That is, the curvature of the flaring disk is important in determining the irradiation flux.

In the limit that the disk has a moderate geometric thickness, one can derive an asymptotic expression for the disk temperature distribution (e.g., Cunningham 1976; Chiang and Goldreich 1997). For simplicity assume that the disk is vertically isothermal at each radius, and that the height of the surface at which the radiation enters the disk is directly proportional to the local scale height H. The last approximation is particularly good when the disk "photosphere" lies at a few scale heights above the midplane (Kenyon & Hartmann 1987; D'Alessio *et al.* 1999, 2001; §8.2). Then, assuming that all the heating is due to irradiation, energy balance requires

$$\sigma T_{\rm d}^4 \propto \frac{L_*}{4\pi R^2}\left(\frac{dH}{dR} - \frac{H}{R}\right), \tag{7.108}$$

with

$$\frac{H}{R} = \frac{c_{\rm s}}{v_\phi} \propto T_{\rm d}^{1/2} R^{1/2}. \tag{7.109}$$

If we assume that T is a power-law function of R, then the term in brackets in equation (7.108) is proportional to H/R; then

$$T_{\rm d} \propto L_*^{2/7} R^{-3/7}. \tag{7.110}$$

As discussed previously, optically thick accretion disks tend to have effective temperatures which vary with radius as $T \propto R^{-3/4}$. Radiative trapping can modify the internal disk temperature from this result, but typical YSO disk models are not very optically thick to the internal disk radiation at large radii (§8.2). Thus the relative importance of irradiation heating vs. viscous heating tends to scale roughly as $\sim R^{-3/7+3/4} \sim R^{9/28}$. T Tauri disks often extend over radial ranges of four orders of magnitude or more; thus, even if viscous heating dominates at small radii, irradiation almost always dominates in outer disk regions, as long as the disk is sufficiently opaque to the radiation from the central region. In turn, because the dominant opacity for this mechanism in YSO disks is that of (small) dust particles, strong irradiation heating requires the suspension of these particles to significant vertical heights. If the dust settles to the midplane, a process invoked in many scenarios of the onset of planetesimal formation, irradiation heating and local disk temperatures decrease (e.g., D'Alessio *et al.* 2006). Observations which constrain dust settling and growth in T Tauri disks are of interest because of their likely relevance to planet formation; we turn to these and other observational tests of our understanding of disk structure and evolution in the following chapter.

8

The disks of pre-main-sequence stars

The idea that the early Sun was surrounded by a rotating flattened nebula or disk out of which the planets formed has had a long history. However, a detailed application of the disk model to pre-main-sequence stars was not made until the seminal work of Lynden-Bell and Pringle (1974). These authors suggested that the excess emission of the low-mass, pre-main-sequence T Tauri stars could be powered by disk accretion; the extended dusty disk accounts for the excess infrared emission of T Tauri stars, while the hot gas predicted at the boundary layer between the star and disk produces the observed ultraviolet continuum emission. Lynden-Bell and Pringle further suggested that T Tauri disks could be quite massive, and might even outshine the central star in their early stages.

In retrospect, researchers in the field were not ready for these insights, partly due to the observational limitations of the time. Complicating the situation, ultraviolet and X-ray observations with the IUE and Einstein satellites in the late 1970s showed that young stars exhibit high-temperature chromospheric and coronal emission at much higher levels than observed on the Sun (e.g., Gahm *et al.* 1979; Cram *et al.* 1980; Walter & Kuhi 1981), undoubtedly as a result of solar-type magnetic activity. Thus, it was natural to assume that this excess optical and ultraviolet emission represented the extreme youthful limit of solar magnetic activity (Herbig 1970; Cram 1979; Calvet *et al.* 1983).

T Tauri stars clearly exhibit extreme levels of magnetic activity, as deduced from X-ray emission (and flaring activity) (Feigelson *et al.* 2007), the presence of large starspots (e.g., Herbst & Shevchenko 1999), and direct measurement of very large photospheric magnetic fields (Johns-Krull *et al.* 1999a; Valenti & Johns-Krull 2004; Johns-Krull 2007). However, in some cases the excess optical emission exceeds the stellar photospheric luminosity (Bertout *et al.* 1988), which is difficult to understand in the context of magnetic fields converting a portion of the stellar energy output into mechanical heating. It is now clear that the (strong) excess emission in T Tauri stars is powered by mass accretion onto the central star. Moreover, the FU Orionis objects are now understood to be systems in which the disk accretion luminosity can exceed the stellar luminosity by as much as two orders of magnitude (Chapter 9), as Lynden-Bell and Pringle suggested might occur.

The early suggestions that dust must be responsible for the excess infrared emission of T Tauri stars (Mendoza 1966; Strom *et al.* 1972; Cohen 1973a,b,c; Cohen & Schwartz 1976; Rydgren *et al.* 1976; Cohen & Kuhi 1979; Rydgren & Vrba 1981) were confirmed by far-infrared *IRAS* observations; radially extended, dusty disks were the only plausible candidates for explaining the observed infrared emission out to long wavelengths (Rucinski 1985). Disks of dust and molecular gas have now been detected by a multitude of imaging

observations, at wavelengths ranging from the ultraviolet to the cm wavelength range (§8.1). There are direct detections of rotation, roughly consistent with Keplerian motion although departures due to self-gravity would be difficult to detect at present.

Thus, the picture proposed by Lynden-Bell and Pringle appears to be generally correct. The angular momenta of collapsing protostellar clouds are large enough that stars are formed with substantial rotating disks around them; accretion powers most of the excess optical and ultraviolet emission of T Tauri stars; and infrared excesses arise from circumstellar accretion disks. However, the disk emission of most T Tauri stars is driven by the absorption of radiation from the central star; only a few of the most rapidly accreting systems have disk emission dominated by local accretion energy release (e.g., Adams & Shu 1986; Kenyon & Hartmann 1987; Chapter 9).

Despite a vast increase in the range and sensitivity of observational techniques that now can be brought to bear in the study of T Tauri disk structure, there are still major uncertainties in how material is transported within disks. While the MRI is an obvious mechanism for angular momentum transport, it is far from clear that T Tauri disks are sufficiently ionized for this mechanism to operate at all radii and vertical heights. Gravitational instabilities are likely to play an important role in the early evolution of protostellar disks, but whether they operate at the later T Tauri stage is uncertain.

The hot continuum excess emission observed at optical and ultraviolet wavelengths, though powered by accretion, probably does not arise from a boundary layer as Lynden-Bell and Pringle suggested. Instead, accretion onto stellar photospheres seems to be mediated by stellar magnetic fields (Uchida & Shibata 1984, 1985; Bertout *et al.* 1988; Camenzind 1990; Königl 1991; Shu *et al.* 1994). The stellar magnetic fields responsible for highly enhanced solar-type activity (coronal X-ray emission, flares, starspots) appear to be strong enough to hold off the accreting disk above the stellar surface, channeling the infalling material into localized regions on the star. The observed hot continuum emission then arises from the accretion energy dissipated when the rapidly moving magnetospheric gas shocks at the stellar surface (Figure 8.1).

The most direct indication of magnetospheric infall comes from analysis of asymmetries in line profiles – specifically, redshifted absorption (as in protostellar envelopes; §5.8). This infall was once thought to be the sign of protostellar collapse (Walker 1972; Wolf *et al.* 1977), but many of these objects are not heavily extincted, as would be expected for infalling dusty envelopes (Chapter 5). We now think that both redshifted absorption and most of the broad emission lines of T Tauri stars are produced in the magnetospheric accretion columns (Calvet & Hartmann 1992; Hartmann *et al.* 1994a; Muzerolle *et al.* 1998a, 2001). Detailed line profile studies indicate that most of the "classical" T Tauri stars or CTTS gain material through stellar magnetospheres (Edwards *et al.* 1994), down to and including young brown dwarfs (Muzerolle *et al.* 2003a).

Some young T Tauri stars are not accreting, and seem not to have dusty disks (at least out to radii of 1–10 AU). These "weak" emission T Tauri stars or WTTS exhibit high levels of chromospheric and coronal emission, which are also present (as indicated by X-ray and narrow line emission) in the CTTS. The differences between CTTS and WTTS allow us to determine which properties are due to disk accretion and which to magnetic activity of the underlying star. Why some stars of the same age are WTTS and others are CTTS is not clear, though the presence of a binary companion can play a role by gravitationally disrupting accretion disks.

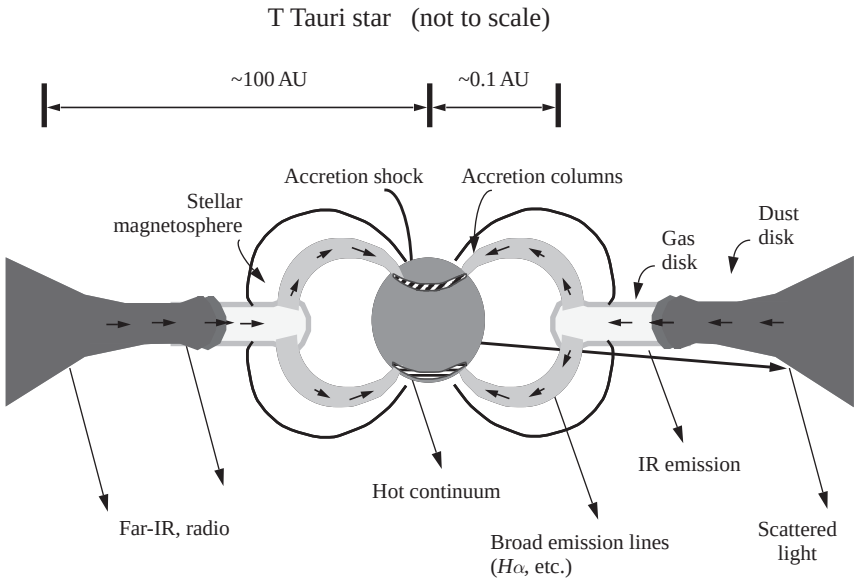

Fig. 8.1. Schematic picture of accretion in T Tauri stars. The pre-main-sequence star is surrounded by an accreting circumstellar disk which emits at infrared, sub-mm, and mm wavelengths. The inner disk is disrupted by stellar magnetic fields, which cause accreting material to be diverted out of the disk and fall rapidly onto the star. This magnetospheric material emits broad emission lines as it falls along the accretion columns, and produces a hot continuum when it crashes into the stellar surface at an accretion shock. The location of the magnetospheric truncation radius is probably inside the radius at which dust is sublimated by radiation from the central star and accretion shock.

Although disk masses are clearly a vital constraint on theories of star and planet formation, they unfortunately remain uncertain. Most mass estimates are based on mm- and sub-mm wavelength observations of dust emission (e.g., Beckwith *et al.* 1990; Andrews & Williams 2005; §8.3). The conversion of sub-mm and mm-wave fluxes to masses is subject to substantial uncertainties in dust opacities, since there is evidence that dust particles in T Tauri disks may be evolving in their sizes and other properties from their interstellar values. Current guesses of opacities indicate disk masses that in many cases are at least as large the minimum disk mass $\sim 0.01\, M_\odot$ needed to account for the heavy elements in the Solar System (assuming an initial solar composition).

Much of the above picture appears to be applicable to intermediate-mass young stars ($M \sim 2 - 4\, M_\odot$), including the possibility of magnetospheric accretion (Muzerolle *et al.* 2004). Indeed, a substantial amount of study has been dedicated to the HAe/Be stars, largely because they are so bright. The frequency of detectable disks among A stars appears to be considerably lower than that of the lower-mass T Tauri stars of the same age, suggesting more rapid disk evolution among the intermediate-mass stars (Hernández *et al.* 2006). The application of disk accretion models to high-mass stars remains problematic, due to the difficulty of observing more distant, confused systems, and the increased importance of photoevaporation/photoionization/radiation pressure (§4.7).

It has been clear since the pioneering studies by Strom *et al.* (1989) and Skrutskie *et al.* (1990) that dusty disks – at least the regions close to the central T Tauri star – tend to disappear (or become optically thin) on timescales of a few to 10 Myr. We now have more detailed studies, thanks mainly to observations with the *Spitzer Space Telescope* and *ISO*, which indicate more subtle signs of dust growth and settling such as expected for the first stages of planetesimal formation (Chapter 12). In this regard the recognition of the "transitional disk" systems (e.g., Calvet *et al.* 2002; D'Alessio *et al.* 2005), in which relatively evacuated inner holes of otherwise substantial dusty disks may be an indication of recent disk clearing by giant planet formation.

In all, the rapid advancement in studies of pre-main-sequence stars suggests that we are beginning to realize the hope expressed by Lynden-Bell and Pringle (1974): "If this interpretation of T Tauri stars is correct, their study will provide new and important evidence on the conditions under which the planets in the solar system were formed."

8.1 Disk imaging

Extensive direct imaging of disks has now been performed at a variety of wavelengths ranging from the optical to the cm range. High-resolution optical imaging possible with *HST* has produced remarkable pictures of disks around young stars, some seen as shadows against the bright Orion Nebula (Figure 1.6), others in light from the central T Tauri star scattered by the outer disk surfaces (Figure 1.7). These images have now been complemented and extended by near-infrared adaptive optics and coronagraphic imaging using large ground-based telescopes (e.g., Close *et al.* 1997). In some cases, these images are providing hints of complex non-axisymmetric structure (Figure 8.2), which may indicate effects of self-gravity or perturbations by companions (compare with Figure 6.4).

Interferometric observations at mm wavelengths have also resolved many nearby disk systems, with direct detections of Keplerian rotation (for example, Koerner *et al.* 1993; Simon

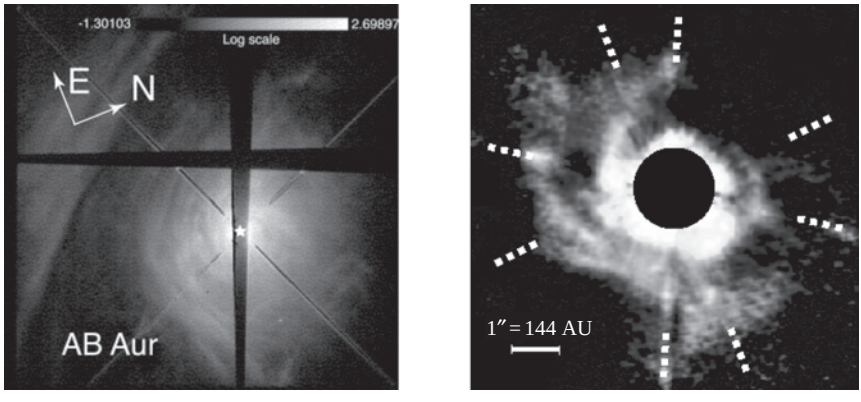

Fig. 8.2. Scattered light images of the Herbig Ae star AB Aur: left, optical image taken in coronagraphic mode with the STIS instrument on board HST (Grady *et al.* 1999, 2005), in a field of 25 arcsec square; right, near-infrared (H band) adaptive optics/coronagraphic image of AB Aur taken with the Subaru telescope (Fukagawa *et al.* 2004), spanning 8 arcsec square (about 110 AU). The disk is very extended and has suggestions of spiral structure (compare with Figure 7.9).

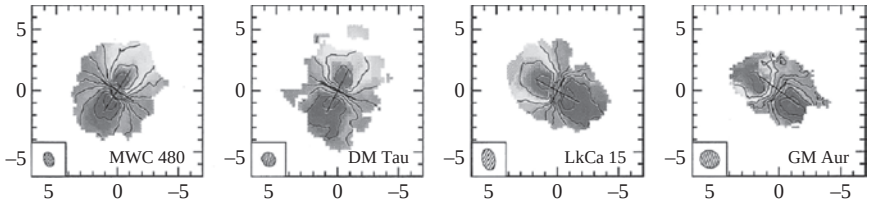

Fig. 8.3. Disk images from observations of ^{12}CO 2-1 (1.3 mm) emission around the HAe/Be star MWC 480 and the T Tauri stars DM Tau, LkCa 15, and GM Aur (see also Figure 8.20). The image dimensions are given in arcsec (1 arcsec ∼140 AU). The contours denote differing curves of constant radial velocity, at spacings of 0.3 km s^{-1} for all but DM Tau, with a spacing of 0.2 km s^{-1}. From Simon *et al.* (2000).

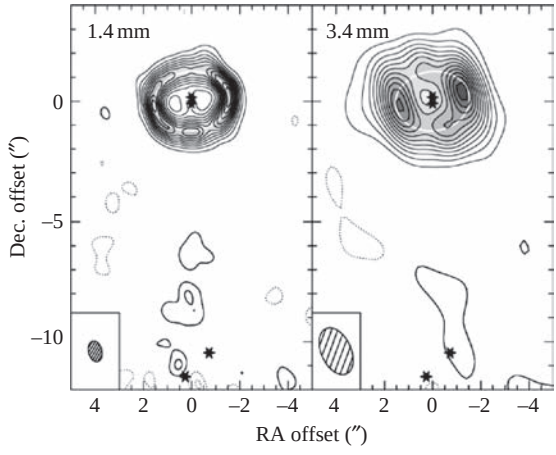

Fig. 8.4. Continuum images at mm wavelengths of the GG Tau multiple system. Torques from the central binary evacuate material, producing a circumbinary disk or ring. The central stars have their own disks, as indicated by near-infrared excesses and accretion (e.g., White *et al.* 1999). GG Tau is a quadruple system; the positions of the outer pair of stars are shown at the bottom of the maps. From Guilloteau *et al.* (1999).

et al. 2000; Figure 8.3). In some cases of relatively large disks, current resolution is sufficient to use the assumed Keplerian rotation of the disk to estimate the central star's mass, helping to constrain stellar evolutionary models (Simon *et al.* 2000). Radio-wavelength interferometry and ground-based adaptive optics observations have also helped clarify the disk structure in multiple star systems, in some cases clearly resolving the circumbinary disk or ring driven by the gravitational torques of the central binary (Figure 8.4).

There are now constraints on inner disk structure from long-baseline near-infrared interferometry of young objects (e.g., Akeson *et al.* 2000, 2005a,b; Monnier & Millan-Gabet 2002; Eisner *et al.* 2003, 2004; Malbet *et al.* 2005; Monnier *et al.* 2005; Millan-Gabet *et al.* 2006). The physical structure of this region remains unclear because most current near-IR interferometers do not include enough telescopes to make well-sampled images. The interferometric results probe emission from regions at or inside the dust destruction radius (where we expect the dust to evaporate due to absorption of radiation from the central star;

e.g., Natta *et al.* 2001; §8.7; Figure 8.1). Unfortunately, it is very difficult to predict what gaseous emission should be detected, as determining the temperature of this optically-thin region presents challenges (see, e.g., Muzerolle *et al.* 2004). In addition, the physics of the region where the magnetosphere truncates the disk is very complex (§10.10).

8.2 Disk SEDs

The *IRAS* satellite made it possible to quantitatively analyze the infrared excess emission of T Tauri stars in terms of dusty disk properties (Adams *et al.* 1987; Kenyon & Hartmann 1987; Calvet *et al.* 1991, 1992; D'Alessio *et al.* 1999, 2001; Chiang & Goldreich 1997). The general form of the typical SED, as shown in Figure 8.5, is a modest decline in emission between about 2 μm and ∼100 μm, with a steep fall-off of emission at longer wavelengths. This behavior strongly suggests that these disks are typically optically thick at infrared wavelengths, so that the SED is determined by the temperature distribution as a function of radius (§7.3), while the steep decrease with increasing wavelength in the mm-wave emission indicates optically thin emission, reflecting the rapidly decreasing dust opacity as well as the Rayleigh–Jeans tail of the dust temperature distribution.

As shown in Figure 8.5, the infrared SEDs generally have a much flatter spectral index than the $\lambda L_\lambda \propto \lambda^{-4/3}$ expected for the steady optically thick accretion disk (§7.3). Flared irradiated disks (Kenyon & Hartmann 1987; §7.9) are required to explain the SED slopes, as flared disks have temperature distributions falling off more slowly with increasing radius (§7.9; equation 7.110). In general local viscous energy release at large radii, far out in the

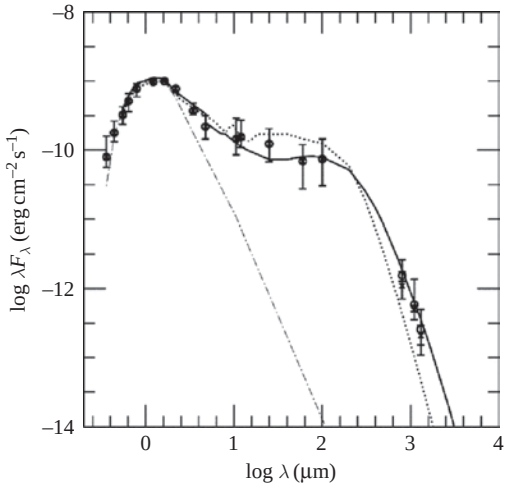

Fig. 8.5. Median SED of K7-M2 T Tauri stars in Taurus (circles), with quartile dispersions (errorbars). The SED of star of similar spectral type without an accretion disk (i.e., a pure photospheric spectrum) is indicated by the dot-dashed curve. The flattening of the infrared emission at long wavelengths provides evidence for models of irradiated flared disks. The dotted curve is the predicted SED for a model with ISM dust, having a maximum size ∼0.3 μm; the solid curve is for a number distribution of dust of radius a proportional to $N(a) \propto a^{-3.5}$ with a maximum size of 1 mm. From D'Alessio *et al.* (2001).

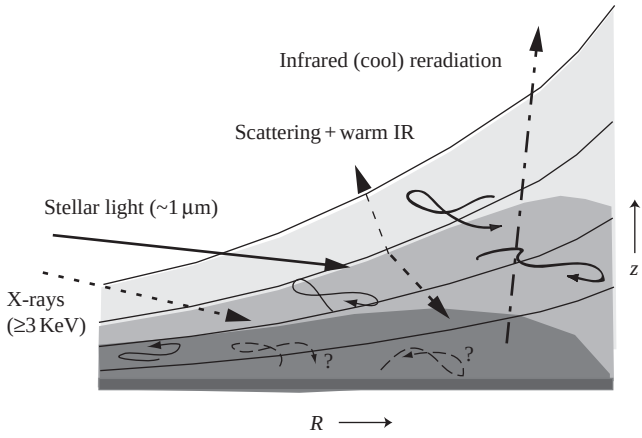

Fig. 8.6. Schematic depiction of T Tauri dusty disk structure. Solid curves are disk scale heights, while increasing density is indicated crudely by darker shaded regions; there may be a dense layer at the midplane with large dust particles. Arrows indicate processes determining thermal energy balance and ionization (see text).
Schematic eddies indicate where turbulence (MRI-driven) may be present; whether the MRI is present in dense central layers (dotted eddies) not ionized by (hard) X-rays is unknown.

gravitational potential well, cannot compete with the heating provided by absorbing radiation from the star and any accretion luminosity arising at small radii. However, for disk flaring to explain the observations in detail, small dust grains must be suspended to at least a few scale heights above the disk midplane, which has implications for understanding grain growth and settling (§12.6).

Figure 8.6 provides a schematic overview of the expected structure of a typical T Tauri disk and the processes responsible for heating and ionization. The density scale heights (solid curves) increase upward in z faster than the cylindrical radius R; this is the flared disk structure. The contours of constant density (gray scale) tend to follow the scale height structure, especially at small radii and high z, but eventually fall toward the midplane because of the general outward decrease of surface density. Disk heating is generally dominated by the dust absorption of light from the central source, which for typical T Tauri stars peaks at wavelengths of order 1 μm. This stellar radiation (solid arrow) is absorbed at a disk photosphere where the (tangential) optical depth is of order unity at the wavelengths of irradiation. The irradiation energy is partly scattered outward (thin upward dashed arrow) and inward (thick downward dashed arrow), and partly absorbed and reradiated at longer wavelengths outward and inward. The inward diffuse disk radiation is absorbed in lower, somewhat cooler layers, which reradiate the energy at even longer wavelengths at which the upper disk is transparent. In the higher-density regions of the disk, collisions with dust heats the gas to similar temperatures, though in upper layers the gas–grain collision rate can be low enough that dust and gas temperatures differ, with higher gas temperatures driven by X-ray and other heating (e.g., Glassgold *et al.* 2004).

A typical temperature distribution in a numerical disk model is illustrated in Figure 8.7 (a simplified version is given by Chiang & Goldreich 1997). In the upper layers of the disk, the dust "sees" the unattenuated stellar radiation field. The dust temperature is given by radiative equilibrium,

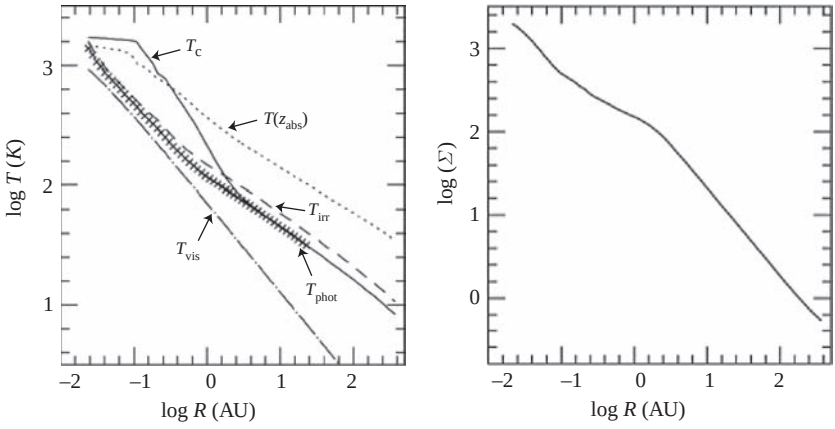

Fig. 8.7. Temperature structure (left) and surface density (right) of a typical (optically thick) T Tauri disk model accreting at $\sim 10^{-8}\, M_\odot\, \mathrm{yr}^{-1}$ with $\alpha = 0.01$ (see text). Note that the surface density at 1 AU is about an order of magnitude less than the standard "minimum mass solar nebula" model (Chapter 12). Modified from D'Alessio *et al.* (1999).

$$\int_0^\infty d\nu\, \kappa_\nu (J_\nu - B_\nu) = 0\,, \tag{8.1}$$

where J_ν is the dilute radiative intensity from the star (plus any accretion shock), B_ν is the Planck function at the dust temperature, and κ is the absorptive opacity. As the dust is typically much colder than the star, and the opacity is generally thought to be a decreasing function of wavelength, the dust in this optically thin region will tend to be hotter than would result from a gray or blackbody approximation (see Appendix 3). This means that the upper disk layers of an irradiated disk will be hotter than the deeper layers. As shown in Figure 8.7, the temperature at the layer where the stellar photons are absorbed, $T(z_{\rm abs})$, is higher than the effective temperature of the disk emission resulting from the irradiation flux $T_{\rm irr}$. The latter is essentially the same as the disk "photospheric" temperature $T_{\rm phot}$ that would be derived by simply treating the irradiation in the blackbody approximation, using the surface of the local disk photosphere at the typical wavelength of disk reradiation (see D'Alessio *et al.* 1999 for details).

The viscous temperature $T_{\rm vis}$ represents the effective temperature the disk would have if accretion were the only energy source (equation 7.55). As shown in Figure 8.7 for a typical T Tauri accretion rate, the viscous heating is relatively unimportant except in the innermost regions of the disk, where it drives the central disk temperature T_c above the upper layer temperature. The central temperature rises because the radiation produced by the internal viscous heating is trapped by the large optical depth (higher temperature radiation "sees" higher dust opacities, so that this effect is most important at smaller radii). The central temperature tends to exhibit a plateau or maximum at values for which dust sublimates; this creates a kind of thermostatic effect, as higher temperatures reduce the dust opacity needed to trap the radiation (D'Alessio *et al.* 1999).

Thus, disks whose heating is dominated by irradiation should have surface layers that are warmer than the deeper layers, except possibly in the innermost regions. The vertical

temperature inversion driven by irradiation can be detected by observing features of larger opacity, which will be formed at higher z and thus appear in emission (Malbet & Bertout 1991; Calvet *et al.* 1991). In particular, small silicate grains exhibit a strong increase in opacity at $\lambda \sim 10\,\mu$m (Figure 4.10), and therefore irradiated disks should exhibit silicate emission features (Calvet *et al.* 1992). This prediction has now been abundantly confirmed by many infrared spectral studies, particularly with the high-sensitivity data available from *ISO* and the *Spitzer Space Telescope* (Figure 8.8).

Irradiated disk models of the type shown in Figure 8.5 can reproduce typical T Tauri disk SEDs provided that there is (small) dust suspended to 3–4 scale heights above the disk midplane (Kenyon & Hartmann 1987). As dust is expected to eventually settle to the midplane, especially from such rarified heights, there may need to be some turbulence to help suspend small dust for T Tauri disk lifetimes.

There is increasing evidence that the dust in T Tauri disks is neither interstellar in its size distribution nor uniformly mixed in the z direction. In Figure 8.5, the dotted curve is a model with complete vertical mixing of dust and gas assuming a typical interstellar dust opacity (Figure 4.10). As can be seen, while the infrared SED is reasonably well-fit, the mm-wave fluxes are vastly underpredicted. Observations at long wavelengths increasingly suggest that there must be dust growth to sizes of $\sim$mm or more; otherwise, unreasonable amounts of mass would be required to explain the magnitude and spectral slope of the long-wavelength emission (Miyake & Nakagawa 1993; D'Alessio *et al.* 2001; Chiang *et al.* 2001; Wilner *et al.* 2005; Rodmann *et al.* 2006; see §8.3). On the other hand, a similar power-law distribution but growth to a maximum of mm-cm sizes results in much better matches to the long-wavelength emission (solid curve), but the silicate emission feature disappears because of the domination of the opacity by particles larger than $10\,\mu$m, contrary to what is observed (e.g., Figure 8.8). Disk models with the best fits to detailed SED observations involve a stratified distribution of dust, with the largest dust particles near the midplane and a lower-mass distribution of small particles near the disk upper and lower surfaces (D'Alessio *et al.* 2006). Such models are qualitatively reasonable, in that the large particles should settle the fastest (§12.6); the suspension of such small particles may be aided by turbulence generated by the MRI (§7.7).

It also appears that models require somewhat less small dust per gas mass in the upper layers of the disk than are typical of the interstellar medium. The clearest evidence for this comes from observations of edge-on disks, which directly show the surfaces which scatter starlight (Figure 8.9). D'Alessio *et al.* (2001) showed that well-mixed models of ISM dust yielded dark dust lanes that were too thick (i.e., the bright scattering surfaces were too far apart); models with some reduction in the amount of small dust, as would be expected as part of the settling process, provide a better comparison to observations (Figure 8.9; also D'Alessio *et al.* 2006).

Another indication of dust settling comes from the overall spectral slopes of disk SEDs. It is evident that if dust settled close to the midplane, the disk SED would have a spectral slope approaching that of the geometrically flat disk, $s \sim -4/3$ (see §§7.4, 7.9). While most objects have much smaller slopes, it is evident from Figure 8.8 that there are a range of properties among T Tauri disks, with some systems exhibiting relatively steep SEDs, presumably implying additional settling of dust.

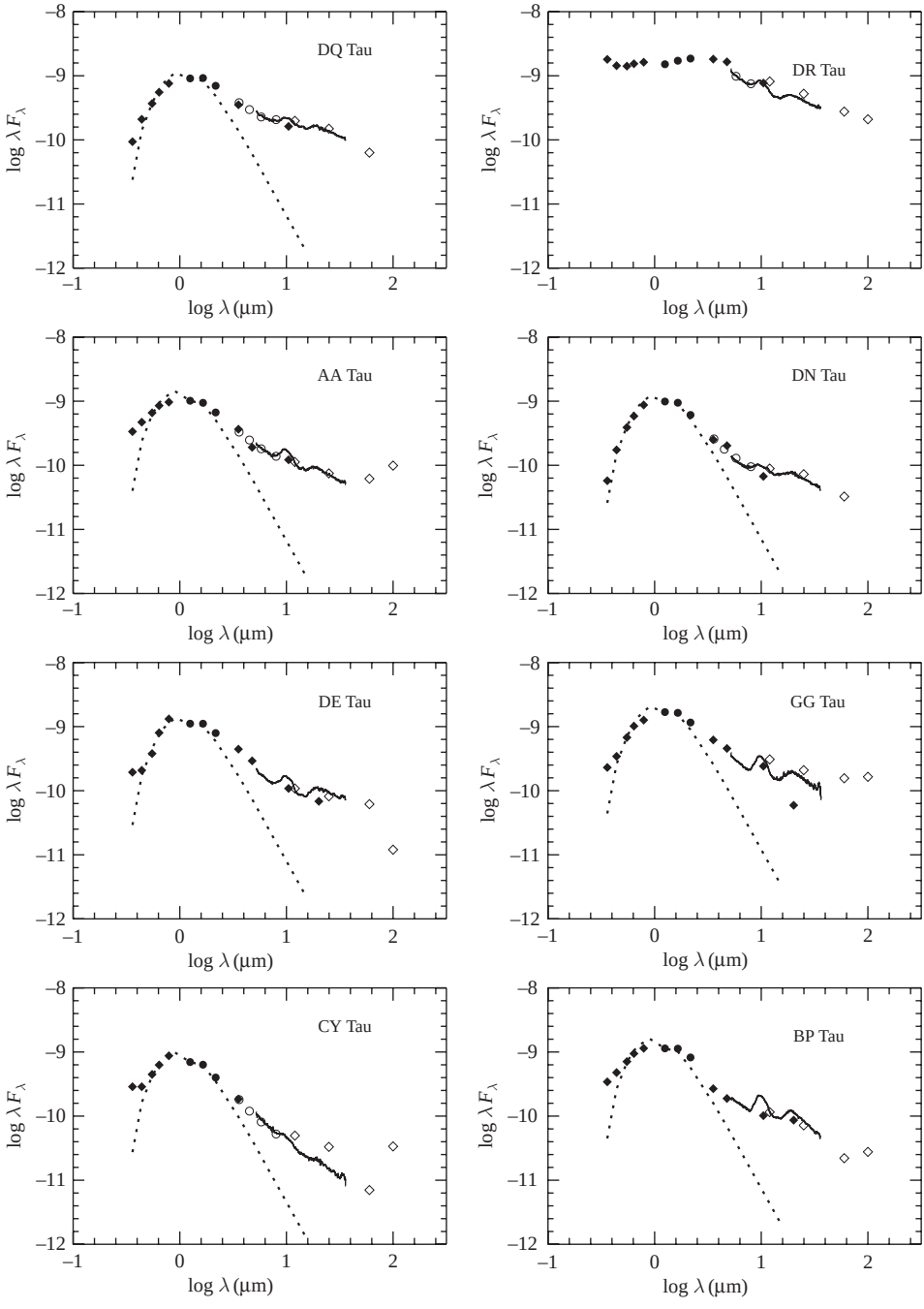

Fig. 8.8. SEDs of T Tauri stars in the Taurus molecular cloud. The vertical axes denote observed fluxes in erg cm^{-2} s^{-1}. The dotted curve denotes the SED for a typical WTTS, with no accretion disk. Circles are photometry from optical studies, the IRAC and MIPS instruments on *Spitzer*, and IRAS at long wavelengths, with spectra from the *Spitzer* IRS spectrograph (solid curve). The long-wavelength emission is much flatter than would be expected from disks heated purely by accretion. In addition, the 10 μm silicate feature is usually seen in emission, as predicted by models where irradiation from the central source dominates the disk heating. (DR Tau is an example of a star where the accretion luminosity dominates the stellar luminosity, making the nature of the central star uncertain.) Modified from Furlan *et al.* (2006).

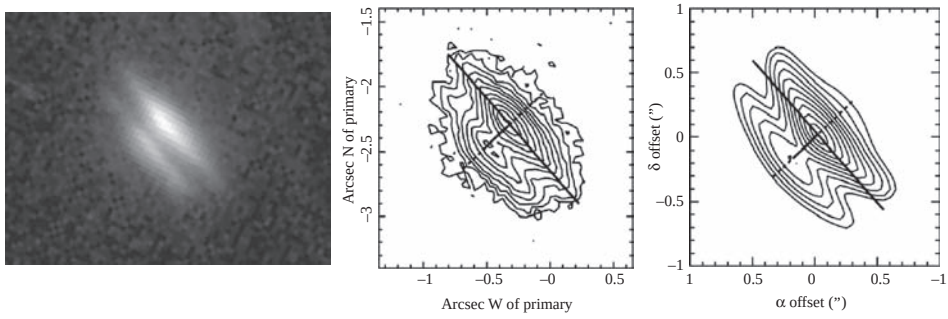

Fig. 8.9. Left, center: HST image of HK Tau c, in gray scale and in contours, from Stapelfeldt *et al.* (1998a); right, model scattering image from D'Alessio *et al.* (2001), with significant deaprtures from interstellar medium dust (see text).

8.3 Long-wavelength emission and disk masses

At very long wavelengths, the excess emission of T Tauri disks declines steeply (Figure 8.5). An optically thick disk with a sharp outer edge will have a spectrum with the Rayleigh–Jeans form $\lambda F_\lambda \propto \lambda^{-3}$ (§7.4). However, the observed spectral slopes are much steeper than this, due to the disk becoming *optically thin*; the spectrum approaches $\lambda F_\lambda \rightarrow \lambda^{-3+\beta}$, where β is the slope of the decreasing dust opacity as a function of wavelength. Because the optically thin emission is proportional to the dust opacity, it is possible to estimate the total dust mass (Beckwith *et al.* 1990). Here we discuss the basic ideas behind these estimates and their limitations.

Suppose for simplicity that the disk is geometrically thin and isothermal in the vertical direction (perpendicular to the disk plane), and that the emission is purely blackbody at the local temperature (which is a function only of cylindrical radius R). Then the apparent luminosity is

$$\nu \hat{L}_\nu = 4\pi d^2 \nu F_\nu = 4\pi\mu \int_{R_i}^{R_d} \nu B_\nu \left[1 - \exp\left(-\frac{\tau_\nu}{\mu}\right)\right] 2\pi R dR\,, \tag{8.2}$$

where F_ν is the flux observed at Earth (corrected for extinction), B_ν is the Planck function, $\mu = \cos i$, and i is the inclination angle of the disk to the line of sight, and τ_ν is the vertical optical depth at cylindrical radius R at frequency ν. The outer and inner radii of the disk are R_d and R_i, respectively. If the optical depth $\tau_\nu >> 1$, then the emission depends solely on the Planck function and thus on the temperature distribution as a function of radius, and is independent of the disk mass, as discussed in the previous chapter. In contrast, when $\tau_\nu << 1$, the emission depends upon the disk surface density distribution,

$$\nu \hat{L}_\nu = 4\pi \int_{R_i}^{R_d} \nu B_\nu k_\nu \Sigma(R)\, 2\pi R dR\,, \tag{8.3}$$

where we have written the optical depth in terms of the opacity k_ν per unit mass,

$$\tau_\nu = k_\nu \Sigma\,. \tag{8.4}$$

If the observed emission occurs at wavelengths where the disk is optically thin, and if the disk temperature as a function of radius is known, measurements of the long-wavelength flux

allow one to estimate the disk mass $M_{\rm d} \propto \Sigma R^2$, with the constant of proportionality depending upon the dependence of the surface density on radius. To illustrate this more explicitly, we make the usual simplifying assumptions that the surface density and temperature can be represented by power laws:

$$T = T_\circ \left(\frac{R}{R_\circ}\right)^{-q} , \tag{8.5}$$

$$\Sigma = \Sigma_\circ \left(\frac{R}{R_\circ}\right)^{-p} . \tag{8.6}$$

To simplify the analysis further we take the long-wavelength limit where $h\nu << kT$, so that $B_\nu = 2\nu^2 kT/c^2$, and assume that the inner radius $R_{\rm i} << R_{\rm d}$. With these assumptions the apparent luminosity becomes (e.g., Beckwith *et al.* 1990)

$$\nu\hat{L}_\nu = \frac{16\pi^2 k}{c^2}\nu^3 k_\nu \Sigma_\circ T_\circ R_\circ^2 \frac{(R_{\rm d}/R_\circ)^{2-p-q}}{2-p-q} . \tag{8.7}$$

The disk mass is

$$M_{\rm d} = \int_{R_{\rm i}}^{R_{\rm d}} 2\pi\Sigma R dR = 2\pi\Sigma_\circ R_\circ^2 \frac{\left(\frac{R_{\rm d}}{R_\circ}\right)^{2-p}}{(2-p)} , \tag{8.8}$$

and therefore

$$\nu\hat{L}_\nu = \frac{8\pi k\nu^3 k_\nu}{c^2} M_{\rm d}\, T_\circ \left(\frac{R_{\rm d}}{R_\circ}\right)^{-q} \frac{2-p}{2-p-q} = \frac{8\pi k\nu^3 k_\nu}{c^2} M_{\rm d}\, T(R_{\rm d}) \frac{2-p}{2-p-q} . \tag{8.9}$$

If the dust opacity k_ν and the outer disk temperature $T(R_{\rm d})$ (or an equivalent scaling temperature $T_\circ$) are known, and if p and q can be determined in some fashion, then disk dust masses can be determined from observed long-wavelength fluxes.

The initial attempts to estimate disk masses in this way were those of Beckwith *et al.* (1990, hereafter BSCG) and Osterloh and Beckwith (1995) from continuum observations at 1.3 mm. The disk temperature distribution can be inferred from the spectral index in the wavelength regions where the disk is optically thick using equation (7.57), simplifying to the case where the disk is vertically isothermal. Then we have

$$\nu\hat{L}_\nu = \frac{16\pi^2 h R_\circ^2}{qc^2} \left(\frac{kT_\circ}{h}\right)^{2/q} \nu^{4-2/q} \int_{x_{\rm in}}^{x_{\rm out}} \frac{x^{1/q-1}\, dx}{(e^x - 1)} . \tag{8.10}$$

In the limit $q = 3/4$ for the steady accretion disk or the geometrically thin and flat irradiated disk, $\nu\hat{L}_\nu \propto \nu^{4/3}$, while for a highly flared disk with $q \sim 1/2$, $\nu\hat{L}_\nu \sim$ constant.

BSCG and Osterloh and Beckwith derived estimated values of q using fits to SEDs, assuming vertical isothermality. Although, as discussed in the previous section, the infrared spectrum is not generally representable by a single power law, these investigators concentrated on fitting the longest-wavelength optically thick emission to fix the outer disk temperature; this is a reasonable approach since most of the disk mass may reside at large radii, and it minimizes parameters.

BSCG and Osterloh and Beckwith assumed $p = 3/2$ for most objects, attributing this to the general result for α disks; but as described in Chapter 7, for steady, constant-α disks, $\Sigma \propto R^{-1}$ for typical values $q \sim 0.5$ (D'Alessio *et al.* 1999). A more recent study using

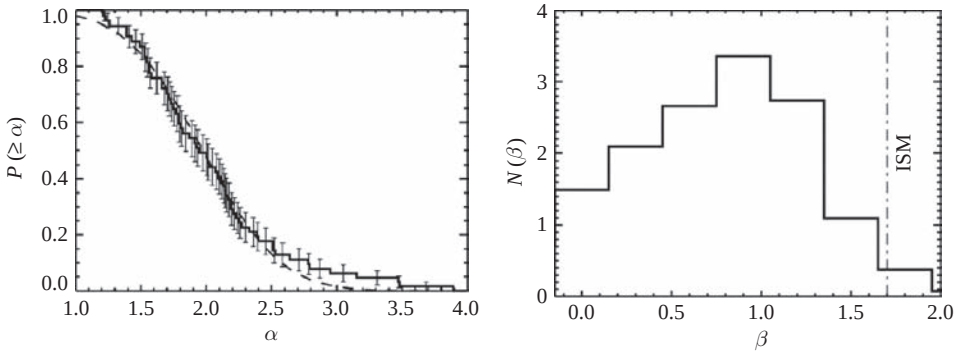

Fig. 8.10. Left: Cumulative distribution of dust continuum spectral indices ($F_\nu \propto \nu^\alpha$) between ~850 and 1330 μm in Taurus. Right: distribution of estimated values of the opacity spectral index β, derived from models as described in the text. From Andrews and Williams (2005, 2007).

(slightly) spatially resolved sub-mm emission suggests a value closer to $p \approx 0.5$, although this is subject to large uncertainties, including the assumption that the dust properties do not vary with radius (Andrews & Williams 2007).

The biggest problem with the analysis of mm–submm emission arises from the uncertainty in the dust opacity. BSCG introduced the frequently used estimate

$$k_\nu = 0.1 \left(\frac{\nu}{10^{12}\, Hz}\right)^\beta \ \mathrm{g\,cm^{-2}}\,, \tag{8.11}$$

with $\beta = 1$. This parameterization matches the form estimated by Hildebrand (1983) at wavelengths $\lambda \lesssim 250\,\mu$m, and is roughly a geometric mean of suggested values at 1 mm (see also Beckwith & Sargent (1991); André *et al.* (1993); Mannings & Emerson (1994)). Figure 8.10 shows a recent analysis of mm-wave emission from disk systems in Taurus. The observed spectral indices (left panel) clearly indicate less steep slopes than would be expected from small dust. Disk SED fitting as described above is needed to make an estimate of the correction needed for the optically thick inner disk regions; the resulting SEDs indicate that the dust opacity spectral index has a median value $\beta \sim 1$, in agreement with equation (8.11). The wide range of estimated values probably indicates some combination of real variations with inadequacies of the simple model analysis.

Using these methods and opacity, BSCG and Osterloh and Beckwith (1995; with some adjustment, see Hartmann *et al.* 1998) found typical disk masses (assuming a gas to dust mass ratio of 100) of order 0.01 $M_\odot$. This is roughly the "minimum mass solar nebula" (MMSN), i.e., the mass needed to account for the present solar system reconstituted to solar composition. These results strongly indicated that many T Tauri disk masses are sufficient to produce giant planet systems. A more recent study by Andrews and Williams (2005) based on sub-mm observations yields a similar result (Figure 8.11). Suggestively, the Andrews and Williams analysis suggests somewhat larger disk masses for Class I objects than Class II systems, as might be expected if the former are in an earlier stage of evolution, with material still being added to the disks from infalling envelopes.

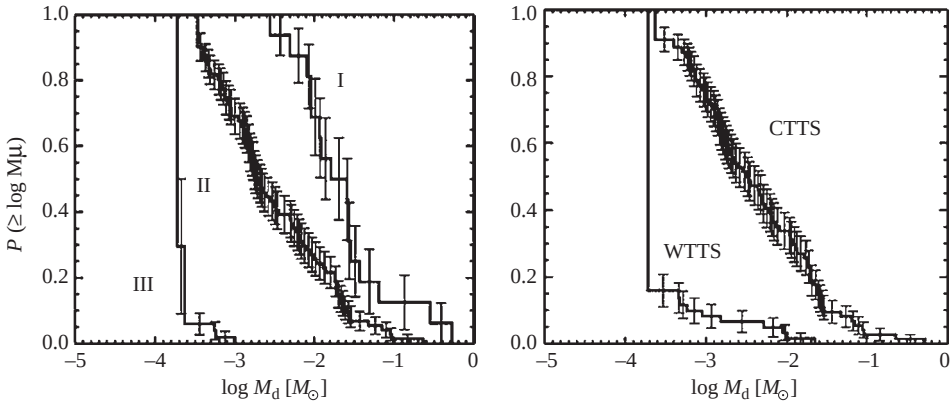

Fig. 8.11. Cumulative distributions of disk masses estimated from 850 μm emission of Taurus objects. The left panel shows the mass distributions segregated by SED class, while the right panel isolates CTTS and WTTS (essentially, accreting vs. non-accreting systems). From Andrews and Williams (2005).

Unfortunately, the dust opacities needed to estimate disk masses from long-wavelength emission are not well constrained, even by the value of β. This is demonstrated in Figure 8.12, where the properties of power-law distributions of grains of typical expected composition are shown. The middle panel shows that distributions with growth up to sizes $\sim$100 μm exhibit large values of β, clearly inconsistent with observations, and that growth up to a maximum radius $a_{\rm max}\sim$1 mm results in the median estimated $\beta \sim 1$. However, grain distributions with infinitely large $a_{\rm max}$ *also* result in $\beta \sim 1$ if the power-law exponent $pg \sim 3.5$, typical of the ISM. Values of $pg = 2.5$ yield much lower values of β for sizes above a cm, but these cannot be ruled out in all cases given the wide range of observational estimates (Figure 8.10).

The upper panel of Figure 8.12 shows that, for the assumed dust properties, the maximum mm-wave dust opacity is roughly the "standard" value of the mm-wave opacity (dashed line). This suggests that the opacity given by equation (8.11) generally *overestimates* the true opacity and thus its use in analyzing sub-mm and mm-wave emission systematically *underestimates* disk masses. Grain growth to mm sizes seems to be indicated; but the dust could grow to much larger sizes and still produce appropriate values of β, provided that the dust grains have an appropriate size distribution. Very small and very large dust grains or rocks contribute little to the mm-wave opacity; thus, the mm-wave value of β will depend upon the distribution of dust sizes through $\sim$100 μm to $\sim$ cm. (Note that the approximation of a single power-law distribution of sizes of solids is for purposes of illustration, rather than necessarily a likely outcome of dust processing in disks.)

The precise values of dust opacity depend upon composition as well, which also contributes some uncertainty (e.g., Henning & Stognienko 1996), and real (small) grains are not likely to be spherical, but complexly shaped or "fractal" instead. Nevertheless, the essential point remains: unless a significant fraction of the mass is in $\sim$mm-sized grains, use of the standard opacity will underestimate the mass present. Moreover, there is much more room in parameter space to underestimate than overestimate the opacity; in principle, one could put large amounts of mass into basketballs or planetesimals which would essentially be undetectable.

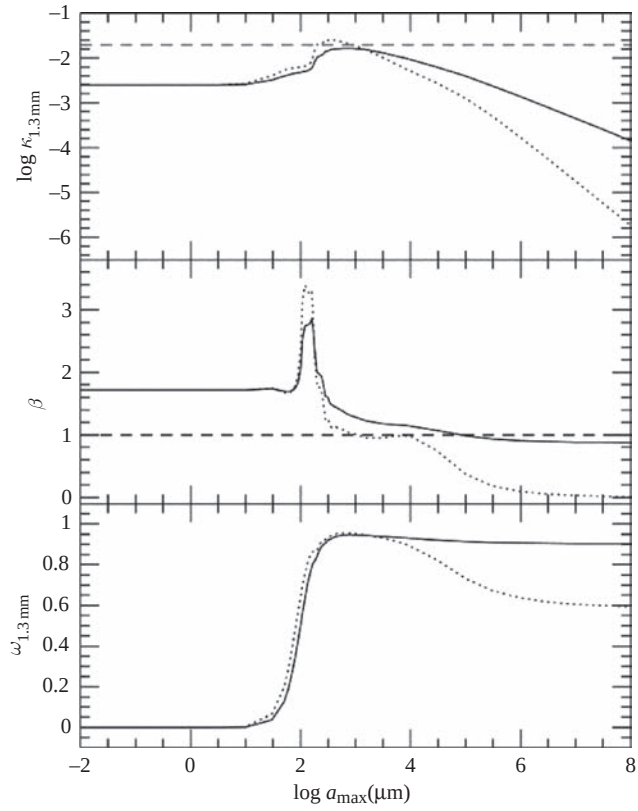

Fig. 8.12. Optical properties for spherical dust grains of a "standard ISM" composition, adopting a power-law distribution of radii $N(a) \propto a^{-pg}$, with $pg = 3.5$ (solid curves) and $pg = 2.5$ (dotted curves), with a maximum grain radius a_{max}. The upper panel shows the mass absorption coefficient at $\lambda = 1.3$ mm as a function of a_{max}; the horizontal dashed line represents the frequently adopted opacity at 1.3 mm from BSCG (equation 8.11). The middle panel shows the value of β calculated between 0.769 and 1.3 mm for the same cases as the upper panel. The horizontal dashed line denotes $\beta = 1$. The bottom panel shows the variation of the albedo at 1.3 mm. From D'Alessio *et al.* (2001).

Finally, one must consider the likely physical situation. Long-wavelength observations are currently most sensitive to emission in the outer disk, partly because most of the mass is likely to reside at large radii (unless there are massive dead zones; §7.6) and partly because the inner regions are probably optically thick. If grain growth has proceeded to mm sizes at radii $\gtrsim$100 AU, it is likely that it has proceeded to even larger sizes at smaller radii, where higher densities lead to faster evolution (§12.5). In general, one would expect growth to differing maximum sizes at differing radii at the same epoch, in which case the mm-wave emission is preferentially sampling regions of the disk with the appropriate maximum dust size. The situation is made even more complex by the probable need to consider dust production by collisions as well as growth by coagulation. At present, it seems safest to regard the present measurements of disk masses as order-of-magnitude values which are probably somewhat underestimated.

8.4 Disk/magnetosphere accretion

As discussed in the previous section, the disks of most T Tauri stars are heated mainly by radiation from the central regions; energy release by accretion (§7.3) is not generally large enough to use the disk SED to estimate accretion rates, or even determine whether the disk is accreting. The clearest signatures of accretion generally come from ultraviolet continuum and line emission arising from gas at temperatures $T \gtrsim 8000$ K.

Figure 8.13 shows Hα (left panel) and optical continuum (right panel) emission as a function of near infrared excesses for a sample of Taurus stars. The WTTS, with photospheric K–L colors, exhibit chromospheric Hα emission; CTTS, with excesses at 3.5 μm (L) indicating the presence of warm dust in the inner disk, generally exhibit much larger Hα equivalent widths. Similarly, solar-type magnetic activity in these stars does not produce continuum excesses; objects with significant continuum emission, or "veiling", have K–L excesses. This correlation demonstrates that disks are connected with optical excess emission; mass accretion is the plausible energy source.

The optical SEDs of some typical T Tauri stars are shown in more detail in Figure 8.14 (compare with Figure 8.8). Gaseous emission is evident from the strong emission in the hydrogen Balmer series and other lines, along with a continuum that is at least partly bound-free hydrogen emission, as indicated by the Balmer jump at $\sim$0.365 μm.

Figure 8.15 shows high-resolution Hα profiles for a typical set of T Tauri stars. The WTTS DI Tau exhibits a typical chromospheric profile, relatively narrow and with a central reversal. The profiles of the other stars show that not only does the equivalent width increase with the presence of a disk, but the line velocity width also increases. The profiles of CTTS show complex behavior: in some cases there is blueshifted absorption, direct evidence for mass loss; while in other cases there are asymmetries in the sense of more blue than red emission

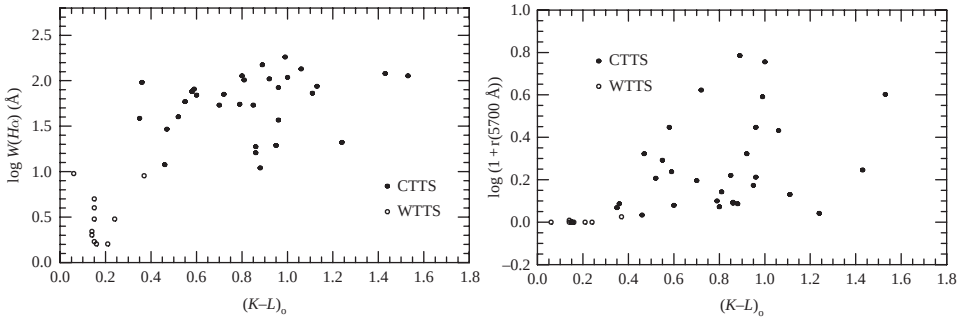

Fig. 8.13. Indicators of hot gas vs. disk emission in late K-early M T Tauri stars. Excess disk emission is identified when the near-infrared K–L index is greater than typical photospheric values $K - L \lesssim 0.3$. (The central wavelengths of K and L are $\sim$2.25 μm and $\sim$3.4 μm, respectively.) In the left panel, the equivalent widths of Hα emission only exceed $W \sim 10$ Å when there is evidence of an inner disk in the near-infrared; smaller levels of Hα emission are chromospheric in origin. In the right-hand panel, excess continuum emission is shown in terms of r, the ratio of hot continuum to stellar photospheric continuum emission at 5700 Å. The correlation of excess Hα and featureless continuum emission with infrared disk emission strongly implicates disk accretion as the mechanism heating the gas. Equivalent width data from Herbig and Bell (1988); reddening-corrected $(K - L)_O$ colors and r-values from Hartigan *et al.* (1995.)

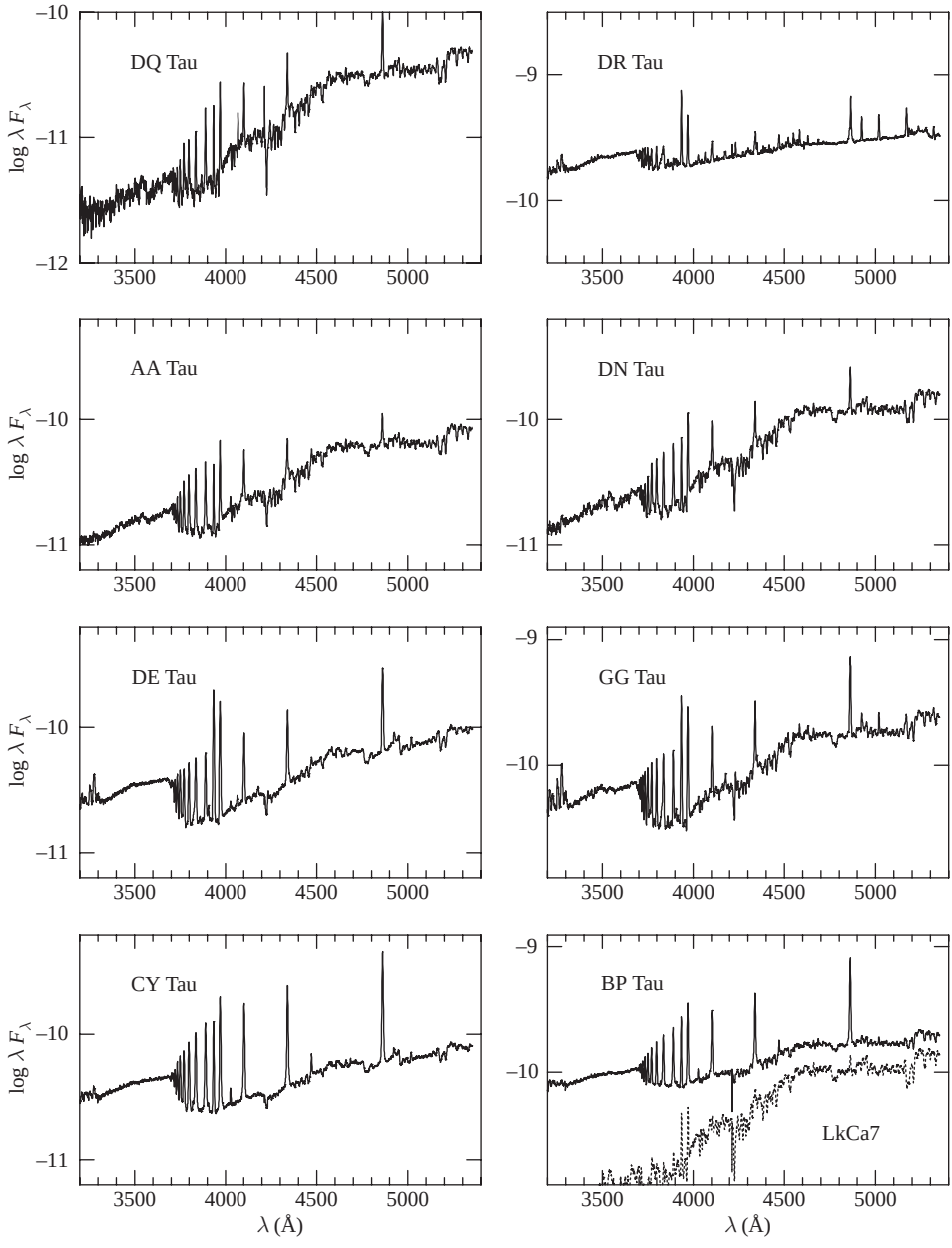

Fig. 8.14. Optical spectra of selected Taurus pre-main-sequence stars, showing the emission lines and hot continuum emission. The excess hot emission is especially apparent in the Balmer continuum shortward of 3650 Å; however, many objects exhibit strong emission at longer wavelengths (DR Tau is an extreme example of this). Comparison with the spectrum of the (non-accreting) WTTS LkCa7 (dotted line, bottom right panel) shows how the hot continuum emission makes the overall spectrum bluer, and how it reduces the apparent equivalent widths of photospheric absorption features. From Gullbring *et al.* (1998).

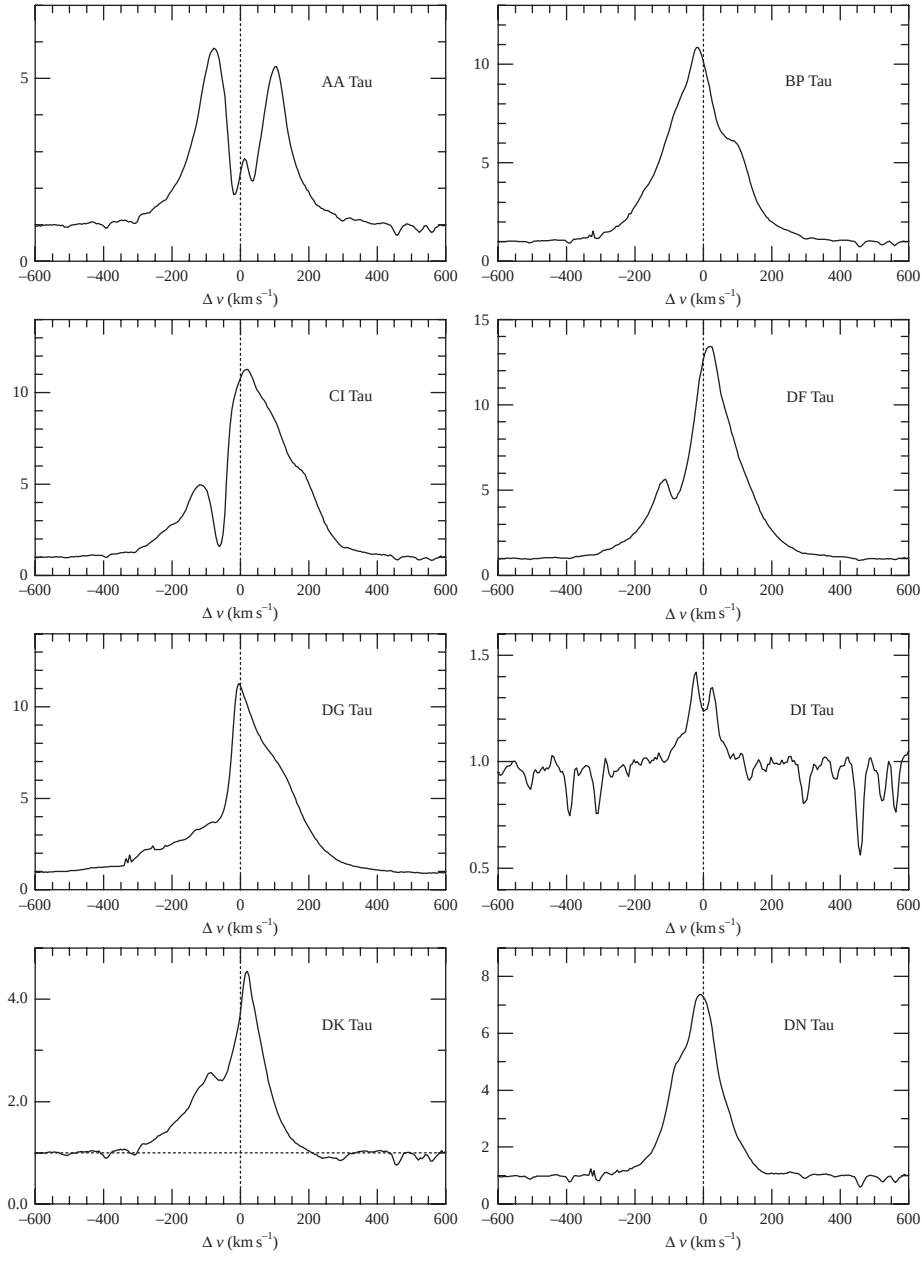

Fig. 8.15. Hα line profiles for T Tauri stars. Observed fluxes are normalized to the stellar continuum, and are plotted as a function of the velocity shift from line center (in the star's rest frame). Most objects show broad emission over ranges $\sim \pm 200$ km s^{-1} from line center. Many stars (CI, DF, DG, DK Tau) show blueshifted absorption probably characterizing mass ejection (Chapter 8), but others (BP, DN Tau) show no evidence for blueshifted wind absorption, and one object (DK Tau) shows evidence for faint redshifted absorption at $\sim +200$ km s^{-1}. DI Tau is a WTTS and therefore does not show the broad Hα profile produced in the infalling magnetospheric gas observed in accreting CTTS (see Chapter 10).

more consistent with infall (§10.10). Confusingly, one can occasionally see both blue- and redshifted absorption (DK Tau in Figure 8.15). We now understand this as due to physically separate flows; there is rapidly infalling material within magnetic flux tubes, in regions close to the star, with lower-density outflow outside of the magnetosphere. Lower opacity lines are more likely to show infall, such as the high Balmer series (Edwards *et al.* 1994); this indicates that the outer flow is optically thin in these lines. In contrast, higher-opacity lines like Hα can become optically thick at lower densities and thus can indicate the outer wind flow.

Boundary layer models (e.g., Lynden-Bell & Pringle 1974) cannot produce the necessary high-velocity infall. On the other hand, stellar magnetic fields may disrupt the disks at several stellar radii away from the stellar surface (Uchida & Shibata 1985; Königl 1991; Camenzind 1990). The accreting material is channeled along the magnetic fields lines as it falls onto the star (Figure 8.1). The accretion flow reaches nearly free-fall velocities; it shocks when it crashes into the stellar surface, producing the hot continuum radiation, while the (broad) emission lines are produced in the rapidly infalling gas within magnetic flux tubes (§10.10). This model explains the magnitude of the velocity widths of many lines (after taking some other line broadening mechanisms into account, e.g., Stark broadening in Hα), consistent with those expected from gravitational free-fall (Bonnell *et al.* 1998; §10.10).

T Tauri stars exhibit very strong magnetic activity, based on observations of strong X-ray activity and the detection of dark starspots covering large fractions of the stellar surface. Measurements of the Zeeman broadening of photospheric absorption lines indicate magnetic field strengths that in principle are sufficiently large to channel the accretion flow (Johns-Krull *et al.* 1999a; Valenti & Johns-Krull 2004; Johns-Krull 2007). Especially significant is the detection of circular polarization in certain emission lines which indicate accretion in strong, ordered magnetic fields (Johns-Krull *et al.* 1999a). Accretion in small, spatially distinct magnetic flux tubes is consistent with the small areas inferred for the hot continua (see section 8.5), and with the photometric modulation of hot spots due to stellar rotation, which require substantial non-axisymmetry in the hot continuum emission (e.g., Bertout *et al.* 1988). In addition, there is evidence for non-equatorial accretion spots (Strassmeier *et al.* 2005), which is not straightforwardly explained by the boundary layer model. Thus, there is every reason to invoke disruption of inner T Tauri disks by stellar magnetospheres.

The magnetospheric model was initially invoked to explain the slow rotation of T Tauri stars; interaction of the stellar magnetic field with a disk at radii where the Keplerian rotation period is of order a week in principle can slow the stellar rotation to a comparable period as it transfers angular momentum to the disk (Königl 1991; Shu *et al.* 1994). Using the photometric periods caused by hot spots (and dark starspots, in the case of non-accreting stars), surveys indicated that stars without close circumstellar disks rotate more slowly than the stars with inner circumstellar disks (Bouvier *et al.* 1993; Edwards *et al.* 1993), consistent with the idea of magnetosphere-disk transfer of angular momentum. The tendency of stars with disks to be somewhat slower rotators has subsequently been reinforced by studies of young clusters (Herbst *et al.* 2002; Lamm *et al.* 2005; Rebull *et al.* 2006), though with more scatter than previously inferred. However, the detailed mechanics of how this spindown can occur is complex; it is not a simple matter to spin down a star while it is accreting higher-angular momentum material (see §10.10). Moreover, the general lack of circular polarization in stellar photospheric lines suggests that large-scale, ordered fields are much smaller than those indicated by Zeeman broadening (e.g., Daou *et al.* 2006); in turn, this may indicate higher-order fields than dipolar, which would make the magnetic field much weaker at large

distances, raising questions as to whether the net stellar field is really strong enough to hold off the disk accretion out to many stellar radii.

In summary, the observed broad line profiles, strong stellar magnetic fields, and non-axisymmetric (and non-equatorial) hot spots confirm the general picture of magnetospheric accretion, although details of the geometry and the size of the magnetospheres remain uncertain (§10.10).

8.5 Accretion rates

Assuming that the hot continuum emission of CTTS is produced by the accreting gas as it shocks at the stellar surface, the steady-state luminosity is

$$L_{\rm hot} \approx \frac{GM\dot{M}}{R_*}\left(1 - \frac{R_*}{R_{\rm m}}\right) , \tag{8.12}$$

while the disk luminosity is*

$$L_{\rm d} \approx \frac{GM\dot{M}}{2R_{\rm m}} + L_{\rm diss} + L_{\rm irrad} . \tag{8.13}$$

Here $R_{\rm m}$ is the magnetospheric radius, where the stellar magnetic field truncates the disk, $L_{\rm diss}$ is the energy dissipated by the stellar magnetic fields passing through the disk if the angular velocity of the magnetic field lines differs from the angular velocity of disk material, and $L_{\rm irrad}$ is the luminosity due to heating by the central star's radiation. The magnitude of $L_{\rm diss}$ is uncertain. At one extreme, if the star is not rotating, and disk material is spun down to match the star before beginning to fall in along the magnetospheric field lines, then $L_{\rm diss} = GM\dot{M}/2R_{\rm m}$, i.e., the equivalent result for the boundary layer (§7.8) but with the magnetospheric radius now playing the role of the inner disk radius. If the inner disk radius is not too far from co-rotating with the stellar magnetic fields, the amount of energy dissipated in the disk is likely to be modest (Kenyon *et al.* 1996). For typical T Tauri stars, the co-rotation radius is probably at $R_{\rm i} \approx$ 3–5 R_*, in which case most of the energy of accretion is radiated in hot continuum emission, not in the disk. (To achieve the necessary infall velocities from gravitational acceleration requires infall from at least $2R_*$; see §10.10.)

Measurements of the hot continuum luminosity therefore can provide estimates of mass accretion rates from equation (8.12) which cannot be derived from disk emission for typical T Tauri stars. Unfortunately, the actual determination of $L_{\rm hot}$ is complicated by several factors, including disentangling the stellar photospheric emission from the excess emission. The hot continuum makes the stellar absorption lines appear weaker, or in the terminology, "veiled". One can estimate the veiling from a knowledge of the true photospheric line depths for the appropriate stellar spectral type (e.g., Hartigan *et al.* 1991), and thus derive the excess emission in wavelength regions where the stellar photosphere dominates. Geometric factors can also introduce errors, given the complex arrangement of accretion, and variability can also be an issue. The biggest problems are estimating source extinction, which affects ultraviolet fluxes strongly, and the broad character of the continuum emission, which ideally requires simultaneous measurements of the excess over wavelengths ranging from the

* The exact amount of energy dissipated in disk and accretion shock depends upon the amount of energy which goes into spinning up (or down) the star, the fraction which goes into a wind, and the potential dissipation of energy as the magnetic field interacts with the disk. The boundary conditions at the inner edge of the disk are uncertain and affect the total disk luminosity (cf. §7.8).

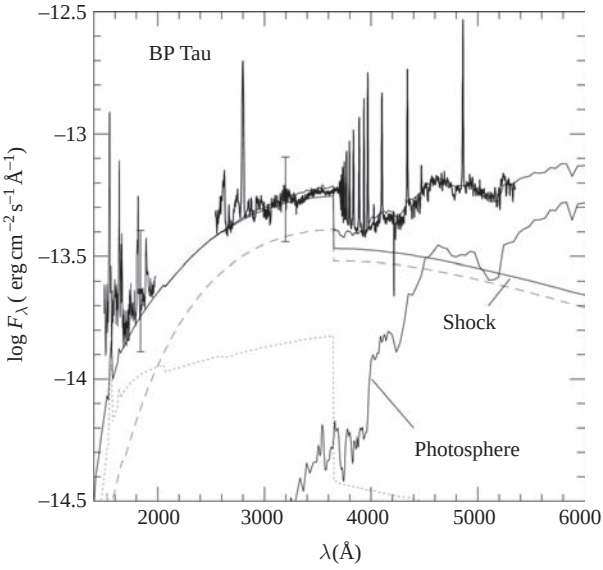

Fig. 8.16. Comparison between observed spectrum (thick solid curve) and an accretion shock model for the CTTS BP Tau. The mean flux levels at 2700 and 1800 Å and the range of variability are indicated by the squares and error bars. The theoretical model (thin solid line) is the sum of shock and photospheric emission. The total shock emission is the sum of the emission from post-shock gas and heated pre-shock gas (dotted line) and the heated atmosphere (dashed line). From Gullbring *et al.* (2000).

ultraviolet to perhaps even 1 μm. These difficulties have limited detailed studies to a few objects, with extrapolation to unobserved wavelength regions using models; in turn these detailed analyses are used to develop calibrations of much more easily obtained data, such as U-band or similar photometric bands vs. accretion luminosity (e.g., Gullbring *et al.* 1998).

Figure 8.16 shows an example of a detailed model calculation of an accretion shock compared with observations (Calvet & Gullbring 1998; see also Gullbring *et al.* 2000). The emission is composed of several components. Shock velocities are of order the free-fall values, ∼200–300 km s^{-1}. The post-shock region produces X-rays and extreme ultraviolet radiation as the gas cools from $\sim 10^6$ K. Most of this high-frequency radiation is absorbed and re-emitted at longer wavelengths; some is emitted downward toward the stellar photosphere, heating it to high temperatures, producing a strong continuum, while the outward radiation heats the less optically thick pre-shock gas, producing among other things the Balmer continuum jump in emission (Figure 8.16).

Detailed models such as in Figure 8.16 suggest that simple photometric measurements of ultraviolet excesses can provide reasonable estimates of accretion rates. Uncertainties still remain; for instance the extinction at ultraviolet wavelengths may depart from standard reddening laws; more "gray" extinction might reduce reddening corrections and therefore reduce accretion rate estimates. On the other hand, veiling at near-infrared wavelengths may be substantially in excess of that predicted by simple uniform shock models (Folha & Emerson 1999; Edwards *et al.* 2006); this might indicate a distribution of shock areas and consequent differing flux levels, implying that current results may underestimate accretion rates.

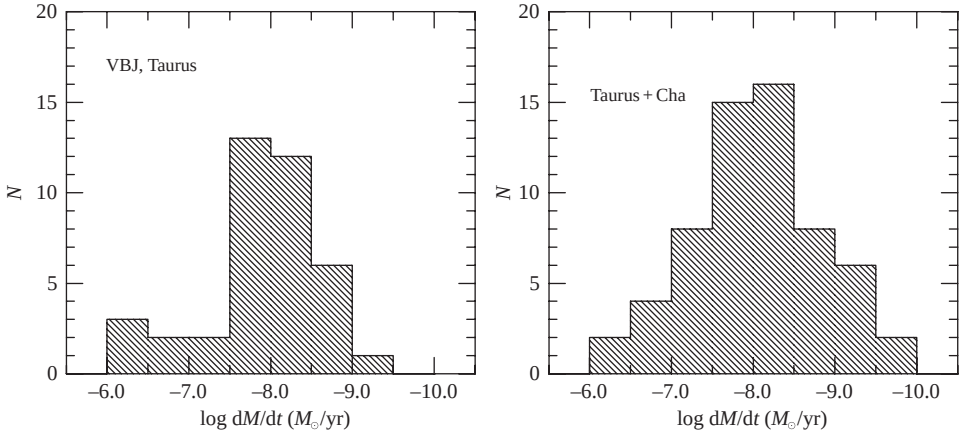

Fig. 8.17. Estimated accretion rates for T Tauri stars. The left-hand panel shows results from Valenti *et al.* (1993) for CTTS mostly in the Taurus cloud, while the right-hand panel illustrates the results from Gullbring *et al.* (1998) and Hartmann *et al.* (1998) for stars in the Taurus and Chamaeleon I regions. Upper limits to mass accretion rates for WTTS are generally well below $10^{-9}\,M_\odot\,\mathrm{yr}^{-1}$.

Figure 8.17 shows two sets of mass accretion rates derived from blue-optical excesses of stars in nearby clouds. For typical stellar parameters $M_* = 0.5\,M_\odot$, $R_* = 2\,R_\odot$, the predicted disk accretion luminosity for a median mass accretion rate of $10^{-8}\,M_\odot\,\mathrm{yr}^{-1}$ is $L_\mathrm{d}(\mathrm{acc}) = GM_*\dot{M}/2R_* \sim 0.08\,L_\odot$. This low value is consistent with the modest infrared excesses generally found in CTTS (Figure 6.3), and indicates that even the inner disk emission in most CTTS is powered by irradiation. The situation is different when the accretion luminosity greatly exceeds that of the central star, as occurs with the most-rapidly accreting T Tauri stars, or the FU Ori objects (Chapter 9). In such cases irradiation from the central star can be ignored, and accretion rates can be inferred from disk luminosities directly, as originally envisaged by Lynden-Bell and Pringle (1974).

Intrinsic time variability of CTTS accretion, which may be responsible for some of the scatter shown in Figure 12.4 is not very well characterized at present (Herbst *et al.* 1994; Gahm 1994, and references therein). Timescales of potential accretion events range from less than one hour to years with amplitudes at the visual band ($\lambda \sim 0.55\,\mu\mathrm{m}$) $V < 0.05$, for the fast events, to several magnitudes in V for longer-term variations (Vrba *et al.* 1993; Gullbring 1994; Gahm *et al.* 1995; Gullbring *et al.* 1996). The variable brightness of the hot continuum may have an analogue in the accreting intermediate polars, which are close binary systems also accreting through magnetospheres (cf. Frank *et al.* 1992).

Herbig (1977b, 1989) has called attention to relatively long-term, substantial variations in the optical emission of CTTS. Typically these "EXor" outbursts involve increases in optical brightness of a few magnitudes and may last for fractions of a year to decades. For example, DR Tau became brighter by about two magnitudes in the B photometric band ($\lambda \sim 0.45\,\mu\mathrm{m}$) in the 1970s and has remained relatively bright since. Because DR Tau is currently a very-strong-emission CTTS (Figures 8.8, 8.14), it is likely that this brightening is due to an increase in the accretion rate, which made the hot continuum emission much brighter. However, at present very little is known about the statistics of such outbursts.

8.6 What drives accretion?

As discussed in §4.6, it is likely that most of the mass of a star initially lands on a disk; it therefore seems likely that gravitational instabilities can dominate the angular momentum transport needed to accrete most of the stellar mass. However, current estimates (e.g., Figure 8.11) suggest disk masses at least an order of magnitude smaller than the values needed for gravitational instability (equation (7.98)). Although it was argued in §8.3 that current disk mass estimates are probably too low, it isn't clear that the disks are really massive enough for gravitational instability to dominate the angular momentum transport, especially close to the star. From equation (7.83), setting $Q \sim 1$ implies $\pi G \Sigma \sim c_s \Omega$; as both the sound speed c_s and especially the angular frequency increase rapidly with decreasing radius, extremely large surface densities are required to make the innermost disk gravitationally unstable.

The other likely mechanism of angular momentum transport is the MRI. However, as discussed in §7.6, the ionization levels in T Tauri disks are likely to be too low to support MRI turbulence in many regions of the disk. Even if one assumes that the MRI can operate because of sufficient dust depletion in upper layers of surface density Σ_a, there are still difficulties. Assuming that the disk is heated primarily by viscous dissipation, and using a layered accretion disk theory, Gammie (1996a) derived an inner disk accretion rate $\dot{M}$ for a standard dust opacity law,

$$\dot{M} = 1.8 \times 10^{-8} \left(\frac{\alpha}{10^{-2}} \right)^2 \left(\frac{\Sigma_a}{100 \, \mathrm{g \, cm^{-2}}} \right)^3 M_\odot \, \mathrm{yr}^{-1} , \tag{8.14}$$

While this model can provide accretion rates in rough agreement with observations, the predicted accretion rates are quite sensitive to the active layer surface density Σ_a. More problematically, this result exhibits no explicit dependence upon the stellar mass, whereas the observational estimates shown in Figure 8.18 indicate a significant correlation, roughly $\dot{M} \propto M_*^2$, albeit with considerable scatter at a given mass.

It is important to note that there are observational selection effects present in Figure 8.18. As pointed out by Clarke and Pringle (2006), continuum excesses much lower than the stellar luminosity are difficult to detect, contributing to the lack of detections in the lower right corner of the figure. In addition, accretion luminosities much larger than that of the stellar luminosity would also make it difficult to and discern the stellar photosphere, and thus the stellar mass, helping to explain the upper envelope of points. However, while these effects are certainly present, they cannot explain the main trend. Hα line profiles are sensitive to mass accretion at rates well below those detectable in continuum emission; indeed, most of the brown dwarf ($M_* < 0.08 \, M_\odot$) accretion rates have been derived from either Hα or Brackett γ emission (Muzerolle *et al.* 2003b; Natta *et al.* 2004). Even at low accretion rates for higher-mass stars, one could detect broad Hα absorption – and this is not seen to the author's knowledge. On the other end of the problem, if accretion luminosities of many T Tauri stars were so high as to completely veil the optical spectrum, one would detect many "continuum" stars; instead, they constitute a small fraction of the population in, for example, Taurus. Thus observational selection effects can somewhat bias any mean trend of $\dot{M}$ vs. M_*, but cannot explain it away. (Another concern is that the accretion rates for the lowest mass stars tend to come from emission line calibrations, rather than continuum excesses as in the higher-mass stars; the investigation of Herczeg and Hillenbrand (2008) suggests that

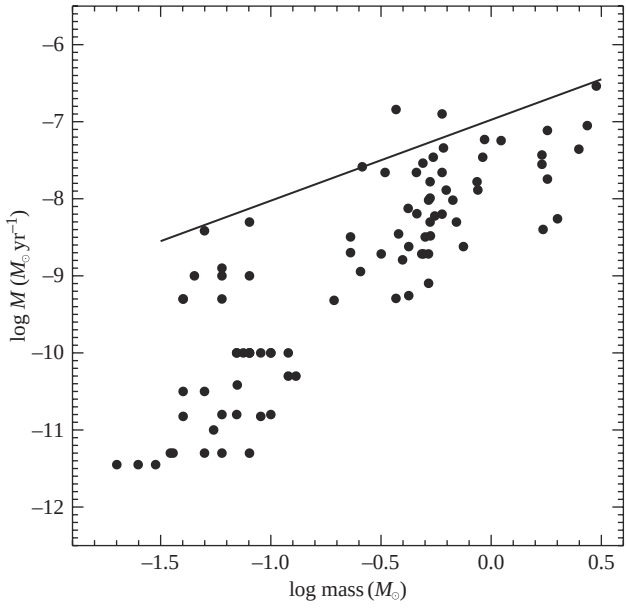

Fig. 8.18. Mass accretion rates for young stars as a function of stellar mass. Data taken from Gullbring *et al.* (1998), White and Ghez (2001), White and Basri (2003), Muzerolle *et al.* 2003b, Calvet *et al.* (2004), Natta *et al.* (2004), and Muzerolle *et al.* (2005). The mass accretion rates for intermediate-mass stars are observed in objects which have not contracted close to the main sequence, i.e., in their F–G star partially convective envelope phase rather than in their eventual A star main-sequence spectral type (see Calvet *et al.* 2004). The solid line corresponds to an accretion rate which would result in amassing 0.1 of the stellar mass in 1 Myr (see text). From Hartmann *et al.* (2006).

Hα measurements underestimate mass accretion rates, but not enough to strongly affect the overall trend of accretion rate vs. mass.)

The T Tauri/Class II/CTTS stage presumably represents the final stages of stellar accretion. It is therefore reasonable to assume that the initial disk masses of these systems are just below that needed for gravitational instability. This means that the disk mass should scale proportionately with the stellar mass (e.g., equation (7.98)). If T Tauri disks are mostly or completely MRI-active, due to small surface densities and/or sufficient numbers of metal ions not absorbed into grains (Fromang *et al.* 2002), then accretion rates should scale as

$$\dot{M} \sim \frac{M_{\rm d}}{t}, \tag{8.15}$$

with constants relating to the assumed viscous properties. For example, using the similarity solution of §7.2, evaluating the constant $C_{\rm g}$ by determining the disk mass at a given time from equation (7.47), assuming that evolution has occured over many viscous times (e.g., $T_{\rm g} \gg 1$ in equation (7.48)), and evaluating the result at the inner disk radius, with $R \to 0$, one finds $\dot{M}(t) = M_{\rm d}/(2t)$. Thus, if the initial disk mass scales with the star, one finds a linear dependence of $\dot{M}$ on M_*. One can achieve an even stronger dependence of the accretion rate on disk mass if viscous evolution is faster in lower-mass objects, for instance if lower-mass stars start out with systematically smaller radii disks (Dullemond *et al.* 2006;

also Hartmann *et al.* 2006). Tilling *et al.* (2008) argue that the data do not really provide a constraint on viscous evolution, given a range of initial T Tauri disk masses generally proportional to the stellar mass, and allowing for observational selection effects.

One potential problem with this kind of model is that it predicts a tight relationship between the current disk mass and the current mass accretion rate. The fully viscous disk model yields low mass accretion rates when disk masses are low; but mm-wave disk emission has been detected from several young brown dwarf disks (Klein *et al.* 2003; Scholz *et al.* 2006) which, despite the uncertainties in dust opacities (§8.3), suggest relatively substantial disks. More generally, this solution requires either MRI activation throughout much of the disks, which seems unlikely, or some other unknown mechanism of angular momentum transport.

It is possible to introduce some dependence of the mass accretion rate on the stellar mass in the Gammie (1996a) layered accretion model by including irradiation from the central star. The accretion rate in the inner disk (and therefore the rate onto the central star) is given by the accretion rate of the layered model at the critical radius R_c where the temperature rises to a level sufficient for thermal ionization to activate the MRI. If we take this to be the (frontally illuminated; Figure 8.1) disk edge at the dust destruction radius (which would both provide enough thermal ionization and remove the electron-absorbing dust), for a fixed dust destruction temperature, $R_c \propto L_*^{1/2}$, then for the viscosity $\nu = \alpha c_s / \Omega$,

$$\dot{M} \propto \nu\Sigma \propto \alpha c_s^2 \Omega^{-1} \Sigma_a \propto \alpha \Sigma_a L_*^{3/4} M_*^{-1/2} . \tag{8.16}$$

For pre-main-sequence stars up to masses of 2 $M_\odot$ or so, the stellar luminosity tends to scale very roughly as $L_* \propto M_*^2$. Therefore in the limit of pure irradiation heating, we would expect

$$\dot{M} \propto \alpha \Sigma_a M_* . \tag{8.17}$$

Thus, the inclusion of irradiation heating results in a layered model in which the accretion rate is no longer independent of stellar mass, with what may be sufficiently sensitive to mass (Tilling *et al.* 2008).

Another possibility is that stellar X-ray emission, which potentially provides MRI activation, also depends upon stellar mass. However, among low-mass stars the ratio of X-ray to stellar luminosity is almost constant, down to brown dwarfs, as indicated by studies of the Orion Nebula Cluster (Flaccomio *et al.* 2003; Preibisch *et al.* 2005). Since the fluxes of both photospheric and X-ray radiation should scale in the same way for the same geometry, it does not seem that there should be an effect. Furthermore, the calculations of Glassgold *et al.* (1997) and Igea and Glassgold (1999) suggest that MRI ionization levels are maintained until the X-rays are very strongly attenuated; this makes the activated total column density depend very slowly on the X-ray luminosity in any case.

The solid line in Figure 8.18 denotes the accretion rate at which 0.1 of the stellar mass would be accreted in 10^6 yr. The absence of stars above this boundary is consistent with the notion that T Tauri disk mass reservoirs need not be so large as to be strongly gravitationally unstable. On the other hand, this does not rule out the possibility of accretion by weak gravitational instability in a disk hovering near $Q \sim 1$, with a gradual dwindling of angular momentum transport. Perhaps the MRI and the gravitational instability combine to produce complicated patterns of accretion which depend upon stellar mass.

8.7 The WTTS

T Tauri stars were originally recognized as young objects found in regions of star formation with strong emission lines, as seen in objective-prism spectra (e.g., Haro *et al.* 1953; Herbig 1954, 1957; Herbig & Kuhi 1963). Stars with weaker, chromospheric Hα emission (e.g., DI Tau, Figure 8.15) were difficult to detect on such low-resolution spectra. X-ray surveys turned out to be much less biased toward accretion activity, resulting in a large expansion of the pre-main-sequence population (see discussion in Montmerle *et al.* 1993). While care must be taken in surveying large areas to avoid including foreground relatively young, magnetically active stars (Briceño *et al.* 1997), increasingly sensitive X-ray surveys have been crucial in rounding out our understanding of pre-main-sequence evolution (e.g., Feigelson *et al.* 2005; Güdel *et al.* 2007, and references therein).

High X-ray emission selects both the strong-excess CTTS and a population of weak Hα emission, which have therefore been called the "weak-emission" T Tauri stars or WTTS. As shown in the left panel of Figure 8.13, WTTS do not show near-infrared excess emission characteristic of disks (see also Wolk & Walter (1996)). Similarly, as shown in the right panel of Figure 8.13, WTTS do not show optical hot continuum emission (veiling) expected for substantial disk accretion. The hot gaseous emission of the WTTS therefore arises from a form of solar-type magnetic chromospheric and coronal activity rather than from disk accretion.

The original definition of a WTTS was that of a young star with $W_\lambda(\mathrm{H}\alpha) < 10\,\text{Å}$ (cf. Herbig & Bell 1988) has been modified to account for the variation of chromospheric Hα fluxes as a function of the effective temperature of the star; this is a natural result of the complicated dependence of chromospheric Hα on the stellar photospheric radiation field (Cram & Mullan 1985). Using large Hα velocity widths as signatures of magnetospheric accretion, White and Basri (2003) devised a more robust way to separate WTTS from CTTS, as shown in Figure 8.19.

The strong chromospheric and coronal emission of WTTS is in the same range as observed in other stars of relative youth, such as the young main-sequence stars in the Pleiades or α Persei clusters, which have ages $\sim$50–100 Myr (Randich *et al.* 1996; Stauffer *et al.* 1994). WTTS may have even stronger coronal X-ray emission than CTTS (Neuhauser *et al.* 1995). However, these emission levels are small fractions of the stellar luminosity, and are easily distinguished from the much larger energy release of disk accretion at ages of $\sim$1 Myr.

Populations of WTTS are found with the same ages as CTTS (Kenyon & Hartmann 1995); thus, although CTTS eventually stop accreting from their disks, and turn into WTTS, age is not the only factor in whether a young star exhibits an accretion disk. Binary companions can render disks dynamically unstable on scales comparable to the binary orbit; this would explain the tendency for binaries to exhibit weaker disk emission and thus exhibit WTTS properties (Jensen *et al.* 1994, 1996; Osterloh & Beckwith 1995; McCabe *et al.* 2006). With the distribution of binary companion stars among solar-type stars peaking at periods of $\sim 6 \times 10^4$ days, or semi-major axes $\sim$30 AU (Duquennoy & Mayor 1991), one might expect that companions are responsible for limiting disk sizes and thus resulting in faster disk evolution. However, binarity does not seem to be the only reason why young WTTS exist, as many binaries exhibit strong dust emission from both circumstellar and circumbinary disks (e.g., Guilloteau *et al.* 1999). Indeed, the CTTS DQ Tau (Figures 8.8, 8.14) manages to accrete and have strong infrared excess emission, even though it is a nearly equal-mass short-period

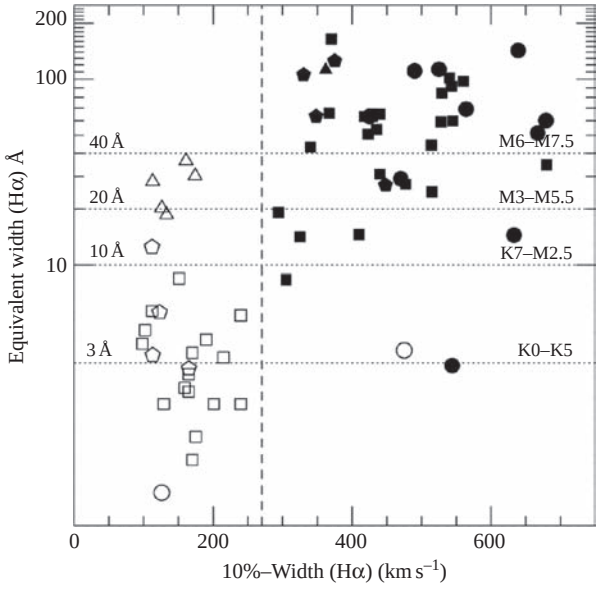

Fig. 8.19. Equivalent widths vs. velocity widths at 10% of peak for Hα lines in T Tauri stars. The velocity widths of optically-veiled, accreting T Tauri stars (CTTS, filled symbols) are systematically larger than the corresponding velocity widths for WTTS. The results suggest that Hα equivalent widths can be used to distinguish CTTS from WTTS reasonably accurately, but that differing limits need to be taken for stars of differing spectral type (see text). From White and Basri (2003).

(15.8 day) binary (Mathieu *et al.* 1997); apparently its eccentric orbit allows material to accrete from the outer disk phased with the orbital period (Basri *et al.* 1997).

8.8 The Herbig Ae/Be stars

The picture of disk structure, accretion, and evolution developed in the preceding sections also appears to be applicable to intermediate-mass young stars ($M \sim 2 - 4\,M_{\odot}$). Hillenbrand *et al.* (1992) pointed out the ubiquity of infrared excesses in these so-called "Herbig Ae/Be systems" and explicitly modeled the emission as dusty disks with high mass accretion rates. Interferometry at mm wavelengths resolved the dust disks of some systems, and traced the disk rotation (e.g., Mannings & Sargent 1997). The interpretation of HAe/Be stars as accreting disk systems has been secured by a variety of measurements (see Millan-Gabet *et al.* 2007).

The 3 μ peak seen in the SEDs emission of many HAe/Be stars (see, for instance, Figure 1.11) initially seemed peculiar, but was naturally explained by Natta *et al.* (2001) and Dullemond *et al.* (2001) as arising from the inner edge of the disk, frontally illuminated, where the disk dust becomes so hot as to evaporate (Figure 8.1). (The same effect is now thought to occur in T Tauri disks; Muzerolle *et al.* 2003b). This disk "wall" produces a large contribution to the near-infrared excess, and can be fit crudely by blackbody emission at roughly 1300–1400 K, comparable to what is expected for dust sublimation (Dullemond *et al.* 2001).

One important difference of the HAe/Be stars compared with T Tauri stars is that the high luminosities of the former imply that the dust destruction radius occurs at much larger radii, of order 0.3–1 AU, as directly verified by near-infrared interferometry (e.g., Millan-Gabet *et al.* 1999, 2001; Monnier & Millan-Gabet 2002; Eisner *et al.* 2003, 2004). The interferometric results are better fit by a "wall" that curves away from the star rather than being a flat plane, as a result of pressure-dependence of dust evaporation and/or grain settling (Isella & Natta 2005; Tannirkulam *et al.* 2007).

In principle disk gas can accrete through the dust destruction wall, especially as the ionization state of such material should be sufficient to sustain the MRI. There is also some evidence for high-velocity infall in a few HAe/Be systems, suggesting that magnetospheric accretion can occur in intermediate-mass pre-main-sequence stars as well as T Tauri stars (Muzerolle *et al.* 2004). The accreting disk material must radiate as it moves inward to the star; this emission may have been detected with near-infrared interferometry (Eisner *et al.* 2007; Tannirkulam *et al.* 2008). The difficulties of calculating the energy balance and thus thermal structure of this accreting gas in the presence of strong ultraviolet radiation which can dissociate gas make theoretical predictions of emission spectra problematic. Muzerolle *et al.* (2004) suggested that this accreting dust-free gas is geometrically thin if not optically thin, so that the dust destruction "wall" is effectively illuminated by the central star rather than being shadowed by the inner disk.

Another issue is whether HAe/Be stars exhibit enough X-ray emission to drive the MRI effectively in the outer disk. Using deep Chandra observations of the very young Orion Nebula Cluster, Stelzer *et al.* (2005) showed that of four of 11 mid B- to late-A were not detected, with X-ray luminosity upper limits much lower than that of the late-type stars in the region; this suggests that the X-rays in the detected objects may be dominated by emission from an unresolved late-type companion star. Telleschi *et al.* (2007) studied the high-resolution X-ray spectrum from AB Aur and concluded that this canonical Herbig Ae/Be star does indeed produce its own X-rays, because its spectrum indicates much lower characteristic temperatures than typical of T Tauri stars (see also Swartz *et al.* 2005). However, the AB Aur spectrum shows a rapid falloff above 1 KeV, whereas photons of energy $\gtrsim$3 KeV are most important for deeply ionizing the disk (Igea & Glassgold 1999); the lack of high-energy photons may reduce MRI activity significantly.

If Herbig Ae/Be stars have reduced MRI activity because of weak or soft X-ray emission, their disk accretion might be driven mainly by gravitational instability. In this case, angular momentum transfer would decay rapidly once the Toomre Q parameter becomes significantly larger than unity, leaving behind a relatively massive disk which only slowly accretes due to the reduced MRI. Speculatively, massive, dense disks might coagulate faster into large bodies, resulting in more rapid disk evolution consistent with the much lower disk frequencies among A stars than among later type stars (e.g., Hernández *et al.* 2005, 2007).

The application of disk accretion models to even higher-mass stars is much more problematic, due to the difficulty of observing more distant, confused systems, and the increased importance of photoevaporation/photoionization/radiation pressure (§4.7).

8.9 The transitional disks

It has been clear since the pioneering studies by Strom *et al.* (1989) and Skrutskie *et al.* (1990) that dusty disks – at least the regions close to the central T Tauri star – tend to disappear (or become optically thin) on timescales of a few to 10 Myr. Recent studies

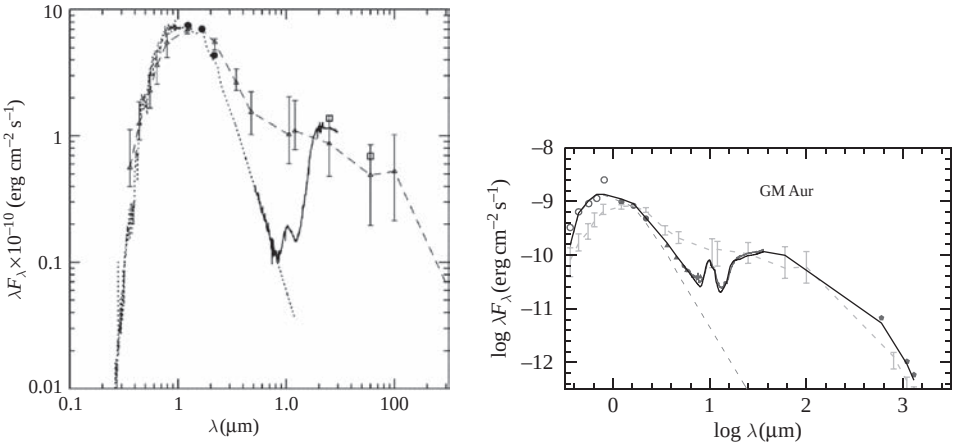

Fig. 8.20. The transitional disks CoKu Tau 4 (left) and GM Aur (right). CoKu Tau 4 is a WTTS, and thus shows no evidence of gas accretion; it exhibits no detectable infrared excess from dust out to ∼10 μm; but the large, rapid rise in emission at longer wavelengths indicates the presence of a typical T Tauri disk, as indicated by the comparison to the median Taurus SED (Figure 8.5). Models indicate that this disk is highly evacuated of gas and dust interior to about 10 AU. In contrast, GM Aur is a CTTS, with significant gas accretion and reduced dust masses within a hole of inner radius ∼24 AU. From D'Alessio *et al.* (2005) and Calvet *et al.* (2005).

(Haisch *et al.* 2001; Carpenter *et al.* 2006; Hernández *et al.* 2007) confirm this general picture, but why some disks "disappear" faster than others is unclear (§12.1).

Generally speaking, when the near-infrared excess disappears, so do the indicators of gas accretion (e.g., Figure 8.13). However, there are a few exceptions to this rule. In particular, thanks largely to the spectral resolution and enhanced sensitivity brought to bear in the 5–35 μm wavelength region by the IRS spectrograph on the *Spitzer Space Telescope*, we now recognize a subset of objects called "transitional disk" systems (e.g., Calvet *et al.* 2002; Calvet *et al.* 2005; D'Alessio *et al.* 2005). The transitional disks have little or no near-infrared excess but very large mid-infrared excesses, comparable to typical T Tauri levels (Figure 8.20). Although some transitional disks do not accrete at detectable levels (CoKu Tau 4), others may have substantial accretion rates. For instance, GM Aur has an estimated accretion rate of $\approx 10^{-8}\, M_\odot\ \mathrm{yr}^{-1}$ (Gullbring *et al.* 1998), suggesting that the accreting gas is less opaque than usual, perhaps due to depletion of small grains. Rice *et al.* (2006a) have suggested that gas pressure gradients at the outer edge of a gap in a disk might hold back some dust, resulting in gas accretion with a lower dust density (see §12.6).

The presence of a relatively massive outer disk with substantial amounts of gas is indicated by the strong mid-infrared excesses seen in these systems. Models for these objects indicate that the abrupt rise of flux with increasing wavelength is due to emission from a relatively well-defined inner disk edge or "wall"; this is a version of the dust walls found in Herbig Ae/Be stars (see previous section), but at much lower temperatures, so they are not the result of dust evaporation. The inferred heights of these walls are large, $z/R \sim 0.2$, in order to produce sufficient infrared excess emission, implying dust suspension to several scale heights above the midplane (D'Alessio *et al.* 2005; Calvet *et al.* 2005; Espaillat *et al.* 2007).

Typical inner wall radii are approximately a few to a few tens of AU; this may be in part an observational selection effect corresponding to the dust temperatures which radiate in the IRS wavelength range.

The presence of a substantial outer disk with weak inner dust emission suggests that the transitional disks represent an early stage of disk clearing. Their low frequency (a few percent of the CTTS) indicates that transitional disks represent a rapidly evolving phase of disk evolution, lasting of order 10^5 yr. While some systems are known to have inner disk clearing due to a binary companion, many others exhibit no evidence of being a multiple system. Thus, many of the transitional disks may be objects in process of coagulating dust into planetesimals or even planets in an "inside–out" process expected theoretically, as evolutionary timescales are thought to increase with increasing radius. These objects will clearly be systems of great interest for future attempts to find giant planets either in formation or during their early evolution.

9

The FU Orionis objects

The remarkable eruptive FU Orionis objects found in star-forming regions are important to our understanding of protostellar accretion disk physics. The best-studied FUors provide the clearest examples of the SED of an optically-thick accretion disk, with observations spanning a decade in wavelength or more. The very high accretion rates of these accretion disk systems imply that the MRI can easily operate through thermal ionization, at least out to radial distances of nearly an AU. In addition, the high temperatures mean that gaseous spectral lines are present which can be used to infer rotation, turbulence, disk surface mass ejection (Chapter 10), and even chromospheric activity. Clues to the magnitude of angular momentum transport can be derived from the timescales of variability of these systems. Finally, the eruptive behavior and high accretion rates for short periods of time provide an unexpected insight into how mass is added to stars during early stellar evolution.

Acceptance of the accretion disk model proposed by Paczynski (1976), Lin and Papaloizou (1985), and Hartmann and Kenyon (1985) was slowed by the optical appearance of FUors, with spectra similar to that of a G supergiant (except rapidly rotating, an otherwise unknown set of objects). An early model for FUors attempted to explain the substantial near-infrared excesses (Cohen & Woolf 1971; Rieke *et al.* 1972; Simon *et al.* 1972; Grasdalen 1973; Simon 1975) by invoking such rapid rotation that the equatorial regions were much more extended, and thus cooler, than the polar regions (Mould *et al.* 1978). This model fails because observations at increasingly long wavelengths require an implausibly flattened stellar structure; moreover, the cool infrared-emitting regions rotate more slowly than the optical photospheres, opposite to what would be predicted for a rotationally extended star, but consistent with Keplerian rotation in a disk (Hartmann & Kenyon 1987a,b). The disk model also can account for the outbursts by analogy with those seen in accreting binary systems, at least in principle.

FU Ori objects must be rapidly accreting systems. Using equation (7.56) to obtain a sufficiently high maximum disk temperature to explain the optical spectrum,

$$T_{\rm max} \sim 6500\, M_{0.5}^{1/4}\, \dot{M}_{-5}^{1/4} R_2^{-3/4}\, {\rm K}\,, \tag{9.1}$$

where $M_{0.5}$ and R_2 are the central star mass and radius in typical units for T Tauri stars of $0.5\, M_\odot$ and $2\, R_\odot$, respectively, and $\dot{M}_{-5}$ is the mass accretion rate in units of $10^{-5}\, M_\odot\, {\rm yr}^{-1}$. Thus, the optical emission from FU Ori disks requires a much higher accretion rate than that typical of T Tauri stars. Observations suggest that the inner disk radii of FU Ori objects are a factor ∼2–3 larger than the value adopted above, requiring mass accretion rates closer to $\sim 10^{-4}\, M_\odot\, {\rm yr}^{-1}$ to explain the observed spectra and accretion luminosities.

FU Ori objects are rare because outbursts at the peak accretion rates $\sim 10^{-4}\, M_\odot\ \mathrm{yr}^{-1}$ cannot last long. On the other hand, the frequency of FU Ori outbursts appears to exceed the expected frequency of star formation in the solar neighborhood by a factor of at least several; thus, at least some stars must have repetitive outbursts, though it is not known whether most low-mass stars undergo FU Ori outbursts. The outbursts are thought to be (relatively) short-lived phenomena, lasting $\sim 10^2$ yr; however, this is quite uncertain, since no known FU Ori has actually yet returned to its pre-outburst state, and there are differences between objects (§9.1).

The total current mass accretion rate for the known FU Ori objects in the solar neighborhood is estimated to be approximately a few to 10% of the rate at which interstellar matter is being converted into stars. This suggests that FU Ori events are responsible for accreting a modest fraction of the total mass of low-mass stars. However, it is quite likely that the present census of FU Ori objects is incomplete, due to difficulties in detecting heavily extincted sources; this view is supported by recent infrared surveys which, although not detecting outbursts, find the spectral signatures of rapid disk accretion. Large-scale infrared surveys are needed to understand the true place of FU Ori objects in early stellar evolution.

It is not clear why disk accretion rates are so variable, although our recognition of the MRI as a major factor in angular momentum transport has led to promising hypotheses. FU Ori outbursts appear to be a phenomenon of the earliest stages of stellar evolution, consistent with the original suggestion by Lynden-Bell and Pringle (1974) that protostellar disks may outshine their central stars at very early ages. The large extinctions and far-infrared emission of many FU Ori objects suggest that they are still experiencing infall from protostellar envelopes. Mass infall to the disk may pile up material until the disk can adjust itself in a violent manner to rid itself of excess material by accreting onto the central star.

The material in this chapter draws on the review by Hartmann and Kenyon (1996) and other references listed therein, including reviews by Herbig (1966, 1977b, 1989) and Reipurth (1990), with recent photometry kindly provided by Mansur Ibrahimov.

9.1 Basic observational properties

FU Ori objects were originally identified by their large outbursts in optical light (Herbig 1966, 1977b; Kolotilov & Petrov 1983, 1985). Figure 9.1 illustrates optical light curves of the three best-studied objects, which all exhibit large increases in optical brightness of ~ 4 mag or more and remain luminous for decades. Though similar in many respects, differences in the light curves show that these objects are not indentical. The two best-studied objects, FU Ori and V1057 Cyg, exhibited very short rise times to maximum light (~ 1 yr), while the rise of V1515 Cyg to maximum has taken more than a decade. The decay timescales can differ dramatically; FU Ori shows a slow decline with an e-folding time $\sim 50-100$ yr; V1057 Cyg initially faded about 10 times faster than FU Ori, but has slowed its rate of decay in recent years; and V1515 Cyg has not yet shown evidence of becoming fainter.

The FU Ori objects are clearly pre-main-sequence systems. They are all spatially and kinematically associated with star-forming regions, and all have reflection nebulae (cf. Goodrich 1987; Figure 9.2). Many objects now assigned to the class by spectroscopic criteria (see p. 190) are heavily extincted, and all have large infrared emission excesses (Weintraub *et al.* 1991). Furthermore, when the optical spectrum can be detected, all FU Ori objects exhibit the strong Li I 0.6707 μm absorption characteristic of young stars (Chapter 11).

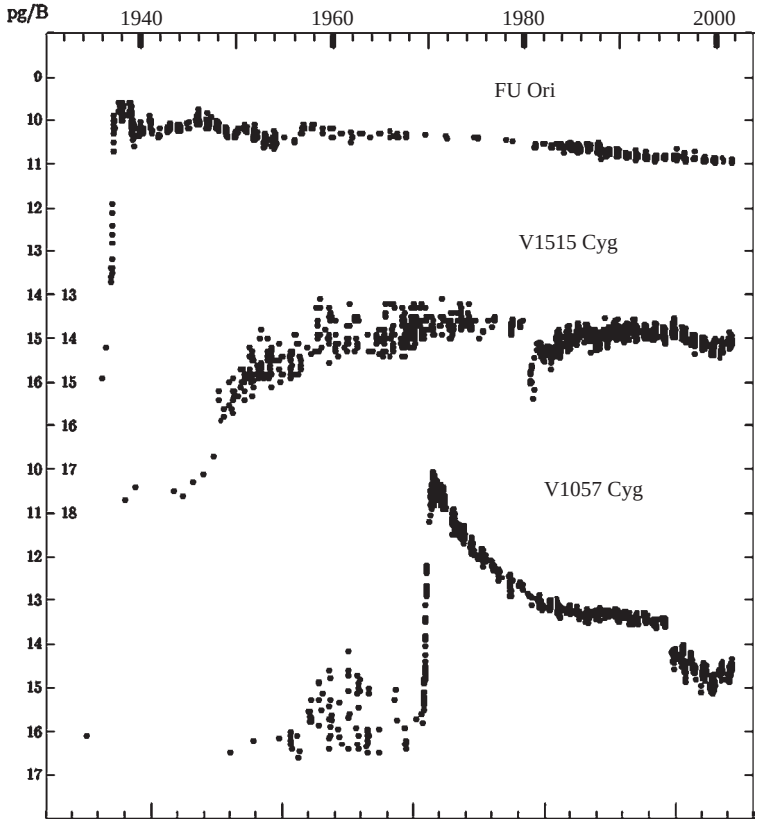

Fig. 9.1. Historical optical photometry of outbursts in three FU Ori objects. Modern photometry is in the B band, to correspond as nearly as possible with archival photographic photometry. Courtesy of Mansur Ibrahimov.

FUors exhibit moderately distinctive optical spectra. Optical spectral types are late F to G (effective temperatures ∼7000–6000 K), and line ratios indicate surface gravities much lower than those typical of T Tauri stars (Figure 9.3). Broad blueshifted absorption is observed in the Balmer and Na I resonance lines, indicating that these objects have powerful winds (Chapter 10); emission components in $H\alpha$ and other wind lines are weak or absent, except for Ca II and Mg II emission which indicates chromospheric activity (e.g., Kenyon *et al.* 1989); thus the FU Ori objects do not exhibit the signatures of magnetospheric accretion seen in T Tauri stars (§§8.4, 10.10).

FU Ori objects have even more distinctive near-infrared spectra. In contradiction with the optical spectral types, FU Oris show strong CO absorption at 2.2 μm and water vapor bands in the near-infrared (∼1–2 μm) region, characteristic of M giant–supergiant atmospheres (effective temperatures $\lesssim$3000 K; see Figure 9.4). Because near-infrared spectra for heavily extincted sources are much easier to obtain than optical spectra, the majority of objects now thought to be FUors are systems which exhibit strong CO and water vapor absorption. In some cases, such as L1551 IRS 5 and V733 Cep (Mundt *et al.* 1985; Stocke *et al.* 1988; Carr *et al.* 1987; Reipurth *et al.* 2007), it is possible to obtain optical spectra (sometimes purely in

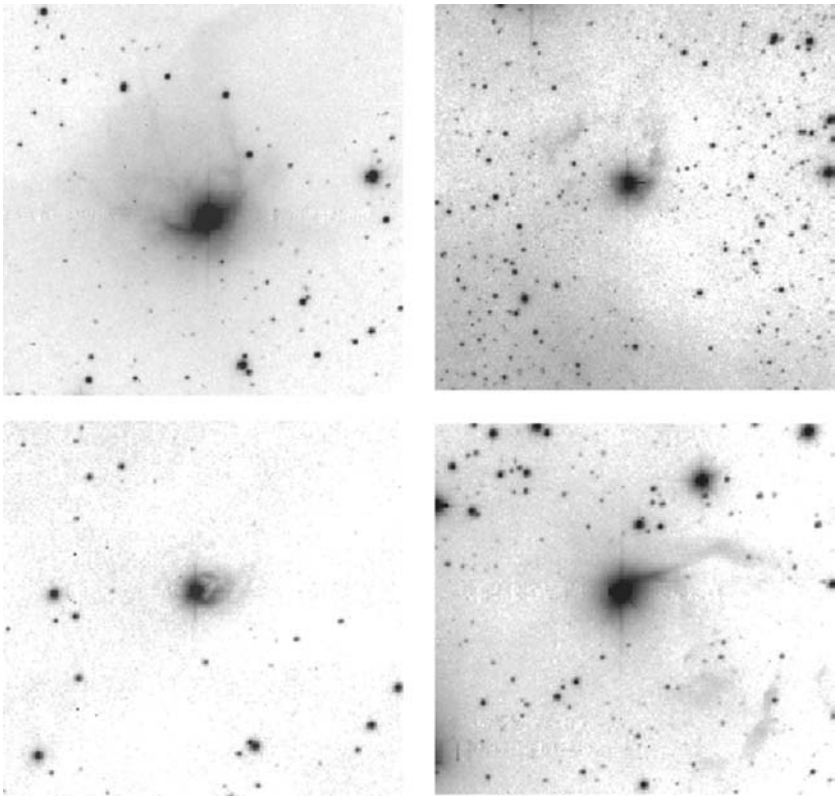

Fig. 9.2. FU Ori (upper left) and V1057 Cyg (upper right); V1515 Cyg (lower left) and Z CMa (lower right) in optical images. Courtesy C. Briceño.

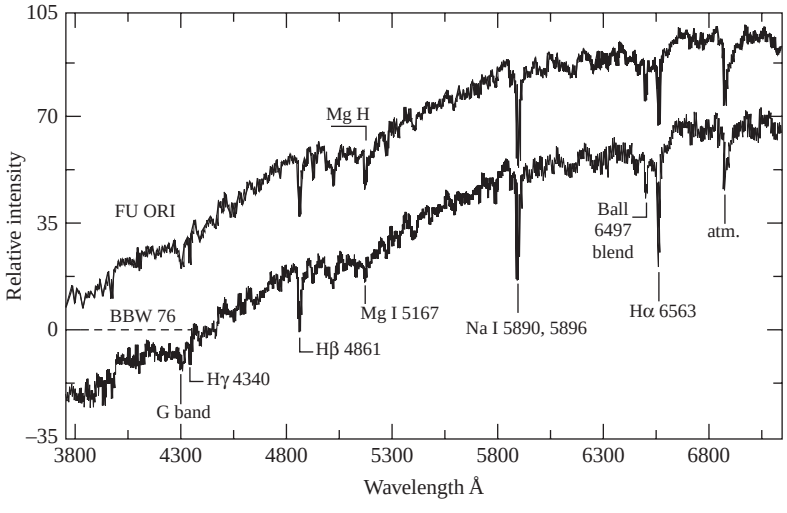

Fig. 9.3. Optical spectra of FU Ori and BBW 76, illustrating typical G supergiant spectral features. These two objects have nearly identical spectra. From Reipurth *et al.* (2002).

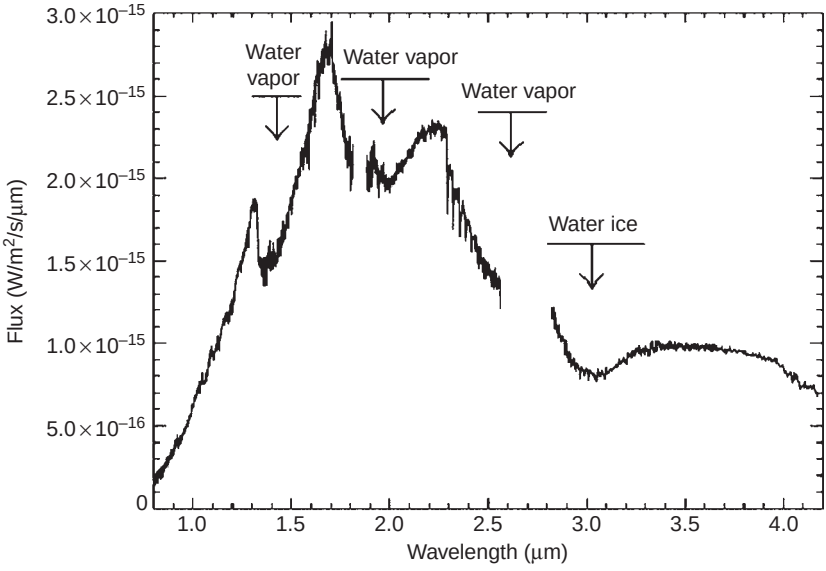

Fig. 9.4. Near-infrared spectrum of the highly embedded young FUor V733 Cep, showing the strong water vapor and CO first vibrational overtone absorption. The spectrum also shows a dip at $\lambda \sim 3\,\mu$m which is due to ice absorption in foreground material. From Reipurth *et al.* (2007).

scattered light along the outflow cavity) which help support the FUor identification. Members of the spectroscopic FUor class (with occasional outburst information) now include Z CMa (Hartmann *et al.* 1989) (which has an embedded companion that dominates the total luminosity; Koresko *et al.* 1991, Haas *et al.* 1993); RNO 1B/C (Staude & Neckel 1991; Kenyon *et al.* 1993); Haro 5a IRS, HH 354 IRS, and HH 381 IRS (Reipurth & Aspin 1997); PP13S (Sandell & Aspin 1998); and possibly V346 Nor (Graham & Frogel 1985). (Some young objects exhibit the CO bands in emission rather than absorption; it is possible that these could be produced in rapidly accreting, FUor-like disks with strong irradiation, either from a hot accretion shock, or possibly from the photospheric emission of an early-type central star; Calvet *et al.* 1991).

A pre-outburst spectrum is available for one FU Ori object (V1057 Cyg), showing the Balmer, Ca II, Fe I, and Fe II emission lines characteristic of an accreting T Tauri star (Herbig 1977b; Figure 8.14). During the outburst of V1057 Cyg, most of the emission lines disappeared. Immediately after the outburst, the initial spectral type was early A ($T_{\rm eff}\sim$9000 K); the spectrum became later (cooler) as V1057 Cyg faded from maximum light. These spectral changes demonstrate that the outburst was not caused by the removal or dispersal of obscuring dust.

9.2 The accretion disk model

The principal tests of the disk interpretation for FUors employ the standard steady, optically thick accretion disk temperature distribution (equation (7.55)),

$$T_{\rm d}^4 = \frac{3GM_*\dot{M}}{8\pi\sigma R^3}\left[1-\left(\frac{R_{\rm i}}{R}\right)^{1/2}\right] \tag{9.2}$$

where R_i is the inner disk radius. As discussed in §7.3, the term in square brackets depends upon the choice of inner boundary condition; this particular form may well not be appropriate for FU Ori objects (§9.7), but we ignore this complication for the present. At first it might be thought surprising that outbursting objects can be treated as steady disks. However, detailed investigations of the best-studied objects have been conducted during epochs considerably after outburst, when the objects were much less variable, and therefore the changes in the mass accretion rates have been slower.

SEDs derived from photometry and IRS spectra of four FU Ori objects are compared with steady, optically thick, blackbody disk model SEDs in Figure 9.5. The disk models, much broader in their SEDs than that of a single-temperature blackbody or stellar photosphere, agree reasonably well with the observations at wavelengths $\lambda \lesssim 10\,\mu$m; the observed emission cannot be explained by a single-temperature blackbody or normal star. In these four objects, the SEDs rise above that of the steady accretion disk model longward of about

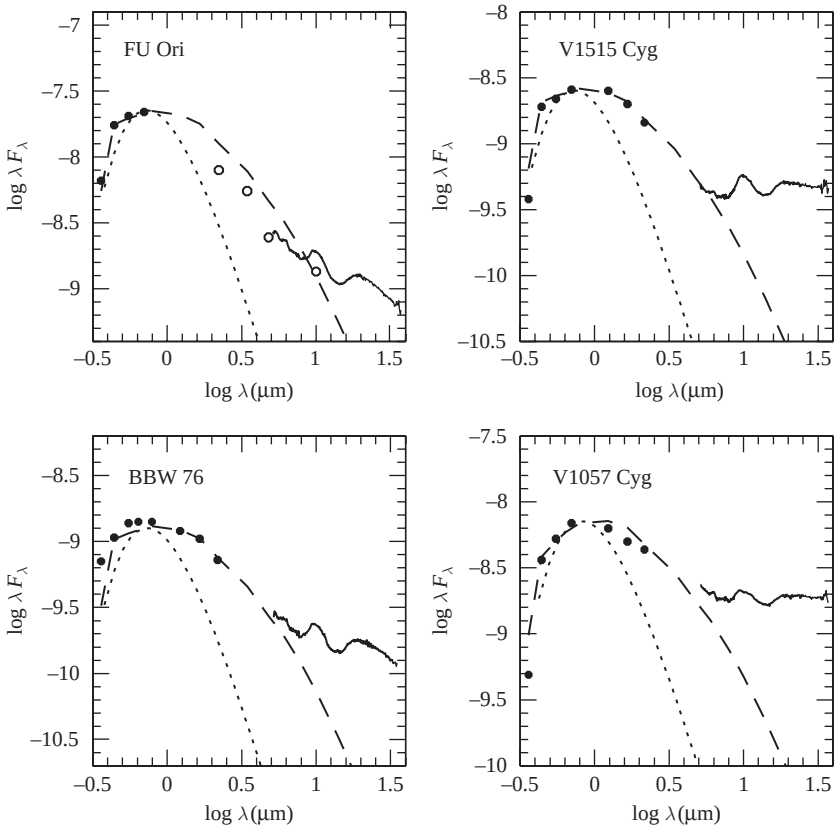

Fig. 9.5. Dereddened SEDs derived from optical near-infrared photometry (dots) and *Spitzer* IRS spectra (curves) of four FU Ori objects, compared with steady, optically thick, accretion disk models (dashed lines) and single-temperature blackbodies (dotted lines). The disk models employ stellar colors at short wavelengths and the blackbody approximation at long wavelengths. Modified from Green *et al.* (2006).

10 μm. This long-wavelength emission, along with the silicate emission peaks, is strongly reminiscent of the SEDs of dusty irradiated T Tauri disks (Figure 8.8). More detailed analysis indicates that the excesses of FU Ori and BBW 76 at wavelengths $\gtrsim$10 μm can be explained with a T Tauri-like flared disk model, but irradiated by the disk rather than a central star and/or accretion shock (Kenyon & Hartmann 1991; Turner *et al.* 1997). The larger excesses of V1057 Cyg and V1515 Cyg probably require extended, possibly infalling, envelopes (Kenyon & Hartmann 1991; Zhu *et al.* 2008; §9.5).

The apparent temperature of the emitting gas in a steady accretion disk varies with the wavelength of observation. At longer wavelengths, outer, cool regions dominate the emission; this is why the disk has a shallower spectral slope at long wavelengths than a single-temperature blackbody. This property enables disk models to explain the variation of spectral type with wavelength observed in FU Ori objects. The difference in temperature of the emitting gas can be recognized from the change in the spectral features.

To demonstrate this more clearly, consider the emission from differing disk annuli. The emergent spectrum of each annulus of a thin disk is approximately that of an independent stellar atmosphere, with local effective temperature $T_{\rm d}(R)$ and vertical surface gravity

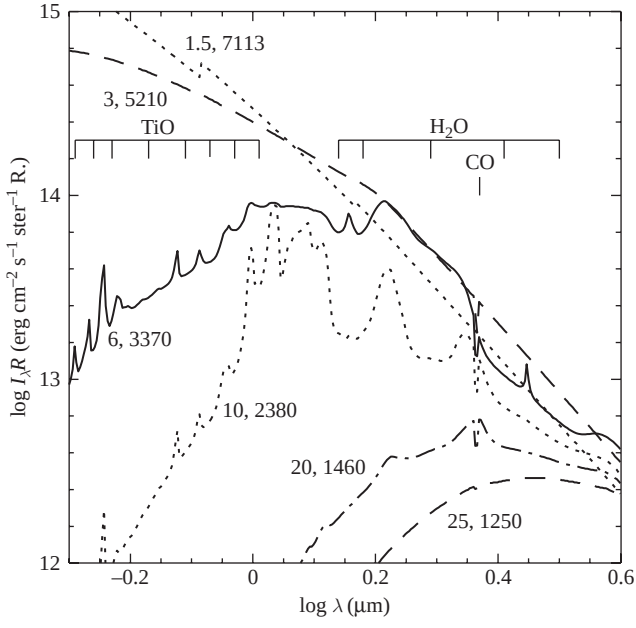

Fig. 9.6. Emission of individual disk annuli for a typical steady disk model for FUors. The intensity at each annulus is weighted by its (cylindrical) radius R to provide an indication of the amount of contribution of each region to the final spectrum (Figure 7.6). Each curve is labeled by the radius of the annulus in units of the inner disk radius, and the effective temperature (in K) of the annulus. The hot inner disk annuli dominate the optical spectrum but do not contribute molecular absorption features in the near infrared. Conversely, disk regions at $R \sim 5$–$10\,R_i$ contribute strong molecular absorption in the 1–2 μm region. The lowest-temperature annulus shows no molecular absorption because continuous dust opacity is assumed to dominate. Calculation courtesy N. Calvet.

$g(R)$.* The spectra are much more sensitive to the temperature than to the precise gravity, so it is adequate to make a rough estimate $g(R) \sim (GM/R^2)(H/R)$ with $H \sim 0.1R$.

Figure 9.6 shows the results of a typical calculation for a steady disk temperature distribution, which approximately reproduces the observed SED of FU Ori. One observes that the hot inner disk regions dominate the optical spectrum, as expected, but do not contribute any molecular features in the near-infrared. In contrast, disk annuli at $R \gtrsim 6\, R_{\rm i}$ contribute strong water vapor features in the 1–2 μm region, and substantial CO first-overtone absorption at 2.2 μm.

By adding up the intensities of the disk annuli, and weighting them by the appropriate area $2\pi R dR$ (cf. equation (7.57)), the spectrum of the disk model can be synthesized. A recent model resulting from this type of computation can account for the optical G-type spectra of FU Ori objects at the same time that it reproduces the near-infrared water vapor and first-overtone CO absorption features (Figure 9.7). (Note that in this calculation, a steady disk model can match the overall SED of FU Ori quite well. The difference between this result and the comparison shown in Figure 9.5 is that a lower extinction – $A_V \sim 1.5$ instead

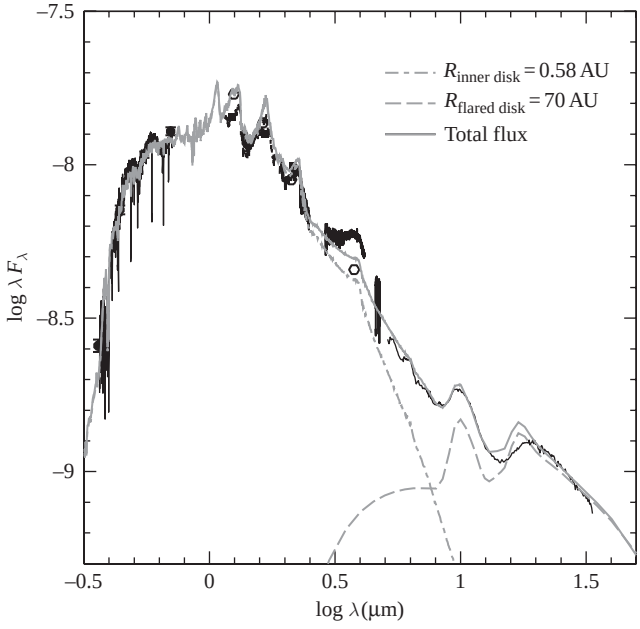

Fig. 9.7. Optical and infrared spectrophotometry of FU Ori (dark curves), compared with a detailed radiative transfer model (gray curves). The addition of a flared dusty disk irradiated from the inner disk regions can explain the long-wavelength fluxes, including the silicate emission features (dashed curve). Modified from Zhu *et al.* (2007, 2008).

* This assumes that all of the energy flowing through the atmosphere is generated at larger optical depths in the disk interior. As discussed in §9.4, this approximation is reasonable for FU Ori disks, which should be extremely dense and optically thick; the viscous energy generation should occur mostly at the high-density internal disk layers, not in the low-density outer disk atmosphere. Irradiation by the central star (§7.9), which acts to make the disk more vertically isothermal or even results in a temperature inversion, can be neglected in the inner disk because the inner disk cannot irradiate itself, and the central star is much less luminous than the disk in outburst.

of 2.2 – was used in Figure 9.7. This illustrates one of the difficulties in analyzing any departures from a steady disk model; without a "standard" spectrum, extinction corrections become uncertain.)

Taken together, Figures 9.3, 9.4, 9.5, and 9.7 illustrate an important point: the presence of *absorption* features in the optical and near- to mid-infrared spectra show that FU Ori and similar systems are *self-luminous*; that is, the energy balance is driven by flux originating at large optical depth, which results in a normal photospheric cooling with increasing height. At $\lambda \sim 10\,\mu$m and $20\,\mu$m, the silicate emission features familiar from T Tauri stars (Figure 8.8) now appear, indicating that the outer disks and/or envelopes are mostly heated from the outside.

9.3 Disk kinematics

Kinematic studies generally provide the clearest tests for the presence of disks. One such test involves line profiles, which are qualitatively different in a disk than in stars. The absorption line shapes of rotating stars are typically parabolic, because there is a large contribution to the total flux from regions near disk center, where projected rotational velocities are small. In contrast, slower-rotating regions in a Keplerian disk lie at larger radii, which are cooler and contribute less to the profile (at least for typical disk temperature distributions). The result is a profile in which the absorption is stronger at some velocity than at line center, i.e., a double-peaked profile.

The line profile produced by a rotating, flat, narrow annulus as a function of velocity shift from line center Δv is of the form

$$\phi(\Delta v) = \left[1 - \left(\frac{\Delta v}{v_{\max}}\right)^2\right]^{-1/2}, \quad -v_{\max} < \Delta v < v_{\max}, \tag{9.3}$$

where $v_{\max} = v_K(R)\sin i$ is the maximum projected rotational velocity of the annulus with Keplerian rotational velocity v_K observed at an inclination angle i. The observed line profile at a given wavelength is the sum of profiles over all annuli, each with a different rotational velocity, and weighted according to the area and flux of each annulus. Only a finite range of radii in the disk contribute significant continuum emission at a given wavelength; for example, as shown in Figure 9.6, annuli with $R \gtrsim 6R_i$ do not contribute significant emission at optical wavelengths, while only regions of the disk with $3R_i \gtrsim R \gtrsim 10R_i$ contribute to the wavelength region near the $2.2\,\mu$m CO absorption bands. Thus, the effect of differential rotation is to smooth the profile given by equation (9.3) but not eliminate its essential "double-peaked" shape.

Figure 9.8 shows optical spectra of FU Ori objects which demonstrate this line doubling. These spectra also exhibit large rotational velocity broadening, ranging from about 45 km s^{-1} for V1057 Cyg to ~110 km s^{-1} in Z CMa. Rapid rotation is also observed in the high-resolution near-infrared spectra of the first-overtone CO absorption in FU Ori and V1057 Cyg (Figure 9.9), as can be seen from both the widths of individual resolved features and the shape of the bandhead. This large rotational velocity broadening is by itself a demonstration that these objects are not normal stars; though the main sequence progenitors of supergiants may have been rapidly rotating, their expansion during evolution off the main sequence makes them slow rotators as M stars.

The measurement of rotational velocities over a wide range of optical and near-infrared wavelengths may be exploited to provide another test of the disk hypothesis. The disk regions

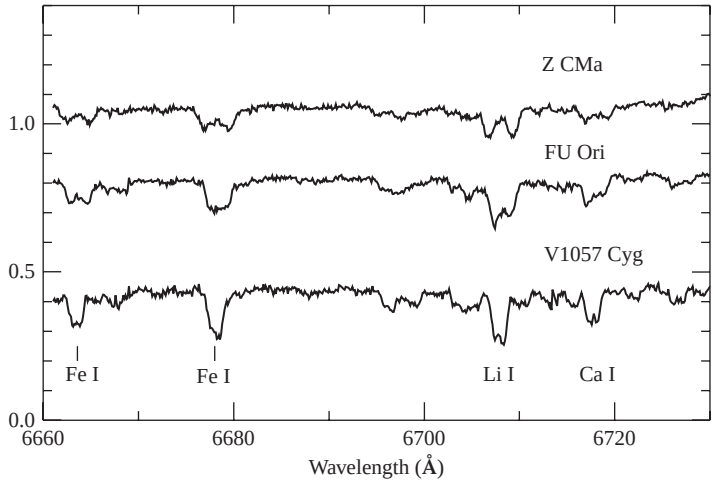

Fig. 9.8. High-resolution red (optical) spectra of three FU Ori objects. The absorption line profiles show evidence for doubling. The sequence from V1057 Cyg → FU Ori → Z CMa illustrates the effect of increasing rotational velocity. The doubling is difficult to detect at the low rotational velocity of V1057 Cyg in the λ6678 feature, because it is a blend of several individual lines. Modified from Hartmann and Kenyon (1996).

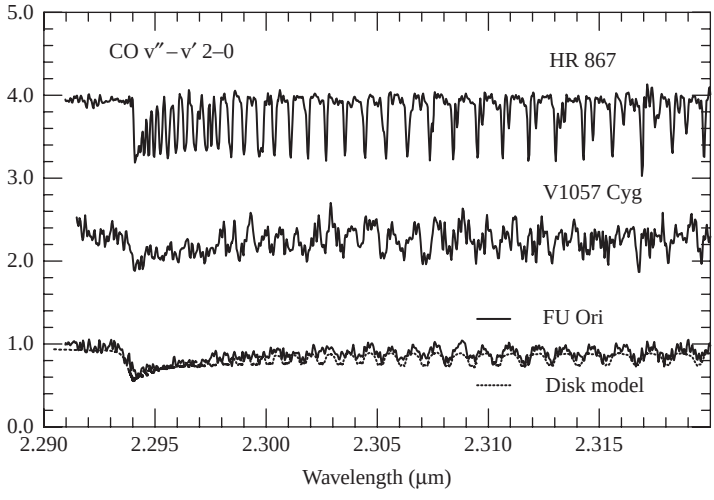

Fig. 9.9. Near-infrared first-overtone ($v'' - v' = 2 - 0$) CO absorption bands in two FU Ori objects. The CO lines are strongly rotationally broadened compared with the bands in the M giant HR 867; the amount of the broadening is consistent with the FU Ori disk model (dashed line; see text). From Hartmann and Kenyon (1996).

responsible for the optical spectrum are hotter and lie at smaller radii than the regions producing the near-infrared spectrum (Figure 9.10). Since the inner disk regions must rotate more rapidly than the outer disk regions, it follows that if the FU Ori objects are disks, the differential rotation should manifest itself as a decreasing rotational velocity with increasing wavelength of observation.

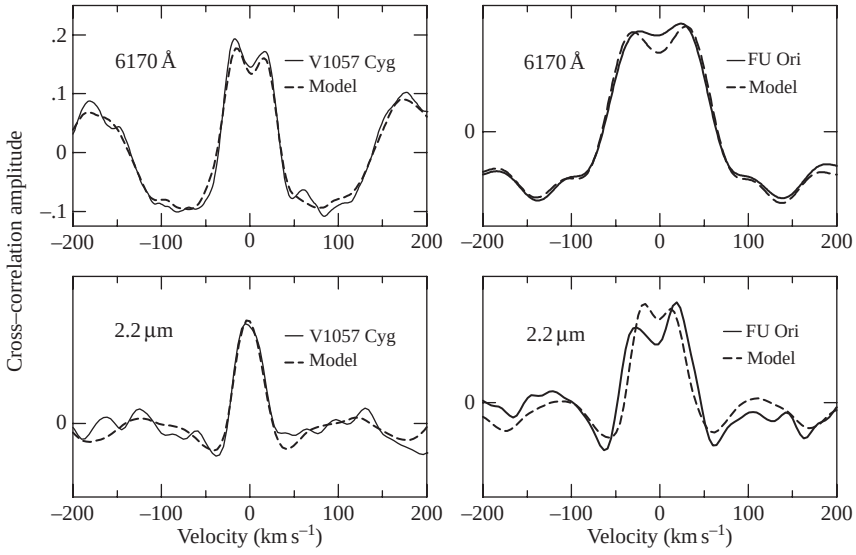

Fig. 9.10. Differential rotation in FU Ori and V1057 Cyg. Cross-correlation peaks show that the intrinsic line widths are larger at optical wavelengths than observed in the $v' - v'' = 2-0$ CO absorption bands at 2.2 μm. Cross-correlation of synthetic disk model spectra with the same templates (dashed lines) demonstrates that the difference in optical and infrared line widths is consistent with the assumption of Keplerian rotation (see text). From Kenyon *et al.* (1988).

Cross-correlation analysis takes advantage of data from many lines to construct an average line profile when the object is rotating much more rapidly than the template spectrum. Figure 9.10 compares optical and infrared cross-correlation peaks for FU Ori and V1057 Cyg, demonstrating that in both objects the broadening observed at 0.6 μm is roughly 1.5 times that observed at 2.2 μm. The observations clearly demonstrate large differential rotation inconsistent with stellar rotation but in the same sense as would be expected for the disk.

To provide a quantitative test of Keplerian rotation, synthetic disk spectra can be computed for the appropriate wavelength regions and then cross-correlated with the same template spectra used to produce the cross-correlations of the real FU Ori objects. The disk model line profiles can be synthesized by convolving the spectrum of each annulus with the appropriate rotational velocity broadening function (9.3), and summing the emission from the individual annuli. Figure 9.10 compares the cross-correlation results of synthetic disk models for FU Ori and V1057 Cyg, scaled to match the observed optical line widths (Kenyon *et al.* 1988). The overall agreement is good, although the predicted differential rotation is perhaps ∼25% larger than observed. One should keep in mind that there are several limitations of the calculation. In particular, the temperature at which the dust opacity begins to dominate the continuous spectrum (e.g., Figure 9.6) affects how much the outer disk regions contribute to the CO absorption features and thus introduces uncertainty in how much these more slowly rotating regions affect the overall line profile widths. Some theoretical models also suggest that the disks of FU Ori objects are so hot that they do not exhibit precisely Keplerian rotation, and are partially supported by radial gas pressure gradients (cf. §9.7).

Note that the double-peaked *shapes* of the cross-correlation peaks for both model and observations are in fairly good agreement with observations of FU Ori at both optical and infrared wavelengths. (The instrumental resolution is not large enough to show clearly the infrared line doubling in the cross-correlation peak of V1057 Cyg in Figure 7.9.)

While the simple steady disk models with pure Keplerian rotation explain the main properties of FU Ori line profiles, the observed lines are often less double-peaked than the models predict. For the strongest lines, mass loss may be important in obscuring the line doubling (§10.3). In the case of weaker lines, Petrov and Herbig (1992) and Herbig *et al.* (2003) have pointed out that line doubling is often not seen, especially in spectra of V1057 Cyg. One possible explanation is that another source of line broadening is present. The temperatures of FU Ori disks, at least in their inner regions, are high enough that the MRI should be active due to thermal ionization; the turbulence generated by MRI activity can generate waves, creating sonic or even supersonic motions in upper disk layers (Figure 9.11). This is a particularly plausible idea for FUors, as the high accretion rates tend to imply that the photospheres are

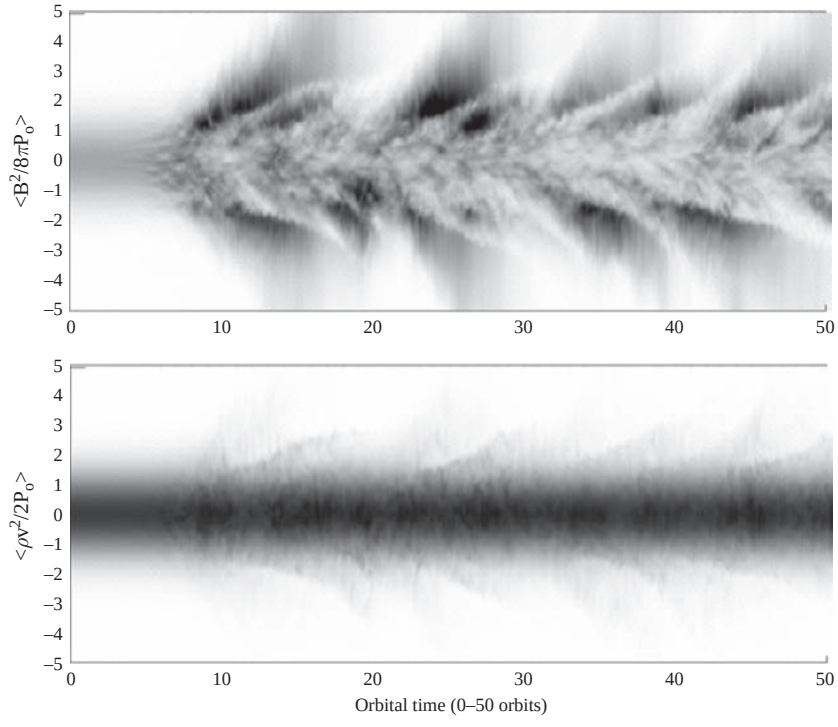

Fig. 9.11. Time-dependent simulation of MRI-driven turbulence in a vertically stratified disk. The vertical axis denotes the z component, while the horizontal axis is elapsed time in orbital periods. This space–time plot shows the time evolution of magnetic (upper panel) and kinetic (lower panel) energies. The central regions are turbulent while the upper layers exhibit subsequent waves of magnetic and kinetic energy fluxes. The velocity dispersion becomes nearly sonic at ± 3 scale heights above the midplane; magnetic waves propagating through the outer disk layers shock, potentially providing significant heating. From Miller and Stone (2000).

several scale heights above the midplane; thus, small-amplitude waves generated in central regions are likely to steepen and shock as they propagate away from the central regions, along the steep vertical density gradient.

The simulation of a vertically stratified disk by Miller and Stone (2000; Figure 9.11) showed waves generated by the MRI in the disk interior can propagate outward and shock; this could produce both "turbulent" line broadening and shock heating at a few scale heights above the midplane. Hartmann *et al.* (2004) found that they needed turbulent velocities approaching twice sonic values in order to explain the CO first-overtone line profiles of FU Ori in detail; and FU Ori also exhibits chromospheric Mg II resonance line emission (Kenyon *et al.* 1989), qualitatively consistent with shock damping of supersonic waves generated from below.

Turbulent line broadening will be most important for objects with small $v \sin i$ values. The projected optical rotational velocities of Z CMa are so large that mildly supersonic turbulence is unimportant relative to the rotational broadening of the line profiles (Figure 9.8) (though turbulence does affect the overall predicted line equivalent widths). Further study of FU Ori spectra might yield insights into MRI-generated turbulence.

9.4 Disk properties

The theory of steady disk emission can be used to estimate physical properties of the FU Ori objects. The observed flux at the Earth is related to the disk accretion luminosity by

$$F = \frac{L_{\rm acc} \cos i}{2\pi d^2}\,, \tag{9.4}$$

where d is the distance to the Earth and i is the inclination of the disk to the line of sight. In practice the dominant uncertainties are the inclination, about which we have only guesses, and the extinction corrections, since the colors of FU Ori objects may well not be those of "normal" stars. Since most of the radiation of FU Ori variables is emitted at optical wavelengths (Figure 9.5), and visual extinctions are typically $A_V \sim 2$–3 mag for the *lightly reddened* objects, uncertainties of a factor of two in the luminosity are to be expected.

The standard disk–boundary layer theory does not apply to FU Ori objects, since they exhibit no evidence of boundary layer emission (§9.7). Nevertheless, let us adopt the standard disk equations for simplicity. Then the accretion luminosity constrains the product of the mass and the accretion rate divided by the inner disk radius,

$$L_{\rm acc} = \frac{G M_* \dot{M}}{2 R_{\rm i}}. \tag{9.5}$$

Consider a "typical" FU Ori object with $L_{\rm acc} = 250\ L_\odot$. Fitting of extinction-corrected SEDs and optical line spectra by steady disk models suggest that the maximum temperature of the disk is $T_{\rm max} \sim 7000$ K, where

$$T_{\rm max} = 0.488 \left(\frac{3 G M \dot{M}}{8\pi\sigma R_{\rm i}^3} \right)^{1/4}\,, \tag{9.6}$$

(equation (7.56)). Combining the luminosity with the maximum temperature results in an estimate of the inner disk radius, $R_{\rm i} \sim 4.5\ R_\odot$, and constrains the product $M \dot{M} \sim 0.75 \times 10^{-4}\ {M_\odot}^2\ {\rm yr}^{-1}$. While these inner disk radii are somewhat larger than typical radii of T Tauri

stars $\sim 2-3\ R_\odot$, the agreement is reasonably satisfactory considering the uncertainty in what is happening to the energy released at the interface between star and disk, if any. (It is possible that the disk advects or carries large amounts of accretion energy into the central star (§9.7), causing the star to expand (§11.4)).

The rotational velocities can be used to estimate the central mass. Steady disk models indicate that the effective emitting radius at $0.6\,\mu$m for $T_{\rm max} = 7000$ K is about 2.5 times the inner radius. Using this result, the apparent optical rotational velocity is

$$v \sin i\ (0.6\,\mu{\rm m}) \sim \left(\frac{GM}{2.5R_i}\right)^{1/2} \sin i \sim 92\, M_{0.5}^{1/2} \sin i \ \ {\rm km\,s^{-1}}\,, \tag{9.7}$$

where $M_{0.5}$ is the central mass in units of one-half solar mass, and we have adopted a typical inner radius $R_i = 4.5\ R_\odot$ (Kenyon *et al.* 1988; §7.6).

The observed optical rotational velocities of the four best-studied FU Ori objects are: Z CMa, $v \sin i \sim 110$ km s^{-1}; FU Ori, $v \sin i \sim 65$ km s^{-1}; V1057 Cyg, $v \sin i \sim 40$ km s^{-1}; and V1515 Cyg, $v \sin i \sim 20$ km s^{-1} (e.g., Figures 9.8, 9.9, 9.10). It is evident that the rotational velocities of Z CMa and FU Ori are consistent with low-mass central stars. In the case of FU Ori, near-infrared interferometry suggests an inclination angle for the disk to the line of sight of $i \sim 55°$ (Malbet *et al.* 2005); adopting this value results in a central stellar mass of $\approx 0.3\ M_\odot$ and a mass accretion rate $\sim 2 \times 10^{-4}\ M_\odot$ yr^{-1} (Kenyon *et al.* 1998; Zhu *et al.* 2007).

The slow rotation of V1057 Cyg and V1515 Cyg requires extremely small central masses unless these objects are observed at a very small inclination. Goodrich (1987) suggested that the circular reflection arcs seen around V1057 Cyg and V1515 Cyg (Figure 9.2) are ovoidal cavities seen nearly along their axis. If these cavities are produced by outflow cavities perpendicular to the disk, parallel to the rotation axis, then these accretion disks may be observed at low inclinations, and the projected rotational velocities can be consistent with masses typical of T Tauri stars.

Assuming that the typical central masses of FU Ori objects are about $0.5\ M_\odot$, maximum disk accretion rates must be $\sim 10^{-4}\ M_\odot$ yr^{-1}. One can then derive a minimum disk mass (prior to outburst) from the length of time of the rapid accretion event. In FU Ori and V1515 Cyg, the estimated outburst lengths ~ 100 yr indicate that the accreted disk mass is $\sim 10^{-2}\ M_\odot$ in one outburst, comparable to the minimum mass solar nebula. For V1057 Cyg the accreted mass during its present outburst will probably be closer to $10^{-3}\ M_\odot$. These values are comparable to the disk masses estimated for T Tauri stars from mm-wave emission (§8.3), but these are merely lower limits to the disk masses, since this is only the material that is accreted over a very short period of time in a single outburst.

It is instructive to consider what the internal disk structure might be like. As mentioned previously, the temperatures in the outbursting region of the disk are high enough that thermal ionization should be high enough for the MRI to operate (§7.5). Using the steady α disk result (7.60),

$$\nu\Sigma = \alpha c_{\rm s} H \Sigma = \frac{\dot{M}}{3\pi}\,, \tag{9.8}$$

and the steady disk temperature distribution (7.55),

$$T_{\rm d}^4 = \frac{3GM\,\dot{M}}{8\pi\sigma R^3}\,. \tag{9.9}$$

Here we have set the factor $[1-(R_{\rm i}/R)^{1/2}]\sim 1$; this approximation makes little difference except at the innermost disk radii, and in any event the inner boundary condition is not well understood (§9.7). We also employ the supplemental equation (7.63),

$$H = c_{\rm s}\left(\frac{R}{v_\phi}\right) = \frac{c_{\rm s}}{\Omega}\,, \tag{9.10}$$

where $\Omega = (GM/R^3)^{1/2}$. Finally, we require a relation between the surface effective temperature $T_{\rm d}$ and the central temperature T at each radius R. Vertically averaging (in z) the opacity, and employing the diffusion approximation,

$$T^4 \simeq T_{\rm d}^4\left(\frac{3}{4}\right)\tau_{\rm R} = \left(\frac{3}{4}\right)T_{\rm d}^4 k_{\rm R}\Sigma\,, \tag{9.11}$$

where the optical depth $\tau_{\rm R}$ through the disk is determined by the Rosseland mean opacity $k_{\rm R}$ (see Frank *et al.* (1992) for details).

With these approximations one can solve for the (vertically averaged) disk structure. Bell and Lin (1994) provide convenient analytic approximations of the opacity for various regimes; in particular, for disk (midplane) temperatures $\gtrsim 10^4$ K,

$$k_{\rm R} \simeq 1.5\times 10^{20}\rho\, T^{-5/2}\,{\rm cm^2\,g^{-1}}\,. \tag{9.12}$$

Using the vertical average $\rho = \Sigma/H$, one can solve for the disk structure for a fixed value of α. After some tedious algebra, the temperature distribution can be written as

$$T \simeq 1.3\times 10^5\,\alpha_{-2}^{-2/9}\,\mu_{0.6}^{5/18}\,\dot{M}_{-4}^{1/3}\,M_{0.5}^{5/18}\,R_{10}^{-5/6}\,{\rm K}\,, \tag{9.13}$$

where $\dot{M}_{-4}$ is the mass accretion rate in units of $10^{-4}\,M_\odot\,{\rm yr^{-1}}$, α_{-2} is the alpha viscosity parameter in units of 10^{-2}, $M_{0.5}$ is once again the mass in units of one-half solar mass, and R_{10} is the cylindrical radius in units of 10 $R_\odot$. Finally, we have set the mean molecular weight $\mu = 0.6$, roughly characteristic of ionized atomic gas.

These results suggest that the innermost disk must be extremely hot in its interior during outburst, far hotter than the surface temperature $\sim$7000 K, as a result of the large optical depths which effectively trap the heat generated by accretion. The internal disk temperature is so large that in the innermost regions the thickness of the disk may not be negligible. For the fiducial parameters at $R = 10\ R_\odot$, $H/R\sim 0.4$; therefore, the thin disk approximations may begin to break down in the inner disk regions. We return to this point when discussing the "missing" boundary layer radiation in §9.7.

The surface density under these assumptions is

$$\Sigma \simeq 5.7\times 10^4\,\alpha_{-2}^{-7/9}\,\mu_{0.6}^{13/18}\,\dot{M}_{-4}^{2/3}\,M_{0.5}^{2/9}\,R_{10}^{-2/3}\,{\rm g\,cm^{-2}}\,. \tag{9.14}$$

This particular disk solution is applicable for temperatures $\gtrsim 10^4$ K. At lower temperatures, the opacity changes character dramatically in a way which may help produce outbursts (§7.5). With the fiducial parameters, $T\sim 10^4$ K occurs at $R_{10}\sim 20\sim 0.87$ AU. The "hot" ($T\gtrsim 10^4$ K) disk mass interior to this radius $R_{\rm out}$ is

$$M_{\rm d}({\rm hot}) \sim 3.4\times 10^{-3}\ \dot{M}_{-4}^{2/3}\,\alpha_{-2}^{-7/9}\,M_{0.5}^{2/9}\left(\frac{R_{\rm out}}{0.87\,{\rm AU}}\right)^{4/3}\ M_\odot\,. \tag{9.15}$$

This result suggests that if $\alpha\gtrsim 10^{-2}$, the disk may store roughly enough mass to fuel one FU Ori outburst within a radius of about 1 AU.

In Chapter 7, we showed that viscous disks evolve on the timescale

$$t_\nu \simeq \frac{R^2}{\nu_{\rm v}} \, . \tag{9.16}$$

With the fiducial parameters, at $R_{\rm out}$ the viscous timescale is approximately $t_\nu \sim 70\,\alpha_{-2}^{-7/9}$ yr, suggesting that the "hot" region of the disk within about 1 AU can in principle account for both the amount of mass accreted and the observed decay timescales of FU Ori accretion events.

A detailed analysis of the IRS spectrum indicates that the accreting region of FU Ori extends to a radius ∼0.5 AU (Zhu *et al.* 2007; Figure 9.7). To explain the decay timescale ∼100 yr at this radius requires a relatively short viscous timescale, and thus a relatively large value of $\alpha \approx 0.1$. This value is somewhat larger than that often seen in numerical simulations, but is more consistent with large values inferred from observations of accreting disks around compact objects (King *et al.* 2007).

These results demonstrate that the inner disks of FU Ori objects must be massive. In FU Ori itself, roughly 0.01 $M_\odot$ must be accreted during a single outburst, with substantial amounts of mass left behind. For reference, the so-called "minimum mass solar nebula" (Chapter 12) contains about 0.002 $M_\odot$ within 1 AU. This suggests that a dead zone model (§7.6) might be appropriate for FUors.

While the long rise time of V1515 Cyg can in principle be explained by a viscous timescale from a large radius, the short rise times of FU Ori and V1057 Cyg cannot be explained in this manner. As discussed in §9.6, thermal instabilities offer a possibility for explaining rapid rises to maximum light.

9.5 Time variability and circumstellar envelopes

Although there is little spectral information available on the rise to maximum light in FU Ori objects, V1057 Cyg has faded substantially since the early 1970s, and its color evolution provides an important clue to physical conditions. After the outburst, the optical and near-infrared spectrum became redder as V1057 Cyg faded, consistent with optical spectra which indicate that V1057 Cyg evolved from an A spectral type near maximum ($T_{\rm eff} \sim 8000$ K (Herbig 1977b)) to a mid-G spectral type ($T_{\rm eff} \sim 6500$ K) at the current epoch. A series of steady accretion disk models with fixed inner radii but decreasing mass accretion rates matches the color evolution with decreasing accretion luminosity fairly well from the optical to wavelengths ∼5 μm, reproducing the observed decrease in amplitude of decay at increasing wavelengths (Kenyon & Hartmann 1991; Figure 9.12).

One observation that steady disk models cannot explain is the observed variation in rotation velocity of V1057 Cyg. Herbig (1989) found that the optical rotational velocity appeared to decrease from about 70 km s^{-1} near peak light to about 45 km s^{-1} in the late 1980s. This is not explicable in terms of steady disk theory; more luminous steady disks have higher temperatures at larger radii, and therefore the optical spectrum should be produced at larger, more slowly rotating regions during outburst. However, time-dependent models for outburst can show the opposite effect, simply because the temperature distribution can deviate substantially from that of a steady disk (Bell *et al.* 1995). While the time-dependent models are suggestive, they are difficult to test in detail using the evolution of the SED, because the disk spectrum is not very much different from that of a single-temperature blackbody

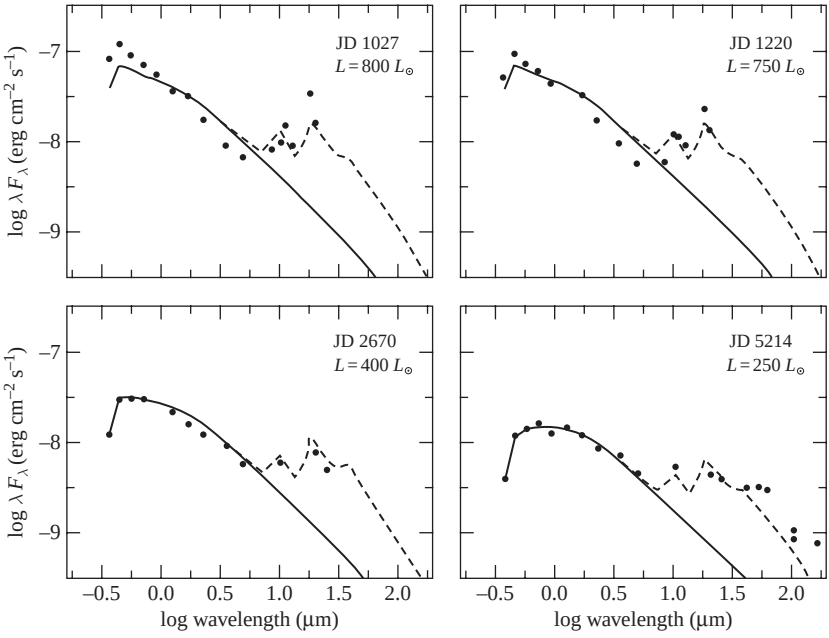

Fig. 9.12. Spectral evolution of V1057 Cyg during decay from maximum light. The central disk becomes redder and can be fitted by a disk model with lower temperatures (solid line) as it fades from maximum. The emission at wavelengths $\lambda \gtrsim 10\,\mu$m decays rapidly, in proportion to the decay of overall system luminosity, consistent with its originating in a circumstellar dust envelope whose emission is powered by absorbing light from the central disk. The dashed line denotes a dusty infalling envelope model, as described in the text. From Kenyon and Hartmann (1991).

over the limited wavelength range observed. Differences in the temperature structure due to time-dependent accretion therefore produce only second-order effects.

As shown in Figure 9.12, the amplitude of variation during the decay in light of V1057 Cyg decreases with increasing wavelength, from the optical through the near-infrared. This can easily be understood in the context of the disk model. The optical wavelengths lie on the blue edge or "Wien side" of the emission from the innermost disk regions, and therefore are the most sensitive to temperature variations. The timescales of variation should also lengthen at longer wavelengths, because the outer regions producing this emission have longer viscous timescales. However, the decay in the fluxes at $\lambda = 10\,\mu$m and $20\,\mu$m is much faster than observed in the near-infrared, but is consistent with the overall change in the system luminosity. Thus, the excess emission at $\lambda \gtrsim 10\,\mu$m is the result of irradiation of the outer regions by the inner disk, consistent with the appearance of silicate emission (Figure 9.5).

The amount of flux emitted in long wavelength radiation is too large to be accounted for by a reasonably flared disk absorbing radiated accretion luminosity and reradiating this energy at longer wavelengths; a circumstellar envelope, presumably a protostellar infalling envelope, with a central outflow cavity provides a better explanation (Kenyon & Hartmann 1991; Green *et al.* 2006; Zhu *et al.* 2008). This model is consistent with interpretations of

the morphology of the scattered light nebulae of V1057 and V1515 Cyg (Goodrich 1987). Moreover, near-infrared interferometry shows that V1057 and V1515 Cyg exhibit much larger sizes than would be expected from a pure thermally emitting disk model (Millan-Gabet *et al.* 2006); scattering off cavity walls on scales of order 5–10 AU would explain these observations. The FUor L1551 IRS 5 is one of the standard objects modeled with infalling protostellar envelopes (Adams *et al.* 1987; Butner *et al.* 1991; §5.4). Thus, many FU Ori objects may have infalling material landing on their outer disks.

9.6 Outburst mechanisms

Mechanisms for explaining the accretion outbursts of FUors fall into three broad classes: an external perturber; accretion of "lumps" or planets; and some kind of inner bottleneck in disk accretion. We consider each of these types of models in turn.

One of the early suggestions to drive accretion was a companion star on an eccentric orbit, whose close passage perturbs the disk, enhancing accretion (Toomre 1985, personal communication; Bonnell & Bastien 1992). One attraction of this mechannism is that most stars are members of multiple systems, and FU Ori itself has a wide companion (Wang *et al.* 2004; Reipurth & Aspin 2004). On the other hand, the companion to FU Ori is far too distant to have caused the outburst in the mid-1930s; moreover, passage probably would have to be at distances of order 10 AU or less, and no evidence of significant radial velocity variation has been seen (Herbig 1977b; Hartmann & Kenyon 1987a; Petrov & Herbig 1992). In addition, successive periastron passages will tend to disrupt the disk, and it is not clear that this mechanism can provide enough outbursts (Bonnell & Bastien 1992 suggest at most three to four recurrences).

If FU Ori disks are highly structured, concentrations of material might fall into the central star and cause outbursts. Vorobyov and Basu (2005, 2006) calculated the evolution of self-gravitating disks in a two-dimensional scheme to follow the evolution for long timescales. They found that young, massive disks would form dense protostellar/protoplanetary mass concentrations that would sporadically accrete into central regions, producing "bursts" of the required magnitude. A concern with this type of calculation is how the disk cooling is evaluated; as discussed in §7.7, whether the disk forms fragments or whether it can readjust relatively smoothly to transport angular momentum is extremely sensitive to the thermal physics, which are difficult to treat correctly.

The second type of mechanism is motivated by the association of FU Ori objects with circumstellar envelopes, high extinction, and their general youth. In this picture, infall from a protostellar envelope has either recently ceased or is still occurring. Unless the disk can accrete at the same rate as material is added to the disk by infall, mass will pile up in the disk until something happens to make disk accretion more efficient. There is no general reason why the spiraling-in of material in a disk should match the free-fall of a protostellar envelope. In particular, if a dead zone is present, piling up of material is essentially guaranteed (§7.6), until some kind of outburst of accretion – perhaps an FU Ori event – occurs.

In any case, the rapid rise times of FU Ori and V1057 Cyg almost certainly require the action of thermal instability, which was originally developed to explain disk outbursts in accreting binary stars. The basic idea behind the thermal instability mechanism has been discussed in detail in many sources (see, e.g., Pringle 1981 and Frank *et al.* 1992); here we provide only an outline. At a radial distance R in the disk, the viscous energy generation, $F_{\rm vis}$, must be balanced by the radiative losses of the disk, $F_{\rm rad}$, in thermal equilibrium.

Integrating the energy equations over the vertical structure of the disk at a fixed radial distance R, and adopting the usual α viscosity treatment, equations (7.22) and (7.59) can be combined to yield

$$F_{\rm vis} = \frac{9}{4}\alpha\Omega\Sigma c_{\rm s}^2 \,, \tag{9.17}$$

while

$$F_{\rm rad} = 2\sigma T_{\rm d}^4 \,. \tag{9.18}$$

We also require the relation (9.11) between the internal disk temperature T and the surface temperature,

$$T^4 \approx \tau_{\rm R} T_{\rm d}^4 \,, \tag{9.19}$$

Combining equations (9.17)–(9.19),

$$\frac{F_{\rm rad}}{F_{\rm vis}} \propto T^3 k_{\rm R}(T,\, P)^{-1} \Sigma^{-2} \alpha^{-1} \tag{9.20}$$

(Kawazoe & Mineshige 1993; D'Alessio 1996).

Now consider a disk annulus initially in thermal equilibrium which is perturbed to a slightly higher internal temperature T. The thermal timescale is much shorter than the viscous timescale, $t_{\rm th} \sim (H/R)^2 t_\nu$ (e.g., Pringle 1981), so it suffices to take $\Sigma \approx$ constant. Then equation (9.20) indicates that the radiative cooling will exceed the viscous heating as long as the opacity does not increase more rapidly with temperature than T^3, and will therefore drive the disk back toward the thermal equilibrium. Conversely, if the opacity increases with increasing temperature faster than T^3, heat is efficiently trapped within the disk, and the surface cooling cannot keep pace with the increasing viscous heating. This leads to a thermal runaway, with the disk temperature increasing rapidly until the character of the opacity changes. Calculations generally indicate that the gas opacity should increase very steeply with increasing temperature for temperatures $\sim$ 3000–10000 K largely because of hydrogen ionization, with the precise range depending somewhat on density. This steep dependence on temperature makes it possible to have thermal instabilities in this temperature range.

To explore the implications of this opacity dependence further, we consider the so-called "S curves" resulting from these assumptions (e.g., Frank *et al.* 1992). The thermal equilibrium equations for a steady-state accretion disk can be recast in terms of the surface (or effective) disk temperature (or mass accretion rates); cf. equation (7.55) and the surface density. Then the loci of thermal equilibrium in the $T_{\rm d}$ vs. Σ plane for a specific disk annulus form an "S"-shaped curve, with a "kink" where the opacity causes thermal instability.

Figure 9.13 shows a schematic S curve typical of the results of detailed calculations. The region above and to the left of the curve corresponds to faster cooling than heating; the region below and to the right of the curve faster heating than cooling. In the limit cycle theory of outbursts, a disk annulus begins in a low accretion rate state at low Σ, lying on the lower branch of an S curve. A perturbation which increases the central temperature tends to drive the disk annulus vertically upward into a region where cooling exceeds heating, so the disk is stable. However, as material piles up in the disk, moving the equilibrium point upwards along the curve, eventually the disk annulus reaches an inflection point (A) in the S curve, at which point a positive temperature perturbation pushes the annulus vertically upward in the log $T_{\rm d}$ vs. log Σ plane, where the disk annulus is thermally unstable. The annulus must jump

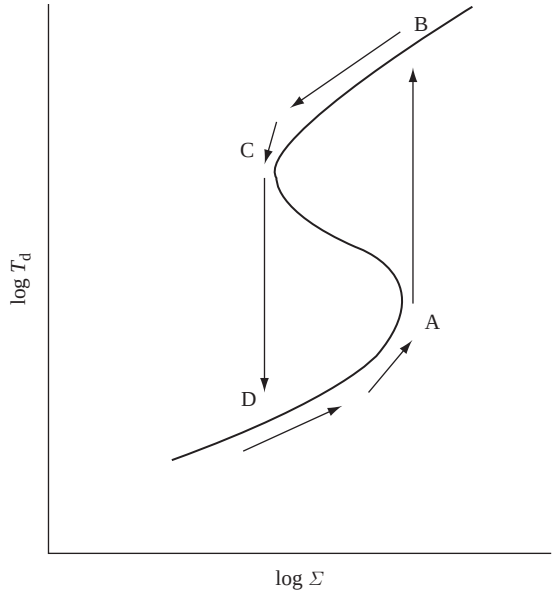

Fig. 9.13. Schematic "S curve" for disk thermal instability, as discussed in the text.

up to the upper branch of the S curve at (B), where the surface (or effective) disk temperature and mass accretion rate are much higher. Eventually, the enhanced accretion onto the central star causes disk material to drain away, dropping Σ to the point (C) beyond which the only stable solution is on the low-accretion rate branch (D).

Thermal instability models have attractions for FU Ori outbursts because: (1) the short rise times observed can be achieved (thermal timescales for the outburst); (2) the predicted inner disk mass fluxes in outburst are $10^{-4}\,M_\odot\,\mathrm{yr}^{-1}$ and the peak surface disk temperature of the disk at this point is just below 10^4 K, in good agreement with observations; and (3) the process can repeat, resulting in multiple events as required by outburst statistics, if there is a mass source which replenishes the disk material accreted during outburst.

A key requirement of the thermal instability model is that of a moderately high accretion rate in the outer disk. At the low temperature end of the unstable regime, the gas opacity is quite low, resulting in an internal disk temperature that is not very much larger than the surface temperature. Thus, we can use the effective temperature at which the disk emits as a useful guide to the regions which can become thermally unstable. Bell and Lin (1994) showed that the critical effective temperature at the transition between the stable and the unstable portions of the S curve is roughly $\sim$2000 K. If we impose a fixed mass accretion rate $\dot{M}_{\mathrm{od}}$ from the outer disk, we can then use this temperature constraint along with equation (7.55) to derive an approximate outer limit radius for the region of thermal instability (Bell and Lin 1994)

$$R_{\mathrm{max}} \approx 20 \left(\frac{\dot{M}_{\mathrm{od}}}{3 \times 10^{-6}\,M_\odot\,\mathrm{yr}^{-1}} \right)^{1/3} \left(\frac{M_*}{M_\odot} \right)^{1/3} \left(\frac{T_{\mathrm{eff}}}{2000\,\mathrm{K}} \right)^{-4/3} R_\odot\,. \qquad (9.21)$$

Disk regions at radii larger than $R_{\max}$ will never become thermally unstable because they cannot become hot enough to enter the required opacity regime. Thus, if there is to be a large amount of mass dumped onto the central star during an outburst, the outer limiting radius of the unstable region must be large; in turn, this tends to require a large outer disk (background) accretion rate.

Lin and Papaloizou (1985) first applied thermal instability models to FU Ori objects and generated optical outburst amplitudes similar to those observed. The eruptions were short-lived, however, and did not produce large infrared outbursts. The reason for this can be seen from equation (9.21). Lin and Papaloizou assumed background mass accretion rates of $\dot{M}_{\rm od} \sim 10^{-7}\, M_\odot\, {\rm yr}^{-1}$, similar to the mass accretion rates of T Tauri stars, but then only the innermost disk regions became thermally unstable, so that very little mass was involved in the eruption; therefore the outburst decayed very quickly. Clarke *et al.* (1990) managed to achieve longer-lasting outbursts with the same low background accretion rate by introducing a very large ($50\times$) perturbation in the surface density. This had the effect of producing a much higher mass flux into the unstable regions, and so triggered an outburst which lasted for ~ 30 yr, qualitatively resembling the decay of V1057 Cyg.

If FU Ori disks are acquiring mass from remnant infalling envelopes at typical protostellar rates $\sim 10^{-6}$–$10^{-5}\, M_\odot\, {\rm yr}^{-1}$ (Chapter 5), this mass source would tend to drive the mass accretion rates of the outer disk closer to values needed to make the thermal instability operate more easily. Kawazoe and Mineshige (1993) first argued that FU Ori outbursts are produced by thermally unstable disks with high mass input rates, and noted the possible correspondence with infall rates. Bell and Lin (1994) and Bell *et al.* (1995) calculated similar models in more detail and showed that many properties of the observed light curves can be reproduced with appropriate model parameters. Bell and Lin (1994) found that models simply fed at the appropriate accretion rate from the outer disk tended to become unstable at inner disk radii first; the instability propagates slowly outward to $R_{\max}$ (see also discussion in Smak (1984)). Under these circumstances, Bell *et al.* (1995) were able to reproduce the slow rise of V1515 Cyg but not the rapid rise times of FU Ori and V1057 Cyg, which require external perturbations.

Unfortunately, many aspects of the thermal instability mechanism depend upon α, which determines the timescales for evolution. Because pure thermal instability is difficult to achieve at large radii, to get enough mass within the region to account for the total mass accreted during outburst, as well as have long viscous decay timescales, Bell and Lin (1994) and Bell *et al.* (1995) required very low $\alpha \sim 10^{-3} - 10^{-4}$. The pure thermal instability model does not seem appropriate now with *Spitzer* IRS data, as models of FU Ori indicate that the high-accretion rate region seen in the absorption spectrum (Figure 9.7) extends out to 0.5–1 AU, much larger than the $\sim$0.1 AU hot region predicted by the model of Bell and Lin (1994).

An interesting modification of the instability picture was introduced by Armitage *et al.* (2001), who invoked the dead zone picture of Gammie (1996a; §7.7) with the new understanding of the MRI to make a composite outburst model. In the picture of Armitage *et al.*, accretion in the massive outer disk is driven by gravitational instability into the inner disk where the MRI is not sufficiently active to prevent material from piling up. However, eventually the surface density becomes so large, and therefore the optical depths become so large that the (presumed) heating by gravitational instability raises the disk temperature, which eventually activates the MRI by thermal ionization. Thus, the dead zone suddenly becomes

active, and a large concentration of material rushes down onto the central star, creating an outburst.

In the Armitage *et al.* model, outbursts lasted a long time ($\sim 10^4$ yr) and had relatively low peak accretion rates $\sim 10^{-5}\, M_\odot\ \mathrm{yr}^{-1}$). However, as they pointed out, if a thermal instability could be activated, timescales could be reduced and outburst magnitudes could be increased. Some preliminary calculations by Zhu *et al.* (2008, in preparation) support this idea. As shown in Figure 9.14, in the low state (upper panels) material piles up at a distance of

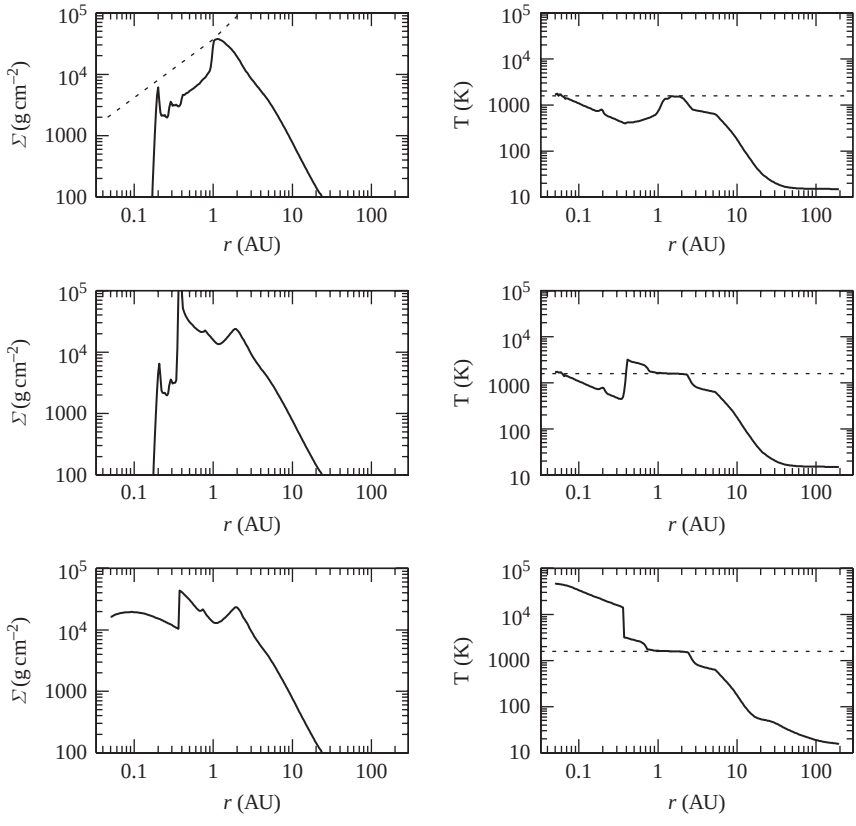

Fig. 9.14. Numerical calculation of a simple dead zone model for FU Ori outbursts. Surface densities (left) and corresponding central temperature structures (right) are shown at selected times during the inert phase (top panels), activation of the MRI (at a temperature $\sim$1500 K, middle panels), and during thermal instability which leads to the outburst in the inner disk (bottom panels). The diagonal dotted line in the upper left panel indicates the approximate surface density above which thermal instability is expected to occur at a high viscosity, while the horizontal dotted lines in the right-hand panels show the temperature at which the MRI is assumed to become activated by thermal ionization. In the upper pair of panels, material piles up in the dead zone due to gravitational torques, with temperatures eventually approaching the MRI activation limit. In the middle panels, the MRI has been activated between a few AU and $\sim$0.5 AU (right middle panel), causing a rapid flow of mass into the inner disk (left middle panel). The bottom panels show the result of thermal instability, producing very high accretion rates. Note the extremely high central temperatures produced in the innermost disk during outburst. From Zhu *et al.* (2008, in preparation).

order 1–2 AU, and gradually approaches the temperature needed for thermal activation of the MRI (here taken to be ∼1500 K). Once the MRI is activated, material rapidly moves in, driving the surface densities up, so that the disk starts to evolve (roughly) along the bottom path of the S-curve (Figure 9.13). Eventually the surface density increases beyond the limit for thermal instability, resulting in a huge jump in central temperatures, approaching 10^5 K in the inner regions (bottom panels in Figure 9.14). Calculations indicate peak accretion rates of $\gtrsim 10^{-4}\, M_\odot\, \mathrm{yr}^{-1}$ and decay timescales of order centuries can be achieved for $\alpha \sim 0.1$, in better agreement with recent observational estimates from compact systems (King *et al.* 2007).

An attractive aspect of this model, at least in general terms, is that the size of the outburst region ∼1 AU seems to be in much better agreement with observations of FU Ori (Zhu *et al.* 2007; Figure 9.7, §9.4). Another promising feature of this mechanism is that it can easily produce repetitive outbursts, as long as material is still being added to the disk by the infalling envelope. The "luminosity problem" of Class I objects (Chapter 5), consistent with direct estimates of current mass accretion rates onto protostars, seems to require that disk accretion rates are often lower than infall rates, as predicted by this model. Instability analysis is complicated, however; further work is needed to test this picture.

One interesting possible consequence of the dead zone picture is that even after infall to the disk ceases, material can still pile up in the dead zone (Chapter 12); thus, smaller and shorter outbursts of accretion might still be generated during the T Tauri phase. Herbig (1977b) drew attention to small optical outbursts observed in pre-main-sequence stars which might constitute a separate class of "EXor" variables, and it is tempting to speculate that the EXor outbursts are produced by instabilities related to piling up material in dead zones.

An idea which combines the two general classes of models is the suggestion by Clarke and Syer (1996) that protoplanets or protostellar companions orbiting in the disk might help to dam up material in the disk, producing conditions suitable for thermal instability (see also Lodato & Clarke 2004). Whether this mechanism requires giant planet formation to occur too rapidly, or whether the thermally unstable region can be large enough to accommodate observations, is an open question.

9.7 The boundary layer problem

The standard boundary layer model (§7.8) predicts large ultraviolet fluxes that are not observed in FU Ori objects (Kenyon *et al.* 1989). The ultraviolet fluxes and spectra of FU Ori and Z CMa show no evidence for appreciable excess emission above that predicted by the disk model. The absence of strong emission lines also points to a lack of boundary layer emission, which, if hotter than 3×10^4 K, and radiating half of the accretion luminosity, should produce enough extreme-ultraviolet photons to ionize a substantial fraction of an FU Ori object's wind; this is inconsistent with observations (Chapter 10).

As discussed in Chapter 8, the standard boundary layer model probably does not apply to T Tauri stars either, because the inner disks are disrupted by stellar magnetic fields. At the high accretion rates of FU Ori objects, one might expect that the dynamic pressure of the disk is sufficient to crush the stellar magnetic fields back up against the outer stellar layers (Shu *et al.* 1994); however, there should be boundary layer emission unless the star is rapidly rotating, unlike typical T Tauri stars.

The most likely explanation for the absence of boundary layer radiation is that FU Ori disks become quite hot internally at small radii, which causes departures from standard thin

disk physics. Returning to the "hot α disk" solution of §7.3, we may combine equations (9.10) and (9.13) to solve for the disk scale height,

$$\frac{H}{R} = \frac{c_s}{v_\phi} \simeq 0.43\,\alpha_{-2}^{-1/9}\,\mu_{0.6}^{-13/36}\,\dot{M}_{-4}^{1/6}\,M_{0.5}^{-13/36}\,R_{10}^{1/12}\,. \tag{9.22}$$

Clarke *et al.* (1990) were the first to suggest that FU Ori disks may be so vertically thick that any radiation generated in the boundary layer is absorbed and diffused in the disk over a distance comparable to $H \sim R$. In this way the heat generated in any boundary layer will be spread over a large area – comparable to the region where most of the viscous disk radiation is generally produced – and therefore no hot emission component will be evident.

More generally, Popham *et al.* (1993, 1996) and Popham (1995) have argued that there may not be a well-defined boundary layer in FU Ori outbursting disks. Keplerian rotation is an adequate approximation for the thin disk only when the gas pressure term in the radial force balance equation (7.99),

$$\frac{v_\phi^2}{R} \approx \frac{1}{\rho}\frac{dP}{dR} + \frac{GM}{R^2}\,, \tag{9.23}$$

can be ignored. This is true only when

$$c_s^2 << \frac{GM}{R}\,, \tag{9.24}$$

which implies $(H/R)^2 << 1$. Since this is probably not true in inner FU Ori disks during outburst, gas pressure forces may become so large that the disk rotates at velocities substantially below the Keplerian velocity because of the pressure support term in equation (9.23). In such a situation the disk rotates more slowly than the local Keplerian angular velocity, and velocity gradients are not steep because of the gas pressure support. The result is that the dissipation of rotational energy is both reduced and less spatially concentrated than the conventional boundary layer.

This model makes the additional interesting prediction that the differential rotation of the disk with radius would be slower than Keplerian. As discussed in §9.3, the observations suggest slightly less differential rotation than Keplerian. While the observations provide some weak support for this picture (Popham *et al.* 1996), the uncertainties in modeling the near-infrared spectra preclude a definite test at this point. Another interesting consequence of this picture is that, even in the absence of magnetospheric interactions or stellar wind spindown, stars may be formed with equatorial rotational velocities less than Keplerian or break-up velocities (Popham 1995).

9.8 Outburst statistics and evolutionary significance

Since FU Ori objects are so rare, their evolutionary significance is somewhat hard to evaluate. Estimates of the star formation rate in the solar neighborhood (Miller & Scalo 1979) suggest that about 2×10^{-2} stars are born per year within 1 kpc of the Sun, where most of the known FU Ori objects are located. If the number of FU Ori outbursts in the same volume is $\sim$5 over the last 60 years, and if every (low-mass) star experiences outbursts, then there must be $\sim$4 outbursts per star. This is clearly a lower limit to the outburst frequency, since many of the more recent FU Oris have been discovered as heavily extincted infrared sources.

If each star experiences a minimum of 4 outbursts, and each outburst accounts for the accretion of $\sim 10^{-2}\ M_\odot$, then the total mass accreted is $\sim 4 \times 10^{-2}\ M_\odot\ \mathrm{yr}^{-1}$, or about 10% of the mass of a typical T Tauri star. Another way of approaching this problem is to note that there are currently ~15 rapidly accreting FU Ori objects within about 1 kpc distance. Not all of these are at maximum light, or as luminous as FU Ori; still, probably $10^{-3}\ M_\odot\ \mathrm{yr}^{-1}$ or more is being accreted in FU Ori objects within 1 kpc, compared with a total mass rate of formation of low-mass stars $M \leq 1\ M_\odot$ of about $6.6 \times 10^{-3}\ M_\odot\ \mathrm{yr}^{-1}$ (Miller & Scalo 1979). This again suggests that ~10% of the mass of low-mass stars is accreted (on average) in FU Ori eruptions. This still leaves the question of when most of a typical star's mass is accreted. One would expect that outbursts or simply rapid disk accretion during Class 0 phases or the most heavily embedded Class I phases account for most of the stellar mass; but demonstrating this convincingly has proved difficult.

10

Disk winds, jets, and magnetospheric accretion

The powerful outflows from pre-main-sequence stars are now understood as a general byproduct of disk accretion. The relation between mass accretion rates and mass loss rates now spans several orders of magnitude by connecting the T Tauri stars with the FU Ori objects. The bipolar nature of these outflows, which begin in the earliest stages of star formation, clearly points to a disk origin. With mass ejection rates of order 10% of the disk accretion rates, outflows represent perhaps as much as half of the energy released by disk accretion.

Neither thermal nor radiation pressures are able to drive the observed rates of mass loss. The inescapable conclusion is that these jets and winds are produced by magnetic acceleration; models show that magnetic fields rotating with the disk naturally produce the necessary collimation along the rotation axis. The precise manner in which this acceleration and collimation takes place is uncertain because the magnetic field structure in the inner disk is not known.

Magnetic fields also play an important role in accretion onto pre-main-sequence stars. The magnetic fields of T Tauri stars are apparently strong enough to hold off disks from the stellar surface; the accreting gas deviates from the disk plane as it falls in along the stellar magnetic field lines, eventually shocking at the stellar surface and producing the observed hot continuum radiation (Figure 8.1). Some of the clearest evidence for magnetospheric accretion comes from the broad, asymmetric emission lines of classical T Tauri stars, which mostly originate in the infalling magnetospheric gas; the infall pattern explains both the velocity widths and the asymmetries of most line profiles. The torques produced by the interaction of the stellar magnetic field with the circumstellar disk can modify the rotation of the central star. This magnetic disk interaction can in principle explain the slow rotation of CTTS relative to WTTS of similar ages. However, how this actually occurs, and whether winds are important as well in stellar spindown, is unclear at present.

This chapter provides an introduction to the complex physical processes involved in disk wind acceleration and magnetospheric accretion.

10.1 Outflows and jets

Many young stars eject powerful, highly collimated, bipolar winds or jets in their early evolution. An enormous literature exists on the ways in which outflows propagate through and interact with the circumstellar medium. The Protostars and Planets V conference volume contains no less than five review articles on the subject (Arce *et al.* 2007; Bally *et al.* 2007; Pudritz *et al.* 2007; Ray *et al.* 2007; Shang *et al.* 2007) and the reader is advised to

consult these articles for details. Here we present only a brief outline of outflows, as the main focus for this book is how accretion and ejection are related at the source.

One of the earliest indications of outflow activity came from the recognition that the Herbig–Haro objects (Herbig 1951, 1952; Haro 1952, 1953) were produced by high-velocity material shocking with the ambient interstellar medium (Schwartz 1975). The discovery of highly collimated emission jets (Dopita *et al.* 1982; Mundt & Fried 1983) added to the picture, as many jets have "knots" of emission similar or identical to those of HH objects. Optical emission lines indicate that the jet gas is being heated to temperatures of several thousand degrees or more, probably mostly by shocks (Schwartz 1975). The detailed motions within jets which can produce shock waves and individual emission knots are complex (Raga 1995; Masson & Chernin 1993); it is likely that time-variability of the ejection is at least partly responsible for some of the jet shocks and knots (Reipurth 1989; Raga 1995). The Herbig–Haro objects may be emission knots in jet material, or emission in the wind as it shocks with the interstellar medium, or emission from interstellar gas in the shock wave (often a bow-shock) which propagates ahead of the jet (cf. Hartigan *et al.* 1987).

Highly collimated optical jets from young stellar objects are often detected in forbidden emission lines, principally [O I] $0.6300, 0.6363\,\mu$m and [S II] $0.6717, 0.6731\,\mu$m. These jets may extend for distances of 10^3–10^4 AU or more from their source (e.g., Figure 1.4), and a few have been traced to distances of $\sim$1 pc from the source (Bally & Devine 1994). Both spectroscopic observations of radial velocities and proper motions of "knots" or bright emission spots in the jets show that the optical emission lines are produced by material flowing outward at $\sim$100–300 km s^{-1}. While optical observations often trace only one side of the jet or outflow (the near, blueshifted side), observations of near-infrared emission in molecular hydrogen and radio-wavelength observations, which are unaffected by extinction, demonstrate that outflows are bipolar (e.g., Bachiller 1996).

Another piece of evidence for rapid mass loss from young objects has come from observations of high-velocity molecular gas in star-forming regions (e.g., Snell *et al.* 1980). These molecular "outflows" are ambient material that has been swept up by the higher-velocity winds and jets. Most of the kinetic energy is quickly dissipated and radiated away as the high-velocity material shocks with the ambient molecular medium. The time-integrated input momentum inferred from the molecular gas motions indicates that outflows from young stars carry away much more momentum than is contained in the radiation field of the central source (Lada 1985), pointing to the need for another acceleration mechanism.

It is important to understand whether the observed jets essentially represent the entire mass ejection, or whether they are simply the dense axis of a more widely diverging wind present in addition to the jet (Shu *et al.* 1995). Reversing the argument presented in the first edition of this book, it now seems clear that jets do not constitute the entirety of mass ejection. Outflows, though relatively collimated, are much wider in opening angle than jets. Most outflow cavities are much wider than the jets aligned along their axis. A clear example of this is L1551 IRS 5, the first pre-main-sequence object with a demonstrated bipolar outflow (Snell *et al.* 1980). As shown in Figure 10.1, the CO outflow is only moderately collimated, as also indicated by the optical cavity (Figure 5.9), while the jets (right panel of Figure 10.1) are much more highly collimated.

Efforts have been made to explain the wider cavities by invoking wiggling or precessing jets, but this does not seem to be a general explanation, given the very long, highly collimated trains of HH objects seen in some cases (Bally & Devine 1994). Another suggestion is

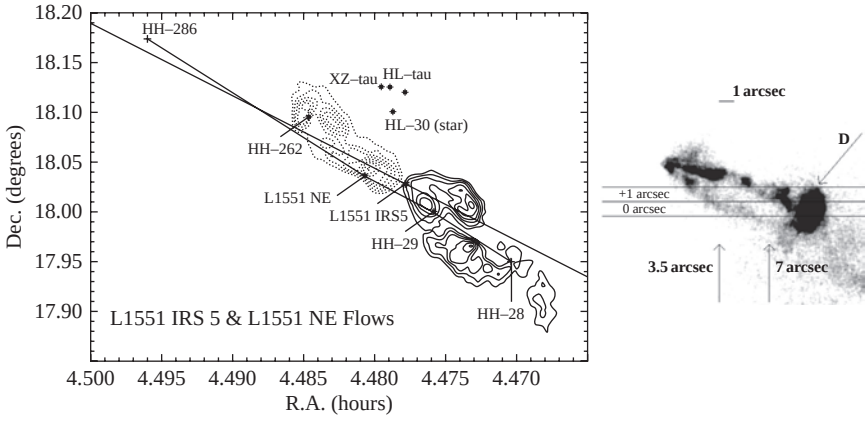

Fig. 10.1. Left: The L1551 outflow as seen in ^{1}2CO. The southwest lobe (solid contours) represents blueshifted emission from -6 to 6 km s^{-1}, and the northeast lobe is redshifted emission from 7 to 21 km s^{-1}. The blueshifted emission fits nicely within the optical cavity as seen in Figure 5.9. (This figure also shows that the region is complex, with additional sources of outflow tending to confuse the picture.) Right: On small scales as seen with HST, the binary FU Ori systems exhibit a pair of highly collimated jets, much narrower than the optical cavity/CO outflow. From Moriarty-Schieven *et al.* 2006 (left) and Fridlund and Liseau (1998) (right).

that multiple jets in the same region contribute to the width of the cavity. This occurs in L1551 IRS 5 (Figure 10.1), but this is unlikely to be a general mechanism, nor can it explain relatively simple cavity geometries. Still another suggestion is that ambient mass off-axis from the jet can be "entrained". There must be some lateral transfer of momentum from the jet as it passes through the molecular medium, which could explain especially narrow outflows, but this seems unlikely to explain many cavities with very large opening angles.

In particular, the T Tauri system provides significant evidence of wind interaction with its large-opening angle cavity (Stapelfeldt *et al.* 1998b). Saucedo *et al.* (2003) mapped out the ultraviolet molecular hydrogen emission along the rims of the cavity (see also Walter *et al.* 2003). This emission is produced by fluorescence with the strong Lyman α emission of the central source (or perhaps of a local shock), *provided* that the H_2 is at temperatures >1000 K to populate the required lower level. The distances at which this emission is seen, >100 AU, are far too large for radiation to account for the necessary heating; the most likely explanation for the molecular hydrogen excitation is that a wide-angle wind produces an oblique shock as it shapes the cavity, resulting in a warm layer of H_2 which can fluoresce.

Perhaps the most direct evidence for wider-angle outflow arises from what appears to have been an ejection event in the XZ Tau binary system. As shown in Figure 10.2, HST images show an expanding bubble in the same direction as a previously detected jet; there are knots of emission which may represent the (narrow) jet within the bubble.

Thus, the observational evidence indicates that jets are accompanied by at least a moderately expanding, wider-angle outflow, a picture which has advantages in terms of understanding the stability of these structures (§10.9). The jets are undoubtedly denser than any surrounding wind, almost certainly exhibit the highest ram pressures ρv^2, and thus will

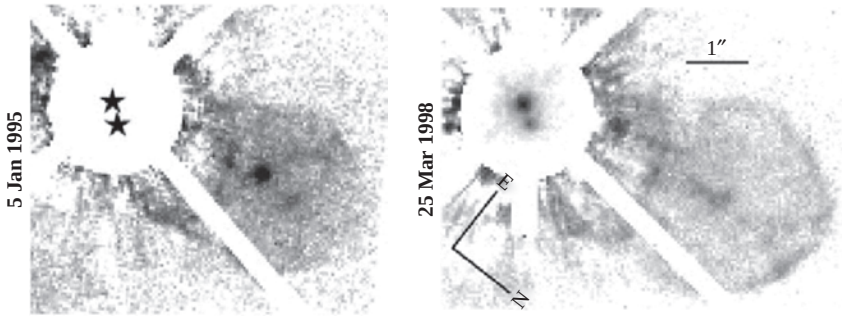

Fig. 10.2. Images of XZ Tau in R-band (0.675 μm) with point-spread function subtraction of the central binary; the 1998 data shows a short exposure inserted into the center. The indication is that of a broad bubble of shocked gas expanding at about 150 km s^{-1} (projected velocity) in the same direction as a previously known jet. The knots bisecting the bubble may be in the collimated jet. From Krist *et al.* (1999).

propagate through the ambient medium most successfully. The jets probably also contain most of the kinetic energy of the outflow as well. Whether jets represent most of the momentum of the flow is another question. The "pencil-beam" large-scale jets seem too collimated to produce much global interaction with the surrounding molecular cloud; a wider-angle, less dramatic outflow could be more important in dispersing molecular gas (Chapter 2).

10.2 P Cygni profiles

Observations with increasing spatial resolution make clear that jets arise near to the central regions of the star-disk system (Ray *et al.* 2007, and references therein). Clues to the nature of the mass ejection on scales too small to resolve can be developed from an analysis of line profiles.

The observational study of wind acceleration relies on the interpretation of velocity shifts and asymmetries in absorption and emission lines. Figure 10.3 illustrates some basic ways in which velocity fields and outflow geometry produce the so-called "P Cygni" profiles. The particular situation illustrated is that of spherically symmetric outflow from a star. The expanding high-velocity outflow produces a broad line profile. Region (1) tends to contribute excess emission toward the observer, either because photons are created in the line, or because stellar photons are scattered into the line of sight. This region produces both blueshifted and redshifted emission. Region (2) would contribute emission at the highest redshifts, but is occulted by the stellar disk. In the case of an optically thick line illustrated in the bottom left-hand panel of Figure 10.3, material in region (3) absorbs light from the star, producing a blueshifted absorption feature. The net result is an asymmetric line profile, with redshifted emission and blueshifted absorption – the canonical P Cygni profile observed in many hot stars.

Variations on this situation can be imagined which change the profile shape. For example, suppose that the star is surrounded by an opaque disk (right-hand panel of Figure 10.3). Then the region of occultation (2) becomes much larger. One can see that the effect of a disk at most inclination angles will be to eliminate the emission preferentially that arises from redshifted material; in the limit where the opaque inner disk edge joins the star, and the disk

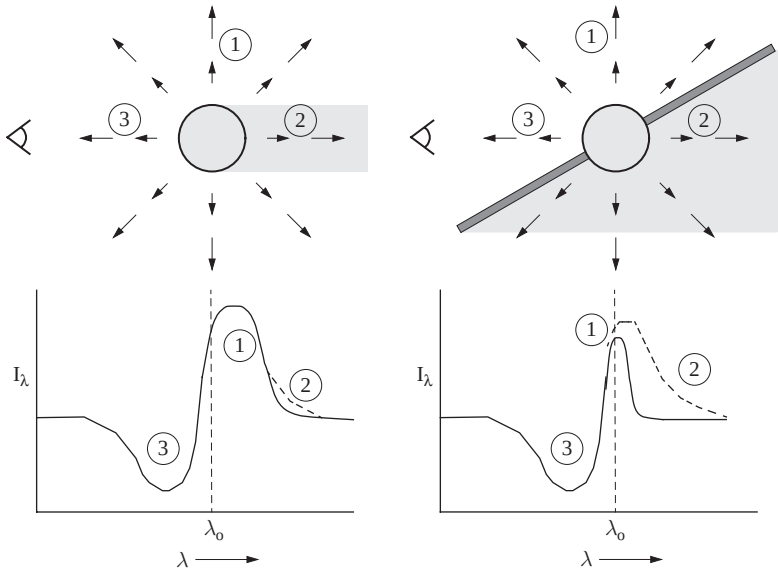

Fig. 10.3. Schematic diagram of geometry responsible for producing P Cygni wind line profiles (see text).

lies in the plane of the sky as seen by the observer, all of the redshifted emission will be occulted, and all that will be left is blueshifted absorption. If the spectral line is optically thin, then the absorption of star light will be negligible. Depending upon the physics of line excitation, region (3) may produce blueshifted *emission* rather than absorption; again, the disk will hide the redshifted material.

The FU Ori objects and the T Tauri stars both show evidence for this disk occultation. In the case of FU Ori systems, the blueshifted spectral features are seen mainly in absorption in permitted atomic transitions, while in the T Tauri stars the occultation is most apparent in blueshifted emission from forbidden (optically thin) lines.

Figure 10.4 illustrates hydrogen Hβ and Na I resonance line profiles in four FU Ori objects. Broad blueshifted absorption is observed, indicating mass ejection at several hundred $\mathrm{km\,s^{-1}}$. There is no evidence for redshifted emission or absorption, indicating that unless the Earth is in some privileged place of observation, occultation of the redshifted outflow must be occurring. This is consistent with the FU Ori objects being optically thick accretion disks.

In contrast, the $H\alpha$ profiles of typical T Tauri stars illustrated in Figure 10.5 (see also Figure 8.15) exhibit qualitatively different profiles. While there is often evidence of a wind from blueshifted absorption, emission wings typically extend out to even larger blueshifted velocities, unlike the situation outlined in Figure 10.3. We now understand the origin of these so-called "type III" P Cygni profiles in T Tauri stars; they are a combination of blueshifted emission arising from the infall region, coupled with substantial Stark line broadening which produces broad wings for very optically thick lines (Muzerolle *et al.* 1998a, 2001). Other spectral lines show redshifted absorption characteristic of magnetospheric infall (§8.4,

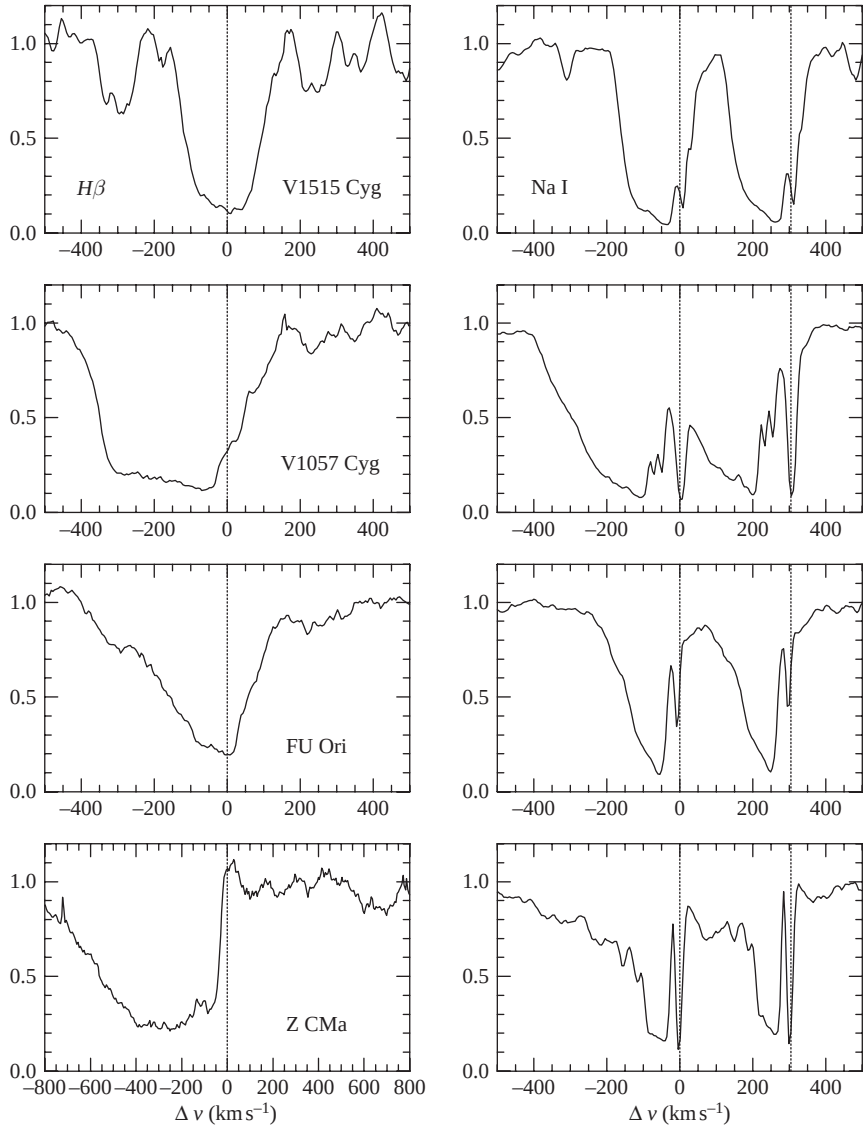

Fig. 10.4. $H\beta$ (left-hand panels) and Na I (right-hand panels) line profiles observed in four FU Orionis objects. The dotted lines indicate the rest velocities for $H\beta$ and the two Na resonance lines. The narrow absorption components of the Na I lines at rest velocities correspond to absorption in the adjacent cold, relatively slowly moving interstellar medium. From Hartmann and Calvet (1995).

10.12). This initially confusing situation – of detecting both infall and outflow simultaneously – is now thought to be the result of mass ejection exterior to the magnetosphere (§10.12); whether outflow or infall dominates the particular line profile depends upon the excitation and optical properties of the particular transition.

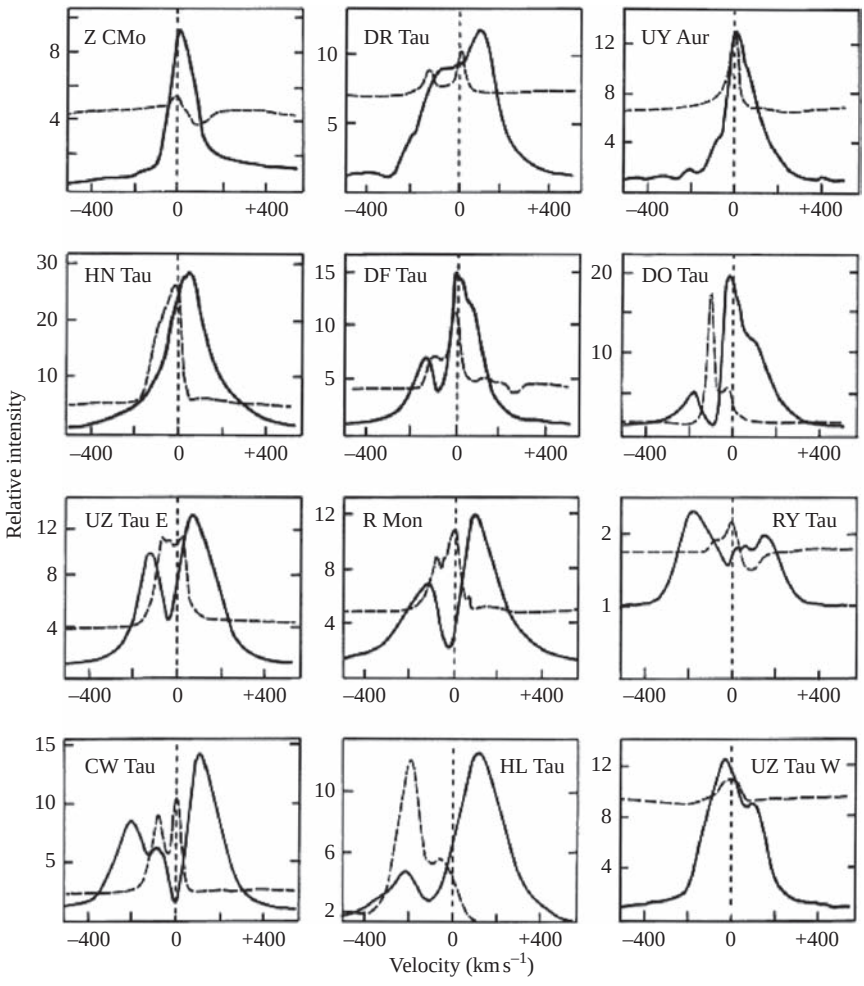

Fig. 10.5. Comparison between Hα profiles (solid curves) with [O I] λ 6300 Å profiles (dashed curves) for some representative T Tauri stars. (Z CMa is a complex close binary consisting of an FU Ori object (Chapter 9) with a highly extincted luminous source that is probably a Herbig Be star.) Blueshifted absorption in $H\alpha$ is often detected, and in many cases corresponds with blueshifted [O I] *emission*; this suggests that the wind/outflow is responsible for both the forbidden line emission as well as the permitted-line absorption. From Edwards *et al.* (1987).

10.3 FU Ori disk winds

Observations demonstrate that the wind of FU Ori itself arises from the surface of the accretion disk. This is possible because wind velocity shifts can be detected in many weak absorption lines formed in the outer disk atmosphere. Because there are many available lines, with widely varying strengths, it is possible to follow the wind as it accelerates away from the disk photosphere.

Figure 10.6 shows a segment of the optical spectrum of FU Ori at high spectral resolution. For comparison the spectrum of another FU Ori object (V1515 Cyg), artificially broadened

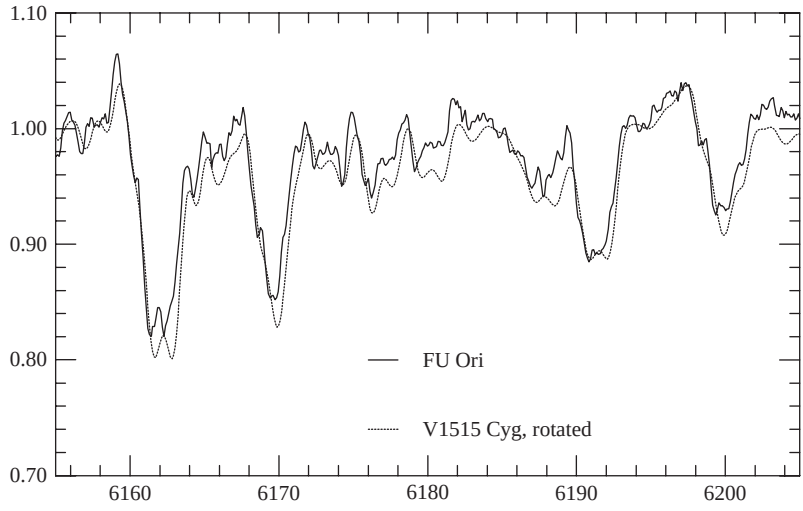

Fig. 10.6. A comparison between the observed spectrum of FU Ori near 6200 Å and a disk model spectrum (dotted line) synthesized by rotationally broadening the V1515 Cyg spectrum (see text). From Hartmann and Calvet (1995).

to match the rotational velocity of FU Ori, is included. Although the absorption features match up reasonably well, the strong lines and blends near 6162, 6170, and 6191 Å are blueshifted in FU Ori relative to the V1515 Cyg spectrum. Apparently, the wind of FU Ori is so strong that the upper photosphere is actually moving outward at detectable rates. Even with this expansion, the blend near 6162 Å is *double-peaked*; this implies that the material is *rotating* like the disk (cf. §7.2) as it expands outward.

Consider what might be observed from the differentially expanding atmosphere of an FU Ori accretion disk. Weak absorption lines, formed near the disk photosphere, will exhibit the "doubled" line profiles produced by disk rotation (§9.3; Figure 9.8), as shown in the uppermost profile (dotted line) in the upper panel of Figure 10.7. Stronger lines will be formed further up in the disk atmosphere, farther from the disk midplane. The atmosphere is cooler in these outer layers, and therefore the absorption profiles of these lines will be deeper, as in a normal stellar atmosphere. Since the gas density is lower at higher levels in the atmosphere, conservation of mass for a (roughly) steady wind implies a larger expansion velocity. The net result is that stronger lines are both deeper and more blueshifted. If the velocity shift due to expansion is small compared with the rotational velocity, the combination of both motions will result in a profile that is dominated by rotation. If the lines are strong enough that the level of line formation in the disk atmosphere is very high, and the velocity of expansion dominates the line profile, the result will be a P Cygni profile with little or no evidence of rotation (e.g., Figure 10.3). Therefore, absorption lines formed in a disk wind should show increasing blueshifts with increasing line strength.

To explore this predicted behavior in more detail, Calvet *et al.* (1993) modeled the FU Ori disk atmosphere as a series of disk annuli, each with its own independent atmosphere; this is justifiable in the plane-parallel limit. The temperature structure of the atmosphere for each annulus was calculated for vertical radiative equilibrium with the appropriate surface

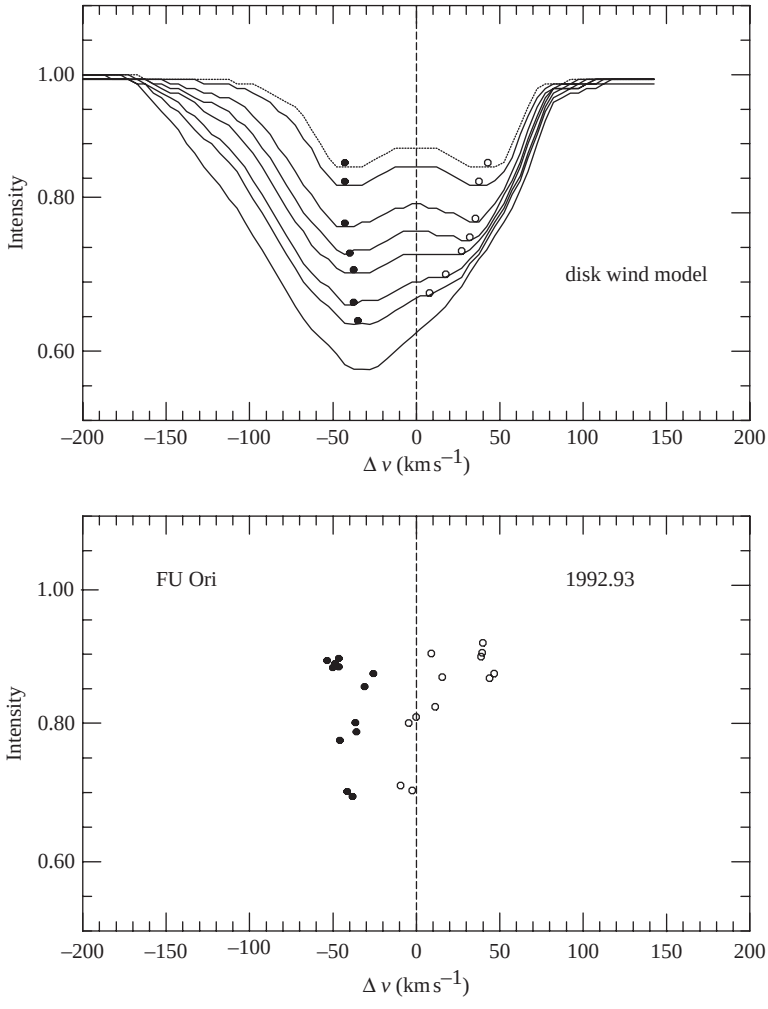

Fig. 10.7. Upper panel: Predicted disk wind profiles for a series of lines with different strengths, taken from Calvet *et al.* (1993). Filled and open circles mark the positions of the absorption dips for the blue and redshifted components, respectively. Lower panel: Velocity shifts of absorption components in FU Ori, from Hartmann and Calvet (1995). See text.

flux at each radius. To make the results more realistic, the effects of ionization balance were included. Profiles were calculated for a series of typical Fe I lines of varying oscillator strengths assuming local thermodynamic equilibrium or LTE (Mihalas 1978), and adopting a linear acceleration of the expanding disk atmosphere combined with Keplerian rotation (see Calvet *et al.* 1993 for details).

The results of these calculations are shown by the sequence of line profiles in the upper panel of Figure 10.7. This sequence quantitatively demonstrates the profile evolution described above. Atomic spectral lines of progressively greater strength compose a sequence of line profiles, with increasing line depth accompanied by an increasing blueshift of the

absorption. An interesting feature of the calculation in the upper panel of Figure 10.7 is that the absorption component on the red side of the line becomes increasingly blueshifted, as would be expected intuitively, but the blue absorption component does not appear to shift much in velocity. This is because the blue component is not an actual feature in the wind velocity profile, but instead is due to the convolution of the rotational broadening profile with the wind expansion profile (Calvet *et al.* 1993).

One simple way of characterizing this evolution of line profiles with increasing line strength is to consider the positions of the two absorption components in the line profiles, marked in the upper panel of Figure 10.7 by the open circles for the redshifted component and filled circles for the blueshifted component. As the line strength increases, the line becomes deeper and so the two absorption components appear at lower residual intensities; the line becomes more blueshifted, and the two absorption features move together. Eventually, for lines strong enough to be formed at a sufficiently high atmospheric level where the expansion velocity dominates the rotation, the two absorption components merge into one blueshifted feature.

This qualitative behavior of line profiles has been observed in FU Ori. The most detailed results were presented by Petrov and Herbig (1992), who measured the profiles of a large number of relatively unblended lines. Petrov and Herbig showed that as the depth of the line increased, the red absorption feature moved to more negative velocities, the blue absorption component remained at almost fixed radial velocity, and the centroid of the line profile became blueshifted, in qualitative agreement with the disk wind model prediction. The lower panel in Figure 10.7 shows confirming measurements of the absorption dip positions (Hartmann & Calvet 1995). The correspondence between the model predictions and the observed dip positions is quite good. The "tomographic" view of the wind obtained by isolating lines of different strengths clearly demonstrates the evolution of the flow from pure Keplerian rotation to outflow, and represents the *only* situation at present where the wind can definitely be shown to arise from the accretion disk. (This effect is not observed in other FU Ori objects such as V1515 Cyg, probably because they have lower mass loss rates; Hartmann & Calvet 1995.)

10.4 T Tauri winds

As discussed in §10.2 (Figure 10.5), the line profiles of $H\alpha$ and other strong lines demonstrate the existence of mass loss in CTTS, along with the presence of blueshifted forbidden-line emission. In addition to the correlation of mass loss with mass accretion, we know that strong mass loss is only detected when inner disks are present, further cementing the relation between disk accretion and outflows.

Some T Tauri stars exhibit spatially resolved jets (e.g., Figure 1.7), which can be observed in optical emission lines such as $H\alpha$, and particularly in forbidden [O I] 6300, 6363 Å and [S II] 6717, 6731 Å emission lines. Optical observations of T Tauri stars have been made with increasing spatial resolution using HST (Ray *et al.* 2007, and references therein), showing that jets can be traced back to the limits of the spatial resolution, typically of order 10–30 AU (Kepner *et al.* 1993; Burrows *et al.* 1996; Ray *et al.* 1996).

An important peculiarity of the forbidden-line profiles is the presence of high-velocity and low-velocity components. As shown in Figure 10.8, stars with large near-infrared excesses (generally rapid accretors) often show two peaks: a high-velocity component with blueshifts of hundreds of $\mathrm{km\,s^{-1}}$, and a low-velocity component, with a blueshift of only $\sim$5 $\mathrm{km\,s^{-1}}$

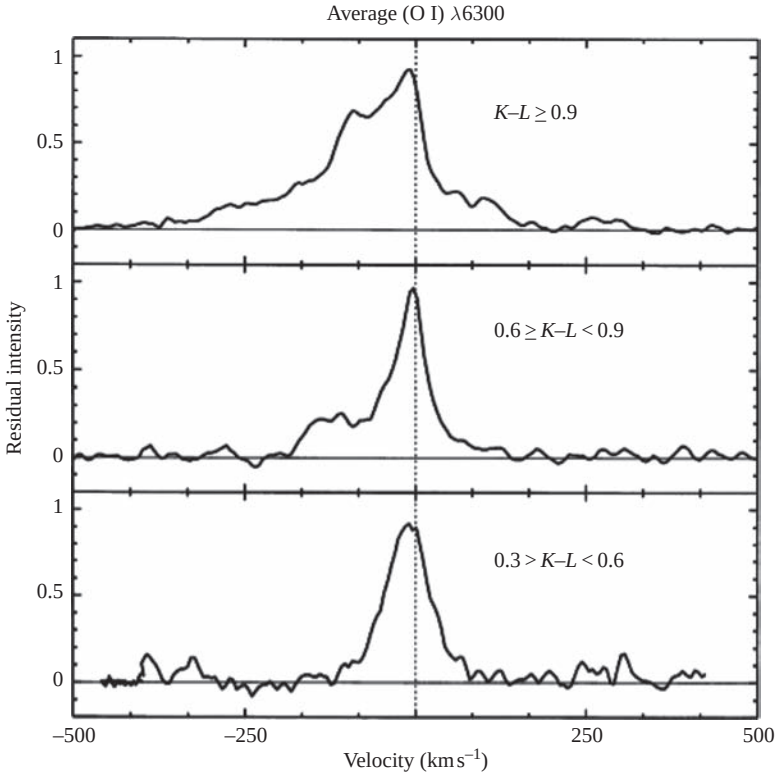

Fig. 10.8. Average [O I] line profiles for CTTS as a function of the magnitude of their near-infrared excess. Stars with large near-IR excess emission, tending to be the most rapidly accreting objects, often exhibit two peaks in [O I] at high and low velocities (upper panel); the high-velocity component is generally associated with a spatially resolved jet. As the magnitude of infrared excess decreases, the high-velocity emission decreases substantially, while the low-velocity component remains. Modified from Hartigan *et al.* (1995).

(Hartigan *et al.* 1995). As the infrared excess decreases (which is usually correlated with a decreasing accretion rate), the high-velocity "jet-like" component decreases in strength, while the low-velocity component tends to remain. Another indication of the discrete nature of these components is that density diagnostics indicate that the low-velocity component exhibits larger electron densities than the high-velocity component (Hartigan *et al.* 1995). The implications of the low-velocity outflow are unclear; they may indicate a wind originating at some significant radial distance in the disk, while the high-velocity jet comes from inner disk regions (Hartigan *et al.* 1995; Kwan & Tademaru 1995).

10.5 Mass loss rates

Mass loss rates have been estimated using the profiles of optically thick permitted spectral lines, with special emphasis on analyzing the blueshifted absorption produced by expansion. Usually it suffices to adopt the Sobolev approximation (§5.8) to calculate the optical depth in terms of physical quantities. In this approximation it is assumed that the

velocity gradients in the expanding atmosphere are large, and therefore only a narrow volume in the wind is responsible for the line absorption and emission at a given velocity shift (see, e.g., Rybicki & Hummer 1978).

In the simplest possible case, that of an absorption line with negligible local emission, the profile is just proportional to $I_c \exp(-\tau_\nu)$, where I_c is the background continuum and τ_ν is the line optical depth at frequency ν. (The background radiation field may be geometrically complex as a result of star, accretion shock, and even disk emission.) Consider a spectral line with a Gaussian line profile of intrinsic velocity width $v_{\rm th}$ due to thermal Doppler motions and any other local velocity broadening. Then the line absorption profile per absorber in the relevant energy level is (Mihalas 1978)

$$\alpha_\nu = \frac{\pi e^2}{mc} \frac{f}{\pi^{1/2} \Delta\nu_{\rm D}} \exp\left[-\left(\frac{\Delta\nu}{\Delta\nu_{\rm D}} \right)^2 \right] , \tag{10.1}$$

where $\Delta\nu_{\rm D} = \nu_o v_{\rm th}/c$ and f is the oscillator strength. Assuming that the absorbing number density N_1 remains constant over the narrow region of interest, located along a line of sight coordinate z at position z_o, the Sobolev optical depth is

$$\tau_v \simeq \int dz\, \alpha_\nu\, N_1 = \frac{\pi e^2}{mc}\, f\, \frac{c}{\nu_o}\, \frac{N_1(z_o)}{|dv/dz|_{z_o}} . \tag{10.2}$$

The position z_o is defined as the point at which the velocity along the line of sight is such that the line is shifted to the frequency of interest, i.e., $\nu = \nu_o(1 + v/c)$. The intrinsic line width $v_{\rm th}$ drops out in this approximation, because only atmospheric regions with velocity shifts $\sim \pm v_{\rm th}/2$ of the central velocity contribute to the optical depth integral along a given line of sight; therefore any increase in thermal velocity width, which reduces the opacity per unit distance, correspondingly increases the distance over which the line can effectively contribute to the absorption, and thus the optical depth at v is unaffected. (This approximation breaks down if the line is so optically thick that damping wings become important.)

An estimate of the wind absorbing optical depth τ_v from analysis of the line profile then yields an estimate of the wind mass loss rate,

$$\dot{M}_{\rm w} \sim (2) \times da\, v\, \mu m_{\rm H}\, N_{\rm H}(v) , \tag{10.3}$$

where the hydrogen number density is

$$N_{\rm H}(v) \propto \tau_v\, |dv/dz| \left(\frac{N_{\rm H}}{N_1} \right) . \tag{10.4}$$

The factor of (2) is intended to account for the bipolar nature of the flow (other treatments often assume spherical wind expansion, so that $2da = 4\pi R^2$). The wind velocity as a function of radius can be prescribed by differing laws or theories; typically, it is assumed that the wind accelerates to its terminal velocity over a few stellar radii in distance.

This method has proved to be difficult to apply either because the lines are too optically thick, or arise from a non-dominant stage of ionization. Combining results for lines with differing excitation can circumvent these problems to some extent. One of the best combinations to use is one or more Balmer lines with the Na I resonance lines; the Balmer lines are more sensitive to temperature than the Na I lines, while the latter more sensitive to electron density. Unfortunately, the number of T Tauri stars with detectable blueshifted Na I (wind) absorption is small. Natta and Giovanardi (1990) derived mass loss rates for a few T Tauri

stars with strong Na I resonance line absorption, finding a range of $\sim 10^{-8}$–$10^{-7}\ M_\odot\ \mathrm{yr}^{-1}$ in reasonable agreement with the strongest mass ejection rates inferred from forbidden emission lines (see p. 226). This method is easier to apply to the FU Ori objects, which have much stronger Na I lines because of the higher mass loss rates (Figure 10.4). In this manner Croswell *et al.* (1987) estimated the mass loss rate of FU Ori to be $\sim 10^{-5}\ M_\odot\ \mathrm{yr}^{-1}$, i.e., an order of magnitude smaller than the disk accretion rate; others were also estimated by Calvet (1998). Overall, the results show that FU Ori objects have much higher mass ejection rates than T Tauri stars.

The high-velocity blueshifted forbidden-line emission of many T Tauri stars can be analyzed to estimate mass ejection rates (e.g., Hartigan *et al.* 1995). The forbidden lines are optically thin and so the total luminosity is proportional to the number of emitting atoms in the observed volume,

$$L_{12} = \int dV\, N_2(\mathrm{A})\, A_{21} E\,, \tag{10.5}$$

where the subscripts 1 and 2 refer to the lower and upper atomic levels of the spectral line being observed in volume V, $N_2(A)$ is the number density of atoms of species A in the upper level 2, A_{21} is the Einstein spontaneous emission probability for the transition, and

$$E = h\nu_{21} \tag{10.6}$$

is the energy of the observed spectral line. If observations are limited to a region of radial extent R_w, and the expansion velocity v_w is estimated from the radial velocity shifts, the (one-sided) mass loss rate is

$$\dot{M}_\mathrm{w} \sim M(\mathrm{A})\frac{v_\mathrm{w}}{R_\mathrm{w}} \sim \frac{v_\mathrm{w}}{R_\mathrm{w}} \int dV\, N_2(\mathrm{A}) \left(\frac{N_\mathrm{A}}{N_2}\right)\left(\frac{N_\mathrm{H}}{N_\mathrm{A}}\right) \mu m_\mathrm{H}\,, \tag{10.7}$$

where $M(\mathrm{A})$ is the mass of species A in the volume under observation, $N_\mathrm{A}/N_\mathrm{H}$ is the abundance of atom A relative to hydrogen, and μ is the mean molecular weight. The mass loss rate can then be determined from observations of the forbidden-line luminosity, if an estimate of the fractional abundance N_2/N_A can be made.

It is often possible to assume that the only processes involved in producing the line emission are collisional excitations between the lower level 1 and the upper level 2, along with spontaneous radiative decay. This is especially true if level 1 is the ground state in which most of the ions reside at any instant. Under these assumptions the equation of statistical equilibrium can be written as

$$N_1 N_\mathrm{e} C_{12} = N_2(\mathrm{A}_{21} + N_e C_{21})\,, \tag{10.8}$$

where C_{12} and C_{21} are the collision rates and N_e is the density of electrons responsible for inducing the collisional transitions (Spitzer 1978). Because the distribution function of the colliding electrons can generally be taken to be Maxwellian, the collision rates are related by the principle of detailed balance (Mihalas 1978),

$$C_{12} = \left(\frac{N_2}{N_1}\right)^* C_{21} = \left(\frac{g_2}{g_1}\right) \exp\left(\frac{-E}{kT}\right) C_{21}\,, \tag{10.9}$$

where the starred quantities refer to the LTE ratios, and the g_i are the statistical weights of the atomic levels. With this result one can write

$$L_{12} = \int dV \, \frac{N_1 N_e \, C_{21} \left(\frac{g_2}{g_1}\right) \exp\left(\frac{-E}{kT}\right)}{1 + N_e \frac{C_{21}}{A_{21}}} \, E \, . \tag{10.10}$$

The collision rate is a function of temperature; usually it is written

$$C_{21} = \frac{8.63 \times 10^{-6} \, \Omega_{21}}{g_2 \, T^{1/2}} \, \mathrm{cm^3 \, s^{-1}} \, , \tag{10.11}$$

where Ω_{21} is usually a slowly varying function of temperature.

To determine mass loss rates we require the number of ions in state 1 relative to the total atomic abundance, N_1/N_A, the gas temperature, and the electron density. Since level 1 is often the ground state of ion A for strong forbidden lines, it is sometimes possible to assume that most of the atoms of species A are in the ground state, i.e., $N_1 \sim N_A$, *if* this is the dominant stage of ionization for A. For example, [O I] and [S II] are likely to be dominant stages of ionization provided the gas temperature is not $>>10^4$ K. This conclusion must be modified for the time-dependent ionization structure of shocks, in which the ionization states are not unique functions of the local density and temperature but depend upon initial shock conditions as well (cf. Hartigan *et al.* 1994). The observed emission in these forbidden lines is likely to be dominated by only those regions where the conditions can produce $N_1 \sim N_A$. This in turn tends to restrict the temperature range relevant to the emission accordingly, although there is no guarantee that *all* of the wind is characterized by these temperatures.

The line emission (equation (10.10)) generally depends upon the electron density. In some cases it is possible to make an independent estimate of the electron density by comparing the emission from different lines. For many T Tauri stars, the ratio of the [S II] 6717, 6731 Å forbidden lines indicates emission in the high-density limit $N_e C_{21} >> A_{21}$, in which case the dependence on electron density is eliminated,

$$L_{12} \sim \int dV \, N_1 A_{21} \left(\frac{g_2}{g_1}\right) \exp\left(\frac{-E}{kT}\right) \, E \, . \tag{10.12}$$

Figure 10.9 shows T Tauri mass loss rates estimated from the [O I] 6300 Å and 6363 Å emission lines, using equations (10.7) and (10.10), and including constraints on electron densities from the [S II] lines (Hartigan *et al.* 1995). To derive these mass loss rates, Hartigan *et al.* adopted an emitting temperature of ∼8000 K for the collision rates, based on results from shock models for jets which suggest that this is the characteristic (post-shock) temperature where most of the emission is radiated. Since $E/k \sim 2.2 \times 10^4$ K for the [O I] lines, the derived mass loss rates are not highly sensitive to the temperature unless it is very much lower than 8000 K.

Shock models actually exhibit a range of temperatures in the cooling gas, and this can be taken into account in detailed calculations (Hollenbach 1985; Hartigan *et al.* 1994). The Hartigan *et al.* (1995) results do not take this into account, mainly because without more information (spatial resolution, etc.) it is difficult to know just how the forbidden-line emitting region is heated, how many shocks there are, etc. These uncertainties plus the likely time-variability of both mass ejection and accretion could account for most of the scatter in Figure 10.9.

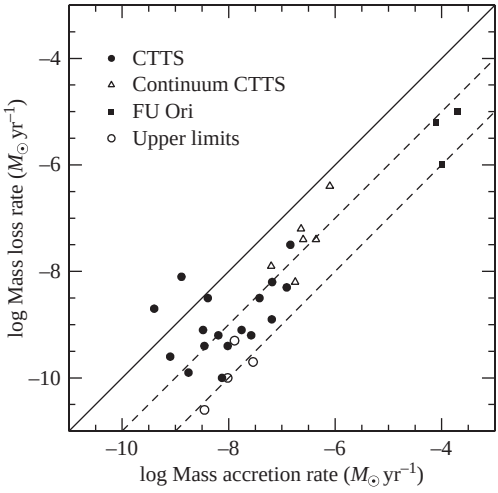

Fig. 10.9. Mass accretion rates vs. mass loss rates. Errors are probably factors of three or more in each coordinate. The solid line is $\dot{M}(\text{wind}) = \dot{M}(\text{accretion})$; the dashed lines are wind mass loss rates of 10% and 1% of the mass accretion rate. Overall, the observations indicate that mass ejection is about 10% of the mass accretion rate, consistent with energetic requirements of driving the mass loss by accretion energy (see text). Taken from Calvet (1998).

The mass loss rates for the three bright FU Ori objects shown in Figure 10.9 are derived from estimates using absorption lines, principally $H\alpha$ and Na I in combination (Figure 10.4; Calvet 1998). Additional confirmation of the mass loss rate of FU Ori itself comes from modeling the velocity shifts in strong photospheric lines (Figure 10.6; Hartmann & Calvet 1995). The optically bright FU Ori objects do not show forbidden-line jet emission, although the heavily extincted binary L1551 IRS 5 does show spatially resolved jet emission (Figure 10.1). Spatially resolved emission may not be detected if insufficient time has elapsed since the outburst; at typical distances of 500–1000 pc, the jet must be $\gtrsim 10^3$ AU long to be resolved from ground-based observations, and it would take about 50 years for the jet to expand this far at 300 km s^{-1}. The reasons why the inner wind does not emit strongly in forbidden lines are less clear, but it may be that the densities are so high in the wind that the forbidden lines are effectively collisionally de-excited (10.8), and the radiative cooling required by any shock heating is accomplished through other (permitted) transitions.

In the case of L1551 IRS 5, Stocke *et al.* (1988) estimated a mass loss rate of $\lesssim 10^{-7}\,M_\odot\,\text{yr}^{-1}$, while Cohen *et al.* (1982) estimated $\dot{M}_\text{w} \lesssim 3.5 \times 10^{-7}\,M_\odot\,\text{yr}^{-1}$ from an analysis of the radio continuum emission from the ionized jet. Osorio *et al.* (2003) estimated the disk accretion rate for each member of the binary as $\sim 2 \times 10^{-6}\,M_\odot\,\text{yr}^{-1}$. The ratio of mass loss to mass accretion rate is consistent with a typical value of 0.1, given the substantial uncertainties in these values. Radio continuum observations of some other FU Ori objects (Rodriguez *et al.* 1990; Rodriguez & Hartmann 1992) suggest *ionized* mass loss rates $\sim 10^{-7}\,M_\odot\,\text{yr}^{-1}$, but these are only lower limits since it is highly likely that FU Ori winds are mostly neutral.

Thus, although there are substantial uncertainties in individual mass loss rates, they appear to be about $\sim 10^{-1}$ of disk mass accretion rates for both T Tauri stars and FU Ori objects. The significance of this can be seen by estimating the amount of energy involved in producing these outflows. The ratio of wind to accretion luminosity is

$$\frac{L_{\rm w}}{L_{\rm acc}} \sim \frac{0.5\,\dot{M}_{\rm w} v_{\rm w}^2}{0.5\,\dot{M}_{\rm a} G M_*/R_i} \sim \frac{\dot{M}_{\rm w} v_{\rm w}^2}{\dot{M}_{\rm a} v_{\rm K}^2}\,, \tag{10.13}$$

where $\dot{M}_{\rm a,w}$ are the accretion and wind mass rates, respectively. The inner edges of FU Ori and T Tauri disks (the latter truncated by the magnetosphere; §10.10) are at $\sim 5\ R_\odot$; assuming a central mass of $0.5\ M_\odot$ for both sets of objects for simplicity, the corresponding Keplerian velocity is $v_{\rm K} \sim 140\ {\rm km\,s^{-1}}$. Wind/jet velocities $v_{\rm w}$ are often seen to extend to $v_{\rm w} = 300\ {\rm km\,s^{-1}}$ or more (Figures 10.4, 10.5). Adopting these values and using $\dot{M}_{\rm w} = 0.1\,\dot{M}_{\rm a}$ results in $L_{\rm w}/L_{\rm acc} \sim 0.5$. This estimate does not take into account the energy needed to overcome the gravitational potential well. Thus, pre-main-sequence accretion disks are extremely efficient in ejecting material, and a significant fraction of accretion energy is injected into outflows.

10.6 Magnetocentrifugal acceleration and collimation

What causes the outflows and jets observed from T Tauri stars and FU Ori objects? In stars like the Sun, the outer coronal atmosphere is sufficiently hot that winds may be thermally driven (probably augmented by magnetic pressure), while in hot stars radiation pressure drives massive winds. Neither of these mechanisms is applicable to the winds of T Tauri stars or FU Ori objects. Thermal pressure is not important when the gas sound speed is very much less than typical escape velocities; the temperatures of FU Ori and T Tauri winds are fairly well constrained to be $\lesssim 10^4$ K, and the associated sound speeds $c_{\rm s} \lesssim 10\ {\rm km\,s^{-1}}$ are very much smaller than typical escape velocities $\sim 100\ {\rm km\,s^{-1}}$. Similarly, radiation pressure is unimportant; radiative driving of winds tends to be most effective for objects with high luminosity to mass ratios like O stars. Moreover, the momentum fluxes of molecular outflows are generally much larger than the photon momentum flux L/c. Although multiple scattering can produce larger momentum fluxes in principle, in practice this is very difficult to arrange (Lada 1985). Finally, neither thermal acceleration or radiation pressure naturally produce highly collimated flows.

The favored mechanism for producing pre-main-sequence outflows is magnetocentrifugal acceleration from the circumstellar disk. Magnetic fields can effectively fling material outward at high rates if they are rotating locally at speeds near the Keplerian velocity (Hartmann & MacGregor 1982). The magnetic fields also collimate the outflow along the rotation axis, an effect initially found by Suess and Nerney (1975) in solar wind models. It seems surprising at first that a mechanism which relies on radially outward motion for the initial acceleration ends up focussing the ejection in the direction perpendicular to the rotation axis, but the collimation results from the toroidal field that is eventually built up in the rotating flow, as illustrated schematically in Figure 10.10. Material is launched initially from the rotating disk along a magnetic field line pointing away from the rotation axis, but at sufficiently large cylindrical radius the field is no longer strong enough to enforce corotation. In this weak magnetic field region, the angular velocity of the gas decreases as it tries to expand away from the rotation axis by conservation of angular momentum. This decreasing angular velocity causes the magnetic field to wind up azimuthally. The azimuthal field exerts

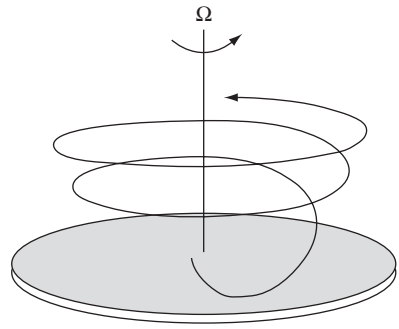

Fig. 10.10. Schematic drawing of a magnetic field line for a magnetocentrifugally driven disk wind, illustrating the azimuthal winding-up of the magnetic field which can lead to collimation around the rotation axis (see text).

a curvature force pointing toward the rotation axis, and this collimates the flow. Although the details of this situation depend upon the detailed magnetic geometry chosen, this general model appears to provide the most likely explanation for collimated pre-main-sequence outflows.

10.7 Magnetohydrodynamic flows

To illustrate some of the basic issues involved in magnetocentrifugal wind acceleration, we briefly outline some basic magnetohydrodynamic (MHD) results. We assume axisymmetric steady flow and infinite conductivity for simplicity, although it may be important to eliminate the latter constraint for the cold material involved in protostellar outflows (Königl 1989). The treatment below follows Mestel's development (1961, 1968). Important discussions have been given by Blandford and Payne (1982), Pudritz and Norman (1983), Lovelace *et al.* (1987), Königl (1989), Pelletier and Pudritz (1992), Lovelace *et al.* (1993), Safier (1993), and Shu *et al.* (1994). Early reviews of the subject have been presented by Königl and Ruden (1993) and Spruit (1996); among the most recent reviews are those of Shang *et al.* (2007) and Pudritz *et al.* (2007).

We take cylindrical coordinates R, ϕ, z, where the total distance from the coordinate center is $r = (R^2 + z^2)^{1/2}$. Splitting the magnetic field and velocity into poloidal and toroidal components, we may write

$$\mathbf{B} = \mathbf{B}_{\rm p} + \mathbf{B}_{\phi}\,, \tag{10.14}$$

$$\mathbf{v} = \mathbf{v}_{\rm p} + R\Omega\hat{\boldsymbol{\phi}}\,, \tag{10.15}$$

where Ω is the angular velocity at R. In the infinite conductivity MHD limit, the electric field in the frame moving with the fluid must vanish, and so the induction equation yields (e.g., Priest 1984)

$$\nabla \times \left(\frac{\mathbf{v}}{c} \times \mathbf{B}\right) = 0\,. \tag{10.16}$$

Using this result and Stokes' theorem,

$$\int \nabla \times (\mathbf{v}_{\rm p} \times \mathbf{B}_{\rm p}) \cdot \mathbf{dA} = \oint d\mathbf{S} \cdot (\mathbf{v}_{\rm p} \times \mathbf{B}_{\rm p}) = 0\,, \tag{10.17}$$

where the integral on the left-hand side is taken over the surface area bounded by the closed curve S. In particular, the line integral on the right-hand side may be taken to be a circle centered on the $\hat{z}$ axis; if the flow is axisymmetric, $\mathbf{v}_\mathrm{p} \times \mathbf{B}_\mathrm{p}$ must be constant on any such circle. Therefore $\mathbf{v}_\mathrm{p} \times \mathbf{B}_\mathrm{p} = 0$, and the poloidal velocity can be written as

$$\mathbf{v}_\mathrm{p} = \kappa \mathbf{B}_\mathrm{p} \,, \tag{10.18}$$

where κ is a scalar quantity. The poloidal velocity is parallel to the poloidal magnetic field as a consequence of the assumed infinite conductivity.

Using the Maxwell equation $\nabla \cdot \mathbf{B} = 0$, the toroidal component of equation (10.16) can be written after some manipulation as

$$(\mathbf{B} \cdot \nabla) \left(\Omega - \kappa \frac{B_\phi}{R} \right) = 0 \,. \tag{10.19}$$

This equation can be interpreted as the change in the second bracketed quantity along a magnetic field line. Therefore, following any individual field line, we have

$$\Omega - \kappa \frac{B_\phi}{R} = \Omega_\circ \,, \tag{10.20}$$

where $\Omega_\circ$ is a constant along the given field line; this is the angular velocity of the *pattern* of the magnetic field in steady flow.

The continuity equation is

$$\nabla \cdot (\rho \mathbf{v}) = 0 = \nabla \cdot (\rho \kappa \mathbf{B}) = (\mathbf{B} \cdot \nabla) \rho \kappa \,. \tag{10.21}$$

Again, this defines a constant along a field line,

$$\rho \kappa = \frac{\rho v_\mathrm{p}}{B_\mathrm{p}} \equiv \eta \,. \tag{10.22}$$

The continuity equation in this form simply states that the mass flux density per unit poloidal magnetic flux density is a constant along a given field line. Equivalently, one may say that the poloidal mass flow is bounded by poloidal magnetic field lines, because the magnetic flux is "frozen in" to the flow.

The momentum equation can be written using the first Maxwell equation as

$$\rho (\mathbf{v} \cdot \nabla) \mathbf{v} = -\rho \nabla \phi - \nabla P + (\nabla \times \mathbf{B}) \times \frac{\mathbf{B}}{4\pi} \,. \tag{10.23}$$

In (rotating) cylindrical coordinates, the toroidal component of the equation of motion is

$$\rho (\mathbf{v} \cdot \nabla) R^2 \Omega = R \left[\frac{(\nabla \times \mathbf{B}) \times \mathbf{B}}{4\pi} \right]_\phi \,. \tag{10.24}$$

After some additional manipulation, this equation can be written as

$$(\mathbf{B} \cdot \nabla) \left(\rho \kappa R^2 \Omega - R \frac{B_\phi}{4\pi} \right) = 0 \,. \tag{10.25}$$

Thus we have yet another quantity conserved along magnetic field lines. Since $\rho\kappa \equiv \eta$ is a constant along a streamline, this constraint can also be written as

$$R^2 \Omega - R \frac{B_\phi}{4\pi} \eta = l \,, \tag{10.26}$$

where l is another constant along the streamline.

The first term on the left-hand side of equation (10.26) is the angular momentum per unit mass carried by the gas. The second term is the angular momentum carried by the magnetic field per unit mass. It is non-zero only if $B_\phi \neq 0$, i.e., the magnetic field must curve in the direction of rotation to exert a torque. We identify l as the total specific angular momentum carried by the flow (Mestel 1968). Then the angular momentum flux along a streamline is

$$\rho v_{\rm p} l = \rho v_{\rm p} R^2 \Omega - R B_{\rm p} \frac{B_\phi}{4\pi} \,. \tag{10.27}$$

These results may be combined to find an equation for the angular velocity of the gas (Mestel 1968),

$$\Omega = \frac{\Omega_\circ - 4\pi\eta^2 l/\rho R^2}{1 - 4\pi\eta^2/\rho} \,. \tag{10.28}$$

One critical parameter controlling the azimuthal motion is

$$\frac{4\pi\eta^2}{\rho} = \frac{4\pi\rho v_{\rm p}^2}{B_{\rm p}^2} \,, \tag{10.29}$$

which represents the ratio of the poloidal ram pressure of the flow to the pressure of the poloidal magnetic field. When the magnetic field is strong, it forces the gas to rotate with the same angular velocity, $\Omega \to \Omega_\circ$; if the magnetic pressure is much lower than the poloidal gas ram pressure, then $\Omega \to l/R^2$, i.e., the gas conserves its angular momentum along the field line.

It is evident that the magnetic field must be strong in the region where the outflow is accelerated to produce strong mass loss. In general the wind density decreases as the gas moves outward, and therefore the flow must pass through a point where equation (10.28) becomes singular; this requires

$$\frac{4\pi\eta^2}{\rho} = \frac{4\pi\rho v_{\rm p}^2}{B_{\rm p}^2} = 1 \,. \tag{10.30}$$

In general, singular points appear in steady flow problems where the flow speed matches the speed of a backward-propagating wave. In this particular case, the singular point is called the Alfvén critical point, because the poloidal velocity matches the Alfvén velocity,

$$V_{\rm a,p}^2 = \frac{B_{\rm p}^2}{4\pi\rho} \,, \tag{10.31}$$

which is the velocity of purely transverse waves along the magnetic field. There are two other pure MHD wave modes – the so-called "fast" and "slow" magnetosonic waves (e.g., Jackson 1962) – and in general the flow must pass through critical points associated with these modes as well (e.g., Weber & Davis 1967).

For smooth flow the numerator of equation (10.28) must also vanish at the Alfvén point, and therefore

$$l = R_{\rm A}^2 \Omega_\circ \,. \tag{10.32}$$

The total angular momentum carried by the flow along a streamline is therefore equal to the value that the gas would have if it rotated at the same angular velocity as the base of the flow out to a cylindrical radius $R_{\rm A}$. Although the actual flow does not precisely co-rotate out to

the Alfvén radius (or, considering all the field lines in space, the Alfvén surface), and the magnetic field carries some of the angular momentum of the flow (equation (10.26)), this picture provides a convenient way of roughly categorizing the outflow into two reasonably distinct regions. Interior to the Alfvén surface, the flow is dominated by the magnetic field, and forced nearly into solid-body rotation; exterior to the Alfvén surface, the poloidal magnetic field becomes less important (although the same is not true of the azimuthal field), and the magnetic field lines become much more wound up (equation (10.28)).

Before leaving the topic of angular momentum conservation it is instructive to consider the qualitative behavior of field lines as a function of angle from rotation axis. Conservation of angular momentum of the flow past the Alfvén point causes the azimuthal velocity of the gas to decrease with increasing (cylindrical) distance from the axis; this in turn causes the field to wrap up toroidally in steady state (to keep the pattern angular velocity $\Omega_\circ$ constant). A field line nearer the axis will wind up less than one tilted closer to the equatorial plane. Thus, the toroidal field will be stronger in more equatorial field lines than axial field lines. This creates a magnetic pressure gradient toward the rotation axis which, when combined with the hoop stresses of the curved field lines, causes the flow to collimate. The Grad–Shafranov equation describes the resulting forces (e.g., Shu *et al.* 1995, Pelletier & Pudritz 1992); as the precise collimation which results depends in a complex way upon various assumptions of field boundary conditions, we restrict the discussion to the above qualitative description.

The momentum equation may also be used to derive an energy constant of the motion in the absence of dissipation. Taking the dot product of the momentum equation with the velocity, and assuming isothermal flow for simplicity,

$$\rho\mathbf{v}\cdot\left[\nabla\frac{v^2}{2}+c_{\rm s}^2\ln\rho-\nabla\frac{GM_*}{(R^2+z^2)^{1/2}}+c_{\rm s}^2\nabla\ \ln\ \rho\right]=\mathbf{v}\cdot\frac{(\nabla\times\mathbf{B})\times\mathbf{B}}{4\pi}\,, \tag{10.33}$$

where $c_{\rm s}$ is the sound speed. After some manipulation, this can be written as

$$\rho\mathbf{v}\cdot\nabla\left[\frac{v^2}{2}+c_{\rm s}^2\ \ln\ \rho-\frac{GM_*}{(R^2+z^2)^{1/2}}-R^2\Omega_\circ\Omega\right]=0\,. \tag{10.34}$$

The term in square brackets,

$$E=\frac{v^2}{2}+c_{\rm s}^2\ \ln\rho-\frac{GM_*}{(R^2+z^2)^{1/2}}-R^2\Omega_\circ\Omega\,, \tag{10.35}$$

is an energy constant along the direction of motion, i.e., along a flow line, and is usually called the Bernoulli constant.

The final term in the energy constant is due to the effects of the magnetic field. To illustrate this more clearly, it can also be written as

$$\begin{aligned}\nabla\cdot(\rho\mathbf{v}(R^2\Omega_\circ\Omega))&=\nabla\cdot(\rho\kappa\mathbf{B}_{\rm p}R^2\Omega_\circ\Omega)=\nabla\cdot\left(\frac{\Omega_\circ RB_\phi\mathbf{B}_{\rm p}}{4\pi}\right)\\&=\nabla\cdot\left(\frac{1}{4\pi}(\mathbf{v}\times\mathbf{B})\times\mathbf{B}\right)=-\nabla\cdot\left(\frac{c}{4\pi}\mathbf{E}\times\mathbf{B}\right)\,.\end{aligned} \tag{10.36}$$

Thus, this energy term corresponds to an electromagnetic Poynting flux, and is responsible for accelerating the outflow in the absence of thermal gas pressure.

10.8 MHD disk winds

To illustrate the essential effects involved in launching a magnetocentrifugal wind, we first assume that the magnetic field in the innermost wind regions is sufficiently strong to enforce co-rotation in the region under consideration (cf. equation (10.28)). Then the Bernoulli constant (10.35) can be approximated as

$$E = \frac{v_{\rm p}^2}{2} + c_{\rm s}^2 \ln \rho - \frac{R^2\Omega_\circ^2}{2} - \frac{GM_*}{(R^2+z^2)^{1/2}} = \frac{v_{\rm p}^2}{2} + c_{\rm s}^2 \ln \rho - \Phi\,, \tag{10.37}$$

where Φ is an effective potential term including the effects of rotation and magnetic fields. The behavior of the flow depends upon the form of Φ, which in turn depends upon the geometry of the flow.

To start with a particularly simple case, suppose that the outflow starts from a ring rotating at $\Omega_\circ$ and is confined to the equatorial plane. Suppose further that the flow is confined to a flux tube whose cross-sectional area A varies as R^2. Then using the continuity equation for the mass flow rate

$$\dot{m}_{\rm w} = \rho A v_{\rm p} = \text{constant}\,, \tag{10.38}$$

and differentiating the Bernoulli constant (10.37) with respect to R, one can substitute for the $\ln\ \rho$ term using (10.38), resulting in

$$(v_{\rm p}^2 - c_{\rm s}^2)\frac{dv_{\rm p}}{dR} = \frac{v_{\rm p}}{R}\left(2c_{\rm s}^2 + R^2\Omega_\circ^2 - \frac{GM_*}{R}\right)\,. \tag{10.39}$$

(Note that for this flow, $v_{\rm p} = v_{\rm r} = v_{\rm R}$, i.e., the poloidal motion is purely radial.) If $\Omega_\circ = 0$ this equation is the familiar steady flow equation for the spherical thermally driven wind (Parker 1963); in this case equation (10.39) is singular at the sonic point $v_{\rm p} = v = c_{\rm s}$; the radius at which the sonic point occurs is then $R_{\rm s} = GM/2c_{\rm s}^2$. The rotational term accounts for the effect of the magnetic field; it has the same sign as the thermal pressure term, and therefore helps accelerate the outflow. This singular point is actually where the flow speed matches the magnetospheric slow mode velocity, but by assuming co-rotation we have effectively assumed very large magnetic field strength and therefore large Alfvén velocity; in this limit the magnetospheric slow mode velocity approaches the sound speed (for radial propagation, see also Blandford & Payne (1982).)

Once the density at the sonic (slow mode) point is found by combining the location of the sonic point from equation (10.39) with the Bernoulli constant, the sonic (or slow mode) point determines the mass flow rate,

$$\dot{m}_{\rm w} = \rho_{\rm s} A_{\rm s} c_{\rm s}\,. \tag{10.40}$$

To illustrate this in more detail, consider first the simple thermally driven case, assuming rotational (and magnetic) effects are negligible. Then the sonic point is the so-called Parker point,

$$R_{\rm P} = \frac{GM_*}{2c_{\rm s}^2}\,, \tag{10.41}$$

and the density at the sonic point can be evaluated in terms of the density $\rho_\circ$ at the starting radius $R_\circ$,

$$\ln \frac{\rho_{\rm s}}{\rho_\circ} = -\frac{1}{2} - \frac{GM_*}{R_\circ c_{\rm s}^2}\left(1 - \frac{R_\circ}{R_{\rm P}}\right)\,. \tag{10.42}$$

If $R_{\rm P} >> R_\circ$, it follows that $GM/R_\circ c_{\rm s}^2 >> 1$. This means that the density at the sonic point must be very much less than the density at the reference level $R_\circ$, and thus the mass loss rate $\dot{m}_{\rm w} \propto \rho_\circ \exp(-(1/2) - GM/R_\circ c_{\rm s}^2)$ will be very low.

Returning to the case with magnetocentrifugal acceleration, the sonic point is given by the cubic equation

$$R_{\rm s}^3 \Omega_\circ^2 + 2c_{\rm s}^2 R_{\rm s} - GM_* = 0\,, \tag{10.43}$$

and the density at the sonic point becomes

$$\ln \frac{\rho_{\rm s}}{\rho_\circ} = -\frac{1}{2} + \frac{-\Phi(R_\circ) + \Phi(R_{\rm s})}{c_{\rm s}^2}\,. \tag{10.44}$$

The effect of the rotating magnetic field is to move the sonic point closer to the initial radius and therefore generally increase the mass loss rate. T Tauri and FU Ori winds are generally quite cold, and so the effect of thermal pressure is rather small, i.e., the Parker radius $R_{\rm p}$ is large (and large in comparison with the sonic point (slow mode) radius). If the rotation at $R_\circ$ is written as a fraction f of the local Keplerian velocity,

$$\Omega_\circ = f\left(\frac{GM_*}{R_\circ^3}\right)^{1/2}\,, \tag{10.45}$$

and assuming that the Parker sonic point is at a much larger radius than the magnetosonic point, equation (10.43) yields approximately

$$R_{\rm s}^3 \approx \frac{R_\circ^3}{f^2}\,. \tag{10.46}$$

Thus as $f \to 1$, the sonic point moves inward to the initial or reference radius $R_\circ$. In the limit that the ring is rotating at the local Keplerian velocity, the sonic point lies right at the ring surface, where the density is large, and therefore large mass fluxes result. Outflow from a disk obviously does not lie precisely in the equatorial plane; however, the above discussion outlines the basic physics of magnetocentrifugal flows.

Consider now the opposite case in which the magnetic field lines are completely vertical, i.e., perpendicular to the disk plane. We suppose that the footpoint in the disk is rotating at the local Keplerian velocity. Now the Bernoulli constant is

$$E = \frac{v_{\rm p}^2}{2} + c_{\rm s}^2 \ln \rho - \frac{GM_*}{2R_\circ} - \frac{GM_*}{(R_\circ^2 + z^2)^{1/2}}\,. \tag{10.47}$$

It is evident that the effective potential term does not vary except on distance scales $\sim R_\circ$, and thus the sonic point of a cold flow will be far above the disk, and the mass loss rate will be vanishingly small. The vertical field configuration does not take advantage of the magnetocentrifugal acceleration which takes place when the field line is tilted with respect to the rotation axis.

From these two limits one can see that there must be some critical angle of the magnetic field line to the rotation axis which allows the sonic point to lie close to the disk surface and thus produce a high mass loss rate. The easiest way to determine this condition is to take the strong-field limit and assume that the sound speed is extremely small, so that thermal effects can be completely neglected. Then the Bernoulli equation simplifies to

$$E = \frac{1}{2} v_{\rm p}^2 + \Phi\,, \tag{10.48}$$

where the "effective" potential is

$$\Phi = -\frac{GM_*}{R_\circ}\left[\frac{1}{2}\frac{R^2}{R_\circ^2} + \frac{R_\circ}{(R^2+z^2)^{1/2}}\right]. \tag{10.49}$$

Consider now a small displacement along the field line, with a coordinate given by s, and

$$ds^2 = dR^2 + dz^2\,. \tag{10.50}$$

At the base of the flow, the disk material is rotating at the local Keplerian velocity. This is an equilibrium state, because $d\Phi/ds = 0$ at $z = 0$. However, if $d^2\Phi/ds^2 < 0$, this equilibrium is *unstable*; any small perturbation along the field line will result in an increased (outward) poloidal velocity from equation (10.48). If θ is the angle between the field line and the disk plane, the critical stability criterion

$$\frac{\partial^2\Phi}{\partial s^2} = 0 \quad (R = R_\circ\,, z = 0) \tag{10.51}$$

requires $\tan^2\theta_c = 3$, or $\theta_c = 60°$ (Blandford & Payne 1982). Disk magnetic field lines which are tipped away from the rotation axis by an angle greater than 30° result in an unstable equilibrium, and rapid outflow will commence at the disk. For smaller tilt angles from the rotation axis, launching of an outflow requires thermal pressure to initiate the motion, and so the mass loss rates will be correspondingly smaller. If the flow is very cold, values of $\theta \geq 60°$ will result in essentially no mass ejection.

A complete analysis of the flow requires consideration of wind behavior at large distances, where the approximation of co-rotation is not valid. The outflow may or may not pass through a fast-mode critical point (Blandford & Payne 1982; Spruit 1996), depending upon how "magnetic" the solution is at large distances, i.e., how much of the energy flow is accounted for by the kinetic energy of the gas vs. how much is contained in the Poynting flux at large distances (equation (10.36)). We will not consider this problem further; although this is of interest for understanding the collimation of jets, it is not essential for understanding the effects of the wind ejection on the disk.

The disk wind carries away both angular momentum and energy from the disk, and therefore may affect disk accretion. To explore this most simply, consider the case where thermal pressure can be neglected. Using (10.34) along a flux tube with area dA,

$$\rho v_{\rm p} dA\left[\frac{v^2}{2} - \frac{GM_*}{(R^2+z^2)^{1/2}} - R^2\Omega_\circ\Omega\right] = \text{constant}\,, \tag{10.52}$$

where $v_{\rm p}$ is the poloidal velocity. This can be written using (10.26) as

$$\rho v_{\rm p} dA\left[\frac{v^2}{2} - \frac{GM_*}{(R^2+z^2)^{1/2}} - \Omega_\circ\left(l + \frac{RB_\phi}{4\pi\eta}\right)\right]. \tag{10.53}$$

Because both $\Omega_\circ$ and l are constants of the motion,

$$\rho v_{\rm p} dA\left[\frac{v^2}{2} - \frac{GM_*}{(R^2+z^2)^{1/2}} + \Omega_\circ l_{\rm B}\right] = \text{constant} = \dot{e}_{\rm w}\,, \tag{10.54}$$

where we identify $\dot{e}_{\rm w}$ as the energy flux along the flux tube, and

$$l_{\rm B} = -\frac{RB_\phi}{4\pi\eta} \tag{10.55}$$

is the (non-constant) angular momentum carried by the magnetic field.

The outflow angular momentum and energy are carried both by the gas and by the magnetic field. However, it is the magnetic field coupling the outflow and disk which is responsible for extracting the energy and angular momentum from the disk needed to drive the outflow. Just above the disk surface, the outflowing gas contains essentially the same angular momentum that it had in the disk, and so its removal does not change the angular momentum per unit mass of the remaining disk material. The magnetic field produces a torque on the disk as it carries away angular momentum; the angular momentum flux carried away by the wind can be evaluated at the base of the flow as

$$\frac{dj_{\rm w}}{dt} = \rho_\circ v_{\rm p0} dA_\circ l_{\rm Bo}\,. \tag{10.56}$$

Suppose now that a magnetic flow tube spans an annular area corresponding to a radial range on the disk of dR at $R_\circ$. In steady state, the flow cannot extract more angular momentum than corresponds to the accretion rate through the disk. Away from the inner disk edge, the angular momentum lost as material accretes through dR at $R_\circ$ is

$$\frac{dj_{\rm acc}}{dt} = \dot{M}\frac{d}{dR}\Omega_K R^2 dR = \frac{1}{2}\dot{M}\Omega_\circ R_\circ^2\frac{dR}{R_\circ}\,. \tag{10.57}$$

If the angular momentum carried away by the wind flux tube spanning dR is exactly equal to the angular momentum transport needed for accretion, the energy carried away by the wind is

$$\dot{e}_{\rm w} = \Omega_\circ l_{\rm Bo}\dot{m}_{\rm w} = \frac{1}{2}\frac{GM_*\dot{M}}{R_\circ}\frac{dR}{R_\circ}\,. \tag{10.58}$$

Therefore, a wind which removes all of the angular momentum needed for disk accretion carries off all of the *local* accretion energy as well. Whether this is *all* of the total accretion energy depends upon whether there is a central torque which does work on the outer disk annuli (§7.3). In the absence of a central torque, making the wind carry away all of the angular momentum results in a non-luminous disk.

An analysis of the solution at large distances is needed to derive the collimation of the flow and the precise asymptotic flow speed. However, a crude estimate of the terminal velocity can be made using the Bernoulli equation (10.35) and the assumptions that most of the angular momentum of the flow is initially carried by the magnetic field, and that the angular momentum asymptotically carried by the magnetic field is negligible; then

$$\frac{v_\infty^2}{2} \sim -\frac{GM_*}{2R_\circ} + \Omega_\circ l_{\rm Bo} \sim -\frac{GM_*}{2R_\circ} + \Omega_\circ^2 R_{\rm A}^2\,. \tag{10.59}$$

Thus the terminal velocity of the flow is typically of the order of the azimuthal velocity at the Alfvén point.

10.9 Applications of MHD disk wind theory

Following the initial self-similar disk wind models investigated for active galactic nuclei by Blandford and Payne (1982), magnetocentrifugal disk wind models for pre-main-sequence objects were constructed by Pudritz and Norman (1983, 1986), Lovelace *et al.* (1987), Königl (1989), Pelletier and Pudritz (1992), Wardle and Königl (1993), Safier (1993), Li (1995), Ferreira and Pelletier (1995), Paatz and Camenzind (1996), Bogovalov and Tsinganos (1999), and Ferreira and Casse (2004), among others. Subsequently, numerical time-dependent simulations have been undertaken (Ouyed & Pudritz 1997a,b, 1999; Krasnopolsky *et al.* 1999, 2003; Ouyed *et al.* 2003; Kudoh *et al.* 2003; Anderson *et al.* 2005). These models assume that the wind arises from a significant range of radii in the disk, and are therefore termed "disk winds". An extreme limit of the disk wind, where only the innermost edge of the disk contributes to the mass loss, has been developed by Shu and collaborators (Shu *et al.* 1994; Najita & Shu 1994), and is called the "X-wind" (Figure 10.11; §10.10).

A variety of magnetocentrifugal wind models can account for the cold, collimated winds of YSOs (see discussion in the reviews of Shang *et al.* 2007 and Pudritz *et al.* 2007). As discussed at the end of §10.5, the outflows of T Tauri stars and FU Ori objects represent a significant energy loss compared with that released by accretion. With the appropriate open magnetic field geometry, the wind can tap into a large fraction of the energy released by disk accretion (equation (10.59)). The winds cannot, in general, account for all of the angular momentum transport, because the disk radiation losses due to accretion energy release are observed in FU Ori objects and in the most rapidly accreting T Tauri stars. It is more plausible to think of accretion energy release driving mass loss, rather than mass loss driving accretion, which would be the case if all the angular momentum were being extracted in the outflow.

Recent spatially resolved kinematics of jets using HST have provided new tests of the predictions of wind models. An example of this is high spatial resolution ($\sim$0.1 arcsec, $\sim$14 AU at the distance of Taurus) imaging of the DG Tau jet. As shown in Figure 10.12, there is some evidence that the higher-velocity outflow is more confined toward the jet axis, with the outer jet exhibiting slower motions. This type of behavior is a natural consequence of a disk wind model (Figure 10.11), where outer jet field lines connect with the disk at larger radii, where the Keplerian rotation is smaller. The X-wind model (Figure 10.11) also may produce

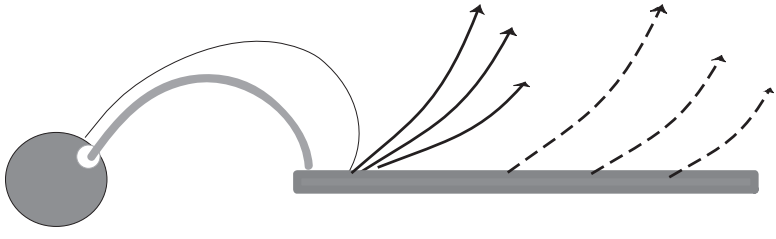

Fig. 10.11. Schematic accretion disk–wind–stellar magnetosphere structure. Magnetic fields which penetrate the disk inside the co-rotation radius (where the angular velocity of the rotating disk matches the angular velocity of the star) allow material to accrete (gray curve); fields penetrating the disk outside of co-rotation help provide a spindown torque (solid dark curve). In the X-wind model, the wind arises from the disk just at co-rotation (arrows), while disk wind models involve mass loss from a wider range of disk radii (dashed arrows).

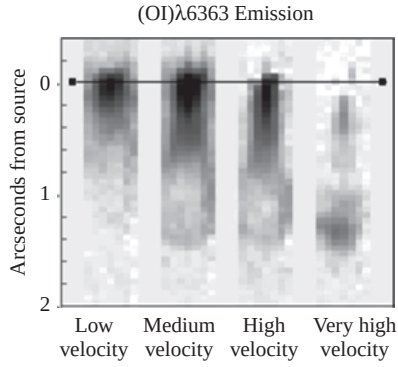

Fig. 10.12. Spectral imaging of the jet of DG Tau in [O I], derived from offset long-slit images (with the slit parallel to the jet axis) using the STIS spectrograph on HST. The four images correspond to adding flux in the velocity bins, from low to high velocity, +73 to -57 km s^{-1}, -58 to -188 km s^{-1}, -189 to -319 km s^{-1}, and -320 to -450 km s^{-1}. The jet is narrower in the higher velocity bins, suggesting a decrease of outflow velocity with decreasing cylindrical distance, as would be expected generally for a disk wind. From Bacciotti *et al.* (2000).

similar results, depending upon how much mass is "loaded" onto field lines; larger densities lead to slower velocities (e.g., Shu *et al.* 1995).

Careful analysis of the jet of DG Tau and a few other objects suggests that rotation may have been detected (Bacciotti *et al.* 2002; Ray *et al.* 2007, and references therein), which of course is a fundamental prediction of the magnetocentrifugal acceleration model. To explore the implications of the detection of rotation quantitatively, we follow the analysis of Anderson *et al.* (2003). There are two constants of the motion along a streamline. One is the specific angular momentum l (equation (10.26)), which can be reformulated using equation (10.22) and setting $R\Omega = v_\phi$,

$$l = R\left(v_\phi^2 - B_\mathrm{p}\frac{B_\phi}{4\pi}\rho v_\mathrm{p}\right) . \tag{10.60}$$

The other constant of the motion is the specific energy E (equation (10.35)), which can be written using a result in equation (10.36)) as

$$E = \frac{v^2}{2} - \Phi + \left(\frac{\Omega_\circ R B_\phi \mathbf{B}_\mathrm{p}}{4\pi\rho v_\mathrm{p}}\right) , \tag{10.61}$$

where Φ is the gravitational potential and the thermal energy term has been ignored, assuming cold flow. Then a new quantity

$$J \equiv E - \Omega_\circ l = \frac{v_\mathrm{p}^2 + v_\phi^2}{2} + \Phi - \Omega_\circ R v_\phi \tag{10.62}$$

can be constructed which is also conserved along a field line.

Next, evaluate equation (10.62) at two locations. First, at the disk launching surface, one can assume that the wind has negligible poloidal velocity v_p and is co-rotating with the disk at the local Keplerian velocity

$$v_{\rm K,o} = \left(\frac{GM_*}{R_\circ}\right)^{1/2} = \Omega_\circ R_\circ v_{\phi,\circ}\,. \tag{10.63}$$

Thus, $J = -3v_{\rm K,o}^2/2$. Next, evaluate J at large distances, where the gravitational potential is negligible; then

$$J = \frac{(v_{\rm p,\infty}^2 + v_{\phi,\infty}^2)}{2 - R_\infty\, v_{\phi,\infty}\, \Omega_\circ}\,. \tag{10.64}$$

Using the relation $v_{\rm K,o} = (GM_*\Omega_\circ)^{1/3}$, equating the values of J results in

$$\Omega_\circ R_\infty v_{\phi,\infty} - \frac{3}{2}(GM_*)^{2/3}\Omega_\circ^{2/3} - \frac{v_{\rm p,\infty}^2 + v_{\phi,\infty}^2}{2} \approx 0\,. \tag{10.65}$$

While this equation is a cubic in $\Omega_\circ^{1/3}$ and can be solved by standard techniques, here we make the approximation that the wind kinetic energy at large distances is considerably larger than the gravitational binding energy at the launch point. Also, typically $v_{\phi,\infty} \gg v_{\rm p,\infty}$, resulting in a final result

$$\Omega_\circ \approx \frac{v_{\rm p,\infty}^2/2}{v_{\phi,\infty}\, R_\infty}\,. \tag{10.66}$$

Therefore, if the jet poloidal and toroidal velocities can be measured at distances of order 10^2 AU (thus far out of the gravitational potential well of the star), and the width of the jet R_∞ can be measured, the angular velocity at the launch point can be determined. In turn, the initial launch radius can be found from $\Omega_\circ = (GM_*/R_\circ^3)^{1/2}$ with an estimate of the stellar mass.

The physical basis of equation (10.66) can be understood as follows. Neglecting the work done against gravity, the final energy of the gas $v_{\rm p,\infty}^2/2$ is provided by the work done by the rotating field on the gas; this is $\Omega_\circ l$. We can approximate the specific angular momentum (see equation (10.32)) by $l \approx v_{\phi,\rm A}R_{\rm A} \approx v_{\phi,\infty}R_\infty$, where the final estimate arises from assuming that the gas roughly conserves its angular momentum beyond the Alfvén radius $R_{\rm A}$. Rearranging terms then yields equation (10.66).

Using a slightly modified version of the relation (10.66) derived from a variety of numerical simulations, Anderson *et al.* (2003) estimated that the low velocity component of the DG Tau jet arises from a region on the disk from $\sim$0.3−4 AU, consistent with the original estimate of Bacciotti *et al.* (2002). A more detailed observation using ultraviolet emission lines by Coffey *et al.* (2007) suggested that the high velocity component in DG Tau arises from radii $\sim$0.2−0.5 AU, while the low velocity jet arises from radii $<$2 AU. All of these estimates are roughly consistent with the suggestion of Hartigan *et al.* (1995) that the low velocity component of T Tauri stars in general could arise from regions $\gtrsim$1 AU, based on interpreting the velocity width in terms of arising near the disk in Keplerian rotation.

One concern about these estimates is that the launch radii are considerably larger than inner disk radii $\lesssim 10\,R_\odot \sim 0.05$ AU; winds from such large radii cannot tap into the inner regions, which have the largest release of gravitational potential energy (§10.5); this makes it difficult to understand the large fraction of accretion energy carried off by jets. The analysis assumes the presence of no flow asymmetries which could masquerade as rotation, an assumption which may be questionable given the probable presence of complex internal shocks needed to heat the radiating jet gas.

It now seems likely that disk winds/X winds with wider opening angles than jets can account for molecular outflows. Matzner and McKee (1999) argued on general grounds that both X-winds and disk winds will exhibit a ram pressure force as a function of cylindrical radius R roughly proportional to $P_{\rm w} = \rho_{\rm w} v_{\rm w}^2 \propto R^{-2}$. Matzner and McKee showed that this kind of wind pressure would sweep up ambient material in a shell with a mass–velocity relation consistent with observations of molecular outflows. Note that with such a flow, the integrated outflow momentum $\int dr\, 2\pi r\, P_{\rm w} \propto \ln r$ can contain a significant contribution from large off-axis distances, while the kinetic energy flux $(1/2)\rho_{\rm w} v_{\rm w}^3$ will be dominated by near-axis regions for flows with typically higher central velocities. The wider-angle outflow helps to reduce or eliminate the kink or sausage instabilities to which narrow jets are subject (Spruit 1996; Anderson *et al.* 2006) by surrounding the jet with material and magnetic fields.

A more general question is whether the required magnetic field strengths are plausible, especially given that the MRI is suppressed when the field is strong (§7.5). The required field strengths can be estimated from the Alfvén point (surface), where both rotational (and poloidal) velocities must be an appreciable fraction of the observed wind terminal velocity. Thus, from the relation (10.30),

$$B_{\rm A}^2 \sim 4\pi \rho_{\rm A} v_{\rm A}^2 \,, \tag{10.67}$$

we estimate

$$B_{\rm A} \sim (\dot{M} v_\infty)^{1/2} R_{\rm A}^{-1} \sim 200\, (\dot{M}_{-5}\, v_{300})^{1/2} \left(\frac{R}{10\ {\rm AU}}\right)^{-1} {\rm G} \,, \tag{10.68}$$

where the mass loss rate $\dot{M}_{-5}$ is measured in units of $10^{-5}\, M_\odot\ {\rm yr}^{-1}$ and the wind velocity v is measured in units of $300\ {\rm km\,s^{-1}}$.

For MHD disk winds to explain FU Ori outflows, the magnetic fields in the wind acceleration region must be of order 10^2 gauss. Detailed models suggest that equipartition fields in the midplane of FU Ori's inner disk might be more like $B_{\rm eq} \sim 10^4$ G; thus, it appears reasonable that field weak enough for the MRI are still strong enough to drive the observed outflows. The situation is less clear for T Tauri stars if the magnetically coupled winds arise from only an active layer rather than the entire disk.

It seems likely, given the presence of MRI turbulence, that the disk field geometry is complex, with both closed and open magnetic field lines at the disk surface, such as present in the Sun, and like the picture of disk fields originally sketched by Blandford and Payne (1982). This complex geometry may help produce the time-variability of mass loss or ejection velocities implied by widely spaced shocks in extended jets (see Bally *et al.* 2007, and references therein).

10.10 Models of magnetospheric accretion

Magnetospheric models were originally developed to investigate disk accretion onto magnetized neutron stars (Ghosh & Lamb 1979) and have also been applied to the highly magnetized white dwarf AM Her systems (see Frank *et al.* 1992 for a discussion). As discussed in §8.4, application of the magnetospheric model was originally motivated by a desire to explain the slow rotation of accreting low-mass stars, CTTS, vs. the somewhat faster-rotating WTTS, by coupling the star to the disk. Early results showing that CTTS rotate faster than WTTS (Edwards *et al.* 1993b; Bouvier *et al.* 1993) have been reinforced by later studies (Herbst *et al.* 2002; Lamm *et al.* 2004, 2005; Dahm & Simon 2005; Rebull

et al. 2006), although there seems to be considerable overlap in rotation periods between WTTS and CTTS.

The way in which the stellar magnetic field interacts with the accretion disk is very complicated and not well understood. Various treatments of the problem have been given by Cameron and Campbell (1993), Ghosh (1995), Ostriker and Shu (1995), Lovelace *et al.* (1995), Armitage and Clarke (1996), Goodson and Winglee (1999), Matt *et al.* (2002), Matt and Pudritz (2004), and Zweibel *et al.* (2006).

The basic idea behind the magnetospheric truncation of the disk can be seen most easily in the context of spherical (free-fall) accretion. Suppose that the magnetic pressure balances the ram pressure of accretion,

$$B^2 = 4\pi\rho v^2 = \dot{M}\frac{v_{\rm in}}{r^2}\,, \tag{10.69}$$

where $v_{\rm in}$ is the infall velocity. In such a situation, the (sufficiently ionized) accreting gas cannot fall in freely; its motion must be restricted or even halted by the magnetic force. If the infall velocity $v_{\rm in}$ is set equal to its maximum value, the free-fall velocity from infinity, and the stellar magnetic field is a dipole, so that $B \propto r^{-3}$, then the radius at which the magnetic field is strong enough to hold off the infall is roughly

$$\frac{r_{\rm T}}{R_*} = \frac{B_o^{4/7} R_*^{5/7}}{\dot{M}^{2/7}(2GM)^{1/7}} = 7.2 B_3^{4/7}\,\dot{M}_{-8}^{-2/7} M_{1/2}^{-1/7} R_2^{5/7}\,, \tag{10.70}$$

where B_3 is the surface magnetic field in kG, $\dot{M}_{-7}$ is the mass accretion rate in $10^{-7}\,M_\odot\,{\rm yr}^{-1}$, $M_{1/2}$ is the central mass in units of 0.5 $M_\odot$, and R_2 is the stellar radius in 2 $R_\odot$. The argument is modified for disk accretion. The true truncation radius $r_{\rm T}$ is in general smaller than given above, because disk ram pressures (dominated by the azimuthal motion) generally are larger than free-fall ram pressures for the same mass accretion rate; the circular velocity is comparable to the free-fall velocity, whereas the disk radial velocities are very small and so the disk densities are large. Nevertheless, equation (10.70) illustrates the basic parameter dependence of the problem; the numerical factor can be modified suitably for the disk accretion case (e.g., Wang 1996).

Measurements of photospheric magnetic fields from line broadening indicate surface magnetic fields of order 2–3 kG (Johns-Krull *et al.* 1999b; Valenti & Johns-Krull 2004; Johns-Krull 2007). Measurements of *emission lines* like He I λ5876 and Ca II λ8498 yield estimates at the level of several kG (Johns-Krull *et al.* 1999a; Valenti & Johns-Krull 2004; Symington *et al.* 2005; Yang *et al.* 2007). Dipole fields of this strength would be able to disrupt T Tauri disks at rather larger radii (equation 10.70). However, measurements of net circular polarization yield much smaller estimates of *global average* fields, providing either upper limits or values of order 100 G (e.g., Daou *et al.* 2006; Yang *et al.* 2007). The polarization results imply that the line broadening is due to kG fields, but with comparable amounts of north and south poles on a given hemisphere; in turn this indicates that much of the field is in higher order moments than dipolar. The observation of polarization in emission lines does not contradict this inference, as these lines probably arise near the accretion shocks (Beristain *et al.* 2001) which cover small areas (typically of order a percent; Calvet & Gullbring 1998; Gullbring *et al.* 2000; Valenti & Johns-Krull 2004). As the lowest-order field – the dipolar field – is the component that survives to the largest distances, the polarization results suggest that the field strengths used in equation (10.70) should be much smaller than a kG.

The discussion of MHD flows in the previous section showed that magnetic fields can transport angular momentum efficiently. A basic parameter of the disk accretion problem is the co-rotation radius, where the Keplerian angular velocity of the disk equals the rotational angular velocity of the star (Figure 10.11). Consider the Bernoulli constant for strong radial magnetic fields (10.37). Taking the radial derivative of this energy constant near the disk truncation radius yields

$$v_{\rm p}\frac{dv_{\rm p}}{dR} = -\frac{GM_*}{R_{\rm T}^2} + R_{\rm T}\Omega_\circ^2 = -\frac{GM_*}{R_{\rm T}^2}(1-f^2)\,, \tag{10.71}$$

where

$$f = \frac{\Omega_\circ}{\Omega_{\rm T}} = \left(\frac{R_{\rm T}}{R_{\rm co}}\right)^{3/2}\,, \tag{10.72}$$

and $R_{\rm co}$ is the co-rotation disk radius at which the Keplerian angular velocity matches that of the star. It can be seen that if $f > 1$, i.e., $R_T > R_{co}$, the sign of the acceleration is positive and the gas will move outward, while for $f < 1$ material moves inward. Thus, magnetic field lines connecting to the disk outside of co-rotation will tend to transfer angular momentum from the star to the disk, while field lines connecting to the disk inside of co-rotation will transfer angular momentum from disk material to the star, allowing the matter to accrete.

Observed emission line profile asymmetries in CTTS provide strong evidence for high-velocity accretion flows, which are not consistent with slow radial infall in disks (§8.4). Temperatures of order 8000 K are needed to explain the Balmer line emission, and so we can assume ideal MHD (i.e., the gas is coupled strongly to the field lines). Moreover, the magnetic field must be strong enough to disrupt the dense disk, so it is reasonable to assume the limit where the magnetic field is sufficiently strong to enforce co-rotation of the gas in the magnetosphere and neglect gas pressure forces. Then the Bernoulli constant can be simply evaluated to find the velocity at radial distance r along a field line which meets the disk near $R_{\rm T}$,

$$v_{\rm P}^2 \simeq \frac{2GM_*}{r}\left(1-\frac{r}{R_{\rm T}}\right) + \Omega_\circ^2(R^2 - R_{\rm T}^2)\,; \tag{10.73}$$

if $R_{\rm T}$ is near the co-rotation radius $R_{\rm co}$, then

$$v_{\rm P}^2 \simeq \frac{2GM_*}{r}\left(1-\frac{r}{R_{\rm T}}\right) + \frac{GM_*}{R_{\rm T}}\left(\frac{R^2}{R_{\rm T}^2} - 1\right)\,. \tag{10.74}$$

Most accreting CTTS are slowly rotating, i.e., $R_{\rm co} \gg R_*$, and so for a first approximation one can ignore the azimuthal velocity, in which case the poloidal velocity is simply that of free-fall (including rotation for slow rotators makes little qualitative difference; Muzerolle *et al.* 2001). If the poloidal structure of the magnetic field is known, then the velocity vectors can also be determined, as well as the density along streamlines from the mass conservation equation.

Using this simple free-fall model, and assuming a non-rotating dipolar magnetosphere, Hartmann *et al.* (1994a) and Muzerolle *et al.* (1998a, 2001) found that it was possible to produce line profiles that look remarkably like observations. The principal uncertainty in the models is the temperature structure; the above calculations assume a simple smooth temperature distribution that is nearly constant over the magnetosphere, but drops near the disk. The infall asymmetry in the Balmer emission lines in both the model and observations

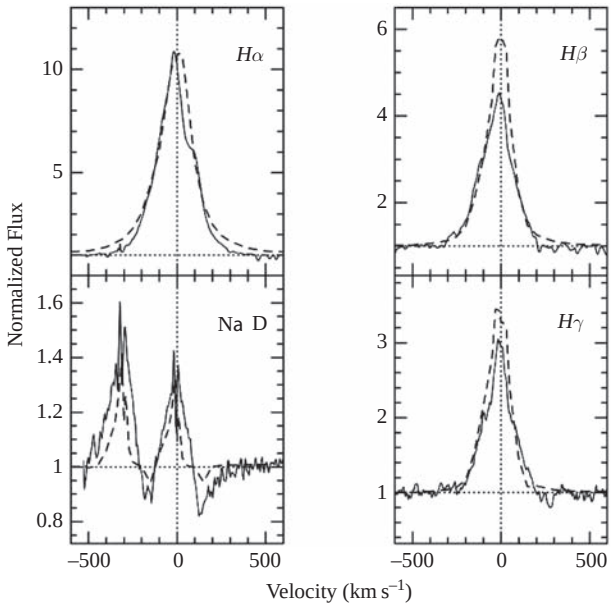

Fig. 10.13. $H\alpha$, $H\beta$, $H\gamma$, and Na I line profiles of the accreting T Tauri stars BP Tau (solid curves) compared with line profiles calculated for a simple magnetospheric infall model. The results show that in the absence of strong wind absorption, the line profiles and asymmetries can be well reproduced by magnetospheric infall. This calculation also demonstrates that differing species can yield strong or weak indications of redshifted absorption using the same velocity field, depending upon excitation conditions and whether the infalling material is aligned in front of the accretion shock along the line of sight. From Muzerolle *et al.* (2001).

of BP Tau is modest (Figure 10.13), while the redshifted absorption is much more prominent in Na I, showing the importance of detailed radiative transfer and statistical equilibrium calculations.

To explain the observed redshifted absorption, and the velocity widths of the underlying emission, it is necessary to invoke infall from $R \gtrsim 1.5R_*$; this is a conservative lower limit which ignores projection effects that make the line-of-sight velocities smaller than the absolute motions. It is very difficult to imagine that any standard boundary layer can form between the disk and star given such large magnetospheric radii, no matter what detailed geometrical form the stellar magnetic fields exhibit. Equation (10.70) indicates that dipolar field strengths of order 100 G would be able to hold off the disk to about $1.9R_*$ for fiducial parameters; thus, limits on global fields from polarization do not yet pose a significant problem for understanding T Tauri line profiles.

In this picture, most of the permitted-line emission of T Tauri stars comes from dense infalling material in the stellar magnetosphere, while the wind arises from outside the magnetosphere (Figure 8.11). Since the emission comes from the magnetosphere, the wind need not be very optically thick in the Balmer lines. In this way Hα, the Balmer line with the largest opacity, can exhibit detectable absorption while the higher Balmer series lines, with much smaller optical depths, can remain relatively transparent, explaining the absence of

blueshifted absorption in the latter (Edwards *et al.* 1994). These results are consistent with the forbidden-line analyses (§10.5) which suggest that T Tauri stars generally have winds with mass loss rates $\sim 10^{-9}\, M_\odot\, \mathrm{yr}^{-1}$, lower than typical accretion rates $\sim 10^{-8}\, M_\odot\, \mathrm{yr}^{-1}$ (§8.5), which (along with small volume filling factors) produce the high densities of the infalling magnetospheric gas.

Another possible indication of magnetospheric accretion is the presence of narrow components in addition to broad components in the emission lines (Hamann & Persson 1992; Batalha *et al.* 1996; Figure 10.14). Muzerolle *et al.* (1998b) suggested that this emission may in part be chromospheric, but might also naturally arise from the post-shock accreting gas – one would expect at least some line emission from this region. Detailed models are yet to be calculated to compare with observation.

While the paradigm of interaction between the stellar magnetosphere and disk is secure, the detailed field geometry is far from clear (e.g., von Rekowski *et al.* 2004). Given the rotational modulation seen in light curves, the stellar field cannot be axisymmetric; but simple non-aligned dipole structures tend to produce highly-collimated funnel flows which would predict much stronger rotational modulation of line profiles than is seen (e.g., Long *et al.* 2007). More broadly, both time-variations and non-axisymmetry almost certainly mean that the coupling region between star and disk cannot always be exactly at co-rotation – and some models demand coupling over a wide region in the disk – in which case magnetic field lines must tend to become twisted. Such twists rapidly lead to a "ballooning out" of closed field lines, with eventual opening up of field lines and possible ejection of mass, with reconnection following (van Ballegooijen 1994; Aly & Kuijpers 1990). The

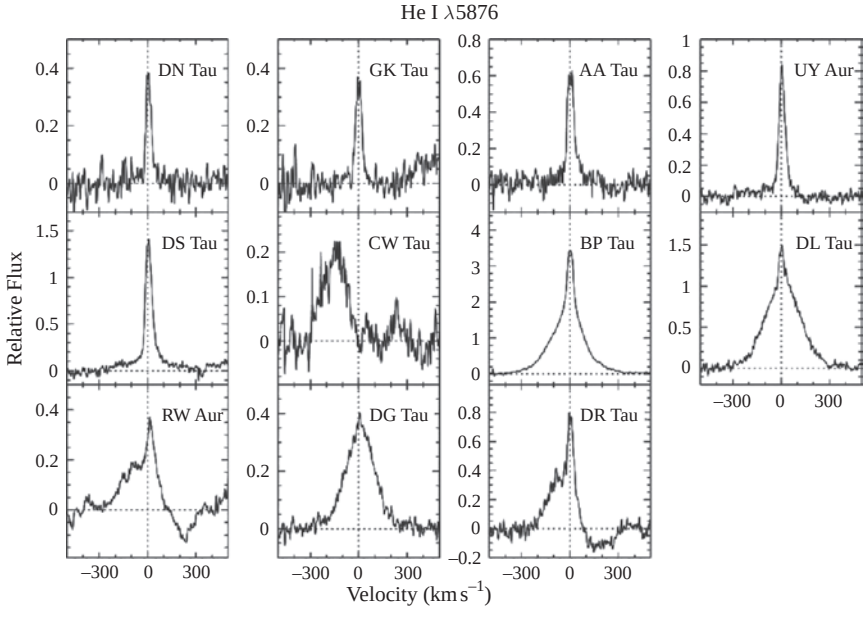

Fig. 10.14. Profiles of the He I λ5876 emission line in various T Tauri stars, showing evidence of a broad component, sometimes with redshifted absorption, along with a narrow component that may be formed in post-shock gas (see text). From Muzerolle *et al.* (1998b).

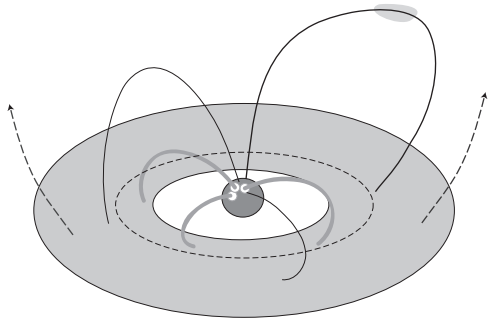

Fig. 10.15. Schematic model of individual stellar magnetic flux tubes connecting with the disk. Field lines (gray) connecting interior to co-rotation (dashed circle) allow accretion onto the star, producing small hot spots. Other field lines (light solid curves) connect to the disk exterior to co-rotation and can spin down the star. Most field lines probably eventually twist up and bulge outward (dark curve), possibly ejecting material (Goodson & Winglee 1999).

real structures of T Tauri magnetospheres may need to be considered as a series of individual loops, some of which connect interior to co-rotation, slowing down disk gas from Keplerian rotation and thus permitting accretion; other field lines attach to the disk outside of co-rotation, transferring angular momentum back to the disk; and almost all field lines eventually twist up and balloon outward (Figure 10.15). One advantage of a picture of many small accreting flux tubes is that it becomes easier to explain the very small covering factors of hot continuum regions, $\lesssim$1% (Calvet & Gullbring 1998; Gullbring *et al.* 2000).

The most uncertain aspect of the magnetospheric picture is the transfer of angular momentum. As matter is being accreted, so is angular momentum; thus, to explain the (generally) slower rotation of the CTTS, there must be some angular momentum transfer outward, either back to the disk or to a magnetically coupled wind. Ghosh and Lamb (1979) accomplished this by postulating a region of finite width through which the disk interacts with the magnetic field, ranging from inside to outside of co-rotation, assuming that the magnetic fields pass through the disk in a steady fashion, being dragged to some extent. That the necessary turbulence or other diffusion of field must occur has never been demonstrated. Shu *et al.* (1994) tried to avoid the wrapping-up problem by postulating that the interaction of the stellar magnetic field with the disk occurs only at a very small region right at co-rotation; however, as indicated above this seems unlikely given time-dependent accretion, magnetic fields, and non-aligned, complex field structure.

The current understanding of angular momentum transfer and stellar spindown is unsettled, with some simulations suggesting that steady magnetospheric braking can occur (Long *et al.* 2007), or that braking occurs in bursts when field lines open up (Goodson & Winglee 1999; Matt *et al.* 2002), or that disk braking is insufficient to spin down T Tauri stars because of the tendency of the field lines to open up (Matt & Pudritz 2004). In addition, the low estimates of global dipolar fields suggest truncation radii well inside of co-rotation, making disk spindown less plausible, though still possible (Johns-Krull 2007). Spindown generally requires magnetic fields tied to the star, leading to suggestions that stellar mass loss is in fact the angular momentum loss mechanism. The problem is that stellar-generated winds do not seem to be effective in producing spindown on timescales less than $\sim$100 Myr; otherwise,

one could not explain the rapidly rotating members of the Pleiades and α Per clusters as the result of contraction to the main sequence (e.g., Stauffer *et al.* 1989). This has lead to suggestions of stellar winds in T Tauri stars that are accretion-powered by some unknown mechanism (Matt & Pudritz 2005; Edwards *et al.* 2006). There is evidence for modest spin-down from the Class I protostellar phase to the T Tauri phase (Covey *et al.* 2005); but it seems clear that most of the angular momentum loss or control of stellar rotation must occur during the protostellar phase, in which physical conditions may be much different than those of the T Tauri phase, perhaps resulting in differing field geometries and spindown effects.

11

Disk accretion and early stellar evolution

The general outlines of pre-main-sequence evolution have been understood for a long time, though many important details remain uncertain. Young low-mass stars initially cannot sustain nuclear fusion in their cores; they must therefore contract gravitationally, generating potential energy which ultimately supplies their radiative losses. This contraction occurs on the Kelvin–Helmholtz timescale,

$$t_{\rm KH} \sim \frac{GM_*^2}{(R_* L_*)}\,, \tag{11.1}$$

where L_* is the stellar luminosity and GM_*^2/R_* is roughly the internal (kinetic plus gravitational potential) energy of a star of mass M_* and radius R_*. Stellar luminosities generally are proportional to a high power of stellar mass (as, e.g., on the hydrogen-burning main sequence); thus, low-mass, low-luminosity stars tend to have extended pre-main-sequence lifetimes, because their Kelvin times are longer than the timescales for the collapse of their parent clouds. In contrast, high-luminosity massive stars exhibit little if any pre-main-sequence evolution because their Kelvin–Helmholtz timescales are as short or shorter than the duration of infall from their natal clouds.

The gravitational contraction of low-mass stars can be slowed or even halted for a modest period of time by deuterium fusion. This slowing of evolution during deuterium burning makes it more likely that low-mass protostars will be observed in this phase, whose location in the HR diagram has been called the stellar "birthline" (Stahler 1983, 1988). While the birthline region appears to be relevant for low-mass pre-main-sequence stars, it is difficult to define a birthline for higher-mass protostars because deuterium fusion cannot be an important energy source for high-luminosity protostars.

One of the principal uses of pre-main-sequence evolutionary theory is to estimate the ages of young stars, providing the most reliable "clocks" we have for determining the timescales of star formation and disk evolution. Systematic errors remain in absolute ages, mostly due to uncertainties in stellar masses for low-mass stars and birthline positions for higher-mass stars. Direct estimates of masses from disk rotation and binary companions are now beginning to make significant improvements in T Tauri age estimates, with important consequences for understanding disk evolution.

11.1 Pre-main-sequence stellar evolutionary tracks

If a low-mass star is much larger than it would be on the hydrogen-burning main sequence, its central temperature will not be sufficiently high to fuse hydrogen in its interior. Under these circumstances, the only energy available to supply the stellar luminosity is the

internal thermal energy (excepting D fusion, treated in §11.3). As energy is lost to space, the internal energy must decrease, and so the star must contract; this contraction continues until the central temperature rises sufficiently that hydrogen fusion begins.

Hayashi *et al.* (1962) and Hayashi (1966) established the modern foundation of pre-main-sequence evolution by showing that low-mass stars above the main sequence are likely to be nearly completely convective (see Shu (1991) for an overview). The interiors of convective stars are found to be nearly adiabatic over most of their mass, because the convection is so efficient at energy transport (Schwarzschild 1958). The stellar interior in this case can be described by a polytropic equation,

$$P\rho^{-\gamma} = K = \text{constant} = P\rho^{-(1+1/n)} \,. \tag{11.2}$$

A convective star composed of a perfect gas has $\gamma = 5/3$ and a polytropic index, $n = 1/(\gamma - 1) = 3/2$ (Chandrasekhar 1967).

The equation of hydrostatic equilibrium (3.13) can be integrated using a polytropic approximation to construct simple models of stellar structure. The qualitative results can be developed from simple arguments. It is clear that polytropes of a given index will have similar internal structures, and thus scaling laws can be developed from general principles. For the $n = 3/2$ polytrope in particular, $P = KT^{5/2}$. From dimensional analysis we can find that the central pressure must scale as $P_c \propto GM_*^2 R_*^{-4}$ and the central temperature (proportional to c_s^2) must scale as $T_c \propto GM_*/R_*$; thus,

$$K \propto M_*^{-1/2} R_*^{-3/2} \,. \tag{11.3}$$

To find the radius of a star of a given mass requires the specification of the constant K, which cannot be found from analyzing only convective energy transport (Schwarzschild 1958). The radiative atmosphere provides the outer boundary condition necessary to specify K; it must be joined to the essentially adiabatic interior. To see this in its simplest form, consider the equation of hydrostatic equilibrium,

$$\frac{1}{\rho}\frac{dP}{dr} = -\frac{GM_*}{R_*^2} = -g \,, \tag{11.4}$$

where we have implicitly assumed that the atmosphere is thin and so the gravitational acceleration g is constant. We then evaluate this equation at the stellar photosphere, which we approximate as a layer of Rosseland mean optical depth $\tau_R = \int k_R \rho dz \sim 2/3$ (see Appendix 3), and having the effective temperature $T_{\rm eff}$ of the star (such that the luminosity is $L_* = 4\pi R_*^2 \sigma T_{\rm eff}^4$). Ignoring the temperature and density variation of the Rosseland mean opacity k_R enables us to integrate the equation of hydrostatic equilibrium to find the pressure at the photosphere,

$$P_{\rm eff} \sim \frac{2}{3}\frac{g}{k_R(P_{\rm eff}, T_{\rm eff})} \,. \tag{11.5}$$

For illustrative purposes, take $k_R \propto \rho T^a$; then $P_{\rm eff} \propto R_* T_{\rm eff}^{-a}$. Equating this pressure to the pressure of the internal adiabatic (polytropic) solution results in

$$T_{\rm eff} \propto R_*^{2.5/(2.5+a)} M_*^{0.5/(2.5+a)} \tag{11.6}$$

and

$$L_* \propto R_*^{(15+2a)/(2.5+a)} M_*^{2/(2.5+a)} \,. \tag{11.7}$$

For stars with effective temperatures $< 5000\,\mathrm{K}$ or so, the opacity is a very steep function of temperature (i.e., $a \sim 10$); this is the same parameter regime where disk thermal instabilities can develop due to this steep dependence on T (§9.6). Thus, equations (11.6) and (11.7) indicate that as the star contracts to compensate for the energy lost through radiation into space, the stellar luminosity decreases much faster than the effective temperature decrease. This means that fully convective pre-main-sequence stars descend nearly vertically in the HR diagram (Figure 1.3).

Detailed solutions for these so-called "Hayashi tracks" are unfortunately complicated by the need to take into account molecular opacities with millions of spectral lines. In addition, the Rosseland mean is strictly only appropriate at large optical depth, where the diffusion approximation holds (Appendix 3); it is not really appropriate to use in outer, more optically thin layers. Finally, the treatment of the energy transport by convection is problematic; the efficiency of convection cannot change abruptly from full to zero transport at a convective–radiative interface, but instead must vary smoothly from the adiabatic limit to the outer, radiative condition. While opacities can in principle be dealt with by increasingly sophisticated numerical transfer calculations, the convective transition is usually done through a "mixing length" treatment (e.g., Mazzitelli 1989) which is heuristic rather than predictive in nature.

As shown in Figure 1.3, the vertical convective tracks are displaced to cooler temperatures as the stellar mass decreases. Thus, the basic uncertainties in the theory translate into uncertainties in the mass of a star with a given luminosity and effective temperature. Empirical calibrations of theoretical evolutionary tracks can be made if the stellar mass can be estimated independently (§11.5).

We next look at the properties of the convective polytrope in more detail. Returning to the equation of hydrostatic equilibrium (3.13), we have

$$\frac{1}{\rho}\frac{dP}{dr} = -\frac{GM_r}{r^2} = -\frac{d\Phi}{dr}\,, \tag{11.8}$$

where M_r is the mass interior to radius r and Φ is the gravitational potential. With the polytropic assumption (11.2), one can integrate equation (11.8) with radius to obtain the ratio of pressure to density at radius r,

$$(n+1)\frac{P}{\rho} = \Phi(R_*) - \Phi(r)\,. \tag{11.9}$$

The total gravitational potential energy of the star is

$$W = -G\int_0^{R_*}\frac{M_r\,dM_r}{r} = \frac{1}{2}\int_0^{R_*}\Phi\,dM_r\,, \tag{11.10}$$

where the final right-hand result can be found by integrating by parts twice (Chandrasekhar 1967). Substituting, one finds

$$W = \frac{1}{2}\int_0^{R_*} dM_r\left[-(n+1)\frac{P}{\rho} + \Phi(R_*)\right] = -\frac{n+1}{2}\int_0^{R_*} P\,dV - \frac{1}{2}\frac{GM_*^2}{R_*}\,, \tag{11.11}$$

where V is the volume and $dM_r = 4\pi r^2\rho dr$.

From the virial theorem for an unmagnetized, non-rotating equilibrium configuration (3.5),

$$\int dV\, 3P = \int dV \rho r \nabla\Phi = \int \frac{dM_r\, GM_r}{r} = -W\,. \tag{11.12}$$

Combining these equations yields

$$W = -\frac{3}{(5-n)}\frac{GM_*^2}{R_*} = -\frac{6}{7}\frac{GM_*^2}{R_*} \tag{11.13}$$

for $n = 3/2$.

The internal thermal energy of the star is

$$U = \int_0^{R_*} c_V\, T\, dM_r = \frac{1}{\gamma-1}\int_0^{R_*}\frac{P}{\rho}\, dM_r = \frac{1}{\gamma-1}\int_0^{R_*} P\, dV\,, \tag{11.14}$$

where c_V is the specific heat at constant volume (Chandrasekhar 1967). Then, for a perfect gas,

$$U = -\frac{W}{3(\gamma-1)} = -\frac{W}{2}\,, \tag{11.15}$$

which is the result required by the virial theorem,

$$2U + W = 0\,. \tag{11.16}$$

Finally, we have the total energy of the polytropic star:

$$E = U + W = \frac{3}{7}\frac{GM_*^2}{R_*} - \frac{6}{7}\frac{GM_*^2}{R_*} = -\frac{3}{7}\frac{GM_*^2}{R_*}\,. \tag{11.17}$$

If the (pre-main-sequence) star does not have an internal fusion energy source, the energy radiated into space (the photospheric luminosity L_*) must cause a corresponding change in the energy of the star:

$$L_* = -\frac{d}{dt}E = -\frac{d}{dt}\frac{3}{7}\frac{GM_*^2}{R_*}\,. \tag{11.18}$$

The negative sign enters because a decrease in the total stellar energy results in a positive luminosity. At fixed stellar mass M_*, the radiation loss L_* will cause the star to contract, releasing gravitational potential energy to replace the energy lost from the stellar surface. By the virial equilibrium equation (11.16), half of this gravitational energy is converted into thermal energy which is needed to replace the surface energy losses to maintain hydrostatic support.

As discussed above, we can approximate Hayashi track evolution by setting the effective temperature to be roughly constant,

$$T_{\rm eff} = \left(\frac{L_*}{4\pi\sigma R_*^2}\right)^{1/4} \approx \text{constant}. \tag{11.19}$$

For times t long after some (arbitrary) starting time, when the radius was much larger than the current radius at time t, combining the constant effective temperature approximation with (11.18) results in

$$L_* = L_\circ\left(\frac{3t}{\tau_{\rm kh}}\right)^{-2/3}\,, \tag{11.20}$$

where

$$\tau_{\rm kh} = \frac{3}{7}\frac{GM_*^2}{R_\circ L_\circ} \tag{11.21}$$

is the Kelvin–Helmholtz timescale and

$$t_\infty = \frac{\tau_{\rm kh}}{3} \tag{11.22}$$

is the age for contraction from infinite radius; $L_\circ$ is the luminosity when the star has a reference radius $R_\circ$. Thus, as the star ages, it contracts and becomes fainter. The rate of decrease in the stellar luminosity (and in the stellar radius) slows with increasing age.

The simple estimate (11.20) does a reasonably good job of explaining the rate of contraction shown in Figure 1.3. As an example, for parameters $M_* = 0.8\,M_\odot$, $R_* = 2\,R_\odot$, and $L_* = 1\,L_\odot$, the Kelvin–Helmholtz time is $\tau_{\rm kh} = 4.3 \times 10^6$ yr, so that the Hayashi track age should be about $t \sim 1.4 \times 10^6$ yr, in reasonable agreement with the tracks.

This simple scaling of contraction rates predicts that stars differing by a factor of ten in age should have luminosities differing by $\Delta \log L \sim 2/3$, approximately what is found in detailed calculations. The principal departure from the power-law decay of the luminosity with time occurs for low-mass stars between the ages of $\sim 10^5$ and $\sim 3 \times 10^5$ yr, and is mostly due to deuterium fusion energy release when the central stellar temperature reaches $\sim 10^6$ K (§11.3). This nuclear energy release slows the stellar contraction, because the star is no longer supplying the energy lost in surface radiation from its internal store of thermal energy; this causes the isochrones to approach each other in Figure 1.2. Deuterium fusion represents a modest energy supply and therefore cannot halt the overall contraction for long. Once the deuterium is completely fused, gravitational contraction resumes unhindered until the star reaches the hydrogen-fusion main sequence.

For stars with masses $\gtrsim 0.8\,M_\odot$, contraction at nearly constant effective temperature eventually stops when the star develops a radiative core. We can understand this qualitatively using the diffusion equation (Appendix 3) and the equation of hydrostatic equilibrium. The radiative gradient is

$$\nabla_R = \frac{d\ln T}{d\ln P} = \frac{3k_{\rm R}P}{64G\pi\sigma T^4}\,\frac{L}{M}\,, \tag{11.23}$$

where quantities are evaluated at a local point r. Convection stops when $\nabla_{\rm R} < 0.4$ (Schwarzschild 1958). A crude estimate is given by $\nabla_{\rm R} \approx k_{\rm R}P/g$; if we then adopt a Kramer's law opacity $k_{\rm R} \propto PT^{-2.5}$, then $\nabla_{\rm R} \approx T^{1/2}/g$. Since the internal temperatures in a similar polytropic structure for a constant stellar mass will scale as $T \propto R_*^{-1}$ and $g \propto R^{-2}$, the radiative gradient becomes smaller as the star contracts, so that central convection will eventually stop (unless hydrogen fusion on the main sequence occurs first, or degeneracy pressure comes into play, halting contraction).

A star that is no longer fully convective then proceeds to the main sequence along nearly horizontal paths in the HR diagram (Henyey *et al.* 1955; Figure 1.3). This change occurs because radiative stars of uniform gaseous composition exhibit a well-defined relation between mass and luminosity (Schwarzschild 1958). In a radiative star the transport of energy can be described by the diffusion equation (Appendix 3) through the interior. Therefore, using a rough scaling argument,

$$\frac{1}{k_{\rm R}\rho}\frac{dT^4}{dr} \sim \frac{1}{<k_{\rm R}\rho>}\frac{T^4}{R_*} \propto \frac{L_*}{R_*^2}\,. \tag{11.24}$$

If we set the mean interior temperature $T \propto M_*/R_*$ (Chapter 2; also see equation (11.37)), and take the mean density $< \rho > \propto M_*/R_*^3$, then we arrive at a crude mass–luminosity relationship

$$M_*^3 < k_{\rm R} >^{-1} \propto L_* . \tag{11.25}$$

For very high-mass stars, where electron scattering dominates, the mean opacity is nearly constant, and $L_* \propto M_*^3$; these stars contract to the main sequence at nearly constant luminosity. For intermediate-mass stars, using a Kramers' opacity leads to $L_* \propto M_*^{5.5} R_*^{-0.5}$; thus, as the star contracts, its luminosity tends to increase (Figure 1.3).

11.2 Protostellar properties

It is reasonably clear that protostars cannot be formed with extremely large radii. A hydrostatic core can only be formed when the star is (very) optically thick, so that it cannot cool on a dynamical timescale and thus rapidly lose pressure support. Because the gas opacity falls so rapidly with decreasing temperature, as discussed in the previous section, pre-main-sequence stars cannot have very low effective temperatures – this is the famous "Hayashi forbidden zone" on the upper right-hand side of the HR diagram. With a minimum effective temperature, a protostar of large radius must have a large luminosity; therefore, the Kelvin–Helmholtz contraction timescale becomes very short. The protostar will contract extremely rapidly until its Kelvin timescale is comparable to if not longer than the infall timescale; thus, the duration of infall helps set the initial protostellar radius.

The first numerical calculations of low-mass protostars formed by collapsing envelopes, in particular those of Larson (1969a,b), indicated that envelopes which collapse on timescales of 10^6 yr form protostars at positions roughly near the 10^6 yr isochrones of Hayashi tracks. Although these results have been superseded by much more detailed calculations, it is remarkable how close Larson's results for initial stellar radii are to those of later, more sophisticated calculations (e.g., Stahler *et al.* (1980a,b); see Shu (1991) for an historical overview, and Boss (1995) for a more recent review).

We follow the argument of Stahler *et al.* (1980a) to illustrate the basic issues. Assume that a hydrostatic core forms early on; the protostellar energy release at time t is then the integral over time of the mass accretion energy release,

$$\int_0^t dt\, 4\pi R_{\rm p}^2 \sigma T_{\rm p}^4 \sim \int_0^t \frac{G M_{\rm p} \dot{M}}{R_{\rm p}} , \tag{11.26}$$

where the subscript p refers to the protostellar mass, radius, and effective temperature. The approximation on the left-hand side assumes relatively free radiation into space, which is plausible (see p. 253). For a constant accretion rate $\dot{M}$, integration with time yields

$$< R_{\rm p} > \sim \left(\frac{G M_{\rm p}^2}{8\pi\sigma < T_{\rm p} >^4 t} \right)^{1/3} , \tag{11.27}$$

where the angular brackets are time-averaged values. Now, compare this with a Hayashi track calculation for the convective polytrope of the same mass (e.g., equation (11.18)),

$$4\pi R_{\rm H}^2 \sigma T_{\rm H}^4 = \frac{d}{dt} \frac{3}{7} \frac{G M_*^2}{R_*} , \tag{11.28}$$

where $T_{\rm H}$ is the effective temperature for the correct outer boundary condition. Integrating this equation with $T_{\rm H}$ = constant yields

$$R_{\rm H} \sim \left(\frac{G M_{\rm p}^2}{28 \pi \sigma T_{\rm H}^4 t} \right)^{1/3} , \tag{11.29}$$

integrating from an infinite radius at $t = 0$. Dividing the two results for the same mass star yields

$$\frac{< R_{\rm p} >}{R_{\rm H}} \sim \left(\frac{7}{2} \frac{T_H^4}{< T_{\rm p} >^4} \right)^{1/3} . \tag{11.30}$$

For the protostellar radius $< R_{\rm p} >$ to be much larger than the Hayashi track condition, the accretion temperature would have to be $\ll T_{\rm H}$. However, because the gas opacity decreases so rapidly with decreasing temperature for low-mass stars – the reason for the vertical tracks in the HR diagram – $< T_p >$ must generally be greater than or equal to $T_{\rm H}$, and thus we do not expect the protostellar radius to be more than a factor of two or so larger than the equivalent Hayashi track radius at a comparable "age" t. (Even for extremely low-mass convective stars, it is difficult for the stellar effective temperature to be much lower than $\sim$2800 K, corresponding to the Hayashi "forbidden region" in the HR diagram; see Figure 1.4). This result also confirms the initial guess that the corresponding $t_{\rm KH}$ cannot be much shorter than the accretion timescale $\sim M/\dot{M}$.

The above derivation in spherical collapse requires the assumption that the infalling envelope does not trap too much of the accretion luminosity, and that dissociation and partial ionization energies are not large. In the case of spherical accretion, Stahler *et al.* (1980a,b) pointed out that the low gas opacities of infalling material make this a reasonable approximation; the backwarming from the envelope arises from the more distant dust-destruction radius, which limits the radiative trapping. The neglect of trapping becomes even more robust in the case of rotating collapse; after the initial core is formed, the angular momentum of the infalling material will deposit mass onto the disk, leaving the central protostar with less obscuring material. Any outflows will also help clear out the inner envelope.

11.3 The "birthline"

The analysis of §11.1 is changed if the protostar is hot enough in its core ($T \sim 10^6$ K) for deuterium fusion to occur. In this case, contraction can be halted as D energy release replenishes the energy lost by radiation. Stahler (1983, 1988) argued that, for a reasonable range of initial conditions and accretion rates, protostars should evolve in such a way that their radii are a strongly constrained function of their mass. The general idea is as follows: The rate of deuterium fusion is a very sensitive function of the central temperature of the protostar, which scales as $T \propto M_{\rm p}/R_{\rm p}$. If the central temperature falls slightly, the star will contract until the temperature rises high enough for fusion; conversely, if the central temperature increases slightly, the resulting rapid increase in luminosity will cause the star to expand and cool in the central regions. This thermostatic effect – keeping the central temperature nearly constant – results in a relatively fixed ratio of mass to radius. Thus, Stahler argued that once spherical accretion ends, the required ratio of $M_{\rm p}/R_{\rm p}$ would result in protostars appearing along a well-defined locus in the HR diagram he called the "stellar birthline", which is roughly consistent with the positions of the *youngest* optically visible stars.

This argument for the existence of a birthline is subject to two important limitations. First, deuterium fusion does not prevent the formation of stars *above* the birthline in the HR diagram; other arguments must be used to fix initial conditions, such as discussed in the previous section. Second, deuterium represents a fairly minor source of energy in general pre-main-sequence evolution. Assuming an interstellar medium abundance ratio of $D/H = 2.5 \times 10^{-5}$, the energy release from deuterium fusion can last

$$E \sim 1.5 \times 10^6 \,\mathrm{yr} \left(\frac{L_*}{L_\odot}\right)^{-1} \left(\frac{M}{M_\odot}\right) . \tag{11.31}$$

Referring to Figure 1.3, one sees that a young $0.3\,M_\odot$ star of luminosity $\sim 0.3\,L_\odot$ might have its contraction slowed by an appreciable amount for ~ 1 Myr, but a $1\ M_\odot$ star with a luminosity of $\sim 5\ L_\odot$ will have its contraction slowed for only ~ 0.3 Myr, comparable to the infall timescale. Thus, we expect D fusion to be most important for low-mass protostars, and unimportant for higher-mass stars. Moreover, even for low-mass protostars, the rate of deuterium addition matters; if the accretion rate is too low, the addition of fresh deuterium cannot compensate for the loss due to fusion.

To illustrate the main physics of the birthline calculations without the complications necessary to address spherical accretion (Stahler 1988), we assume accretion occurs through a disk or magnetospheric hot spots which cover only a small fraction of the stellar surface. In this case, most of the stellar photosphere can radiate freely to space, unaffected by accretion. Under these conditions, we expect typical low-mass pre-main-sequence stars or stellar cores to be completely convective, and therefore adopt the $n = 3/2$ polytropic approximation. We further neglect the rotational energy of the star for simplicity; this should not be a bad approximation for most T Tauri stars, which are slowly rotating. The treatment here follows that of Hartmann *et al.* (1997; see also Palla & Stahler 1992).

Suppose a small mass of gas Δm is added to the star, with gravitational potential energy

$$\Delta W = -\frac{G M_* \Delta m}{R} \tag{11.32}$$

and internal energy

$$\Delta U = \epsilon \, \frac{G M_* \Delta m}{R} , \tag{11.33}$$

where ϵ is introduced to parameterize the thermal energy content of the accreted material (e.g., Prialnik & Livio 1985). The star then readjusts to a polytropic configuration with mass $M_* + \Delta m$ and radius $R_* + \Delta R$. We assume that this mass is added over a time Δt, and that the surface luminosity of the star during this time is L_*. Then conservation of energy requires (cf. equation (11.18))

$$L_* \Delta t - \frac{3}{7} \frac{G(M_* + \Delta m)^2}{(R_* + \Delta R)} = -\frac{3}{7} \frac{G M_*^2}{R_*} - \frac{G M_* \Delta m}{R_*} (1 - \epsilon) + L_{\rm D} \Delta t , \tag{11.34}$$

where $L_{\rm D}$ is the deuterium fusion luminosity (see also Palla & Stahler 1992). Expanding this equation to first order, writing $\dot{M} = \Delta m / \Delta t$, and letting $\Delta t \to 0$, we have

$$L_* = -\frac{3}{7} \frac{G M_*^2}{R_*} \left[\left(\frac{1}{3} - \frac{7\epsilon}{3} \right) \frac{\dot{M}}{M_*} + \frac{\dot{R}_*}{R_*} \right] + L_{\rm D} . \tag{11.35}$$

In the limit that $\dot{M} = 0$ and $L_{\rm D} = 0$, the standard gravitational contraction result (11.18) is recovered.

The first two terms on the right-hand side of equation (11.35) account for change in the energy of the star due to the accreted matter. To isolate the basic effects, assume that the surface photospheric luminosity and the deuterium fusion luminosity are small (equivalently, assume that a finite mass and energy are added on a short enough timescale that surface energy losses and deuterium fusion energy release are negligible). First, suppose $\epsilon << 1/7$, so that the material is accreted "cold". Then the accretion of matter will cause the star to contract ($\dot{R}_* < 0$). The physical reason for this is that the cold accreted material does not support itself; the star must readjust to generate additional thermal energy (pressure) to support this material. In the case of a (convective) $n = 3/2$ polytrope, the star must contract. Conversely, if $\epsilon > 1/7$, then the accretion of warm material will tend to make the star expand (e.g., Prialnik & Livio 1985). For sufficiently large accretion rates and ϵ, the accreting star may become radiative, in which case the star may expand rapidly and this treatment is invalid, as discussed below (see also §9.7).

We can relate ϵ to other physical quantities by noting that, for a perfect gas,

$$T_{\rm acc}\,\Delta m = \frac{\Delta U}{c_V} = \frac{(\gamma-1)\mu\, m_{\rm H}}{k}\,\Delta U = \frac{2}{3}\frac{\mu m_{\rm H}}{k}\Delta U\,, \tag{11.36}$$

where $T_{\rm acc}$ is the temperature of the accreting gas, k is Boltzmann's constant, $m_{\rm H}$ is the mass of the hydrogen atom, ΔU is the change in internal energy due to the accreted gas, and c_V is the ratio of specific heats at constant volume. An average internal temperature can be calculated for the $n = 3/2$ polytrope,

$$M\langle T\rangle \equiv \int T\,dM = \int \frac{u}{c_V}\,dM = \frac{2}{7}\frac{\mu\, {\rm m}_H}{k}\frac{GM^2}{R}\,, \tag{11.37}$$

where u is the specific internal energy. Substituting for ΔU from (11.33) and solving for ϵ using (11.36) and (11.37),

$$\epsilon = \frac{3}{7}\frac{T_{\rm acc}}{\langle T\rangle}\,. \tag{11.38}$$

The critical value $\epsilon_{\rm c} = 1/7$ then corresponds to $T_{\rm acc} = (1/3)\langle T\rangle$, i.e., the temperature of the accreting material is a considerable fraction of the average internal temperature of the star.

As emphasized by Stahler (1988), the fusion of deuterium can play a crucial role in setting the evolutionary tracks of low-mass protostars. Deuterium energy generation is proportional to $\rho T^{14.8}$; integrating over the interior of an $n = 3/2$ polytrope,

$$L_{\rm D} = 1.92\times 10^{17}\, f\left[\frac{D}{H}\right]\left(\frac{M_*}{M_\odot}\right)^{13.8}\left(\frac{R_*}{R_\odot}\right)^{-14.8} L_\odot \tag{11.39}$$

(Stahler 1988). Here f is the fractional concentration of deuterium relative to its initial number abundance, which is taken to be $[D/H] = 2.5\times 10^{-5}$. This equation assumes that the convection in the star instantaneously and thoroughly mixes all the deuterium, so that f is spatially constant at any time within the star. The strong dependence on stellar mass and radius arises from the steep dependence of the deuterium fusion on the central temperature, which is $\propto M_*/R_*$.

Because of the importance of $L_{\rm D}$, evolutionary calculations must consider the variation of f,

$$\frac{df M_*}{dt} = \dot{M} - \frac{L_{\rm D}}{\beta_{\rm D}}\,, \tag{11.40}$$

where $\beta_{\rm D}$ is the total energy available from deuterium fusion per gram of material (Stahler 1988). Rearranging this, we may write

$$\frac{df}{dt} = \frac{\dot{M}}{M_*}\left(1 - f - \frac{L_{\rm D}}{L_{\rm DSS}}\right), \tag{11.41}$$

where $L_{DSS} = \beta_D \dot{M}$ is the steady luminosity release that would be produced if the deuterium in the accreted material were instantaneously fused; numerically, for the assumed deuterium abundance,

$$L_{\rm DSS} = 1.5\left(\frac{\dot{M}}{10^{-6}\ M_\odot\ {\rm yr}^{-1}}\right)\ L_\odot\,. \tag{11.42}$$

The resulting evolution of the protostellar core can be calculated if the photospheric radiative losses are known. In this case, the surface photospheric radiative losses are the same as for an isolated pre-main-sequence star because accretion effects are limited to only a small area of the photosphere. The detailed form of $L_*(M_*, R_*)$ can be taken in principle from the results of stellar structure calculations. For illustrative purposes one may adopt the following fit to the "CMA" stellar evolutionary tracks of D'Antona and Mazzitelli (1994):

$$L_* = 1\left(\frac{M_*}{0.5\ M_\odot}\right)^{0.9}\left(\frac{R_*}{2\ R_\odot}\right)^{2.34}\ L_\odot \tag{11.43}$$

(Hartmann *et al.* 1997). This fit is only approximate and appropriate for the regime $0.3\ M_\odot \le M_* \le 1\ M_\odot$.

Figure 11.1 shows evolutionary tracks calculated for two different mass accretion rates, rates which might correspond to infall estimates (Chapters 4, 5). The curves have been calculated by simultaneously solving (11.35), (11.39), (11.41), and (11.43), starting with a low-mass core of small radius, and assuming that accretion is "cold" ($\epsilon = 0$). These disk accretion curves depart only modestly from the spherical accretion results of Stahler (1988; solid dots in Figures 11.1, 11.2). In part, the differences between the two treatments derive from Stahler's use of more detailed stellar interior calculations and a careful treatment of

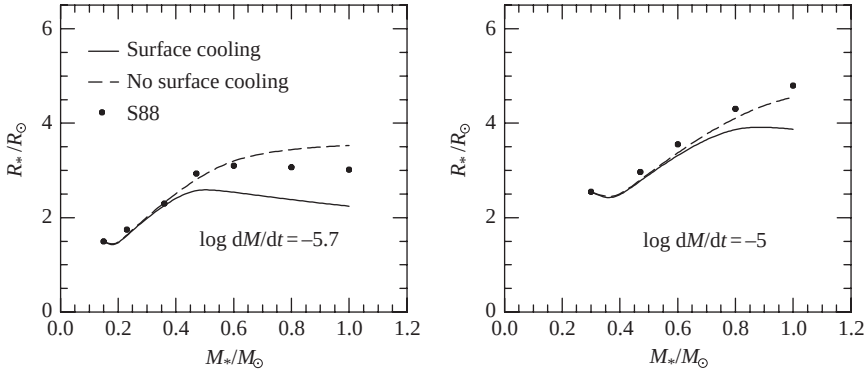

Fig. 11.1. Birthline evolutionary tracks for two different mass accretion rates. The dots correspond to the results of Stahler (1988) and the curves are calculated from the simple evolutionary model for cold disk accretion (§9.5). From Hartmann *et al*. (1997).

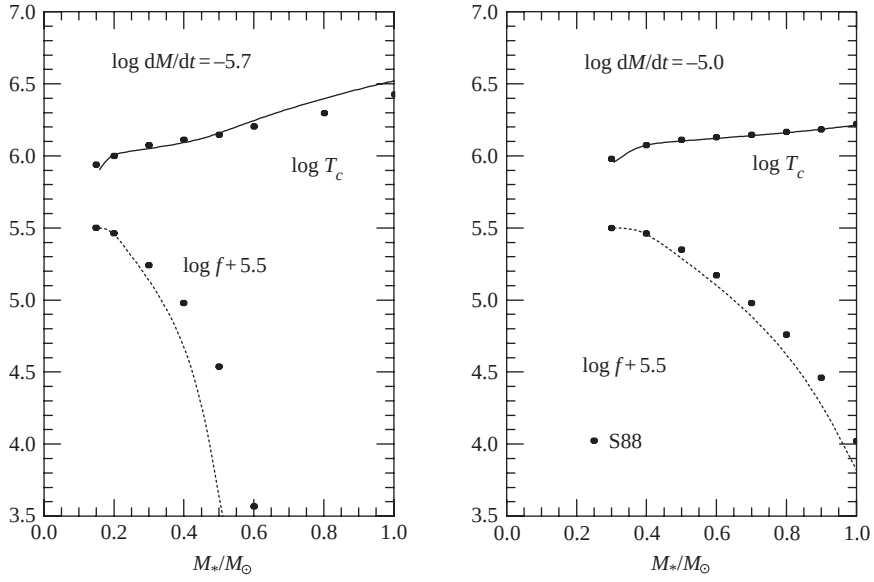

Fig. 11.2. Variation of central protostellar temperature and deuterium concentration f corresponding to the evolutionary tracks shown in Figure 11.1 (the "surface cooling" case). Dots show the original results of Stahler (1988); curves use the simple method described in the text. From Hartmann *et al.* (1997).

the accreting material. However, it appears that the main reason for the differences between disk and spherical accretion is the difference in outer boundary conditions. Stahler assumed much smaller stellar photospheric radiative energy losses L_* (see discussion in Hartmann *et al.* 1997). To illustrate this, the dashed lines in Figure 11.1 show the effect of setting $L_* = 0$ in the simple model calculations. The resulting $R_*(M_*)$ relations track the original calculations of Stahler more closely.

There is an initial $M_* \propto R_*$ dependence, which extends to higher masses at higher accretion rates; this is the region where the concentration of deuterium remains high, and so the central stellar temperature must remain fixed (Figure 11.2). At higher masses the $R_p(M_p)$ relation flattens out when the available deuterium is mostly fused into heavier elements (Figure 11.2), allowing the star to heat up beyond the point of deuterium fusion.

To clarify the effect of the photospheric radiative energy loss, which is assumed not to be blocked or trapped by the accreting material, it is useful to compare L_* to the steady-state luminosity that would occur if deuterium were fused as it is accreted into the protostar, $L_{\rm DSS}$. If $L_* < L_{\rm DSS}$, the demands on deuterium fusion are low, and the concentration f remains high. However, for $L_* > L_{\rm DSS}$ the energy losses require fusing deuterium at a rate faster than is supplied through accretion, and f must drop. This behavior is shown explicitly in Figure 11.3. The evolutionary tracks turn over slightly before $L_* = L_{\rm DSS}$ because some energy must be invested in heating the star to help support the weight of the cold accreting material. The corresponding deuterium concentrations are shown in Figure 11.2. As the stellar luminosity becomes increasingly large, the deuterium becomes depleted, allowing the star to have a higher central temperature and thus contract below the deuterium main sequence.

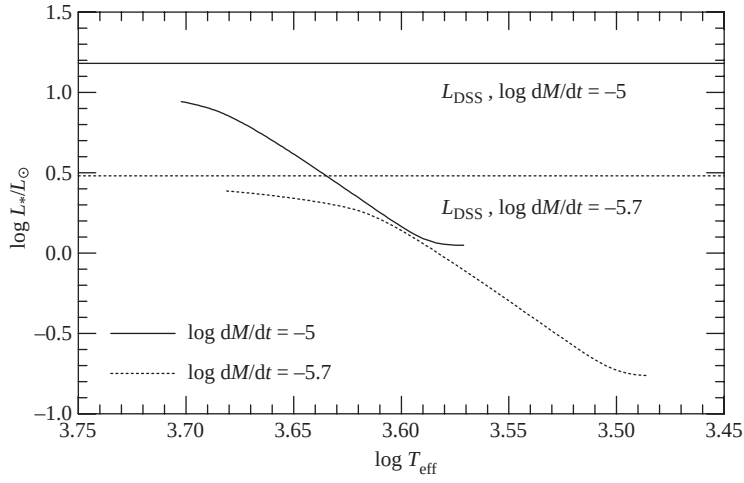

Fig. 11.3. HR diagram tracks for the "surface cooling" calculations of Figure 9.2. The evolutionary tracks initially follow the $R_* \propto M_*$ relation when the deuterium fusion luminosity is high; however, once the (proto)star approaches the steady-state luminosity L_{DSS} the evolutionary tracks become more horizontal, because the energy represented by the fresh deuterium being accreted is now balanced by the photospheric radiative losses (see text). From Hartmann *et al.* (1997).

The above discussion deals with the case where the protostar is completely convective. However, as shown in §11.1, at higher masses and luminosities one may expect the star to become radiative. To show the resulting qualitative differences from convective protostar accretion in a heuristic way, consider the differences between the $n = 1.5$ convective polytrope and an $n = 3$ polytrope, which can be taken as a rough approximation to the structure of a radiative star; for the latter,

$$E_3 = -\frac{3}{4}\frac{GM^2}{R}\,. \tag{11.44}$$

Consider the addition of a cold shell of small mass δM, and thus energy $E_s = -GM\delta M/R_\circ$, to a star of initial mass and radius $M_\circ$, $R_\circ$. The star must readjust to the additional weight by thermalizing part of the additional energy. Suppose this happens fast enough that the energy loss by radiation can be neglected. Then

$$\begin{aligned} -\frac{3}{4}\frac{GM_\circ^2}{R_\circ} - \frac{GM_\circ\delta M}{R_\circ} &= -\frac{3}{4}\frac{GM_\circ^2}{R_\circ}\frac{(1+\delta M/M_\circ)^2}{(1+\delta R/R_\circ)} \\ &\simeq -\frac{3}{4}\frac{GM_\circ^2}{R_\circ}\left((1+\frac{2\delta M}{M_\circ} - \frac{\delta R}{R_\circ}\right)\,. \end{aligned} \tag{11.45}$$

Equating terms, we find

$$\frac{GM_\circ\delta M}{2R_\circ} \simeq \frac{3}{4}\frac{GM_\circ^2}{R_\circ}\frac{\delta R}{R_\circ}\,; \tag{11.46}$$

since $\delta R > 0$, the star *expands* rather than contracts. Thus one may expect the birthline evolution of higher-mass stars to result in expansion and increased luminosity as mass is added – and this is seen in the detailed results of Palla and Stahler (1992).

However, birthlines for stars with masses $\gtrsim 1\, M_\odot$ must be regarded as highly uncertain. Even at low masses, birthline positions depend upon the accretion rate; moreover, birthline positions also differ for differing assumed initial masses and radii (Stahler 1988; Hartmann *et al.* 1997). These difficulties are even greater for higher-mass stars, because as discussed previously deuterium fusion cannot represent a significant energy source at higher luminosities. This means that birthlines for intermediate-mass stars and high-mass stars are very sensitive to the assumed initial conditions.

In their theoretical calculations of intermediate-mass birthlines, Palla and Stahler (1992) assumed that the initial protostellar cores are essentially the same for all stars; the result is birthlines which lie well above observed positions of young stars in the HR diagram. There is no theoretical justification for the assumption of initially equal core or starting masses; indeed, one might expect that the initial core mass to scale with the final mass of the star. Moreover, as Palla and Stahler (1992) show, even with similar initial core properties, a plausible range of accretion rates produces distinctly differing birthline properties. Finally, given observational uncertainties and likely variations in initial conditions for different stars of similar mass, it seems plausible that one should aim for lower birthline positions for intermediate-mass stars in the HR diagram. As discussed further in §11.5, lower birthlines would produce ages for intermediate-mass stars in better agreement with those of lower- and higher-mass stars.

11.4 Birthlines: comparison with observations

Figure 11.4 shows a comparison of the cold disk accretion birthlines (left panel) with the HR diagram positions of Taurus stars (e.g., Figure 1.3). The birthline tracks in the low-mass region pass near the upper envelope of the stellar positions. It is not necessary for the birthline to pass above all HR diagram positions of young stars, given observational errors and uncertainties (such as unresolved binaries) and the possibility that stars may form (slightly) above the birthline.

Ideally, one would like to test the birthline calculations with observations of protostars. The right panel of Figure 11.4 shows data for Class I sources, with effective temperatures estimated from the analysis of near-infrared spectra by Doppmann *et al.* (2005) and luminosities from Kenyon and Hartmann (1991). This figure indicates that the main problem with testing the birthline hypothesis for Class I objects comes from the large uncertainties in the luminosity. Doppmann *et al.* used observed near-infrared fluxes with a guess at reddening and a correction to increase the apparent fluxes by a factor of $\sim$2 to account for the fact that these objects are generally observed in scattered light. It seems preferable to use the apparent bolometric (infrared) luminosity, which is less likely to be affected by inclination, though there is always some uncertainty due to the non-spherical nature of protostellar envelopes (Chapter 5). Another uncertainty derives from the presence of accretion luminosity. The open circles in the right panel of Figure 11.4 represent DG Tau – a very rapidly accreting, heavily veiled T Tauri star – and L1551 IRS 5, a binary FUor (§5.4, Chapter 9). It is thus no surprise that these objects lie well above the birthline.

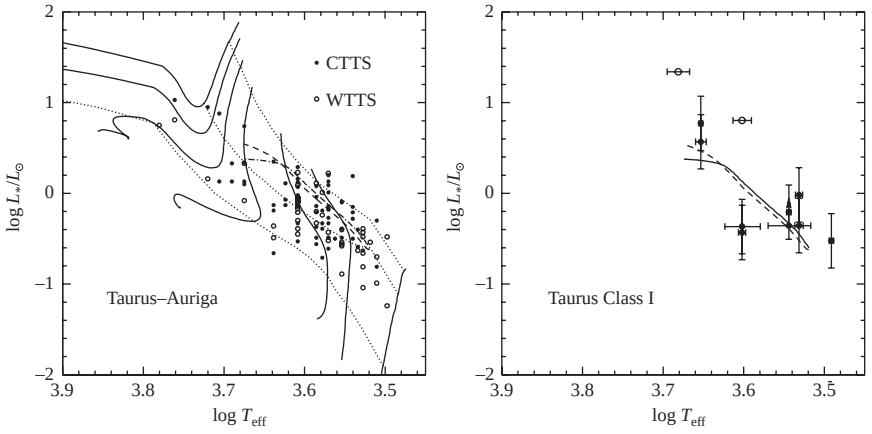

Fig. 11.4. Left: stellar evolutionary tracks for low-temperature ($\epsilon = 0$) disk accretion, compared with observed HR diagram positions of T Tauri stars in the Taurus–Auriga star-forming region, modified slightly from the results of Figure 11.1, by interpolating in the D'Antona and Mazzitelli (1994) CMA tracks to improve the calibration of $L_*(M_*, R_*)$ (see text). The heavy solid lines correspond to birthline accretion rates of $\dot{M} = 2 \times 10^{-6}\ M_\odot\ {\rm yr}^{-1}$ (lower) and $\dot{M} = 10^{-5}\ M_\odot\ {\rm yr}^{-1}$ (upper). The light solid lines show the CMA pre-main-sequence evolutionary tracks of D'Antona and Mazzitelli for masses of 0.1, 0.3, 0.5, 1, 1.5, and 2.5 $M_\odot$. The dashed lines show isochrones for 1×10^5 yr, 1×10^6 yr, and 1×10^7 yr. The HR diagram positions of T Tauri stars in the Taurus–Auriga molecular cloud, segregated between weak-emission (WTTS) and strong-emission (CTTS) stars, are taken from Kenyon and Hartmann (1995). These birthline tracks roughly pass through the upper envelope of the apparent HR diagram positions of the T Tauri stars, and correspond roughly to $t \sim 3 \times 10^5$ yr Hayashi track calculations. Right: properties of Taurus Class I objects compared to the birthlines in the left-hand panel, with effective temperatures taken from Doppmann *et al.* (2005) and (bolometric) luminosities from Kenyon and Hartmann (1995).

The comparisons between observation and theory shown in Figure 11.4 indicate that the properties for low-mass Class I objects are roughly consistent with expected birthline positions, and that most low-mass T Tauri stars appear to have contracted slightly below the birthline(s), as expected. (The accretion rates of T Tauri stars are unlikely to be large enough to have a significant effect on normal Hayashi track contraction; Hartmann *et al.* 1997).

As discussed in §5.1, accretion rates inferred from luminosities of Class I objects (and even many Class 0 objects) are considerably lower than the rates used in these calculations – rates which are needed to form the star on a reasonable timescale. This suggests that the bulk of the protostellar mass is amassed during short bursts of very rapid accretion. Prialnik and Livio (1985) showed that rapid accretion of material with finite thermal energy content onto a fully convective, main sequence, low-mass star can cause the star to become partially radiative and expand substantially. This can occur even when $\epsilon < 1/7$, for which our assumption of a convective polytropic star would result in contraction (in the absence of deuterium fusion). If the timescale for changing the thermal energy of the star is short in comparison with the thermal equilibrium timescale, thermal equilibrium cannot be established, which is necessary for the star to remain convective. The constraint that the thermal time of the star be shorter than the thermal energy addition timescale,

$$t_{\rm th} = \frac{E}{L_*} < t_{\rm U} = E\left(\frac{\epsilon GM\dot{M}}{R}\right)^{-1} \tag{11.47}$$

corresponds to

$$\epsilon\, GM\frac{\dot{M}}{R} < L_* \,. \tag{11.48}$$

This condition states that convection could be suppressed if ϵ is greater than the ratio of intrinsic stellar luminosity to the accretion luminosity. Rapid accretion during the FU Ori phase might expand the star, explaining the somewhat larger inner radii inferred for these disks (Chapter 9).

It is not known at present whether episodic accretion modifies birthline calculations substantially from steady-state results. If the bursts of accretion are relatively short compared with evolutionary timescales, and if large amounts of thermal energy are not advected into the stellar interior, it may be possible to consider these birthline results as applying to a suitable time-average of protostellar accretion. Even if significant amounts of thermal energy are advected into the star during an FU Ori outburst, if the outburst is short enough, this extra energy may not be integrated fully into the star but radiated away during long periods between outbursts, so that the steady cold accretion birthline calculations might still be relevant with suitable time averaging.

11.5 Age estimates

Typically, stellar ages are estimated by placing stars in the HR diagram and then comparing it with theoretical isochrones. In addition to observational errors discussed in the following section, theoretical evolutionary tracks are somewhat uncertain, and often do not consider birthline effects, but instead start the calculations at very large stellar radii. Here we adopt a schematic approach to illustrate some of the difficulties involved in estimating ages.

The elapsed time $t_{\rm b}$ that a low-mass, fully convective, pre-main-sequence star has been contracting since the end of major accretion is (e.g., equation 11.22)

$$t_{\rm b} = \frac{\tau_{\rm KH}}{3} - \frac{\tau_{\rm KH}}{3}({\rm birth}) = \frac{GM_*^2}{7R_*L_*} - \frac{GM_*^2}{7R_\circ L_\circ}({\rm birth})\,, \tag{11.49}$$

where the terms labeled "birth" denote quantities at the star's birth position. This equation explicitly shows which stellar properties need to be determined to produce an age estimate, and also emphasizes the potential importance of the birthline correction (the second term on the right-hand side).

If a low-mass star is old enough that the birthine correction is unimportant, then $t_{\rm b} \propto M_*^2 T_{\rm eff}^2 L_*^{-3/2}$. The main uncertainty then usually comes from the error in determining the stellar mass. The sensitivity of the atmospheric opacity to temperature which makes contraction occur at nearly constant temperature (§11.1) also results in low-mass stars having a small spread in effective temperature over a substantial range in mass. Differing theoretical treatments of the outer boundary conditions typically result in differences in estimated ages for a given stellar luminosity and effective temperature of roughly a factor of two for stars of masses $\sim 0.8 - 0.3\,M_\odot$.

Substantial improvements in this area are coming from direct mass estimates from binary motion and disk kinematics. As an example of how to use equation (11.49), masses estimated

from disk kinematics of a few Taurus CTTS from Simon *et al.* (2000) indicate in a median age (without birthline correction) $\sim$2 Myr (e.g., Table 2.1), in reasonable agreement with several theoretical evolutionary tracks.

For stars more massive than $\sim 1\,M_\odot$, and especially those on radiative tracks (e.g., Figure 1.3), a similar result to equation (11.49) can be obtained, with $M_*^2/(R_* L_*)$ still the important quantity. For these stars the mass uncertainty is relatively unimportant, given the strong dependence of their luminosities on mass (§11.1), as well as removing the need to treat convective effects and better-understood opacities. However, now the birthline correction becomes much more important, due to the unimportance of deuterium fusion and the importance of the initial thermal energy content during protostellar formation. Indeed, at masses of $\sim 4\,M_\odot$ and more, stars are formed essentially on the main sequence, so that there is essentially no pre-main-sequence evolution. Thus, the young higher-mass stars will be assigned erroneously large ages by using evolutionary tracks which assume initially large radii. In clusters where we expect star formation to be roughly coeval, the birthline problem shows up as a systematic variation of cluster age with stellar mass.

The classic example of the mass-dependence of ages derived without birthline corrections is the Orion Nebula Cluster. As shown in Figure 11.5, the intermediate-mass stars appear to be substantially older by many Myr than *either* the low-mass stars *or* the high-mass stars. Taken at face value, this would imply that the cluster existed for several Myr forming only $\sim 2 - 4\,M_\odot$ stars without forming any low-mass (or high-mass) stars. Other very young

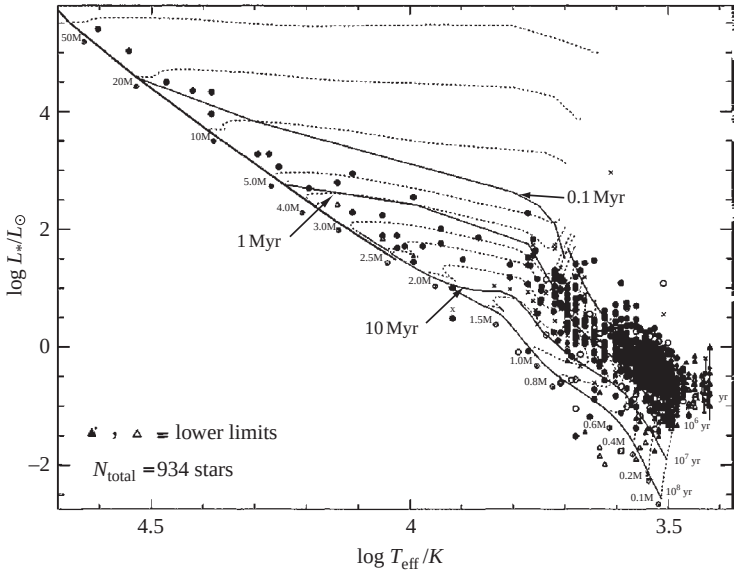

Fig. 11.5. HR diagram for the Orion Nebula Cluster. As indicated by theoretical isochrones without birthline corrections, the low-mass stars have ages $\lesssim$1 Myr; the A and late B stars near the main sequence with masses between $\sim 2\,M_\odot$ and $\sim 4\,M_\odot$ have ages between 1 and 10 Myr; and the high-mass stars have ages between 1 and 0.1 Myr, or even less. Rather than envisioning cluster formation over many Myr, starting only with intermediate-mass stars, it seems more likely that large birthline corrections must be applied to the ages of the intermediate-mass stars. Modified from Hillenbrand (1997).

clusters show similar behavior. As we never observe such a strange mass function in young clusters, it must be that there is a mass-dependent error in the isochrones. The most plausible explanation of this discrepancy is that the birthline correction is large for the intermediate-mass stars; that is, they start out much closer to the main sequence than the low-mass stars. As the massive stars clearly start out essentially on the main sequence, while the low-mass stars start out well above the main sequence, the intermediate-mass stars simply represent the transition between these two states.

In detail, the mass-dependence of the isochrones becomes apparent even at masses of order 1 $M_\odot$. As shown in the left panel of Figure 11.6, the slightly hotter Taurus stars – of masses $\gtrsim$1 $M_\odot$ – seem much older than the lower-mass objects using the birthline of Palla and Stahler (1999). The right panel of Figure 11.6 shows the HR diagram corresponding to these age determinations, with the relative positions of the Palla and Stahler (1999) birthline along with the somewhat lower birthlines calculated for cold accretion. It is evident that the lower birthlines will produce a smaller age differential as a function of stellar mass.

Alternatively, one might argue that the ages of the low-mass stars have been underestimated. Hillenbrand and White (2004) found that most evolutionary calculations were in good agreement with observations for $M_* \gtrsim 1.2\,M_\odot$, but systematically underpredicted the dynamical masses by 10–30% for the lower-mass stars. From equation (11.49), this implies that many tracks systematically underestimate low-mass ages by factors of $\sim$20 to $\sim$ 70%$\times$ (see discussion in Mathieu *et al.* 2007), not enough to explain the large ages of many of the hotter stars in Figure 11.6. This comparison reinforces the conclusion that the ages of $1 - 13\,M_\odot$ pre-main-sequence stars must be considered particularly uncertain due to their poorly constrained birthline positions.

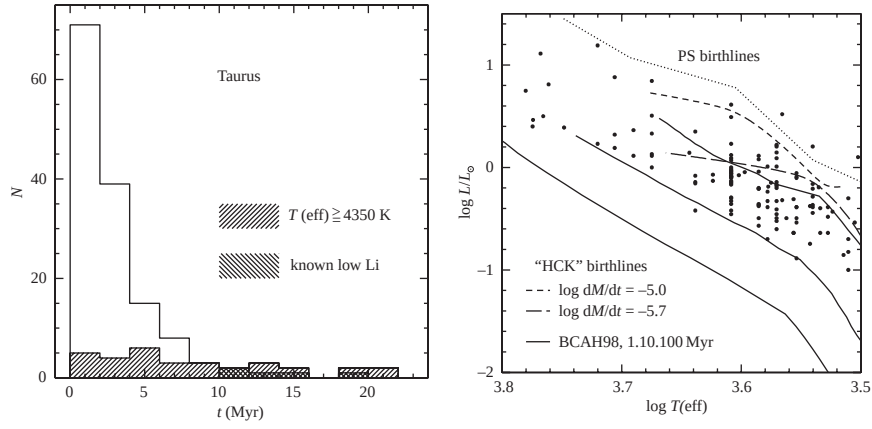

Fig. 11.6. Left: Histogram of Taurus stellar ages using Palla and Stahler (1999) tracks. One type of hatching indicates stars with effective temperatures $\geq$4500 K, which are generally of higher mass. The other hatching indicates stars with low Li abundances, which are unlikely to be members (see §11.6 for further discussion). Right: HR diagram corresponding to the histogram on the left, showing the Baraffe *et al.* (1998) isochrones: from top to bottom, ages of 1, 10, and 100 Myr. The birthlines of Hartmann *et al.* (1997) are shown as dashed curves (see Figure 11.4); the upper dotted curve is the birthline from Palla and Stahler. The general trend of the higher-temperature stars to fall along older isochrones is apparent. Modified from Hartmann (2003).

11.6 Star formation histories

The distribution of ages among stellar populations in molecular clouds and young clusters can provide insight into the processes of star and cluster formation. In addition to the uncertainties discussed in the previous section – mass estimates for low-mass stars, birthline corrections for intermediate-mass stars – other observational difficulties come into play which have made attempts to detail star formation histories problematic.

One major problem is simply distance. We have very few accurate parallaxes (except for some recent VLBA results; Torres *et al*. 2007), even for the nearest star-forming regions; the various methods – fitting main sequences, using extinction maps to tell where clouds start – have their limitations. Assigning a single distance to the nearest clouds can be problematic. For example, consider a 20 pc depth for a cloud at 140 pc – quite reasonable for extended regions such as Taurus. This corresponds to a factor of 1.44 in luminosity; and because $t \propto L^{-3/2}$ on Hayashi tracks, this results in a change of 1.73 in age. This is a *logarithmic* age error, relative to the average age determination; a 0.73 Myr age error for a true 1-Myr-old population is a 7.3 Myr age error for a 10-Myr-old population.

Another problem which mostly results from the lack of individual distances is contamination by non-members. While it is easy to assign membership to accreting CTTS, WTTS are more difficult to separate from foreground stars. Even strong solar-type magnetic activity (i.e., X-ray emission) is problematic, as the X-ray luminosities of young stars do not decay substantially until they are older than about 100 Myr (see discussion in Briceño *et al.* 1997).

A useful diagnostic is the Li I 6707 Å line, which can be strong in late-type pre-main-sequence stars. Li is fused in stellar interiors at central temperatures of 3×10^6 K or more. Fully convective stars will mix surface and central layers, resulting in Li depletion at varying pre-main-sequence ages depending upon the stellar mass. For stars of masses between about 0.3 and 0.8 $M_\odot$, depletion timescales are estimated to be of order 10–20 Myr (see discussion in White & Hillenbrand 2005). Thus, the presence of strong Li absorption in such stars is a clear indication of pre-main-sequence membership. However, this diagnostic is much less useful for lower- and higher-mass stars. The contraction time for lower-mass stars is so long that Li is not destroyed until ages of 30–100 Myr or more, making membership problematic. More massive stars develop radiative cores, making mixing inefficient and thus slowing Li depletion; empirically, the detection of strong Li absorption in stars hotter than early K-type only indicates ages less than or comparable to that of the Pleaides ($\sim$ 100 Myr; Briceño *et al.* 1997).

Another major difficulty is the presence of unresolved binaries. An excellent example of the effect of binaries is the young cluster NGC 2362 (Figure 11.7), which shows a very sharp lower distribution of stars and a clear secondary sequence displaced by $\Delta V = 0.75$ magnitudes, which would be the spread for equal-mass binaries (i.e., a factor of two in luminosity). Again, this is a *logarithmic* error, a factor to be applied to the average age of the region. It is important to recognize the binary sequence. For example, Moitinho *et al.* (2001) found an age for NGC 2362 of $\sim 5^{+1}_{-2}$ Myr, and Jeffries *et al.* (2007) found an age of 9 ± 2 Myr for the young cluster NGC 2169; however, ignoring unresolved binaries would have resulted in age spreads of a factor of $2^{3/2} = 2.8$ in age.

Finally, it is apparent that errors in extinction corrections can add to uncertainties in ages and thus increase age spreads in star-forming regions. When placing stars in the HR diagram using spectral types and photometry, extinction corrections affect the luminosity but obviously not the spectral type. When studying overall age spreads in a region, rather than

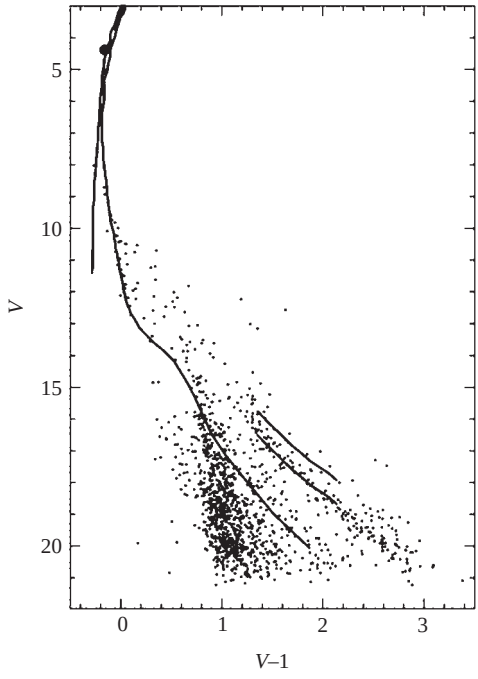

Fig. 11.7. Color-magnitude diagram of the ∼5 Myr-old cluster NGC 2362. The lower solid curve indicates the inferred cluster isochrone, with the upper solid curve displaced upward by 0.75 magnitudes to account for equal-brightness binaries. There is no evidence for significant age spread in this cluster. From Moitinho *et al.* (2001).

individual ages, it is often better to consider a color–magnitude diagram such as V vs. $V–I$ (e.g., Figure 11.7), because reddening vectors tend to be along isochrones (at least for the late-type stars), minimizing the effects of extinction errors.

With the above discussion in mind, return now to the apparent age distribution in Taurus shown in the left-hand panel of Figure 11.6. There is a large peak in the youngest age bin with a fall-off toward older ages. Some asymmetry in the distribution is expected simply because, as discussed above, most observational errors are logarithmic; when plotting in linear age bins, this results in a skewing of the distribution, and tends to result in a pileup of stars in the lowest age bin (compare with the right-hand panel of Figure 11.6, where the luminosities and isochrones are plotted logarithmically; see Hartmann 2001). Next, part of the "older" tail of stars are the higher-mass systems, which as discussed in the previous section probably have spuriously large apparent ages due to inadequate birthline corrections. Finally, detailed spectroscopic study of several of the older stars shows that they have depleted their Li, and therefore are likely older, foreground systems (Figure 11.6; Hartmann 2003).

This leaves only a few reasonably well-studied CTTS in Taurus which seem to be much older than the rest of the population. One of these systems is HL Tau, which is faint because it is extincted by a circumstellar envelope, and is seen not directly but in scattered light (Figure 5.16). Because the scattered light is less reddened than the direct light of the central source, simple reddening corrections will underestimate the true extinction to the object.

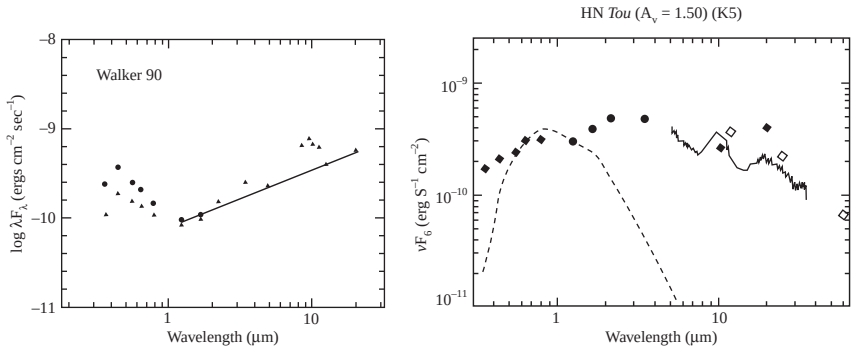

Fig. 11.8. SEDs of possible edge-on disk systems. Left, Walker 90 = Lk Ha 25 = V590 Mon; right, HN Tau. From Rydgren and Vrba (1987) and Furlan *et al.* (2006).

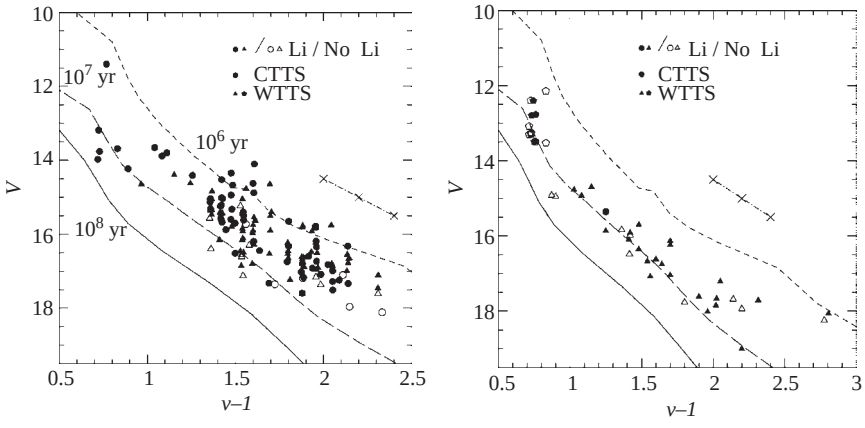

Fig. 11.9. Color–magnitude diagrams for two clusters in the Cep OB2 association, located at essentially the same distance. The younger cluster, Tr 37 (left), has an estimated age of ∼4 Myr, but clearly contains even younger stars in some molecular material along the edge of its expanding H II region. The older cluster, NGC 7160 (right), exhibits no star formation, and has a well-defined cluster isochrone consistent with an age ∼10 Myr. The spread of apparent ages in NGC 7160 appear to be due mostly to unresolved binaries. This is made clearer by comparison with the more populous cluster NGC 2362 (right), which shows an extremely well-defined cluster isochrone. The lower solid curve indicates the expected cluster sequence, with the upper solid curve displaced upward by 0.75 magnitudes to account for equal-brightness binaries. From Sicilia-Aguilar *et al.* (2005).

Another possible explanation for faint CTTS is that they are edge-on disk systems. The scattered light off the disk upper surfaces (e.g., Figure 8.9) will be relatively unreddened, and give a misleadingly low estimate of the extinction to the central source. The classical example of this is the A star Walker 90 (V590 Mon), which appears to be below the main sequence at the distance of its cluster, NGC 2264. Its SED (Figure 11.8) gives the impression that the mid-infrared luminosity substantially exceeds the "stellar" luminosity. This cannot be, whether the powering radiation comes from the star or from the accretion shock; the inference is that the object is seen only in scattered light at optical wavelengths,

underestimating its true luminosity. Occultation by a disk is a likely explanation. HN Tau, an underluminous CTTS in Taurus, has similar properties in its SED (Figure 11.8). It is perhaps surprising that there are fewer examples of edge-on disk systems, as disks with thicknesses $H(\mathrm{phot})/R \gtrsim 0.1$ should account for $\gtrsim$10% of the population, assuming random inclinations to the line of sight. The likely explanation is that such objects tend to drop out of observational samples because they are very faint, especially at optical and near-infrared wavelengths.

This is not to say that star-forming regions never exhibit significant age spreads. For example, the young cluster Tr 37 in the Cep OB2 association (§2.3; Figure 2.4) shows a significant age spread in comparison with the older cluster at the same distance, NGC 7160 (Figure 11.9). (Note the hint of a binary sequence in NGC 7160.) This age spread of 3–4 Myr is understandable; even though the central O7 star of Tr37 has removed all gas from the central cluster regions, protostars are still being formed in the molecular gas surrounding the expanding H II region (Sicilia-Aguilar *et al.* 2006). This example emphasizes that age spreads in a particular volume of space are in general an upper limit – sometimes an extreme upper limit – to the timescales of the *local* conversion of molecular gas into stars. Given the observational uncertainties, it is rather remarkable that the main age spreads estimated in nearby molecular clouds are so short; that star formation is highly dynamic is undeniable.

12

Disk evolution and planet formation

The discovery of many extrasolar planetary systems over the last decade, most with properties considerably different from those of the solar system, has revolutionized thinking about the processes of planet formation. An entire book could be devoted to the vast literature that has arisen on this complex topic. The aim of the present chapter is limited to outlining a few relevant astrophysical constraints on disk evolution and to sketch some of their potential implications for planet formation.

Our current lack of understanding of angular momentum transport in protoplanetary disks is a major obstacle to understanding how planets form. The presence or absence of a dead zone (§7.6) can strongly affect dust coagulation/planetesimal growth rates by piling up material over time; the activation or lack of same of the MRI will affect disk turbulence, which in turn affects the rates at which dust settles and grows in the disk. Astrophysical clues to these processes are meager at present, though there is evidence that settling and growth of small dust particles is at least somewhat limited by turbulence.

Dust disks within a few to 20 AU of the central star tend to "clear" (i.e., become undetectable in infrared excesses) on timescales of a few Myr. Individual systems exhibit a wide range of clearing timescales; some low-mass stars of ages $\sim$1 Myr have no detectable disks, while of order 5% of stars of ages $\sim$10 Myr exhibit substantial disk emission. The transitional disks (§8.8) provide evidence that some dust clearing can occur without complete gas removal, as many of these objects are still accreting gas even though they have strongly reduced infrared excesses. However, most T Tauri stars without detectable infrared excesses show no detectable gas accretion, suggesting that gas and dust clearing are generally related.

While dust can "disappear" without changing location simply by growing to large sizes, the disappearance of gas requires either accretion into the star, accretion into (giant) planets, or dispersal. Originally, gas was thought to be cleared from disks by the impact of strong T Tauri winds; but we now know that these flows are accretion-driven disk winds, which tend to be ejected away from the disk plane rather than along it. Stellar winds are undoubtedly present, but are much weaker than accretion-driven outflow and thus unlikely to clear disks rapidly enough.

The most popular explanation of gas removal at present is photoevaporation by the extreme ultraviolet radiation of the central star. In this model, Lyman continuum photons from the central star ionize disk gas, heating it to temperatures of order 10^4 K; at radii where the escape velocity is a significant fraction of the sound speed $\sim$10 km s^{-1}, an ionized wind will be set up which can drain the disk of gas, typically at radii beyond a few AU. Unfortunately, there are large uncertainties in the magnitude of stellar EUV fluxes, which translate

into substantial uncertainties in gas evaporation timescales. Disks may also be evaporated by the radiation from neighboring massive stars (§12.4, Figure 1.5), but this is likely to affect only the modest fraction of recently formed T Tauri stars sufficiently near to a massive star with a strong ionizing radiation field (e.g., an O star).

It seems likely that at least some of the disk clearing observed is due to accretion into giant planets which sweep up both dust and gas. The wide range of timescales for clearing suggest that giant planet formation typically occurs more rapidly than previously thought (2–5 Myr rather than 5–10 Myr). The significant range in disk evolutionary timescales suggests that initial conditions play an important role in setting planet formation timescales. A parameter likely to be important is the initial system angular momentum; modest differences in angular momenta can translate into significant differences in initial disk sizes and thus in dynamical timescales.

Dust, planetesimals, and planets migrate within the nebula. Many estimates suggest that radial migration could easily be far too rapid, leaving behind few if any planets with the bulk of the solids ending up in the central star. Addressing this problem on the frontier of planet formation theory requires advances in our understanding of disk structure, the detailed manner in which bodies interact with the disk, and rates and mechanisms of planetesimal accretion.

12.1 Clearing of optically thick disks

Figure 12.1 shows the estimated fractions of young stars in various groups with large near-to-mid-infrared excesses as a function of age. The results of the many studies incorporated into this figure demonstrate that the infrared emission characteristic of optically thick disks disappears on timescales of 1–10 Myr. The groups or clusters represented in Figure 12.1 span a substantial range of environments, but there is no clear evidence yet that disk frequencies depend significantly on local conditions.

One must consider the range of disk radii probed by these observations to understand the detailed implications for disk evolution. In some cases, particularly the youngest systems in Figure 12.1, disk frequencies have been estimated from observations only out to wavelengths $\lambda \sim 3.6\,\mu$m, and thus trace only inner disk emission. Now that the *Spitzer Space Telescope* has routinely detected small excesses above photospheric levels at longer wavelengths, $\lambda \sim$ 8–10 μm, it is possible to evaluate disk clearing over a much larger radial range.

Figure 12.2 shows results from *Spitzer* for a typical young system, the ∼3-Myr-old σ Ori cluster. The dense grouping of points along the lower part of the plot shows photospheric detections, with the width of the distribution corresponding to observational error; this illustrates the ability of the IRAC camera to detect small excesses, even down to the brown dwarf regime. Most of the stars with disks exhibit excesses consistent with optically thick, flared disks. A few systems have lower excesses (middle region, between bottom and middle horizontal dotted lines). In some cases this can be explained by optically thick but geometrically flat (i.e., non-flared) disks; others have weak emission in the 3.6–8.0 μm IRAC region but strong emission at longer wavelengths (boxed symbols), which suggests that they are transitional disk systems (§8.8). In all, the relatively small numbers of objects in the region of intermediate excesses suggests that the timescale for transitioning between optically thick disks and optically thin, undetectable disks is short, perhaps an order of magnitude shorter than the system ages (i.e., a few times 10^5 yr at most).

Detailed studies of nearby regions using the IRS spectrometer on board *Spitzer* have pushed these results to even longer wavelengths. Long exposures with IRS can detect stellar

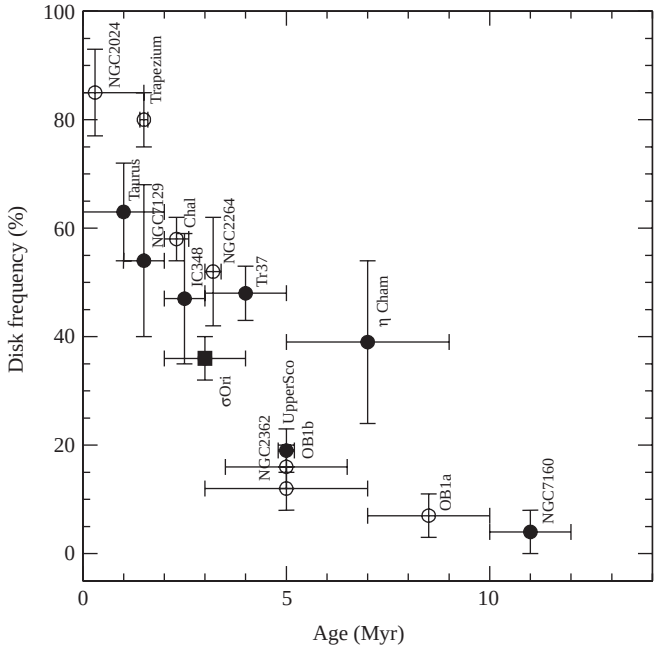

Fig. 12.1. Fraction of stars with near-infrared disk emission as a function of the age of the stellar group. Open circles represent the disk frequency for stars in the T Tauri mass range, derived using JHKL observations: NGC2024, Trapezium, NGC2264 and NGC2362 from Haisch *et al.* (2001), Chamaleon I from Gómez and Kenyon (2001), and Orion OB1a and OB1b sub-associations from Hernández *et al.* (2005). Solid symbols represent the disk frequency calculated for stars in the TTS mass range using IRAC data: Taurus from Hartmann *et al.* (2005), NGC7129 from Gutermuth *et al.* (2004), IC348 from Lada *et al.* (2006), Tr 37 and NGC7160 from Sicilia-Aguilar *et al.* (2006), Upper Scorpius from Carpenter *et al.* (2006), η Chameleontis from Megeath *et al.* (2005), and the σ Orionis cluster. Modified from Hernández *et al.* (2007).

photospheres of nearby systems out to wavelengths $\sim$30 μm. In general, relatively few Class III objects seem to exhibit strong excesses at 20–30 μm (e.g., Furlan *et al.* 2006, Hernández *et al.* 2007). For example, Padgett *et al.* (2006) found that only 2 out of 83 WTTS in Taurus exhibited excesses only at 24 μm but not at shorter wavelengths. Thus, although the disk frequencies of Figure 12.1 are direct measures only in the near infrared (3.6 μm) at worst, and the IRAC range ($\sim$8 μm) at best, the results provide reasonable estimates of the frequency of objects with or without significant infrared excesses out to $\sim$30 μm.

The blackbody temperature of a spherical dust grain of radius a, absorbing geometrically with a cross-section πa^2 and emitting uniformly over its surface area $4\pi a^2$, is

$$T_{\rm bb} = 88 \left(\frac{R}{10\,{\rm AU}}\right)^{-1/2} \left(\frac{L}{L_\odot}\right)^{-1/4} {\rm K}\,, \tag{12.1}$$

According to the Wien law, blackbody emission should peak at $\lambda \sim 30\,\mu$m for this fiducial temperature $\sim$90 K. Thus, given *Spitzer* sensitivity for nearby objects, current disk statistics relying on IRS and MIPS 24 μm data are adequate estimates of the frequency of significant

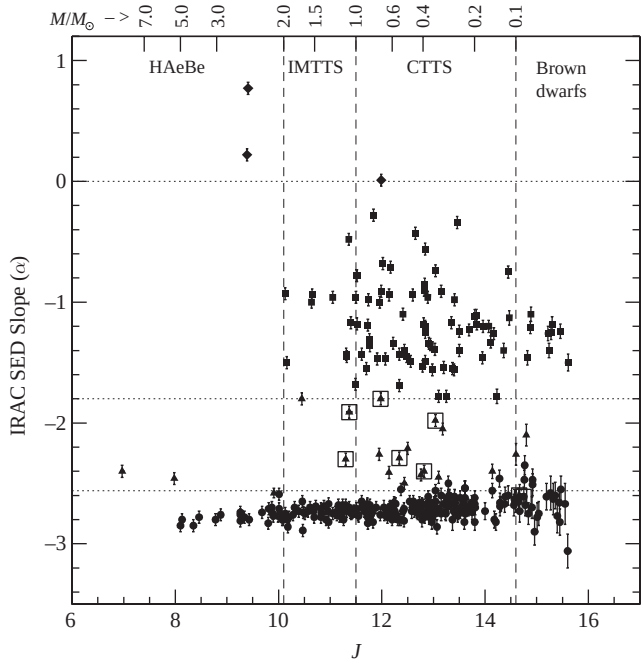

Fig. 12.2. Infrared excess emission as a function of J magnitude in the young σ Ori cluster, as measured by the slope $\alpha = d\log(\lambda F_\lambda)/d\log\lambda$ over the IRAC range from 3.6 to 8 μm (see text). Approximate mass ranges are shown on the upper axis, with vertical dashed lines indicating typical ranges for various types of young stars. Moving from bottom to top, the horizontal dotted lines indicate approximate divisions between objects with little or no photospheric excess, the lower limit of typical optically thick disks, and Class I (protostellar) objects. The boxed symbols denote objects with large 24 μm excesses suggesting that they are transitional disks. Filled symbols denote certain members, while open symbols denote possible members. From Hernández *et al.* (2007).

amounts of small dust within about 10 AU of the central stars. Colder dust can still be detected ∼20 μm from emission on the Wien side of the blackbody spectrum if the excesses are sufficiently large. As an example of this, the transitional disk system GM Aur, with strong excesses due to dust exterior to 24 AU, is easily detected by IRS (Figure 8.20).

Less is known about the presence of gas in the inner 10–20 AU. Najita *et al.* (2003) surveyed the CO $v'' - v'$ 1–0 emission from a range of T Tauri stars, which probably arises in gaseous disk regions within $\lesssim$1 AU. As shown in Figure 12.3, the small sample available so far indicates that major reductions in the gaseous component accompany major reductions in near-infrared excess. A more widely available indicator is gaseous accretion rates onto the central stars; as discussed in §8.3, objects without near-infrared excesses generally exhibit little or no indication of accretion (with the transitional disks constituting many if not all of the exceptions; §8.8). As small dust is thought to inhibit MRI activity (§7.5), one would expect that dust-cleared gaseous disks would be especially prone to turbulent angular momentum transport, and thus should be actively accreting. Thus, small dust clearing and gas clearing in the inner disk are correlated, with the transitional disks providing a few exceptions in the sense of less small dust for a given gas accretion rate.

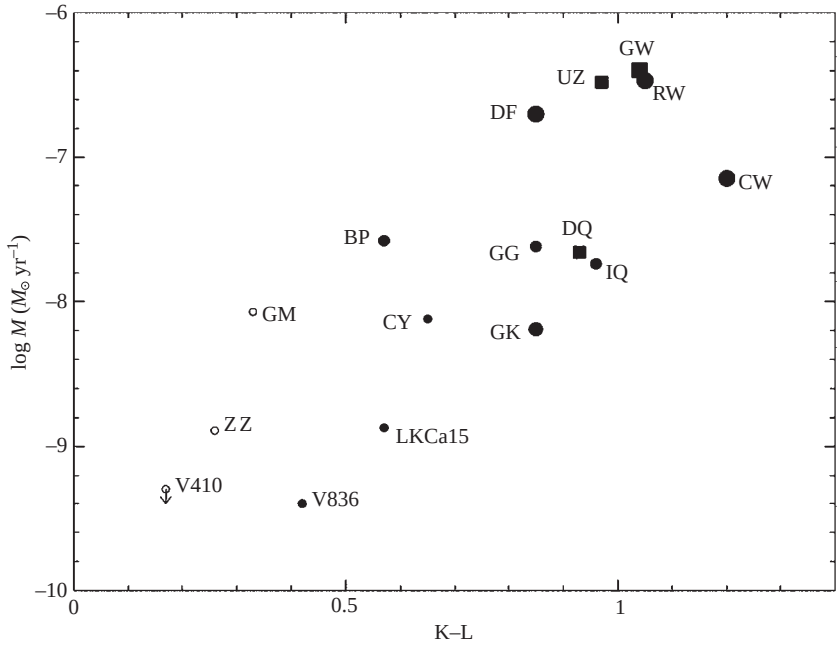

Fig. 12.3. Comparison of the disk accretion rate and K–L color for sources with observations of CO vibrational fundamental emission. Stars without detected CO emission are shown as open symbols, and spectroscopic binaries are plotted as squares. Objects with low or undetectable near-infrared excess and mass accretion were not detected in CO. From Najita *et al.* (2003).

Timescales for outer disk gas and/or dust clearing are much less well known. The WTTS in nearby, young regions such as Taurus tend to exhibit very little sub-mm to mm-wave emission (e.g., Figure 8.11). Whether this is an indication of nearly simultaneous disk evolution over a huge range of radii or simply a reflection of initial conditions (such as an initially small, and thus rapidly evolving, disk) is not clear.

12.2 Viscous disk evolution

The observational evidence shows that some mechanism(s) clear dust and gas from protoplanetary disks over timescales of 1–10 Myr, with a median timescale of roughly 3 Myr. Aside from planet formation, perturbations due to binary companions, photoevaporation, coagulation, and general dust evolution may also play important roles in clearing disks. We begin by considering viscous accretion.

T Tauri disks accrete; and this fact alone requires disks to evolve. To outline the basic issues, we return to the simple model of self-similar viscous disk evolution discussed in §7.2 under the assumption that the temperature structure of the disk is determined mostly by irradiation from the central star, and that the disk is nearly isothermal vertically. As discussed in Chapter 8, these approximations are probably not too bad for the outer disk, which tends to control the evolution. We further make the extremely simplifying assumption that the outer disk is reasonably "flared" (§§7.9, 8.2), so that the disk temperature varies as

$$T(R) \sim 10 \left(\frac{100\,\mathrm{AU}}{R} \right)^{1/2} \mathrm{K}\,, \tag{12.2}$$

where the normalization is very roughly what would be expected for a typical 1 $L_\odot$ T Tauri star. Finally, we assume that the viscosity can be represented with a constant α formalism (§7.4). With these assumptions, $\nu_\mathrm{v} \propto R$, and the similarity solutions of §7.2 hold. (The effect of the decrease in luminosity of the central star during evolution (§11.1) on the disk temperature is neglected here.) In particular, for an "initial" disk radius R_1 (see §7.2, equations (7.46)–(7.48)), the similarity solution yields

$$\Sigma \sim 1.4 \times 10^3 \, \frac{e^{-R/(R_1 t_\mathrm{d})}}{(R/R_1)\; t_\mathrm{d}^{3/2}} \left(\frac{M_\mathrm{d}(0)}{0.1\; M_\odot} \right) \left(\frac{R_1}{10\; AU} \right)^{-2} \mathrm{g\,cm^{-2}}\,, \tag{12.3}$$

and

$$\dot{M} \sim 6 \times 10^{-7} \, \frac{e^{-R/(R_1 t_\mathrm{d})}}{t_\mathrm{d}^{3/2}} \left(1 - \frac{2R}{R_1\, t_\mathrm{d}} \right) \left(\frac{M_\mathrm{d}(0)}{0.1\; M_\odot} \right) \times \left(\frac{R_1}{10\,\mathrm{AU}} \right)^{-1} \left(\frac{\alpha}{10^{-2}} \right) \left(\frac{M_*}{0.5\; M_\odot} \right)^{-1/2} \left(\frac{T_{100}}{10\,\mathrm{K}} \right) \; M_\odot\,\mathrm{yr}^{-1}\,, \tag{12.4}$$

where $M_\mathrm{d}(0)$ is the initial disk mass, M_* is the stellar mass, and the time t_d is related to the true elapsed time by

$$t_\mathrm{d} = 1 + \frac{t}{t_\mathrm{s}}\,; \tag{12.5}$$

the scaling time is

$$t_\mathrm{s} \sim 8 \times 10^4 \left(\frac{R_1}{10\,\mathrm{AU}} \right) \left(\frac{\alpha}{10^{-2}} \right)^{-1} \left(\frac{M_*}{0.5\; M_\odot} \right)^{1/2} \left(\frac{T_{100}}{10\,\mathrm{K}} \right)^{-1} \mathrm{yr}\,, \tag{12.6}$$

where T_{100} is the temperature at 100 AU.

In this model, the expansion of the transition radius R_t (§5.2), which can be considered as a characteristic disk size scale, is

$$R_\mathrm{t} \sim 5\, t_\mathrm{d} \left(\frac{R_1}{10\; AU} \right) \mathrm{AU}\,. \tag{12.7}$$

The overall behavior of this solution can be understood in a heuristic way as follows. The angular momentum of the disk is essentially constant, except for the small amount accreted onto the star (which is formally ignored in the similarity solution). Thus the angular momentum of the disk, $J_\mathrm{d} \propto M_\mathrm{d} R_\mathrm{t}^{1/2}$ for a Keplerian disk, is constant. Because the characteristic disk radius expands as $R_\mathrm{t} \propto t$ at long times, the disk mass must therefore vary as $M_\mathrm{d} \propto R_\mathrm{t}^{-1/2} \propto t^{-1/2}$ and the mass accretion rate must vary as $\dot{M} = dM_\mathrm{d}/dt \propto t^{-3/2}$.

Figure 12.4 compares this similarity solution using the fiducial parameters (solid curve) to the estimated disk mass accretion rates for late K-early M stars in several different nearby star-forming regions as a function of age. While the trend of decreasing mass accretion rate with increasing age is roughly reproduced, there is a large scatter at any given age. This scatter plus concerns about systematic effects do not permit a very definitive test of this

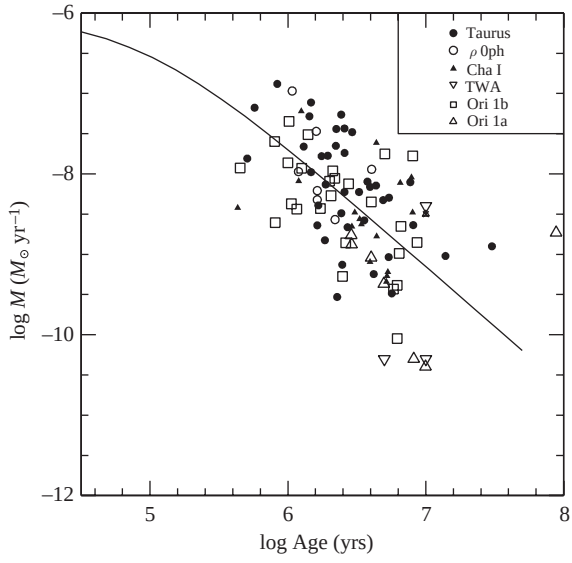

Fig. 12.4. Mass accretion rates determined from blue-ultraviolet excess emission as a function of the estimated stellar age, for typical T Tauri stars in a variety of regions. The solid curve is a model of the form given in equation (12.4). Courtesy N. Calvet.

model (Hartmann *et al.* 1998). This solution also predicts disk masses of about 0.03 $M_\odot$ at $t = 1\,\mathrm{Myr}$, a few times larger than the recent disk mass estimates from sub-mm wave measurements *for the standard dust opacity* (8.11), though more consistent with estimates based on gas accretion rates (see §8.6). This solution also predicts that $R_\mathrm{t} \sim 60\,\mathrm{AU}$ at $t \sim 10^6\,\mathrm{yr}$; the "outer" disk radius measured in various ways, such as mm emission, might be a factor of two or so larger than this. Larger disks are certainly observed (e.g., Figure 8.3), but this might be the result of an initially large R_1. Note that the results are not very sensitive to the assumed starting radius R_1 when $t \gg t_\mathrm{s}$.

While this similarity solution is almost certainly inapplicable to real disks in any detail, it is useful to demonstrate some of the basic disk physics and how things may scale with varying parameters. For example, the fiducial viscosity parameter $\alpha = 10^{-2}$ is reasonably consistent with numerical simulations of the MRI, although some empirical studies suggest values as much as an order of magnitude larger (§7.5). Using an $\alpha = 0.1$ would result in ten times as large an accretion rate early on, and roughly 10 times faster disk clearing, as the disk expands to sizes of order 10^3 AU in only $\sim$1 Myr. In principle, one could constrain values of α in the outer disk by measuring outer disk radii; in practice, this is difficult observationally because the surface brightness of disks falls off so rapidly with increasing distance.

With this solution, disk masses vary slowly with time, $M_\mathrm{d} \propto t^{-1/2}$. Sub-mm mass estimates exhibit two orders of magnitude scatter at a given age in Taurus (Andrews & Williams 2005), which means either a wide range in initial disk masses, or a wide range in dust evolution at a given age, or both. The essential point for the present discussion is that pure viscous evolution takes a long time to empty out disk mass. It does not yield the "two timescale" behavior (e.g., Clarke *et al.* 2001) – slow decay of accretion with rapid clearing – implied by disk frequencies (§8.1).

12.3 Binaries

The presence of a binary companion star can have very strong effects on disk structure and evolution. A secondary star will gravitationally perturb the disk of the primary, tending to excite a spiral wave in the disk; this gives rise to a torque between the secondary and the disk, in a manner analogous to the gravitationally unstable disk (Figure 7.1). The faster-moving disk will tend to transfer angular momentum to the secondary, resulting in the disk moving inward. Over time, this torque results in a truncation of the primary disk, such that it (roughly) stays within the Roche lobe of the primary star – the region in which a test particle is gravitationally bound to the primary (Papaloizou & Pringle 1977). The secondary may maintain its own disk within its own Roche lobe. For circular orbits, an analytic approximation to the Roche lobe radius is given by Eggleton (1983) as

$$\frac{R_{\rm i}}{a} \approx \frac{0.49\, q_{\rm i}^{2/3}}{0.6\, q_{\rm i}^{2/3} + \ln\left(1 + q_{\rm i}^{1/3}\right)}\,, \tag{12.8}$$

where a is the semi-major axis of the binary orbit and

$$q_1 = \frac{m_1}{m_2} = \frac{1-q}{q} \quad \text{and} \quad q_2 = \frac{m_2}{m_1} = \frac{q}{1-q}\,. \tag{12.9}$$

Binaries with eccentric orbits – the majority – will tend to clear out even larger regions of disks (e.g., Pichardo *et al.* 2005).

If the stars have much more angular momentum than their disks, the disks will essentially be confined by the binary orbit and accrete more rapidly than they would otherwise. Figure 12.5 shows a set of calculations for the simple viscous disk model of the previous section modified to prevent the disk from expanding beyond a certain radius. As shown in the figure, disk evolution proceeds roughly like the similarity solution until the disk reaches the outer boundary; at that point the disk can no longer expand and simply drains out onto the central mass, resulting in an exponentially decreasing disk mass. The timescales shown in Figure 12.5 show that for $\alpha = 0.01$ and truncation radii of 15–30 AU, disk clearing due to accretion can become very effective at ages of order 2–3 Myr. Putting this in perspective, for a mass ratio $q = 0.5$, the binary semi-major axis would be roughly a factor of three larger than these truncation radii (equation (12.8)). Thus, given a typical binary semi-major axis of 30 AU (Duquennoy & Mayor 1991; Figure 6.1), many binary systems should have very short disk lifetimes (unless $\alpha \ll 10^{-2}$).

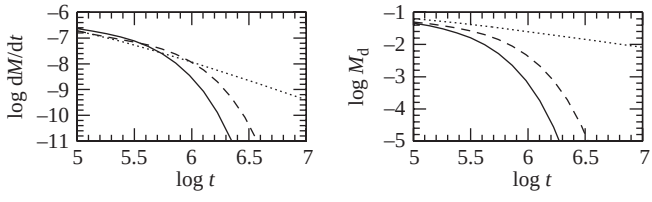

Fig. 12.5. Effect of preventing disk expansion on the evolution of disk mass and accretion rate of the simple viscous disk model. The dotted curves show the similarity solution of equations (12.3) and (12.4), while the dashed and solid curves denote the behavior of the disk for forced disk truncation at radii of 30 and 15 AU, respectively (see text).

Circumbinary disks can be present at distances sufficiently larger than the binary orbit, again constrained by Roche lobe limits. Such disks can be prevented from accreting due to tidal torques, and will eventually spread out as angular momentum is added from the inner binary (Pringle 1991b). The poster child for circumbinary disk systems is GG Tau (Roddier *et al.* 1996; Guilloteau *et al.* 1999; Krist *et al.* 2005; Figure 8.4). The inner region is relatively cleared out to ∼150 AU, with perhaps some inner dust (Krist *et al.* 2005). McCabe *et al.* (2002) estimate a semi-major axis for the binary orbit of 35^{+22}_{-8} AU, with a modest eccentricity of $e \sim 0.3 \pm 0.2$; thus, the ring appears to reside well outside the binary orbit as expected.

Somewhat surprisingly, both GG Tau Aa and Ab appear to be accreting from their circumstellar disks (White *et al.* 1999). The orbital elements suggest that the inner disks are expected to be truncated at sizes of order 10–20 AU; one might expect such disks to empty out on timescales of ∼1 Myr (Figure 12.5). Age estimates are often difficult, but in the case of GG Tau we can use the dynamical total mass estimated by Simon *et al.* (2000) of 1.28 $M_\odot$ from the dynamics of the circumstellar ring. If we assign a mass of 0.7 $M_\odot$ to Aa, use the luminosity of 0.84 $L_\odot$ estimated by White *et al.* (1999), and adopt $T = 4000$ K for the K7 spectral type of Aa, then the estimated stellar radius is 1.9 $R_\odot$. We may then use equation (11.49) to find a maximum contraction age (without birthline correction) of about 1.3 Myr. This result suggests that GG Tau A may not be accreting for much longer. Alternatively, this calculation suggests that the effective or average α in the cirumstellar disks of GG Tau Aa and Ab cannot be much larger than 0.01; otherwise the disks would have emptied out by now.

Although it has been clear for some time that, statistically speaking, disks are less frequently present in binary systems (see, e.g., Mathieu *et al.* 2000), but as in the case of GG Tau, indvidual binary or multiple systems can still retain disks. Inner disks can last for some time before being drained by accretion onto the central star, outer circumbinary disks can last considerably longer, and accretion may or may not occur depending upon the age of the system, the binary separation, or even the eccentricity of the binary orbit. Understanding the behavior of disks in binary systems requires close attention to the specifics of individual systems.

12.4 Disk evaporation

T Tauri stars emit copious amounts of high-energy radiation, partly due to stellar magnetic activity and also partly due to accretion, if present. In particular, Lyman continuum photons from the central regions can ionize hydrogen, generally heating it to temperatures typical of H II regions, ∼10 000 K. At radii where the resulting sound speed c_s is comparable to the gravitational potential well,

$$R_g \sim \frac{G M_*}{c_s^2} , \tag{12.10}$$

the gas can flow outward and escape from the system, producing a thermally driven wind. Mass loss will probably start somewhat inside of R_g; if we adopt the simple steady thermally driven wind model, we find the sonic point occurs at (equation (10.39) without rotation)

$$R_s \sim \frac{G M_*}{2 c_s^2} \sim 3.6 \frac{M_*}{M_\odot} \text{ AU} , \tag{12.11}$$

where we have set the mean molecular weight to 0.67, appropriate for a gas of cosmic abundance with ionized hydrogen and neutral helium. Thus, ionizing photons have the potential for removing disk gas at radii of a few to 10 AU from the central star.

To see the essential physics of the problem with a minimum of geometrical complication, assume that a volume of $4\pi R^3$ must be ionized, where R is a characteristic radius of escape. This estimate is justified because the gas must maintain its ionization over the disk to a distance comparable to its escape radius to flow out of the gravitational potential well. The balance between photoionization and recombination leads to the typical Strömgren sphere result (e.g., Spitzer 1978),

$$\Phi = 4\pi R^3 n_{\rm e} n_{\rm p} \alpha_{\rm B} \,, \tag{12.12}$$

where Φ is the flux of ionizing photons from the central source, $n_{\rm e}$ and $n_{\rm p}$ are the electron and proton densities, respectively, and $\alpha_{\rm B}$ is the Case B recombination rate for hydrogen (assuming that all recombinations directly to the ground state result in the emission of ionizing photons which are then locally absorbed – the so-called "on-the-spot approximation".) Setting the electron and proton densities to be equal to each other and to the hydrogen density, $n_{\rm e} = n_{\rm p} = n_{\rm H}$, we may write the photoevaporative mass loss rate as

$$\dot{M} \sim 4\pi n_{\rm p} \mu m_{\rm p} c_{\rm s} R^2 \,, \tag{12.13}$$

where the expansion velocity is estimated to be the sound speed. Rearranging, we have

$$\dot{M} \sim (4\pi)^{1/2} \Phi \alpha_{\rm B}{}^{-1/2} \mu m_{\rm H} c_{\rm s} R^{1/2} \,. \tag{12.14}$$

The ionized gas will have a temperature of $\sim 10^4$ K. Then the sound speed is $c_{\rm s} sim 10$ km s^{-1}, the recombination rate is $\alpha_{\rm B} = 2.6 \times 10^{13}$ cm^{-6} s^{-1}, and $\mu = 1.4$ to add the (neutral) helium mass to the proton mass. The final result for the mass loss rate is then

$$\dot{M} \sim 10^{-9} \Phi_{41}^{1/2} R_{10}^{1/2} \; M_\odot \; {\rm yr}^{-1} \,, \tag{12.15}$$

where Φ_{41} is the Lyman continuum flux in units of 10^{41} s^{-1} and R_{10} is a characteristic scale of the flow in units of 10 AU. This estimate illustrates the potential of photoevaporation to remove disk gas over evolutionarily interesting timescales.

Much more sophisticated treatments of the outflow have been considered by Hollenbach *et al.* (1994), Clarke *et al.* (2001), Font *et al.* (2004), and Alexander *et al.* (2006a,b). There are generally two limits of wind behavior. The first is when the wind is optically thick to the Lyman continuum photons; thus the wind absorbs the central source photons before they reach the disk. The wind then reradiates some of these photons by direct recombination to the ground state, producing a "diffuse" radiation field which irradiates the disk. In this case the density of the wind near the disk is found to be $n_{\rm w} \propto R^{-5/2}$, where R is the cylindrical radius (Hollenbach *et al.* 1994). The mass loss rate then is concentrated toward small radii,

$$\frac{d\dot{M}}{dR} \propto 2\pi R \, n_{\rm w} c_{\rm s} \propto R^{-1/2} \,. \tag{12.16}$$

The other limit occurs when the wind is not optically thick to the ionizing radiation, and the disk receives "direct" ionizing illumination from the central star. In this case $n_{\rm w} \propto R^{-3/2}$ and the mass loss is weighted toward larger radii,

$$\frac{d\dot{M}}{dR} \propto 2\pi R \, n_{\rm w} c_{\rm s} \propto R^{1/2} \,. \tag{12.17}$$

In general one expects the inner disk regions to match the "direct case" more nearly (because of limited attenuation) and the "diffuse case" at large radii.

Detailed numerical solutions of the coupled hydrodynamics and ionization balance problem were presented by Alexander *et al.* (2006a) for the case in which the inner disk has drained and the direct flux dominates. The resulting mass loss rates for a 1 $M_\odot$ central star and an ionizing flux $\Phi_{41} = 1$ were $\dot{M} \sim 10^{-9}\ M_\odot\,\mathrm{yr}^{-1}$, comparable to the rough estimate above (equation (12.15)). For comparison, Clarke *et al.* (2001) estimated $\dot{M} \sim 4 \times 10^{-10}\ M_\odot\,\mathrm{yr}^{-1}$ for the optically thick case.

Combining photoevaporative winds with simple viscous accretion models such as those of §12.2 results in a two-stage evolution (Clarke *et al.* 2001; Matsuyama *et al.* 2003; Alexander *et al.* 2006b). Viscous evolution dominates in early stages, depleting the disk as it accretes onto the central star. The disk accretion rates decrease with time (equation (12.4)); when they fall below the photoevaporation rate, the outer disk can no longer supply mass to the inner disk. The inner disk then drains out rapidly on its relatively short viscous timescale, leading to the development of an inner disk hole. In the second stage, the evaporation of the outer disk proceeds more rapidly because of the absence of an inner disk wind, and eventually photoionization disperses the disk. The most detailed calculations of this combined evolution are those of Alexander *et al.* (2006b), who find typical inner disk clearing on timescale of a few Myr and full disk dispersion on timescales of order 10 Myr, assuming $\Phi_{41} = 10$.

The effects of gas evaporation on small dust and therefore disk clearing are somewhat uncertain. The photoevaporative wind itself is unlikely to remove any but the very smallest dust, due to its low density (Takeuchi *et al.* 2005). Dust settling, migration, growth, and collisional replenishment and/or destruction further complicate the situation (§12.6). However, once the inner disk drains away, removing gas from the inner disk, dust removal by radiation pressure and/or Poynting–Robertson drag (§12.10) can be rapid. In addition, a decreasing gas density with decreasing radius will result in stopping the migration of the dust (Rice *et al.* 2003). Thus, the removal of inner disk gas is likely to be correlated with the removal of inner small dust.

The photoevaporative model clearly can produce inner disk holes, as seen in the transitional disks (§8.8), but there are some difficulties in applying this mechanism to all systems. The model predicts inner disk clearing when the photoevaporative mass loss rate is larger than the disk accretion rate – otherwise, the outer disk replenishes the inner disk faster than evaporative loss. However, Najita *et al.* (2007) pointed out that several transitional disk systems are estimated to have accretion rates well above the $10^{-9}\ M_\odot\,\mathrm{yr}^{-1}$ estimate of the evaporative rate. In addition many of the transitional disk systems seem to have relatively massive disks, whereas the simple viscous evolution model would predict lower mass disks when accretion rates are low.

Another problem is to estimate the true ionizing fluxes. Models of the accretion shock (Calvet & Gullbring 1998; Gullbring *et al.* 2000; Figure 8.16) generally indicate little emission in the Lyman continuum; thus, the EUV radiation most probably results from enhanced solar-type magnetic activity. There are no direct measurements of the Lyman continuum flux for any solar-type star at present other than the Sun; this is because even a trace amount of interstellar neutral hydrogen suffices to completely absorb emission just shortward of 912 Å, the Lyman limit. Alexander *et al.* (2005) attempted to use emission-measure analyses of the ultraviolet lines of T Tauri stars to estimate Lyman continuum fluxes, with estimates ranging from 10^{41}–10^{44} photons s^{-1}, which would strongly photoevaporate disks. However, it is

extremely difficult to estimate the photoionizing flux from this kind of analysis. Lyman continuum emission due to stellar chromospheric activity generally is estimated to originate in relatively low-temperature gas, $T \sim 10\,000$ K, where emission measure analyses are uncertain. (The Lyman continuum arises at such temperatures because hydrogen becomes ionized above 10 000 K.) A flux of 10^{44} photons s^{-1} is implausible because it represents emission of nearly 1 $L_\odot$ in the Lyman continuum, more than the X-ray or (most) accretion luminosities. A flux comparable to the typical X-ray luminosity $L_x \sim 10^{30}$ erg s^{-1} would imply a photon flux closer to 10^{41} photons s^{-1}, which would allow disks to survive for several Myr, as observed. Moreover, if accretion is actively proceeding, the magnetospheric accretion columns and/or the inner disk wind could easily be optically thick in the Lyman continuum, preventing ionizing photons from reaching the outer disk.

Ribas *et al.* (2005) used data from the Far Ultraviolet Spectroscopic Explorer and the International Ultraviolet Explorer, among other missions, to estimate short-wavelength emission fluxes from nearby solar-type stars. For the youngest star in their sample, EK Dra (age ∼100 Myr), they used the flux evolution in other wavelengths to scale to the Sun in the 360–920 Å band to arrive at an equivalent photon flux of about 4×10^{39}photons s^{-1}. If this flux can be taken to be typical of low-mass T Tauri stars, the result suggests evaporation of disks due to stellar magnetic activity occurs on timescales of order 10 Myr or more. Whether photoevaporation plays a major role in the strong disk evolution from 1–10 Myr remains unclear, if not unlikely.

Disks close to a hot luminous star can be photoevaporated rapidly due not only to EUV (Lyman continuum) radiation but also by far-UV (∼1000 Å) radiation, which can heat the gas to temperatures ∼1000 K as electrons are driven off grains. The FUV radiation thus can drive a wind off the outer disk, and may be more important in many systems if most of the disk mass resides at large distances. We have clear examples of this disk photoevaporation in the Orion Nebula, with direct HST observations of "proplyds" (§1.6; Figure 1.6). However, it is important to note that the disk systems must be relatively close to the ionizing star for photoevaporation of this type to be effective. For example, Störzer and Hollenbach (1999) estimate that disk systems must come within ∼0.3 pc of the ionizing star θ^1 C Ori in the Orion Nebula for evaporation to become important. As the half-mass radius of the Orion Nebula Cluster is ≈0.8 pc (Hillenbrand & Hartmann 1998), it is quite likely that the majority of stars in the Orion Nebula will not have their disks externally photoevaporated.

12.5 Dust evolution

Dust grains in the disk generally are thought to evolve to larger sizes, with a decreasing population of small grains with increasing age. During this overall growth, dust is expected to settle vertically and drift radially. This evolution of dust in size and position in the disk can reduce and ultimately eliminate infrared excess emission. For present purposes we simply sketch some basic ideas; useful reviews are given by Weidenschilling and Cuzzi (1993), Cuzzi and Weidenschilling (2006), and Dominik *et al.* (2007).

Consider first vertical settling in a non-turbulent disk. While the gas scale height is maintained by frequent collisions, dense dust grains feel much less support and so they tend to settle toward the midplane. The equation of motion in the vertical (z) direction is

$$\frac{dv_z}{dt} = -\frac{GM_* z}{R^3} + \frac{F_\mathrm{d}}{m_\mathrm{g}} = -\Omega^2 z + \frac{F_\mathrm{d}}{m_\mathrm{g}}\,, \tag{12.18}$$

where $F_{\rm d}$ is the drag force acting on the particle, $m_{\rm g}$ is its mass, Ω is the Keplerian angular frequency, and the other symbols have their usual meaning. For concreteness we take the Epstein drag formula, valid in the limit when the gas mean free path is larger than the spherical particle radius a and v_z is less than the sound speed $c_{\rm s}$; then (Weidenschilling 1977)

$$F_{\rm d} = -\frac{4\pi}{3} a^2 \rho c_{\rm s} v_z \,. \tag{12.19}$$

Generally particles will rapidly approach terminal velocity such that

$$v_z = -\Omega^2 z \frac{m}{4/3\pi a^2 \rho c_{\rm s}} = -\Omega^2 z \left(\frac{a\rho_{\rm g}}{\rho c_{\rm s}}\right) = -\Omega^2 z t_{\rm e} \,, \tag{12.20}$$

where $t_{\rm e}$ is the "stopping time" of the particle. Thus, the characteristic settling time of a particle is

$$t_{\rm sett} = (\Omega^2 t_{\rm e})^{-1} \,. \tag{12.21}$$

This settling timescale is extremely rapid. To illustrate, a typical minimum-mass solar nebula at 1 AU might have a gas density of order $\sim 10^{-13}$ g cm^{-3} at 4 scale heights above the midplane; then 1 μm-sized grains will have stopping times of a few hours and settling times of a few hundred years. Moreover, as grains collide at least some will stick, increasing the mass-to-surface area ratio, which makes settling happen even faster. Short settling timescales were a reason why there was initially some resistance to the concept of flared dusty disks.

Although it is clear that T Tauri disks are "flared", only a relatively small amount of dust need be suspended to make a flared "surface" which can more effectively intercept light from the central regions, and reradiate the energy downward into the disk. As shown in Figure 4.10, for an ISM-like distribution with small dust the opacity is of order 10^2 cm^2 g^{-1}, so that a vertical optical depth of unity requires a surface density of only 0.02 g cm^{-2}. Using Figure 8.7 (which probably represents a relatively low-mass disk), it appears that even at 100 AU only a few percent of the mass of the dust need be suspended in the form of small grains (which are required to explain silicate emission features; §8.2, Figure 8.5), and much less at smaller radii.

The simple estimate in equation (12.19) underestimates the true drag force for realistic small particles, which are not spherical. Instead, growth initially proceeds by sticking particles together into long chains and "fractal-like" structures, which have surface areas growing roughly as their masses (e.g., Weidenschilling & Cuzzi 1993; Wurm & Blum 1998). However, it does not appear that enhanced drag for fractal grains can account for the extended periods of dust suspension, as particles keep growing on rapid timescales and eventually compactify (Dominik *et al.* 2007).

Another important question is the role of turbulence. Vertical turbulent motions can help delay or slow settling; and it seems essential that T Tauri disks have at least some turbulent regions, if the MRI is to drive the observed accretion. Unfortunately, the levels of turbulence and their spatial distribution within disks are highly uncertain (§7.6). Moreover, turbulence can actually enhance the depletion of small dust particles if they can be mixed by turbulence down to lower layers where they are then accreted onto larger objects (Dullemond & Dominik 2005).

Dullemond and Dominik (2005) and Tanaka *et al.* (2005) considered the long-term evolution of dust particles in disks. In both treatments, the disk interior to about 10 AU becomes

optically thin on timescales of 0.1 to 1 Myr, as dust particles settle and coalesce into larger bodies. The evolution of the mm fluxes is slower because of longer timescales of accumulation in the outer disk, with substantial reductions in mm-wave emission on timescales of 10 Myr. One might expect that turbulence would lengthen settling and growth timescales, but Dullemond and Dominik find faster growth due to turbulent mixing. The rapid clearing of the inner dust disk in these two sets of models is inconsistent with observations, leading Dullemond and Dominik to argue that ongoing dust destruction is required to repopulate the small particle distribution.

As dust grains settle they are increasingly likely to collide with, and accrete, other particles; this growth eventually makes them settle to the disk midplane in a dense layer. Further growth is enhanced by radial drift, which promotes further accretion. This radial drift is caused by the difference in the azimuthal velocities of gas and dust. The equation of motion for the (slowly accreting) gas in the midplane is

$$\frac{v_{v_\phi}^2}{R} = \frac{1}{\rho}\frac{dP}{dR} - \frac{GM_*}{R^2}\,. \tag{12.22}$$

In general the gas pressure gradient is outward, which results in the gas rotating at a velocity slightly below Keplerian. A dense body will feel a reduced or negligible radial pressure force and then will orbit at a velocity close to Keplerian. This means that the body will feel a headwind, which results in a drag force transferring angular momentum to the gas from the body; as a result the body moves inward. From equation (12.22) one can estimate the gas rotation rate as

$$v_{v_\phi}^2 \sim v_{\rm K}^2 - c_{\rm s}^2\,, \tag{12.23}$$

and therefore the departure from Keplerian rotation is of order

$$\delta v \sim \frac{v_{\rm K}}{2}\left(\frac{c_{\rm s}^2}{v_{\rm K}^2}\right)\,. \tag{12.24}$$

Typically, $\delta v \sim 1 - 3 \times 10^{-3} v_{\rm K}$; even this modest velocity difference can have important effects.

Small particles basically move with the gas and thus have slow drift velocities; large bodies feel negligible drag force and thus do not migrate due to this process (though they can migrate due to gravitational torques; §12.7). On intermediate size scales, the "smaller" and "larger" regimes have differing behavior. For the smaller range, the particles basically rotate with the gas, and thus are in sub-Keplerian motion; they then tend to fall toward the central star until they achieve a terminal velocity. The radial equation of motion then reads

$$v_{\rm R}\frac{dv_{\rm R}}{R} + \frac{GM_*}{R^2} = \frac{1}{\rho}\frac{dP}{dR} = -\frac{v_{\rm R}}{t_{\rm e}}\,. \tag{12.25}$$

Setting $dP/dR \sim \rho c_{\rm s}^2/R$, the terminal radial velocity is

$$v_{\rm R} \sim \frac{c_{\rm s}^2 t_{\rm e}}{R} \sim 2\Omega t_{\rm e}\delta v\,. \tag{12.26}$$

When the bodies are large enough that they decouple strongly from the rotation of the gas, they feel a headwind and thus lose angular momentum and migrate inward. This results in a radial inward velocity of

$$v_{\rm R} \sim \frac{2\delta v}{\Omega t_{\rm e}}\,. \tag{12.27}$$

The maximum radial drift velocity of $v_{\rm R} = \delta v$ occurs when $\Omega t_{\rm e} = 1$ (Weidenschilling 1977). For typical disk models, this maximum velocity is achieved for bodies on the size of cm to m, depending upon radial position. With $\delta v \gtrsim 10^{-3}$, such bodies can migrate into the central star on timescales of a thousand orbits or less. Even cm-sized particles at distances of 100 AU may drift inward on timescales of order 1 Myr (Takeuchi & Lin 2005).

What happens to these bodies is uncertain. For example, the difference in velocities between objects within an order of magnitude of meter size can result in their complete shattering or disruption, as gravity is unimportant on these scales as are electrostatic forces – the so-called "rubble piles" appear to be easy to disrupt, though a high porosity might improve matters by allowing "crushing" to occur (see, e.g., discussion in Cuzzi & Weidenschilling 2006, Benz & Jutzi 2007). Turbulent eddies or whirlpools might help collect these objects at low velocities so that they can accrete (e.g., Rice *et al.* 2006b), or alternatively disperse them more widely.

What can observations tell us, in view of the vast complexity of the processes affecting dust? As discussed in §8.3, sub-mm and mm wavelength observations strongly imply growth of grains well beyond typical sizes in the diffuse interstellar medium. The most recent spatially resolved observations at long wavelengths indicate grain growth to at least cm sizes at radii $\gtrsim$100 AU (Natta *et al.* 2004; Wilner *et al.* 2005; Rodmann *et al.* 2006), based on the observed low spectral indices (§8.2). As discussed above, this is consistent with models showing rapid growth (e.g., Dominik & Dullemond 2005; Tanaka *et al.* 2005). On the other hand, if radial drift operates, it should remove grains of these sizes fairly rapidly, leading Takeuchi and Lin (2005) to argue that replenishment of mm to cm-sized dust due to collisions of larger bodies must be occurring – analogous to inferences of small dust production in debris disks (§12.10).

Similarly, the rapid inner disk clearing of small dust predicted by models like those of Tanaka *et al.* (2005) and Dominik and Dullemond (2005) is inconsistent with the SEDs of many objects. Furlan *et al.* (2005, 2006) found that better fits to the observed Spitzer IRS spectra resulted from models with a significant amount of dust settling, with levels of depletion of 10^{-2} to 10^{-3} from interstellar medium values of small dust, but this is far more small dust than in the aforementioned models. (Note that Sano *et al.* (2000) estimated that depletions of order 10^{-4} are needed for the MRI to operate robustly in upper disk layers; §7.5). Again, another possible solution to this problem is to invoke continued production of small dust by collisions between larger bodies.

There is some modest evidence for decreasing disk flaring with increasing age, as would be expected from settling/growth models (Hernández *et al.* 2007), but the trend is relatively weak, in part because there is a wide range of behavior at a given age. A sample of Spitzer IRS SEDs from the Taurus star-forming region (Figure 12.6) shows a variety of SED slopes and silicate emission strengths in this relatively young population. There is a slight trend for the silicate emission strength to be weaker relative to the continuum in disks with steeper slopes – less flaring – and presumably more settling; this would suggest a correlation of increased settling with increased grain growth (which weakens the silicate features).

Smooth 10 μm features are consistent with amorphous silicates such as are typical of the diffuse interstellar medium; the squarish or structured silicate features seen in some

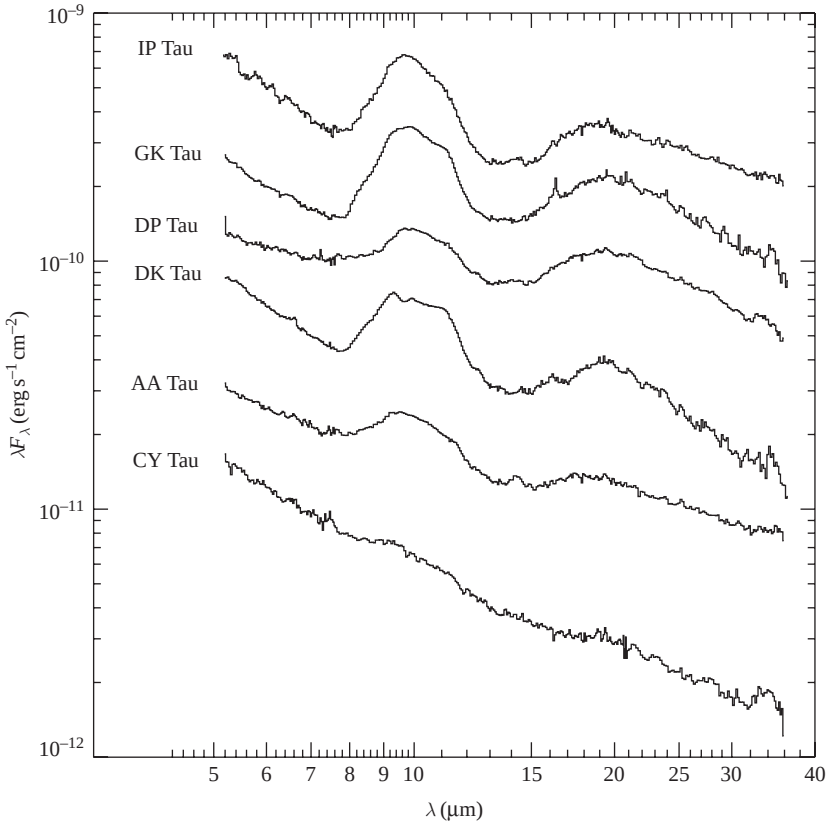

Fig. 12.6. Infrared spectral energy distributions of a sample of Taurus young stars, observed with the IRS instrument on the *Spitzer Space Telescope*. Each object shown is representative of 10–20 systems in Taurus. The strength of the 10 μm and 20 μm silicate emission features is widely variable, as shown. Objects with SEDs similar to that of CY Tau, with almost no silicate emission, tend to have steeper SEDs, suggesting that the least flared disks (presumably the most settled disks) also have the weakest silicate feature (suggesting grain growth to sizes beyond a few μm (see text). Data from Furlan *et al.* (2006); plot courtesy E. Furlan.

objects in Figure 12.6 are the result of the presence of crystals. The mystery is that to produce crystalline structure in initially amorphous particles requires heating to $T \sim 1000$ K, while the regions in which the silicate features are produced have temperatures $T \lesssim 300$ K. The observation of crystalline silicate features in cold regions has lead to various proposed mechanisms to move substantial amounts of material from 0.1 AU, where such temperatures might be achieved naturally, to nearly 1 AU; however, this is easier said than done. Watson *et al.* (2008) found that there is a statistical correlation with the fraction of crystalline silicates in disk upper layers with the amount of disk flaring, i.e., the spectral slope of the disk continuum becomes steeper as the crystalline fraction increases. One wonders whether the production of such heating might not be due to in situ production by collisions among larger bodies. Interferometric observations suggest that crystallinity is more pronounced in the inner disk regions of Herbig Ae/Be stars than at outer disk radii (van Boekel *et al.* 2006),

which could be consistent either with limited outward transport or with production by local collisions, which would be more frequent in inner regions.

Meteorites provide abundant evidence of a variety of heating events in the early solar nebula (see, e.g., Lauretta & McSween 2006). The mechanisms responsible for this heating, especially for the mm-sized, roundish chondrules, are controversial. Much work remains to be done before the detailed solar system results can be folded in with astrophysical constraints to provide a more comprehensive picture of solids in protoplanetary disks.

12.6 Core accretion and planet formation

The other obvious mechanism for clearing disk material is the formation of massive planets, which can act in a manner similar to binaries, but with the potential of sweeping out material over a wide range of disk radii if many objects form at differing distances. While small (terrestrial) planets will eventually clear regions of small dust, they do not capture substantial amounts of gas. Given the evidence for gas clearing accompanying dust clearing (§8.1), giant planets need to be invoked in many cases. Giant planet formation generally requires the accretion of substantial amounts of gas; in addition, large planets can dam up the gas attempting to accrete from the outer disk, allowing the inner disk gas to drain away via accretion.

Two general mechanisms have been suggested as the main means of giant planet formation: core accretion and gaseous gravitational instability. In the core accretion model, solid bodies accumulate via collisions until the resulting core is sufficiently large that its gravity can pull in surrounding gas (see Lissauer & Stevenson 2007 for a recent review). The gaseous gravitational instability is simply a case of fragmentation (§7.7). A kind of hybrid model posits that the gravitational fragmentation occurs in a dense dust layer, forming cores rapidly that then accrete gas from the nebula.

Beyond the evidence for a core in Saturn, the large fractions of ice and rock in Uranus and Neptune, and the possible core of Jupiter, the core accretion model has the advantage that something like this must occur to make the terrestrial planets. One might expect that, if grain growth to cm sizes occurs in less than 10 Myr at radii of 100 AU, growth to much larger bodies must have occurred at radii of order 1 AU in even shorter timescales, as suggested by the calculations discussed in the previous section.

There is some concern that core accretion might proceed too slowly to explain the observed disk clearing on timescales as short as 1–2 Myr in significant numbers of stars. There are two potential bottlenecks in the process. One is the formation of km-sized planetesimals from cm-sized objects. Such bodies are thought to be held together lightly – too large for effective sticking and too small for gravity to become important – and, as bodies of differing sizes have differing velocities due to gas drag (previous section), collisions between these objects might shatter them rather than build them up. In addition, the rapid migration of such bodies (see section 12.5) requires fast agglomeration, even for km-sized objects (Ward 1997; §12.9).

Various schemes of dust concentration might help avoid shattering by reducing relative motions and increasing densities, perhaps through vortices or eddies (e.g., Klahr & Bodenheimer 2006) or in other turbulent structures (Cuzzi *et al.* 2001). Alternatively, the probable development of a dense dust layer at the disk midplane led Goldreich and Ward (1973) to suggest that planetesimals might form by gravitational instability; however, there are

difficulties with this model. Weidenschilling (1980, 1984; also Cuzzi *et al.* 1993) pointed out that the formation of such a dense dust layer would necessarily generate turbulence which would work against gravitational collapse. In a typical nebular model, the disk surface density is well below that required by the Toomre criterion, and so an unstable dust layer must have a density dominated by particles. However, such a (large) dust or particle layer will try to rotate at Keplerian velocity, faster than the partially pressure-supported gas above/below it, as discussed above. Thus, a shear develops which tends to inflate the dust layer and prevents gravitational instabilities from growing. (Whether this also applies to a very high surface density region, such as might develop in dead zone models, is an open question.) An implication of these results is that strong enhancements of large dust particles can cause some turbulence even in dead zones. Radial drift might also help in the concentration of solids (Youdin & Shu 2002).

Once km-sized planetesimals are made, collisions among them can lead to the building of terrestrial planets and giant planet cores. The remaining bottleneck is that of accumulating gas. Assuming a sufficiently large core can be assembled rapidly, the time required to reach the epoch of runaway accretion depends upon the opacity of the growing planetary envelope. The energy released by accretion of planetesimals and gravitational contraction of the envelope must be radiated by the outer envelope; the higher the opacity, the larger the envelope. A larger envelope in turn reduces the rate at which the planet can accumulate gas, because there is less "room" to accrete within the planet's gravitational domain (roughly, its "Hill sphere", within which the planet's gravity overcomes the tidal forces of the central star). Hubickyj *et al.* (2005) showed that, with sufficiently massive cores, giant planets can form within 1 Myr for an opacity ∼2% of interstellar values. These authors attribute the reduction in opacity (dominated by dust) to rainout of solid materials in the planetary envelope; as grain growth almost certainly preceeds core formation, reduced dust opacity is an extremely plausible assumption.

12.7 Gaseous gravitational instability and planet formation

Boss (2003) has championed the idea of formation of giant planets through gaseous gravitational instability. The chief attractions of this idea are: first, that we expect disks to be relatively massive initially; and second, this mechanism avoids all the uncertainties involved with core accretion – grain growth, settling, turbulence, and migration.

There are difficulties with this idea, however, starting with theoretical constraints using a vertically averaged approach (e.g., Rafikov 2005). We can write the cooling timescale as the energy content of the disk $\Sigma c_s^2/(\gamma - 1)$ divided by its (two) surface cooling rate, $2\sigma T_{\rm eff}^4$. Using the simple relation between the effective temperature $T_{\rm eff}$ and central temperature T_c for an optically thick gray radiative disk (Hubeny 1990)

$$T_c^4 = \frac{3}{8}\tau T_{\rm eff}^4 \,, \tag{12.28}$$

the cooling time can be written as

$$t_c \sim \frac{\Sigma c_s^2}{\gamma - 1}\,\frac{4\tau_R}{3\sigma T_c^4} \tag{12.29}$$

where $\tau_R = \Sigma k_R/2$ is the vertical Rosseland mean optical depth. For gravitational instability, we require $Q \sim 1 \sim c_s\Omega/(\pi G\Sigma)$; rearranging,

$$t_c\Omega \sim \frac{1}{(\pi G)^2}\,\frac{c_s^4}{\gamma-1}\,\frac{2k_R}{3\sigma T_c^4}\left(\frac{GM}{R^3}\right)^{3/2} . \tag{12.30}$$

If we adopt the Rosseland mean opacity of Bell and Lin (1994) for temperatures lower than about 170 K, $k_R \approx 2\times10^{-4}T^2$, then numerically we have

$$t_c\Omega \sim 4\times10^4 (M/M_\odot)^{3/2} R_{10}^{-9/4} . \tag{12.31}$$

Recall that numerical experiments suggest $t_c\Omega \sim 3$ for gravitational fragmentation (Gammie 2001; Johnson & Gammie 2003; Rice *et al.* 2003; §7.7). This is qualitatively reasonable; unless a perturbation can condense on a timescale shorter than an orbital period, it will tend to shear out. These results suggest that if such gravitational fragmentation occurs at all, it would be at large radii, $R \sim 100$ AU; but then disks tend to become optically thin, changing the analysis.

These considerations apply to linear perturbations. It is easy to imagine producing highly non-linear perturbations in a disk due to the collapse of a very strongly non-axisymmetric protostellar cloud core (§6.2). However, the disk would be strongly perturbed at early times, suggesting that if fragmentation were to occur, it would tend to be during the protostellar phase – especially as the disk is more likely to be relatively massive in comparison with the central star during this phase. Fragmentation before most of the disk mass has fallen in poses problems. The danger is that either the fragments continue to accrete mass from the continuing infall and become companion stars, not planets (e.g., Bate & Bonnell 1997), or that the continuing infall leads to massive disk accretion, forcing the fragments into the central star during Type II migration (see next section).

Even if fragmentation could occur after infall ceases, one would still expect it to be more important early on, when the disk is more massive. It is not obvious how initial gravitational instability would explain the observed clearing of disks over millions of years.

12.8 Migration

The discovery of hot Jupiters (i.e., massive planets very close to the central star) made it painfully obvious that planets can migrate substantial distances inward. (Hot Jupiters are very difficult to form in situ because disks probably can't contain enough mass at such radii, condensation of ices and even dust is more difficult, etc.) Making planets move large distances does not seem to be a problem; if anything, many investigations suggest that it is all too easy to have most or all planets and planetesimals accreted into their central stars, leaving little or nothing behind.

Beyond the radial drift of small bodies discussed in §12.6, planetesimals and planets may migrate through gravitational interactions with disks by one of three basic mechanisms. Using the typical astronomical convention of adopting uninformative names, these mechanisms are called Type I, II, and III migration, and operate as follows (see also discussion in Papaloizou *et al.* 2007).

Type I. A body of sufficient mass to have a small but non-negligible gravitational effect on the disk will excite spiral density waves, which have the form shown in the right-hand panel of Figure 7.1 (with the body in the center of the perturbation labeled "2"). The resulting torques thus are analogous to the case of gravitational instability; the trailing arm takes up

angular momentum from the body, while the leading inner arm adds angular momentum. In general, the torques from the outer arm exceed those of the inner arm; as a result, the body migrates inward. The migration timescales for objects of masses $\sim 10\, M_\oplus$ are very short, suggesting difficulties in having the core-accretion model work for Jupiter-like objects (e.g., Ward 1997; D'Angelo *et al.* 2003). Possible solutions to this problem include keeping cores significantly below $\sim 10\, M_\oplus$, having rapid gas accretion to form the giant planet before migration into the central star, and/or reducing the Type I migration rate by interactions with the turbulently structured disk, resulting in more of a random-walk migration (Nelson & Papaloizou 2004).

Type II. The exertion of torques on the spiral arm by a body implies opposing torques applied to the disk. The body imparts angular momentum to the outer disk and takes up angular momentum from the inner disk. Large planets – typically on the order of Saturn mass – can open a gap when the gravitational torques exceed the gap-closing viscous and pressure effects (e.g., Lin & Papaloizou 1986a). The planet then migrates inward, carried along with the disk accretion (Lin & Papaloizou 1986b). Nominally, the migration time is expected to be the viscous timescale, although a low-mass disk may not be able to affect a more massive planet significantly (e.g., Edgar 2007 and references therein).

Type III migration involves torques involving material flowing through the co-orbital region. Because the disk structure and flows are so complicated in this region, many uncertainties remain. Migration apparently can be either inward or outward, and very rapid, and may only be important in massive disks.

Attempts have been made to incorporate migration into models of planet formation. Ida and Lin (2004) ignored Type I migration because it was too rapid and concentrated on Type II migration for gas giants. Assuming completely viscous disks, Ida and Lin adopted a value of $\alpha \sim 10^{-4}$ for their simulations, to be consistent with an estimated photoevaporation time of order 10 Myr. This value is much lower than typical numerical simulations yield, $\sim 10^{-2}$, which is also the value used for the simple viscous evolution model of §2.2. Low values of $\alpha \sim 10^{-4}$ presumably are required to make the viscous timescale at 10 AU (equation (12.6)) long enough for planets to form; viscosities two orders of magnitude higher could easily end up with the accretion of all the giant planets into the central star, with perhaps infrequent exceptions where conditions are just right (say, with timely outer disk photoevaporation) to halt the Type II motion. Such low viscosities seemingly imply that the MRI is highly inefficient, as would be the case if dead zones are present.

12.9 Disk gaps and holes

Theory indicates that even massive planets open disk gaps about them that are no more than about a factor of two or three wide in radius. The transitional disks (§8.8), on the other hand, exhibit behavior much more like inner disk holes, with substantial clearing at radii ranging over more than an order of magnitude. One possibility is that Type II migration is not occurring, or is slowed down sufficiently such that the material inside the gap has a much shorter viscous time than material outside the gap, resulting in the rapid accretion and evacuation of the inner disk. Another possibility is that multiple bodies are present and their gaps are overlapping. High-resolution imaging is needed to explore these possibilities.

It is difficult to detect disk gaps from SEDs. A gap of a factor of two in radius would correspond to a gap in the temperature distribution of the disk of a factor of only $\sim 2^{1/2}$ or less. To put this in perspective, the FWHM of a blackbody SED is roughly factor of three

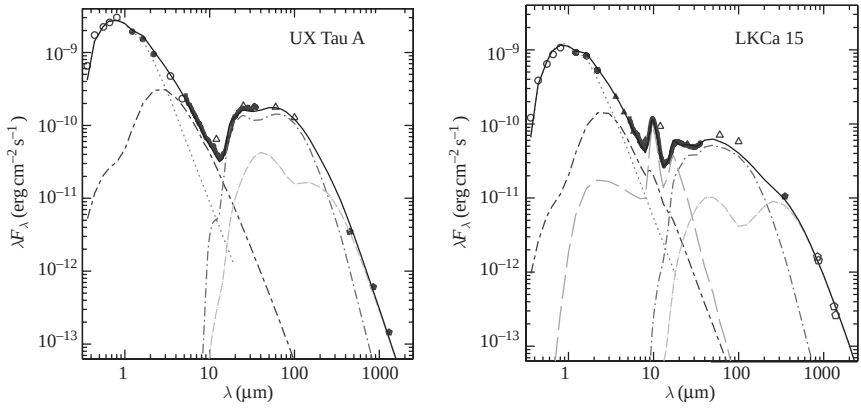

Fig. 12.7. SEDs of UX Tau A (left) and LkCa 15 (right), along with models. UX Tau A appears to have optically thick emission from a region close to the star, with a disk gap of about 56 AU. LkCa 15 has a small amount of optically thin dust within a gap of outer radius of about 46 AU, consistent with mm-wave interferometry (Piétu *et al.* 2006). The solid curves are total model fluxes to compare with observations; moving sequentially to longer wavelengths, the dotted curves show the stellar photosphere, long dot-long dash curves inner disk dust emission, dot-dash curves emission from the disk "wall" facing the star, and light dot-dashed curves outer disk emisison. Modified from Espaillat *et al.* (2007).

in wavelength; this implies that emission from optically thick disk annuli with temperature differences less than a factor of three will overlap in the spectrum.

Detailed analysis of a few stars with *Spitzer* IRS spectra has identified a few potential gap systems. UX Tau A appears to be a good candidate, with a very large dropout in infrared flux in the 10 μm region, but what appears to be an optically-thick inner disk wall (Espaillat *et al.* 2007; Figure 12.7). LkCa 15 shows a more subtle mid-infrared dip (Figure 12.7), but the inference of a large gap is supported by mm-wave interferometry (Piétu *et al.* 2006). The presence of a few systems with very large gaps suggest that many more systems with small gaps exist; interferometry with ALMA should be able to test this conjecture.

12.10 Debris disks

After the optically thick phase, many older stars exhibit optically thin, low-mass (in small grains), and gas-poor disks. The prototype of these systems is β Pic (Smith & Terrile 1984), imaged as an edge-on disk. By now many other optically thin dust disks have resolved images (§1.6; Figure 1.10). Because of their relatively small amounts of dust emission (e.g., Figure 1.11, most of the optically thin dust disks originally were found around relatively luminous nearby objects – main sequence stars of types A–F – given the limited sensitivity of the *IRAS* satellite (Backman & Paresce 1993); however, it is clear that older low-mass stars can also have optically thin disks (e.g., Greaves *et al.* 1998). These optically thin systems are called "debris disks", because it appears that this dust must be replenished continually to avoid removal by radiation pressure or infall due to Poynting–Robertson drag, both in the absence of significant amounts of gas (see, e.g. Backman & Paresce 1993).

A detailed treatment of both radiation pressure and the Poynting–Robertson effect is given by Burns *et al.* (1979); here we sketch the main ideas. Radiation pressure on a spherical dust

grain of radius a exceeds the gravitational attraction of star of luminosity L_* and mass M_* when

$$\frac{\pi a^2}{4/3\pi a^3 \rho_{\rm g}} \frac{L_*}{4\pi c G M_*} \sim 0.2 \left(\frac{a}{\mu{\rm m}}\right)^{-1} \left(\frac{\rho_g}{3\,{\rm g\,cm^{-3}}}\right)^{-1} \left(\frac{L_*}{L_\odot}\right) \left(\frac{M_*}{M_\odot}\right)^{-1} > 1\,, \quad (12.32)$$

where we have assumed a geometrical cross-section for the interaction with radiation. Thus, even for T Tauri stars, small grains with $a \lesssim 0.1\,\mu$m can be blown away rapidly, and for A stars, with typical ratios of L_*/M_* of 10 or more in solar units, only grains of sizes $>1\,\mu$m will resist radiative expulsion.

To estimate the Poynting–Robertson timescale, consider for simplicity the above dust grain to be in circular orbit at r. In its rest frame the grain sees a component of radiation pressure opposing its motion due to aberration, proportional to v_ϕ/c, where v_ϕ is its azimuthal velocity. This component of the radiation pressure force produces a torque on the particle, reducing its angular momentum and causing it to fall in. In this simplified example, assuming slow drift so that the particle is always on radial orbits, we have

$$\frac{dr v_\phi}{dt} \approx \frac{L_*}{4\pi r^2 c} \frac{3\pi a^2}{4\pi a^3 \rho_{\rm g}} \frac{v_\phi}{c}\,, \quad (12.33)$$

where $\rho_{\rm g}$ is the density of the particle. Using $r v_\phi = (G M_* r)^{1/2}$,

$$\frac{dr^{1/2}}{dt} \approx \frac{L_*}{4\pi r^{3/2} c^2} \frac{3}{4 a_{\rm g}^\rho}\,. \quad (12.34)$$

Integrating, we find the timescale for the particle to move from r to $r \to 0$,

$$t_{\rm PR} \approx \frac{4\pi a \rho_{\rm g}}{3} \frac{\pi c^2 r^2}{L_*} \approx 2.2 \times 10^3 \left(\frac{a}{\mu{\rm m}}\right) \rho_{\rm g} r_{\rm AU}^2 \frac{L_\odot}{L_*}\,{\rm yr}\,. \quad (12.35)$$

Therefore, for dust with sizes <1 mm, Poynting–Robertson timescales at 1 AU are short – and out to considerably larger radii for the higher-luminosity intermediate-mass stars. Because of the short timescales for the removal of dust, debris disks are taken to be signatures of solid bodies of significant size (planetesimals, asteroids, comets) which continually collide and release small dust.

Statistically significant surveys of debris disks have been made possible with the advent of the *Spitzer Space Telescope* (e.g., Chen *et al.* 2005; Rieke *et al.* 2005; Gorlova *et al.* 2006; Meyer *et al.* 2006; Siegler *et al.* 2007; Trilling *et al.* 2008; Currie *et al.* 2007). These studies suggest that debris disk frequencies around solar-type (F–G) stars are 10–30% at ages less than 1 Gyr, and can be of order 15% for several Gyr. There is some evidence for a peak in dust production at ages of around 10 Myr (Hernández *et al.* 2006; Currie *et al.* 2007), with a decay in production thereafter, as predicted by the models of Kenyon and Bromley (2005). As most of the detected excesses are much larger than that estimated for the zodiacal dust in our solar system, also continually produced by the collision of solid bodies, the true frequency of debris disk systems is likely to be much larger than quoted above.

Taken in conjunction with optically thick disk frequencies of order 50% or more at ages of a few Myr, the commonality of debris disk systems suggests that the frequency of planetary systems is much larger than represented by the current radial velocity detections. Indeed, there are suggestions that some of the brightest excess systems are the result of transient

dust production by collisions between large bodies (Rieke *et al.* 2005), though this is not certain (Wyatt *et al.* 2007).

Direct imaging of many debris disks shows various kinds of structures – warps, non-axisymmetric emission – which can plausibly be attributed to the perturbing gravity of giant planets (e.g., Heap *et al.* 2000; Holland *et al.* 2003). In addition, most of these systems yield evidence of inner evacuation of at least some dust species (for example, the ring system HR 4796; Koerner *et al.* 1998, Jayawardhana *et al.* 1998; Figure 1.10). This again suggests the presence of large bodies in the inner regions which can sweep disks clear.

12.11 Speculations

As discussed in §8.3, grain growth to up to at least cm sizes appears to happen over relatively short timescales at radii $\lesssim$100 AU. Unless growth is halted at meter-sized objects, it is difficult to believe that growth to much larger bodies has not occurred at 1 AU. Indeed, without substantial large bodies already present at 1 Myr, it is difficult to understand how disks could clear in 3 Myr. Thus, the author's speculation is that many T Tauri disks, even though optically thick from 0.1 to hundreds of AU, already have substantial planetesimals in the inner disk which are hidden from view by clouds of small dust (Figure 12.8). A substantial number of bodies spread over a significant range of radii would also help explain the inner disk holes of transition objects. Collisions among these bodies might also generate enough heated material to produce in situ crystalline (i.e., annealed) dust.

The question then becomes: Why are exoplanet frequencies so low? Current results from radial velocity surveys suggest that of order 10% of solar-type stars have massive planets within 5 AU, much less than the $\sim$60% of stars which have substantial gas and dust disks at ages of 1 Myr (Figure 12.1). For the reasons sketched earlier in this chapter neither accretion nor photoevaporation are likely explanations. Reconciling the radial velocity results with disk frequencies may require that most systems form relatively small Uranus- or

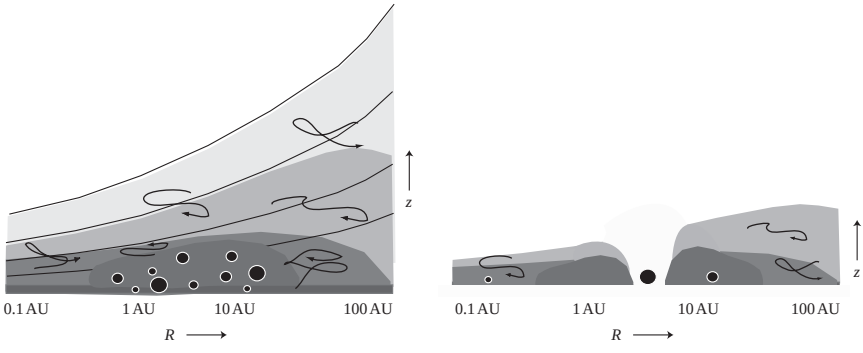

Fig. 12.8. Two speculative pictures of typical T Tauri disks, with actively accreting, turbulent upper layers, a dead zone in inner, midplane regions. On the left, even a fully active disk probably has planetesimal formation in some regions even at ages of 1–2 Myr, hidden by the small dust in upper layers. On the right, even small gaps opened by giant planets would be difficult to detect purely by SED analysis; improvements in mm-wave interferometric imaging with ALMA will undoubtedly show much more evidence for disk gaps, perhaps most likely in the most evolved, settled disks.

Neptune-mass planets; or that Jupiter-mass planets are typically formed at very large radii; or that most planets are accreted into their host stars.

Figure 12.1, by demonstrating a range of clearing timescales, suggests that initial conditions are important. Initial angular momentum is a likely candidate for explaining this range; larger disks presumably should evolve more slowly. The current data provide a hint that clearing from ∼60% of disks to ∼10% of disks occurs over 3–5 Myr, with the last 5–10% of disks taking much longer – 10 Myr – to clear. If this apparent trend holds up with more data, it might provide a further clue to disk evolution.

Our limited understanding of disk structure and dynamics is a major obstacle to understanding planet formation. The layered disk model, with a low-viscosity region or dead zone, may be important in avoiding excessively rapid Type II migration. A dead zone could result in faster particle growth, both due to higher surface densities and lower turbulence, making enormous differences in estimated timescales for planetesimal formation, and might have profound effects on migration (e.g., Matsumura *et al*. 2007). Finally, the large uncertainties in disk mass measurements directly demonstrate that much remains to be learned about the physical conditions leading to planet formation.

Appendix 1 Basic hydrodynamic and MHD equations

Here we list some basic MHD and gas-dynamic equations for reference. Derivations and further discussion may be found, for example, in Priest (1984) and Shu (1992).

We assume a non-relativistic, one-component fluid of density ρ and velocity $\mathbf{v}$. The equation of continuity or mass conservation,

$$\frac{\partial \rho}{\partial t} + \nabla \cdot (\rho \mathbf{v}) = \mathbf{0}\,, \tag{A1.1}$$

is sometimes written as

$$\frac{D\rho}{Dt} + \rho \nabla \cdot \mathbf{v} = \mathbf{0}\,, \tag{A1.2}$$

where the total time derivative

$$\frac{D}{Dt} = \frac{\partial}{\partial t} + \mathbf{v} \cdot \nabla \tag{A1.3}$$

is sometimes called the convective time derivative, or the derivative following a fluid element; $\partial/\partial t$ is the time derivative at a fixed location in space.

The momentum equation is

$$\rho \frac{D\mathbf{v}}{Dt} = -\nabla P - \rho \nabla \Phi + \mathbf{F}\,, \tag{A1.4}$$

where P is the gas pressure, Φ is the gravitational potential, and $\mathbf{F}$ includes other forces on the volume. The gravitational potential is determined by Poisson's equation

$$\nabla^2 \Phi = 4\pi G \rho\,. \tag{A1.5}$$

If magnetic fields are present then the momentum equation becomes (using Gaussian cgs units)

$$\rho \frac{D\mathbf{v}}{Dt} = -\nabla P - \rho \nabla \Phi + \frac{1}{c}\,\mathbf{J} \times \mathbf{B}\,, \tag{A1.6}$$

where $\mathbf{J}$ is the current density and $\mathbf{B}$ is the magnetic field strength, and the net charge is assumed to be zero. If the fluid velocity is much smaller than the speed of light c, then it is possible to neglect the "displacement current" term, $\partial \mathbf{E}/\partial t$, in Maxwell's equation

$$\nabla \times \mathbf{B} - \frac{1}{c}\frac{\partial \mathbf{E}}{\partial t} = \frac{4\pi}{c}\,\mathbf{J}\,. \tag{A1.7}$$

Then

$$\frac{1}{c}\,\mathbf{J} \times \mathbf{B} = \frac{1}{4\pi}(\nabla \times \mathbf{B}) \times \mathbf{B}\,, \tag{A1.8}$$

and with a vector identity one may then write the momentum equation as

$$\rho \frac{d\mathbf{v}}{dt} = -\nabla P - \rho \nabla \phi - \frac{1}{8\pi} \nabla B^2 + \frac{1}{4\pi} (\mathbf{B} \cdot \nabla) \mathbf{B} . \tag{A1.9}$$

Ohm's law gives the current density **J** in terms of the electric and magnetic fields,

$$\mathbf{J} = \sigma \left(\mathbf{E} + \frac{\mathbf{v}}{c} \times \mathbf{B} \right) , \tag{A1.10}$$

where σ is the conductivity of the fluid. In the simple ideal MHD limit that we consider in this book, the conductivity is assumed to be effectively infinite, so that

$$\mathbf{E} + \frac{\mathbf{v}}{c} \times \mathbf{B} = 0 . \tag{A1.11}$$

Using this result, we can derive the "flux-freezing" result...
The first law of thermodynamics can be written as

$$du = -P d \left(\frac{1}{\rho} \right) + T \, ds , \tag{A1.12}$$

where u is the internal energy of the fluid, T is the temperature, and s is the entropy. For an ideal polytropic gas, $u = c_V T$, where c_V is the specific heat at constant volume. The generalized energy equation is

$$\rho \frac{D}{Dt} \left(u + \frac{v^2}{2} \right) = -\Lambda_{\rm r} - \nabla \cdot \mathbf{q} + H_e + \mathbf{v} \cdot \left(\frac{1}{c} \mathbf{J} \times \mathbf{B} - \nabla P + \mathbf{F} \right) , \tag{A1.13}$$

where $\Lambda_{\rm r}$ are the radiative energy losses, **q** is the conductive flux, and $H_{\rm e}$ represents the sum of all other heating sources, including viscous dissipation (see, e.g., Priest (1984)).

Appendix 2 Jeans masses and fragmentation

The Jeans mass is a concept frequently used to discuss gravitational instabilities, although the background state assumed is not usually realizable (cf. Binney & Tremaine 1987), i.e., the assumption of constant background density does not generally represent a solution consistent with hydrostatic equilibrium.

Assume that the velocity and density can be represented by a mean state plus a small fluctuation, so that $\mathbf{v} = \mathbf{v}_\circ + \delta\mathbf{v}$, $\rho = \rho_\circ + \delta\rho$. Then linearizing the equations of mass conservation and momentum for the case of no magnetic pressure (Appendix 1),

$$\frac{\partial}{\partial t}\delta\mathbf{v} = -\frac{1}{\rho_\circ}\nabla c_\mathrm{s}^2\delta\rho - \nabla\Phi\,, \tag{A2.1}$$

$$\frac{\partial}{\partial t}\delta\rho + \delta\mathbf{v}\cdot\nabla\rho_\circ = -\rho_\circ\nabla\cdot\delta\mathbf{v}\,, \tag{A2.2}$$

where it is assumed that $\mathbf{v}_\circ = \mathbf{0}$, and that the equilibrium state is

$$\frac{c_\mathrm{s}^2}{\rho_\circ}\nabla\rho_\circ = -\nabla\Phi_\circ\,. \tag{A2.3}$$

Using the Poisson equation relating the gravitational potential to the density,

$$\nabla^2\Phi = 4\pi G\rho\,. \tag{A2.4}$$

Making the further simplification (obviously inconsistent with the above) that the background density $\rho_\circ$ is constant, one can combine the equations to arrive at

$$\frac{\partial^2\delta\rho}{\partial t^2} = \rho_\circ\left(\frac{c_\mathrm{s}^2}{\rho_\circ}\nabla^2\delta\rho + 4\pi G\delta\rho\right)\,. \tag{A2.5}$$

Taking a plane wave of the form

$$\delta\rho = \delta\rho_\circ e^{i(\omega t - kx)}\,, \tag{A2.6}$$

the resulting dispersion equation is

$$\omega^2 = c_\mathrm{s}^2\,(k^2 - k_\mathrm{J}^2)\;,\quad k_\mathrm{J}^2 = 4\pi G\frac{\rho_\circ}{c_\mathrm{s}^2}\,. \tag{A2.7}$$

When $k < k_\mathrm{J}$, ω is imaginary; thus, there are exponentially decaying and exponentially increasing solutions; the latter correspond to gravitational instability, i.e., the density grows without limit.

It is usual to define the Jeans mass by

$$M_{\rm J} = \left(\frac{2\pi}{k_{\rm J}}\right)^3 \rho_\circ = \left(\frac{\pi c_{\rm s}^2}{G}\right)^{3/2} \rho_\circ^{-1/2} \,. \tag{A2.8}$$

For a given temperature and density, masses greater than the Jeans mass will be unstable to gravitational collapse, based on this analysis. However, this solution has been called the 'Jeans swindle' (e.g., Spitzer 1978; Binney & Tremaine 1987) because the background state does not correspond to any physical equilibrium. In certain cases the Jeans mass is a useful guide to the likely scales of gravitational instability (Chapter 2).

One situation for which the assumption of a constant uniform background density as an equilibrium state is correct is the special case of a uniform, infinite, and infinitely thin sheet of matter (or a thin sheet where gradients in the perpendicular (z) direction can be neglected). Then the conservation equations can be integrated vertically (in z), and the surface density Σ takes the place of the volume density:

$$\frac{\partial}{\partial t}\Sigma + \nabla \cdot (\Sigma \delta \mathbf{v}) = 0 \,, \tag{A2.9}$$

$$\Sigma \frac{\partial}{\partial t}\delta \mathbf{v} = -\nabla \mathbf{P} - \Sigma \nabla \Phi \,, \tag{A2.10}$$

where the pressure has been vertically integrated. Linearizing as before, and starting from rest,

$$\frac{\partial}{\partial t}\delta\Sigma + \Sigma_\circ \nabla \cdot \delta \mathbf{v} = \mathbf{0} \,, \tag{A2.11}$$

$$\Sigma_\circ \frac{\partial}{\partial t}\delta \mathbf{v} = -c_{\rm s}^2 \nabla \delta\Sigma - \Sigma_\circ \nabla \Phi \,. \tag{A2.12}$$

We assume here implicitly that the gradient in the background state pressure balances the gradient of the background potential. These gradients must be in the z direction by symmetry. We can use this fact with Gauss' law to derive the potential, by integrating the surface field $-\nabla\Phi$ over a pillbox of area $2dA$ encompassing the sheet at $z = 0$; then

$$2\,(-\nabla\Phi)\,dA = -4\pi G \Sigma\, dA \,, \tag{A2.13}$$

so that

$$\nabla\Phi = 2\pi G \Sigma \,. \tag{A2.14}$$

Therefore,

$$\lim_{\epsilon\to\infty} \int_{-\epsilon}^{+\epsilon} dz\, \nabla^2\Phi = \lim_{\epsilon\to\infty} \left[\nabla\Phi\mid_{+\epsilon} - \nabla\Phi\mid_{-\epsilon}\right] = 4\pi G\Sigma \,. \tag{A2.15}$$

From basic definitions, this implies

$$\nabla^2\Phi = 4\pi G \Sigma \delta(z) \,, \tag{A2.16}$$

where δ is the Dirac delta function.

As before, we analyze behavior for a plane wave perturbation in the x direction,

$$\delta\Phi = \delta\Phi_a\, e^{i(kx-\omega t)} \,, \tag{A2.17}$$

where $\delta\Phi_a$ is a (constant) amplitude. This equation can only apply in the plane $z = 0$; for $z \neq 0$,

$$\nabla^2 \delta\Phi = 0\,. \tag{A2.18}$$

There is only one continuous function which satisfies both these constraints, and also goes to zero at large z,

$$\delta\Phi = \delta\Phi_a\, e^{i(kx-\omega t)-|kz|}\,. \tag{A2.19}$$

Returning to the Gauss' law evaluation,

$$\lim_{\epsilon\to\infty}\left[\frac{\partial}{\partial z}\delta\Phi\mid_{+\epsilon} - \frac{\partial}{\partial z}\delta\Phi\mid_{-\epsilon}\right] = -2\mid k\mid \delta\Phi_a = 4\pi G\delta\Sigma\,, \tag{A2.20}$$

so that

$$\Phi_a = -\frac{2\pi G\delta\Sigma}{\mid k\mid}\,. \tag{A2.21}$$

Substitution of this result into the linearized equations leads to the dispersion relation

$$\omega^2 = c_{\rm s}^2 k^2 - 2\pi G\Sigma_\circ \mid k\mid\ . \tag{A2.22}$$

Again, when $\omega^2 < 0$, exponential growth occurs, so the sheet is gravitationally unstable for

$$\mid k_{\rm J}\mid < 2\pi G\frac{\Sigma_\circ}{c_{\rm s}^2}\,. \tag{A2.23}$$

Thus, just as in the basic Jeans mass calculation, wavelengths greater than $\lambda_{\rm J} > 2\pi/k_{\rm J}$ are unstable. However, the sheet dispersion relation differs in an important way from the basic Jeans mass result. Defining a growth rate $\Gamma = -i\omega$, and taking only real positive k,

$$\Gamma^2 = 2\pi G\Sigma_\circ k - c_{\rm s}^2 k^2\,, \tag{A2.24}$$

so that $\Gamma \to 0$ as $k \to 0$. The growth rate has a maximum at $k_{\rm max} = k_{\rm J}/2$, unlike the basic Jeans mass calculation, where the growth rate is largest for $k \to 0$.

A stability analysis for infinite filaments yields results similar to those for sheets, in the sense that the critical wavelengths (Jeans lengths) are of the order of the characteristic dimension of the medium. Here we consider the isothermal case, following Larson (1985). Assume a cylinder infinitely extended in the z direction. The filament has a density structure as a function of cylindrical radius R of (Ostriker 1964)

$$\rho = \rho_0\left(1 + \frac{R^2}{(4H^2)}\right)^{-2}\,, \tag{A2.25}$$

where the scale height H is given by

$$H = \frac{c_{\rm s}^2}{(2G\Sigma_0)}\,, \tag{A2.26}$$

and Σ_0 is the surface density taken perpendicular to the filament through its center. The critical wavenumber is then (Stodolkiewicz 1963)

$$k_{\rm c}H = 0.798\,. \tag{A2.27}$$

The critical mass is

$$M_{\rm c} = 7.88 \frac{c_{\rm s}^4}{G^2 \Sigma_\circ} \,, \tag{A2.28}$$

which has obvious analogies to the case of the sheet. The dispersion relation has not been worked out in detail for this case, but Larson (1985) estimates that the maximum rate occurs for $k_{\rm max} \sim 0.5 k_{\rm c}$, similar to the case of the sheet. The maximum linear growth rate is estimated to correspond to an e-folding timescale of roughly

$$\tau_{\rm e} \sim 3.6 \frac{H}{c_{\rm s}} \,. \tag{A2.29}$$

An interesting property of the infinite isothermal filament is that it has a critical (maximum) line density (mass per unit length in the z direction), which is a function only of temperature (Ostriker 1964):

$$m_{\rm c} = \frac{2 c_{\rm s}^2}{G} \,. \tag{A2.30}$$

This is equivalent to assuming that the external pressure at the outer boundary is negligible, so that integrals of the density distribution extend effectively to infinity in R. Assuming a mean molecular weight of $2.36 m_{\rm H}$, this line density corresponds to

$$m_{\rm c} = 16.3 \, T_{10} \;\; M_\odot \, {\rm pc}^{-1} \,, \tag{A2.31}$$

where T_{10} is the gas temperature in units of 10 K. Line densities above this critical value result in collapse in the R direction. The Jeans length in the z dimension for the cylinder of critical line density is then

$$\lambda_{\rm c} = 3.94 \, \frac{c_{\rm s}^2}{(G \Sigma_0)} \,. \tag{A2.32}$$

As discussed in Chapter 2, the above discussion can be used as a guide to preferred scales of fragmentation, but the assumed initial static conditions are unrealistic, as finite sheets and filaments tend to collapse faster than linear growth rates; non-linear perturbations must be present in the sheets and filaments for them to collapse faster than global modes and thus fragment.

Appendix 3 Basic radiative transfer

Here we briefly review some basic equations of radiative transfer. A detailed discussion of radiation transport is beyond the scope of this work; the most thorough treatment can be found in Mihalas (1978).

The specific intensity $I_\nu(\theta, \phi)$ is defined to be the amount of energy in a unit frequency interval around ν passing through a unit area into unit solid angle in the direction (θ, ϕ) per unit time. Dealing with this quantity has the advantage that it is invariant except for sources and sinks of radiation. The total flux of energy F_ν through an area dA is then

$$F_\nu = \int_0^{2\pi} d\phi \int_0^{\pi} d\theta \sin\theta \cos\theta \, I_\nu \,, \tag{A3.1}$$

where θ is the polar angle measured from the normal to the surface and ϕ is the azimuthal angle. The total luminosity L_ν from an object is then the integral of F_ν over the entire surface of the object, and the total radiative energy loss L is $\int_0^\infty L_\nu d\nu$.

A special case of interest is that of a flat uniform surface which radiates as a blackbody. That is, the intensity emitted into space from this surface at all angles is the Planck function B_ν. Then the flux emitted by the surface, using the assumption of axisymmetry, is

$$F_\nu = \int_0^{2\pi} d\phi \int_0^{\pi/2} d\theta \sin\theta \cos\theta B_\nu = 2\pi \int_0^1 d\mu \mu B_\nu = \pi B_\nu \,, \tag{A3.2}$$

where $\mu = \cos\theta$ and the total flux per unit area integrated over all frequencies is $\int_0^\infty d\nu \pi B_\nu = \sigma T^4$.

The time-independent radiative equation for the change of the intensity over a path s is

$$\frac{dI_\nu}{ds} = -k_\nu I_\nu + j_\nu \,, \tag{A3.3}$$

where k_ν is the opacity per unit volume, and j_ν is the emissivity. The term $k_\nu I_\nu$ represents the absorption of radiation by the medium, while the emissivity represents sources of additional radiation.

In plane-parallel geometry, with vertical height z, and with θ measured from the vertical, the transfer equation can be written as

$$\mu \frac{dI_\nu}{d\tau_\nu} = I_\nu - S_\nu \,, \tag{A3.4}$$

where

$$d\tau_\nu = -k_\nu dz \,, \qquad S_\nu = \frac{j_\nu}{k_\nu} \,. \tag{A3.5}$$

The formal solution of the plane-parallel transfer equation for the intensity emerging from the surface of the medium (where $\tau_\nu = 0$) is

$$I_\nu(0) = \int_0^{\tau_\nu} S_\nu(t') e^{-t'/\mu} \frac{dt'}{\mu} + I_\nu(\tau_\nu) e^{-\tau_\nu/\mu} . \tag{A3.6}$$

The total intensity along the ray is the sum of the underlying intensity $I_\nu(\tau_\nu)$, attenuated by the total absorption through the medium of optical depth τ_ν, and the contribution from the emission of the medium, represented by the source function S_ν.

The formal solution is generally not very useful because the source function is not known a priori; usually S_ν depends upon the optical depth and other properties of the medium, as well as on the radiation fields present. In the general case, the transfer solution is obtained iteratively.

One special case of particular interest is that of extinction (by dust, for example) in an absorbing slab of material far from the source. In this case $S_\nu = 0$ and only one angle of inclination needs to be taken into account, so that the observed flux

$$F_\nu(\text{obs}) = I_\nu \, d\Omega \, \exp[-\tau_\nu(\text{total}) = F_\nu(\text{true}) \, \exp[-\tau_\nu(\text{total})] , \tag{A3.7}$$

where $d\Omega$ is the solid angle subtended by the source at the observer and $\tau_\nu(\text{total})$ is the total optical depth along the path to the source. Usually extinction at a given wavelength or frequency is expressed in magnitudes. The magnitude scale is related to fluxes F by $m_1 - m_2 = -2.5 \log(F_1/F_2)$; then the extinction A_ν in magnitudes (the reduction in brightness due to the absorbing screen) is related to the extinction optical depth by $A_\nu = 1.086 \tau_\nu(\text{total})$.

For all cases considered in detail here we may take azimuthal symmetry. Thus, the integral over solid angle becomes

$$\oint \frac{d\Omega}{4\pi} = \left(\frac{1}{2}\right) \int_{-1}^{1} d\mu . \tag{A3.8}$$

We define the moments

$$J_\nu = \left(\frac{1}{2}\right) \int_{-1}^{1} d\mu \, I_\nu ; \quad H_\nu = \left(\frac{1}{2}\right) \int_{-1}^{1} d\mu \, \mu \, I_\nu ; \quad K_\nu = \left(\frac{1}{2}\right) \int_{-1}^{1} d\mu \, \mu^2 \, I_\nu . \tag{A3.9}$$

The quantity J_ν is the mean intensity and $4\pi H_\nu$ is the total flux of energy per unit area, while $4\pi K_\nu/c$ is the radiation pressure (Mihalas 1978). (Note that all of these quantities are per unit interval frequency at frequency ν.)

For simplicity assume that S_ν is isotropic. Then the first two moments of the transfer equation yield

$$\frac{dH_\nu}{d\tau_\nu} = J_\nu - S_\nu ; \qquad \frac{dK_\nu}{d\tau_\nu} = H_\nu . \tag{A3.10}$$

Recasting the first equation as

$$\frac{dH_\nu}{dz} = -k_\nu (J_\nu - S_\nu) , \tag{A3.11}$$

and if there is no net energy production in the atmosphere, as is often the case,

$$\frac{d}{dz} \int_0^\infty H_\nu d\nu = 0 , \tag{A3.12}$$

and so

$$\int_0^\infty k_\nu (J_\nu - S_\nu) d\nu = 0\,, \tag{A3.13}$$

which is the condition of radiative equilibrium. For example, the models of dusty infalling envelopes discussed in §4.2 generate little energy except at the center; therefore the enforcement of radiative equilibrium provides the solution for the envelope source function and hence the emergent spectrum.

To see the general nature of the solutions, we make the approximation that the opacity as a function of frequency $k_\nu = k$ is constant. Then the two moments of the transfer equation can be integrated over frequency,

$$\frac{dH}{d\tau} = 0\,, \qquad \frac{dK}{d\tau} = H\,, \tag{A3.14}$$

which can be easily integrated to yield

$$K = H\tau + \text{constant}\,, \qquad J = S\,. \tag{A3.15}$$

To complete the solution, one requires a closure relation between J and K and a boundary condition. One simple approximation is to assume that, in this plane-parallel region, the radiation is restricted to streaming only in two opposing directions,

$$I = I_+ \,\delta\left(\mu - \frac{1}{\sqrt{3}}\right) + I_- \,\delta\left(\mu + \frac{1}{\sqrt{3}}\right)\,, \tag{A3.16}$$

where δ is the Dirac delta function. With this choice of mean angle, $J = 3K$, which is also the result for the nearly isotropic radiation fields expected at a large optical depth (cf. Mihalas 1978). Assuming that the incoming radiation field $I_- = 0$ at the outer boundary $\tau = 0$ of the atmosphere, it is straightforward to show that $J(\tau = 0) = \sqrt{3}H$. The solution of the transfer equation for this case becomes

$$J = S = 3H\left(\tau + \frac{1}{\sqrt{3}}\right)\,. \tag{A3.17}$$

If one further assumes that the source function is equal to the Planck function $B = \int_0^\infty B_\nu \, d\nu = \sigma T^4/\pi$, and defines the effective temperature by $4\pi H = \sigma T_{\rm eff}^4$, the temperature structure of the atmosphere is given by the standard gray atmosphere equation

$$T^4 = \left(\frac{3}{4}\right) T_{\rm eff}^4 \left(\tau + \frac{1}{\sqrt{3}}\right)\,. \tag{A3.18}$$

Thus, the atmosphere can be taken to be approximately radiating as a blackbody, with effective temperature $T_{\rm eff}$, with the radiation arising from a surface where $\tau \sim 0.76$. (The equation for the gray plane-parallel atmosphere can be solved to arbitrary accuracy, but the exact solution is not of great interest because the opacity is never constant with frequency.)

For dusty protostellar envelopes, one is generally interested in situations in which the atmosphere cannot be approximated as plane-parallel. We therefore also consider the transfer equation in spherical coordinates,

$$\mu \frac{\partial I_\nu}{\partial r} + \frac{(1-\mu^2)}{r} \frac{\partial I_\nu}{\partial \mu} = -k_\nu (I_\nu - S_\nu)\,. \tag{A3.19}$$

Taking moments as before,

$$\frac{\partial H_\nu}{\partial r} + \frac{2H_\nu}{r} = -k_\nu (J_\nu - S_\nu)\,, \tag{A3.20}$$

$$\frac{\partial K_\nu}{\partial r} + \frac{(3K_\nu - J_\nu)}{r} = -k_\nu H_\nu\,, \tag{A3.21}$$

where the total energy emitted in $d\nu$ at ν is $L_\nu = 16\pi^2 r^2 H_\nu$.

We consider first the case in which the envelope is optically thin, which is relevant to dusty envelopes surrounding YSOs at low frequencies. In this case clearly $H_\nu \propto r^{-2}$. If we further assume that all of the radiation is provided by a central "core" with uniform intensity $I_{\rm c}$, then

$$J_\nu = \frac{1}{2}\int_{\mu_{\rm min}}^{1} d\mu I_{\rm c} = \frac{I_{\rm c}}{2}\left[1 - \left(1 - \frac{R_{\rm c}^2}{r^2}\right)^{1/2}\right]\,, \tag{A3.22}$$

where $\mu_{\rm min}$ corresponds to the angle tangent to the stellar surface and $R_{\rm c}$ is the radius of the core. It is simple to show that in the limit $r >> R_{\rm c}$,

$$J_\nu \rightarrow I_{\rm c}\frac{R_{\rm c}^2}{4r^2} \rightarrow H_\nu \rightarrow K_\nu\,. \tag{A3.23}$$

At the other extreme, suppose that the optical depth is very large. In this circumstance one expects the radiation field to be nearly isotropic and to approach LTE. This implies $J_\nu \simeq 3K_\nu$ and $S_\nu \simeq B_\nu \simeq J_\nu$. Equation (A3.21) becomes

$$\frac{1}{k_\nu}\frac{dB_\nu}{dr} = \frac{1}{k_\nu}\frac{dB_\nu}{dT}\frac{dT}{dr} = -3H_\nu\,. \tag{A3.24}$$

Defining the Rosseland mean opacity

$$\frac{1}{k_{\rm R}} = \int_0^\infty \frac{(1/k_\nu)\,(dB_\nu/dT)\,d\nu}{\int_0^\infty (dB_\nu/dT)\,d\nu}\,, \tag{A3.25}$$

and integrating over frequency, one arrives at the well-known diffusion equation from the theory of stellar structure (cf. Schwarschild 1958)

$$L = -\frac{64\pi\sigma r^2 T^3}{3k_{\rm R}}\frac{dT}{dr}\,. \tag{A3.26}$$

Finally, we consider an approximate solution for the gray (constant) opacity case where sphericity is important. In this case the radiation field tends to be peaked in the radial direction. For illustrative purposes we take $K = J$. Then

$$\frac{dJ}{dr} + \frac{2J}{r} = -kH = -\frac{kL}{16\pi^2 r^2}\,. \tag{A3.27}$$

Suppose that the opacity per unit volume has a power-law dependence, $k = k_\circ (r/r_\circ)^{-n}$ ($n > 1$). Then

$$\frac{dJ}{dr} + \frac{2J}{r} = \frac{k_\circ L}{16\pi^2 r_\circ^2}\left(\frac{r_\circ}{r}\right)^{2+n}\,. \tag{A3.28}$$

This has the solution

$$J = J_1\left(\frac{r_\circ}{r}\right)^{1+n} + J_2\left(\frac{r_\circ}{r}\right)^2\,, \tag{A3.29}$$

where J_1 and J_2 are constants; the second term is the solution to the homogeneous equation. Solving in terms of the radial optical depth

$$\tau_{\rm r} = \int_r^\infty k dr = \frac{k_\circ r_\circ}{n-1}\left(\frac{r}{r_\circ}\right)^{1-n}, \tag{A3.30}$$

and using the boundary condition that as $\tau \to 0$, $J \to H$, the result is

$$J = \frac{L}{16\pi^2 r^2}(\tau_r + 1), \tag{A3.31}$$

which has obvious similarities to the plane-parallel case.

List of symbols

a	Area element (Chapter 10)
a	semi-major axis (Chapter 12)
A	Atomic species (Chapter 10)
A_{ij}	Einstein spontaneous emission probability
B	magnetic field
$B_{\rm p}$	poloidal magnetic field (Chapter 10)
B_ν	Planck function
B_ϕ	toroidal magnetic field (Chapter 10)
c	speed of light
$c_{\rm s}$	isothermal sound speed
c_V	ratio of specific heats at constant volume
C_{ij}	collisional transition rate between (atomic) levels
dj/dt	angular momentum flux per unit magnetic flux tube (Chapter 10)
$\dot{e}_{\rm w}$	wind energy flux per unit magnetic flux tube (Chapter 10)
E	energy
f	oscillator strength
F	radiant energy flux per unit area
g	disk annulus torque
g_i	statistical weight of atomic level i
G	gravitational constant
h	Planck constant
h	specific angular momentum (Chapter 7)
H	disk scale height
I_ν	specific intensity
J	angular momentum
J	current density (Chapter 10)
k	Boltzmann constant, wavenumber
l	angular momentum constant on magnetic field line (Chapter 10)
$l_{\rm B}$	angular momentum on field line carried by magnetic field (Chapter 10)
L	luminosity
$L_{\rm acc}$	accretion luminosity
$L_{\rm b}$	bolometric luminosity
$L_{\rm d}$	disk luminosity
$L_{\rm D}$	deuterium fusion luminosity

$L_{\rm DSS}$	steady-state deuterium fusion luminosity
L_*	stellar luminosity
$m_{\rm H}$	mass of hydrogen atom
M_*	stellar mass
$M_{\rm d}$	disk mass
$M_{\rm J}$	Jeans mass
M_r	mass interior to radius r
$M_{\rm cl}$	mass of cloud
$\dot{M}$	mass infall or accretion rate
$\dot{M}_{\rm w}$	wind mass loss rate
n	number density
n	power-law index of infall density distribution (Chapter 4)
n	polytropic index (Chapter 11)
$N_{\rm H_2}$	number density of hydrogen molecules
p	impact parameter (Chapter 5)
p	power-law dependence of surface density on radius (Chapter 8)
P	gas pressure
q	power-law dependence of temperature on radius (Chapter 8)
q	mass ratio of binary (Chapter 12)
Q	Toomre parameter for gravitational instability
r	radial distance
$r_{\rm c}$	centrifugal radius (Chapter 4)
r_λ	photospheric radius at wavelength λ (Chapter 5)
R	cylindrical radius distance
$R_{\rm cl}$	radius of cloud
$R_{\rm co}$	disk co-rotation radius
$R_{\rm m}$	magnetospheric (disk truncation) radius
$R_{\rm s}$	sonic point radius (Chapter 10)
$R_{\rm T}$	disk truncation radius
R_*	stellar radius
S_ν	source function
t	time
$t_{\rm c}$	cooling time
t_e	characteristic stopping time of dust grain (Chapter 12)
$t_{\rm kh}$	Kelvin–Helmholtz timescale
T	temperature (K)
$< T >$	mean internal stellar temperature
$T_{\rm d}$	disk surface or effective temperature
$T_{\rm eff}$	(stellar) effective temperature
$t_{\rm ff}$	free-fall time
T_g	non-dimensional time for disk similarity solution
$T_{\rm max}$	disk peak temperature
τ	optical depth
u	velocity, r/r_c (Chapter 4)
U	internal thermal energy of star
UBVRIJHKL	Standard optical near-infrared, broad-band photometric magnitudes
v	velocity

$v_{\rm p}$	poloidal velocity (Chapter 10)
$v_{\rm th}$	thermal velocity width
v_ϕ	azimuthal velocity
v_ϕ	toroidal velocity (Chapter 10)
$v_{\rm K}$	Keplerian velocity
$v_{\rm R}$	radial velocity (cylindrical coordinates; Chapter 12)
V	volume, velocity
w	turbulent velocity
$w_{\rm D}$	drift velocity
W	gravitational potential energy of star
x	non-dimensional radial distance (Chapter 4)
α	orbital angle (Chapter 4), viscosity parameter
α	overdensity (Chapter 3), non-dimensional density (Chapter 4)
$\alpha_{\rm B}$	Case B hydrogen recombination coefficient
α_m	line absorption cross-section (Chapter 5)
α_ν	line absorption cross-section at frequency ν
β	exponent of dust opacity vs. frequency
γ	angle between incoming ray and disk normal
$\delta(x)$	Dirac delta function
ϵ	thermal energy content of accreted material (Chapter 11)
η	parameter for flattened collapse models (Chapter 4)
η	ratio between mass and magnetic flux (Chapter 10)
θ	polar angle in cylindrical coordinates
$\theta_\circ$	streamline polar angle of rotating collapse solution at infinity (Chapter 3)
κ	epicyclic frequency (Chapter 7)
κ	Scalar relation between v and B (Chapter 10)
κ_g	wavenumber for disk torque decomposition (Chapter 7)
$\kappa_{\rm J}$	critical wavenumber for Jeans instability
$\kappa_{\rm R}$	Rosseland mean opacity
κ_λ	opacity per unit mass at wavelength λ
κ_ν	opacity per unit mass at frequency ν
λ	wavelength, mean free path (Chapter 7)
$\lambda_{\rm J}$	Jeans length
μ	mean molecular weight in hydrogen masses
ν	frequency
ν_υ	viscosity
ρ	gas mass density
σ	cross-section for collisions (Chapter 3)
σ	Stefan–Boltzmann constant
Σ	surface density
τ	optical depth
ϕ	potential; gravitational, effective
Φ	flux of ionizing photons
Φ_B	magnetic flux
ξ	initial mass function
ω	angular frequency
Ω	angular velocity

Bibliography

Abramowitz, M., & Stegun, I. A. 1972, *Handbook of Mathematical Functions* (Dover: New York), p. 591
Adams, F. C., & Fatuzzo, M. 1996, *Ap.J.*, **464**, 256
Adams, F. C., Hollenbach, D., Laughlin, G., & Gorti, U. 2004, *Ap.J.*, **611**, 360
Adams, F. C., Lada, C. J., & Shu, F. H. 1987, *Ap.J.*, **312**, 788 (ALS)
Adams, F. C., Lada, C. J., & Shu, F. H. 1988, *Ap.J.*, **326**, 865
Adams, F. C., & Myers, P. C. 2001, *Ap.J.*, **553**, 744
Adams, F. C., Ruden, S. P., & Shu, F. H. 1989, *Ap.J.*, **347**, 959
Adams, F. C., & Shu, F. H. 1986, *Ap.J.*, **308**, 836
Ahmic, M., Jayawardhana, R., Brandeker, A., Scholz, A., van Kerkwijk, M. H., Delgado-Donate, E., & Froebrich, D. 2007, *Ap.J.*, **671**, 2074
Akeson, R. L., Ciardi, D. R., van Belle, G. T., Creech-Eakman, M. J., & Lada, E. A. 2000, *Ap.J.*, **543**, 313
Akeson, R. L., *et al.* 2005a, *Ap.J.*, **622**, 440
Akeson, R. L., *et al.* 2005b, *Ap.J.*, **635**, 1173
Ali, B., & Depoy, D. 1995, *A.J.*, **109**, 709
Allen, L., *et al.* 2007, *Protostars and Planets V*, eds. B. Reipurth, D. Jewitt, and K. Keil (Tucson: University of Arizona Press), p. 361
Alexander, R. D., Clarke, C. J., & Pringle, J. E. 2005, *M.N.R.A.S.*, **358**, 283
Alexander, R. D., Clarke, C. J., & Pringle, J. E. 2006a, *M.N.R.A.S.*, **369**, 216
Alexander, R. D., Clarke, C. J., & Pringle, J. E. 2006b, *M.N.R.A.S.*, **369**, 229
Alibert, Y., Mousis, O., Mordasini, C., & Benz, W. 2005, *Ap.J.Lett.*, **626**, L57
Alves, J. F., Lada, C. J., & Lada, E. A. 2001, *Nature*, **409**, 159
Aly, J. J., & Kuijpers, J. 1990, *A&Ap.*, **227**, 473
Ambartsumian, J. A. 1947, *Stellar Evolution and Astrophysics* (Yerevan: Acad. Sci. Armenian SSR)
Anderson, J. M., Li, Z.-Y., Krasnopolsky, R., & Blandford, R. D. 2003, *Ap.J.Lett.*, **590**, L107
Anderson, J. M., Li, Z.-Y., Krasnopolsky, R., & Blandford, R. D. 2005, *Ap.J.*, **630**, 945
Anderson, J. M., Li, Z.-Y., Krasnopolsky, R., & Blandford, R. D. 2006, *Ap.J.Lett.*, **653**, L33
André, P., Deeney, B. D., Phillips, R. B., & Lestrade, J.-F. 1992, *Ap.J.*, **401**, 667
André, P., & Montmerle, T. 1994, *Ap.J.*, **420,** 837
André, P., Montmerle, T., & Feigelson, E. D. 1987, *A.J.*, **93**, 1192
André, P., Motte, F., & Bacmann, A. 1999, *Ap.J.Lett.*, **513**, L57
André, P., Phillips, R. B., Lestrade, J.-F., & Klein, K.-L. 1991, *Ap.J.*, **376,** 630
André, P., Ward-Thompson, D., & Barsony, M. 1993, *Ap.J.*, **406**, 122
Andre, P., Ward-Thompson, D., & Barsony, M. 2000, *Protostars and Planets IV*, eds. B. Reipurth, D. Jewitt, and K. Keil (Tucson: University of Arizona Press), p. 59
Andrews, S. M., & Williams, J. P. 2005, *Ap.J.*, **631**, 1134
Andrews, S. M., & Williams, J. P. 2007, *Ap.J.*, **659**, 705
Anglada, G., Rodriguez, L. F., Canto, J., Estalella, R., & Lopez, R. 1987, *A&Ap.*, **186**, 280
Appenzeller, I., Jankovics, I., & Östreicher, R. 1984, *A&Ap.*, **141,** 108
Appenzeller, I., & Tscharnuter, W. M. 1974, *A&Ap.*, **30**, 423
Arce, H. G., Shepherd, D., Gueth, F., Lee, C.-F., Bachiller, R., Rosen, A., & Beuther, H. 2007, *Protostars and Planets V*, eds. B. Reipurth, D. Jewitt, & K. Keil (Tucson: University of Arizona Press), 245
Armitage, P. J., & Clarke C. J. 1996, *M.N.R.A.S.*, **280**, 458
Armitage, P. J., Livio, M., & Pringle, J. E. 2001, *M.N.R.A.S.*, **324**, 705

Arons, J., & Max, C. E. 1975, *Ap.J.Lett.*, **196**, L77
Aspin, C., Barbieri, C., Boschi, F., Di Mille, F., Rampazzi, F., Reipurth, B., & Tsvetkov, M. 2006, *A.J.*, **132**, 1298
Aspin, C., & Reipurth, B. 2003, *A.J.*, **126**, 2936
Artymowicz, P., & Lubow, S. H. 1996a, in *Disks and Outflows around Young Stars*, eds. S. V. W. Beckwith, J. Staude, A. M. Quetz, & A. Natta (Berlin: Springer), p. 115
Artymowicz, P., & Lubow, S. H. 1996b, *Ap.J.*, **467**, L77
Bacciotti, F., Mundt, R., Ray, T. P., Eislöffel, J., Solf, J., & Camezind, M. 2000, *Ap.J.Lett.*, **537**, L49
Bacciotti, F., Ray, T. P., Mundt, R., Eislöffel, J., & Solf, J. 2002, *Ap.J.*, **576**, 222
Bachiller, R. 1996, *Ann. Rev. Astr. Ap.*, **34**, 111
Backman, D. E., & Paresce, F. 1993, in *Protostars and Planets III*, eds. E. H. Levy & J. I. Lunine (Tucson: University of Arizona Press), p. 1253
Bacmann, A., André, P., Puget, J.-L., Abergel, A., Bontemps, S., & Ward-Thompson, D. 2000, *A&Ap.*, **361**, 555
Balbus, S. A., & Hawley, J. F. 1991, *Ap.J.*, **376**, 214
Balbus, S. A., & Hawley, J. F. 1998, *Rev. Mod. Phys.*, **70**, 1
Balbus, S. A., & Papaloizou, J. C. B. 1999, *Ap.J.*, **521**, 650
Ballesteros-Paredes, J. 2006, *M.N.R.A.S.*, **372**, 443
Ballesteros-Paredes, J., Hartmann, L., & Vázquez-Semadeni, E. 1999, *Ap.J.*, **527**, 285
Ballesteros-Paredes, J., & Hartmann, L. 2007, *Revista Mexicana de Astronomia y Astrofisica*, **43**, 123
Ballesteros-Paredes, J., Klessen, R. S., Mac Low, M.-M., & Vazquez-Semadeni, E. 2007, *Protostars and Planets V*, eds. B. Reipurth, D. Jewitt, & K. Keil (Tucson: University of Arizona Press), p. 63
Bally, J., & Devine, D. 1994, *Ap.J.*, **428**, L65
Bally, J., Reipurth, B., & Davis, C. J. 2007, *Protostars and Planets V*, eds. B. Reipurth, D. Jewitt, & K. Keil (Tucson: University of Arizona Press), 215
Bally, J., Sutherland, R. S., Devine, D., & Johnstone, D. 1998, *A.J.*, **116**, 293
Bally, J., Stark, A. A., Wilson, R. W., & Langer, W. D. 1987, *Ap.J.Lett.*, **312**, L45
Baraffe, I., Chabrier, G., Allard, F., & Hauschildt, P. H. 1998, *A&Ap.*, **337**, 403
Basri, G., & Bertout, C. 1989, *Ap.J.*, **341**, 340
Basri, G., Johns-Krull, C. M., & Mathieu, R. D. 1997, *A.J.*, **114**, 781
Basri, G., Marcy, G. W., & Valenti, J. A. 1992, *Ap.J.*, **390**, 622
Bastien, P., & Ménard, F. 1988, *Ap.J.*, **326**, 334
Bastien, P., & Ménard, F. 1990, *Ap.J.*, **364**, 232
Batalha, C. C., Stout-Batalha, N. M., Basri, G., & Terra, M. A. O. 1996, *Ap.J.Supp.*, **103**, 211
Bate, M. R., & Bonnell, I. A. 1997, *M.N.R.A.S.*, **285**, 33
Bate, M. R., Bonnell, I. A., & Bromm, V. 2002, *M.N.R.A.S.*, **332**, L65
Bate, M. R., Bonnell, I. A., & Bromm, V. 2003, *M.N.R.A.S.*, **339**, 577
Beck, R. 2001, *Space Sci. Rev.*, **99**, 243
Beck, T. L., Schaefer, G. H., Simon, M., Prato, L., Stoesz, J. A., & Howell, R. R. 2004, *Ap.J.*, **614**, 235
Beckwith, S. V. W., & Sargent, A. I. 1991, *Ap.J.*, **381**, 250
Beckwith, S. V. W., Sargent, A. I., Chini, R. S., Güsten, R. 1990, *A.J.*, **99**, 924 (BSCG)
Beckwith, S. V. W., Sargent, A. I., Koresko, C. D., & Weintraub, D. A. 1989, *Ap.J.*, **343**, 393
Beichman, C. A., Boulanger, F., & Moshir, M. 1992, *Ap.J.*, **386**, 248
Beichman, C. A., Myers, P. C., Emerson, J. P., Harris, S., Mathieu, R., Benson, P. J., & Jennings, R. E. 1986, *Ap.J.*, **307**, 337
Bell, K. R., & Lin, D. N. C. 1994, *Ap.J.*, **427**, 987
Bell, K. R., Lin, D. N. C., Hartmann, L. W., & Kenyon S. J. 1995, *Ap.J.*, **444**, 376
Benson, P. J., & Myers, P. C. 1989, *Ap.J.Supp.*, **71**, 89
Benz, W., & Jutzi, M. 2007, *IAU Symp.*, **236**, 223
Beristain, G., Edwards, S., & Kwan, J. 2001, *Ap.J.*, 551, 1037
Bergin, E. A., Hartmann, L. W., Raymond, J. C., & Ballesteros-Paredes, J. 2004, *Ap.J.*, **612**, 921
Bergin, E. A., Maret, S., van der Tak, F. F. S., Alves, J., Carmody, S. M., & Lada, C. J. 2006, *Ap.J.*, **645**, 369
Bergin, E. A., Alves, J., Huard, T., & Lada, C. J. 2002, *Ap.J.Lett.*, **570**, L101
Bertout, C. 1989, *Ann. Rev. Astr. Ap.*, **27**, 351
Bertout, C., Basri, G., & Bouvier, J. 1988, *Ap.J.*, **330**, 350
Bieging, J. H., & Cohen, M. 1985, *Ap.J.Lett.*, **289**, L5
Binney, J., & Tremaine, S. 1987, *Galactic Dynamics* (Princeton: Princeton University Press).
Blaes, O. M., & Balbus, S. A. 1994, *Ap.J.*, **421**, 163

Blandford, R. D., & Payne, D. G. 1982, *M.N.R.A.S.*, **199**, 883
Blitz, L. 1991, in *The Physics of Star Formation and Early Stellar Evolution*, eds. C. J. Lada & N. D. Kylafis (Dordrecht:Kluwer). p. 3
Blitz, L., & Shu, F. H. 1980, *Ap.J.*, **238**, 148
Blitz, L., & Spergel, D. N. 1991, *Ap.J.*, **379**, 631
Bodenheimer, P. 1978, *Ap.J.*, **224**, 488
Bogovalov, S., & Tsinganos, K. 1999, *M.N.R.A.S.*, **305**, 211
Böhm, K. H. 1990, in *Structure and Dynamics of the Interstellar Medium*, eds. G. Tenorio-Tagle, M. Moles, & J. Melnick (Berlin: Springer), 282
Bok, B. J., & Reilly, E. F. 1947, *Ap.J.*, **105**, 255
Boland, W., & DeJong, T. 1984, *A&Ap.*, **134**, 87
Boley, A. C., Mejía, A. C., Durisen, R. H., Cai, K., Pickett, M. K., & D'Alessio, P. 2006, *Ap.J.*, **651**, 517
Bonnell, I., & Bastien, P. 1992, *Ap.J.*, **401**, 654
Bonnell, I., & Bate, M. R. 1994, *M.N.R.A.S.*, **271**, 999
Bonnell, I. A., Bate, M. R., & Price, N. M. 1996a, *M.N.R.A.S.*, **279**, 121
Bonnell, I. A., Bate, M. R., Clarke, C. J., & Pringle, J. E. 1996b, *M.N.R.A.S.*, **285**, 201
Bonnell, I. A., Bate, M. R., & Vine, S. G. 2003, *M.N.R.A.S.*, **343**, 413
Bonnell, I. A., Clarke, C. J., Bate, M. R., & Pringle, J. E. 2001, *M.N.R.A.S.*, **324**, 573
Bonnell, I. A., & Davies, M. B. 1998, *M.N.R.A.S.*, **295**, 691
Bonnell, I. A., Larson, R. B., & Zinnecker, H. 2007, *Protostars and Planets V*, eds. B. Reipurth, D. Jewitt, & K. Keil (Tucson: University of Arizona Press), p. 149
Bonnell, I., Martel, H., Bastien, P., Arcoragi J.-P., & Benz, W. 1991, *Ap.J.*, **377**, 553
Bonnell, I. A., Smith, K. W., Meyer, M. R., Tout, C. A., Folha, D. F. M., & Emerson, J. P. 1998, *M.N.R.A.S.*, **299**, 1013
Bonnell, I. A., Vine, S. G., & Bate, M. R. 2004, *M.N.R.A.S.*, **349**, 735
Bonnor, W. B. 1956, *M.N.R.A.S.*, **112**, 195
Boogert, A. C. A., Hogerheijde, M. R., & Blake, G. A. 2002, *Ap.J.*, **568**, 761
Boogert, A. C. A., *et al.* 2004, *Ap.J.Supp.*, **154**, 359
Bontemps, S., André, P., Terebey, S., & Cabrit, S. 1996, *A&Ap.*, **311**, 858
Bontemps, S., *et al.* 2001, *A&Ap.*, **372**, 173
Boss, A. P. 1993, *Ap.J.*, **410**, 157
Boss, A. P. 1995, in *Circumstellar Disks, Outflows, and Star Formation*, eds. S. Lizano, & J. M. Torrelles, *Rev. Mex. Astr. Astrof., Serie de Conferencias*, 1, 165
Boss, A. P. 2002, *Ap.J.*, **568**, 743
Boss, A. P. 2003, *Ap.J.*, **599**, 577
Boss, A. P. 2005, *Ap.J.*, **622**, 393
Boss, A. P., & Black, D. C. 1982, *Ap.J.*, **258**, 270
Boss, A. P., & Yorke, H. W. 1995, *Ap.J.*, **439**, 55L
Boulares, A., & Cox, D. P. 1990, *Ap.J.*, **365**, 544
Bourke, T. L., Myers, P. C., Robinson, G., & Hyland, A. R. 2001, *Ap.J.*, **554**, 916
Bouvier, J., & Bertout, C. 1992, *A&Ap.*, **263**, 113
Bouvier, J., Bertout, C., Benz, W., & Mayor, M. 1986, *A&Ap.*, **165**, 110
Bouvier, J., Cabrit, S., Fernandez, M., Martin, E. L., Matthews, J. M. 1993, *A&Ap.*, **272**, 176
Bouy, H., Brandner, W., Martín, E. L., Delfosse, X., Allard, F., & Basri, G. 2003, *A.J.*, **126**, 1526
Brandenburg, A., Nordlund, A., Stein, R. F., & Torkelsson, U. 1996, *Ap.J.*, **458**, L45
Briceño, C., Hartmann, L., Stauffer, J. R., Gagné, M., Stern, R. A., & Caillault, J.-P. 1997, *A.J.*, **113**, 740
Briceño, C., Hartmann, L., Stauffer, J., & Martín, E. 1998, *A.J.*, **115**, 2074
Briceño, C., Luhman, K. L., Hartmann, L., Stauffer, J. R., & Kirkpatrick, J. D. 2002, *Ap.J.*, **580**, 317
Briceño, C., *et al.* 2004, *Ap.J.Lett.*, **606**, L123
Bryden, G., Chen, X., Lin, D. N. C., Nelson, R. P., & Papaloizou, J. C. B. 1999, *Ap.J.*, **514**, 344
Burgasser, A. J., Kirkpatrick, J. D., Reid, I. N., Brown, M. E., Miskey, C. L., & Gizis, J. E. 2003, *Ap.J.*, **586**, 512
Burkert, A., & Bodenheimer, P. 1993, *M.N.R.A.S.*, **264**, 798
Burkert, A., & Hartmann, L. 2004, *Ap.J.*, **616**, 288
Burns, J. A., Lamy, P. L., & Soter, S. 1979, *Icarus*, **40**, 1
Burrows, C. J., Stapelfeldt, K. R., Watson, A. M., Krist, J. E., Ballester, G. E., Clarke, J. T., Crisp, D., Gallagher, J. S., III., Griffiths, R. E., Hester, J. J., Hoessel, J. G., Holtzman, J. A., Mould, J. R., Scowen, P. A., Trauger, J. T., & Westphal, J. A. 1996, *Ap.J.*, **473**, 437

Butner, H. M., Evans, N. J. II, Lester, D. F., Levreault, R. M., & Strom, S. E. 1991, *Ap.J.*, **376**, 636
Butner, H. M., Lada, E. A., & Loren, R. B. 1995, *Ap.J.*, **448**, 207
Butner, H. M., Natta, A., & Evans, N. J., II. 1994, *Ap.J.*, **420**, 326
Cabot, W., & Pollack, J. B. 1992, *Geophys. Astrophys. Fluid Dyn.*, **64**, 97
Cabrit, S., & Bertout, C. 1992, *A&Ap.*, **261**, 274
Cabrit, S., Guilloteau, S., Andre, P., Bertout, C., Montmerle, T., Schuster, K. 1996, *A&Ap.*, **305**, 527
Calvet, N. 1997, in *Herbig-Haro Flows and the Birth of Low-Mass Stars*, *IAU Symposium 182*, eds. B. Reipurth & C. Bertout, p. 417
Calvet, N. 1998, *Am. Inst. Phys. Conf. Ser.*, **431**, 495
Calvet, N., Basri, G., & Kuhi, L. V. 1983, *Ap.J.*, **268**, 739
Calvet, N., D'Alessio, P., Hartmann, L., Wilner, D., Walsh, A., & Sitko, M. 2002, *Ap.J.*, **568**, 1008
Calvet, N., & Gullbring, E. 1998, *Ap.J.*, **509**, 802
Calvet, N., & Hartmann, L. 1992, *Ap.J.*, **386**, 239
Calvet, N., Hartmann, L., & Kenyon, S. J. 1991, *Ap.J.*, **383**, 752
Calvet, N., Hartmann, L., & Kenyon, S. J. 1993, *Ap.J.*, **402**, 623
Calvet, N., Hartmann, L., Kenyon, S. J., & Whitney, B. A. 1994, *Ap.J.*, **434**, 330
Calvet, N., Hartmann, L., & Strom, S. E. 1997, *Ap.J.*, **481**, 912
Calvet, N., Magris, G. C., Patino, A., & D'Alessio, P. 1992, *Revista Mexicana de Astronomia y Astrofisica*, **24**, 27
Calvet, N., Muzerolle, J., Briceño, C., Hernández, J., Hartmann, L., Saucedo, J. L., & Gordon, K. D. 2004, *A.J.*, **128**, 1294
Calvet, N., Patino, A., Magris, G. C., & D'Alessio, P. 1991, *Ap.J.*, **380**, 617
Calvet, N., *et al.* 2005, *Ap.J.Lett.*, **630**, L185
Camenzind, M. 1990, *Reviews in Modern Astronomy* (Springer-Verlag: Berlin), 3, p. 234
Cameron, A. C., & Campbell, C. G. 1993, *A&Ap.*, **274**, 309
Cantó, J., D'Alessio, P., & Lizano, S. 1995, in *Circumstellar Disks, Outflows, and Star Formation*, eds. S. Lizano, & J. M. Torrelles, *Rev. Mex. Astr. Astrof., Serie de Conferencias*, 1, 217
Carpenter, J. M., Hillenbrand, L. A., & Skrutskie, M. F. 2001, *A.J.*, **121**, 3160
Carpenter, J. M., Hillenbrand, L. A., Skrutskie, M. F., & Meyer, M. R. 2002, *A.J.*, **124**, 1001
Carpenter, J. M., Mamajek, E. E., Hillenbrand, L. A., & Meyer, M. R. 2006, *Ap.J.*, **651**, L49
Carr, J. S., Harvey, P. M., Lester, D. F. 1987, *Ap.J.*, **321**, L71
Carr, J. S., Tokunaga, A. T., Najita, J., Shu, F. H., & Glassgold, A. E. 1993, *Ap.J.*, **411**, L37
Caselli, P., & Myers, P. C. 1995, *Ap.J.*, **446**, 665
Cassen, P., & Moosman, A. 1981, *Icarus*, **48**, 353
Castor, J., McCray, R., & Weaver, R. 1975, *Ap.J.Lett.*, **200**, L107
Cernicharo, J. 1991, in *The Physics of Star Formation and Early Stellar Evolution*, eds. C. J. Lada & N. D. Kylafis (Dordrecht: Kluwer), p. 287
Chabrier, G. 2003, *Pub. Astr. Soc. Pac.*, **115**, 763
Chandler, C. J., & Sargent, A. I. 1993, *Ap.J.*, **414**. L29
Chandrasekhar, S. 1960, *Proc. Nat Acad. Sci.*, **46**, 53
Chandrasekhar, S. 1961, *Hydrodynamic and Magnetohydrodynamic Stability* (Oxford: Oxford University Press)
Chandrasekhar, S. 1967, *An Introduction to the Study of Stellar Structure* (New York: Dover)
Chandrasekhar, S., & Fermi, E. 1953, *Ap.J.*, **118**, 116
Chen, C. H., Jura, M., Gordon, K. D., & Blaylock, M. 2005, *Ap.J.*, **623**, 493
Chernin, L. M., & Masson, C. R. 1995, *Ap.J.*, **443**, 181
Cesaroni, R., Galli, D., Lodato, G., Walmsley, C. M., & Zhang, Q. 2007, *Protostars and Planets V*, eds. B. Reipurth, D. Jewitt, and K. Keil (Tucson: University of Arizona Press), p. 197
Chiang, E. I., & Goldreich, P. 1997, *Ap.J.*, **490**, 368
Chiang, E. I., Joung, M. K., Creech-Eakman, M. J., Qi, C., Kessler, J. E., Blake, G. A., & van Dishoeck, E. F. 2001, *Ap.J.*, **547**, 1077
Choi, M., Evans, N. J., II., Gregerson, E. M., & Wang, Y. 1995, *Ap.J.*, **448**, 742
Churchwell, E., Wood, D. O. S., Felli, M., & Massi, M. 1987, *Ap.J.*, **321**, 516
Ciolek, G. E., & Basu, S. 2000, *Ap.J.*, **529**, 925
Ciolek, G. E., & Basu, S. 2001, *Ap.J.*, **547**, 272
Clarke, C. J., Armitage, P. J., Smith, K. W., & Pringle, J. E. 1995, *M.N.R.A.S.*, **273**, 639
Clarke, C. J., Gendrin, A., & Sotomayor, M. 2001, *M.N.R.A.S.*, 328, 485
Clarke, C. J., Lin, D. N. C., & Papaloizou, J. C. B. 1989, *M.N.R.A.S.*, **236**, 495

Clarke, C. J., Lin, D. N. C., & Pringle, J. E 1990, *M.N.R.A.S.*, **242**, 439
Clarke, C. J., & Pringle, J. E. 1991, *M.N.R.A.S.*, **249**, 588
Clarke, C. J., & Pringle, J. E. 2006, *M.N.R.A.S.*, **370**, L10
Clarke, C. J., & Syer, D. 1996, *M.N.R.A.S.*, **278**, L23
Clemens, D. P., & Barvainis, R. E. 1988, *Ap.J.Supp.*, **68**, 257
Close, L. M., Richer, H. B., & Crabtree, D. R. 1990, *A.J.*, **100**, 1968
Close, L. M., Roddier, F., Northcott, M. J., Roddier, C., & Graves, J. E. 1997, *Ap.J.*, **478**, 766
Close, L. M., Siegler, N., Freed, M., & Biller, B. 2003, *Ap.J.*, **587**, 407
Coffey, D., Bacciotti, F., Ray, T. P., Eislöffel, J., & Woitas, J. 2007, *Ap.J.*, **663**, 350
Cohen, M. 1973a,b,c, *M.N.R.A.S.*, **161**, 85–105
Cohen, M., Bieging, J., & Schwartz, R. D. 1982, *Ap.J.*, **253**, 707
Cohen, M., Emerson, J. P., & Beichman, C. A. 1989, *Ap.J.*, **339**, 455
Cohen, M., & Kuhi, L. V. 1979, *Ap.J.Supp.*, **41**, 743
Cohen, M., & Schwartz, R. D. 1976, *M.N.R.A.S.*, **174**, 137
Cohen, M., & Woolf, N. J. 1971, *Ap.J.*, **169**, 543
Corbelli, E., Palla, F., & Zinnecker, H. eds., 2005, *The Initial Mass Function 50 Years Later* (Springer: Dordrecht)
Covey, K. R., Greene, T. P., Doppmann, G. W., & Lada, C. J. 2005, *A.J.*, **129**, 2765
Covino, E., Alcala, J. M., Allain, S., Bouvier, J., Terranegra, L., & Krautter, J. 1997, *A&Ap.*, **328**, 187
Covino, E., Terranegra, L., Vittone, A. A., Russo, G. 1984, *A.J.*, **89**, 1868
Cram, L. E. 1979, *Ap.J.*, **234**, 949
Cram, L. E., Giampapa, M. S., & Imhoff, C. L. 1980, *Ap.J.*, **238**, 905
Cram, L. E., & Mullan, D. J. 1985, *Ap.J.*, **294**, 626
Crutcher, R. M. 1999, *Ap.J.*, **520**, 706
Crutcher, R. M. 2005, *ASP Conference Series 343*, eds. A. Adamson, C. Aspin, C. J. Davis, & T. Fujiyoshi, p. 111
Crutcher, R. M., Mouschovias, T. Ch., Troland, T. H., & Ciolek, G. E. 1994, *Ap.J.*, **427**, 839
Croswell, K., Hartmann, L., & Avrett, E. H. 1987, *Ap.J.*, **312**, 227
Cunningham, C. 1976, *Ap.J.*, **208**, 534
Cunningham, A., Frank, A., & Hartmann, L. 2005, *Ap.J.*, **631**, 1010
Curry, C. L. 2002, *Ap.J.*, **576**, 849
Curry, C., Pudritz, R. E., & Sutherland, P. G. 1994, *Ap.J.*, **434**, 206
Currie, T., Kenyon, S., Balog, Z., Rieke, G., Bragg, A., & Bromley, B. 2007, *Ap.J.*, **672**, 558
Cuzzi, J. N., Dobrovolskis, A. R., & Champney, J. M. 1993, *Icarus*, **106**, 102
Cuzzi, J. N., Hogan, R. C., Paque, J. M., & Dobrovolskis, A. R. 2001, *Ap.J.*, **546**, 496
Cuzzi, J. N., & Weidenschilling, S. J. 2006, *Meteorites and the Early Solar System II*, 353
Dahm, S. E., & Simon, T. 2005, *A.J.*, **129**, 829
D'Alessio, P. 1996, PhD Thesis, Universidad Nacional Autonoma de Mexico
D'Alessio, P., Calvet, N., & Hartmann, L. 1997, *Ap.J.*, **474**, 397
D'Alessio, P., Calvet, N., & Hartmann, L. 2001, *Ap.J.*, **553**, 321
D'Alessio, P., Calvet, N., Hartmann, L., Franco-Hernández, R., & Servín, H. 2006, *Ap.J.*, **638**, 314
D'Alessio, P., Calvet, N., Hartmann, L., Lizano, S., & Cantó, J. 1999, *Ap.J.*, **527**, 893
D'Alessio, P., *et al.* 2005, *Ap.J.*, **621**, 461
D'Angelo, G., Kley, W., & Henning, T. 2003, *Ap.J.*, **586**, 540
Dame, T. M. 1993, in *Back to the Galaxy*, eds. S. S. Holt & F. Verter, AIP Conference, 278, p. 267
Dame, T. M., Ungerechts, H., Cohen, R. S., DeGeus, E. J., Grenier, I. A., May, J., Murphy, D. C., Nyman, L.-A., & Thaddeus, P. 1987, *Ap.J.*, **322**, 706
Dame, T. M., Hartmann, D., & Thaddeus, P. 2001, *Ap.J.*, **547**, 792
D'Antona, F., & Mazzitelli, I. 1994, *Ap.J.Supp.*, **90**, 467
Daou, A. G., Johns-Krull, C. M., & Valenti, J. A. 2006, *A.J.*, **131**, 520
de Avillez, M. A., & Mac Low, M.-M. 2001, *Ap.J.Lett.*, **551**, L57
de Bruijne, J. H. J. 1999, *M.N.R.A.S.*, **310**, 585
DeCampli, W. M. 1981, *Ap.J.*, **244**, 124
de Geus, E. J., de Zeeuw, P. T., & Lub, J. 1989, *A&A.*, **216**, 44
de Pree, C. G., Rodriguez, L. F., & Goss, W. M. 1995, *Revista Mexicana de Astronomia y Astrofisica*, **31**, 39

Di Francesco, J., Evans, N. J., II, Caselli, P., Myers, P. C., Shirley, Y., Aikawa, Y., & Tafalla, M. 2007, *Protostars and Planets V*, eds. B. Reipurth, D. Jewitt, & K. Keil (Tucson: University of Arizona Press), 17
Di Francesco, J., Myers, P. C., Wilner, D. J., Ohashi, N., & Mardones, D. 2001, *Ap.J.*, **562**, 770
de Geus, E. J. 1992, *A&Ap.*, **262**, 258
DeGeus, E. J., Bronfman, L., & Thaddeus, P. 1990, *A&Ap.*, **231**, 137
Dominik, C., Blum, J., Cuzzi, J. N., & Wurm, G. 2007, *Protostars and Planets V*, eds. B. Reipurth, D. Jewitt, & K. Keil (Tucson: University of Arizona Press), p. 783
Dopita, M. A., Schwartz, R. D., & Evans, I. 1982, *Ap.J.*, **263**, L73
Doppmann, G. W., Greene, T. P., Covey, K. R., & Lada, C. J. 2005, *A.J.*, **130**, 1145
Doty, S. D., Everett, S. E., Shirley, Y. L., Evans, N. J., & Palotti, M. L. 2005, *M.N.R.A.S.*, **359**, 228
Draine, B. T., & Lee, H. M. 1984, *Ap.J.*, **285**, 89
Duchêne, G., Ghez, A. M., McCabe, C., & Ceccarelli, C. 2005, *Ap.J.*, **628**, 832
Dullemond, C. P., & Dominik, C. 2005, *A&Ap.*, **434**, 971
Dullemond, C. P., Dominik, C., & Natta, A. 2001, *Ap.J.*, **560**, 957
Dullemond, C. P., Natta, A., & Testi, L. 2006, *Ap.J.Lett.*, **645**, L69
Duquennoy, A., & Mayor, M. 1991, *A&Ap.*, 248, 485
Dutrey, A., Guilloteau, S., Duvert, G., Prato, L., Simon, M., Schuster, K., & Menard, E. 1996, *A&Ap.*, **309**, 493
Dyck, H. M., Simon, T., & Zuckerman, B. 1982, *Ap.J.Lett.*, **255**, L103
Dyson, J. E. 1987, in *Circumstellar Matter, IAU Symposium 122*, eds. I. Appenzeller & C. Jordan (Dordrecht: Reidel), p. 159
Ebert, R. 1955, *Zs. Ap.*, **37**, 217
Ebert, R., von Hoerner, S., & Temesvary, S. 1960, *Die Enstehung von Sternen durch Kondensation diffuser Materie* (Berlin: Springer-Verlag), p. 184.
Edgar, R. G. 2007, *Ap.J.*, **663**, 1325
Edwards, S. 1995, in *Circumstellar Disks, Outflows, and Star Formation*, eds. S. Lizano, & J. M. Torrelles, *Rev. Mex. Astron. Astrofis., Serie de Conferencias*, 1, p. 309
Edwards, S., Cabrit, S., Strom, S., Heyer, I., Strom, K., & Anderson, E. 1987, *Ap.J.*, **321**, 473
Edwards, S., Fischer, W., Hillenbrand, L., & Kwan, J. 2006, *Ap.J.*, **646**, 319
Edwards, S., Hartigan, P., Ghandour, L., & Andrulis, C. 1994, *A.J.*, **108,** 1056
Edwards, S., Mundt, R., & Ray, T. 1993, in *Protostars and Planets III*, eds. E. H. Levy & J. I. Lunine (Tucson: University of Arizona Press), p. 567
Edwards, S., Strom, S. E., Hartigan, P., Strom, K. M., Hillenbrand, L. A., Herbst, W., Attridge, J., Merrill, K. M., Probst, R., & Gatley, I. 1993, *A.J.*, **106**, 372
Efstathiou, A., & Rowan-Robinson, M. 1991, *M.N.R.A.S.*, **252**, 528
Eggleton, P. P. 1983, *Ap.J.*, **268**, 368
Eisenhauer, F., Quirrenbach, A., Zinnecker, H., & Genzel, R. 1998, *Ap.J.*, **498**, 278
Eisner, J. A., Chiang, E. I., Lane, B. F., & Akeson, R. L. 2007, *Ap.J.*, **657**, 347
Eisner, J. A., Lane, B. F., Akeson, R. L., Hillenbrand, L. A., & Sargent, A. I. 2003, *Ap.J.*, **588**, 360
Eisner, J. A., Lane, B. F., Hillenbrand, L. A., Akeson, R. L., & Sargent, A. I. 2004, *Ap.J.*, **613**, 1049
Eisner, J. A., Hillenbrand, L. A., White, R. J., Akeson, R. L., & Sargent, A. I. 2005, *Ap.J.*, **623**, 952
Elmegreen, B. G. 1991, in *The Physics of Star Formation and Early Stellar Evolution*, eds. C. J. Lada & N. D. Kylafis (Dordrecht:Kluwer), p. 35
Elmegreen, B. G. 1997, *Ap.J.*, **486**, 944
Elmegreen, B. G. 2000, *Ap.J.*, **530**, 277
Elmegreen, B. G. 2007, *Ap.J.*, **668**, 1064
Elmegreen, B. G., & Lada, C. J. 1977, *Ap.J.*, **214**, 725
Elmegreen, B. G., & Scalo, J. 2004, *Ann. Rev. Astr. Ap.*, **42**, 211
Espaillat, C., Calvet, N., D'Alessio, P., Hernández, J., Qi, C., Hartmann, L., Furlan, E., & Watson, D. M. 2007, *Ap.J.Lett.*, **670**, L135
Evans, N. J., II, Balkum, S., Levreault, R. M., Hartmann, L., & Kenyon, S. 1994, *Ap.J.*, **424**, 793
Falgarone, E. 1996, CO: Twenty-Five Years of Millimeter-Wave Spectroscopy, *IAU Symposium 170*, eds. Latter *et al.* (Kluwer), p. 119
Falgarone, E., *et al*. 1998, A&Ap., **331**, 669
Fatuzzo, M., & Adams, F. C. 2002, *Ap.J.*, **570**, 210
Feigelson, E. D., *et al.* 2005, *Ap.J.Supp.*, **160**, 379

Feigelson, E. D., Casanova, S., Montmerle, T., Guibert, J. 1993, *Ap.J.*, **416**, 623
Feigelson, E. D., & DeCampli, W. M. 1981, *Ap.J.*, **243**, L89
Feigelson, E. D., Jackson, J. M., Mathieu, R. D., Myers, P. C., & Walter, F. M. 1987, *A.J.*, **94**, 1251
Feigelson, E. D., & Kriss, G. A. 1981, *Ap.J.*, **248**, L35
Feigelson, E. D., & Kriss, G. A. 1989, *Ap.J.*, **338**, 262
Feigelson, E., Townsley, L., Güdel, M., & Stassun, K. 2007, *Protostars and Planets V*, p. 313
Ferreira, J., & Casse, F. 2004, *Ap.J.Lett.*, **601**, L139
Ferreira, J., & Pelletier, G. 1995, *A&Ap.*, **295**, 807
Fiedler, R. A., & Mouschovias, T. Ch. 1993, *Ap.J.*, **415**, 680
Fischer, W., Edwards, S., Hillenbrand, L., & Kwan, J. 2005, *Protostars and Planets V*, 8075
Flaccomio, E., Damiani, F., Micela, G., Sciortino, S., Harnden, F. R., Jr., Murray, S. S., & Wolk, S. J. 2003, *Ap.J.*, **582**, 398
Flaccomio, E., Micela, G., Sciortino, S., Favata, F., Corbally, C., & Tomaney, A. 1999, *A&Ap.*, **345**, 521
Fleming, T., & Stone, J. M. 2003, *Ap.J.*, **585**, 908
Folha, D. F. M., & Emerson, J. P. 1999, *A&Ap.*, **352**, 517
Folha, D., Emerson, J., & Calvet, N. 1997, *Poster Proceedings of IAU Symposium 182*, eds. F. Malbet & A. Castets (Grenoble: Observatoire de Grenoble)
Font, A. S., McCarthy, I. G., Johnstone, D., & Ballantyne, D. R. 2004, *Ap.J.*, **607**, 890
Foster, P. N., & Chevalier, R. A. 1993, *Ap.J.*, **416**, 303
Franciosini, E., Pallavicini, R., & Sanz-Forcada, J. 2006, *A&Ap.*, **446**, 501
Franco, J., Tenorio-Tagle, G., Bodenheimer, P., Rozyczka, M., & Mirabel, I. F. 1988, *Ap.J.*, **333**, 826
Frank, J., King, A., & Raine, D. 1992, *Accretion Power in Astrophysics*, 2nd edition (Cambridge University Press)
Fricke K. 1969, *A&Ap.*, **1**, 388
Fridlund, C. V. M., & Liseau, R. 1998, *Ap.J.Lett.*, **499**, L75
Fromang, S., Terquem, C., & Balbus, S. A. 2002, *M.N.R.A.S.*, **329**, 18
Fukagawa, M., *et al.* 2004, *Ap.J.Lett.*, **605**, L53
Fukui, Y., Iwata, T., Mizuno, A., Bally, J., & Lane, A. P. 1993, in *Protostars and Planets III*, eds. E. H. Levy & J. I. Lunine (Tucson: University of Arizona Press), p. 603
Fuller, G. A. 1994, in *Clouds, Cores, and Low-Mass Stars*, eds. D. P. Clemens & R. Barvainis, Astronomical Society of the Pacific Conference Series, 65, p. 3
Fuller, G. A., & Myers, P. C. 1992, *Ap.J.*, **384**, 523
Fuller, G. A., & Myers, P. C. 1993, *Ap.J.*, **418**, 273
Furesz, G., Hartmann, L., Megeath, S. T., Szentgyorgyi, A. H., & Hamden, E. T. 2008, *Ap.J.*, **676**, 1109
Furlan, E., *et al.* 2005, *Ap.J.Lett.*, **628**, L65
Furlan, E., *et al.* 2006, *Ap.J.Supp.*, **165**, 568
Furlan, E., McClure, M., Calvet, N., Hartmann, L., D'Alessio, P., Forrest, W. J., Watson, D. M., Uchida, K. I., Sargent, B., Green, J. D., & Herter, T. L. 2008, *Ap.J.Suppl.*, **176**, 184
Gahm, G. F. 1981, *Ap.J.*, **242**, L163
Gahm G. F. 1994, in *Flares and Flashes*, eds. J. Greiner, H. W. Duerbeck, & R. E. Gershberg, IAU Coll. No. 151 (Berlin: Springer), p. 203
Gahm, G. F., Fredga, K., Liseau, R., & Dravins, D. 1979, *A&Ap.*, **73,** L4
Gahm, G. F., Lodén K., Gullbring E., Hartstein D. 1995, *A&Ap.***301**, 89
Galli, D., & Shu, F. H. 1993a,b, *Ap.J.*, 417, **220**, 243
Galli, D., Lizano, S., Shu, F. H., & Allen, A. 2006, *Ap.J.*, **647**, 374
Gammie, C. F. 1996a, *Ap.J.*, **457**, 355
Gammie, C. F. 1996b, *Ap.J.*, **462**, 725
Gammie, C. F. 2001, *Ap.J.*, **553**, 174
Gammie, C. F., & Ostriker, E. C. 1996, *Ap.J.*, **466**, 814
Genzel, R., & Stutzski, J. 1989, *Ann. Rev. Astr. Ap.*, **27**, 41
Ghez, A. M., Neugebauer, G., Gorham, P. W., Haniff, C. A., Kulkarni, S. R., Matthews, K., Koresko, C., & Beckwith, S. 1991, *A.J.*, **102**, 2066
Ghez, A. M., Neugebauer, G., & Matthews, K. 1993, *A.J.*, **106**, 2005
Ghosh, P. 1995, *M.N.R.A.S.*, **272**, 763
Ghosh, P., & Lamb, F. K. 1979, *Ap.J.*, **234**, 296
Giampapa, M. S., Basri, G. S., Johns, C. M., & Imhoff, C. 1993, *Ap.J.Supp.*, **89**, 321
Giampapa, M. S., Calvet, N., Imhoff, C. L., & Kuhi, L. V. 1981, *Ap.J.*, **251**, 113

Gibb, E. L., *et al.* 2000, *Ap.J.*, **536**, 347
Gilmore, G., & Howell, D. eds. 1998, The Stellar Initial Mass Function (38th Herstmonceux Conference), ASP Conference Proceedings, 142
Gizis, J. E., Reid, I. N., Knapp, G. R., Liebert, J., Kirkpatrick, J. D., Koerner, D. W., & Burgasser, A. J. 2003, *A.J.*, **125**, 3302
Glassgold, A. E., Najita, J., & Igea, J. 1997, *Ap.J.*, **480**, 344
Glassgold, A. E., Najita, J., & Igea, J. 2004, *Ap.J.*, **615**, 972
Goldreich, P., & Lynden-Bell, D. 1965, *M.N.R.A.S.*, **130**, 125
Goldsmith, P. F. 1988, in *Molecular Clouds in the Milky Way*, eds. R. L Dickman, R. L. Snell, & J. S. Young, Lecture Notes in Physics (Berlin: Springer), **315**, p. 1
Goldreich, P., & Ward, W. R. 1973, *Ap.J.*, **183**, 1051
Gomez, M., Hartmann, L., Kenyon, S. J., & Hewett, R. 1993, *A.J.*, **105**, 1927
Gómez, M., & Kenyon, S. J. 2001, *A.J.*, **121**, 974
Goodman, A. A., Benson, P. J., Fuller, G. A., Myers, P. C. 1993, *Ap.J.*, **406**, 528
Goodman, A. A., Crutcher, R. M., Heiles, C., Myers, P. C., & Troland, T. H. 1989, *Ap.J.*, **338**, L61
Goodrich, R. W. 1987, *Pub. Astr. Soc. Pac.*, **99**, 116
Goodson, A. P., & Winglee, R. M. 1999, *Ap.J.*, **524**, 159
Gorlova, N., Rieke, G. H., Muzerolle, J., Stauffer, J. R., Siegler, N., Young, E. T., & Stansberry, J. H. 2006, *Ap.J.*, **649**, 1028
Grady, C. A., *et al.* 2005, *Ap.J.*, **630**, 958
Grady, C. A., Woodgate, B., Bruhweiler, F. C., Boggess, A., Plait, P., Lindler, D. J., Clampin, M., & Kalas, P. 1999, *Ap.J.Lett.*, **523**, L151
Graham, J. A., & Frogel, J. A. 1985, *Ap.J.*, **289**, 331
Grasdalen, G. L. 1973, *Ap.J.*, **182**, 781
Grasdalen, G. L., Sloan, G., Stout, M., Strom, S. E., & Welty, A. D. 1989, *Ap.J.Lett.*, **339**, L37
Greaves, J. S., Holland, W. S., Moriarty-Schieven, G., Jenness, T., Dent, W. R. F., Zuckerman, B., McCarthy, C., Webb, R. A., Butner, H. M., Gear, W. K., Walker, H. J. 1998, *Ap.J. Lett.*, **506**, L133
Green, J. D., Hartmann, L., Calvet, N., Watson, D. M., Ibrahimov, M., Furlan, E., Sargent, B., & Forrest, W. J. 2006, *Ap.J.*, **648**, 1099
Greene, T. P., & Meyer, M. R. 1995, *Ap.J.*, **450**, 233
Greene, T. P., Wilking, B. A., Andre, P., Young, E. T., & Lada, C. J. 1994, *Ap.J.*, **434**, 614
Greenhill, L. J., Chandler, C. J., Reid, M. J., & Humphreys, E. M. L. 2005, *Protostars and Planets V*, p. 8614
Gregersen, E. M., Evans, N. J., II., Mardones, D., & Myers, P. C. 2000, *Ap.J.*, **533**, 440
Gregory, S. G., Jardine, M., Simpson, I., & Donati, J.-F. 2006, *M.N.R.A.S.*, **371**, 999
Güdel, M., *et al.* 2007, *A&Ap.*, **468**, 353
Guilloteau, S., Dutrey, A., & Simon, M. 1999, *A&Ap.*, **348**, 570
Gullbring E. 1994, *A&Ap.*, **287**, 131
Gullbring, E., Barwig, H., Chen, P. S., Gahm, G., & Bao, M. X. 1996, *A&Ap.*, **307**, 791
Gullbring, E., Calvet, N., Muzerolle, J., & Hartmann, L. 2000, *Ap.J.*, **544**, 927
Gullbring, E., Hartmann, L., Briceno, C., & Calvet, N. 1998, *Ap.J.*, **492**, 323
Gutermuth, R. A., Megeath, S. T., Muzerolle, J., Allen, L. E., Pipher, J. L., Myers, P. C., & Fazio, G. G. 2004, *Ap.J.Supp.*, **154**, 374
Haas, M., Christou, J. C., Zinnecker, H., Ridgway, S. T., Leinert, Ch. 1993, *A&Ap.*, **269**, 282
Haisch, K. E., Lada, E. A., & Lada, C. J. 2001, *Ap.J.Lett.*, **553**, L153
Hamann, F., & Persson, S. E. 1992, *Ap.J.Supp.*, **82**, 247
Haro, G. 1952, *Ap.J.*, **115**, 572
Haro, G. 1953, *Ap.J.*, **117**, 73
Haro, G., Iriarte, B., & Chavira, E. 1953, *Bol. Obs. Tonantzintla y Tacubaya*, **8**, 3
Hartigan, P., Edwards, S., & Ghandour, L. 1995, *Ap.J.*, **452**, 736
Hartigan, P., Hartmann, L., Kenyon, S. J., Strom, S. E., & Skrutskie, M. F. 1990, *Ap.J.*, **354**, 25L
Hartigan, P., Morse, J. A., & Raymond, J. 1994, *Ap.J.*, **346**, 125
Hartigan, P., Raymond, J., & Hartmann, L. 1987, *Ap.J.*, **316**, 323
Hartigan, P., Strom, S., Edwards, S., Kenyon, S., Hartmann, L., Stauffer, J., & Welty, A. 1991, *Ap.J.*, **382**, 617
Hartmann, L. 2001, *A.J.*, **121**, 1030
Hartmann, L. 2002, *Ap.J.*, **578**, 914
Hartmann, L. 2003, *Ap.J.*, **585**, 398

Hartmann, L., Avrett, E. H., Loeser, R., & Calvet, N. 1990, *Ap.J.*, **349**, 168
Hartmann, L., Ballesteros-Paredes, J., & Bergin, E. A. 2001, *Ap.J.*, **562**, 852
Hartmann, L., & Burkert, A. 2007, *Ap.J.*, **654**, 988
Hartmann, L., Boss, A., Calvet, N., & Whitney, B. 1994a, *Ap.J.Lett.*, **430**, L49
Hartmann, L., & Calvet, N. 1995, *A.J.*, **109**, 1846
Hartmann, L., Calvet, N., Allen, L., Chen, H., & Jayawardhana, R. 1999, *A&J*, **118**, 1784
Hartmann, L., Calvet, N., & Boss, A. 1996, *Ap.J.*, **464**, 387
Hartmann, L., Calvet, N., Gullbring, E., & D'Alessio, P. 1998, *Ap.J.*, **495**, 385
Hartmann, L., Cassen, P., & Kenyon, S. J. 1997, *Ap.J.*, **475**, 770
Hartmann, L., D'Alessio, P., Calvet, N., & Muzerolle, J. 2006, *Ap.J.*, **648**, 484
Hartmann, L., Hewett, R., Stahler, S., & Mathieu, R. D. 1986, *Ap.J.*, **309**, 275
Hartmann, L., Hewett, R., & Calvet, N. 1994b, *Ap.J.*, **426**, 669
Hartmann, L., Hinkle, K., & Calvet, N. 2004, *Ap.J.*, **609**, 906
Hartmann, L., Jones, B. F., Stauffer, J. R., & Kenyon, S. J. 1991, *A.J.*, **101**, 1050
Hartmann, L., & Kenyon, S. J. 1996, *Ann. Rev. Astr. Ap.*, **34**, 207
Hartmann, L., & Kenyon, S. J. 1985, *Ap.J.*, **299**, 462
Hartmann, L., & Kenyon, S. J. 1987a, *Ap.J.*, **312**, 243
Hartmann, L., & Kenyon, S. J. 1987b, *Ap.J.*, **322**, 393
Hartmann, L., Kenyon, S. J., Hewett, R., Edwards, S., Strom, K. M., Strom, S. E., & Stauffer, J. R. 1989, *Ap.J.*, **338**, 1001
Hartmann, L., & MacGregor, K. B. 1982, *Ap.J.*, **259**, 180
Hartmann, L., Soderblom, D. R., & Stauffer, J. R. 1988, *A.J.*, **93**, 907
Hartmann, L., Megeath, S. T., Allen, L., Luhman, K., Calvet, N., D'Alessio, P., Franco-Hernandez, R., & Fazio, G. 2005, *Ap.J.*, **629**, 881
Harvey, D. W. A., Wilner, D. J., Lada, C. J., Myers, P. C., & Alves, J. F. 2003, *Ap.J.*, **598**, 112
Hawley, J. F., Gammie, C. F., & Balbus, S. A. 1995, *Ap.J.*, **440**, 742
Hawley, J. F., Gammie, C. F., & Balbus, S. A. 1996, *Ap.J.*, **464**, 690
Hayashi, C. 1966, *Ann. Rev. Astr. Ap.*, **4**, 171
Hayashi, C., Hoshi, R., & Sugimoto, D. 1962, *Prog. Theor. Phys. Suppl.*, **22**, 1
Hayashi, M., Ohashi, N., & Miyama, S. 1993, *Ap.J.*, **418**, L71
Heiles, C., Goodman, A. A., McKee, C. F., & Zweibel, E. G. 1993, in *Protostars and Planets III*, eds. E. H. Levy & J. I. Lunine (Tucson: University of Arizona Press), p. 279
Heap, S. R., Lindler, D. J., Lanz, T. M., Cornett, R. H., Hubeny, I., Maran, S. P., & Woodgate, B. 2000, *Ap.J.*, **539**, 435
Heiles, C., & Troland, T. H. 2005, *Ap.J.*, **624**, 773
Heitsch, F., Slyz, A. D., Devriendt, J. E. G., Hartmann, L. W., & Burkert, A. 2006, *Ap.J.*, **648**, 1052
Heitsch, F., Burkert, A., Hartmann, L. W., Slyz, A. D., & Devriendt, J. E. G. 2005, *Ap.J.Lett.*, **633**, L113
Heitsch, F., Mac Low, M. M., & Klessen, R. S. 2001, *Ap.J.*, **547**, 280
Heitsch, F., Hartmann, L. W., Slyz, A. D., Devriendt, J. E. G., & Burkert, A. 2008, *Ap.J.*, **674**, 316.
Hennebelle, P., & Audit, E. 2007, *A&Ap.*, 465, 431; 465, 445
Henney, W. J., O'Dell, C. R., Meaburn, J., Garrington, S. T., & Lopez, J. A. 2002, *Ap.J.*, **566**, 315
Henning, T., & Stognienko, R. 1996, *A&Ap.*, **311**, 291
Henriksen, R., André, P., & Bontemps, S. 1997, *A&Ap.*, **323**, 549
Henyey, L. G., LeLevier, R., & Levee, R. D. 1955, *Pub. Astr. Soc. Pac.* , **67**, 154
Herbig, G. H. 1951, *Ap.J.*, **114**, 697
Herbig, G. H. 1952, *J. Roy. Astr. Soc. Canada*, **46**, 222
Herbig, G. H. 1954, *Ap.J.*, **119**, 483
Herbig, G. H. 1958, *Ap.J.*, **128**, 259
Herbig, G. H. 1960, *Ap.J.Supp.*, **4**, 337
Herbig, G. H. 1962, *Adv. Astr. Ap.* , **1**, 47
Herbig, G. H. 1966, *Vistas Astron.*, **8**, 109
Herbig, G. H. 1970, *Mem. Roy. Soc. Scie. Liege, Ser. 5*, **59**, 13
Herbig, G. H. 1977a, *Ap.J.*, **214**, 747
Herbig, G. H. 1977b, *Ap.J.*, **217**, 693
Herbig, G. H. 1989, in *ESO Workshop on Low-Mass Star Formation and Pre-Main Sequence Objects*, ed. B. Reipurth (Garching: ESO), p. 233
Herbig, G. H. 1998, *Ap.J.*, **497**, 736

Herbig, G. H., & Bell, K. R. 1988, *Third Catalog of Emission-Line Stars of the Orion Population*, Lick Observatory Bulletin No. 1111. (HBC)
Herbig, G. H., & Kuhi, L. V. 1963, *Ap.J.*, **137**, 398
Herbig, G. H., Petrov, P. P., & Duemmler, R. 2003, *Ap.J.*, **595**, 384
Herbig, G. H., & Terndrup, D. M. 1986, *Ap.J.*, **307**, 609
Herbig, G. H., Vrba, F. J., & Rydgren, A. E. 1986, *A.J.*, **91**, 575
Herbst, W., Bailer-Jones, C. A. L., Mundt, R., Meisenheimer, K., & Wackermann, R. 2002, *A&Ap.*, **396**, 513
Herbst, W., Herbst, D. K., Grossman, E. J., & Weinstein D. 1994, *A.J.*, **108**, 1906
Herbst, W., & Shevchenko, V. S. 1999, *A.J.*, **118**, 1043
Herczeg, G. J., & Hillenbrand, L. A. 2008, *Ap.J.*, in press
Herczeg, G. J., Linsky, J. L., Walter, F. M., Gahm, G. F., & Johns-Krull, C. M. 2006, *Ap.J.Supp.*, **165**, 256
Hernández, J., Calvet, N., Hartmann, L., Briceño, C., Sicilia-Aguilar, A., & Berlind, P. 2005, *A.J.*, **129**, 856
Hernández, J., Briceño, C., Calvet, N., Hartmann, L., Muzerolle, J., & Quintero, A. 2006, *Ap.J.*, **652**, 472
Hernández, J., *et al.* 2007, *Ap.J.*, **662**, 1067
Heyvaerts, J., & Norman, C. A. 1989, *Ap.J.*, **347**, 1055
Heyvaerts, J., Priest, E. R., & Bardou, A. 1996, *Ap.J.*, **473**, 403
Hildebrand, R. H. 1983, *Quart. J. Roy. Astr. Soc.*, **24**, 267
Hillenbrand, L. 1997, *A.J.*, **113**, 1733
Hillenbrand, L. A., Bauermeister, A., & White, R. J. 2007, to appear in *Cool Stars 14*, ed. G. van Belle, 2007, ASP Conference Series
Hillenbrand, L. A., & Hartmann, L. W. 1998, *Ap.J.*, **492**, 540
Hillenbrand, L. A., Strom, S. E., Vrba, F. J., & Keene, J. 1992, *Ap.J.*, **397**, 613
Hillenbrand, L. A., & White, R. J. 2004, *Ap.J.*, **604**, 741
Hogerheijde, M. R., van Dishoeck, E. F., Blake, G. A., & van Langevelde, H. J. 1997, *Ap.J.*, **489**, 293
Hogerheijde, M. R., van Langevelde, H. J., Mundy, L. G., Blake, G. A., & van Dishoeck, E. F. 1997, *Ap.J.Lett.*, **490**, L99
Holland, W. S., *et al.* 2003, *Ap.J.*, **582**, 1141
Holland, W. S., Greaves, J. S., Dent, W. R. F., Wyatt, M. C., Zuckerman, B., Webb, R. A., McCarthy, C., Coulson, I. M., Robson, E. I., Gear, W. K. 2003, *Ap.J.*, **582**, 1141
Hollenbach, D. 1985, *Icarus*, **61**, 36
Hollenbach, D., Johnstone, D., Lizano, S., & Shu, F. 1994, *Ap.J.*, **428**, 654
Hollenbach, D., & Natta, A. 1995, *Ap.J.*, **455**, 133
Hollenbach, D. J., Yorke, H. W., & Johnstone, D. 2000, in *Protostars and Planets IV*, eds. V. Mannings, A. P. Boss, & S. Russell (Tucson: University of Arizona Press), p. 401
Hoyle, F. 1953, *Ap.J.*, **118**, 513
Hubeny, I. 1990, *Ap.J.*, **351**, 632
Hubickyj, O., Bodenheimer, P., & Lissauer, J. J. 2005, *Icarus*, **179**, 415
Huenemoerder, D. P., Lawson, W. A., & Feigelson, E. D. 1994, *M.N.R.A.S.*, **271**, 967
Hunter, C. 1963, *M.N.R.A.S.*, **126**, 299
Hunter, C. 1977, *Ap.J.*, **218**, 834
Ida, S., & Lin, D. N. C. 2004, *Ap.J.*, **604**, 388
Igea, J., & Glassgold, A. E. 1999, *Ap.J.*, **518**, 848
Imhoff, C. L., & Giampapa, M. S. 1980, *Ap.J.*, **239**, L115
Isella, A., & Natta, A. 2005, *A&Ap.*, **438**, 899
Jackson, J. D. 1962, *Classical Electrodynamics* (New York: Wiley)
Jappsen, A.-K., Klessen, R. S., Larson, R. B., Li, Y., & Mac Low, M.-M. 2005, *A&Ap.*, **435**, 611
Jayawardhana, R., Fisher, S., Hartmann, L., Telesco, C., Pina, R., & Fazio, G. 1998, *Ap.J.Lett.*, **503**, L79
Jeffries, R. D., Maxted, P. F. L., Oliveira, J. M., & Naylor, T. 2006, *M.N.R.A.S.*, **371**, L6
Jeffries, R. D., Oliveira, J. M., Naylor, T., Mayne, N. J., & Littlefair, S. P. 2007, *M.N.R.A.S.*, **376**, 580
Jensen, E. L. N., Mathieu, R. D., & Fuller, G. A. 1994, *Ap.J.*, **429**, L29
Jensen, E. L. N., Mathieu, R. D., & Fuller, G. A. 1996, *Ap.J.*, **458,** 312
Jijina, J. & Adams, F. C. 1996, *Ap.J.*, **462**, 874
Johns, C. M., & Basri, G. 1995a, *A.J.*, **109,** 2800
Johns, C. M., & Basri, G. 1995b, *Ap.J.*, **449,** 341
Johns-Krull, C. M. 2007, *Ap.J.*, **664**, 975
Johns-Krull, C. M., & Basri, G. 1997, *Ap.J.*, **474,** 433
Johns-Krull, C. M., Valenti, J. A., Hatzes, A. P., & Kanaan, A. 1999a, *Ap.J.Lett.*, **510**, L41

Johns-Krull, C. M., Valenti, J. A., & Koresko, C. 1999b, *Ap.J.*, **516**, 900
Johnson, B. M., & Gammie, C. F. 2003, *Ap.J.*, **597**, 131
Johnstone, D., Hollenbach, D., & Bally, J. 1998, *Ap.J.*, **499**, 758
Johnstone, D., Wilson, C. D., Moriarty-Schieven, G., Joncas, G., Smith, G., Gregersen, E., & Fich, M. 2000, *Ap.J.*, **545**, 327
Jones, C. E., & Basu, S. 2002, *Ap.J.*, **569**, 280
Jones, C. E., Basu, S., & Dubinski, J. 2001, *Ap.J.*, **551**, 387
Jones, B. F., & Herbig, G. H. 1979, *A.J.*, **84,** 1872
Jones, B. F. & Walker, M. F. 1988, *A.J.*, **95,** 1755
Jørgensen, J. K., *et al.* 2006, *Ap.J.*, **645**, 1246
Joy, A. H. 1945, *Ap.J.*, **102,** 168
Julian, W. H., & Toomre, A. 1966, *Ap.J.*, **146,** 810
Kahn, F. D. 1974, *A&Ap.*, **37**, 149
Kawazoe, E., & Mineshige, S. 1993, *Pub. Astr. Soc. Japan*, **45**, 715
Keene, J., & Masson, C. R. 1990, *Ap.J.*, **335**, 635
Kenyon, S. J., & Bromley, B. C. 2005, *A.J.*, **130**, 269
Kenyon, S. J., Calvet, N., & Hartmann, L. 1993, *Ap.J.*, **414**, 676 (KCH)
Kenyon, S. J., Gomez, M., Marzke, R. O., & Hartmann, L. 1994, *A.J.*, **108**, 251
Kenyon, S. J., Hartmann, L., Strom, K. M, & Strom, S. E. 1990, *A.J.*, **99**, 869
Kenyon, S. J., & Hartmann, L. 1987, *Ap.J.*, **323**, 714
Kenyon, S. J., & Hartmann, L. 1990, *Ap.J.*, **349**, 197
Kenyon, S. J., & Hartmann, L. 1991, *Ap.J.*, **383**, 664
Kenyon, S. J., & Hartmann, L. 1995, *Ap.J.Supp.*, **101**, 117
Kenyon, S. J., Hartmann, L., Gomez, M., Carr, J. S., & Tokunaga, A. 1993, *A.J.*, **105**, 1505
Kenyon, S. J., Hartmann, L., & Hewett, R. 1988, *Ap.J.*, **325**, 231
Kenyon, S. J., Hartmann, L., Imhoff, C. L., & Cassatella, A. 1989, *Ap.J.*, **344**, 925
Kenyon, S. J., Hartmann, L., & Kolotilov, E. A. 1991, *Pub. Astr. Soc. Pac.*, **103**, 1069
Kenyon, S. J., Yi, I., & Hartmann, L. 1996, *Ap.J.*, **462**, 439
Kepner, J., Hartigan, P., Yang, C., & Strom, S. 1993, *Ap.J.*, **415**, L119
Keto, E. 2003, *Ap.J.*, **599**, 1196
Kim, S. S., Figer, D. F., Kudritzki, R. P., & Najarro, F. 2006, *Ap.J.Lett.*, **653**, L113
King, A. R., Pringle, J. E., & Livio, M. 2007, *M.N.R.A.S.*, **376**, 1740
Kirk, J. M., Ward-Thompson, D., & André, P. 2005, *M.N.R.A.S.*, **360**, 1506
Klahr, H., & Bodenheimer, P. 2006, *Ap.J.*, **639**, 432
Klein, R., Apai, D., Pascucci, I., Henning, T., & Waters, L. B. F. M. 2003, *Ap.J.Lett.*, **593**, L57
Klein, R. I., Fisher, R., & McKee, C. F. 2004, *Revista Mexicana de Astronomia y Astrofisica Conference Series*, **22**, 3
Klessen, R. S. 2001, *Ap.J.*, **556**, 837
Klessen, R. S., & Burkert, A. 2001, *Ap.J.*, **549**, 386
Klessen, R. S., & Burkert, A. 2000, *Ap.J.Supp.*, **128**, 287
Klessen, R. S., Heitsch, F., & Mac Low, M. M. 2000, *Ap.J.*, **535**, 887
Konopacky, Q. M., Ghez, A. M., Rice, E. L., & Duchêne, G. 2007, *Ap.J.*, **663**, 394
Kolotilov, E. A., & Petrov, P. P. 1983, *Pis'ma Astr. Zh.*, **9**, 171
Kolotilov, E. A., & Petrov, P. P. 1985, *Pis'ma Astr. Zh.*, **11**, 846
Königl, A. 1989, *Ap.J.*, **342**, 208
Königl, A. 1991, *Ap.J.Lett.*, **370**, L39
Königl, A., & Ruden, S. P. 1993, in *Protostars and Planets III*, eds. E. H. Levy & J. I. Lunine (Tucson: University of Arizona Press), p. 641
Köhler, R., Petr-Gotzens, M. G., McCaughrean, M. J., Bouvier, J., Duchêne, G., Quirrenbach, A., & Zinnecker, H. 2006, *A&Ap.*, **458**, 461
Koerner, D. W., Chandler, C. J., & Sargent, A. I. 1995, *Ap.J.*, **452**, L69
Koerner, D. W., Ressler, M. E., Werner, M. W., & Backman, D. E. 1998, *Ap.J.Lett.*, **503**, L83
Koerner, D. W., & Sargent, A. I. 1995, *A.J.*, **109**, 2138
Koerner, D. W., Sargent, A. I., & Beckwith, S. V. W. 1993, *Icarus*, **106**, 2
Koresko, C. D. 2000, *Ap.J.Lett.*, **531**, L147
Koresko, C. D., Beckwith, S. V. W., Ghez, A. M., Matthews, K., & Neugebauer, G. 1991, *A.J.*, **102**, 2073
Krasnopolsky, R., Li, Z.-Y., & Blandford, R. 1999, *Ap.J.*, **526**, 631

Krasnopolsky, R., Li, Z.-Y., & Blandford, R. D. 2003, *Ap. Space Sci.*, **287**, 75
Kraus, A. L., White, R. J., & Hillenbrand, L. A. 2005, *Ap.J.*, **633**, 452
Krist, J. E., *et al.* 1999, *Ap.J.Lett.*, **515**, L35
Krist, J. E., Stapelfeldt, K. R., Ménard, F., Padgett, D. L., & Burrows, C. J. 2000, *Ap.J.*, **538**, 793
Krist, J. E., *et al.* 2005, *A.J.*, **130**, 2778
Kroupa, P. 2000, *New Astron.*, **4**, 615
Kroupa, P. 2002, *Science*, **295**, 82
Kroupa, P., Tout, C. A., & Gilmore, G. 1990, *M.N.R.A.S.*, **244**, 76
Kroupa, P., Tout, C. A., & Gilmore, G. 1993, *M.N.R.A.S.*, **262**, 545
Kuan, P. 1975, *Ap.J.*, **202**, 425
Kudoh, T., Matsumoto, R., & Shibata, K. 2003, *Ap. Space Sci.*, **287**, 99
Kuhi, L. V. 1964, *Ap.J.*, **140**, 1409
Kuiper, T. B. H., Rodriguez-Kuiper, E. N., & Zuckerman, B. 1978, *Ap.J.*, **219**, 129
Kurtz, S., Cesaroni, R., Churchwell, E., Hofner, P., & Walmsley, C. M. 2000, *Protostars and Planets IV*, p. 299
Kwan, J., & Tademaru, E. 1995, *Ap.J.*, **454**, 382
Lada, C. J. 1985, *Ann. Rev. Astr. Ap.*, **23**, 267
Lada, C. J. 1987, in *Star Forming Regions*, *IAU Symposium 115*, eds. M. Peimbert & J. Jugaku (Dordrecht: Reidel), p. 1
Lada, C. J., & Lada, E. A. 2003, *Ann. Rev. Astr. Ap.*, **41**, 57
Lada, C. J., & Wilking, B. A. 1984, *Ap.J.*, **287**, 610
Lada, E. A., Evans, N. J., II., Depoy, D. L., Gatley, I. 1991, *Ap.J.*, **371**, 171
Lada, C. J., *et al.* 2006, *A.J.*, **131**, 1574
Ladd, E. F., Adams, F. C., Casey, S., Davidson, J. A., Fuller, G. A., Harper, D. A., Myers, P. C., & Padman, R. 1991, *Ap.J.*, **382**, 555
Ladd, E. F., Fuller, G. A., Padman, R., Myers, P. C., & Adams, F. C. 1995, *Ap.J.*, **439**, 771
Lago, M. T. V. T. 1984, *M.N.R.A.S.*, **210**, 323
Lamm, M. H., Bailer-Jones, C. A. L., Mundt, R., Herbst, W., & Scholz, A. 2004, *A&Ap.*, **417**, 557
Lamm, M. H., Mundt, R., Bailer-Jones, C. A. L., & Herbst, W. 2005, *A&Ap.*, **430**, 1005
Larson, R. B. 1969a,b, *M.N.R.A.S.*, **145**; 271, 297
Larson, R. B. 1972, *M.N.R.A.S.*, **157**, 121
Larson, R. B. 1980, *Rev. Mex. Astron. Astrof.*, **7**, 219
Larson, R. B. 1981, *M.N.R.A.S.*, **194**, 809
Larson, R. B. 1983, *M.N.R.A.S.*, **190**, 321
Larson, R. B. 1984, *M.N.R.A.S.*, **206**, 197
Larson, R. B. 1985, *M.N.R.A.S.*, **214**, 379
Larson, R. B. 1992, *M.N.R.A.S.*, **256**, 641
Larson, R. B. 2005, *M.N.R.A.S.*, **359**, 211
Larson, R. B. & Starrfield, S. 1971, *A&Ap.*, **13**, 190.
Laughlin, G., & Bodenheimer, P. 1994, *Ap.J.*, **436**, 335
Laughlin, G., Korchagin, V., & Adams, F. C. 1998, *Ap.J.*, **504**, 945
Lauretta, D. S., & McSween Jr., H. Y. eds. 2006, *Meteorites and the Early Solar System II* (Tucson: University of Arizona Press)
Lay, O. P., Carlstrom, J. E., Hills, R. E., & Phillips, T. G. 1994, *Ap.J.*, **434**, L75
Lee, C. W., & Myers, P. C. 1999, *Ap.J. Supp.*, **123**, 233
Leinert, C. H., Zinnecker, H., Weitzel, N., Christou, J., Ridgeway, S. T., Jameson, R., Haas, M., & Lenzen, R. 1993, *A&Ap.*, **278**, 129
Leitherer, C., Robert, C., & Drissen, L. 1992, *Ap.J.*, **401**, 596
Li, Z.-Y. 1995, *Ap.J.*, **444**, 848
Li, Z. Y., & McKee, C. F. 1996, *Ap.J.*, **464**, 373
Li, Z. Y., & Shu, F. H. 1996, *Ap.J.*, **468**, 261
Lim, J., & Takakuwa, S. 2006, *Ap.J.*, **653**, 425
Lin, D. N. C., & Papaloizou, J. C. B. 1980, *M.N.R.A.S.*, **191**, 37
Lin, D. N. C., & Papaloizou, J. C. B. 1985, in *Protostars and Planets II*, eds. D. C. Black & M. C. Matthews (Tucson: University of Arizona Press), p. 981
Lin, D. N. C., & Papaloizou, J. 1986a, *Ap.J.*, **307**, 395
Lin, D. N. C., & Papaloizou, J. 1986b, *Ap.J.*, **309**, 846

Lin D. N. C., & Pringle J. E. 1990, *Ap.J.*, **358**, 515
Lissauer, J. J., & Stevenson, D. J. 2007, in *Protostars and Planets V*, eds. B. Reipurth, D. Jewitt, & K. Keil (Tucson: University of Arizona Press), p. 591
Livio, M. 1995, in *Cataclysmic Variables*, eds. A. Bianchini *et al.* (Dordrecht: Kluwer), p. 349
Lizano, S., & Shu, F. H. 1989, *Ap.J.*, **342**, 834
Lizano, S., & Torrelles, J. M. eds. 1995, *Circumstellar Disks, Outflows, and Star Formation, Rev. Mex. Astr. Astrof., Serie de Conferencias*, 1
Lodato, G., & Clarke, C. J. 2004, *M.N.R.A.S.*, **353**, 841
Lodato, G., & Rice, W. K. M. 2005, *M.N.R.A.S.*, **358**, 1489
Long, M., Romanova, M. M., & Lovelace, R. V. E. 2005, *Ap.J.*, **634**, 1214
Long, M., Romanova, M. M., & Lovelace, R. V. E. 2007, *M.N.R.A.S.*, **374**, 436
Looney, L. W., Mundy, L. G., & Welch, W. J. 1997, *Ap.J.Lett.*, **484**, L157
López-Corredoira, M., Cabrera-Lavers, A., Mahoney, T. J., Hammersley, P. L., Garzón, F., & González-Fernández, C. 2007, *A.J.*, **133**, 154
Loren, R. B., Wooten, A., & Wilking, B. A. 1990, *Ap.J.*, **365**, 269
Lovelace, R. V. E., Romanova, M. M., & Bisnovatyi-Kogan, G. S. 1995, *M.N.R.A.S.*, **275**, 244
Lovelace, R. V. E., Romanova, M. M., & Contoupoulos, J. 1993, *Ap.J.*, **403**, 158
Lovelace, R. V. E., Wang, J. C. L., & Sulkanen, M. E. 1987, *Ap.J.*, **315**, 504
Lubow, S., Papaloizou, J. C. B., & Pringle, J. E. 1994, *M.N.R.A.S.*, **268**, 1010
Luhman, K. L. 2000, *Ap.J.*, **544**, 1044
Luhman, K. L. 2001, *Ap.J.*, **560**, 287
Luhman, K. L. 2003a, *IAU Symp.*, **211**, 103
Luhman, K. L., Stauffer, J. R., Muench, A. A., Rieke, G. H., Lada, E. A., Bouvier, J., & Lada, C. J. 2003b, *Ap.J.*, **593**, 1093
Luhman, K. L. 2004, *Ap.J.*, **617**, 1216
Luhman, K. L. 2007, *Ap.J.S*, **173**, 104
Lynden-Bell, D., & Pringle, J. E. 1974, *M.N.R.A.S.*, **168**, 603
Mac Low, M.-M., & Klessen, R. S. 2004, *Rev. Mod. Phys.*, **76**, 125
Malbet, F., & Bertout, C. 1991, *Ap.J.*, **383**, 814
Malbet, F., Rigaut, F., Bertout, C., & Léna, P. 1993, *A&Ap.*, **271**, L9
Malbet, F., *et al.* 2005, *A&Ap.*, **437**, 627
Mamajek, E. E., Lawson, W. A., & Feigelson, E. D. 1999, *Ap.J.*, **516**, L77
Mannings, V., & Emerson, J. P. 1994, *M.N.R.A.S.*, **267**, 361
Mannings, V., & Sargent, A. I. 1997, *Ap.J.*, **490**, 792
Mardones, D., Myers, P. C., Tafalla, M., Wilner, D. J., Bachiller, R., & Garay, G. 1997, *Ap.J.*, **504**, 900
Marschall, L. A., Karshner, G. B., & Comins, N. F. 1990, *A.J.*, **99**, 1536
Masson, C. R., & Chernin, L. M. 1993, *Ap.J.*, **414**, 230
Mathieu, R. D. 1994, *Ann. Rev. Astr. Ap.*, **32**, 465
Mathieu, R. D., Baraffe, I., Simon, M., Stassun, K. G., & White, R. 2007, *Protostars and Planets V*, 411
Mathieu, R. D., Ghez, A. M., Jensen, E. L. N., & Simon, M. 2000, *Protostars and Planets IV*, 703
Mathieu, R. D., Stassun, K., Basri, G., Jensen, E. L. N., Johns-Krull, C. M., Valenti, J. A., & Hartmann, L. W. 1997, *A.J.*, **113**, 1841
Mathis, J. 1990, *Ann. Rev. Astr. Ap.*, **28**, 37
Matsumura, S., Pudritz, R. E., & Thommes, E. W. 2007, *Ap.J.*, **660**, 1609
Matsuyama, I., Johnstone, D., & Hartmann, L. 2003, *Ap.J.*, **582**, 893
Matsuyama, I., Johnstone, D., & Murray, N. 2003, *Ap.J.Lett.*, **585**, L143
Matt, S., Goodson, A. P., Winglee, R. M., & Böhm, K.-H. 2002, *Ap.J.*, **574**, 232
Matt, S., & Pudritz, R. E. 2004, *Ap.J.Lett.*, **607**, L43
Matt, S., & Pudritz, R. E. 2005, *Ap.J.Lett.*, **632**, L135
Matzner, C. D., & McKee, C. F. 1999, *Ap.J.Lett.*, **526**, L109
Mayne, N. J., Naylor, T., Littlefair, S. P., Saunders, E. S., & Jeffries, R. D. 2007, *M.N.R.A.S.*, **375**, 1220
Mazzitelli, I. 1989, in *ESO Workshop on Low-Mass Star Formation and Pre-Main Sequence Objects*, ed. B. Reipurth (ESO:Garching), p. 433
McCabe, C., Duchêne, G., & Ghez, A. M. 2002, *Ap.J.*, **575**, 974
McCabe, C., Ghez, A. M., Prato, L., Duchêne, G., Fisher, R. S., & Telesco, C. 2006, *Ap.J.*, **636**, 932
McCaughrean, M. J. & Stauffer, J. 1994, *A.J.*, **108**, 1382
McCaughrean, M. J., & O'Dell, C. R. 1996, *A.J.*, **111**, 1977

McCullough, P. R., Fugate, R. Q., Christou, J. C., Ellerbroek, B. L., Higgins, C. H., Spinhirne, J. M., Cleis, R. A., & Moroney, J. F. 1995, *Ap.J.*, **438**, 394
McKee, C. F. 1989, *Ap.J.*, **345**, 782
McKee, C. F., & Ostriker, E. C. 2007, *Ann. Rev. Astr. Ap.*, **45**, 565
McKee, C. F., Zweibel, E. G., Goodman, A. A., & Heiles, C. 1993, in *Protostars and Planets III*, eds. E. H. Levy & J. I. Lunine (Tucson: University of Arizona Press), p. 327
Megeath, S. T., Hartmann, L., Luhman, K. L., & Fazio, G. G. 2005, *Ap.J.Lett.*, **634**, L113
Megeath, S. T., Thaddeus, P., & Hartmann, D. 2001, Personal communication.
Megeath *et al.* 2008, in preparation
Meibom, S., Mathieu, R. D., & Stassun, K. G. 2006, *Ap.J.*, **653**, 621
Mendoza, E. E. 1966, *Ap.J.*, **143**, 1010
Mestel, L. 1961, *M.N.R.A.S.*, **122**, 473
Mestel, L. 1963, *M.N.R.A.S.*, **126**, 553
Mestel, L. 1965, *Quart. J. Roy. Astr. Soc.* , **6**, 161
Mestel, L. 1968, *M.N.R.A.S.*, **138**, 359
Mestel, L. 1985, in *Protostars and Planets II*, eds. D. C. Black & M. S. Mathews (Tucson: University of Arizona Press), p. 81
Mestel, L., & Spitzer, L., Jr 1956, *M.N.R.A.S.*, **116**, 503
Meyer, M. R., *et al.* 2006, *P.A.S.P.*, **118**, 1690
Mihalas, D. 1978, *Stellar Atmospheres* (San Francisco: Freeman)
Millan-Gabet, R., Schloerb, F. P., Traub, W. A., Malbet, F., Berger, J. P., & Bregman, J. D. 1999, *Ap.J.Lett.*, **513**, L131
Millan-Gabet, R., Schloerb, F. P., & Traub, W. A. 2001, *Ap.J.*, **546**, 358
Millan-Gabet, R., *et al.* 2006, *Ap.J.*, **641**, 547
Millan-Gabet, R., Malbet, F., Akeson, R., Leinert, C., Monnier, J., & Waters, R. 2007, *Protostars and Planets V*, p. 539
Miller, G. E. & Scalo, J. M. 1979, *Ap.J.Supp.*, **41**, 513
Miller, K. A., & Stone, J. M. 2000, *Ap.J.*, **534**, 398
Miyake, K., & Nakagawa, Y. 1993, *Icarus*, **106**, 20
Mizuno, A., Onishi, T., Yonekura, Y., Nagahama, T., Ogawa, H., & Fukui, Y. 1995, *Ap.J.*, **445**, L161
Momose, M., Ohashi, N., Kawabe, R., Nakano, T., & Hayashi, M. 1998, *Ap.J.*, **504**, 314
Monnier, J. D., & Millan-Gabet, R. 2002, *Ap.J.*, **579**, 694
Monnier, J. D., *et al.* 2005, *Ap.J.*, **624**, 832
Montmerle, T., Feigelson, E. D., Bouvier, J., & André, P. 1993, in *Protostars and Planets III*, eds. E. H. Levy & J. I. Lunine (Tucson: University of Arizona Press), p. 689
Montmerle, T., Koch-Miramond, L., Falgarone, E., Grindlay, J. E. 1983, *Ap.J.*, **269**, 182
Moriarty-Schieven, G. H., Johnstone, D., Bally, J., & Jenness, T. 2006, *Ap.J.*, **645**, 357
Motte, F., Andre, P., & Neri, R. 1998, *A&Ap.*, **336**, 150
Moitinho, A., Alves, J., Huélamo, N., & Lada, C. J. 2001, *Ap.J.Lett.*, **563**, L73
Mould, J. R., Hall, D. N. B., Ridgway, S. T., Hintzen, P., Aaronson, M. 1978, *Ap.J.*, **222**, L123
Mouschovias, T. Ch. 1976, *Ap.J.*, **206**, 753
Mouschovias, T. Ch. 1991, in *The Physics of Star Formation and Early Stellar Evolution*, eds. C. J. Lada & N. D. Kylafis (Dordrecht: Kluwer) pp. 61, 449
Mouschovias, T. Ch., & Spitzer, L. 1976, *Ap.J.*, **210**, 326
Muench, A. A., Lada, E. A., Lada, C. J., & Alves, J. 2002, *Ap.J.*, **573**, 366
Mundt, R. 1984, *Ap.J.*, **280**, 749
Mundt, R. 1985, in *Protostars & Planets II*, eds. D. C. Black & M. S. Mathews (Tucson: University of Arizona Press), p. 414
Mundt, R., Brugel, E. W., & Bührke, T. 1987, *Ap.J.*, **319,** 275
Mundt, R., & Fried, J. W. 1983, *Ap.J.*, **274**, L83
Mundt, R., Ray, T. P., Bührke, T., Raga, A. C., & Solf, J. 1990, *A&Ap.*, **232**, 37
Mundt, R., Stocke, J., Strom, S. E., Strom, K. M., & Anderson, E. R. 1985, *Ap.J.Lett.*, **297**, L41
Mundt, R., Walter, F. M., Feigelson, E. D., Finkenzeller, U., Herbig, G. H., & O'Dell, A. P. 1983, *Ap.J.*, **269**, 229
Mundy, L. G., Looney, L. W., Erikson, W., Grossman, A., Welch, W. J., Forster, J. R., Wright, M. C. H., Plambeck, R. L., Lugten, J., & Thornton, D. D. 1996, *Ap.J.*, **464,** L169
Muzerolle, J., Calvet, N., & Hartmann, L. 1998a, *Ap.J.*, **492**, 743

Muzerolle, J., Hartmann, L., & Calvet, N. 1998b, *A.J.*, **116**, 455
Muzerolle, J., Hartmann, L., & Calvet, N. 1998c, *A.J.*, **116**, 2965
Muzerolle, J., Calvet, N., & Hartmann, L. 2001, *Ap.J.*, **550**, 944
Muzerolle, J., Hillenbrand, L., Calvet, N., Briceño, C., & Hartmann, L. 2003a, *Ap.J.*, **592**, 266
Muzerolle, J., Calvet, N., Hartmann, L., & D'Alessio, P. 2003b, *Ap.J.Lett.*, **597**, L149
Muzerolle, J., D'Alessio, P., Calvet, N., & Hartmann, L. 2004, *Ap.J.*, **617**, 406
Muzerolle, J., Luhman, K. L., Briceño, C., Hartmann, L., & Calvet, N. 2005, *Ap.J.*, **625**, 906
Myers, P. C. 1983, *Ap.J.*, **270**, 105
Myers, P., & Benson, P. J. 1983, *Ap.J.*, **266**, 309
Myers, P. C., Fuller, G. A., Goodman, A. A., & Benson, P. J. 1991, *Ap.J.*, **376**, 561
Myers, P. C., & Fuller, G. A. 1992, *Ap.J.*, **396**, 631
Myers, P. C., Fuller, G. A., Mathieu, R. D., Beichman, C. A., Benson, P. J., Schild, R. E., & Emerson, J. P. 1987, *Ap.J.*, **319**, 340
Myers, P. C., & Goodman, A. A. 1988a, *Ap.J.Lett.*, **326**, L27
Myers, P. C., & Goodman, A. A. 1988b, *Ap.J.*, **329**, 392
Myers, P. C., Goodman, A. A., Heiles, C., & Güsten, R. 1995, *Ap.J.*, **442**, 177
Myers, P. C., & Khersonsky, V. K. 1995, *Ap.J.*, **442**, 186
Myers, P. C., Mardones, D., Tafalla, M., Williams, J. P., & Wilner, D. J. 1995, *Ap.J.*, **449**, L65
Najita, J. R., Strom, S. E., & Muzerolle, J. 2007, *M.N.R.A.S.*, **378**, 369
Natta, A. 1993, *Ap.J.*, **412**, 761
Najita, J., Carr, J. S., Glassgold, A. E., Shu, F. H., & Tokunaga, A. T. 1996, *Ap.J.*, **462**, 919
Najita, J., Carr, J. S., & Mathieu, R. D. 2003, *Ap.J.*, **589**, 931
Najita, J., Carr, J. S., & Tokunaga, A. T. 1996, *Ap.J.*, **456**, 292
Natta, A., Prusti, T., Neri, R., Thi, W. F., Grinin, V. P., & Mannings, V. 1999, *A&Ap.*, **350**, 541
Natta, A., Prusti, T., Neri, R., Wooden, D., Grinin, V. P., & Mannings, V. 2001, *A&Ap.*, **371**, 186
Natta, A., Testi, L., Muzerolle, J., Randich, S., Comerón, F., & Persi, P. 2004, *A&Ap.*, **424**,
Natta, A., Testi, L., Neri, R., Shepherd, D. S., & Wilner, D. J. 2004, *A&Ap.*, **416**, 179, 603
Najita, J., & Shu, F. H. 1994, *Ap.J.*, **429**, 808
Nakamura, F., Hanawa, T., & Nakano, T. 1995, *Ap.J.*, **444**, 770
Nakamura, F., & Li, Z.-Y. 2005, *Ap.J.*, **631**, 41
Nakano, T. 1984, *Fund. Cosmic Phys.*, **9**, 139
Nakano, T., & Nakamura, T. 1978, *Pub. Astr. Soc. Japan*, **30**, 671
Narayan, R., & Popham, R. 1994, in *Theory of Accretion Disks – 2*, eds. W. J. Duschl, J. Frank, Meyer, F., Meyer-Hofmeister, E., & Tschnarnuter, W. M. (Dordrecht: Kluwer), p. 293
Natta, A., & Giovanardi, C. 1990, *Ap.J.*, **356**, 646
Nelson, R. P., & Papaloizou, J. C. B. 1993, *M.N.R.A.S.*, **265**, 905
Nelson, R. P., & Papaloizou, J. C. B. 2004, *M.N.R.A.S.*, **350**, 849
Neufeld, D. A., & Hollenbach, D. J. 1994, *Ap.J.*, **428**, 170
Neuhauser, R., Sterzik, M. F., Schmitt, J. H. M. M., Wichmann, R., & Krautter, J. 1995, *A&Ap.*, **297**, 391
Nomura, H., Aikawa, Y., Tsujimoto, M., Nakagawa, Y., & Millar, T. J. 2007, *Ap.J.*, **661**, 334
O'Dell, C. R. 2001, *Ann. Rev. Astr. Ap.*, **39**, 99
O'Dell, C. R., & Wen, Z. 1994, *Ap.J.*, **436**, 194
O'Dell, C. R., Wen, Z., & Hu, X. 1993, *Ap.J.*, **410**, 696
Ogilvie, G. I. 2003, *M.N.R.A.S.*, **340**, 969
Ohashi, N., Hayashi, M., Ho, P. T. P., Momose, M., & Hirano, N. 1996, *Ap.J.*, **466**, 317
Onishi, T., Mizuno, A., Kawamura, A., Ogawa, H., & Fukui, Y. 1996, *Ap.J.*, **465**, 815
Onishi, T., Mizuno, A., Kawamura, A., Ogawa, H., & Fukui, Y. 1998, *Ap.J.*, **502**, 296
Onishi, T., Mizuno, A., Kawamura, A., Tachihara, K., & Fukui, Y. 2002, *Ap.J.*, **575**, 950
Osorio, M., D'Alessio, P., Muzerolle, J., Calvet, N., & Hartmann, L. 2003, *Ap.J.*, **586**, 1148
Ossenkopf, V., & Henning, Th. 1994, *A&Ap.*, **291**, 943
Osterloh, M., & Beckwith, S. V. W. 1995, *Ap.J.*, **439**, 288
Ostriker, J. 1964, *Ap.J.*, **140**, 1056
Ostriker, E. C., Gammie, C. F., & Stone, J. M. 1999, *Ap.J.*, **513**, 259
Ostriker, E. C., & Shu, F. H. 1995, *Ap.J.*, **447**, 813
Ostriker, E. C., Shu, F. H., & Adams, F. C. 1992, *Ap.J.*, **399**, 192
Ouyed, R., & Pudritz, R. E. 1997a, *Ap.J.*, **482**, 712
Ouyed, R., & Pudritz, R. E. 1997b, *Ap.J.*, **482**, 794
Ouyed, R., & Pudritz, R. E. 1999, *M.N.R.A.S.*, **309**, 233

Ouyed, R., Clarke, D. A., & Pudritz, R. E. 2003, *Ap.J.*, **582**, 292
Paatz, G., & Camenzind, M. 1996, *A&Ap.*, **308**, 77
Paczynski, B. 1976, cited in Trimble, V., *Quart. J. Roy. Astr. Soc.*, **17**, 25
Padoan, P., & Nordlund, Å. 2002, *Ap.J.*, **576**, 870
Padoan, P., & Nordlund, Å. 2004, *Ap.J.*, **617**, 559
Padoan, P., Nordlund, Å., Kritsuk, A. G., Norman, M. L., & Li, P. S. 2007, *Ap.J.*, **661**, 972
Padgett, D. L., *et al.* 2006, *Ap.J.*, **645**, 1283
Padgett, D. L., Brandner, W., Stapelfeldt, K. R., Strom, S. E., Terebey, S., & Koerner, D. 1999, *A.J.*, **117**, 1490
Palla, F., & Stahler, S. W. 1992, *Ap.J.*, **392**, 667
Palla, F., & Stahler, S. W. 1993, *Ap.J.*, **418**, 414
Palla, F., & Stahler, S. W. 1999, *Ap.J.*, **525**, 772
Palla, F., & Stahler, S. W. 2000, *Ap.J.*, **540**, 255
Palla, F., & Stahler, S. W. 2002, *Ap.J.*, **581**, 1194
Papaloizou, J. C. B., & Lin, D. N. C. 1995, *Ann. Rev. Astr. Ap.*, **33**, 505
Papaloizou, J. C. B., Nelson, R. P., Kley, W., Masset, F. S., & Artymowicz, P. 2007, *Protostars and Planets V*, p. 655
Papaloizou, J., & Pringle, J. E. 1977, *M.N.R.A.S.*, **181**, 441
Parker, E. N. 1963, *Interplanetary Dynamical Processes* (New York: Wiley).
Parker, E. N. 1966, *Ap.J.*, **145**, 811
Passot, T., & Vazquez-Semadeni, E. 2003, *A&Ap.*, **398**, 845
Passot, T., Vázquez-Semadeni, E., & Pouquet, A. 1995, *Ap.J.*, **455**, 536
Patel, N. A., Goldsmith, P. F., Heyer, M. H., Snell, R. L., & Pratap, P. 1998, *Ap.J.*, **507**, 241
Patel, N. A., *et al.* 2005, *Nature*, **437**, 109
Pelletier, G., & Pudritz, R. E. 1992, *Ap.J.*, **394**, 117
Penston, M. V. 1969, *M.N.R.A.S.*, **144**, 425
Pessah, M. E., Chan, C.-k., & Psaltis, D. 2006, arXiv:astro-ph/0612404
Petrov, P. P., Gullbring, E., Ilyin, I., Gahm, G. F., Tuominen, I., Hackman, T., & Loden, K. 1996, *A&Ap.*, **314**, 821
Petrov, P. P., & Herbig, G. H. 1992, *Ap.J.*, **392**, 209
Pichardo, B., Sparke, L. S., & Aguilar, L. A. 2005, *M.N.R.A.S.*, **359**, 521
Piétu, V., Dutrey, A., Guilloteau, S., Chapillon, E., & Pety, J. 2006, *A&Ap.*, **460**, L43
Podosek, F. A., & Cassen, P. 1994, *Meteoritics*, **29**, 6
Pollack, J. B., Hollenbach, D., Beckwith, S., Simonelli, D. P., Roush, T., & Fong, W. 1994, *Ap.J.*, **421**, 615
Pollack, J. B., Hubickyj, O., Bodenheimer, P., Lissauer, J. J., Podolak, M., & Greenzweig, Y. 1996, *Icarus*, **124**, 62
Popham, R. 1995, *Ap.J.*, **467**, 749
Popham, R., Kenyon, S., Hartmann, L., & Narayan, R. 1996, *Ap.J.*, **473**, 422
Popham, R., Narayan, R., Hartmann, L., & Kenyon, S. 1993, *Ap.J.*, **415**, L127
Portegies Zwart, S., Gaburov, E., Chen, H.-C., & Gumlrkan, M. A. 2007, *M.N.R.A.S.*, **378**, L29
Preibisch, T., Günther, E., & Zinnecker, H. 2001, *A&J.*, **121**, 1040
Preibisch, T. & Zinnecker, H. 1999, *A.J.*, **117**, 2381
Prialnik, D., & Livio, J. 1985, *M.N.R.A.S.*, **216**, 37
Preibisch, T., *et al.* 2005, *Ap.J.Supp.*, **160**, 582
Priest, E. R. 1984, *Solar Magneto-hydrodynamics* (Dordrecht: Reidel).
Pringle, J. E. 1981, *Ann. Rev. Astr. Ap.*, **19**, 137
Pringle, J. E. 1989, *M.N.R.A.S.*, **236**, 107
Pringle, J. E. 1991a, NATO ASIC Proc. 342: *The Physics of Star Formation and Early Stellar Evolution*, eds. N. Kylafis & C. Lada, p. 437
Pringle, J. E. 1991b, *M.N.R.A.S.*, **248**, 754
Pudritz, R. E., & Norman, C. A. 1983, *Ap.J.*, **274**, 677
Pudritz, R. E., & Norman, C. A. 1986, *Ap.J.*, **301**, 571
Pudritz, R. E., Ouyed, R., Fendt, C., & Brandenburg, A. 2007, *Protostars and Planets V*, p. 277
Pudritz, R. E., Pelletier, G., & Gomez de Castro, A. I. 1991, in *The Physics of Star Formation and Early Stellar Evolution*, eds. C. J. Lada & N. D. Kylafis (Dordrecht: Kluwer), p. 539
Pudritz, R. E., Wilson, C. D., Carlstrom, J. E., Lay, O. P., Hills, R. E., & Ward-Thompson, D. 1996, *Ap.J.Lett.*, **470**, L123

Qi, C., *et al.* 2004, *Ap.J.Lett.*, **616**, L11
Rafikov, R. R. 2005, *Ap.J.Lett.*, **621**, L69
Raga, A. C. 1993, *Ap. Space Sci.*, **208**, 163
Raga, A. C. 1989, in *ESO Workshop on Low Mass Star Formation and Pre-Main Sequence Objects*, ed. B. Reipurth (Garching: ESO Conference and Workshop Proceedings No. 33), p. 281
Raga, A. C. 1995, in *Circumstellar Disks, Outflows, and Star Formation*, eds. S. Lizano, & J. M. Torrelles, *Rev. Mex. Astr. Astrof., Serie de Conferencias*, 1, 103
Ramírez, S. V., *et al.* 2004, *A.J.*, **128**, 787
Randich, S., Schmitt, J. H. M. M., Prosser, C. F., & Stauffer, J. R. 1996, *A&Ap.*, **305**, 785
Ray, T., Dougados, C., Bacciotti, F., Eislöffel, J., & Chrysostomou, A. 2007, *Protostars and Planets V*, p. 231
Ray, T. P., Mundt, R., Dyson, J. E., Falle, S. A. G., & Raga, A. C. 1996, *Ap.J.*, **468**, L103
Rebull, L. M., Stauffer, J. R., Megeath, S. T., Hora, J. L., & Hartmann, L. 2006, *Ap.J.*, **646**, 297
Reid, M. J., Menten, K. M., Greenhill, L. J., & Chandler, C. J. 2007, *Ap.J.*, **664**, 950
Reipurth, B. 1990, in *Flare Stars in Star Clusters, IAU Symposium 137*, eds. L. V. Mirzoyan, B. R. Petterson, M. K. Tsvetkov (Dordrecht: Kluwer), p. 229
Reipurth, B. 1989, in *ESO Workshop on Low Mass Star Formation and Pre-Main Sequence Objects*, ed. B. Reipurth (Garching: ESO Conference and Workshop Proceedings No. 33), p. 247
Reipurth, B. 1991 in *The Physics of Star Formation and Early Stellar Evolution*, eds. C. J. Lada & N. D. Kylafis (Dordrecht:Kluwer), p. 497
Reipurth, B. 1997, in *Herbig-Haro Flows and the Birth of Low-Mass Stars, IAU Symposium 182*, eds. B. Reipurth & C. Bertout (Dordrecht: Kluwer), p. 3
Reipurth, B., & Aspin, C. 1997, *A.J.*, **114**, 2700
Reipurth, B., & Aspin, C. 2004, *Ap.J.Lett.*, **608**, L65
Reipurth, B., Aspin, C., Beck, T., Brogan, C., Connelley, M. S., & Herbig, G. H. 2007, *A.J.*, 133, 1000
Reipurth, B. & Bertout, C. 1997, eds., *Herbig-Haro Flows and the Birth of Low-Mass Stars, IAU Symposium 182* (Dordrecht: Kluwer)
Reipurth, B., & Clarke, C. 2001, *A.J.*, **122**, 432‘
Reipurth, B., Hartmann, L., Kenyon, S. J., Smette, A., & Bouchet, P. 2002, *A.J.*, **124**, 2194
Reipurth, B., Pedrosa, A., & Lago, M. T. V. T. 1996, *A&AS*, **120**, 229
Reipurth, B., & Zinnecker, H. 1993, *A&Ap.*, **278**, 81
Reyes-Ruiz, M., & Stepinski, T. F. 1995, *Ap.J.*, **438**, 750
Ribas, I., Guinan, E. F., Güdel, M., & Audard, M. 2005, *Ap.J.*, **622**, 680
Rice, W. K. M., Armitage, P. J., Bate, M. R., & Bonnell, I. A. 2003, *M.N.R.A.S.*, **339**, 1025
Rice, W. K. M., Armitage, P. J., Wood, K., & Lodato, G. 2006a, *M.N.R.A.S.*, **373**, 1619
Rice, W. K. M., Lodato, G., & Armitage, P. J. 2005, *M.N.R.A.S.*, **364**, L56
Rice, W. K. M., Lodato, G., Pringle, J. E., Armitage, P. J., & Bonnell, I. A. 2006b, *M.N.R.A.S.*, **372**, L9
Richling, S., & Yorke, H. W. 2000, *Ap.J*, **539**, 258
Rieke, G. H., *et al.* 2005, *Ap.J.*, **620**, 1010
Rieke, G., Lee, T., & Coyne, G. 1972, *Pub. Astr. Soc. Pac.* , **84**, 37
Rincon, F., Ogilvie, G. I., & Proctor, M. R. E. 2007, *Phys. Rev. Lett.*, **98**, 254502
Roddier, C., Roddier, F., Northcott, M. J., Graves, J. E., & Kim, J. 1996, *Ap.J.*, **463,** 326
Rodmann, J., Henning, T., Chandler, C. J., Mundy, L. G., & Wilner, D. J. 2006, *A&Ap.*, **446**, 211
Rodriguez, L. F., & Hartmann, L. W. 1992, *Rev. Mex. Astr. Astrof.*, **24,** 135
Rodriguez, L. F., Hartmann, L. W., & Chavira, E. 1990, *Pub. Astr. Soc. Pac.* , **102**, 1413
Rodríguez, L. F., *et al.* 1998, *Nature*, **395**, 355
Rozyczka, M., & Spruit, H. C. 1993, *Ap.J.*, **417**, 677
Rucinski, S. M. 1985, *A.J.*, **90**, 2321
Ruden, S. P., & Pollack, J. B. 1991, *Ap.J.*, **375**, 740
Rybicki, G. B., & Hummer, D. G. 1978, *Ap.J.*, **219**, 654
Rydgren, A. E., Strom, S. E., & Strom, K. M. 1976, *Ap.J.Supp.*, **30**, 307
Rydgren, A. E., & Vrba, F. J. 1981, *A.J.*, **86**, 1069
Rydgren, A. E., & Vrba, F. J. 1987, *P.A.S.P.*, **99**, 482
Ryu, D., & Goodman, J. 1992, *Ap.J.*, **338**, 438
Saito, M., Kawabe, R., Kitamura, Y., & Sunada, K. 1996, *Ap.J.*, **473**, 464
Safier, P. 1993, *Ap.J.*, **408**, 115
Safier P. 1995, *Ap.J.*, **444**, 818

Salpeter, E. E. 1955, *Ap.J.*, **121**, 161
Sandell, G., & Aspin, C. 1998, *A&Ap.*, **333**, 1016
Sandell, G., & Weintraub, D. A. 2001, *Ap.J.Supp.*, **134**, 115
Sano, T., Miyama, S. M., Umebayashi, T., & Nakano, T. 2000, *Ap.J.*, **543**, 486
Sano, T., Inutsuka, S.-I., Turner, N. J., & Stone, J. M. 2004, *Ap.J.*, **605**, 321
Saucedo, J., Calvet, N., Hartmann, L., & Raymond, J. 2003, *Ap.J.*, **591**, 275
Scalo, J. M. 1986, *Fund. Cos. Phys.*, **11**, 1
Scalo, J. M. 1996, *Fund. Cosmic Physics*, **11**, 1
Scalo, J. M. 1990, in *Physical Processes in Fragmentation and Star Formation*, Proceedings of the Workshop, Rome, Italy (Dordrecht:Kluwer), p.151
Scalo, J., & Elmegreen, B. G. 2004, *Ann. Rev. Astr. Ap.*, **42**, 275
Shirley, Y. L., Evans, N. J., II., & Rawlings, J. M. C. 2002, *Ap.J.*, **575**, 337
Shirley, Y. L., Nordhaus, M. K., Grcevich, J. M., Evans, N. J., II., Rawlings, J. M. C., & Tatematsu, K. 2005, *Ap.J.*, **632**, 982
Schneider, S., & Elmegreen, B. G. 1979, *Ap.J.Supp.*, **41**, 87
Schneider, G., *et al.* 1999, *Ap.J.Lett.*, **513**, L127
Scholz, A., Jayawardhana, R., & Wood, K. 2006, *Ap.J.*, **645**, 1498
Schwartz, R. D. 1975, *Ap.J.*, **195**, 631
Schwartz, R. D. 1983, *Ann. Rev. Astr. Ap.*, **21**, 209
Schwarzschild, M. 1958, *Structure and Evolution of the Stars* (New York: Dover)
Shakura, N. I., & Sunyaev, R. A. 1973, *A&Ap.*, **24**, 337
Shang, H., Li, Z.-Y., & Hirano, N. 2007, *Protostars and Planets V*, 261
Shapiro, S. L., & Teukolsky, S. A. 1983, *Black Holes, White Dwarfs, and Neutron Stars*, The Physics of Compact Objects (Wiley: New York), p. 450 ff.
Shepherd, D. S., & Churchwell, E. 1996, *Ap.J.*, **472**, 225
Shepherd, D. S., Claussen, M. J., & Kurtz, S. E. 2001, *Science*, **292**, 1513
Shirley, Y. L., Nordhaus, M. K., Grcevich, J. M., Evans, N. J., II., Rawlings, J. M. C., & Tatematsu, K. 2005, *Ap.J.*, **632**, 982
Shu, F. H. 1977, *Ap.J.*, **214**, 488
Shu, F. H. 1991, in *The Physics of Star Formation and Early Stellar Evolution*, eds. C. J. Lada & N. D. Kylafis (Dordrecht: Kluwer), p. 376
Shu, F. H. 1992, *The Physics of Astrophysics*, vol. 2 *(Gas Dynamics)* (Mill Valley: University Science Books).
Shu, F. H. 1995, in *Circumstellar Disks, Outflows, and Star Formation*, eds. S. Lizano, & J. M. Torrelles, *Rev. Mex. Astr. Astrof., Serie de Conferencias*, **1**, 375
Shu, F. H., Adams, F. C., & Lizano, S. 1987, *Ann. Rev. Astr. Ap.*, **25**, 23
Shu, F. H., Galli, D., Lizano, S., & Cai, M. 2006, *Ap.J.*, **647**, 382
Shu, F. H., Galli, D., Lizano, S., Glassgold, A. E., & Diamond, P. H. 2007, *Ap.J.*, **665**, 53
Shu, F., Najita, J., Ostriker, E. C., & Shang, H. 1995, *Ap.J.*, **455**, L155
Shu, F., Najita, J., Ostriker, E., Wilkin, F., Ruden, S., & Lizano, S. 1994, *Ap.J.*, **429**, 781
Shu, F. H., Tremaine, S., Adams, F. C., & Ruden, S. P. 1990, *Ap.J.*, **358**, 495
Sicilia-Aguilar, A., Hartmann, L. W., Hernández, J., Briceño, C., & Calvet, N. 2005, *A.J.*, **130**, 188
Sicilia-Aguilar, A., *et al.* 2006, *Ap.J.*, **638**, 897
Siegler, N., Close, L. M., Cruz, K. L., Martín, E. L., & Reid, I. N. 2005, *Ap.J.*, **621**, 1023
Siegler, N., Muzerolle, J., Young, E. T., Rieke, G. H., Mamajek, E. E., Trilling, D. E., Gorlova, N., & Su, K. Y. L. 2007, *Ap.J.*, **654**, 580
Siess, L., Dufour, E., & Forestini, M. 2000, *A&Ap.*, **358**, 593
Simon, T. 1975, *Pub. Astr. Soc. Pac.* , **87**, 317
Simon, M., Dutrey, A., & Guilloteau, S. 2000, *Ap.J.*, **545**, 1034
Simon, M., Ghez, A. M., Leinert, Ch., Cassar, L., Chen, W. P., Howell, R. R., Jameson, R. F., Matthews, K., Neugebauer, G., & Richichi, A. 1995, *Ap.J.*, **443**, 625
Simon, T., Morrison, N. D., Wolff, S. C., & Morrison, D. 1972, *Pub. Astr. Soc. Pac.* , **84**, 644
Skinner, S. L. 1993, *Ap.J.*, **408**, 660
Skrutskie, M. F., Dutkevich, D., Strom, S. E., Edwards, S., Strom, K. M., & Shure, M. A. 1990, *A.J.*, **99**, 1187
Smak, J. 1984, *Pub. Astr. Soc. Pac.* , **96**, 5
Smith, B. A., & Terrile, R. J. 1984, *Science*, **226**, 1421

Snell, R. L., Loren, R. B., & Plambeck, R. L. 1980, *Ap.J.Lett.*, **239**, L17
Spitzer, L., Jr 1968, in *Nebulae and Interstellar Matter, Stars and Stellar Systems*, vol. 7, eds. B. Middlehurst & L. H. Aller (Chicago: University of Chicago Press), p. 1
Spitzer, L., Jr. 1978, *Physical Processes in the Interstellar Medium* (New York: Wiley).
Spruit, H. 1996, in *Physical Processes in Binary Stars*, eds. R. A. M. J. Wijers, M. B. Davies, & C. A. Tout (Dordrecht: Kluwer).
Stahler, S. W. 1983, *Ap.J.*, **274**, 822
Stahler, S. W. 1988, *Ap.J.*, **332**, 804
Stahler, S. W., Shu, F. H., & Taam, R. E. 1980a, *Ap.J.*, **241**, 637
Stahler, S. W., Shu, F. H., & Taam, R. E. 1980b, *Ap.J.*, **242**, 226
Stahler, S. W., & Walter, F. M. 1993, in *Protostars and Planets III*, eds. E. H. Levy & J. I. Lunine (Tucson: University of Arizona Press), p. 405
Stapelfeldt, K. R., Burrows, C. J., Krist, J. E., Trauger, J. T., Hester, J. J., Holtzman, J. A., Ballester G. E., Casertano, S., Clarke, J. T. Crisp, D., Evans, R. W., Gallagher, J. S., III., Griffiths, R. E., Hoessel, J. G., Mould, J. R., Scowen, P. A., Watson, A. M., & Westphal, J. A. 1995, *Ap.J.*, **449**, 888
Stapelfeldt, K. R., Krist, J. E., Menard, F., Bouvier, J., Padgett, D. L., & Burrows, C. J. 1998a, *Ap.J.Lett.*, **502**, L65
Stapelfeldt, K. R., *et al.* 1998b, *Ap.J.*, **508**, 736
Staude, H. J., & Neckel, T. 1991, *A&Ap.*, **244**, L13
Staude, H. J., & Neckel, T. 1992, *Ap.J.*, 400, 556
Stauffer, J. R., Caillault, J.-P., Gagne, M., Prosser, C. F., & Hartmann, L. W. 1994, *Ap.J.Supp.*, **91**, 625
Stauffer, J. R., Hartmann, L. W., & Barrado y Navascues, D. 1995, *Ap.J.*, **454**, 910
Stauffer, J. R., Hartmann, L. W., & Jones, B. F. 1989, *Ap.J.*, **346**, 160
Stelzer, B., Flaccomio, E., Montmerle, T., Micela, G., Sciortino, S., Favata, F., Preibisch, T., & Feigelson, E. D. 2005, *Ap.J.Supp.*, **160**, 557
Stemwedel, S. W., Yuan, C., & Cassen, P. 1990, *Ap.J.*, **351**, 206
Stepinski, T. 1995, in *Circumstellar Disks, Outflows, and Star Formation*, eds. S. Lizano, & J. M. Torrelles,*Rev. Mex. Astr. Astrof., Serie de Conferencias*, 1, 267
Stocke, J. T., Hartigan, P. M., Strom, S. E., Strom, K. M., Anderson, E. R., Hartmann, L. W., & Kenyon, S. J. 1988, *Ap.J.Supp.*, **68**, 229
Stodolkiewicz, J. S. 1963, *A&A*, **13**, 30
Stolte, A., Brandner, W., Grebel, E. K., Lenzen, R., & Lagrange, A.-M. 2005, *Ap.J.Lett.*, **628**, L113
Stone, J. M., & Balbus, S. A. 1996, *Ap.J.*, **464**, 364
Stone, J. M., Hawley, J. F., Gammie, C. F., & Balbus, S. A. 1996, *Ap.J.*, **463**, 656
Stone, J. M., & Norman, M. L. 1994, *Ap.J.*, **433**, 746
Stone, J. M., Ostriker, E. C., & Gammie, C. F. 1998, *Ap.J.Lett.*, **508**, L99
Störzer, H., & Hollenbach, D. 1999, *Ap.J.*, **515**, 669
Strassmeier, K. G., Rice, J. B., Ritter, A., Küker, M., Hussain, G. A. J., Hubrig, S., & Shobbrook, R. 2005, *A&Ap.*, **440**, 1105
Strom, S. E. 1972, *Pub. Astr. Soc. Pac.*, **84**, 745
Strom, S. E., Edwards, S., & Skrutski, M. 1993, in *Protostars and Planets III*, eds. E. H. Levy & J. I. Lunine (Tucson: University of Arizona Press), p. 837
Strom, K. M., Strom, S. E., Kenyon, S. J., & Hartmann, L. 1988, *A.J.*, **95**, 534
Strom, S. E., Strom, K. M., Brooke, A. L., Bregman, J., & Yost, J. 1972, *Ap.J.*, **171**, 267
Strom, K. M., Strom, S. E., Edwards, S., Cabrit, S., & Skrutskie, M. F. 1989, *A.J.*, **97**, 1451
Suess, S. T., & Nerney, S. F. 1975, *Solar Phys.*, **40**, 487
Swartz, D. A., Drake, J. J., Elsner, R. F., Ghosh, K. K., Grady, C. A., Wassell, E., Woodgate, B. E., & Kimble, R. A. 2005, *Ap.J.*, **628**, 811
Symington, N. H., Harries, T. J., Kurosawa, R., & Naylor, T. 2005, *M.N.R.A.S.*, **358**, 977
Tafalla, M., Mardones, D., Myers, P. C., Caselli, P., Bachiller, R., & Benson, P. J. 1998, *Ap.J.*, **504**, 900
Takakuwa, S., *et al.* 2004, *Ap.J.Lett.*, **616**, L15
Takeuchi, T., Clarke, C. J., & Lin, D. N. C. 2005, *Ap.J.*, **627**, 286
Takeuchi, T., & Lin, D. N. C. 2005, *Ap.J.*, **623**, 482
Tamura, M., Gatley, I., Waller, W., & Werner, M. W. 1991, *Ap.J.*, **374**, L25
Tanaka, H., Himeno, Y., & Ida, S. 2005, *Ap.J.*, **625**, 414
Tannirkulam, A., Harries, T. J., & Monnier, J. D. 2007, *Ap.J.*, **661**, 374
Tannirkulam, A., *et al.* 2008, preprint

Teixeira, P. S., *et al.* 2006, *Ap.J.Lett.*, 636, L45
Telleschi, A., Güdel, M., Briggs, K. R., Skinner, S. L., Audard, M., & Franciosini, E. 2007, *A&Ap.*, **468**, 541
Terebey, S., Chandler, C. J., & Andre, P. 1993, *Ap.J.*, **414**, 759
Terebey, S., Shu, F. H., & Cassen, P. 1984, *Ap.J.*, **286**, 529 (TSC)
Tomley, L., Cassen, P., & Steiman-Cameron, T. 1991, *Ap.J.*, **382**, 530
Tomley, L., Steiman-Cameron, T. Y., & Cassen, P. 1994, *Ap.J.*, **422**, 850
Toomre, A. 1964, *Ap.J.*, **139**, 1217
Torres, R. M., Loinard, L., Mioduszewski, A. J., & Rodríguez, L. F. 2007, *Ap.J.*, **671**, 1813
Tout, C. A., & Pringle, J. E. 1992, *M.N.R.A.S.*, **259**, 604
Tilling, I., Clarke, C. J., Pringle, J. E., & Tout, C. A. 2008, *M.N.R.A.S.*, **385**, 1530
Trilling, D. E., *et al.* 2008, *Ap.J.*, **674**, 1086
Troland, T. H., Crutcher, R. M., Goodman, A. A., Kazes, I., & Myers, P. C. 1996, *Ap.J.*, **471**, 302
Tobin *et al.* 2008, in preparation
Truelove, J. K., Klein, R. I., McKee, C. F., Holliman, J. H., II, Howell, L. H., & Greenough, J. A. 1997, *Ap.J.Lett.*, **489**, L179
Tscharnuter, W. 1991, in *The Physics of Star Formation and Early Stellar Evolution*, eds. C. J. Lada & N. D. Kylafis (Dordrecht:Kluwer), p. 411
Turner, N. J. J., Bodenheimer, P., & Bell, K. R. 1997, *Ap.J.*, **480**, 754
Uchida, Y., & Shibata, K. 1984, *Pub. Astr. Soc. Japan*, **36**, 105
Uchida, Y., & Shibata, K. 1985, *Pub. Astr. Soc. Japan*, **37**, 515
Ulrich, R. K. 1976, *Ap.J.*, **210**, 377
Ulrich, R. K., & Knapp, G. R. 1979, *Ap.J.*, **230**, L99
Umebeyashi, T., & Nakano, T. 1988, *Prog. Theor. Phys. Suppl.*, **96**, 151
Umebeyashi, T., & Nakano, T. 1990, *M.N.R.A.S.*, **243,** 103
Ungerechts, H., & Thaddeus, P. 1987, *Ap.J.Supp.*, **63**, 645
Valenti, J. A., Basri, G., & Johns, C. M. 1993, *A.J.*, **106**, 2024
Valenti, J. A., & Johns-Krull, C. M. 2004, *Ap. Space Sci.*, **292**, 619
van Ballegooijen, A. A. 1994, *Space Sci. Rev.*, **68**, 299
van Boekel, R., *et al.* 2006, *Proc. SPIE*, **6268**, 13
van Buren, D., Mac Low, M.-M., Wood, D. O. S., & Churchwell, E. 1990, *Ap.J.*, **353**, 570
Vázquez-Semadeni, E., Gómez, G. C., Jappsen, A. K., Ballesteros-Paredes, J., González, R. F., & Klessen, R. S. 2007, *Ap.J.*, **657**, 870
Velikhov, E. P. 1959, *Soviet Phys.-JETP*, **36**, 995 (*JETP Lett.*, **35**, 1398)
Vishniac, E. T., & Diamond, P. 1989, *Ap.J.*, **347**, 447
Vishniac, E. T., & Diamond, P. 1992, *Ap.J.*, **398**, 561
von Rekowski, B., Brandenburg, A., Dobler, W., & Shukurov, A. 2004, *Ap. Space Sci.*, **292**, 493
Vorobyov, E. I., & Basu, S. 2005, *Ap.J.Lett.*, **633**, L137
Vorobyov, E. I., & Basu, S. 2006, *Ap.J.*, **650**, 956
Vrba F. J., Chugainov, P. F., Weaver W. B., & Stauffer J. S. 1993, *A.J.*, **106**, 1608
Wada, K., & Norman, C. A. 2001, *Ap.J.*, **547**, 172
Walker, C. K., Lada, C. J., Young, E. T., Maloney, P. R., & Wilking, B. A. 1986, *Ap.J.Lett.*, **309,** L47
Walker, M. F. 1972, *Ap.J.*, **175**, 89
Walter, F. M. 1986, *Ap.J.*, **306**, 573
Walter, F. M., Brown, A., Mathieu, R. D., Myers, P. C., & Vrba, F. J. 1988, *A.J.*, **96**, 297
Walter, F. M., & Kuhi, L. V. 1981, *Ap.J.*, **250**, 254
Walter, F. M., Vrba, F. J., Mathieu, R. D., Brown, A., & Myers, P. C. 1994, *A.J.*, **107**, 692
Walter, F. M., *et al.* 2003, *A.J.*, **126**, 3076
Wang, H., Apai, D., Henning, T., & Pascucci, I. 2004, *Ap.J.Lett.*, **601**, L83
Wang, Y., Evans, N. J. II., Zhou, S., & Clemens, D. P. 1995, *Ap.J.*, **454**, 217
Wang, Y.-M. 1995, *Ap.J.*, **449**, L153
Wang, Y.-M. 1996, *Ap.J.*, **465**, L111
Ward, W. R. 1997, *Ap.J.Lett.*, **482**, L211
Wardle, M., & Königl, A. 1993, *Ap.J.*, **410**, 218
Ward-Thompson, D., André, P., Crutcher, R., Johnstone, D., Onishi, T., & Wilson, C. 2007, *Protostars and Planets V*, p. 33
Watson, D. M. *et al.* 2008, *Ap.J.*, in press

Webb, R. A., Zuckerman, B., Platais, I., Patience, J., White, R. J., Schwartz, M. J., & McCarthy, C. 1999, *Ap.J.*, **512**, L63
Weber, E. J., & Davis, L., Jr. 1967, *Ap.J.*, **148**, 217
Weidenschilling, S. J. 1977, *M.N.R.A.S.*, **180**, 57
Weidenschilling, S. J. 1980, *Icarus*, **44**, 172
Weidenschilling, S. J. 1984, *Icarus*, **60**, 553
Weidenschilling, S. J., & Cuzzi, J. N. 1993, in *Protostars and Planets III*, eds. E. H. Levy & J. I. Lunine (Tucson: University of Arizona Press), p. 1031
Weinberger, A. J., Becklin, E. E., Schneider, G., Smith, B. A., Lowrance, P. J., Silverstone, M. D., Zuckerman, B., & Terrile, R. J. 1999, *Ap.J.Lett.*, **525**, L53
Weintraub, D. A., Sandell, G., & Duncan, W. D. 1991, *Ap.J.*, **382**, 270
Welch, W. J., Hartmann, L., Helfer, T., & Briceño, C. 2000, *Ap.J.*, **540**, 362
Welty, A. D., Strom, S. E., Edwards, S., Kenyon, S. J., & Hartmann, L. W. 1992, *Ap.J.*, **397**, 250
White, R. J., & Basri, G. 2003, *Ap.J.*, **582**, 1109
White, R. J., & Ghez, A. M. 2001, *Ap.J.*, **556**, 265
White, R. J., Ghez, A. M., Reid, I. N., & Schultz, G. 1999, *Ap.J.*, **520**, 811
White, R. J., Greene, T. P., Doppmann, G. W., Covey, K. R., & Hillenbrand, L. A. 2007, *Protostars and Planets V*, eds. B. Reipurth, D. Jewitt, & K. Keil (Tucson: University of Arizona Press), 117
White, R. J., & Hillenbrand, L. A. 2004, *Ap.J.*, **616**, 998
White, R. J., & Hillenbrand, L. A. 2005, *Ap.J.Lett*, **621**, L65
Whitney, B. A., & Hartmann, L. 1992, *Ap.J.*, **395**, 529
Whitney, B. A., & Hartmann, L. 1993, *Ap.J.*, **402**, 605
Whitworth, A. P., Bhattal, A. S., Francis, N., & Watkins, S. J. 1996, *M.N.R.A.S.*, **283**, 1061
Wilking, B. A., & Lada, C. J. 1983, *Ap.J.*, **274**, 698
Williams, J. P., DeGeus, E. J., & Blitz, L. 1994, *Ap.J.*, **428**, 693
Williams, J. P., Lee, C. W., & Myers, P. C. 2006, *Ap.J.*, **636**, 952
Williams, J. P., Myers, P. C., Wilner, D. J., & di Francesco, J. 1999, *Ap.J.Lett.*, **513**, L61
Wilner, D. J., D'Alessio, P., Calvet, N., Claussen, M. J., & Hartmann, L. 2005, *Ap.J.Lett.*, **626**, L109
Wilner, D. J., Holman, M. J., Kuchner, M. J., & Ho, P. T. P. 2002, *Ap.J.Lett.*, **569**, L115
Wilner, D. J., Myers, P. C., Mardones, D., & Tafalla, M. 2000, *Ap.J.Lett.*, **544**, L69
Wilson, B. A., Dame, T. M., Masheder, M. R. W., & Thaddeus, P. 2005, *A&AP.*, **430**, 523
Winkler, K.-H., & Newman, M. J. 1980a,b, *Ap.J.*, **236**, 210, & 238, 311
Winters, W. F., Balbus, S. A., & Hawley, J. F. 2003, *M.N.R.A.S.*, **340**, 519
Wolf, B., Appenzeller, I., & Bertout, C. 1977, *A&Ap.*, **58**, 163
Wolfire, M. G., & Cassinelli, J. P. 1986, *Ap.J.*, **310**, 207
Wolfire, M. G., & Cassinelli, J. P. 1987a, *Ap.J.*, **315**, 315
Wolfire, M. G. & Cassinelli, J. P. 1987b, *Ap.J.*, **319**, 850
Wolk, S. J., & Walter, F. M. 1996, *A.J.*, **111**, 2066
Wood, D. O. S., & Churchwell, E. 1989a, *Ap.J.*, **340**, 265
Wood, D. O. S., & Churchwell, E. 1989b, *Ap.J.Supp.*, **69**, 831
Wood, K., Kenyon, S. J., Whitney, B., & Turnbull, M. 1998, *Ap.J.*, **497**, 404
Wood, D. O. S., Myers, P. C., & Daugherty, D. A. 1994, *Ap.J.Supp.*, **95**, 457
Wünsch, R., Gawryszczak, A., Klahr, H., & Różyczka, M. 2006, *M.N.R.A.S.*, **367**, 773
Wurm, G., & Blum, J. 1998, *Icarus*, **132**, 125
Wyatt, M. C., Smith, R., Su, K. Y. L., Rieke, G. H., Greaves, J. S., Beichman, C. A., & Bryden, G. 2007, *Ap.J.*, **663**, 365
Wyse, A. B., & Mayall, N. U. 1942, *Ap.J.*, **95**, 24
Yang, H., Johns-Krull, C. M., & Valenti, J. A. 2007, *A.J.*, **133**, 73
Yi, S. K., Kim, Y.-C., & Demarque, P. 2003, *Ap.J.Supp.*, **144**, 259
Yorke, H. W., & Sonnhalter, C. 2002, *Ap.J.*, **569**, 846
Yorke, H. W., Tenorio-Tagle, G., & Bodenheimer, P. 1983, *A&Ap.*, **127**, 313
Yorke, H. W., Bodenheimer, P., & Laughlin, G. 1993, *Ap.J.*, **411**, 274
Youdin, A. N., & Shu, F. H. 2002, *Ap.J.*, **580**, 494
Yun, J. L., & Clemens, D. P. 1990, *Ap.J.Lett.*, **365**, L73
Zhang, Q., Hunter, T. R., & Sridharan, T. K. 1998, *Ap.J.Lett.*, **505**, L151
Zhou, S. 1994, *Ap.J.*, **442**, 685
Zhou, S., Evans, N. J., II, Kömpke, C., & Walmsley, C. M. 1993, *Ap.J.*, **404**, 232

Zhou, S., & Evans, N. J. II 1994, in *Clouds, Cores, and Low-Mass Stars*, *PASP Conference Series Vol. 65*, eds. D. P. Clemens & R. Barvainis, p. 183
Zhou, S., Wu, Y., Evans, N. J., II, Fuller, G. A., & Myers, P. C. 1989, *Ap.J.*, **346**, 168
Zhu, Z., Hartmann, L., Calvet, N., Hernandez, J., Muzerolle, J., & Tannirkulam, A.-K. 2007, *Ap.J.*, **669**, 483
Zhu, Z. *et al*. 2008, *Ap.J*, in press
Zinnecker, H. 1982, in *Symposium on the Orion Nebula to Honor Henry Draper*, eds. A. E. Glassgold *et al.* (New York: New York Academy of Sciences), p. 226
Zinnecker, H., & Yorke, H. 2007, *Ann. Rev. Astr. Ap.*, **45**, 481
Zuckerman, B., & Evans, N. J., II., 1974, *Ap.J.Lett.*, **192**, L149
Zweibel, E. G., Hole, K. T., & Mathieu, R. D. 2006, *Ap.J.*, **649**, 879

Index